DOCTOR OF SCIENCE (DSC)

The Influence of Modifiers on the Properties of Commercial Glasses

Mendes Da Silva, Rita

Award date:
2023

Awarding institution:
University of Bath

The Influence of Modifiers on the Properties of Commercial Glasses

submitted by

Rita Mendes da Silva

for the degree of Doctor of Philosophy

of the

University of Bath

Department of Physics

September 2022

Abstract

The structure of zinc aluminosilicate glasses $(ZnO)_x(Al_2O_3)_y(SiO_2)_{1-x-y}$, where $0 \leq x \leq 1$, $0 \leq y \leq 1$ and $x + y \leq 1$, was investigated by neutron diffraction (ND), X-ray (XRD) diffraction and ^{27}Al magic angle spinning nuclear magnetic resonance (NMR). The majority of the Al atoms reside in fourfold coordinated sites for all the investigated glasses, with the fraction of fivefold coordinated sites increasing with the alumina content for compositions where $R = x/y < 1$. The results were interpreted with the help of an analytical model developed by Gammond et al [1] for the amorphous aluminosilicate materials. The model predicts Al-O bond distances that are typical of fourfold and fivefold coordinated aluminium atoms. It also explains the conditions where in different ranges of composition zinc behaves as network modifier or as a charge-compensating species. The more compact coordination environment of Zn-O is related to an enhanced probability of zinc finding non-bridging oxygen (NBO) atoms as nearest-neighbors, i.e, zinc behaves as a network modifier. The higher Zn-O coordination environment found in the $R < 1$ region and in compositions with higher SiO_2 mol% is related to Zn^{2+} ions stabilizing the Al^{3+} ions in tetrahedral $(AlO_4)^-$, i.e, zinc behaves as a charge compensating species.

The structure of the magnesium aluminosilicate glasses $(MgO)_x(Al_2O_3)_y(SiO_2)_{1-x-y}$, where $0 \leq x \leq 1$, $0 \leq y \leq 1$ and $x + y \leq 1$, was explored by X-ray diffraction and aided by the results obtained from ^{27}Al magic angle spinning NMR, ND and ND with isotopic substitution. For all the glasses the majority of the Al atoms reside in fourfold coordinated sites with a substantial fraction appearing in fivefold coordinated sites only for compositions where $R = x/y \leq 1$ (peraluminous regime). The results were interpreted with the Gammond et al model [1]. For compositions with $R > 1$ the glass network consists mainly of SiO_4 and AlO_4 tetrahedra, which are linked through bridging oxygen (BO) atoms to form an aluminosilicate network. Here, Mg^{2+} act mainly as network modifiers where they associate with non-bridging oxygen (NBO) atoms. For compositions with $R < 1$, Mg^{2+} ions act mainly as a charge-compensating

species where it stabilises the Al^{3+} ions in tetrahedral units. In this region there is also an insufficient number of Mg^{2+} ions to stabilise all the Al^{3+} ions, which requires some fraction of these ions to behave as network modifier/charge compensating species in a similar way to Mg^{2+}. This behaviour explains the higher coordinated Al(V) and Al(VI) species present in the glass that are not part of the aluminosilicate network.

X-ray and neutron diffraction with magnesium isotope substitution was used to measure the structure of diopside, $CaMgSi_2O_6$. The neutron diffraction analyses used the value of a recent measurement of the scattering length of ^{25}Mg isotope. The diffraction results for the glass show a broad asymmetric distribution of Mg-O nearest neighbors with a small Mg-O coordination number of 4.40(5) in which magnesium has the role of a network modifier. The results demonstrate the power of neutron diffraction with magnesium isotope substitution to provide unambiguous site-specific information on the glass structure. In particular, it removes the uncertainty associated with the overlap between the Mg-O and Ca-O correlations.

The structure of crystalline and amorphous materials in the sodium (Na) super-ionic conductor (NASICON) system $Na_{1+x}Al_xGe_{2-x}(PO_4)_3$ with $x = 0$, $x = 0.4$ or $x = 0.8$ was investigated by ND and XRD. The results for the crystalline materials confirm the existence of corner-sharing PO_4, GeO_6 and AlO_6 units. These polyhedral units are linked to form a 3-dimensional network with Na^+ ions residing in interstitial cavities. In the more disordered structures such as the as-prepared glass the XRD and ND results show the formation of sub-octahedral Ge and Al centered units, which leads to the creation of non-bridging oxygen (NBO) atoms. When the as-prepared glass is relaxed by thermal annealing, there is an increase in the Ge and Al coordination numbers that leads to a decrease in the fraction of NBO atoms. The influence of these materials on the ion mobility is discussed. A structural model is used for the glassy composition $x = 0$ which relies on the formation of $Na_2P_6GeO_{18}$ super-structural units. The super-structural units can grow in size by a reaction in which NBO atoms on the $P^{(3)}$ motifs are used to convert $Ge^{(4)}$ to $Ge^{(6)}$ units, where superscripts denote the number of bridging oxygen atoms.

Finally, the structure of glassy materials in the Na super-ionic conductor (NASICON) system $Na_{1+x}Ti_2Si_xP_{3-x}O_{12}$ with $x = 0.8$ or $x = 1.0$ was investigated by X-ray and neutron diffraction. Here, neutron and X-ray results are consistent with a glass network comprising tetrahedral PO_4 and SiO_4 units in which titanium has a sub-octahedral coordination environment with a mean Ti-O coordination number of 5.17(4) for $x = 0.8$ versus 4.86(4) for $x = 1.0$. A mismatch of 8% is found between the P-O and Si-O bond lengths, which can allow the incorporation of Si into the P sites of the NASICON

crystal structure.

Acknowledgements

Firstly I would like to thank my supervisors Dr. Anita Zeidler and Professor Philip Salmon for the opportunity of studying amorphous materials. This project made me gained skills in neutron diffraction and further develop my knowledge in X-ray scattering at synchrotron sources in an international environment, which I am grateful for. In particular, I thank Anita for providing guidance during the project and support during experiments and writing phase. I thank Phil for valuable discussions of neutron and X-ray diffraction results.

I thank Dr. Lawrence Gammond for his friendship, precious data discussion and being always available to answer any annoying question that would come up. A deep thanks to Dr. Michela Buscemi for her friendship, support during the beginning of my PhD and for our laughs in and outside Bath.

I would like to thank Dr. Alex Hannon for his help with the neutron diffraction experiments on GEM diffractometer at ISIS and his advice on experiment details and data analysis for neutrons and X-rays. I also thank Dr. Henry Fischer for his help with the neutron diffraction experiments on D4c diffractometer at ILL and his lovely conversations at lunch. I thank Chris Benmore for performing the X-ray diffraction experiments in the 6-ID-D beamline at APS. I aknowledge Hesamadin Mohamadi for providing some sample preparation.

I thank Dr. Bruce Aitken and Dr. Randall Youngman at Corning Inc. for providing the zinc aluminosilicate glasses and performing the ^{27}Al magic angle spinning (MAS) nuclear magnetic resonance (NMR) experiments and help in experiment details. I also thank all the collaborators involved with the study of NAGP and NTPS samples, especially Prof. Ana Candida Rodrigues, Prof. Hellmut Eckert and Dr. Igor Silva for sharing their expertise in the NASICON materials and provide the ^{27}Al, ^{29}Si and ^{31}P NMR experiments.

To my roommates Luanne, Cheryl and Tsepo I am grateful for the injections of positiv-

ity we were always giving to each other, for our funny moments in the kitchen, movie nights and to get to know more Bristol and Cardiff with you. To the PhD students at Bath, specially Anastasia, Tom, Thijs, Lewis, Liam, Philip and David I thank for the pub nights, Dungeons and Dragons, salsa and board and video games that made our PhDs more enjoyable. To my amazing partner David Collomb I thank for his unconditional love, support and companionship that made me grow as a person.

Para as minhas amigas da ilha, Mariana e Adriana, eu agradeço a amizade e carinho e que apesar de nos termos conhecido quando tinhamos apenas dez anos quando nos voltamos a ver faz-me ter a certeza que o tempo não passou. Eu quero agradecer à minha família, especialmente às minhas avós a quem dedico esta tese, que me ajudaram a tornar na mulher forte e trabalhadora que sou hoje. Nunca vou esquecer as longas horas de conversa sobre conselhos da vida que me ajudaram a ultrapassar o meu doutoramento e que me fizeram ver ao final do dia o que realmente importa. Aos meus tios por estarem sempre presentes e prontos a ajudar mesmo à distância. Finalmente, aos meus dois irmãos Sofia e Alvarino, por serem compreensivos em qualquer situação e espero que saibam que apesar de estar longe ainda quero ser a irmã mais velha que olha por vocês.

Contents

Chapter 1

Introduction

Glass is an intriguing material that has been fabricated for about five thousand years but the discipline of glass science is only one hundred years old. This means that humans have perfected the technology of glass-making like temperatures, times, ingredients, processes, etc [2]. Over the centuries people have developed and used glass across various applications courtesy of its many attractive qualities such as its transparency, chemical inertness, environmental friendliness and resistance to fracture. Example applications of a disordered material such as glass include; optics [3, 4], geophysics [5], nuclear waste storage [6, 7] and complex biological systems such as bone tissue regeneration [8–10]. The architectural glass market also plays a huge role in everyday life providing transparency, structural performance and safety.

Glasses are typically formed when a liquid at high temperatures is quenched quickly through its glass transition temperature, so that crystallisation cannot occur. However the subtle differences in the way glasses are fabricated can result in distinctive changes in their properties. This has spawned a significant research interest in the way glasses are made. Furthermore, these properties can also vary with changes in the glass composition. From the point of view of a consumer, glass strength and the glass resistance to corrosion [11] are important properties to take into account. Additionally, good glasses are normally stable, but they can be leached by water or other chemicals [12, 13]. Alkali and alumina inclusions makes a good improvement in these glasses because it increases their durability. Other properties, essential for specific applications like refractive index, electrical conductivity, thermal expansion, transparency to or absorption of radiation are also vital to consider when developing new glassy materials [14]. Numerous advanced processes including tempering, laminating, coating,

bending and casting [2] make glass a high-end product to meet civilization standards and needs.

Silicates and aluminosilicates are the basis of the modern glass industry [15]. They are important cultural, societal and geological materials. SiO_2 is mostly present in the glass composition because of its low thermal expansion (0.5×10^{-6} K^{-1}), high thermal stability ($\approx$ 1000°C) and high ultraviolet transmission [16]. It was present in tools and ornamental objects during the paleolithic. Nowadays, it is present in smartphone screens and optical fibers [17]. Silicate glasses are formed by a network of SiO_4^{4-} tetrahedral units and can be modified by the introduction of network modifier metal cations or conditional network forming aluminium cations.

The addition of aluminium in silicate glasses is known to improve mechanical properties such as chemical durability or hardness. One well known example of an aluminosilicate glass in industry is the Gorilla glass [18] present in smartphones and tablets from Corning Inc. The Al^{3+} ion forms $(AlO_4)^-$ groups in the glass in which when an alkali ion is added place themselves in the network of the SiO_4 tetrahedra, increasing its polymerization. The proportion of AlO_5 and AlO_6 is small and will depend on the glass synthesis, pressure, composition and the presence of metal cations.

Cationic network modifiers like Na, Mg, Ca and Zn can be added to silicate and aluminosilicate structures to improve particular desired properties of the fabricated glass [19]. These network modifiers are typically present as ions that create non-bridging oxygen atoms, which alter the glass network. Elements bonded to oxygen like Si, B, P, Ge; constitute an extended network and they are known as the network-formers. The B-, P- and Si-O bonds are the strongest interactions (normally covalent) whereas network modifier, M-O bonds are weak (normally ionic). Alkali (Li, Na, K) and alkaline-earth (Ca, Mg) metal cations can play either a network modifier role breaking Si-O-Si bonds, or a charge-compensating role, ensuring electrical neutrality of trivalent cations like Al^{3+}. In Al-free silicate glasses, there are only network modifiers that break Si-O-Si bonds and form weak bonds with the non-bridging oxygen (NBO) anions.

As stated above phosphorous is also classified as a network-former. Phosphate glasses are built from a network of tetrahedral PO_4, where at least one of the oxygen atoms is non-bridging. When modifier cations enter the glass network, there is breakage of P-O-P bonds to form P-NBO and terminal oxygens are linked to these modifiers. Al_2O_3 can also be added to the phosphate glasses to improve their chemical durability, where it is connected to phosphate tetrahedra through P-O-Al bonds. The research on phosphate glasses has been increasing exponentially over the past years. The fact that they have

a much lower chemical resistance than silicate glasses made them at first unattractive for new research. However, glasses containing P_2O_5 also possess unique properties that allow them to be employed in fields where no other material can achieve the same performance. Phosphates have made extraordinary achievements as bioglasses or glass-ceramics [8], as laser host materials [20] and in glass matrices for stabilizing radioactive waste [21–23]. They can be manipulated to have a chemical composition similar to that of mineral bone [24] and their bio-compatible and bioresorbable properties make them promising candidates for biomedical applications such as implant materials for targeted tissue repair [9]. Furthermore, they have found success as solid electrolytes for rechargeable batteries. The crystalline phases are related to the NASICON (Na superionic conductor) structural type [25], which have a high electrical conductivity among the solid electrolytes. Therefore, aluminosilicates and phosphates have a bright future ahead with further new developments and challenges to overcome.

The phosphate, silicate and aluminosilicate glasses studied for their interesting properties and vast applications mentioned before are oftentimes complex because they are made of multiple elements. Nevertheless different techniques such as diffraction, are used to determine the bulk structure of disordered materials and complete information will involve contributions from multiple experimental and simulation techniques.

Diffraction experiments in amorphous materials do not show sharp Bragg peaks in the diffraction pattern which means there is a lack of long-range order and periodicity. However, diffraction patterns provide information on the atomic structure of a system in the form of the total pair distribution function, $D(r)$, which provides a measure of the probability of finding two atoms a distance r apart and the areas under the peaks are associated with the number of atoms in the coordination spheres. It probes both short- and intermediate- range order, being very sensitive to the nature and extent of disorder in glasses and liquids, and is an essential tool to understand the structural differences between amorphous and crystalline materials.

The work presented in this thesis makes use of X-ray diffraction (XRD), Neutron Diffraction with (NDIS) and without (ND) isotopic substitution to obtain information on the structure of crystalline and glassy materials. Neutrons and X-rays are complementary probes, as the neutrons scatter mostly from the nuclei of atoms, whereas the X-rays are scattered by the electrons via electromagnetic forces [26]. Different isotopes of the same chemical species can have different scattering cross-sections for neutrons which is exploited by the NDIS technique.

The aim of this work is to understand how different concentrations of network modifiers

(Ca, Mg, Zn and Na) affect the glasses structure and hence its properties. The thesis is organized as follows: Chapter 2 gives the essential theory for neutron and X-ray diffraction experiments and the data correction procedures. Chapter 3 describes the diffraction instrumentation of the neutron and X-ray synchrotron sources. In chapter 4, the structure of zinc aluminosilicate glasses was studied by X-ray and neutron diffraction where ^{27}Al magic angle spinning (MAS) nuclear magnetic resonance (NMR) results were used to help fitting the data and give complementary information on the glass network. In chapter 5 the results of magnesium aluminosilicate glasses obtained from X-ray diffraction is given where ^{27}Al MAS NMR spectroscopy results are also used to help fitting the data. Chapter 6 discusses the coordination environment of Mg and Ca in the diopside glass by using NDIS and XRD.

The results from ND and XRD of crystalline and amorphous Na-Al-Ge-P-O (NAGP) materials are presented in chapter 7. The information obtained from the pair distribution function analysis makes use of ^{31}P and ^{27}Al MAS NMR and provides a model that describes the glass structure and how the structure changes with different times of annealing and temperature. In chapter 8, the results from experimentation on Na-Si-Ti-P-O (NTSP) glasses from XRD and ND are presented. These are also compared with the NAGP materials when Ti^{4+} is used instead of Ge^{4+} ions. Finally, an overall summary of the results and conclusions is given in chapter 9 as well as suggestions for future work.

Chapter 2

Neutron and X-Ray Diffraction Theory

2.1 Scattering Theory

In a scattering experiment, an incident neutron with a wave-vector k_i undergoes scattering through a sample such that the scattered particle emerges with a wave-vector k_f. The scattering vector Q is defined as [26].

$$\vec{Q} = \vec{k_i} - \vec{k_f}, \tag{2.1}$$

where $k = \frac{2\pi}{\lambda}$ and λ is the wavelength of the particle. A schematic representation of this scattering event is shown in figure 2-1.

The energy transfer in the scattering event for a neutron of mass m_n will be

$$\Delta E = E_i - E_f = \frac{|\hbar k_i|^2}{2m_n} - \frac{|\hbar k_f|^2}{2m_n}, \tag{2.2}$$

where $\hbar = \frac{h}{2\pi}$ and h is the Planck constant. Applying the cosine rule to the scattering triangle in figure 2-1, it follows that

$$Q^2 = k_i^2 + k_f^2 - 2k_i k_f \cos(2\theta), \tag{2.3}$$

where 2θ is the scattering angle. By assuming the static approximation, the energy exchange between a neutron and a sample, ΔE, is much smaller than the incident energy, E_i, such that $\Delta E/E_i \ll 1$, it follows from equation 2.2 that

$$|k_i| = \frac{2\pi}{\lambda_i} \approx |k_f| = \frac{2\pi}{\lambda_f}. \tag{2.4}$$

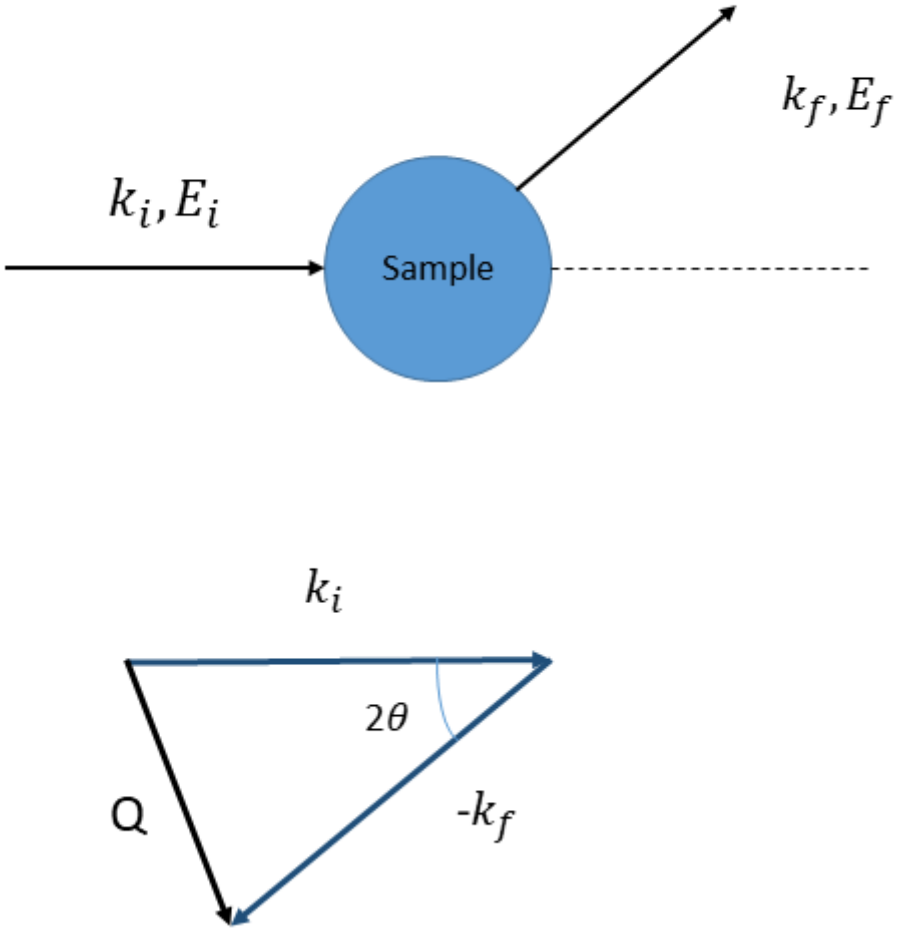

Figure 2-1: Schematic representation of a scattering event and the resulting scattering angle.

By applying equation 2.4 to equation 2.3, the magnitude of the scattering vector becomes

$$Q = \frac{4\pi}{\lambda} \sin(\theta). \tag{2.5}$$

The scattering geometry for a diffraction experiment is shown in figure 2-2. A collimated beam of incident neutrons with flux ϕ is scattered by a sample at the origin of coordinates. The neutrons scattered are counted by a detector of area dS at a distance R from the origin and subtending a small solid angle $d\Omega = dS/R^2$.

During a diffraction experiment in the small sample limit, the quantity measured is the differential cross section which is defined as

$$\frac{d\sigma}{d\Omega}(\theta) = \frac{\text{number of quanta scattered into solid angle d}\Omega \text{ per second}}{\phi \; d\Omega}, \tag{2.6}$$

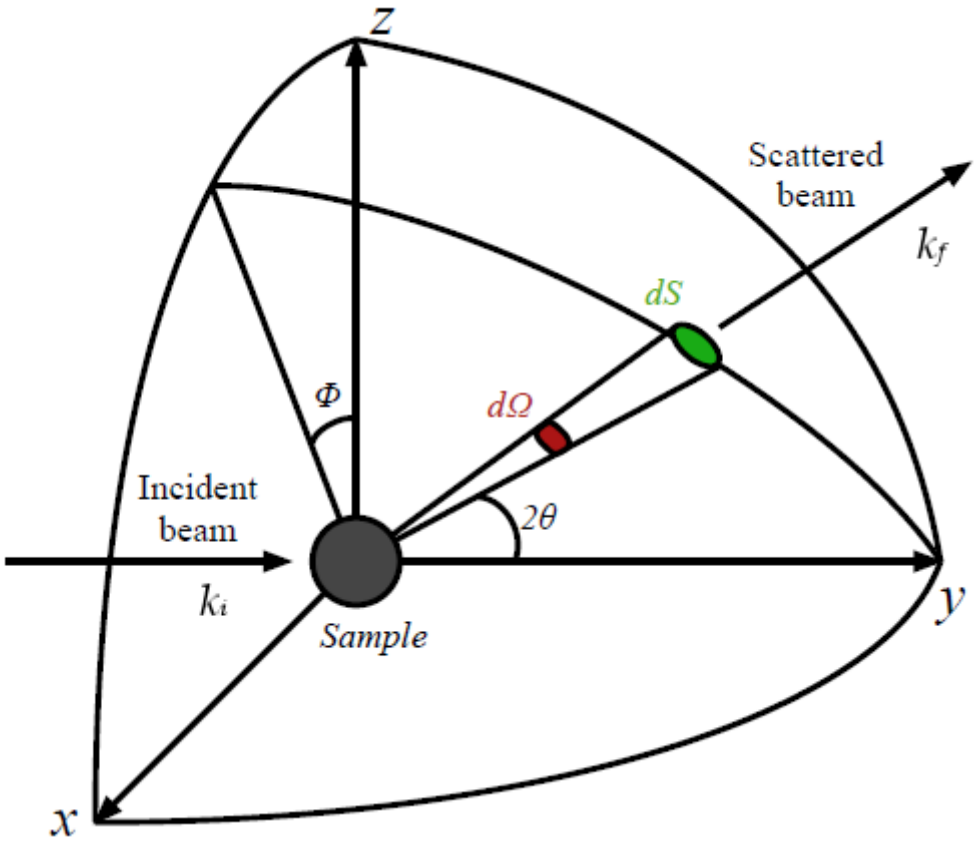

Figure 2-2: The geometry of a diffraction experiment into a detector of surface area dS. The origin of the coordinates is the position of the sample and the y-axis adopts the direction of the incident wave vector k_i. Reproduced from [27].

2.2 Neutron Diffraction

Neutrons interact with the nucleus of the atom by the strong nuclear force. Although they have the advantage of deep penetration, the interaction happens at short distances which results in weak scattering [26]. To overcome this problem, large samples are needed to obtain a good scattering signal in comparison with X-rays. For a multicomponent system with N atoms of n different chemical species, the differential scattering cross section in the small sample limit is [28]

$$\frac{1}{N}\frac{d\sigma}{d\Omega}(Q) = F(q) + \sum_{\alpha} c_{\alpha}(b^2_{\alpha,\mathrm{coh}} + b^2_{\alpha,\mathrm{inc}})[1 + P_{\alpha}(Q)]. \tag{2.7}$$

$F(Q)$ is the total structure factor which contains the structural information, $P_{\alpha}(Q)$ is the Plazcek correction associated with the inelastic scattering for chemical species α [29]. The self-scattering term is given by the sum of the squares of the coherent and incoherent scattering lengths ($b_{\alpha,\mathrm{coh}}$ and $b_{\alpha,\mathrm{inc}}$ respectively) for all species α weighted by their concentration c_{α}.

The total structure factor $F(Q)$ can be written in terms of the Faber-Ziman partial structure factors $S_{\alpha\beta}$ [30] as

$$F(Q) = \sum_{\alpha}\sum_{\beta} c_{\alpha}c_{\beta}b_{\alpha}b_{\beta}[S_{\alpha\beta}(Q) - 1], \tag{2.8}$$

The Faber-Ziman convention describes the correlations between pairs of nuclei of chemical species α and β. The normalised neutron total structure factor $S_N(Q)$ is defined as

$$S_N(Q) = \frac{F(Q)}{\langle b\rangle^2} + 1, \tag{2.9}$$

where $\langle b\rangle = c_{\alpha}b_{\alpha} + c_{\beta}b_{\beta} + ...$ is the average neutron scattering length. The real space information is obtained by taking the Fourier transform of $F(Q)$, which is called the total pair distribution function $G(r)$

$$\begin{aligned} G(r) &= \frac{1}{2\pi^2 r n_0}\int_0^{\infty} QF(Q)\sin(Qr)dQ \\ G(r) &= \sum_{\alpha}\sum_{\beta} c_{\alpha}c_{\beta}b_{\alpha}b_{\beta}[g_{\alpha\beta}(r) - 1], \end{aligned} \tag{2.10}$$

where n_0 is the atomic number density and $g_{\alpha\beta}(r)$ is the probability of finding an atom of chemical species β at a distance r from an atom of chemical species α [28].

The coordination number can be expressed by:

$$\overline{n}_{\alpha}^{\beta} = 4\pi n_0 c_{\beta} \int_{r_1}^{r_2} g_{\alpha\beta}(r) r^2 dr. \tag{2.11}$$

$\bar{n}_{\alpha}^{\beta}$ describes the average number of atoms β that are around an atom α, where r_1 and r_2 are the inner and outer radius, respectively, of a spherical shell. If the peak in $g_{\alpha\beta}(r)$ is not symmetrical, it can be helpful to define a weighted mean peak position given by

$$\overline{r}_{\alpha\beta} = \frac{\int_{r_1}^{r_2} r g_{\alpha\beta}(r) dr}{\int_{r_1}^{r_2} g_{\alpha\beta}(r) dr}, \tag{2.12}$$

where $g_{\alpha\beta}(r)$ is obtained from the sum of the Gaussian functions fitted to the first peak, and r_1 and r_2 define the overall extent of this peak.

In the low-r limit *G(r)* can be written as

$$G(r \to 0) = G(0) = -\sum_{\alpha} \sum_{\beta} c_{\alpha} c_{\beta} b_{\alpha} b_{\beta}, \tag{2.13}$$

which represents the distance below the closest approach between two atoms. Unphysical features in $G(r)$ due to Fourier transform artefacts therefore, oscillate around this low-r limit. A possible self-consistency check is to set the low-r oscillations of a $G(r)$ function equal to $G(0)$ and then back-Fourier transform the result. The back-Fourier transform should be in good overall agreement with the measured $F(Q)$ function.

Another self-consistency check is the sum-rule relation (obtained from equation 2.10 at $r \to 0$) that is given by [31]

$$\int_0^{\infty} F(Q) Q^2 dQ = 2\pi^2 n_0 G(0). \tag{2.14}$$

The partial structure factors and the partial pair-distribution functions can be written as

$$S_{\alpha\beta}(Q) - 1 = \frac{4\pi n_0}{Q} \int_0^{\infty} r[g_{\alpha\beta}(r) - 1] \sin(Qr) dr \tag{2.15}$$

$$g_{\alpha\beta}(r) - 1 = \frac{1}{2\pi^2 r n_0} \int_0^\infty Q[S_{\alpha\beta}(Q) - 1] \sin(Qr) dQ. \tag{2.16}$$

2.2.1 Modification Functions

In a neutron diffraction experiment, the diffractometer can only access a limited Q-range. The total structure factor will be truncated by the maximum Q-value such that it will be multiplied by a step modification function, which is defined as

$$M(Q) = \left\{ \begin{array}{ll} 1 & \text{if } Q \leq Q_{\max} \\ 0 & \text{if } Q > Q_{\max} \end{array} \right\}. \tag{2.17}$$

The Fourier transform of $M(Q)$ is given by

$$M(r) = \frac{1}{\pi} \int_0^{Qmax} \cos(Qr) dQ = \frac{Q_{\max}}{\pi} \sin(Q_{\max} r). \tag{2.18}$$

A Lorch modification function [32], *L(Q)*, can also be used instead of a step modification function in order to reduce Fourier transform artefacts that affect the real space function. *L(Q)* is defined as

$$L(Q) = \left\{ \begin{array}{ll} \frac{\sin(\frac{\pi Q}{Q_{\max}})}{\frac{\pi Q}{Q_{\max}}} & \text{if } Q \leq Q_{\max} \\ 0 & \text{if } Q > Q_{\max} \end{array} \right\}. \tag{2.19}$$

The density correlation function is defined as [33]

$$D_{\exp}(r) = \frac{2}{\pi} \int_0^\infty Q \frac{F(Q)}{\langle b \rangle^2} \sin(Qr) M(Q) dQ. \tag{2.20}$$

Equation 2.20 can be rewritten as

$$\begin{aligned} D_{\exp}(r) &= 4\pi n_0 r \frac{G(r)}{\langle b \rangle^2} \otimes M(r) \\ &= 4\pi n_0 \sum_\alpha^n \sum_\beta^n \frac{c_\alpha c_\beta b_\alpha b_\beta}{\langle b \rangle^2} r g_{\alpha\beta}(r) \otimes M(r) - 4\pi n_0 r, \end{aligned} \tag{2.21}$$

where $\otimes$ is the convolution operator. A Gaussian function of width $\sigma_{\alpha\beta}(i)$ and centered

at $r_{\alpha\beta}(i)$ has an area which gives the coordination number $\bar{n}^{\beta}_{\alpha}(i)$, where i is $rg_{\alpha\beta}(r)$. The fitted density function is

$$D_{\text{fit}}(r; r_{\alpha\beta}, \bar{n}^{\beta}_{\alpha}, \sigma_{\alpha\beta}) = \sum_{i} \Bigg[\omega_{\alpha\beta}(i) \frac{\bar{n}^{\beta}_{\alpha}(i)}{c_{\beta}(i) r_{\alpha\beta}(i)} \frac{1}{\sqrt{2\pi}\sigma_{\alpha\beta}(i)} \times \exp\Big(\frac{-[r - r_{\alpha\beta}(i)]^2}{2[\sigma_{\alpha\beta}(i)]^2} \Big) \otimes M(r) \Bigg] - 4\pi n_0 r. \tag{2.22}$$

The weighting factor $\omega_{\alpha\beta}(i)$ is given by

$$w_{\alpha\beta}(i) = \left\{ \begin{array}{ll} \frac{2c_{\alpha}c_{\beta}b_{\alpha}b_{\beta}}{\langle b \rangle^2} & \text{if } \alpha \neq \beta \\ \frac{c^2_{\alpha}b^2_{\alpha}}{\langle b \rangle^2} & \text{if } \alpha = \beta \end{array} \right\}. \tag{2.23}$$

Accurate peak positions and coordination numbers are obtained by minimizing the goodness of the fit parameter R_{χ} [34], which is

$$R_{\chi}(r_{\alpha\beta}, \bar{n}^{\beta}_{\alpha}, \sigma_{\alpha\beta}) = \sqrt{\frac{\sum_i [D_{\text{exp}}(r_i) - D_{\text{fit}}(r_i)]^2}{\sum_i D^2_{\text{exp}}(r_i)}}. \tag{2.24}$$

If Q_{max} given by the diffractometer has a large value such that *M(Q)* has a negligible effect on *F(Q)*, then *D(r)* can be written in terms of its partial pair density correlation functions $d_{\alpha\beta}(r)$ [35],

$$D(r) = \sum_{\alpha}^{n} \sum_{\beta}^{n} c_{\alpha}c_{\beta}b_{\alpha}b_{\beta}d_{\alpha\beta}(r), \tag{2.25}$$

where

$$d_{\alpha\beta}(r) = 4\pi n_0 r[g_{\alpha\beta}(r) - 1]. \tag{2.26}$$

2.3 Neutron Diffraction with Isotopic Substitution

Performing a neutron diffraction experiment with isotopic substitution (NDIS) consists of measuring $F(Q)$ for samples with identical structure and chemical composition, but with different isotopic composition for at least one of the species α.

Figure 2-3 shows an example of the scattering length varying between elements and isotopes of the same element.

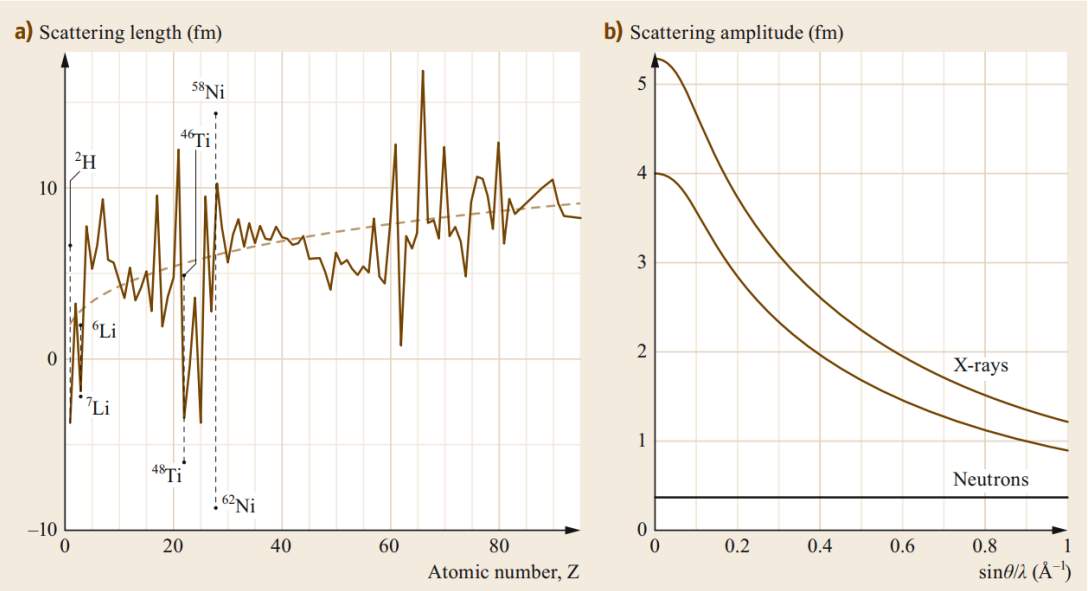

Figure 2-3: (a) Neutron scattering lengths as a function of the atomic number Z. The dashed curve shows the slow increase of the potential scattering. (b) X-ray and neutron scattering amplitudes as a function of $\sin\theta/\lambda$. Reproduced from [2].

2.3.1 Difference Functions

In a complex multi-component system it is sometimes challenging to measure the full set of partial structure factors in a neutron diffraction experiment. However, by only considering a pair of isotopically enriched samples the information obtained is simplified. By calculating a first-order difference (FOD) function $\Delta F(Q)$ between the total structure factors individual pair correlations are removed from the diffraction patterns [30].

Consider a case of a four component system (Si, Mg, Ca, O) in diopside. Let $^{\text{nat}}$Mg and ^{25}Mg represent the isotopes of Mg such that $^{\text{nat}}F(Q)$ and $^{25}F(Q)$ are the corresponding

total structure factors given by

$$
\begin{aligned}
{}^{\mathrm{nat}}F(Q) = {} & c_{\mathrm{Ca}}^2 b_{\mathrm{Ca}}^2 [S_{\mathrm{CaCa}}(Q) - 1] + c_{\mathrm{Si}}^2 b_{\mathrm{Si}}^2 [S_{\mathrm{SiSi}}(Q) - 1] + c_{\mathrm{O}}^2 b_{\mathrm{O}}^2 [S_{\mathrm{OO}}(Q) - 1] \\
& + c_{^{\mathrm{nat}}\mathrm{Mg}}^2 b_{^{\mathrm{nat}}\mathrm{Mg}}^2 [S_{^{\mathrm{nat}}\mathrm{Mg}^{\mathrm{nat}}\mathrm{Mg}}(Q) - 1] + 2 c_{^{\mathrm{nat}}\mathrm{Mg}} c_{\mathrm{O}} b_{^{\mathrm{nat}}\mathrm{Mg}} b_{\mathrm{O}} [S_{^{\mathrm{nat}}\mathrm{MgO}}(Q) - 1] \\
& + 2 c_{\mathrm{Ca}} c_{\mathrm{O}} b_{\mathrm{Ca}} b_{\mathrm{O}} [S_{\mathrm{CaO}}(Q) - 1] + 2 c_{\mathrm{Si}} c_{\mathrm{O}} b_{\mathrm{Si}} b_{\mathrm{O}} [S_{\mathrm{SiO}}(Q) - 1] \\
& + 2 c_{^{\mathrm{nat}}\mathrm{Mg}} c_{\mathrm{Ca}} b_{\mathrm{natMg}} b_{\mathrm{Ca}} [S_{^{\mathrm{nat}}\mathrm{MgCa}}(Q) - 1] \\
& + 2 c_{^{\mathrm{nat}}\mathrm{Mg}} c_{\mathrm{Si}} b_{^{\mathrm{nat}}\mathrm{Mg}} b_{\mathrm{Si}} [S_{^{\mathrm{nat}}\mathrm{MgSi}}(Q) - 1] + 2 c_{\mathrm{Si}} c_{\mathrm{Ca}} b_{\mathrm{Si}} b_{\mathrm{Ca}} [S_{\mathrm{SiCa}}(Q) - 1].
\end{aligned}
\tag{2.27}
$$

and

$$
\begin{aligned}
{}^{25}F(Q) = {} & c_{\mathrm{Ca}}^2 b_{\mathrm{Ca}}^2 [S_{\mathrm{CaCa}}(Q) - 1] + c_{\mathrm{Si}}^2 b_{\mathrm{Si}}^2 [S_{\mathrm{SiSi}}(Q) - 1] + c_{^{25}\mathrm{Mg}}^2 b_{^{25}\mathrm{Mg}}^2 [S_{^{25}\mathrm{Mg}^{25}\mathrm{Mg}}(Q) - 1] \\
& + c_{\mathrm{O}}^2 b_{\mathrm{O}}^2 [S_{\mathrm{OO}}(Q) - 1] + 2 c_{^{25}\mathrm{Mg}} c_{\mathrm{O}} b_{^{25}\mathrm{Mg}} b_{\mathrm{O}} [S_{^{25}\mathrm{MgO}}(Q) - 1] \\
& + 2 c_{\mathrm{Ca}} c_{\mathrm{O}} b_{\mathrm{Ca}} b_{\mathrm{O}} [S_{\mathrm{CaO}}(Q) - 1] + 2 c_{\mathrm{Si}} c_{\mathrm{O}} b_{\mathrm{Si}} b_{\mathrm{O}} [S_{\mathrm{SiO}}(Q) - 1] \\
& + 2 c_{^{25}\mathrm{Mg}} c_{\mathrm{Ca}} b_{^{25}\mathrm{Mg}} b_{\mathrm{Ca}} [S_{^{25}\mathrm{MgCa}}(Q) - 1] \\
& + 2 c_{^{25}\mathrm{Mg}} c_{\mathrm{Si}} b_{^{25}\mathrm{Mg}} b_{\mathrm{Si}} [S_{^{25}\mathrm{MgSi}}(Q) - 1] + 2 c_{\mathrm{Si}} c_{\mathrm{Ca}} b_{\mathrm{Si}} b_{\mathrm{Ca}} [S_{\mathrm{SiCa}}(Q) - 1].
\end{aligned}
\tag{2.28}
$$

The difference function $\Delta F_{\mathrm{Mg}}(Q)$ eliminates all those pair-correlation functions that do not involve magnesium and is given by

$$\begin{aligned}\Delta F_{\mathrm{Mg}}(Q) =& {}^{\mathrm{nat}}F(Q) - {}^{25}F(Q) \\ &= c_{\mathrm{Mg}}^2(b_{^{\mathrm{nat}}\mathrm{Mg}}^2 - b_{^{25}\mathrm{Mg}}^2)[S_{\mathrm{MgMg}}(Q) - 1] \\ &+ 2c_{\mathrm{Mg}}c_{\mathrm{O}}b_{\mathrm{O}}(b_{^{\mathrm{nat}}\mathrm{Mg}} - b_{^{25}\mathrm{Mg}})[S_{\mathrm{MgO}}(Q) - 1] \\ &+ 2c_{\mathrm{Mg}}c_{\mathrm{Si}}b_{\mathrm{Si}}(b_{^{\mathrm{nat}}\mathrm{Mg}} - b_{^{25}\mathrm{Mg}})[S_{\mathrm{MgSi}}(Q) - 1] \\ &+ 2c_{\mathrm{Mg}}c_{\mathrm{Ca}}b_{\mathrm{Ca}}(b_{^{\mathrm{nat}}\mathrm{Mg}} - b_{^{25}\mathrm{Mg}})[S_{\mathrm{MgCa}}(Q) - 1]\end{aligned} \tag{2.29}$$

The Mg-α correlations with $\alpha \neq$ Mg can also be eliminated by forming the difference function

$$\begin{aligned}\Delta F(Q) &= [b_{^{\mathrm{nat}}\mathrm{Mg}}\,{}^{25}F(Q) - b_{^{25}\mathrm{Mg}}\,{}^{\mathrm{nat}}F(Q)]/(b_{^{\mathrm{nat}}\mathrm{Mg}} - b_{^{25}\mathrm{Mg}}) \\ &= 2c_{\mathrm{Ca}}c_{\mathrm{O}}b_{\mathrm{Ca}}b_{\mathrm{O}}[S_{\mathrm{CaO}}(Q) - 1] + 2c_{\mathrm{Si}}c_{\mathrm{O}}b_{\mathrm{Si}}b_{\mathrm{O}}[S_{\mathrm{SiO}}(Q) - 1] \\ &+ c_{\mathrm{Ca}}^2b_{\mathrm{Ca}}^2[S_{\mathrm{CaCa}}(Q) - 1] + c_{\mathrm{Si}}^2b_{\mathrm{Si}}^2[S_{\mathrm{SiSi}}(Q) - 1] \\ &+ c_{\mathrm{O}}^2b_{\mathrm{O}}^2[S_{\mathrm{OO}}(Q) - 1] + 2c_{\mathrm{Ca}}c_{\mathrm{Si}}b_{\mathrm{Ca}}b_{\mathrm{Si}}[S_{\mathrm{CaSi}}(Q) - 1] \\ &- c_{\mathrm{Mg}}^2b_{^{\mathrm{nat}}\mathrm{Mg}}b_{^{25}\mathrm{Mg}}[S_{\mathrm{MgMg}}(Q) - 1].\end{aligned} \tag{2.30}$$

Applying a Fourier transform to the functions $\Delta F_{\mathrm{Mg}}(Q)$ and $\Delta F(Q)$ follows respectively,

$$\begin{aligned}\Delta G_{\mathrm{Mg}}(r) &= c_{\mathrm{Mg}}^2(b_{^{\mathrm{nat}}\mathrm{Mg}}^2 - b_{^{25}\mathrm{Mg}}^2)[g_{\mathrm{MgMg}}(Q) - 1] \\ &+ 2c_{\mathrm{Mg}}c_{\mathrm{O}}b_{\mathrm{O}}(b_{^{\mathrm{nat}}\mathrm{Mg}} - b_{^{25}\mathrm{Mg}})[g_{\mathrm{MgO}}(Q) - 1] \\ &+ 2c_{\mathrm{Mg}}c_{\mathrm{Si}}b_{\mathrm{Si}}(b_{^{\mathrm{nat}}\mathrm{Mg}} - b_{^{25}\mathrm{Mg}})[g_{\mathrm{MgSi}}(Q) - 1] \\ &+ 2c_{\mathrm{Mg}}c_{\mathrm{Ca}}b_{\mathrm{Ca}}(b_{^{\mathrm{nat}}\mathrm{Mg}} - b_{^{25}\mathrm{Mg}})[g_{\mathrm{MgCa}}(Q) - 1],\end{aligned} \tag{2.31}$$

and

$$\begin{aligned}\Delta G(r) = {} & 2c_{\mathrm{Ca}}c_{\mathrm{O}}b_{\mathrm{Ca}}b_{\mathrm{O}}[S_{\mathrm{CaO}}(Q)-1] + 2c_{\mathrm{Si}}c_{\mathrm{O}}b_{\mathrm{Si}}b_{\mathrm{O}}[S_{\mathrm{SiO}}(Q)-1] \\ & + c_{\mathrm{Ca}}^2 b_{\mathrm{Ca}}^2[S_{\mathrm{CaCa}}(Q)-1] + c_{\mathrm{Si}}^2 b_{\mathrm{Si}}^2[S_{\mathrm{SiSi}}(Q)-1] \\ & + c_{\mathrm{O}}^2 b_{\mathrm{O}}^2[S_{\mathrm{OO}}(Q)-1] + 2c_{\mathrm{Ca}}c_{\mathrm{Si}}b_{\mathrm{Ca}}b_{\mathrm{Si}}[S_{\mathrm{CaSi}}(Q)-1] \\ & - c_{\mathrm{Mg}}^2 b_{^{\mathrm{nat}}\mathrm{Mg}}b_{^{25}\mathrm{Mg}}[S_{\mathrm{MgMg}}(Q)-1].\end{aligned} \tag{2.32}$$

2.4 Neutron Diffraction Data Corrections and Analysis

In a neutron diffraction experiment i.e, no longer in the small sample limit, it is necessary to take into account physical processes like absorption and multiple scattering when a sample inside a container is placed in a diffractometer. Therefore, it is important to subtract the diffracted intensities coming from the sample container and the background.

The attenuation corrections resulting from absorption and scattering have been calculated by Paalman and Pings [36] (1962) for the case of an illuminated sample of cylindrical geometry in an annular container. The attenuation coefficients are denoted by $A_{i,j}(\theta)$ which means the events where neutrons are scattered in medium i and attenuated in medium j.

In the following section, the data corrections are valid for a single incident wavelength used in neutron reactor sources. However, for a spallation source experiment the corrections will be both angle and wavelength dependent.

2.4.1 Attenuation, Multiple Scattering and Inelasticity Corrections

In the small sample limit the neutrons are not attenuated by the sample and there is no multiple scattering effect. $I_S(\theta)$ is the single scattered intensity and is given by

$$I_S(\theta) = a(\theta)N_S\frac{d\sigma}{d\Omega}(\theta), \tag{2.33}$$

where N_S is the number of scattering centres in the beam, $a(\theta)$ is the calibration coefficient which converts cross-sections into measured intensities and $\frac{d\sigma}{d\Omega}(\theta)$ is the

differential scattering cross section for the sample as mention in section 2.1.

In the non small sample limit, the background corrected intensity in the case of a container-less sample with a cylindrical geometry is given by

$$I_S^E(\theta) = A_{S,S}(\theta)I_S(\theta) + a(\theta)M_S(\theta), \tag{2.34}$$

where $A_{S,S}$ is the attenuation coefficient for scattering in the sample and attenuated by sample and $M_S(\theta)$ is the multiple scattering cross section [37] which is defined as

$$M_S(\theta) = N_S A_{S,S}(\theta)\frac{\sigma_S}{4\pi}\Delta_S(\theta)[1 + P_S(\theta)]. \tag{2.35}$$

σ_S is the total scattering cross section of the sample and is wavelength dependent, $\Delta_S(\theta)$ is the ratio of multiple scattering to single scattering and $P_S(\theta)$ is the Placzek correction [29] factor of the sample.

During a neutron diffraction experiment, the intensity of the scattered neutrons measured for the sample S inside its container C is denoted $I_{SC}^E(\theta)$ and is written as

$$I_{SC}^E(\theta) = A_{S,SC}(\theta)I_S(\theta) + A_{C,SC}(\theta)I_C(\theta) + a(\theta)M_{SC}(\theta), \tag{2.36}$$

where I_C is the single scattered intensity measured for the container and $M_{SC}(\theta)$ is the multiple scattering cross section for the sample in the container. The background corrected intensity for the empty container is given by

$$I_C^E(\theta) = A_{C,C}(\theta)I_C(\theta) + a(\theta)M_C(\theta), \tag{2.37}$$

where $M_C(\theta)$ is the multiple scattering cross section of the empty container. The differential scattering cross section can then be calculated by combining equations 2.33, 2.36 and 2.37 such that

$$\frac{d\sigma}{d\Omega}(\theta)\bigg|_S = \frac{1}{N_S A_{S,SC}(\theta)}\left[\frac{I_{SC}^E(\theta)}{a(\theta)} - M_{SC}(\theta) - \frac{A_{C,SC}(\theta)}{A_{C,C}(\theta)}\left(\frac{I_C^E(\theta)}{a(\theta)} - M_C(\theta)\right)\right]. \tag{2.38}$$

2.4.2 Vanadium Normalisation

Vanadium is used in neutron diffraction experiments as a normalization standard because it has a small coherent and a large incoherent scattering cross section, i.e, $\sigma_{V,\text{coh}}$ = 0.01838(12) barn and $\sigma_{V,\text{inc}}$ = 5.08(6) barn, respectively [38]. The background corrected intensity for vanadium, $I_V^E(\theta)$ is given by

$$I_V^E(\theta) = A_{V,V}(\theta)I_V(\theta) + a(\theta)M_V(\theta). \tag{2.39}$$

$I_V(\theta)$ is the single scattered intensity for vanadium and $M_V(\theta)$ is the multiple scattering cross section. $I_V(\theta)$ and $M_V(\theta)$ are defined as

$$I_V(\theta) = a(\theta)N_V\frac{d\sigma}{d\Omega}(\theta)\bigg|_V = a(\theta)N_V\frac{\sigma_V}{4\pi}[1 + P_V(\theta)], \tag{2.40}$$

$$M_V(\theta) = N_V A_{V,V}(\theta)\frac{\sigma_V}{4\pi}\Delta_V(\theta)[1 + P_V(\theta)], \tag{2.41}$$

where N_V is the number of vanadium scattering centres in the neutron beam, $\sigma_V \simeq \sigma_{V,\text{inc}} = 4\pi b_{V,\text{inc}}^2$ is the scattering cross section, $P_V(\theta)$ is the Placzek correction factor and $\Delta_V(\theta)$ is the ratio of multiple scattering to single scattering. The background corrected intensity for vanadium, $I_V^E(\theta)$ can be rewritten as

$$I_V^E(\theta) = a(\theta)A_{V,V}(\theta)N_V\left(\frac{\sigma_V}{4\pi}[1 + P_V(\theta)][1 + \Delta_V(\theta)]\right), \tag{2.42}$$

and the calibration coefficient is

$$a(\theta) = \frac{I_V^E(\theta)}{A_{V,V}(\theta)N_V\left(\frac{\sigma_V}{4\pi}[1 + P_V(\theta)]\right)(1 + \Delta_V(\theta))}. \tag{2.43}$$

Figure 2-4 summarizes the data corrections procedure for a neutron diffraction experiment.

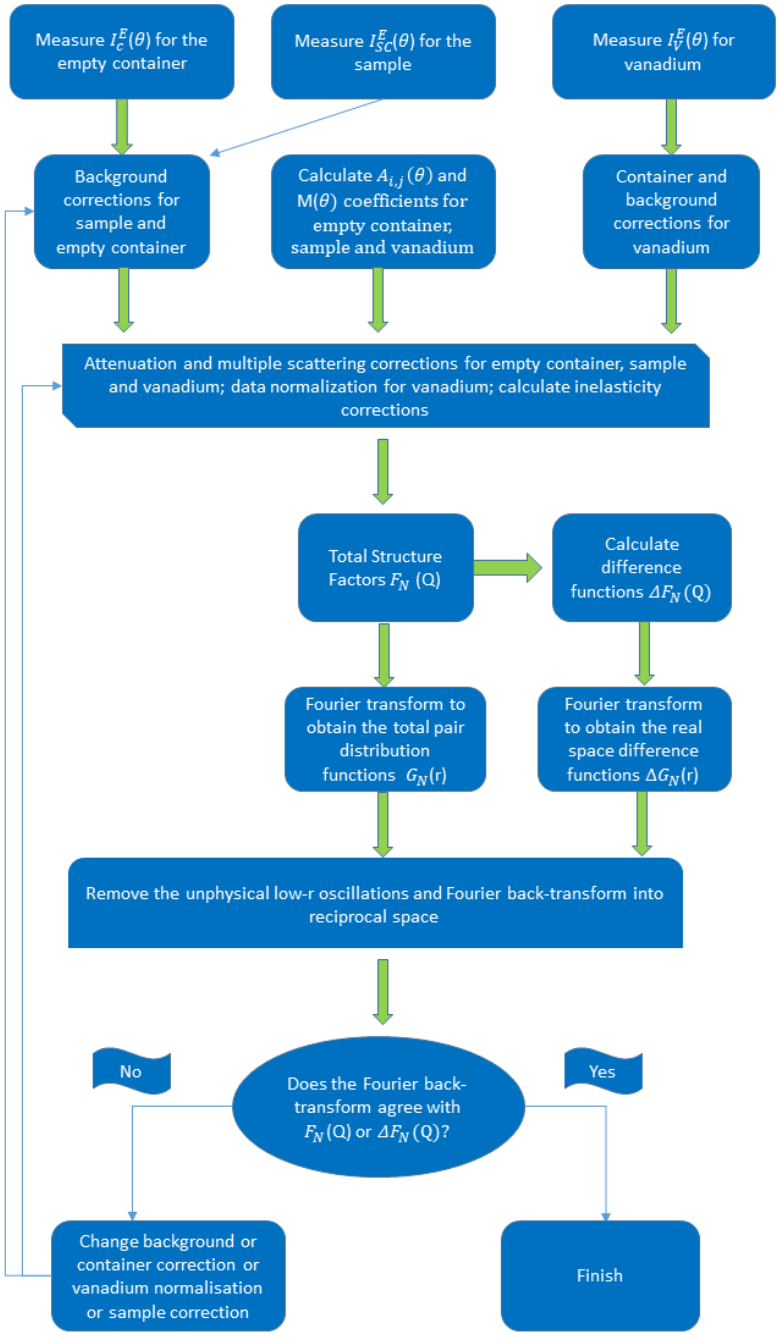

Figure 2-4: Data analysis procedure for a neutron diffraction experiment.

2.5 X-Ray Diffraction Data Correction and Analysis

X-ray photons consist of oscillating electric and magnetic fields. Although they do not have charge or mass, the charge of the electrons in the material interacts with these magnetic and electric fields [26]. The static approximation is valid since the scattering in X-rays is originated from the electron cloud with high incident energies of the order of keV.

The total structure factor formalism for X-ray diffraction is the same as for neutron diffraction but the neutron scattering lengths will be replaced by the X-ray form factors, *f(Q)* [30]. The *f(Q)* is dependent on the scattering vector Q and the energy of the incident X-ray photons E_0 and is defined as

$$r_e f(Q, E_0) = r_e[Z f_{\text{falloff}}(Q) + f'(E_0) + i f''(E_0)], \tag{2.44}$$

where $r_e = 2.818$ fm is the radius of an electron, $f(Q, E_0)$ is the atomic form factor, Z is the atomic number and $f_{\text{falloff}}(Q)$ is the atomic form factor's modulation varying from 1 at Q = 0 to 0 at Q = ∞. $f'(E_0)$ and $f''(E_0)$ denote the real and imaginary parts of the anomalous term, respectively, of the atomic form factor and because it involves inner core electron clouds having small radii, its Q-dependence is generally weak enough to be ignored.

Instead of the Placzek correction, additional inelastic scattering and re-emission processes like Compton scattering, fluorescence and resonant-Raman scattering contribute to the total scattering and must be corrected for to obtain the Rayleigh-Thomson (Ray-T) differential scattering cross section pertinent to diffraction.

The total X-ray scattering cross section is given by [28]

$$\begin{aligned}\left[\frac{d\sigma}{d\Omega}(Q)\right]^X_{\text{Total}} &= F_X(Q) + \sum_\alpha^n c_\alpha f_\alpha(Q)^2 + \left[\frac{d\sigma}{d\Omega}(Q)\right]^X_{\text{Compton}} \\ &+ \left[\frac{d\sigma}{d\Omega}\right]^X_{\text{Fluorescence}} + \left[\frac{d\sigma}{d\Omega}(Q)\right]^X_{\text{r-Raman}} + \left[\frac{d\sigma}{d\Omega}(Q)\right]^X_{\text{Other}},\end{aligned} \tag{2.45}$$

where c_α is the atomic fraction and $f_\alpha(Q)$ is the atomic form factor for chemical species α. The second term of the equation is denoted as self scattering.

At energies far enough from an absorption edge the processes such as fluorescence, resonant-Raman scattering and/or other are negligible with the exception of Compton

scattering. The anomalous terms of the form factor, and hence their energy dependence, are also negligible at energies far from an absorption edge. The total structure factor for X-rays is then

$$F_X(Q) = \sum_{\alpha}^{n}\sum_{\beta}^{n} c_\alpha c_\beta f_\alpha(Q) f_\beta(Q)[S_{\alpha\beta}(Q) - 1]. \tag{2.46}$$

The total scattering intensity is written as the normalized total X-ray structure factor, $S_X(Q)$,

$$S_X(Q) = \frac{F_X(Q)}{\sum_{\alpha}^{n}\sum_{\beta}^{n} c_\alpha c_\beta f_\alpha(Q) f_\beta(Q)} + 1, \tag{2.47}$$

which oscillates around 1 at high Q and so,

$$S_X(Q) = 1 + \frac{1}{\langle f(Q)\rangle^2}\sum_{\alpha}\sum_{\beta} c_\alpha c_\beta f_\alpha(Q) f_\beta(Q)\left[S_{\alpha\beta}(Q) - 1\right], \tag{2.48}$$

where $\langle f(Q)\rangle = \sum_\alpha c_\alpha f_\alpha(Q)$.

To obtain $\frac{d\sigma}{d\Omega}(Q)$ for a sample it is necessary to subtract the scattering contributions from the sample container and background in a similar way to neutron diffraction [30].

The single scattered intensity measured for a sample, $I_S(Q)$, is given by

$$I_S(Q) = aN_S\left[\frac{d\sigma}{d\Omega}(Q)\right]^X_{\text{Total}}, \tag{2.49}$$

where a is the calibration coefficient. The total X-ray differential scattering cross section and total X-ray structure factor is

$$\begin{aligned}\left[\frac{d\sigma}{d\Omega}(Q)\right]^X_{\text{Total}} &= \left[\frac{d\sigma}{d\Omega}(Q)\right]^X_{\text{Ray-T}} + \left[\frac{d\sigma}{d\Omega}(Q)\right]^X_{\text{Compton}} \\ &= F(Q) + \sum_\alpha c_\alpha f_\alpha(Q)^2 + \left[\frac{d\sigma}{d\Omega}(Q)\right]^X_{\text{Compton}}\end{aligned} \tag{2.50}$$

$$F(Q) = \left[\frac{d\sigma}{d\Omega}(Q)\right]^X_{\text{Total}} - \sum_\alpha c_\alpha f_\alpha(Q)^2 - \left[\frac{d\sigma}{d\Omega}(Q)\right]^X_{\text{Compton}}. \tag{2.51}$$

Figure 2-5 summarizes the data corrections procedure for a X-ray diffraction experiment.

2.6 Coordination Numbers

In a given range r, where all the partial pair distribution functions are zero except the α-β partial pair distribution function $g_{\alpha\beta}(r)$, the mean coordination number $\bar{n}_{\alpha}^{\beta}$ is calculated by

$$\bar{n}_{\alpha}^{\beta} = \frac{4\pi n_0}{c_\alpha b_\alpha b_\beta} \int_{r_1}^{r_2} [G(r) - G(0)] r^2 dr. \tag{2.52}$$

The first peak in $g_{\alpha\beta}(r)$ contains the nearest-neighbor information mentioned above. Assuming is does not overlap with other $g_{\alpha\beta}(r)$ functions then the structural information can be accessed directly from the total pair distribution function. However, most of the times it is necessary to take into account the effects of overlapping peaks and Fourier transform artefacts. The following sub-sections describes the programs used to fit the total pair distribution functions for X-rays and neutrons. These two techniques allow access to wide Q range domains and thus offer a good resolution of bond lengths and numbers of first neighbors. Table 2.1 summarizes a comparison and the main information possible to obtain between XRD and ND.

2.6.1 PXFIT

PXFIT is a program [39] to fit the pair distribution function measured by X-ray diffraction. The computational method for the fitting has a subroutine that calculates the peak function for a given set of parameters ($r_{\alpha\beta}$, $\sigma_{\alpha\beta}$, $\bar{n}_{\alpha}^{\beta}$) and a least squares subroutine that optimizes the parameters of the peak, so it fits the experimental $T(r)$ function as closely as possible, where

$$T(r) = D(r) + T^0(r), \tag{2.53}$$

and $T^0(r) = 4\pi n_0 r$. The function $T(r)$ can also be written as

$$T(r) = 4\pi n_0 r[G(r) - G(0)]. \tag{2.54}$$

The contribution to the distinct scattering $S_X(Q)$ from each atom pair (α, β) is weighted by the form factor $f_\alpha(Q) f_\beta(Q)$, i.e, it decays strongly with increasing Q.

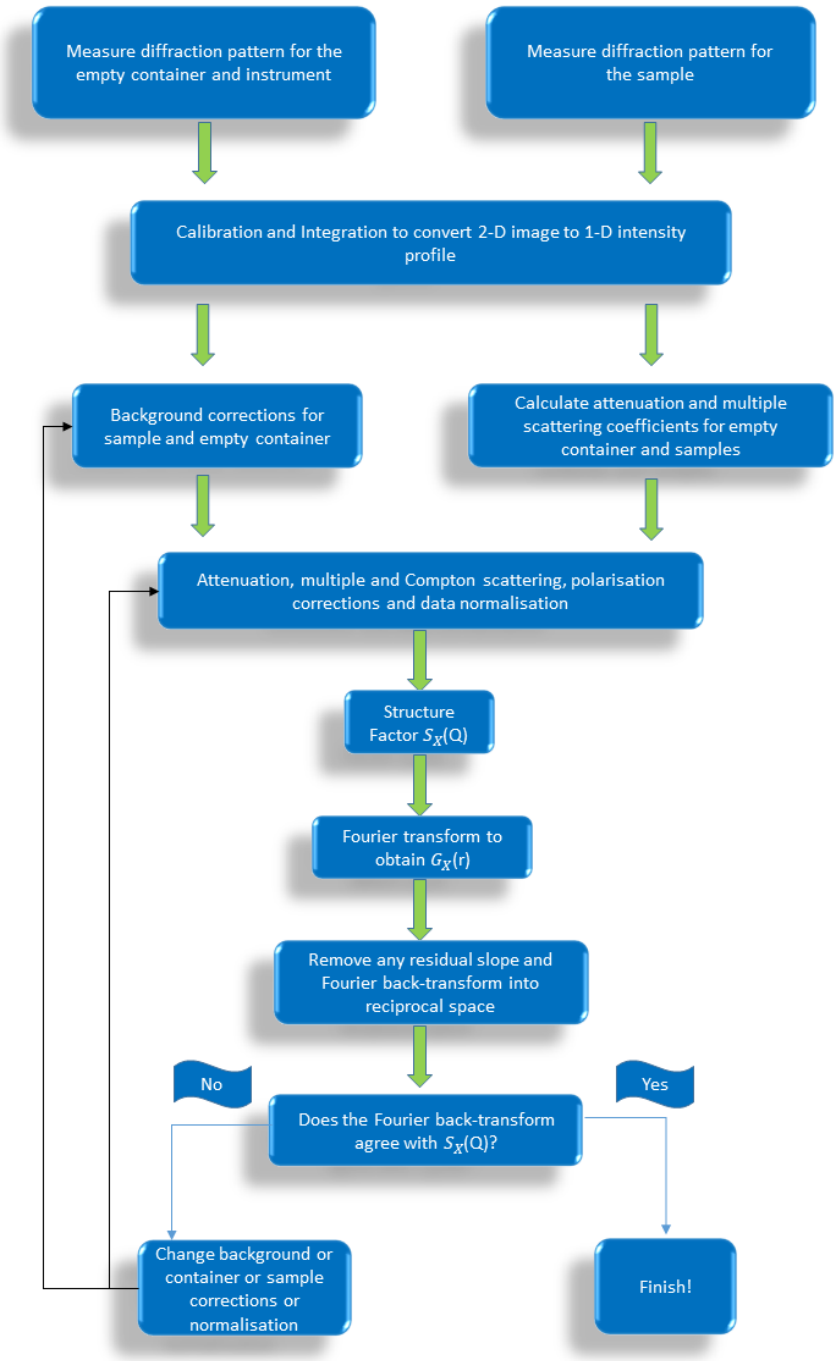

Figure 2-5: Data analysis procedure for an X-ray experiment.

X-ray Diffraction	**Neutron Diffraction**
Interaction with the electronic cloud	Interaction with the nucleus
$f(Q, E_0)$ atomic form factor	b neutron scattering length
Strong variation of scattered intensity with θ	Constant, independent of θ
Information on high Z elements	Almost independent from Z
Weak scattering for low Z elements	Light elements are visible
Weak difference for elements with close Z	Distinction of elements with close Z
f varies with energy (anomalous scattering)	b can vary at some energies for some elements (anomalous scattering limited)
f cannot distinguish isotopes from the same element	b varies among isotopes of the same element (isotopic substitution)
Small samples	Large samples
Radiation can cause damage	Radiation can cause activation
No magnetic information	Magnetic information is possible
Experiments are quick	Experiments can take several hours

Table 2.1: Comparison between X-ray and neutron diffraction.

The function $p^i_{\alpha\beta}(Q)$ is Fourier transformed using the same modification function and $Q_{\max}$, as has been used to obtain the experimental $T(r)$. The calculation of the peak function starts in reciprocal space, but the fitting is performed in real space. In order to distinguish between features in $D(r)$ that describe the glass structure from those that are an artifact of $M(r)$, each peak i in $rg_{\alpha\beta}(r)$ can be represented by the Gaussian function

$$p^i_{\alpha\beta}(r) = \frac{1}{4\pi n_0}\frac{\bar{n}^\beta_\alpha(i)}{c^i_\beta r^i_{\alpha\beta}}\frac{1}{\sqrt{2\pi}\sigma^i_{\alpha\beta}}\exp\left[-\frac{(r-r^i_{\alpha\beta})^2}{2(\sigma^i_{\alpha\beta})^2}\right]. \tag{2.55}$$

The contribution of each peak $p^i_{\alpha\beta}(r)$ to $S(Q)-1$ is given by

$$p^i_{\alpha\beta}(Q) = W^i_{\alpha\beta}\frac{\bar{n}^\beta_\alpha}{c^i_\beta}\frac{\sin(Qr^i_{\alpha\beta})}{Qr^i_{\alpha\beta}}\exp\left[-\frac{Q^2(\sigma^i_{\alpha\beta})^2}{2}\right], \tag{2.56}$$

and

$$W^i_{\alpha\beta} = \frac{(2-\delta_{\alpha\beta})c^i_\alpha c^i_\beta f^i_\alpha(Q) f^i_\beta(Q)}{\langle f(Q)\rangle^2}, \tag{2.57}$$

where $\delta_{\alpha\beta}$ is the Kronecker delta. Each $p^i_{\alpha\beta}(Q)$ function is Fourier transformed to real space using the same $M(Q)$ function as used for the experimental data. For a selected region in r-space, the method of least squares is then used to fit an appropriate sum of these Fourier transforms to $T(r)\otimes M(r)$. Coordination numbers and peak positions were calculated from $T(r)$ by PXFIT.

2.6.2 RDFgenfit

RDFgenfit is a program to fit the pair distribution function measured by neutron diffraction [40]. The program is written in python and uses the Scipy curve fitting routine [41] to calculate $D_{\text{fit}}(r)$ and refine the peak parameters $r_{\alpha\beta}(i)$, $\sigma_{\alpha\beta}(i)$ and $\bar{n}^\beta_\alpha(i)$ by the least-squares method. It reads $D_{\exp}(r)$; the r range that the data is fitted; the sample properties; such as weighting factors ($w_{\alpha\beta}$), concentration of second species (c_β) and number density (n_0); and experimental details such as $Q_{\max}$.

After inserting their details, an initial guess of peak parameters with minimum and maximum values is given and $D_{\text{fit}}(r)$ is calculated from those. The output file of the program displays $D_{\exp}(r)$, $D_{\text{fit}}(r)$, R_χ and each peak's contribution to $D_{\text{fit}}(r)$. The

peak parameters can be refined and constrained to get the best agreement between $D_{\mathrm{exp}}(r)$ and $D_{\mathrm{fit}}(r)$, i.e, where R_{χ} is as close to zero as possible.

Chapter 3

Instrumentation

In this chapter, a description of the neutron and X-ray instrumentation used is given along with the NMR and Raman spectroscopy theory. Neutron diffraction experiments were performed using the nuclear reactor at the Institut Laue Langevin (ILL) in Grenoble and the ISIS pulsed neutron source at the Rutherford Appleton Laboratory in Didcot. The X-ray diffraction experiments were perfomed at the Advanced Photon Source (APS) in Chicago.

3.1 The ISIS Spallation Neutron Source

At ISIS the neutrons are produce by a process called spallation. An example of a typical spallation reaction is given by

$$^{184}_{74}\mathrm{W} + p \longrightarrow F^* + G^* + 20n + \text{ Energy}, \tag{3.1}$$

where F^* and G^* are the fragments of the original $^{184}_{74}$W nucleus.

An ion source produces H^- ions which are accelerated and separated into bunches by a Radio Frequency Quadrupole (RFQ) accelerator at regular intervals. Each bunch is then accelerated in a linear accelerator (LINAC) to 70 MeV [43]. When the H^- ions enter the synchrotron, a thin Al_2O_3 foil strips off the electrons, leaving a beam of protons. The synchrotron has a 163 m circumference ring of magnets that bend and focus the beam into a circle.

The proton beam at 800 MeV is guided towards target Station 1 and target Station 2 as shown in Figure 3-1. The proton pulses are extracted at a rate of 50 Hz, with 4/5 of

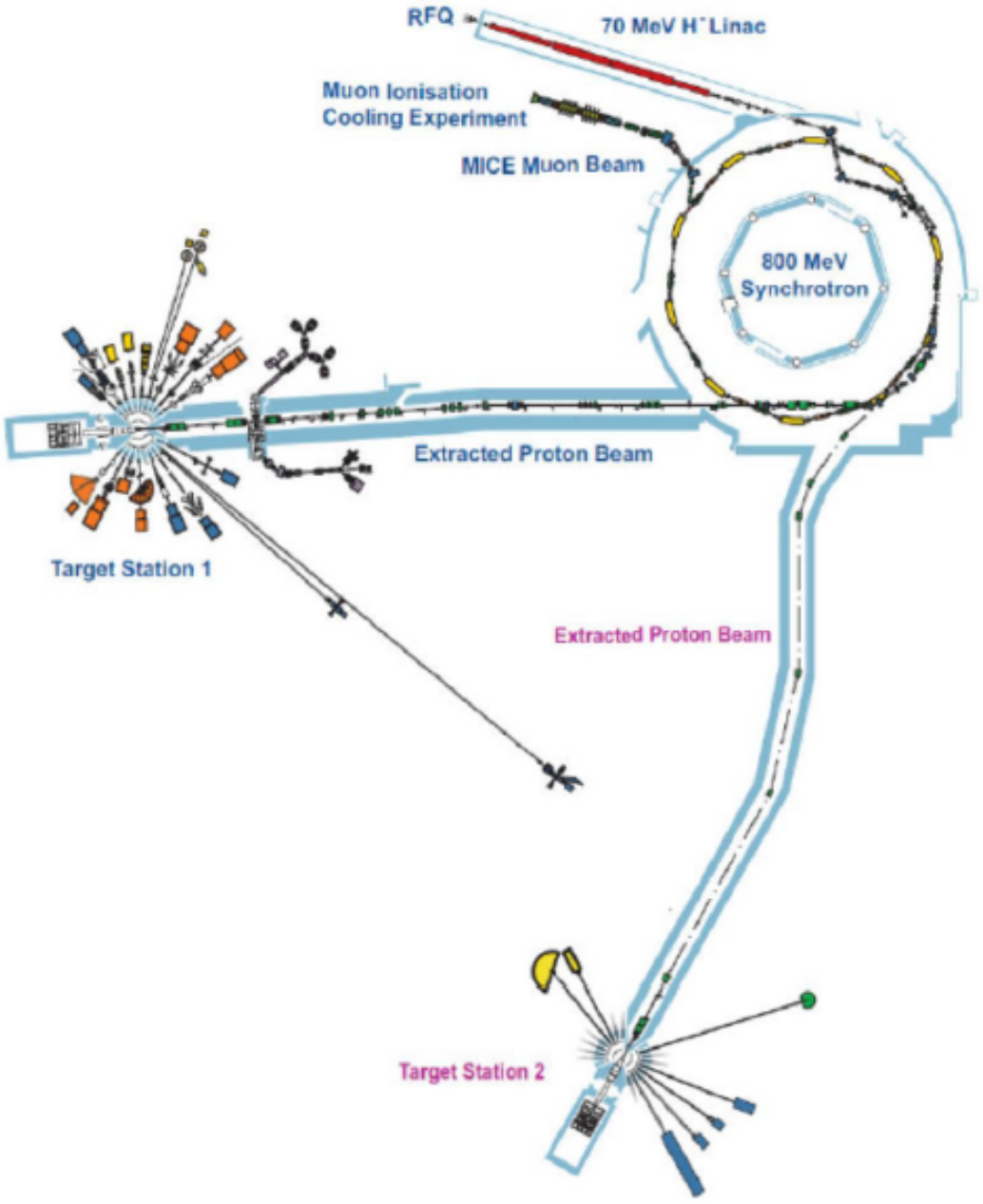

Figure 3-1: Schematic Representation of the ISIS spallation neutron source [42].

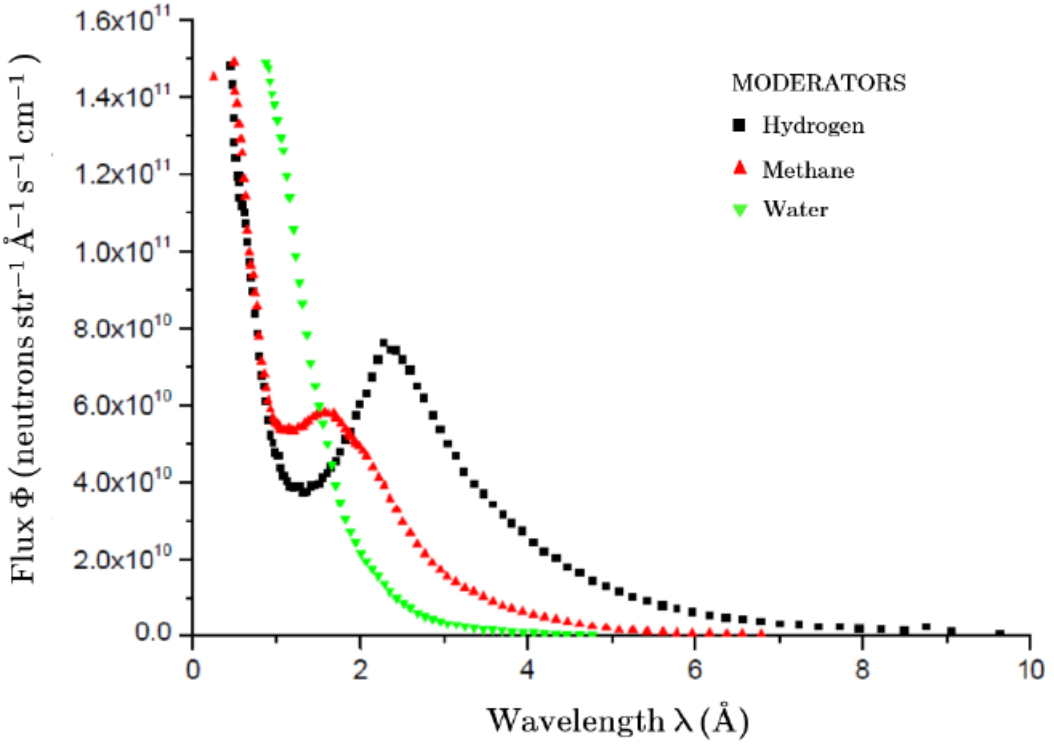

Figure 3-2: The energy/wavelength distributions of the three moderators used at ISIS [45].

the pulses guided to target station 1 and 1/5 guided to target station 2. They are then fired at a tungsten target where the neutrons are produced as a result of the spallation process.

These high intensity neutron pulses are then slowed down by moderators in order to give a suitable wavelength distribution. Three moderators (figure 3-2) with different energy/wavelength distributions are available at ISIS: hydrogen-, methane- and water-based [44]. Neutrons that have reached thermal equilibrium with the moderator have a Maxwellian distribution of energies with a peak that is characteristic of the moderator temperature. Finally, the neutrons arrive at the neutron diffractometers, in this case GEM, located at Target Station 1.

3.1.1 The GEM Diffractometer

The GEneral Materials diffractometer, GEM, as shown in figure 3-3, is an instrument to study both amorphous and crystalline materials. An important characteristic of GEM is the detector array, divided into 9 detector banks, which covers a large area (7.270 m^2)

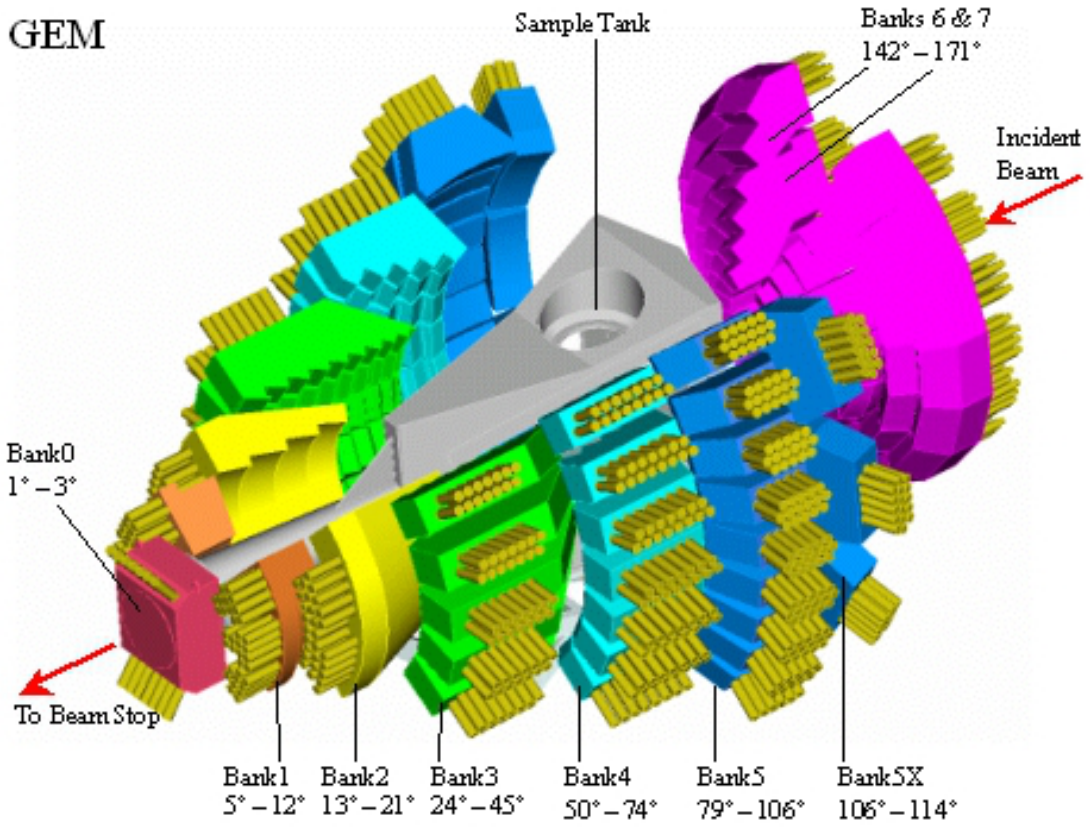

Figure 3-3: Schematic Representation of the GEM diffractometer [47].

and a large range in scattering angles from 1.2° to 171.4°. These two characteristics provide data with high counting rate, low signal to noise ratio and large Q-range [46].

GEM receives neutrons after they have been slowed down by a liquid methane moderator at temperatures between 100 and 110 K. The primary flight path from moderator to sample has a length $L_1 = 17$ m. Neutron-absorbing $^{10}B_4C$ slits are used to define the beam shape and a series of choppers are used to reduce background scattering from the beam and define an energy range of neutrons that prevents consecutive pulses of neutrons from overlapping. The incident beam passes through four beam monitors to measure the incident flux.

The secondary flight path, L_2, varies depending on the scattering angle ranging from 1.0 to 2.8 m (1.21° to 171°, respectively). Table 3.1 gives the average scattering angle for each detector bank. The detectors used on GEM are Li-based ZnS scintillators where the neutron and lithium reacts via

Detector Bank	Scattering Angle $2\theta(^\circ)$
1	2.2
2	9.0
3	17.5
4	35.1
5	62.4
6	92.8
7	110.1
8	146.1
9	160.7

Table 3.1: Average scattering angle for each of the nine detector banks of the GEM diffractometer.

$$\text{neutron} + {}^{6}_{3}\text{Li} \longrightarrow {}^{3}_{1}\text{H}^{2-} + {}^{4}_{2}\text{He}^{2+}, \tag{3.2}$$

to produce an electrical signal.

The sample is contained within an evacuated steel tank with aluminium windows between the sample and detectors to reduce background scattering. A long flight path and access to high energy neutrons from the spallation source leads to high-Q resolution in reciprocal space. The scattering vector has a wide range of 0.15 $\text{Å}^{-1} \leq Q \leq 60$ Å^{-1}, which minimizes Fourier transform artefacts and improves real-space resolution when doing pair distribution function analyse.

The neutron wavelength is calculated from the time-of-flight technique. It starts by measuring the time of flight t taken for a neutron to travel a total flight path L from the moderator to the detector. The De Broglie equation is

$$\lambda = \frac{h}{m_n v}, \tag{3.3}$$

where h is Planck's constant, m_n is the neutron mass and v is the neutron velocity which can be calculated from the distance and the time taken

$$v = \frac{L_1 + L_2}{t}, \tag{3.4}$$

where L_1 is the moderator sample-distance and L_2 is the sample-detector distance.

Using equation 2.5, the scattering vector can be rewritten as

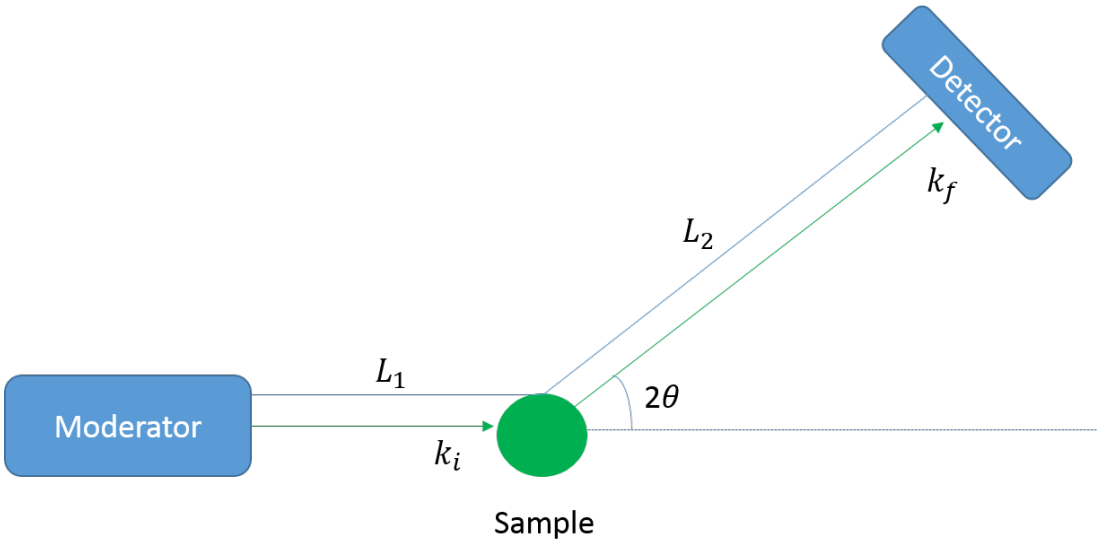

Figure 3-4: Schematic representation of a time-of-flight diffraction experiment.

$$Q = \frac{4\pi m}{ht}(L_1 + L_2)\sin(\theta). \tag{3.5}$$

Figure 3-4 shows a schematic representation of the time-of-flight process.

3.2 The Institut Laue-Langevin (ILL) Neutron Reactor Source

The ILL is a reactor source where the neutrons are produced in a nuclear fission reaction process, via

$$^{235}_{92}\mathrm{U} + {}^{1}n \longrightarrow {}^{91}_{36}\mathrm{Kr}^{*} + {}^{145}_{56}\mathrm{Ba}^{*} + \mathrm{Energy} \tag{3.6}$$

$$^{91}_{36}\mathrm{Kr}^{*} + {}^{145}_{56}\mathrm{Ba}^{*} \longrightarrow {}^{90}_{36}\mathrm{Kr} + {}^{144}_{56}\mathrm{Ba} + 2n + \gamma, \tag{3.7}$$

where the unstable nuclei are denoted by asterisk.

A small quantity of the emitted neutrons sustains the chain reaction while the majority of neutrons are used for neutron scattering experiments after being slowed down by a moderator [48]. This works because of a series of collisions with the nuclei of the moderating material, which reduces the kinetic energy of the neutrons.

The ILL has different types of moderators that provides a range of energies, and hence wavelengths, for the experiments. The moderators used are a hot graphite source at 2400 K, a thermal D_2O source at 300 K and two cold D_2 sources at 20 K. A representation of the reactor source is shown in Figure 3-5.

3.2.1 The D4c Diffractometer

D4c is a high precision diffractometer mostly dedicated for the study of disordered materials. It has low background and high count rate, which enables high precision measurements over the entire accessible Q range. It is one of the instruments that receive neutrons from the hot graphite moderator [50]. A representation of D4c is given in figure 3-6 and a photograph of the instrument is shown in figure 3-7.

The neutrons are selected from a copper monochromator, wich provides three possible wavelengths of 0.35 Å, 0.5 Å or 0.7 Å corresponding to the lateral faces of (331), (220) and (200). To remove harmonic $\lambda/2$ contamination, the neutrons are passed through a Rh filter for $\lambda = 0.5$ Å [50], which was the wavelength used in this work. To reduce background scattering, collimation is provided by neutron absorbing materials such as boron, cadmium or gadolinium. Figure 3-8 shows a schematic representation of a neutron diffraction experiment at the ILL neutron source.

To normalize the incident beam intensity, the neutron flux is measured by a monitor

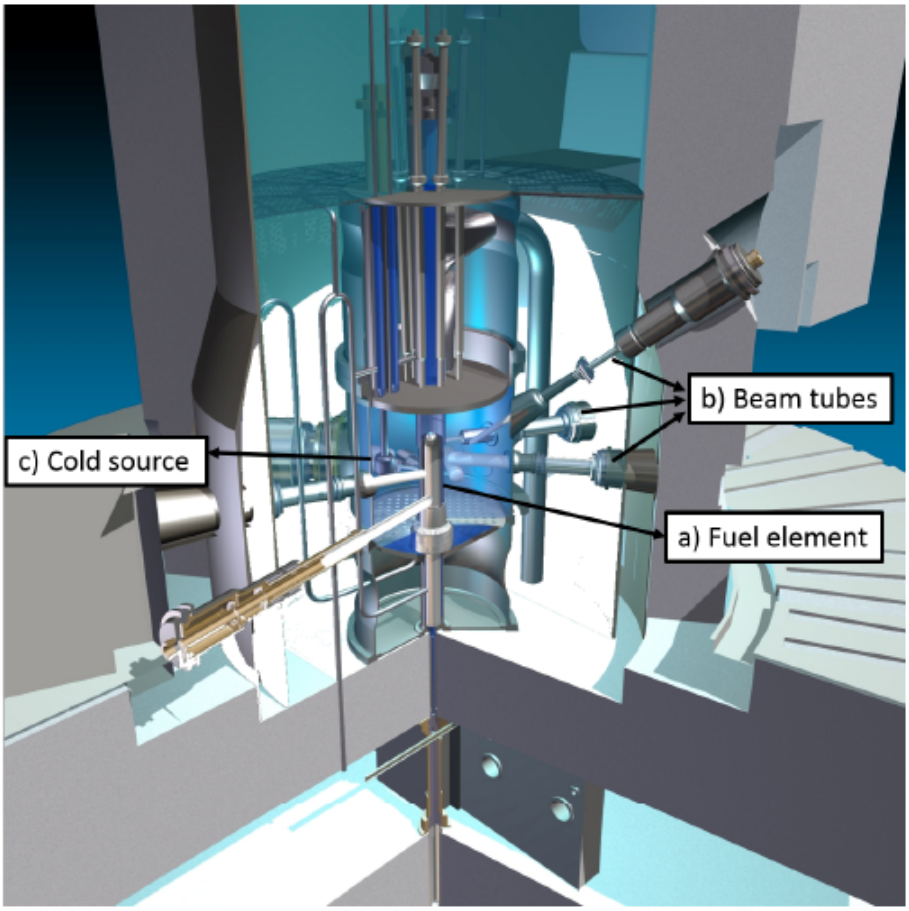

Figure 3-5: A 3D image of the reactor at the ILL [49].

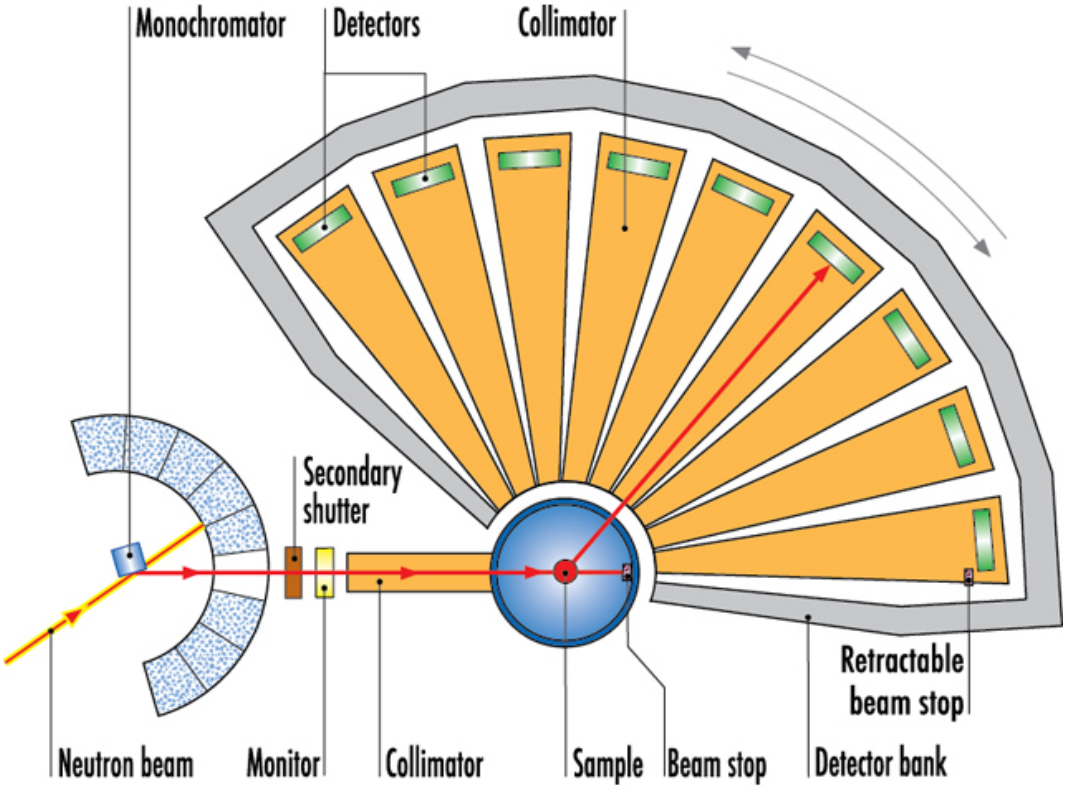

Figure 3-6: Representation of the D4c instrument at the ILL [51].

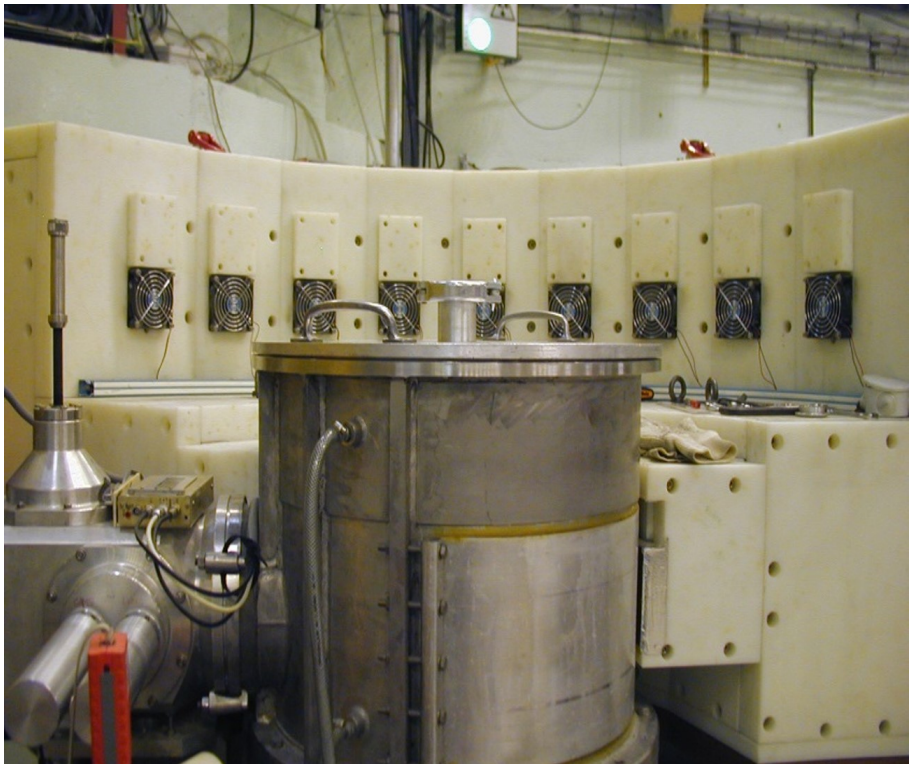

Figure 3-7: The diffractometer D4c at ILL. The aluminium bell jar contains the sample holder and the detector array is held within the white polymer shielding.

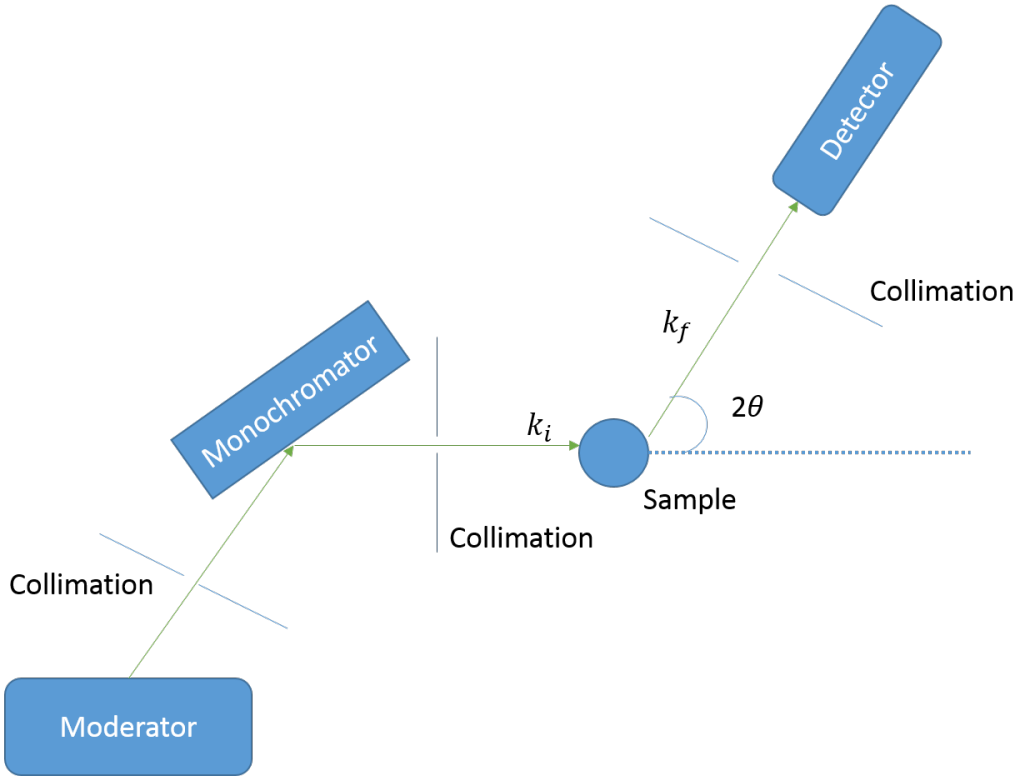

Figure 3-8: Schematic representation of a diffraction experiment at a continuous neutron source.

placed between the monochromator and the beam-slits [50]. Beam-slits adjust the beam geometry giving a maximum illuminated height of 5 cm in the vertical direction and width of 2 cm in the horizontal direction. The sample is contained within an evacuated aluminium bell jar and each detector has its own evacuated collimation tube to minimize background scattering. Background scattering originating from the beam is reduced by beamstops, which prevent any direct pathway between straight-through beam and detector.

The D4c diffractometer has 9 detector banks that operate with ^{3}He detection gas, which reacts with the incoming neutron to form charged particles via

$$\text{neutron} + {}^3_2\text{He} \longrightarrow {}^3_1\text{H}^- + \text{proton}. \tag{3.8}$$

These charged particles interact with the microstrip detectors to produce an electrical signal. The detector array can be rotated around the sample position to obtain data for an angular range of $1.5\ ^\circ \leq 2\theta \leq 137\ ^\circ$. The Q range covered by the detector depends on the selected incident wavelength and can be calculated using equation 2.5 as,

$$\begin{aligned} 0.5\ \text{Å}^{-1} \leq Q \leq 33.4\ \text{Å}^{-1} \text{ for } \lambda = 0.35\ \text{Å}, \\ 0.3\ \text{Å}^{-1} \leq Q \leq 23.4\ \text{Å}^{-1} \text{ for } \lambda = 0.5\ \text{Å}, \\ 0.2\ \text{Å}^{-1} \leq Q \leq 16.7\ \text{Å}^{-1} \text{ for } \lambda = 0.7\ \text{Å}. \end{aligned} \tag{3.9}$$

To determine the relative efficiency of each detector cell the diffraction pattern of a vanadium rod is measured. All detector cells will then be normalized with respect to each other and with a relative scaling factor for each detector cell.

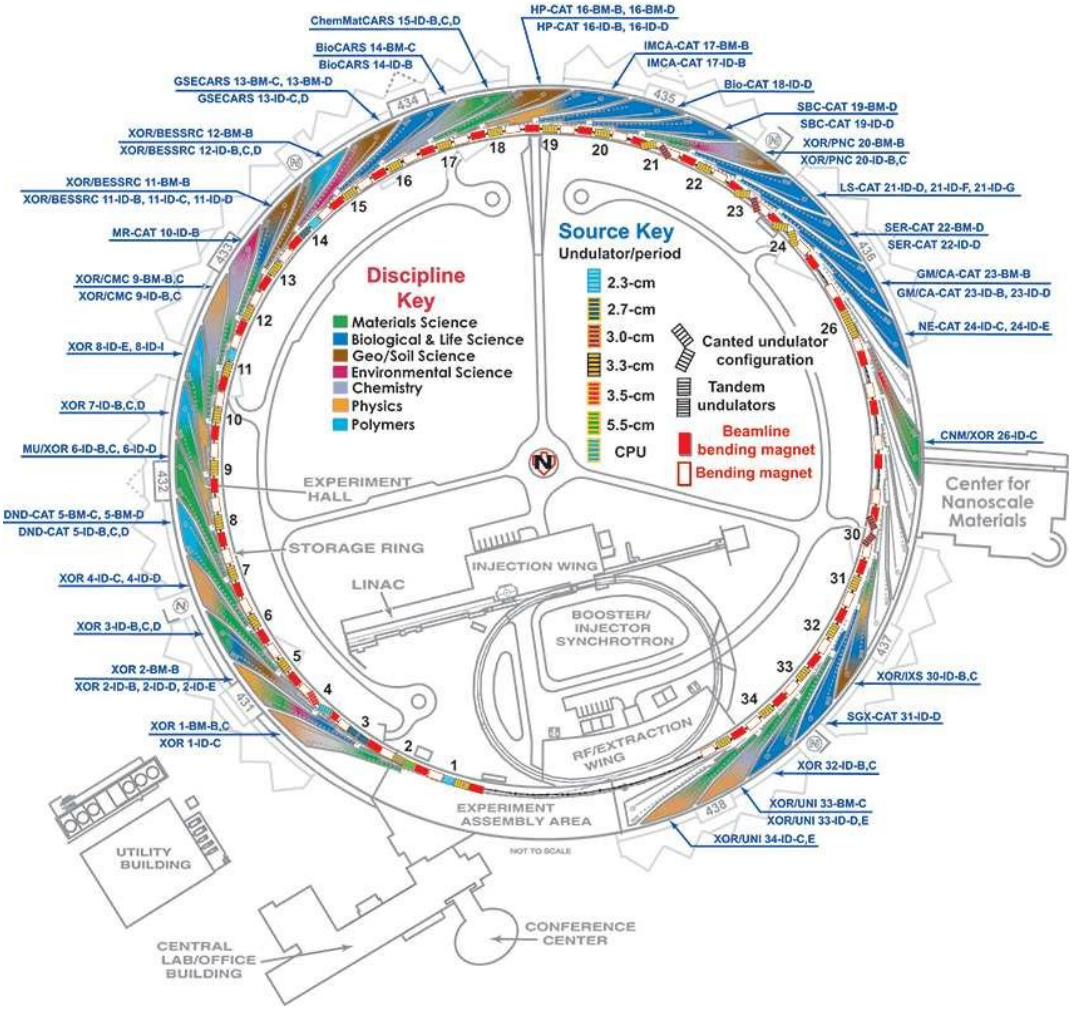

Figure 3-9: Schematic Representation of the Advanced Photon Source (APS) at the Argonne National Laboratory, USA [52].

3.3 The Advanced Photon Source

The Advanced Photon Source (APS) (figure 3-9) produces X-ray beams with high energy and high brightness. It consists of a linear accelerator, a booster synchrotron, an electron storage ring and an experiment hall. To produce the X-ray beams, a cathode is heated to approximately 1000 °C which emits electrons. The electrons enter the linear accelerator were they are accelerated to 450 MeV by high voltage alternating electric fields [53]. The electrons will then be injected into the booster synchrotron were they are accelerated from 450 MeV to 7 GeV in 1.5 seconds (99.9999% of the speed of light) by electrical fields in radio frequency cavities. The high speed electrons will be injected into the storage ring which has a circumference of 1104 m. The storage

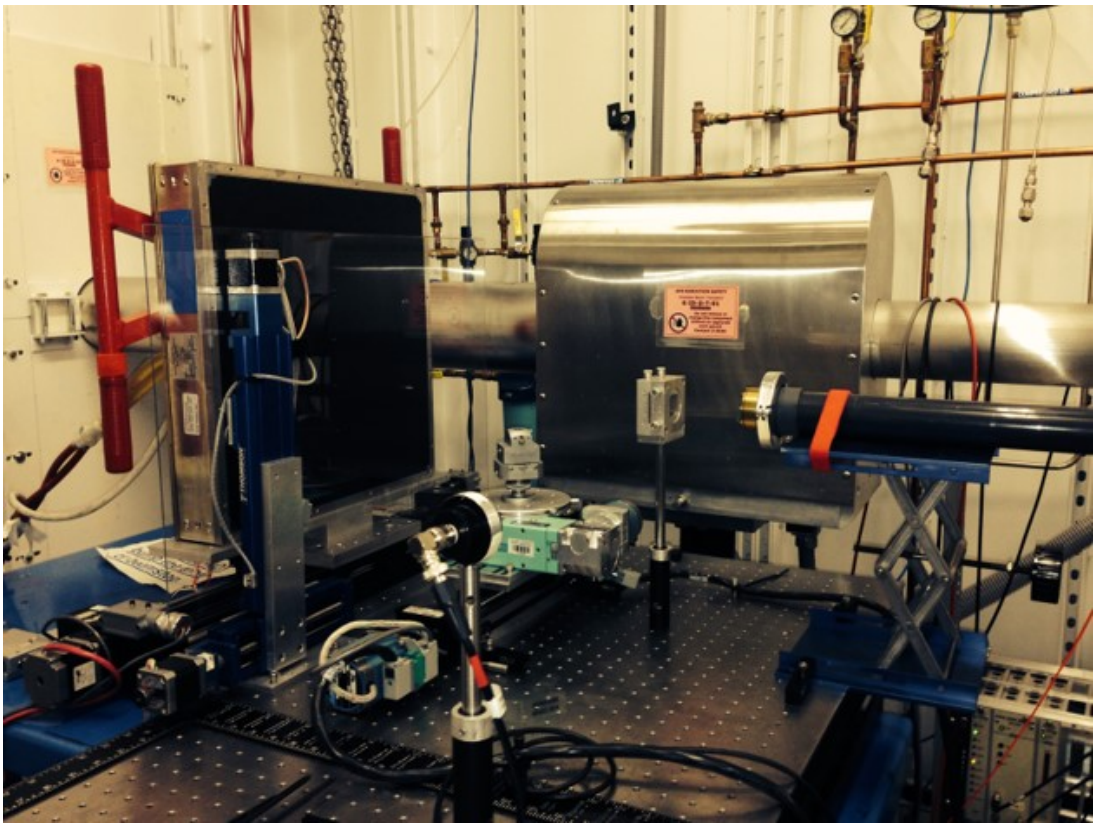

Figure 3-10: The 6-ID-D diffractometer at APS.

ring has more than 1000 magnets that produce a very narrow beam.

3.3.1 The 6-ID-D Diffractometer

The 6-ID-D diffractometer is situated in Sector 6 at the APS (Figure 3-9). This X-ray beamline produces high energies which varies between 50 to 130 KeV, which are commonly used for magnetic X-ray scattering, high energy X-ray diffraction and powder diffraction. The selection of the photon energy is made by the monochromator, which in this case is a silicon mono-crystal with (311) planes in reflection and the detector is an amorphous silicon area detector [54]. The 6-ID-D diffractometer can be seen in figure 3-10.

The detector has 2048×2048 pixels across, with each pixel 200 × 200 μm wide. The scintillator layer consists of 500 μm thick thallium doped CsI crystals. The 2048×2048 array is made of 16×8 subpanels each 128 pixels horizontally and 256 pixels vertically [55]. The subpanels offset are dealt with by a dark image subtraction.

3.4 Nuclear Magnetic Resonance Spectroscopy

Nuclear Magnetic Resonance Spectroscopy (NMR) is a technique which takes advantage of the magnetic properties of an atomic nuclei of a certain element that has a non-zero spin. The nuclei of a certain element will absorb and re-emit energy in the form of electromagnetic radiation. This energy has a specific resonance frequency, which is dependent on the magnetic properties of the isotope of the atom and on the strength of the applied magnetic field.

During an NMR experiment a constant magnetic field is applied to the sample to polarize or align the magnetic nuclear spins. A radio frequency pulse is then applied to perturb the alignment of the nuclear spins. The two fields are chosen to be perpendicular to each other in order to maximize the NMR signal strength. The response by the total magnetization of the nuclear spins of the material studied can give information on structure, chemical environment, dynamics and reaction state of molecules.

These nuclei have a magnetic moment, μ, given by

$$\mu = \gamma I, \tag{3.10}$$

where γ is the gyromagnetic ratio specific to each nucleus. In the absence of an external magnetic field B_0, the magnetic moments of nuclei are oriented randomly in space and there is no energy difference for a particular orientation. When its present, μ interacts with B via the Hamiltonian $\mu \cdot B_0$, producing energy levels, i.e, a splitting between the nuclear spin levels. This effect is called the Zeeman interaction [56]. For the common $I = 1/2$ (^{31}P, ^{29}Si) case, the difference between the energy levels is given by

$$\Delta E = \hbar \gamma B_0, \tag{3.11}$$

where $\hbar$ is the reduced Planck constant.

In the Zeeman effect, the splitted nuclei is able to absorb radio-frequency radiation of the exact energy ΔE. This excites the transition of some nuclear spins to higher energy levels. The excited spins then return to the ground state due to relaxation processes and release energy into the lattice. The two types of relaxation are spin-lattice (longitudinal) relaxation and spin-spin (transversal, energy conversing) relaxation. However, the magnetic moments being in B_0 are not perfectly aligned with it. They precess around the axis of B_0 with a frequency specific for each isotope called the Larmor frequency which is given by

$$w = -\gamma B_0. \tag{3.12}$$

The excitation radio frequency should match the Larmor frequency otherwise the NMR phenomenon cannot be observed.

Different nuclei such as ^{27}Al, ^{29}Si, ^{31}P; do not resonate all at the same frequency due to the magnetic shielding effect of the electrons. They will experience different local magnetic fields and hence give signals at different frequencies. The different local magnetic fields due to interactions with a nucleus' neighbors in the first and second coordination spheres will slightly change the ΔE. This small change in the energy levels causes a change in the frequency required for the transitions of nuclei from one energy level to a higher one. In other words, different degree of nuclear shielding will give different peaks in an NMR spectrum. The chemical shift, δ, is given by

$$\delta = \frac{w_s - w_{ref}}{w_{ref}}, \tag{3.13}$$

where w_s is the Larmor frequency of a nucleus and w_{ref} is the Larmor frequency of the same isotope in a specific reference.

A quadrupolar nucleus is a nucleus with a spin quantum number greater than 1/2. For example, nuclei ^{17}O and ^{27}Al have spin 5/2. Unlike in the nuclei with the spin 1/2, such as ^{1}H and ^{29}Si, the Zeeman splitting for such nuclei gives more than two energy levels. NMR signals of such nuclei are typically complicated due to strong quadrupolar interactions causing complex line broadening as well as the appearance of several lines arising from the various allowed energy transitions.

In solid state NMR spectroscopy lines are broad due to anisotropic nuclear spin interactions. They are much broader than in liquid state NMR. In liquids, these interactions are averaged out because of the rapid motion of the particles. To improve the spectral resolution by narrowing the NMR lines, the MAS NMR technique is used [57]. This technique involves spinning a sample at the "magic angle" of $\theta_m = 54.74°$ to the magnetic field B_0 (Figure 3-11). Such spinning removes dipolar interactions and averages chemical shift anisotropy and the first order quadrupolar interactions. It improves the quality of a spectrum and permits the analysis and quantification of NMR lines. Elements with $I > 1/2$ need a second order treatment. The first order term is removed by magic angle spinning (MAS) and the second order term is removed by triple quantum magic angle spinning (3Q MAS). The 3Q MAS NMR technique [58] is able to switch between two angles, therefore removing the second order term and cancelling out the

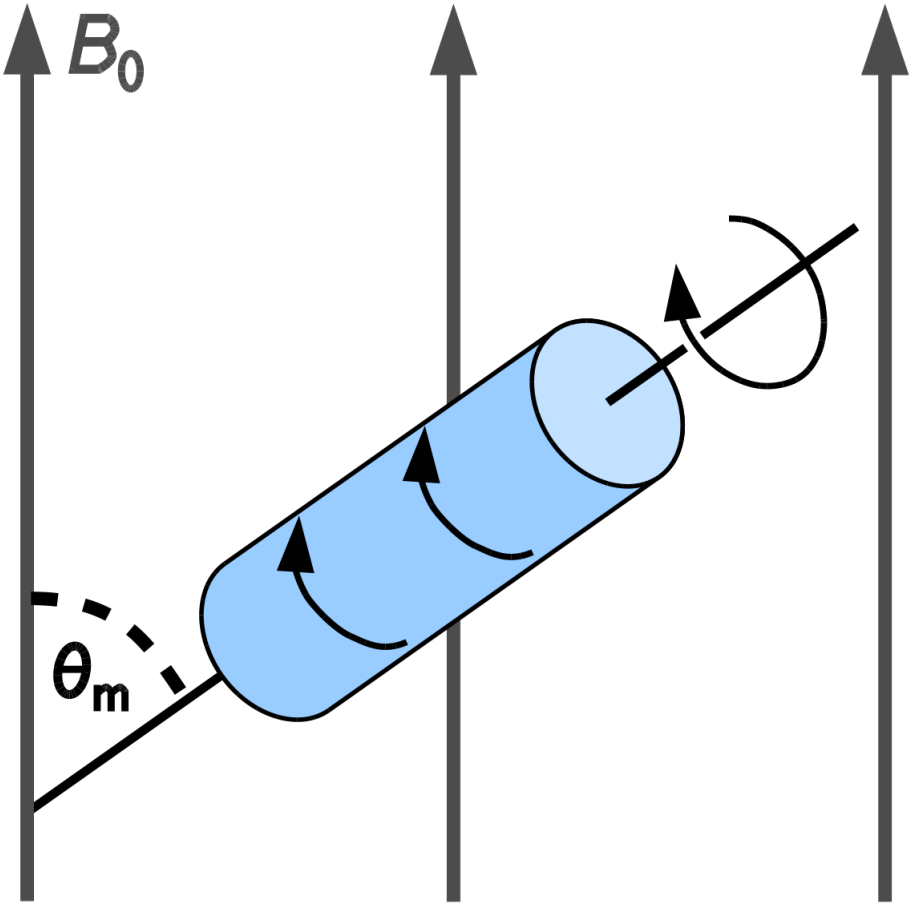

Figure 3-11: Illustration of the Magic Angle Spinning (MAS) technique. A sample is rotating in a magnetic field, B_0, at the angle $\theta_m = 57.4°$. Reproduced from [59].

quadrupolar interaction.

MAS NMR and 3Q MAS NMR spectroscopies have been used extensively to look at ^{29}Si and ^{27}Al in the structure of aluminosilicate glasses. MAS NMR is sensitive to the local chemical structure in glasses such as tetrahedral bond angles, bond distances and the fraction of bridging oxygen atoms. The absorption frequency of the probe nucleus will shift depending on the degree to which nearby electrons shield the probe nucleus from the external magnetic field. Different bonding sites or environments of the nuclei will shield the probe nucleus differently so the bonding environment of the probe nucleus is deduced from the absorption frequency shift in the data.

All the measurements in this work were carried out using a Bruker DSX 500 (figure 3-12) spectrometer at a magnetic field of 16.4 T (182.34 MHz resonance frequency).

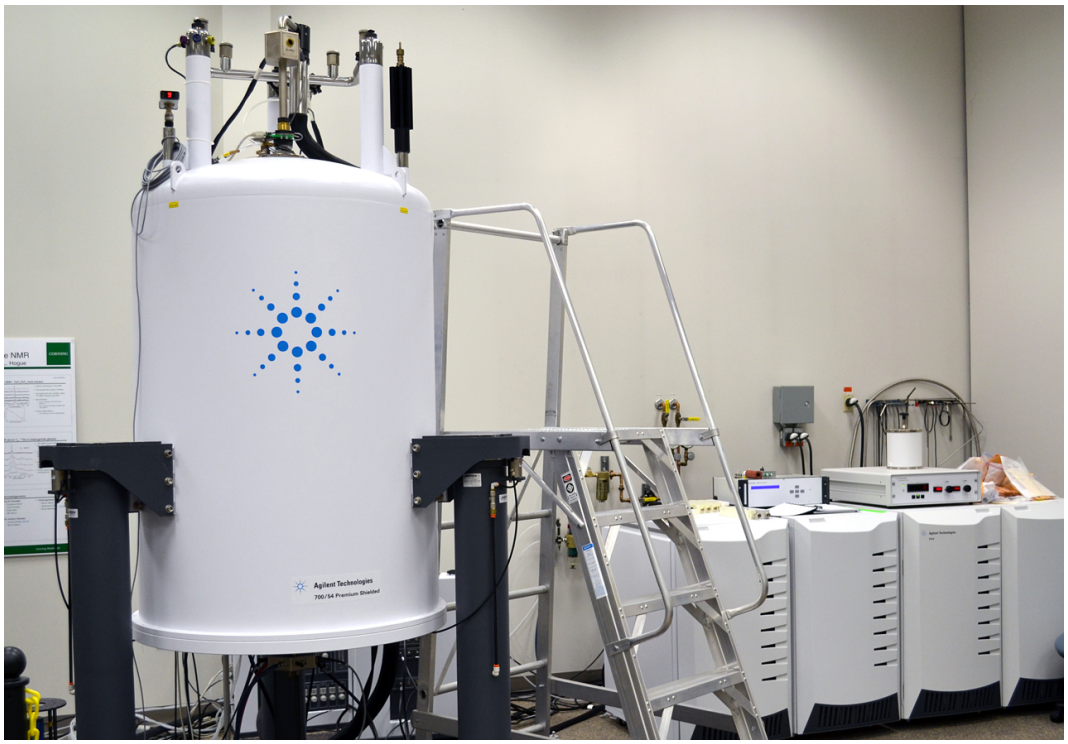

Figure 3-12: 16.4T magnet and NMR spectrometer at Corning Inc.,USA.

The experimental details are slightly different depending on the samples used and are described in the next relevant chapters.

3.5 Raman Spectroscopy

Raman spectroscopy uses inelastic scattering of monochromatic light, in this case a laser. The laser light interacts with a molecule resulting in energy of photons being shifted up or down. This shift in the photon energy provides information about the vibrational modes in the sample, which refers to the chemical bonds and symmetry of molecules [60, 61]. For this reason, Raman spectroscopy gives a qualitative fingerprint in which a molecule can be identified.

An incoming photon excites the system from its initial state to a virtual state which depends on the photon energy, $h\nu$. This state is very unstable and the system relaxes back to a lower energy by emitting a photon. The majority of light undergoes elastic (Rayleigh) scattering when the system relaxes to its original state via the emission of a photon of identical energy. A small proportion of light experience inelastic (Raman) scattering where the system relaxes to a different state due to the interaction with a vibrational excitation. In this situation, the emitted photon will either be red-shifted as it loses energy (Stokes) or blue-shifted as it gains energy (anti-Stokes) [62]. Therefore, this process allows the determination of the various vibrational state energies in a system by analysis of the change in photon energy after scattering from the material, known as Raman spectroscopy. Figure 3-13 shows the energy levels in a material and their relation to light scattering processes.

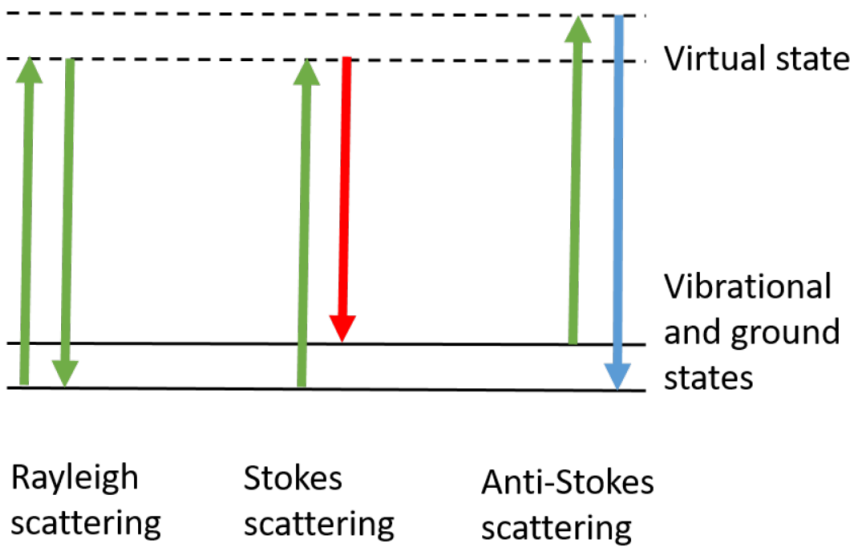

Figure 3-13: Energy diagram associated with light scattering processes.The excitation and emission processes are represented by the up and down arrows respectively.

The intensity of Raman scattered light is very weak compared to the excitation intensity. For this reason, high intensity sources such as lasers operating in the visible range of the spectrum are typically used. Although scattering occurs in all directions away from the point of excitation, many Raman spectroscopy techniques use back-scattering geometry such that only the photons travelling directly back towards the source are detected.

The mechanism of Raman scattering is treated with semi-classical theory that takes into account light as a wave of oscillating electric field which induces a displacement within a material. The energy-momentum transfer in this process is described with a quantum mechanical context by considering allowed phonon modes interacting with photons [63, 64].

The polarisation of a material perturbed by an electric field, $\vec{E}$, from a light source is

$$\vec{P} = \epsilon_0 \chi \vec{E}, \tag{3.14}$$

where ϵ_0 is the permitivity in free space and χ is the dielectric susceptibility of the material. The electric field from the incident light source has a periodic dependence on time t and space $\vec{r}$, given by

$$\vec{E}(\vec{r}, t) = \vec{E}(\vec{k}_i, \nu_i) \cos\left(\vec{k}_i \cdot \vec{r} - \frac{\nu_i}{2\pi} t\right), \tag{3.15}$$

where ν_i is the frequency and k_i is the wavevector. The dielectric susceptibility contains an oscillatory component as a consequence of the vibration of the atoms in the material. The resulting displacement in the material is

$$\vec{u}(\vec{r}, t) = \vec{u}(\vec{q}, w) \cos(\vec{q} \cdot \vec{r} - wt), \tag{3.16}$$

where w is the angular frequency ($w = 2\pi\nu$) and $\vec{q}$ is the wavevector of the phonon. Assuming that the displacement $u(\vec{r}, t)$ is small, χ can be expanded in a first order Taylor series as

$$\chi_{jk}(\vec{k}_i, w_i) \approx \chi_{jk}(\vec{k}_i, w_i) + \frac{\partial_{\chi_{jk}}(\vec{k}_i, w_i)}{\partial u_l} u_l. \tag{3.17}$$

The labels j, k, and l run over the spatial coordinates x, y and z. The polarisability is re-written as

$$P(\vec{r},\vec{u},t) \propto f(\vec{k}_i,\nu_i,\vec{q},w)\times \\ \left\{\cos\left[(\vec{k}_i+\vec{q})\cdot\vec{r}-\left(\frac{\nu_i}{2\pi}+w\right)t\right]+\cos\left[(\vec{k}_i-\vec{q})\cdot\vec{r}-\left(\frac{\nu_i}{2\pi}-w\right)t\right]\right\}, \tag{3.18}$$

where $f(\vec{k}_i,\nu_i,\vec{q},w)$ is a function containing the Raman tensors which determine the amplitude of the various allowed modes via selection rules.

Equation 3.18 shows that the polarisability contains two oscillatory terms for scattered light, $\left(\frac{\nu_i}{2\pi}+w\right)$ and $\left(\frac{\nu_i}{2\pi}-w\right)$. The corresponding transfer of momentum is $(\vec{k}_i+\vec{q})$ or $(\vec{k}_i-\vec{q})$, suggesting that the scattered light will contain photons which have either gained (+) or lost (-) energy and momentum by interaction with a particular phonon. Therefore, the conservation laws can be written as

$$h\nu_f = h\nu_i \pm \hbar w, \tag{3.19}$$

$$\vec{k}_f = \vec{k}_i \pm \vec{q}. \tag{3.20}$$

Phonon frequencies are orders of magnitude lower than the frequency of visible light and therefore the approximation $\nu_i = \nu_f$ in equation 3.19 can be made. The photon momentum is directly proportional to the frequency and the refractive index, n, of the material by $\vec{k} = 2\pi n\nu/c$ and based on the previous approximation, $\vec{k}_f \approx \vec{k}_i = \vec{k} = 2\pi n\nu/c$. From equation 3.20 the phonon momentum is $|q| = |k_f - k_i|$. During a Raman experiment using backscattering geometry, the outgoing photon travels directly back towards the source along the same path as the incoming photon. They have opposite directions $\vec{k}_f = -\vec{k}$ and $\vec{k}_i = \vec{k}$, leading to

$$|q| \approx |k_f - k_i| \approx 2k \approx \frac{4\pi n\nu}{c}. \tag{3.21}$$

The probability of a phonon occupying a particular state is calculated by Bose-Einstein statistics and therefore, their total population depends on a thermal distribution. The ratio of Stokes, I_S, to anti-Stokes, I_A intensities for a single mode is

$$\frac{I_{as}}{I_s} = \left(\frac{\frac{\nu_i}{2\pi}+w}{\frac{\nu_i}{2\pi}-w}\right)^4 \exp\left(-\frac{\hbar w}{kT}\right), \tag{3.22}$$

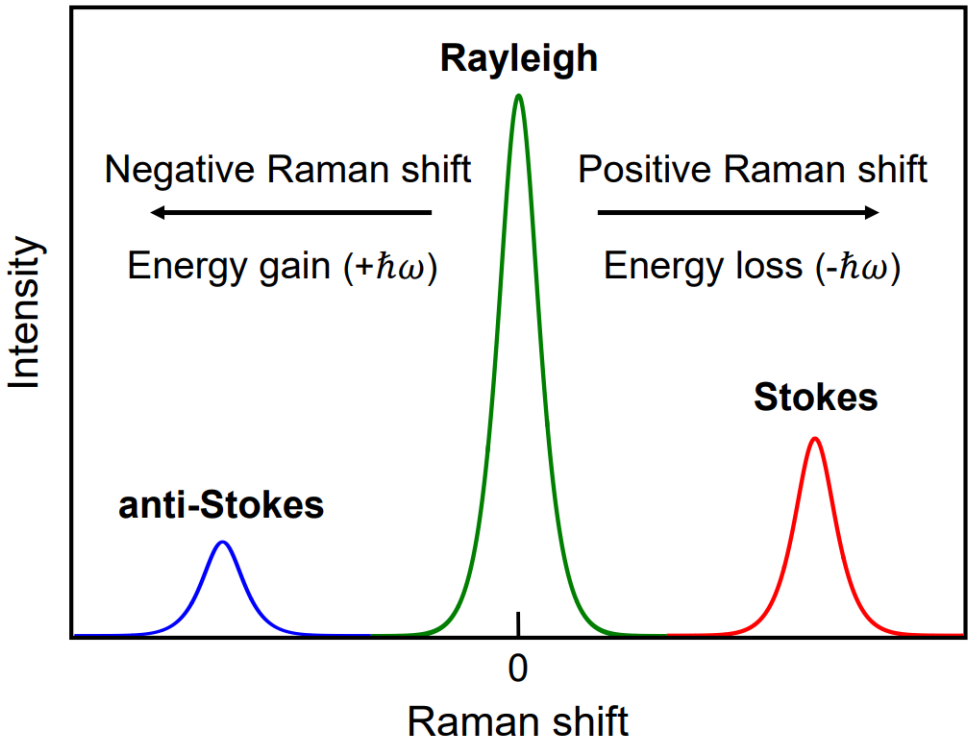

Figure 3-14: Relative intensities of different scattering processes in a Raman spectrum. The colours indicate the energy gain (blue-shifted) and energy loss (red-shifted) of the inelastic processes compared to the elastic (green) process. Reproduced from [65].

where $\hbar w$ is the energy of a particular phonon mode and T is the temperature.

At ambient conditions the intensity of Stokes scattering is much higher than that of anti-Stokes (Figure 3-14). The Rayleigh scattering is orders of magnitude larger in intensity than Raman scattering and is filtered in experiments to allow the detection of the Raman signal. The energy loss (Stokes signal) is referred to as positive shift whereas the energy gain (Anti-Stokes signal) is referred to as negative shift. The Stokes and Anti-Stokes lines will occur for each phonon frequency in the material, known as Raman bands. The lineshape of Raman bands are described by a convolution of Gaussian and Lorentzian functions.

Raman spectroscopy measurements were made using a Renishaw InVia Raman spectrometer (Figure 3-15) in backscattering geometry using a laser excitation wavelength of 532 nm with a corresponding grating of 1800 1/mm. The spectrometer laser filter has a cut-off below 60 cm^{-1}.

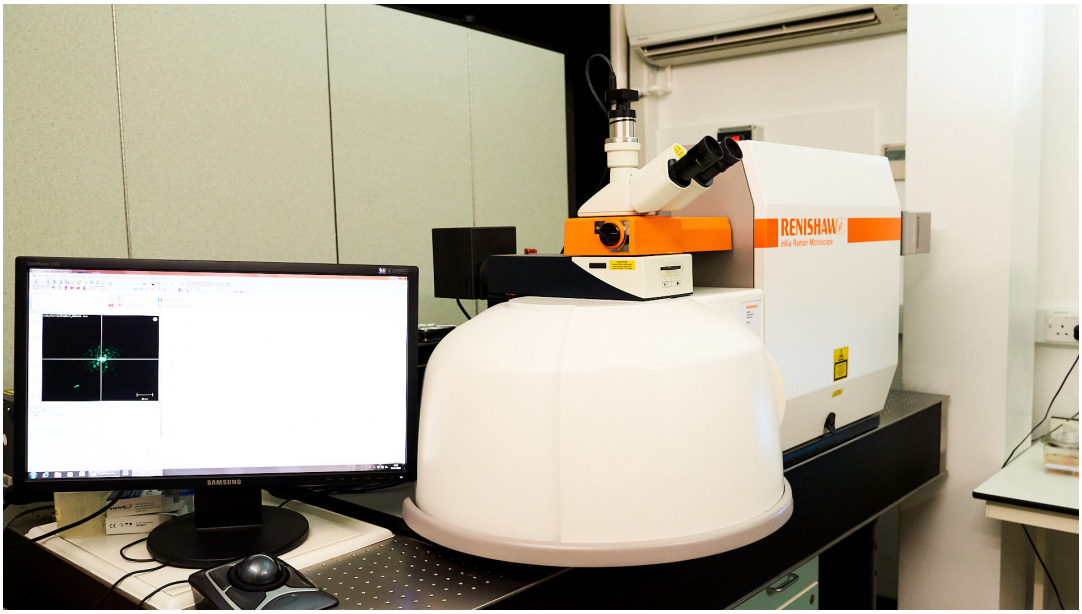

Figure 3-15: The Renisham InVia Raman microscope at the University of Bath. Photo provided by [66].

Chapter 4

Structure of Zinc Aluminosilicate Glasses

4.1 Introduction

Aluminosilicate glasses are of great technological importance where they have a huge variety of applications that impact the everyday life of humans ranging from fiber [67] to display glasses [12]. However, the glass forming ability in aluminosilicates is challenging and it will be dependent on the cations used. The zinc (ZAS)- and magnesium (MAS)-aluminosilicate glasses have very similar glass forming domains except that MgO-SiO_2 glasses can be obtained in a large composition range. Zn^{2+} ions have a lesser glass forming ability than Mg^{2+} since no binary ZnO-SiO_2 glasses can be formed. The ZAS system is important in glass-ceramics due to the opportunity to crystallize gahnite ($ZnAl_2O_4$) [68, 69] or willemite (Zn_2SiO_4) [70, 71] and no ternary compounds (Figure 4-1). These crystals can be doped with rare earths and transition elements providing efficient luminescence [72]. A wide range of compositions covering the ZAS glass forming diagram is dominated by the stability of the gahnite region.

Zinc plays an important role as an additive to improve the glass forming domain mechanical properties such as strength and hardness. The $(ZnO)_x(Al_2O_3)_y$ $(SiO_2)_{1-x-y}$ system has a high glass transition temperature and a low coefficient of thermal expansion which can be used as a stabilizer to improve the chemical resistance of the material [16]. This makes zinc a good candidate for various applications, ranging from commercial glass and glass ceramics to high performance optical glasses [73–76]. Zinc oxide is important in bioactive glass where the zinc ion is responsible for bone formation, resorption, soft tissue regeneration and stimulates cellular protein synthesis [77].

Zinc is also a useful antibacterial agent in glass-ionomer-based cements [78] and ceramic coatings [79]. In borosilicate glasses, zinc is added to commercial nuclear waste applications [7].

Understanding the atomic scale structure is a key to explain the glass' different properties mentioned above. In this chapter X-ray and neutron diffraction experiments were carried out to unravel the structure of aluminosilicate glasses with different amounts of zinc. Raman spectroscopy and MAS NMR on ^{27}Al and ^{29}Si experiments were also done to provide complementary information on the role of zinc in the ZAS system.

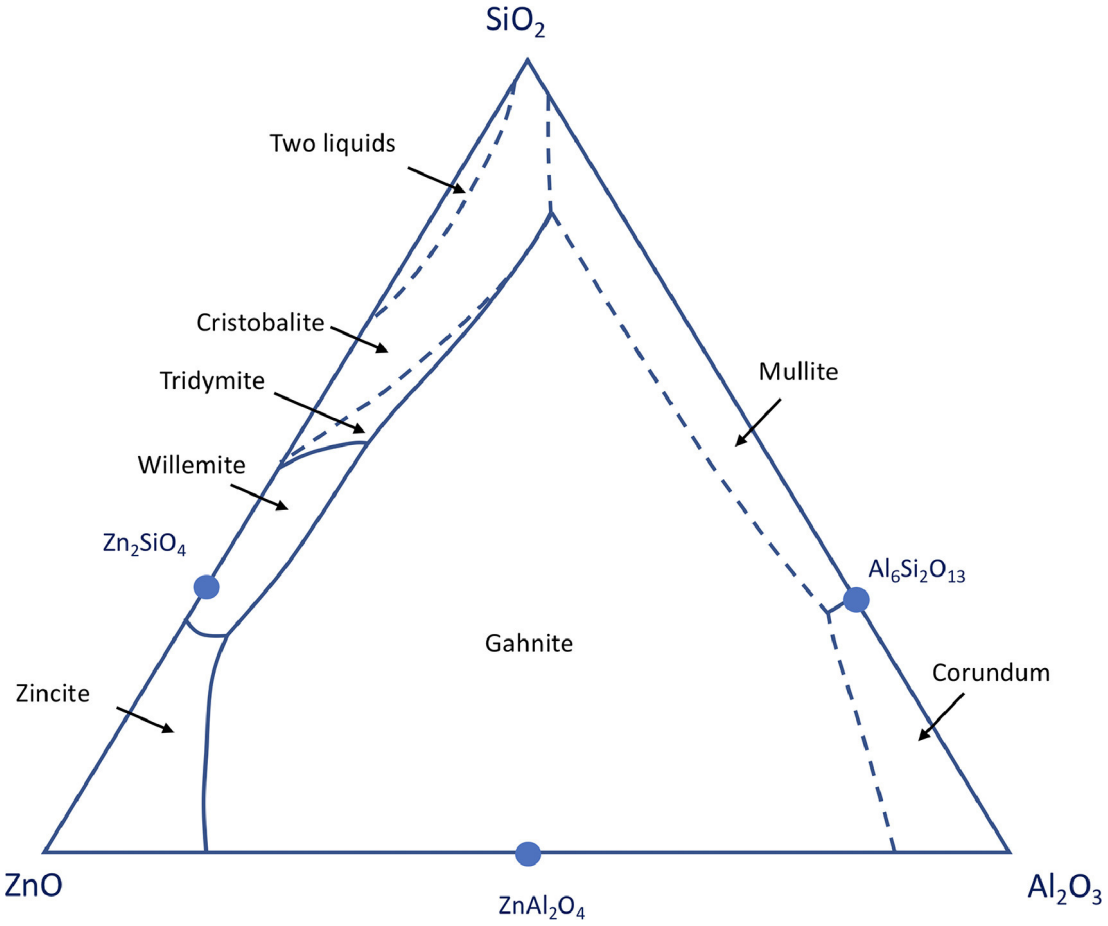

Figure 4-1: The ZAS ternary phase diagram showing the crystalline phases. Reproduced from [80].

4.2 Experiment

4.2.1 Sample Preparation

Two batches of zinc aluminosilicate glasses were prepared as described below. Their respective concentrations are shown in table 4.1. The densities of the ZAS samples were measured using a helium pycnometer (MICRO-ULTRAPYC 1200e) and their values are presented in table 4.2.

The first batch of ZAS samples was prepared at Corning Inc., USA. Powders of ZnO (Zochem), Al_2O_3 (Alfa Aesar) and high purity sand (US silica) were used. A 900 g of ball-milled material was melted at 1650°C for ≈ 20 h in covered platinum crucibles and quenched by pouring onto a steel table. The as-prepared glasses were annealed at 650 °C for 1 h and then allowed to cool by cutting the furnace power. The batch weight for the ZAS glasses changed by no more than 0.02 g, so there was negligible deviation from the batch composition.

The second batch of ZAS samples was prepared in Bath, England, where powders of ZnO (Aldrich, ≥ 99.999%), Al_2O_3 (Sigma, 99.998%) and SiO_2 (Alfa Aesar, 99.9%) were used. The raw materials were dried at 1000 °C for 1-2 h. For each sample, a batch of powder of mass ≈ 4 g was melted at 1600 °C (ZAS60.15p55) or 1650 °C (ZAS50.7p5, ZAS50.17p36 and ZAS65.17p5) in a covered Pt/Rh crucible for 2h. The glasses were quenched by placing the bottom of the crucible into a water bath (ZAS65.17p5) or using a copper block cooled in liquid nitrogen (all other samples). For the ZAS50.7p5 composition the sample was ground and the melt and quench procedure was repeated to ensure glass homogeneity. The overall mass loss during processing was ≈ 1%, which is probably related to the loss of water re-adsorbed after the initial drying procedure. The composition of each glass was taken from the batch composition. It was not possible to prepare homogeneous alumina-free zinc silicate glasses by conventional melt quenching or by aerodynamic levitation with laser heating in accordance with the findings from [80].

The crystalline Zn_2SiO_4 phase I, willemite, was prepared using the procedure adapted from [81]. ZnO (Aldrich, ⩾ 99.999%) and SiO_2 (Alfa Aesar, 99.9%) powders were dried at 1000 °C for 2 h, mixed to give the correct stoichiometry and ≈ 3 g of material was pelleted under a pressure of ≈ 0.74 GPa during five minutes. The pellets were sintered at 1000 °C for 18 h and were finely ground using an agate pestle and mortar. The resultant powder was pelleted and sintered at 1250 °C for 24 h in a covered Pt/Rh crucible. The grinding, pelleting and sintering cycle was then repeated. The willemite

Samples	Batch	ZnO [mol%]	Al_2O_3 [mol%]	SiO_2 [mol%]
Zn_2SiO_4	2	66.67	0	33.33
ZAS50.7p5	2	42.5	7.5	50
ZAS50.10	1	40.0	10.0	50
ZAS50.12p5	1	37.5	12.5	50
ZAS50.17p36	2	32.64	17.36	50
ZAS50.22p22	1	27.78	22.22	50
ZAS50.25	1	25.0	25.0	50
ZAS50.27p78	1	22.22	27.78	50
ZAS60.13p33	1	26.67	13.33	60
ZAS60.15p55	2	24.45	15.55	60
ZAS60.17p78	1	22.22	17.78	60
ZAS60.20	1	20.0	20.0	60
ZAS60.22p22	1	17.78	22.22	60
ZAS65.17p5	2	17.5	17.5	65
ZAS70.13p33	1	16.67	13.33	70
ZAS70.15	1	15.0	15.0	70
ZAS70.16p67	1	13.33	16.67	70

Table 4.1: Concentration, in mol%, of ZnO, Al_2O_3 and SiO_2 for each of the ZAS samples.

crystal structure was confirmed by powder X-ray diffraction [70].

4.2.2 6-ID-D Experiment

The high energy X-ray diffraction experiment on the ZAS glasses was done at room temperature using the 6-ID-D diffractometer at the APS. The photon energy of the square incident beam was 100.233 keV, corresponding to a wavelength of 0.1236 Å. The ground glasses were loaded into kapton polyimide tubes of 1.80(1) mm internal diameter and 0.051(6) mm wall thickness. The scattered X-rays were detected using a Varex 4343CT amorphous silicon flat panel detector which was placed at a distance of $\approx$ 311(1) mm from the sample position as deduced from the diffraction pattern measured for crystalline CeO_2.

Diffraction patterns were measured for each sample in its capillary, an empty capillary and the empty instrument. The data were converted to one-dimensional diffraction patterns using FIT2D [84]. The program PDFgetX2 [85] was used for corrections to background scattering, beam polarization, attenuation and Compton scattering.

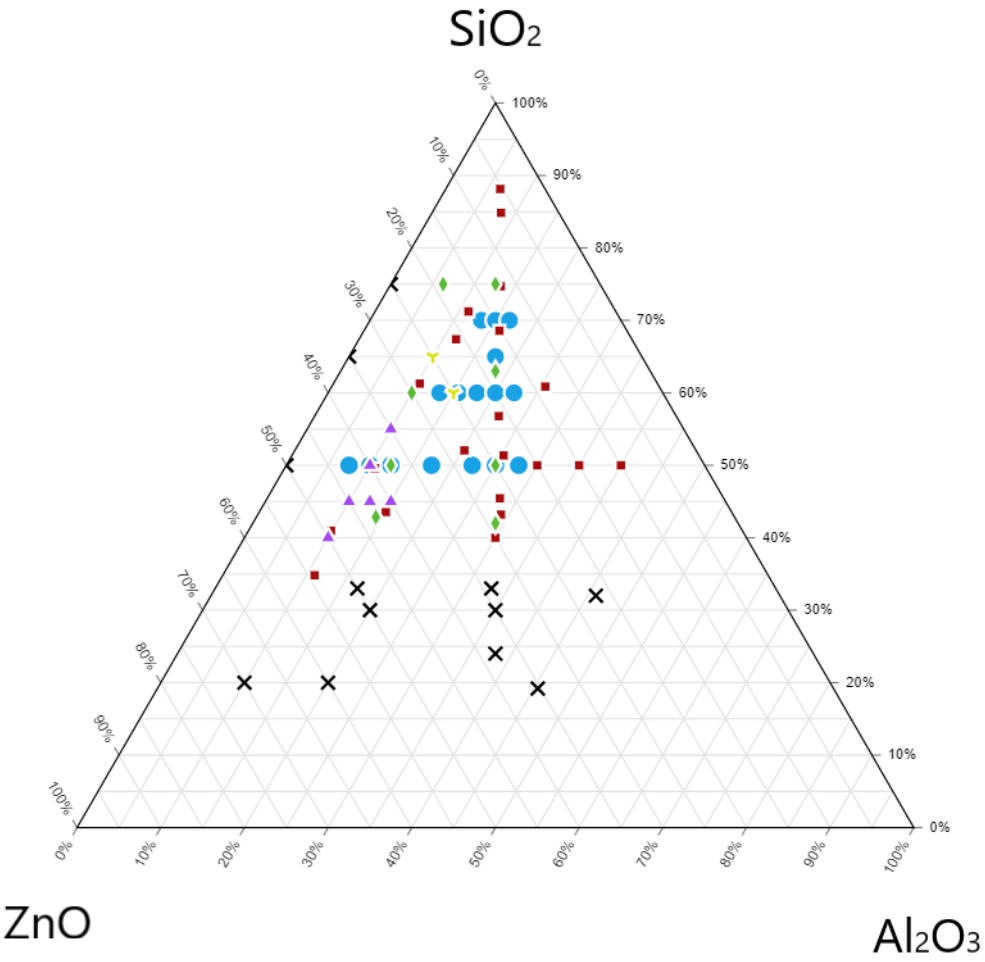

Figure 4-2: Glass forming composition (in blue) for the ZAS system studied. Glasses found from previous investigations are also shown. The red square were taken from [80], purple triangle [74], green diamonds [82] and yellow wye [83]. The black crosses [80,82] correspond to compositions for which no glass could be obtained and they are either crystalline, partially crystallized or phase separated.

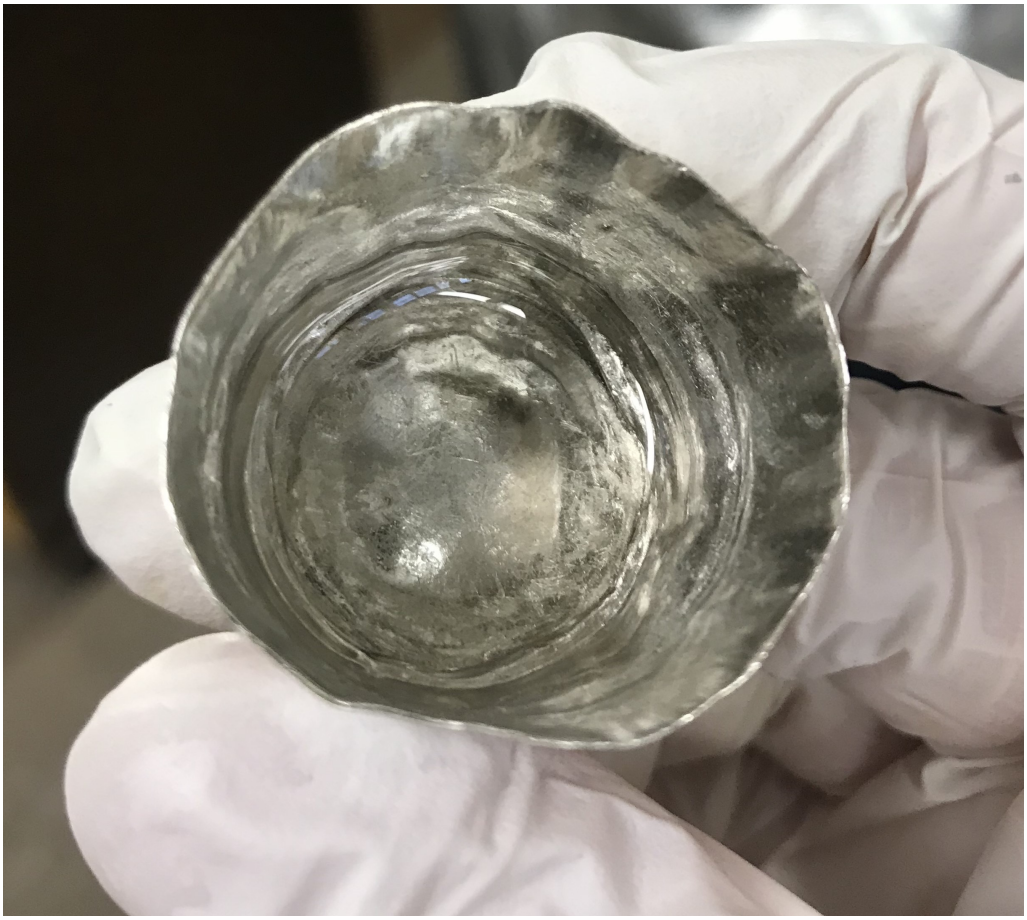

Figure 4-3: Samples ZAS50.10 glass in a Pt-10%Rh crucible after quenching. The sample looks completely clear and glassy.

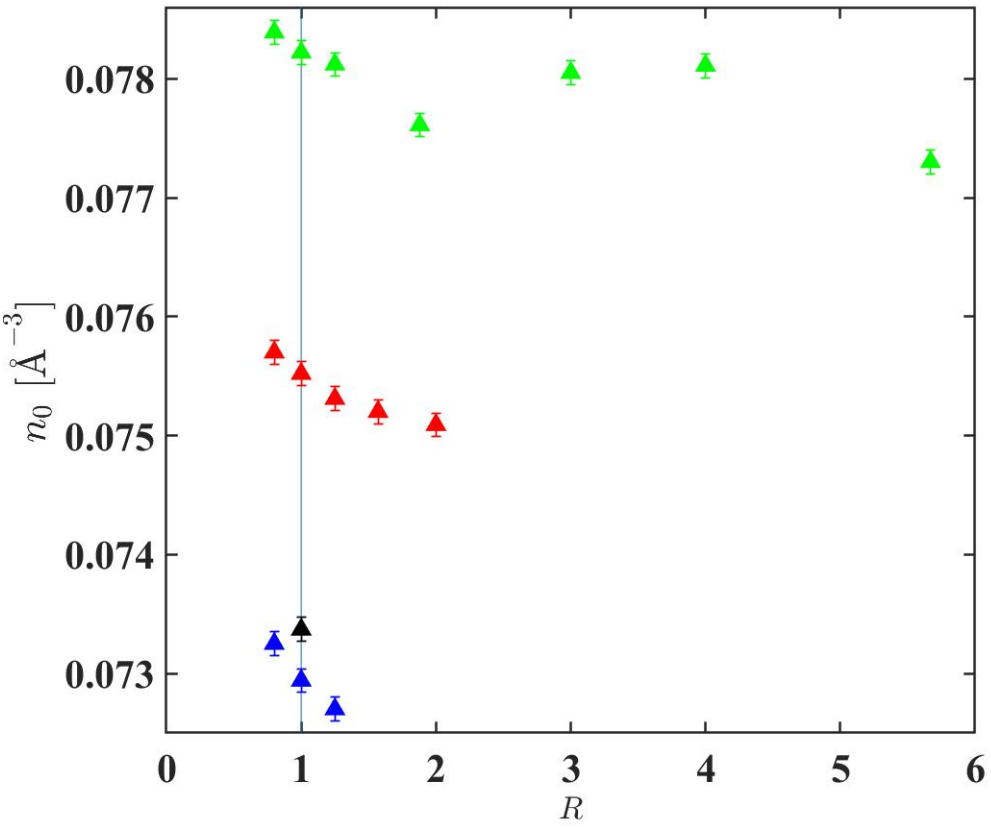

Figure 4-4: Number density, n_0, as a function of the ratio $R(c_{ZnO}/c_{Al_2O_3})$ for the ZAS glasses. The green data points show the n_0 values along the 50 mol% SiO_2 tie-line. The red data points show the n_0 values along the 60 mol% SiO_2 tie-line. The black data point show the n_0 value for the 65 mol% SiO_2 and the blue data points show the n_0 values along the 70 mol% SiO_2 tie-line.

Samples	ρ [g/cm^3]	ρ Corning Inc. [g/cm^3]	n_0 [Å^{-3}]
Zn_2SiO_4	4.224(5)	-	0.0799(10)
ZAS50.7p5	3.403(5)	-	0.0773(1)
ZAS50.10	3.3723(8)	3.371	0.07811(2)
ZAS50.12p5	3.3047(5)	3.304	0.07805(1)
ZAS50.17p36	3.170(1)	-	0.0776(1)
ZAS50.22p22	3.0849(5)	3.087	0.07812(1)
ZAS50.25	3.033(1)	3.038	0.07822(3)
ZAS50.27p78	2.986(1)	2.997	0.07839(3)
ZAS60.13p33	2.9656(7)	2.976	0.07509(2)
ZAS60.15p55	2.924(1)	-	0.0752(3)
ZAS60.17p78	2.8841(5)	2.893	0.07531(1)
ZAS60.20	2.8498(9)	2.853	0.07552(2)
ZAS60.22p22	2.8161(8)	2.827	0.07570(2)
ZAS65.17p5	2.730(1)	-	0.07337(8)
ZAS70.13p33	2.6957(9)	2.707	0.07270(2)
ZAS70.15	2.6749(6)	2.680	0.07294(2)
ZAS70.16p67	2.6572(4)	2.656	0.07325(1)

Table 4.2: The measured mass density, ρ, and corresponding number density n_0 for the ZAS samples. The density measured by Corning Inc. is also shown for comparison.

4.2.3 GEM Experiment

Two neutron diffraction experiments were carried out at ISIS using the GEM diffractometer. The first set of experiments was done with samples from batch 1 and the second set of experiments was done using samples from batch 2.

The samples were ground and loaded either into a 10.3 mm (batch 1) or a 8.3 mm (batch 2) vanadium can. Each vanadium can was placed in an ultrasonic bath for 10 minutes to achieve a higher packing of the sample. The glasses were mounted in the sample changer which centers each sample in turn in the neutron beam and diffraction patterns were measured for each of them. Diffraction patterns were also measured for empty vanadium cans and the empty instrument to correct for background scattering, and a V-Nb (5.14%) rod with a coherent scattering length of zero for normalization purposes.

4.2.4 Nuclear Magnetic Resonance Spectroscopy

^{29}Si MAS NMR Experiment of crystalline Zn_2SiO_4

^{29}Si MAS NMR was conducted at 4.7 T using an Agilent DD2 spectrometer, a double-resonance 5 mm MAS NMR probe and a wide-bore (89 nm) superconducting magnet.

Element	b [fm]
Zn	5.680(5)
Al	3.449(5)
Si	4.1491(10)
O	5.803(4)

Table 4.3: The bound coherent neutron scattering lengths, b, for the chemical elements Zn, Al, Si and O [38]. The values will be used to calculate the values in table 4.4.

Samples	$\langle b \rangle$ [fm]
ZAS50.7p5	5.351
ZAS50.10	5.322
ZAS50.12p5	5.295
ZAS50.17p36	5.245
ZAS50.22p22	5.201
ZAS50.25	5.177
ZAS50.27p78	5.154
ZAS60.13p33	5.252
ZAS60.15p55	5.231
ZAS60.17p78	5.210
ZAS60.20	5.191
ZAS60.22p22	5.172
ZAS65.17p5	5.198
ZAS70.13p33	5.221
ZAS70.15	5.205
ZAS70.16p67	5.191

Table 4.4: Average neutron scattering lengths, $\langle b \rangle$, with ± 0.005 fm for each of the ZAS samples.

The powdered Zn_2SiO_4 was packed into a 5 mm outer diameter zirconia MAS NMR rotor, providing sample spinning of 7 KHz. Single pulse experiments were made with a $\pi/2$ pulse widths of 5.4 μs, recycle delay of 900 s and signal averaging of 86 scans.

^{29}Si MAS NMR data was processed using the software Agilent VnmrJ (Agilent) without any extra line broadening and the ^{29}Si NMR frequency was referenced to an external tetramethylsilane (TMS) standard at 0.0 ppm.

^{27}Al MAS NMR Experiment

^{27}Al NMR Spectroscopy was performed to obtain information about the structure of aluminum contained in the ZAS system. The measurements were done at Corning Incorporated (USA).

For the batch 1 ZAS glasses, it was used an Agilent DD2 spectrometer and a Variant T3 1.6 mm MAS (Magic Angle Spinning) NMR probe with an external magnetic field of 16.4 T (182.34 MHz resonance frequency). The powdered ZAS glasses were packed into 3.2 mm zirconia rotors with the sample spinning at 22 KHz using compressed nitrogen. 0.6 μs radio-frequency (RF) pulses were used to excite the ^{27}Al central transitions and the data was collected using a 2 s recycle delay and averaging of 400-1000 scans.

For the batch 2 ZAS glasses the ^{27}Al MAS NMR was conducted at 16.4 T using an Agilent DD2 spectrometer, a triple resonance 3.2 mm MAS NMR probe and a shielded narrow-bore superconducting magnet. The powdered glasses were loaded into low-Al zirconia rotors with an outer diameter of 3.2 mm. These sample holders still give a weak background signal around 0 ppm, which was treated in the fitting protocol. Single pulse experiments were used to collect data with a 0.6 μs pulse width ($\pi/12$ tip angle), a 4 s recycle delay between scans and a signal averaging of 1000 scans. Sample spinning was computer controlled to 22.0 KHz, using compressed nitrogen. Processing was done using commercial software Agilent VnmrJ without line broadening. The shift referencing was done with an external solution of aqueous aluminum nitrate at 0.0 ppm.

All the ^{27}Al MAS NMR spectra were analysed in the DMFIT program [86], which uses Czjzek line shapes to simulate the second-order quadrupolar broadened peaks from Al in different coordination environments. The spectra was optimized by varying the quadrupolar coupling constant (C_Q), isotropic chemical shift (δ_{iso}) and the Gaussian distribution.

4.2.5 Raman Spectroscopy

Unpolarized Raman spectra were recorded at room temperature using a Renishaw In-Via Raman microscope with a $\times 50$ objective lens. No special sample preparations were made in advance for the experiment. The Raman experiment was performed in back-scattering geometry using a He-Cd laser excitation wavelength of 532 nm with a grating of 1800 1/mm. The laser was focused onto the sample with a beam diameter of ≈ 2.5 μm.

The spectrometer laser filters usually have a cut-off below $50-60$ cm^{-1}. For the ZAS glasses the Raman spectra were measured between $100-1300$cm^{-1} The laser power was kept sufficiently low to avoid any damage to the sample surface over extended periods.

4.3 Results

4.3.1 Nuclear Magnetic Resonance Spectroscopy

^{29}Si MAS NMR

The ^{29}Si MAS-NMR spectrum measured for crystalline Zn_2SiO_4 is shown in figure 4-5. The spectrum shows a single resonance at -70.87 ppm and is consistent with previous ^{29}Si MAS NMR measurements for willemite [87–90]. The single peak is characteristic of the monomeric orthosilicate SiO_4 unit, i.e, a single silicon environment with Q^0.

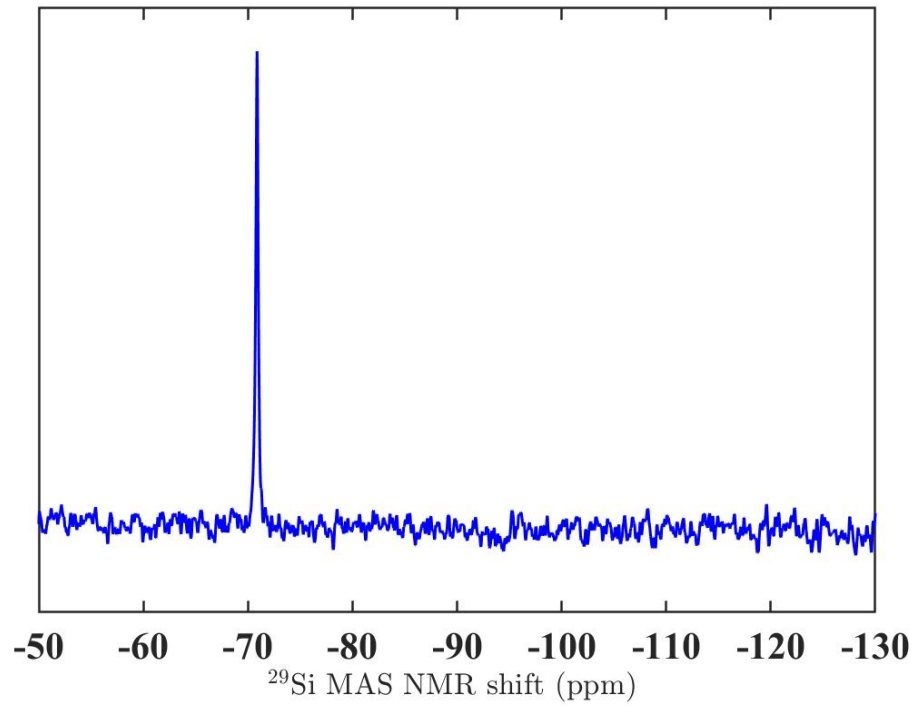

Figure 4-5: ^{29}Si MAS NMR spectrum of crystalline Zn_2SiO_4 sample.

^{27}Al MAS NMR

Figures 4-6, 4-7, 4-8 and 4-9 show the ^{27}Al MAS NMR spectra measured for the zinc aluminosilicate glasses from batch 1 and 2.

The ^{27}Al MAS NMR spectra were fitted in DMFit [86] using Czjzek line shapes to represent the second-order quadrupolar broadened peaks from aluminium in different coordination environments. The fits are shown in figures 4-10, 4-11 and 4-12. The parameters describing the fitted line shapes are listed in tables 4.5 and 4.6.

The ZAS spectra show two distinct contributions, a dominant contribution centered at $\approx$ 60 ppm and a second one centered at $\approx$ 35 ppm. These two signals are assigned to Al(IV) (higher chemical shift) and Al(V) (lower chemical shift), respectively [91–99]. A weak signal is also seen at $\approx$ 5 ppm that corresponds to Al(VI) units. The isotropic chemical shift, $\delta(^{27}\mathrm{Al})$, for Al(IV) species varies with composition and is related to different polymerized environments around AlO_4 tetrahedra.

The results show that, as the alumina content increases, the fraction of fourfold coordinated aluminum Al(IV) decreases and the fraction of higher coordinated aluminum increases. For all the ZAS glasses Al(IV) is the majority species and fivefold coordinated aluminum Al(V) is the second most abundant species. For compositions with $R \geqslant 1$, sixfold coordinated aluminum Al(VI) occurs rarely ($\leqslant 2.6\%$). For the compositions with $R < 1$ (peraluminous regime) the proportion of Al(V) and Al(VI) species increases along both 50, 60 and 70 mol% SiO_2 tie-lines. This is expected since not enough Zn is present to ensure local charge balance of $(AlO_4)^-$ tetrahedra. The chemical shift of the Al(V) and Al(VI) contributions are almost independent of the silica content.

Figure 4-13 shows the Al-O coordination numbers as a function of R and their respective values are listed in table 4.7.

Samples	Coordination Environment	Area (%)	$\delta(^{27}\mathrm{Al})$	$\Delta\delta(^{27}\mathrm{Al})$	C_Q
ZAS50.10	Al(IV)	94.3	65.1	15.3	8.37
	Al(V)	4.5	34.4	17.2	5.68
	Al(VI)	1.2	8.0	15.6	5.22
ZAS50.12p5	Al(IV)	94.7	65.6	15.2	8.48
	Al(V)	4.2	35.3	14.4	6.53
	Al(VI)	1.1	7.0	16.0	5.11
ZAS50.22p22	Al(IV)	90.5	66.8	14.9	9.04
	Al(V)	6.9	35.5	14.2	5.94
	Al(VI)	2.6	10.7	23.7	4.84
ZAS50.25	Al(IV)	85.8	66.8	15.3	9.06
	Al(V)	11.0	36.9	15.1	6.50
	Al(VI)	3.2	10.7	23.7	4.84
ZAS50.27p78	Al(IV)	81.8	66.8	15.4	9.28
	Al(V)	14.6	37.5	14.3	7.04
	Al(VI)	3.6	13.1	19.2	6.91
ZAS60.13p33	Al(IV)	87.8	64.4	16.9	8.13
	Al(V)	11.1	39.5	17.0	8.35
	Al(VI)	1.1	2.0	11.9	3.49
ZAS60.17p78	Al(IV)	91.9	65.6	16.0	9.25
	Al(V)	7.2	37.3	10.8	8.30
	Al(VI)	0.9	2.0	12.0	3.61
ZAS60.20	Al(IV)	87.4	66.0	16.4	9.32
	Al(V)	11.4	37.9	11.8	8.42
	Al(VI)	1.2	2.0	14.1	2.92
ZAS60.22p22	Al(IV)	86.3	66.0	16.2	9.82
	Al(V)	12.4	37.6	11.4	8.27
	Al(VI)	1.3	3.9	13.9	3.96
ZAS70.13p33	Al(IV)	89.7	65.8	15.9	9.22
	Al(V)	9.0	37.8	11.4	8.87
	Al(VI)	1.3	2.2	11.7	3.92
ZAS70.15	Al(IV)	88.4	65.9	16.3	9.58
	Al(V)	10.3	37.6	11.9	8.43
	Al(VI)	1.3	2.1	14.9	3.26
ZAS70.16p67	Al(IV)	82.1	66.0	17.1	9.34
	Al(V)	16.0	38.4	13.1	8.42
	Al(VI)	1.9	2.0	16.5	2.68

Table 4.5: Parameters obtained from the Czjek fits to the ^{27}Al MAS NMR spectra measured for the batch 1 ZAS glasses. The parameters correspond to the peak area ($\pm$2%), ^{27}Al MAS NMR shift $\delta(^{27}\mathrm{Al})(\pm 1$ ppm), full-width at half-maximum (FWHM) of a Gaussian distribution of these shifts $\Delta\delta(^{27}\mathrm{Al})$ ($\pm$2 ppm), and average quadrupolar coupling constant C_Q ($\pm$0.2 MHz).

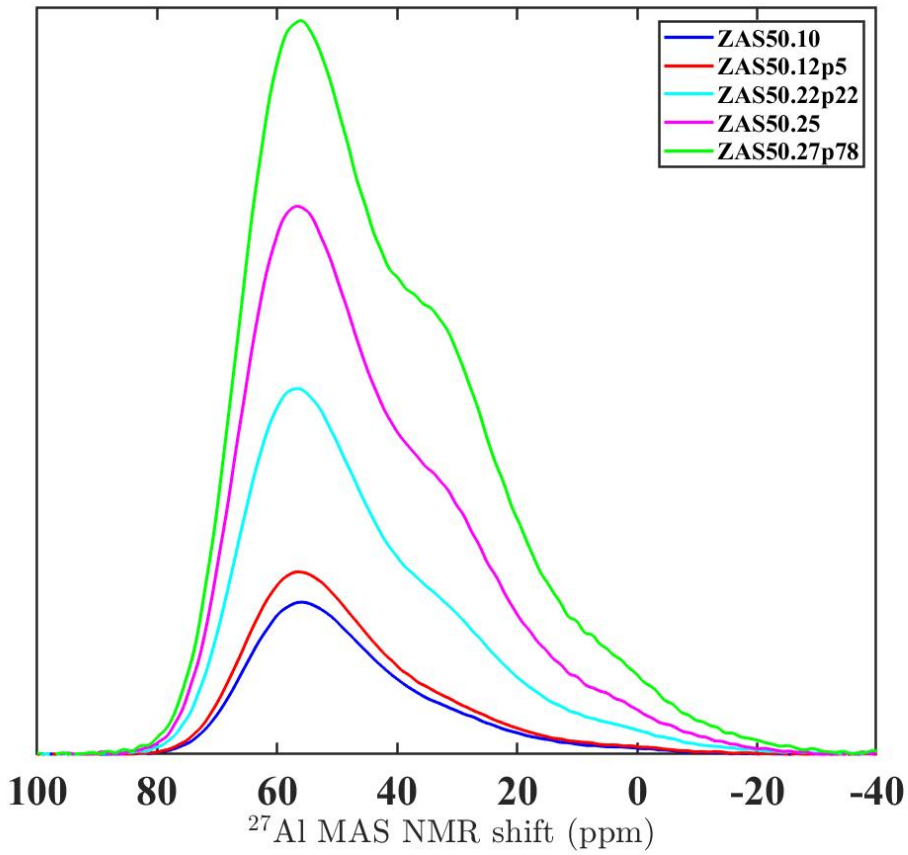

Figure 4-6: ^{27}Al MAS NMR spectra for the batch 1 ZAS glasses along the 50 mol% SiO_2 tie-line. The curves are offset vertically for clarity of presentation.

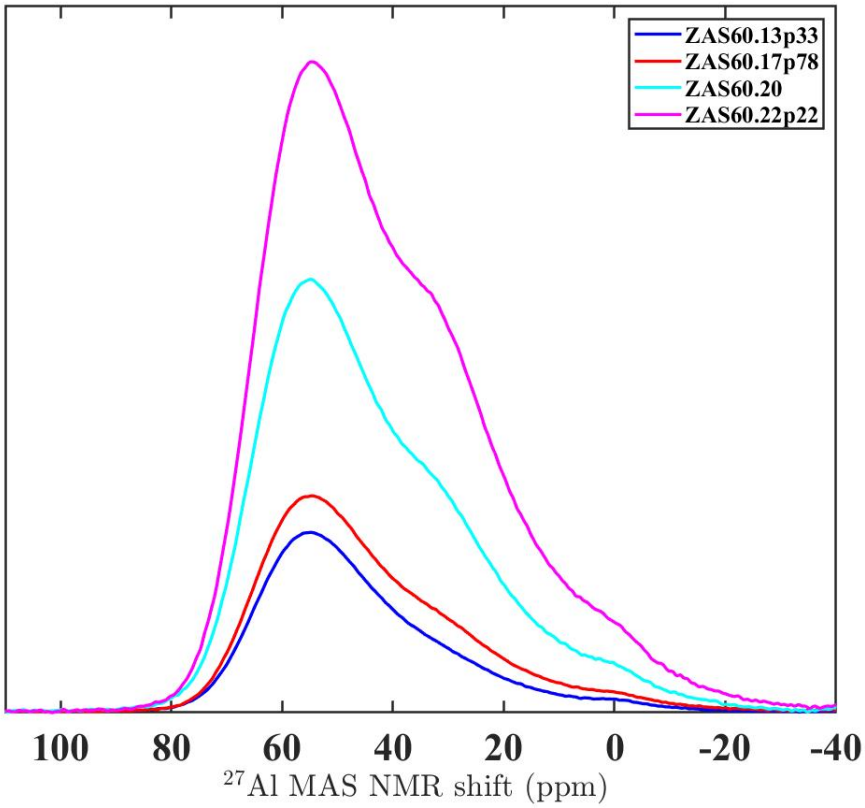

Figure 4-7: ^{27}Al MAS NMR spectra for the batch 1 ZAS glasses along the 60 mol% SiO_2 tie-line. The curves are offset vertically for clarity of presentation.

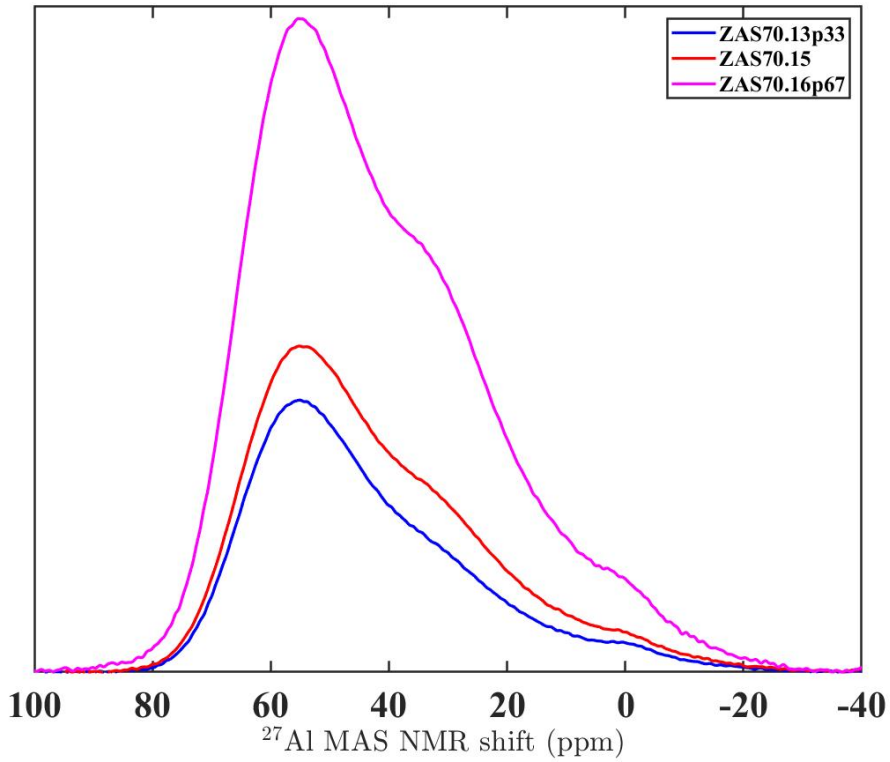

Figure 4-8: ^{27}Al MAS NMR spectra for the batch 1 ZAS glasses along the 70 mol% SiO_2 tie-line. The curves are offset vertically for clarity of presentation.

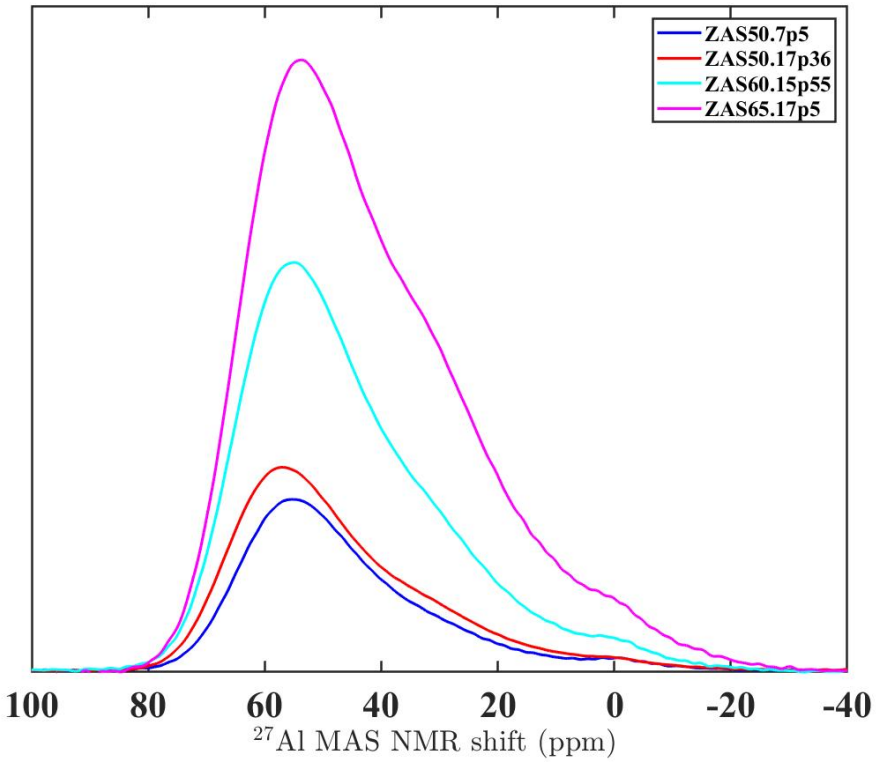

Figure 4-9: ^{27}Al MAS NMR spectra for the batch 2 ZAS glasses. The curves are offset vertically for clarity of presentation.

Samples	Coordination Environment	Area (%)	$\delta(^{27}\mathrm{Al})$	$\Delta\delta(^{27}\mathrm{Al})$	C_Q
	Al(IV)	94.85	64.74	15.79	8.48
ZAS50.7p5	Al(V)	3.88	34.86	13.88	6.22
	Al(VI)	1.27	4.25	24.17	2.47
	Al(IV)	93.61	66.84	15.16	8.90
ZAS50.17p36	Al(V)	5.02	36.38	11.91	7.03
	Al(VI)	1.37	4.14	24.17	2.47
	Al(IV)	86.65	65.10	16.46	8.47
ZAS60.15p55	Al(V)	10.73	35.73	21.83	5.53
	Al(VI)	2.62	6.18	20.84	4.26
	Al(IV)	85.29	64.74	16.57	9.23
ZAS65.17p5	Al(V)	11.64	36.74	17.44	6.77
	Al(VI)	3.07	7.69	24.19	4.43

Table 4.6: Parameters obtained from the Czjek fits to the ^{27}Al MAS NMR spectra measured for the batch 2 ZAS glasses. The parameters correspond to the peak area (±2%), ^{27}Al MAS NMR shift $\delta(^{27}\mathrm{Al})$(±1 ppm), full-width at half-maximum (FWHM) of a Gaussian distribution of these shifts $\Delta\delta(^{27}\mathrm{Al})$ (±2 ppm), and average quadrupolar coupling constant C_Q (±0.2 MHz).

Samples	Al(IV) [%]	Al(V) [%]	Al(VI) [%]	$\bar{n}^{\mathrm{O}}_{\mathrm{Al}}$
ZAS50.7p5	94	4	2	4.08(7)
ZAS50.10	94.29	4.49	1.22	4.07(7)
ZAS50.12p5	94.66	4.21	1.13	4.06(7)
ZAS50.17p36	93	5	2	4.09(7)
ZAS50.22p22	90.5	6.89	2.61	4.12(7)
ZAS50.25	85.85	10.96	3.2	4.17(7)
ZAS50.27p78	81.85	14.55	3.6	4.22(7)
ZAS60.13p33	87.83	11.06	1.11	4.13(7)
ZAS60.15p55	86	11	3	4.17(7)
ZAS60.17p78	91.88	7.18	0.94	4.09(7)
ZAS60.20	87.44	11.35	1.2	4.14(7)
ZAS60.22p22	86.28	12.4	1.32	4.15(7)
ZAS65.17p5	85	12	3	4.18(7)
ZAS70.13p33	89.67	8.99	1.34	4.12(7)
ZAS70.15	88.35	10.32	1.34	4.13(7)
ZAS70.16p67	82.11	15.95	1.94	4.20(7)

Table 4.7: Al speciation in ZAS glasses measured by ^{27}Al MAS NMR. For each composition, the calculated average Al-O coordination number is given with a typical measurement error.

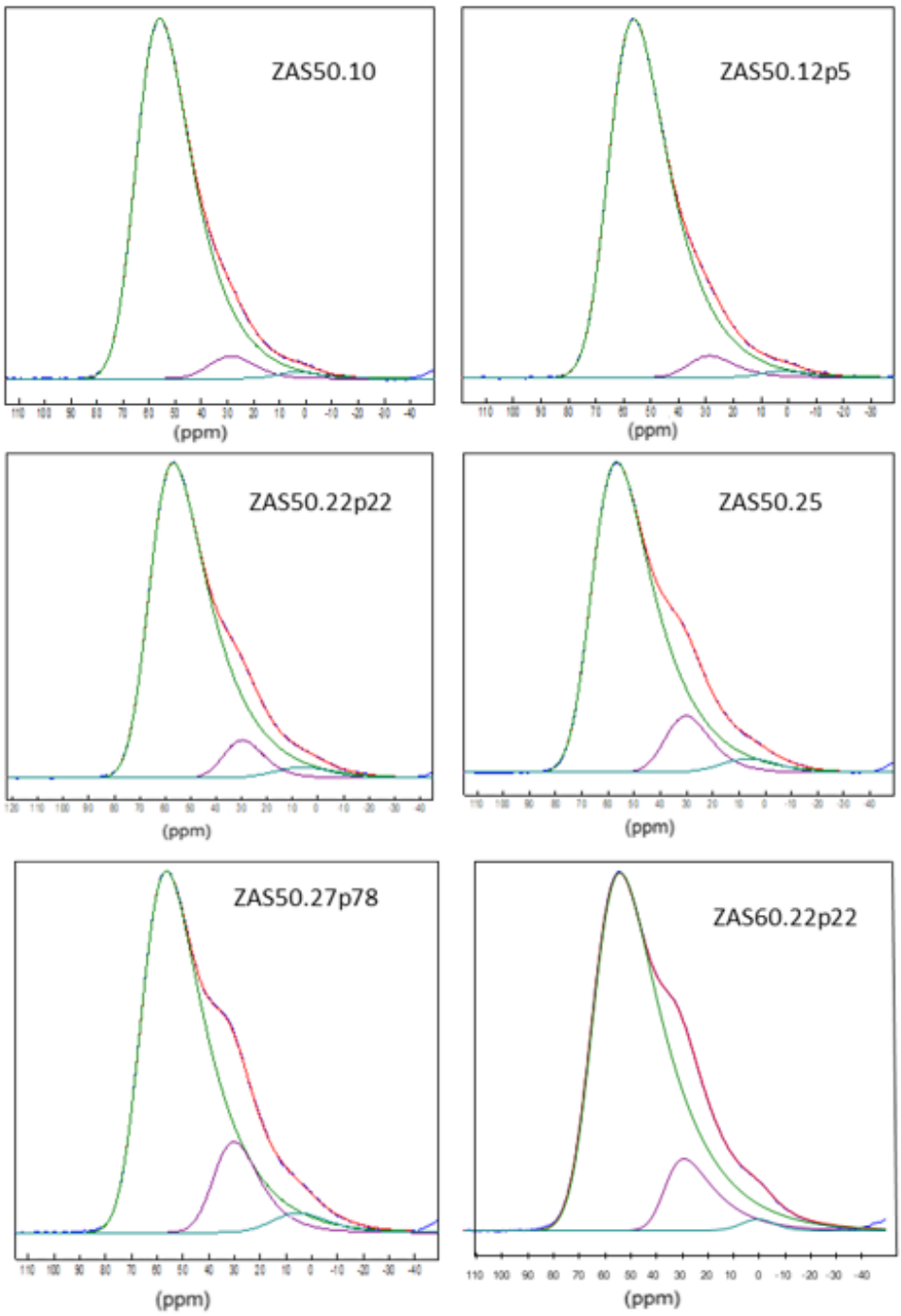

Figure 4-10: Gaussian fits to the MAS NMR spectra shown in figures 4-6 and 4-7 for the batch 1 ZAS glasses along the 50 and 60 mol% SiO_2 tie-line. The green curve corresponds to Al(IV), the purple curve corresponds to Al(V) and the blue curve corresponds to Al(VI). The sum of the fitted functions is given by the red curve, which overlays the measured data (black curve) at most values of $\delta(^{27}\mathrm{Al})$.

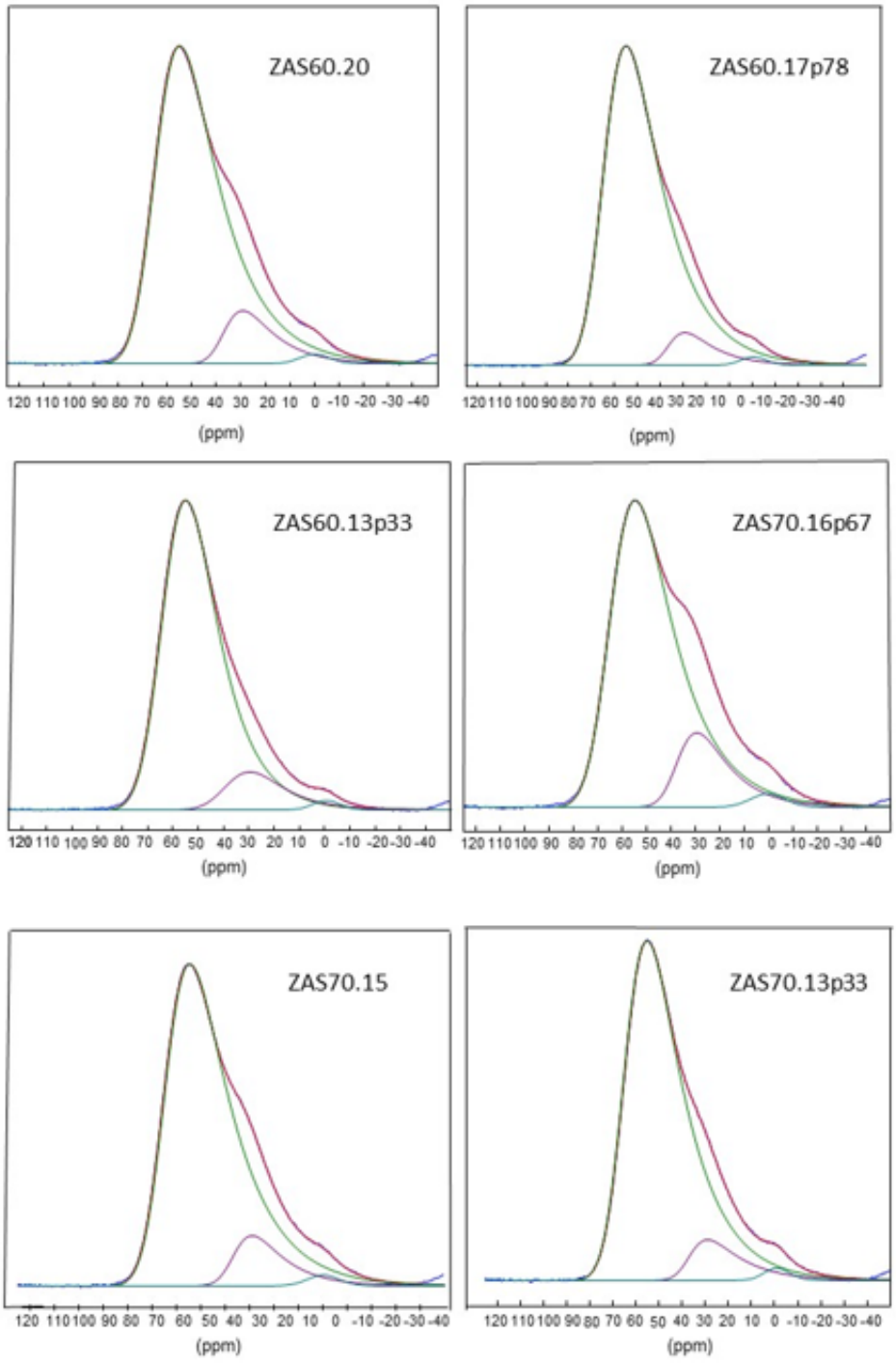

Figure 4-11: Gaussian fits to the MAS NMR spectra shown in figures 4-6 and 4-7 for the batch 1 ZAS glasses along the 60 (continuation) and 70 mol% SiO_2 tie-line. The green curve corresponds to Al(IV), the purple curve corresponds to Al(V) and the blue curve corresponds to Al(VI). The sum of the fitted functions is given by the red curve, which overlays the measured data (black curve) at most values of $\delta(^{27}\mathrm{Al})$.

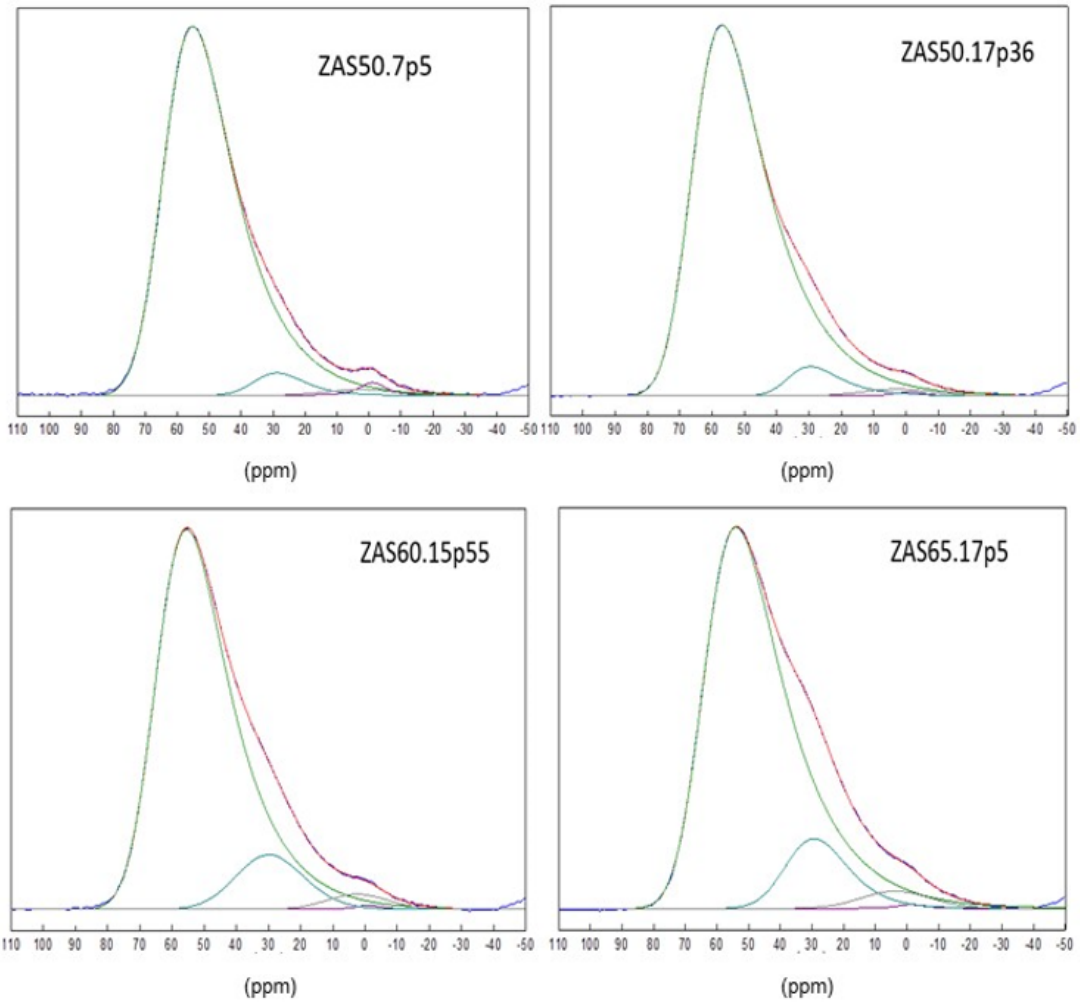

Figure 4-12: Gaussian fits to the MAS NMR spectra shown in figures 4-6 and 4-7 for the batch 2 ZAS glasses. The green curve corresponds to Al(IV), the blue curve corresponds to Al(V) and the purple curve corresponds to Al(VI). The sum of the fitted functions is given by the red curve, which overlays the measured data (black curve) at most values of $\delta(^{27}\mathrm{Al})$.

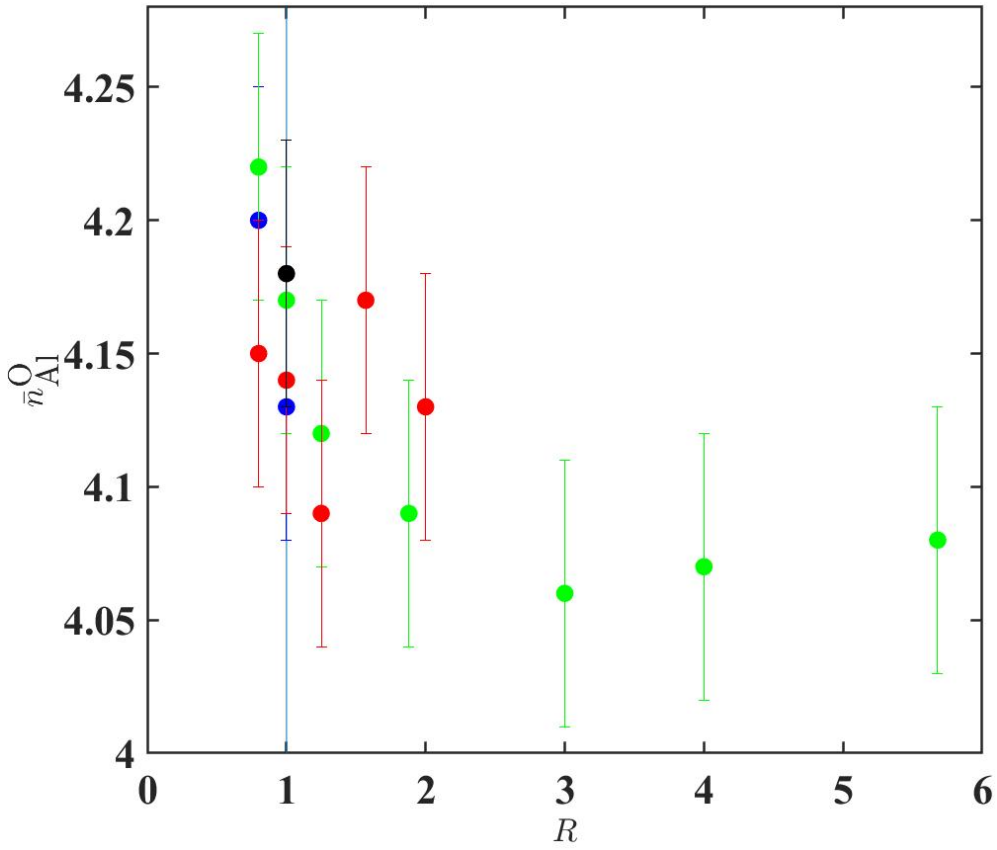

Figure 4-13: Al-O coordination number as a function of the ratio R. The green data points show the coordination numbers along the 50 mol% SiO_2 tie-line. The red data points show the coordination numbers along the 60 mol% SiO_2 tie-line. The black data point show the coordination number for the 65 mol% SiO_2 and the blue data points show the coordination numbers along the 70 mol% SiO_2 tie-line. The cyan line at $R = 1$ indicates the tectosilicate composition.

4.3.2 X-ray Difraction

The X-ray total structure factors $S_X(Q)$ of ZAS glasses are shown in figures 4-14, 4-15, 4-17 and 4-16. All $S_X(Q)$ functions adopt the usual three peak structure at small Q values which are listed in table 4.8, along with their respective $Q_{\max}$ used in the Fourier transformation. These three main peaks are related to ordering on different real-space length scales [100] although the presence of overlapping partial structure factors with composition-dependent weighting factors makes it challenging to interpret. Figures 4-18, 4-19, 4-21 and 4-20 show the $D_X(r)$ functions for the ZAS glasses. The functions show well defined peaks at $r \approx 1.6$ and $r \approx 2.0$ Å which is attributed to Si-O and Zn-O peaks, respectively. The Zn-O peak includes a shoulder on the high r- side which is typical of ZAS glasses [80,82]. The peak at $r \approx 2.63$ Å is mainly due to O-O correlations originating from SiO_4 tetrahedra.

The fitted $D_X(r)$ functions are shown in figures 5-16, 5-18 and 5-19. A peak at $r \approx 1.76$ Å is attributed to the Al-O distance in tetrahedral units. It is not easy to identify Al-O contributions due to the r- space resolution of the X-ray diffractometer [101] and the low weighting factor. For this reason, the neutron diffraction data in the ZAS glasses helped constrain the Al-O peak position.

As the Al_2O_3 content increases the Zn-O peak decreases in the $D_X(r)$ functions. The Si-O and O-O peak distances remain at $r \approx 1.62$ Å and $r \approx 2.63$ Å, respectively, for all compositions even though both peaks get sharper with higher SiO_2 content. The $D_X(r)$ functions show a peak in the range 3.0-3.5 Å which corresponds mainly to Zn-Zn but also to Zn-Si and Zn-Al contributions. Above 3.5 Å there is an overlap between the different contributions which makes it difficult to extract information.

Tables 4.9, 4.10 and 4.11 show the fitted parameters with the corresponding goodness-of-fit, R_χ, over the fitted range 1.30-3.20 Å for the ZAS samples. For each $D_X(r)$ fit, one peak was assigned to Si-O correlations, one peak to Al-O correlations, two peaks to Zn-O correlations, one peak to O-O correlations and one peak was assigned to Zn-Zn correlations. The average coordination number for Si-O was fixed to 4 and the average coordination numbers for Al-O were fixed to the values obtained from ^{27}Al MAS NMR measurements. The results of the Zn-O coordination numbers as a function of R are shown in figure 4-25.

Sample	Q_{FSDP} [Å^{-1}]	Q_{PP} [Å^{-1}]	Q_3 [Å^{-1}]	Q_{max} [Å^{-1}]
ZAS50.7p5	-	-	-	-
ZAS50.10	2.411(1)	4.465(1)	6.445(2)	27.76
ZAS50.12p5	2.192(1)	4.474(1)	6.455(2)	26.18
ZAS50.17p36	-	-	-	-
ZAS50.22p22	1.977(1)	4.512(1)	6.498(2)	28.66
ZAS50.25	1.931(1)	4.523(1)	6.513(2)	26.36
ZAS50.27p78	1.900(1)	4.533(1)	6.519(2)	26.3
ZAS60.13p33	1.901(1)	4.502(1)	6.485(2)	28.1
ZAS60.15p55	-	-	-	-
ZAS60.17p78	1.843(1)	4.522(1)	6.503(2)	28.02
ZAS60.20	1.846(1)	4.527(1)	6.505(2)	27.96
ZAS60.22p22	1.790(1)	4.541(1)	6.522(2)	27.96
ZAS65.17p5	-	-	-	-
ZAS70.13p33	1.701(1)	4.535(1)	6.513(2)	27.72
ZAS70.15	1.685(1)	4.540(1)	6.521(2)	27.84
ZAS70.16p67	1.690(1)	4.557(1)	6.525(2)	27.74

Table 4.8: The positions of the first three peaks Q_{FSDP}, Q_{PP} and Q_3 in the $S_X(Q)$ functions for the ZAS glasses shown in figures 4-14, 4-15 and 4-16. The Q_{max} values used in the Fourier transformation are also listed.

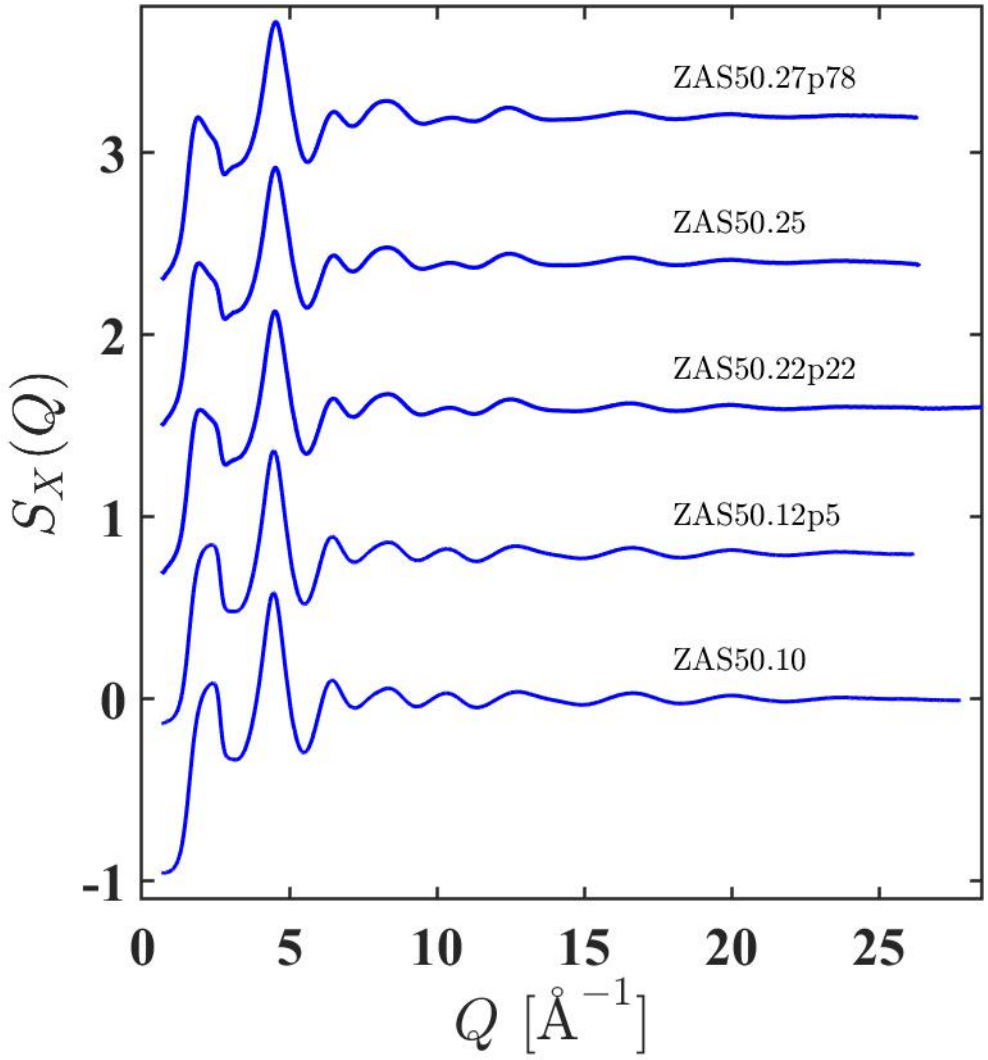

Figure 4-14: Total structure factors $S_X(Q)$ for the ZAS glasses along the 50 mol% SiO_2 tie-line. The error bars are smaller than the line thickness at most Q values. The curves are offset vertically for clarity of presentation.

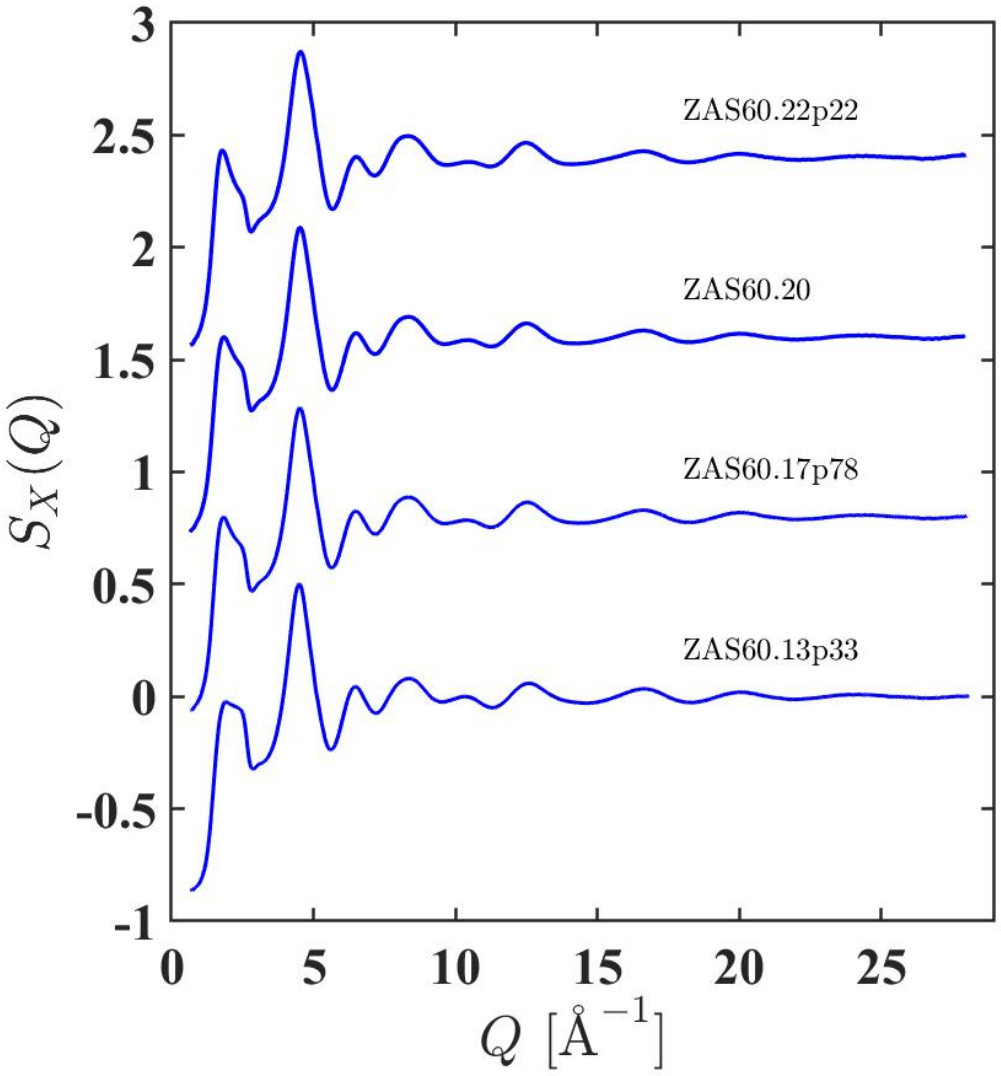

Figure 4-15: Total structure factors $S_X(Q)$ for the ZAS glasses along the 60 mol% SiO_2 tie-line. The error bars are smaller than the line thickness at most Q values. The curves are offset vertically for clarity of presentation.

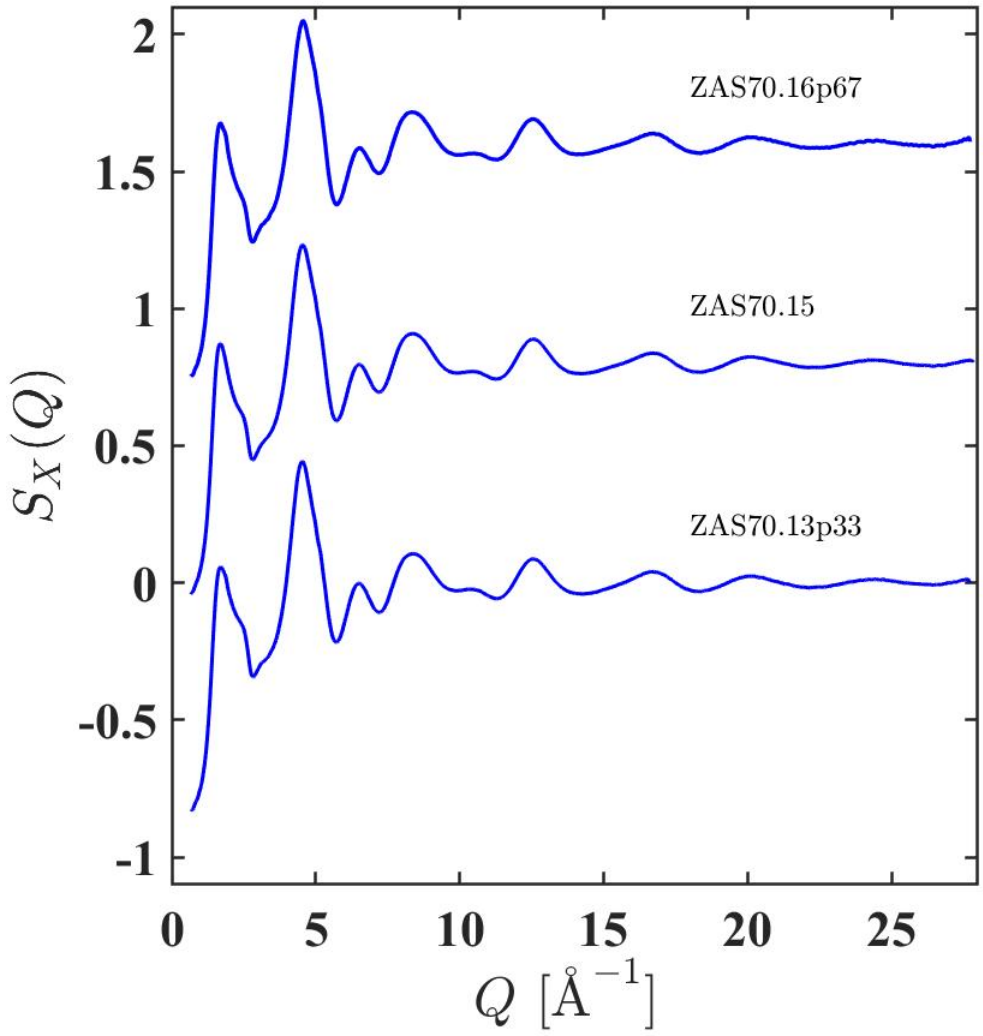

Figure 4-16: Total structure factors $S_X(Q)$ for the ZAS glasses along the 70 mol% SiO_2 tie-line. The error bars are smaller than the line thickness at most Q values. The curves are offset vertically for clarity of presentation.

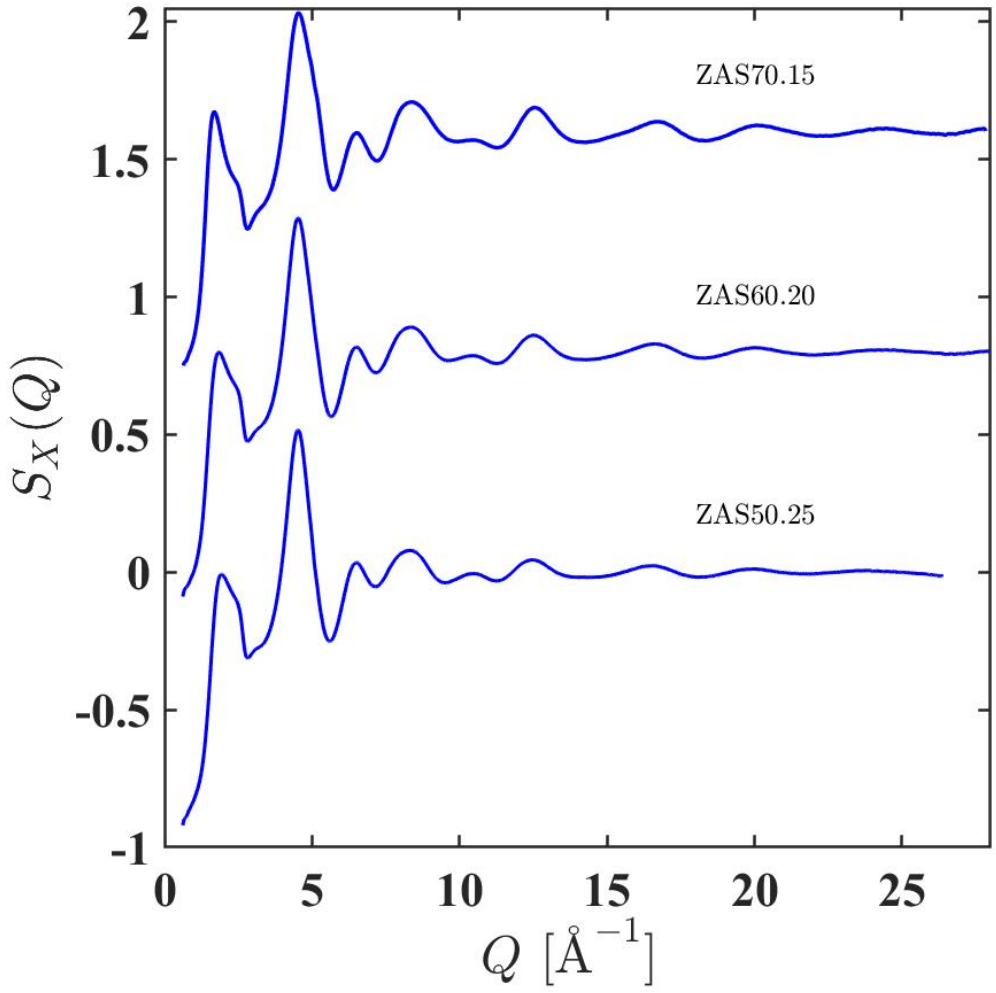

Figure 4-17: Total structure factors $S_X(Q)$ for the ZAS glasses along the $R = 1$ tie-line. The error bars are smaller than the line thickness at most Q values. The curves are offset vertically for clarity of presentation.

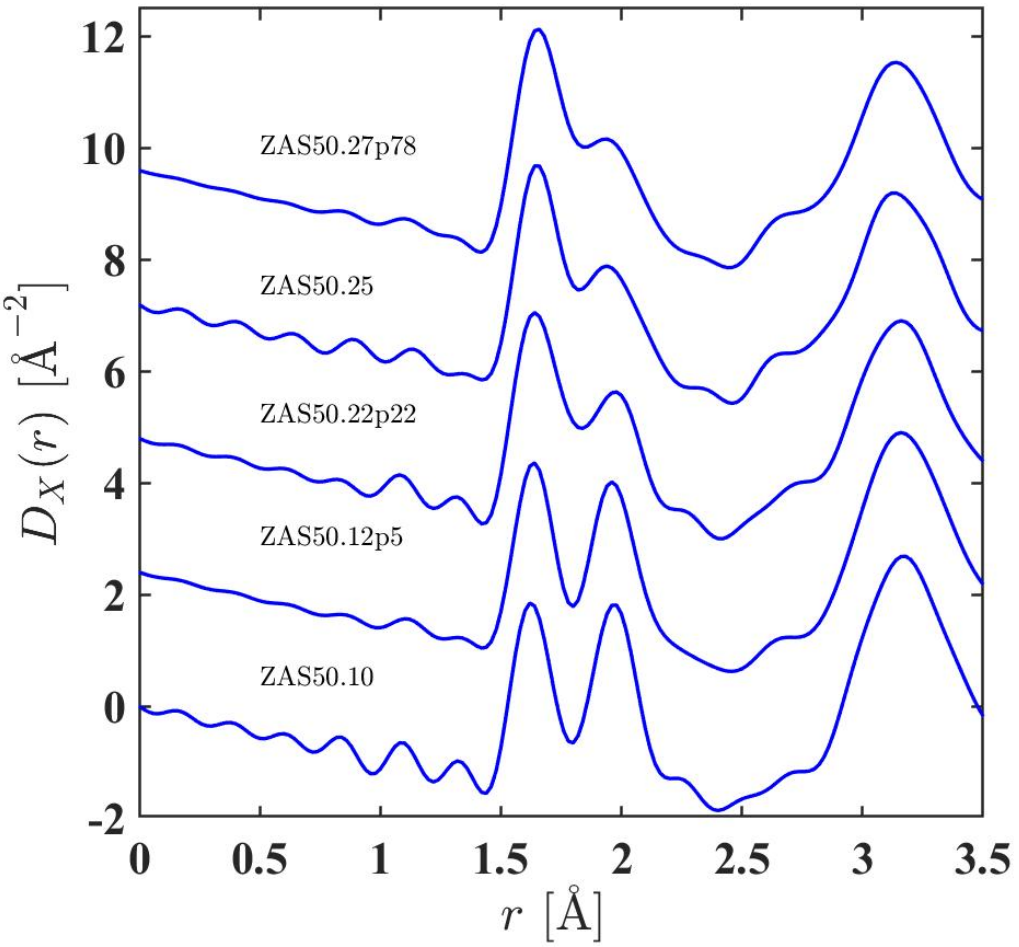

Figure 4-18: $D_X(r)$ functions for the ZAS glasses along the 50 mol% SiO_2 tie-line. The curves were obtained by Fourier transforming the corresponding reciprocal space data shown in figure 4-14. The curves are offset vertically for clarity of presentation.

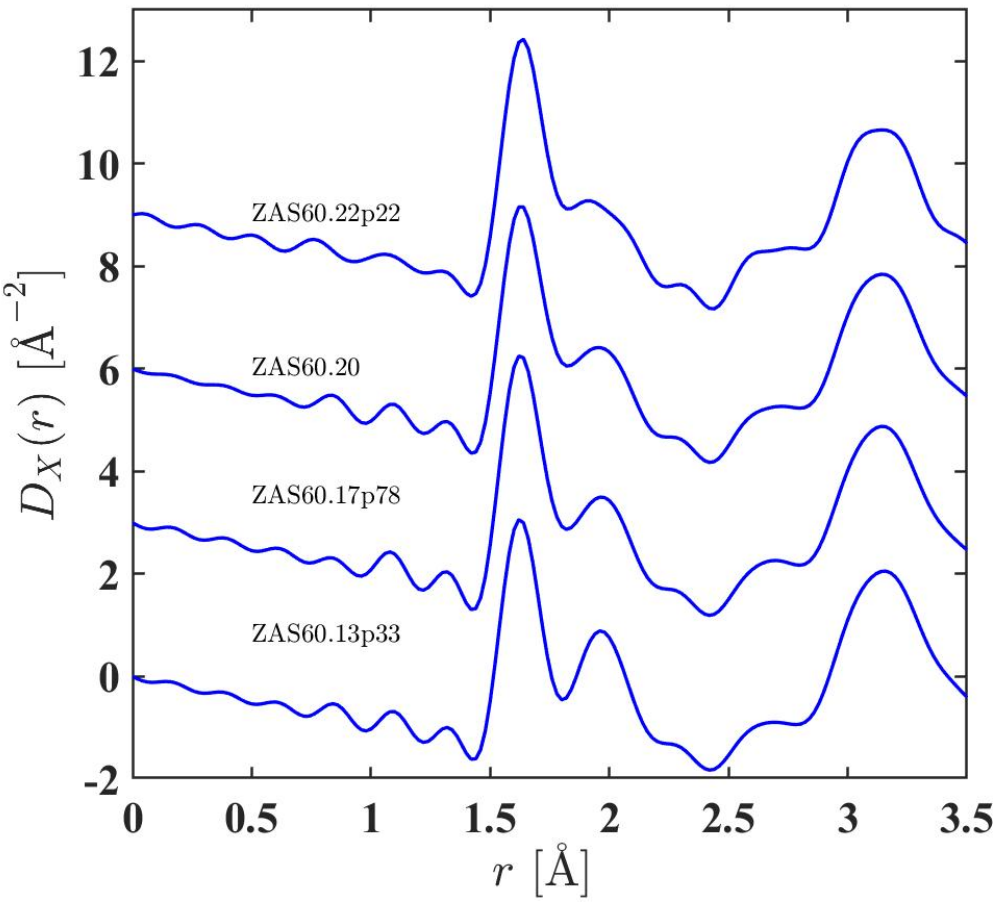

Figure 4-19: $D_X(r)$ functions for the ZAS glasses along the 60 mol% SiO_2 tie-line. The curves were obtained by Fourier transforming the corresponding reciprocal space data shown in figure 4-15. The curves are offset vertically for clarity of presentation.

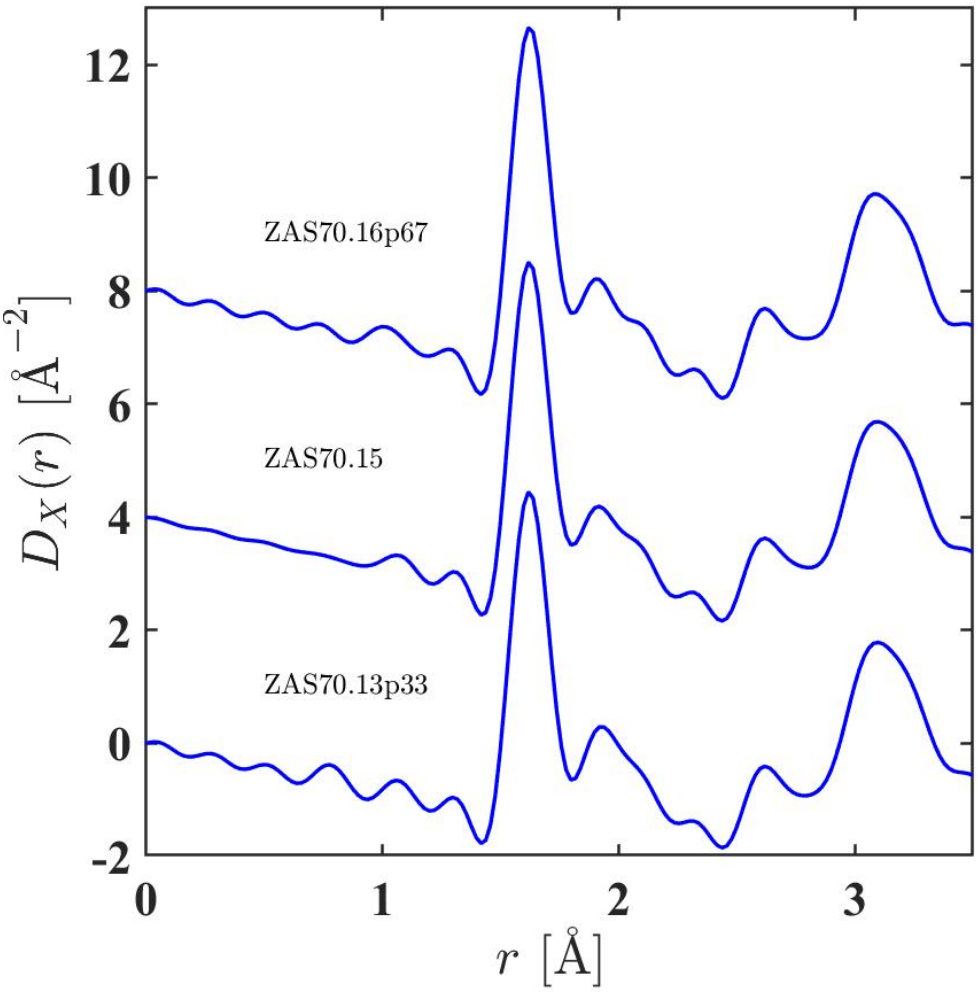

Figure 4-20: $D_X(r)$ functions for the ZAS glasses along the 70 mol% SiO_2 tie-line. The curves were obtained by Fourier transforming the corresponding reciprocal space data shown in figure 4-16. The curves are offset vertically for clarity of presentation.

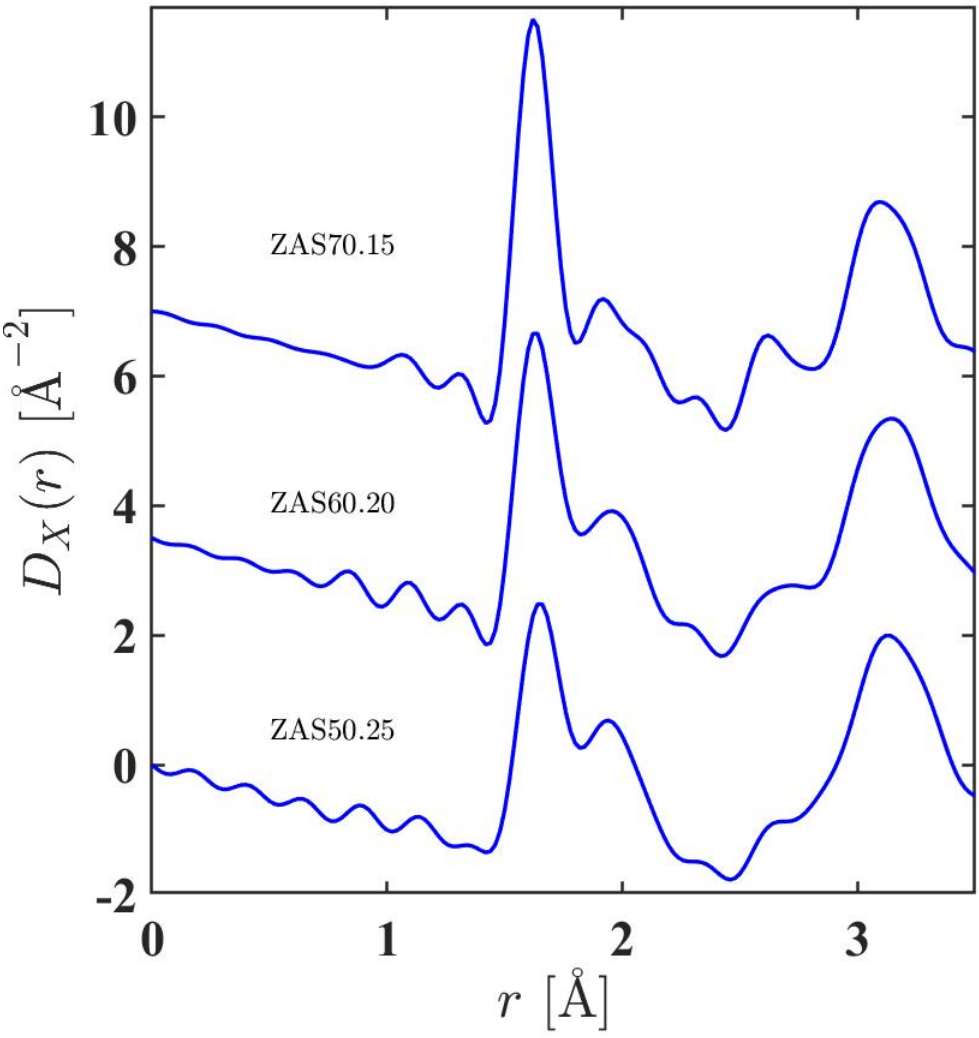

Figure 4-21: $D_X(r)$ functions for the ZAS glasses along the $R = 1$ tie-line. The curves were obtained by Fourier transforming the corresponding reciprocal space data shown in figure 4-21. The curves are offset vertically for clarity of presentation.

Sample	Atom pair	r [Å]	$\sigma_{\alpha\beta}$ [Å]	$\bar{n}_\alpha^\beta$	R_χ [%]
ZAS50.10	Si-O	1.619(1)	0.049(1)	4*	5.42
	Al-O	1.779(3)	0.046(1)	4.07*	
	Zn-O	1.970(1)	0.073(2)	2.88(9)	
	Zn-O	2.169(6)	0.162(6)	1.74(4)	
	Zn-O (sum)	2.614(4)	0.117(3)	4.62(8)	
	O-O			4.89(11)	
	Zn-Zn	3.199(6)	0.261(4)	12.0(3)	
ZAS50.12p5	Si-O	1.6262(9)	0.0604(9)	4*	4.79
	Al-O	1.764(4)	0.100(3)	4.06*	
	Zn-O	1.9763(9)	0.0888(9)	3.43(3)	
	Zn-O	2.256(5)	0.140(3)	1.41(4)	
	Zn-O (sum)	2.620(3)	0.112(2)	4.84(8)	
	O-O			4.73(2)	
	Zn-Zn	3.200(5)	0.269(3)	12.7(3)	
ZAS50.22p22	Si-O	1.621(1)	0.062(1)	4*	6.31
	Al-O	1.778(2)	0.082(1)	4.12*	
	Zn-O	1.977(2)	0.069(1)	2.18(4)	
	Zn-O	2.149(4)	0.150(5)	2.80(9)	
	Zn-O (sum)			4.98(10)	
	O-O	2.624(7)	0.133(4)	5.0(3)	
	Zn-Zn	3.198(1)	0.282(1)	15.5(9)	
ZAS50.25	Si-O	1.631(1)	0.0718(8)	4*	4.00
	Al-O	1.778(2)	0.108(2)	4.17*	
	Zn-O	1.992(1)	0.090(1)	3.03(3)	
	Zn-O	2.254(4)	0.150(4)	2.19(4)	
	Zn-O (sum)			5.22(8)	
	O-O	2.642(2)	0.124(2)	5.04(8)	
	Zn-Zn	3.186(4)	0.273(3)	16.0(3)	
ZAS50.27p78	Si-O	1.6344(8)	0.0730(7)	4*	4.46
	Al-O	1.776(2)	0.119(1)	4.22*	
	Zn-O	1.991(2)	0.097(1)	3.13(4)	
	Zn-O	2.257(4)	0.139(3)	2.18(5)	
	Zn-O (sum)			5.31(10)	
	O-O	2.637(2)	0.125(2)	5.03(6)	
	Zn-Zn	3.187(5)	0.278(3)	17.9(3)	

Table 4.9: Parameters obtained from Gaussian peak fits to the $D_X(r)$ functions for the ZAS glasses along the 50 mol% SiO_2 tie-line. The fitted functions are shown in figure 4-22. The parameters denoted by an * are fixed. R_χ is given for the fitted range 1.30-3.20 Å.

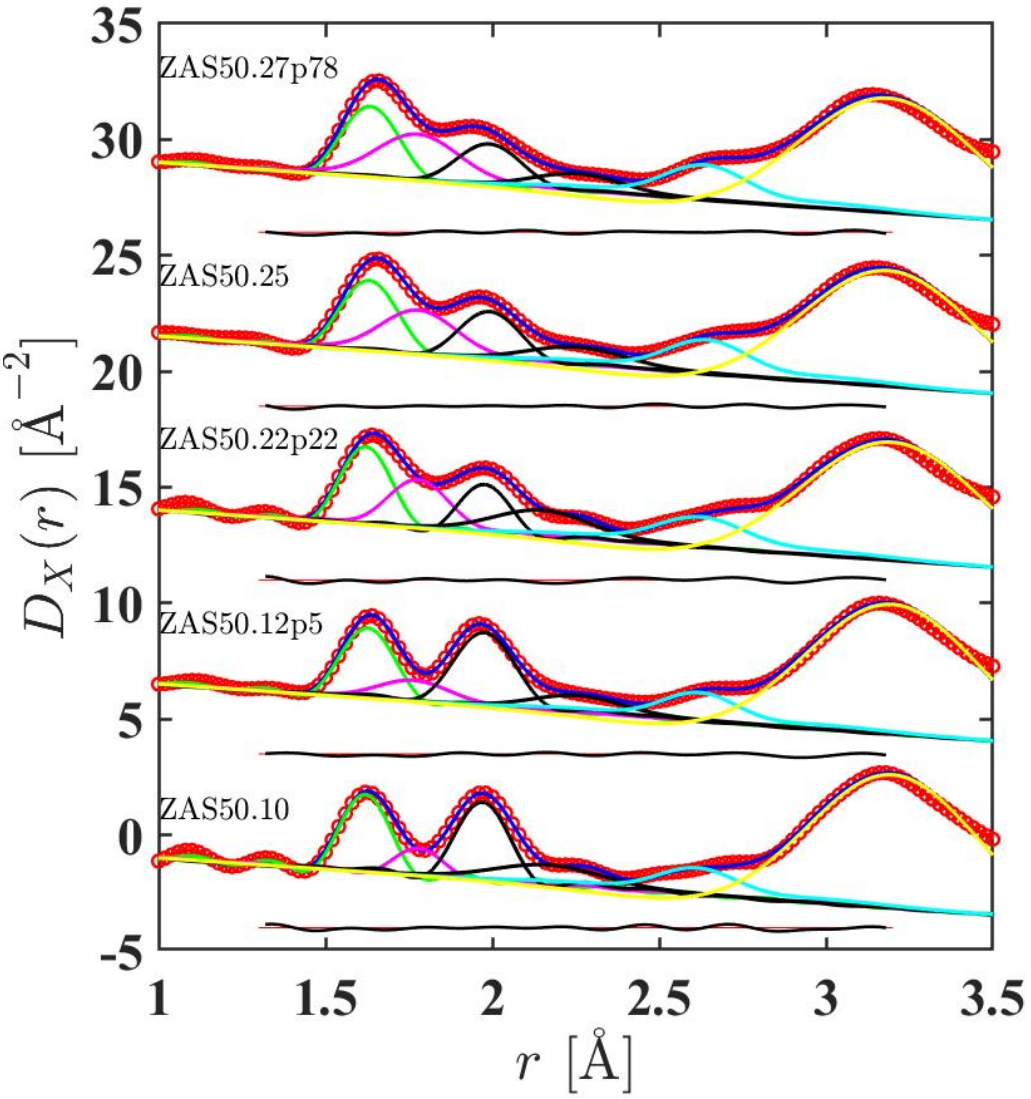

Figure 4-22: The fitted $D_X(r)$ functions for the ZAS glasses along the 50 mol% SiO_2 tie-line. The red circles are the data, the blue solid curves are the fits and the other curves show the contribution from Si-O (green), Al-O (magenta), Zn-O (black), O-O (cyan) and Zn-Zn (yellow) correlations. The displaced black solid curve gives the residual (fit subtracted from measured data). The O-O and Zn-Zn correlations are introduced to constrain the peaks fitted at smaller r values.

Sample	Atom pair	$r_{\alpha\beta}$ [Å]	$\sigma_{\alpha\beta}$ [Å]	$\bar{n}_\alpha^\beta$	R_χ [%]
ZAS60.13p33	Si-O	1.6174(9)	0.056(1)	4*	6.39
	Al-O	1.773(3)	0.073(2)	4.13*	
	Zn-O	1.976(1)	0.076(1)	2.72(5)	
	Zn-O	2.187(7)	0.160(7)	2.16(8)	
	Zn-O (sum)	2.624(3)	0.113(3)	5.12(10)	
	O-O			4.88(8)	
	Zn-Zn	3.183(7)	0.257(5)	13.41(39)	
ZAS60.17p78	Si-O	1.6167(9)	0.058(1)	4*	7.40
	Al-O	1.77(2)	0.077(3)	4.09*	
	Zn-O	1.986(2)	0.082(1)	3.11(7)	
	Zn-O	2.235(7)	0.140(6)	2.18(8)	
	Zn-O (sum)	2.627(3)	0.112(2)	5.29(9)	
	O-O			4.89(2)	
	Zn-Zn	3.190(2)	0.271(1)	16.1(1)	
ZAS60.20	Si-O	1.619(1)	0.062(1)	4*	7.45
	Al-O	1.782(3)	0.085(2)	4.14*	
	Zn-O	1.993(4)	0.083(4)	3.10(10)	
	Zn-O	2.239(8)	0.147(8)	2.26(11)	
	Zn-O (sum)	2.639(3)	0.120(3)	5.36(10)	
	O-O			5.60(10)	
	Zn-Zn	3.163(6)	0.243(5)	15.17(10)	
ZAS60.22p22	Si-O	1.6215(7)	0.061(9)	4*	7.34
	Al-O	1.789(2)	0.092(1)	4.15*	
	Zn-O	2.001(2)	0.082(2)	2.73(5)	
	Zn-O	2.244(6)	0.168(6)	3.02(9)	
	Zn-O (sum)	2.638(2)	0.114(2)	5.75(7)	
	O-O			5.11(7)	
	Zn-Zn	3.165(2)	0.257(3)	17.50(10)	

Table 4.10: Parameters obtained from Gaussian peak fits to the $D_X(r)$ functions for the ZAS glasses along the 60 mol% SiO_2 tie-line. The fitted functions are shown in figure 4-23. R_χ is given for the fitted range 1.30-3.20 Å.

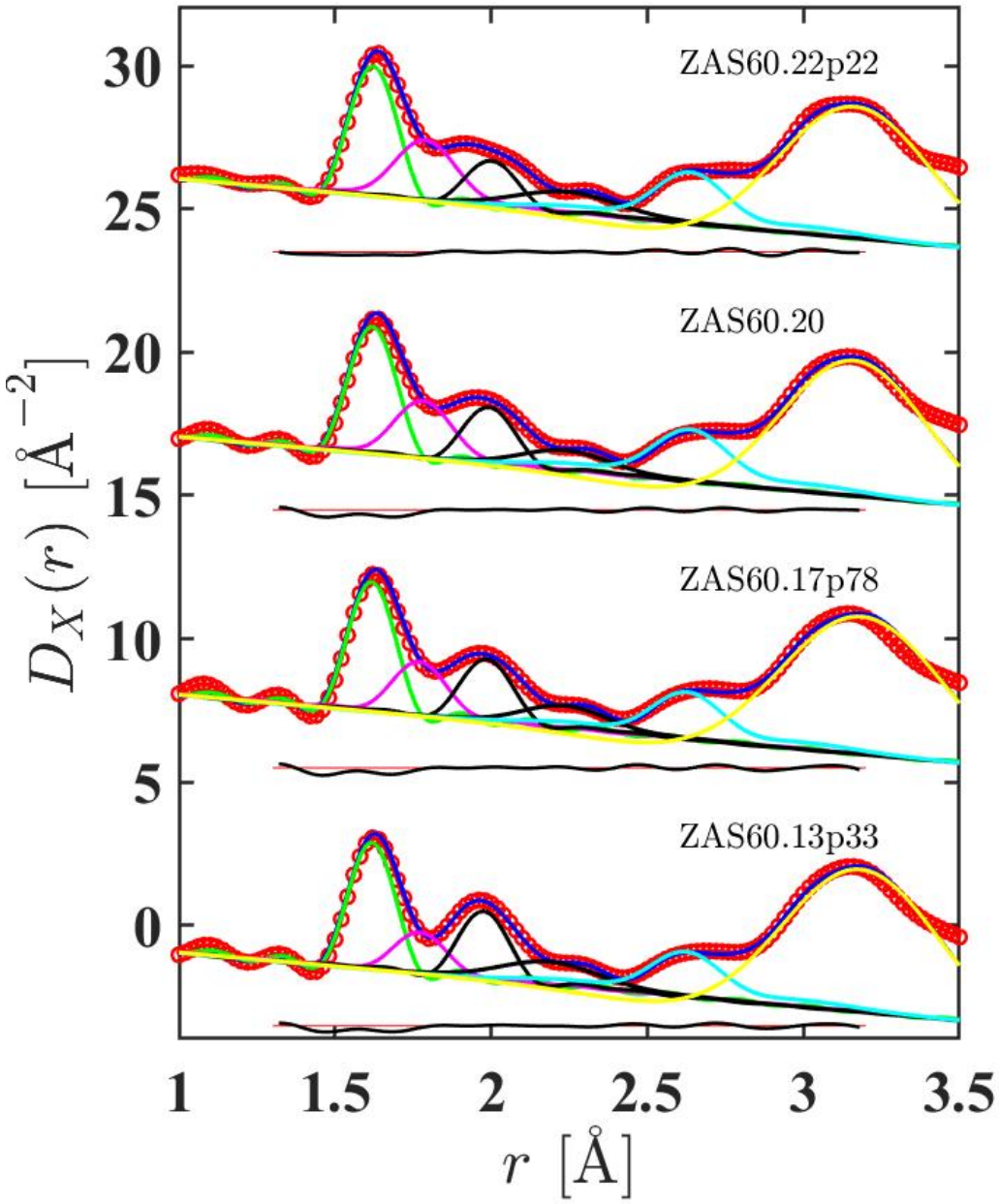

Figure 4-23: The fitted $D_X(r)$ functions for the ZAS glasses along the 60 mol% SiO_2 tie-line. The red circles are the data, the blue solid curves are the fits and the other curves show the contribution from Si-O (green), Al-O (magenta), Zn-O (black), O-O (cyan) and Zn-Zn (yellow) correlations. The displaced black solid curve gives the residual (fit subtracted from measured data). The O-O and Zn-Zn correlations are introduced to constrain the peaks fitted at small r values.

Sample	Atom pair	$r_{\alpha\beta}$ [Å]	$\sigma_{\alpha\beta}$ [Å]	$\bar{n}_{\alpha}^{\beta}$	R_{χ} [%]
	Si-O	1.6193(7)	0.0585(8)	4*	
	Al-O	1.789(5)	0.103(5)	4.12*	
	Zn-O	2.001(4)	0.098(4)	3.48(10)	
ZAS70.13p33	Zn-O	2.322(10)	0.150(9)	2.34(10)	6.64
	Zn-O (sum)			5.82(10)	
	O-O	2.635(3)	0.098(2)	5.00(9)	
	Zn-Zn	3.146(6)	0.228(5)	14.8(5)	
	Si-O	1.6173(8)	0.060(1)	4*	
	Al-O	1.789(4)	0.094(6)	4.13*	
	Zn-O	1.994(4)	0.082(4)	2.89(10)	
ZAS70.15	Zn-O	2.249(1)	0.149(2)	2.92(11)	7.39
	Zn-O (sum)			5.81(10)	
	O-O	2.628(3)	0.102(2)	5.05(10)	
	Zn-Zn	3.156(7)	0.241(6)	17.3(6)	
	Si-O	1.6182(6)	0.0573(6)	4*	
	Al-O	1.794(2)	0.093(2)	4.2*	
	Zn-O	1.996(3)	0.081(2)	3.62(10)	
ZAS70.16p67	Zn-O	2.222(9)	0.140(7)	2.32(12)	6.94
	Zn-O (sum)			5.94(10)	
	O-O	2.638(2)	0.114(2)	5.02(2)	
	Zn-Zn	3.129(2)	0.203(1)	18.9(1)	

Table 4.11: Parameters obtained from Gaussian peak $D_X(r)$ fits to the r space functions for the ZAS glasses along the 70 mol% SiO_2 tie-line. The fitted functions are shown in figure 4-24. The parameters denoted by an * are fixed. R_{χ} is given for the fitted range 1.30-3.20 Å.

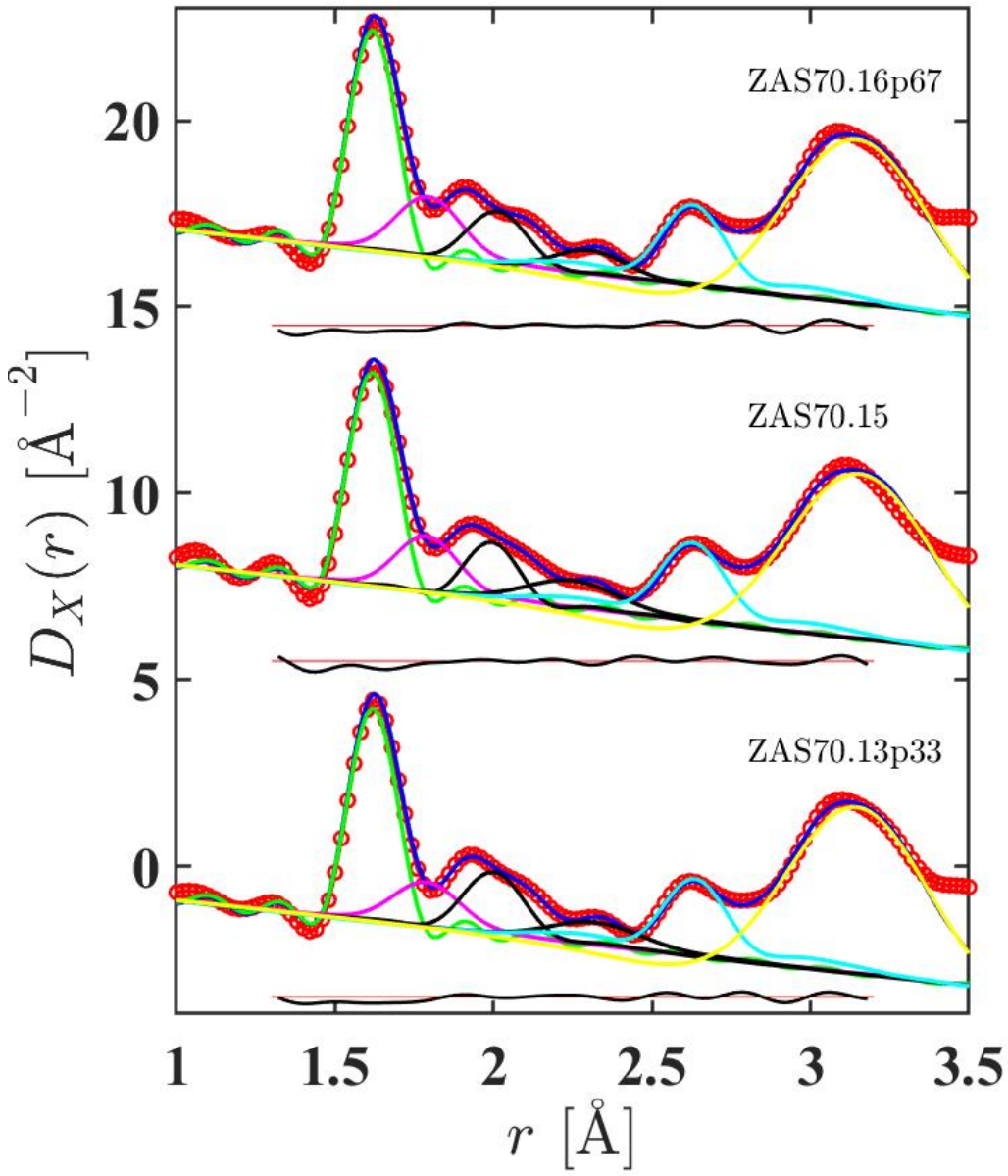

Figure 4-24: The fitted $D_X(r)$ functions for the ZAS glasses along the 70 mol% SiO_2 tie-line. The red circles are the data, the blue solid curves are the fits and the other curves show the contribution from Si-O (green), Al-O (magenta), Zn-O (black), O-O (cyan) and Zn-Zn (yellow) correlations. The displaced black solid curves gives the residual (fit subtracted from measured data). The O-O and Zn-Zn correlations are introduced to constrain the peaks fitted at small r values.

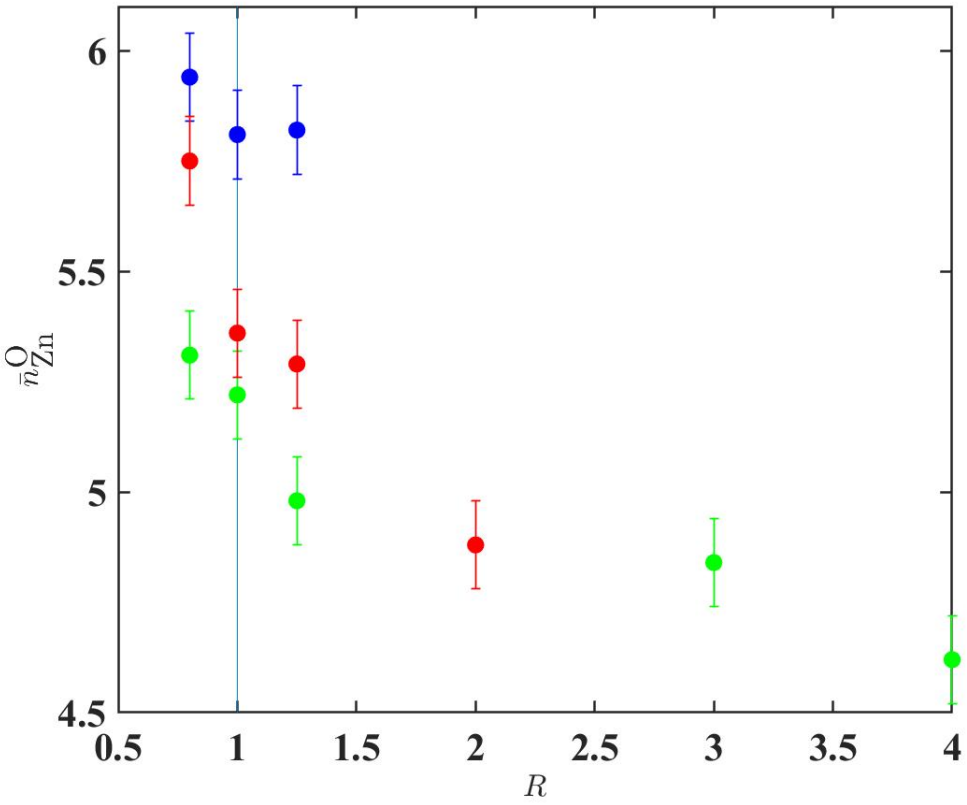

Figure 4-25: Zn-O coordination number as a function of the ratio R obtained from the $D_X(r)$ fits. The green data points show the coordination numbers along the 50 mol% SiO_2 tie-line. The red data points show the coordination numbers along the 60 mol% SiO_2 tie-line and the blue data points show the coordination numbers along the 70 mol% SiO_2 tie-line. The cyan line at $R = 1$ indicates the tectosilicate composition.

4.3.3 Neutron diffraction

Zn2SiO4 crystal

In most crystalline structures, Zn^{2+} is tetrahedrally coordinated ($\alpha-Zn_2SiO_4$) [70, 71] with Zn-O distances in the range 1.85-2.04 Å and, rarely, octahedrally coordinated with longer Zn-O distances at 1.98-2.26 Å.

For willemite, Zn_2SiO_4, the $S_N(Q)$ function is shown in figure 4-27 where Bragg peaks are observed. The $S_N(Q)$ function was Fourier transformed with $Q_{\max} = 31.95$ Å^{-1}, using a step modification function to obtain the total pair distribution function $D_N(r)$ (Figure 4-28). The $D_N(r)$ function shows 4 well defined peaks at $r \approx 1.635$ Å, $r \approx 1.96$ Å, $r \approx 2.67$ Å and $r \approx 3.22$ Å. The very small peak at $r \approx 2.4$ Å is due to a Fourier transform artefact.

The first peak is due to Si-O correlations within SiO_4 tetrahedra and the second peak is attributed to Zn-O correlations within ZnO_4 tetrahedra. For tetrahedral SiO_4 and ZnO_4 motifs, the nearest neighbor O-O correlations are expected to be at $r_{OO} = \sqrt{8/3} r_{SiO} = 2.67$ Å and $r_{OO} = \sqrt{8/3} r_{ZnO} = 3.20$ Å, respectively. Although the peak at $r \approx 2.67$ Å is mainly due to O-O correlations within SiO_4, the peak at $r \approx 3.22$ Å will have contributions from O-O correlations within ZnO_4 but also contributions from Zn-Zn and Zn-Si correlations.

The fitted $D_N(r)$ function is shown in figure 4-29. One peak was assigned to Si-O correlations, two peaks were assigned to Zn-O correlations and one peak was assigned to O-O correlations. Although there is only a Zn-O coordination number of 4 for Zn_2SiO_4 crystals (Figure 4-26), two peaks needed to be fit for the Zn-O peak in order to cover the entire area.

Table 4.12 shows the fitted parameters with the corresponding goodness-of-fit R_χ, over the fitted range 1.30-2.90 Å. The average coordination number of Si-O was taken from ^{29}Si MAS NMR measurements.

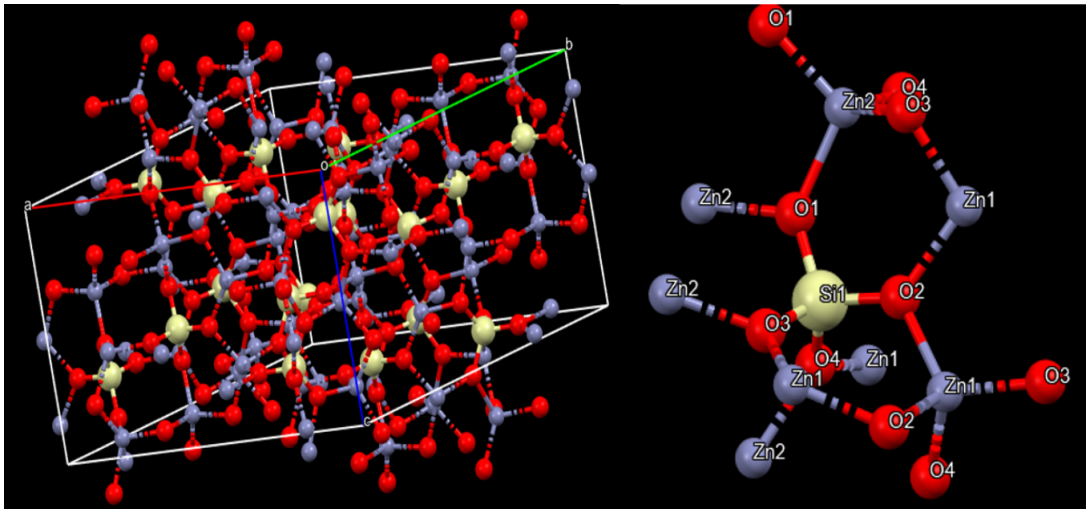

Figure 4-26: Ball and stick model for the Zn_2SiO_4 crystal produced by using the program Mercury [102] for crystallographic data. The CIF file was taken from [70].

Atom-pair	$r_{\alpha\beta}$[Å]	$\sigma_{\alpha\beta}$ [Å]	$\bar{n}_\alpha^\beta$	R_χ [%]
Si-O	1.635(1)	0.046(5)	4.00(5)	
Zn-O	1.945(1)	0.046(5)	2.00(9)	
Zn-O	2.000(1)	0.071(5)	2.00(9)	
Zn-O(sum)			4.00(10)	
O-O	2.669(1)	0.081(5)	3.00(10)	
Zn-O	3.084(1)	0.053(5)	0.50*	
Zn-Si	3.190(1)	0.098(5)	4.00*	
Zn-Zn	3.214(1)	0.106(5)	4.00*	7.54
O-O	3.236(1)	0.123(5)	6.00*	
Zn-O	3.364(1)	0.165(5)	1.50*	
O-O	3.450(1)	0.124(5)	2.00*	
Si-O	3.498(1)	0.088(5)	2.00*	
Zn-O	3.710(1)	0.181(5)	7.50*	
Si-O	3.820(1)	0.186(5)	6.00*	

Table 4.12: Parameters obtained from Gaussian $D_N(r)$ peak fits to the r-space function for the crystalline Zn_2SiO_4. The fitted function is shown in figure 4-29. R_χ is given for the fitted range 1.30-3.80 Å.

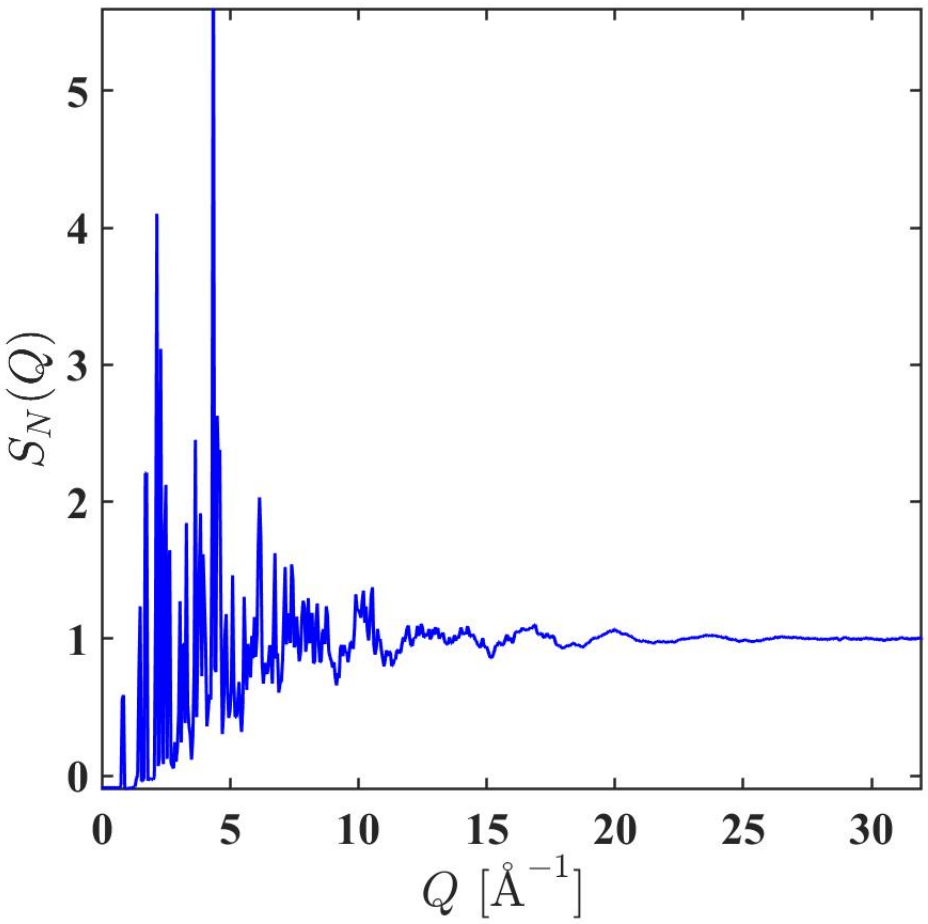

Figure 4-27: Total structure factor $S_N(Q)$ for the crystalline Zn_2SiO_4 sample with $Q_{\max} = 31.95$ Å^{-1}. The error bars are smaller than the line thickness at most Q values.

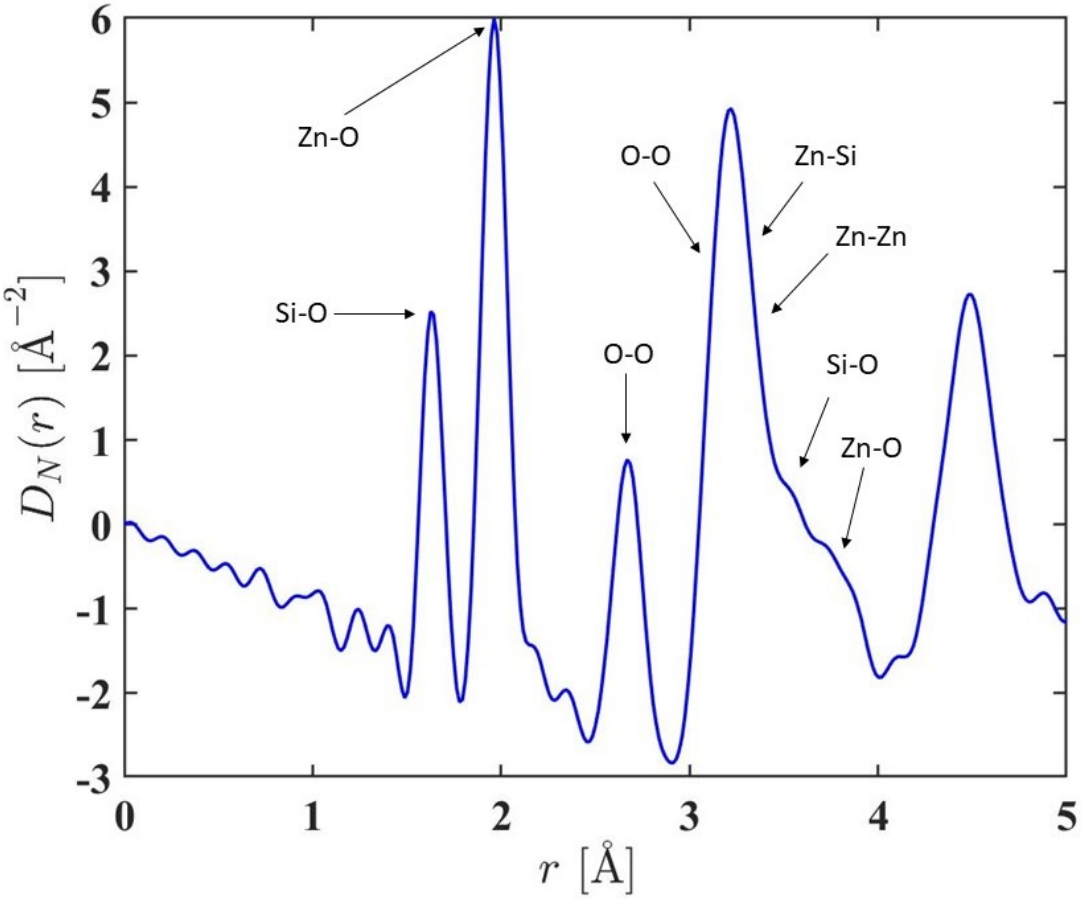

Figure 4-28: $D_N(r)$ function for the crystalline Zn_2SiO_4 sample. The curve was obtained by Fourier transforming the corresponding reciprocal space data shown in figure 4-27. Arrows indicate peak assignments based on the element-element distances found in the crystal structure [70, 71].

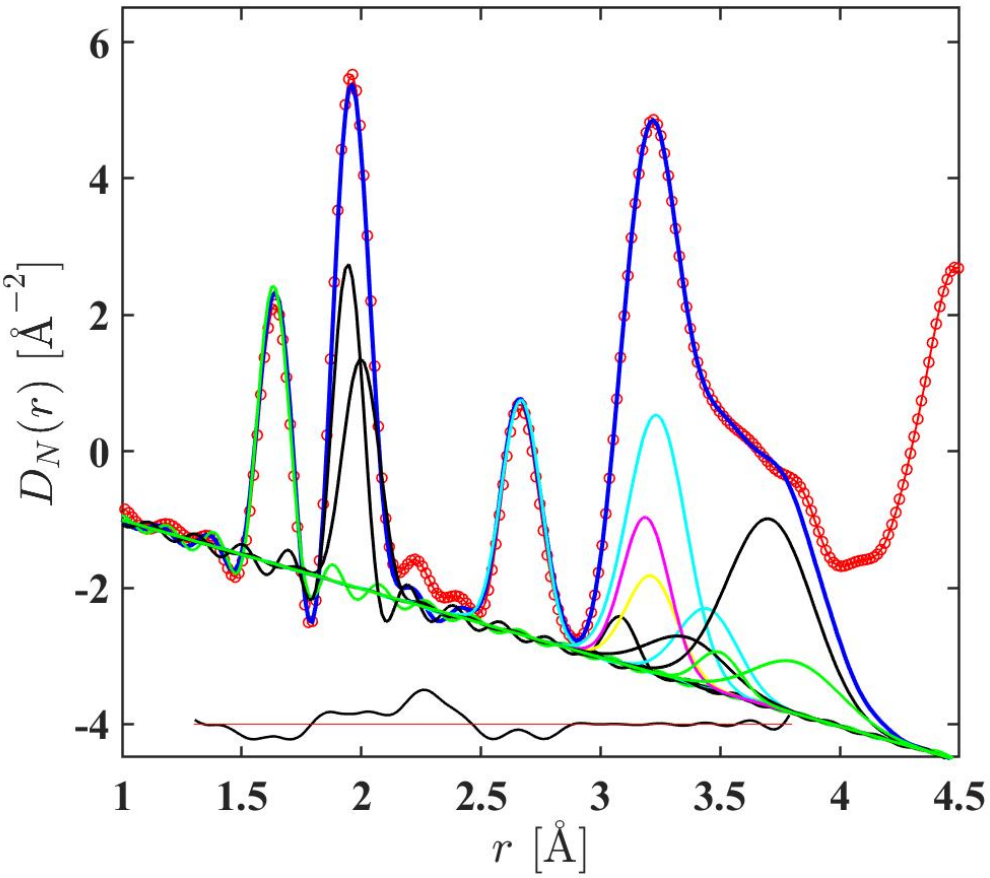

Figure 4-29: The fitted $D_N(r)$ function for the Zn_2SiO_4 crystal. The red circles are the data, the blue solid curves are the fits and the other curves show the contribution from Si-O (green), Zn-O (black), Zn-Si (magenta), Zn-Zn (yellow) and O-O (cyan) correlations. The displaced black solid curves gives the residual (fit subtracted from measured data).

$(ZnO)_x(Al_2O_3)_y(SiO_2)_{1-x-y}$ glasses

The neutron total structure factors $S_N(Q)$ of ZAS glasses are shown in figures 4-30, 4-31, 4-32 and 4-33 and the weighting factors for the partial pair distribution functions are given in table 4.14. All $S_N(Q)$ functions adopt the usual three peak structure at small Q values which are listed in table 4.13, along with their respective $Q_{\max}$ values used for the Fourier transformation.

The FSDP occurs in the range from 1.584(1)-1.790(1) $Å^{-1}$ and is in agreement with previous neutron diffraction experiments [82] on similar compositions for the zinc aluminosilicate glasses. This peak becomes less broad and more intense as the SiO_2 content increases and is an important assignment to the medium range order [100].

The $S_N(Q)$ were Fourier transformed using a step modification function to get the total pair distribution function $D_N(r)$ (Figures 4-34, 4-35, 4-36 and 4-37). The $D_N(r)$ functions show defined peaks at $r \approx 1.6$ Å, $r \approx 1.77$ Å, $r \approx 2.0$ Å and $r \approx 2.66$ Å which correspond to Si-O, Al-O, Zn-O and O-O correlations respectively. As the SiO_2 content increases, the peaks attributed to Si-O and O-O correlations become sharper. However, the Si-O and O-O peak positions remain at $r \approx 1.62$ Å and $r \approx 2.66$ Å for all compositions, enforcing the presence of SiO_4 tetrahedra.

In contrast with the $D_X(r)$ functions, the $D_N(r)$ functions do not show a peak at $r \approx 3.18$ Å. This is due to the low neutron weighting factors for correlations involving zinc. Above 3.5 Å there is an overlap between different contributions which makes it difficult to extract information. The fitted $D_N(r)$ functions are shown in figures 4-38, 4-39 and 4-41. For each $D_N(r)$ fit one peak was assigned to Si-O correlations, one peak to Al-O correlations, two peaks to Zn-O correlations and one peak was assigned to O-O correlations.

Tables 4.15, 4.16, 4.17 and 4.18 show the fitted parameters with the corresponding goodness-of-fit, R_χ, over the fitted range 1.30-2.80 Å. The O-O correlations were fitted in order to constrain the peaks at small r-values and because the O-O peak has a well defined minimum there is no need to fit beyond 2.8 Å like in the $D_X(r)$ fits.

The $D_N(r)$ functions were firstly fitted by fixing the parameters from the $D_X(r)$ fits. Then the fitted parameters were refined slowly starting by the peak widths and then the peak positions. If the fit doesn't have an overall good agreement with the data, the coordination numbers of O-O are also refined slightly until R_χ is as close to zero as possible. The average coordination number of Si-O was fixed to 4 and the average coordination numbers for Al-O were fixed to the values obtained from ^{27}Al MAS NMR

measurements. The Zn-O coordination numbers as a function of R are shown in figure 4-42.

Sample	Q_{FSDP} [Å^{-1}]	Q_{PP} [Å^{-1}]	Q_3 [Å^{-1}]	Q_{max} [Å^{-1}]
ZAS50.7p5	1.717(1)	2.664(1)	4.491(2)	47.2
ZAS50.10	1.790(1)	2.706(1)	4.542(2)	45.95
ZAS50.12p5	1.767(1)	2.712(1)	4.575(2)	49.1
ZAS50.17p36	1.700(1)	2.668(1)	4.629(2)	45.2
ZAS50.22p22	1.749(1)	2.715(1)	4.898(2)	46.05
ZAS50.25	1.753(1)	2.717(1)	4.935(2)	45.3
ZAS50.27p78	1.739(1)	2.720(1)	4.956(2)	46.4
ZAS60.13p33	1.675(1)	2.744(1)	5.085(2)	49.3
ZAS60.15p55	1.610(1)	2.703(1)	5.022(2)	47.45
ZAS60.17p78	1.675(1)	2.743(1)	5.077(2)	48.0
ZAS60.20	1.669(1)	2.745(1)	5.082(2)	47.5
ZAS60.22p22	1.661(1)	2.748(1)	5.074(2)	48.8
ZAS65.17p5	1.584(1)	2.721(1)	5.053(2)	48.05
ZAS70.13p33	1.595(1)	2.771(1)	5.154(2)	48.95
ZAS70.15	1.599(1)	2.798(1)	5.151(2)	47.15
ZAS70.16p67	1.596(1)	2.775(1)	5.150(2)	45.85

Table 4.13: The positions of the first three peaks Q_{FSDP}, Q_{PP} and Q_3 in the $S_N(Q)$ functions shown in figures 4-30, 4-31 and 4-32 for the ZAS glasses. The Q_{max} values used in the Fourier transformation are also listed.

Sample	w_{SiO}	w_{AlO}	w_{ZnO}	w_{OO}	$G(0)$
Zn_2SiO_4	0.128(8)	-	0.352(22)	0.359(11)	-0.306(9)
ZAS50.7p5	0.187(29)	0.047(7)	0.217(33)	0.431(33)	-0.286(22)
ZAS50.10	0.184(24)	0.061(8)	0.202(26)	0.438(28)	-0.283(18)
ZAS50.12p5	0.182(21)	0.076(9)	0.187(22)	0.445(26)	-0.280(16)
ZAS50.17p36	0.177(20)	0.102(11)	0.158(18)	0.458(25)	-0.275(15)
ZAS50.22p22	0.173(20)	0.128(15)	0.131(16)	0.469(28)	-0.270(16)
ZAS50.25	0.170(21)	0.141(18)	0.116(15)	0.476(15)	-0.268(17)
ZAS50.27p78	0.168(23)	0.155(21)	0.102(14)	0.482(33)	-0.266(18)
ZAS60.13p33	0.217(28)	0.080(11)	0.132(17)	0.473(31)	-0.276(18)
ZAS60.15p55	0.215(28)	0.092(12)	0.120(16)	0.478(31)	-0.274(18)
ZAS60.17p78	0.212(29)	0.104(14)	0.107(15)	0.483(33)	-0.271(18)
ZAS60.20	0.209(31)	0.116(17)	0.096(14)	0.488(36)	-0.269(20)
ZAS60.22p22	0.207(33)	0.127(21)	0.084(14)	0.493(14)	-0.268(40)
ZAS65.17p5	0.230(37)	0.103(17)	0.085(14)	0.495(40)	-0.270(22)
ZAS70.13p33	0.253(44)	0.080(14)	0.083(15)	0.497(43)	-0.273(24)
ZAS70.15	0.251(46)	0.089(17)	0.074(14)	0.501(46)	-0.271(25)
ZAS70.16p67	0.248(51)	0.098(20)	0.065(14)	0.505(51)	-0.269(27)

Table 4.14: The neutron weighting factors (in barn) for the partial pair distribution functions in $D_N(r)$ for the ZAS glasses. The $G(0)$ values are also listed.

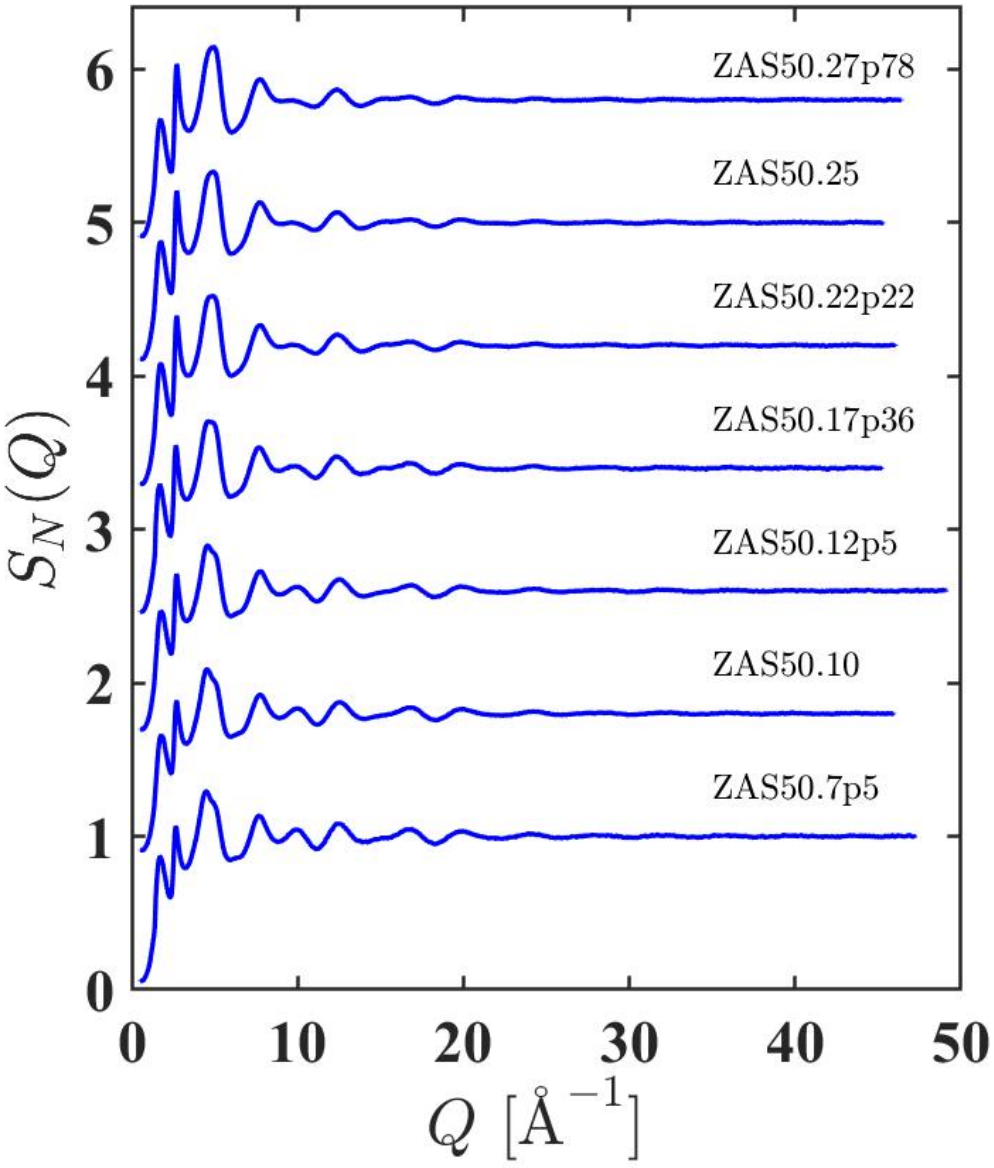

Figure 4-30: Total structure factors $S_N(Q)$ for the ZAS glasses along the 50 mol% SiO_2 tie-line. The error bars are smaller than the line thickness at most Q values. The curves are offset vertically for clarity of presentation.

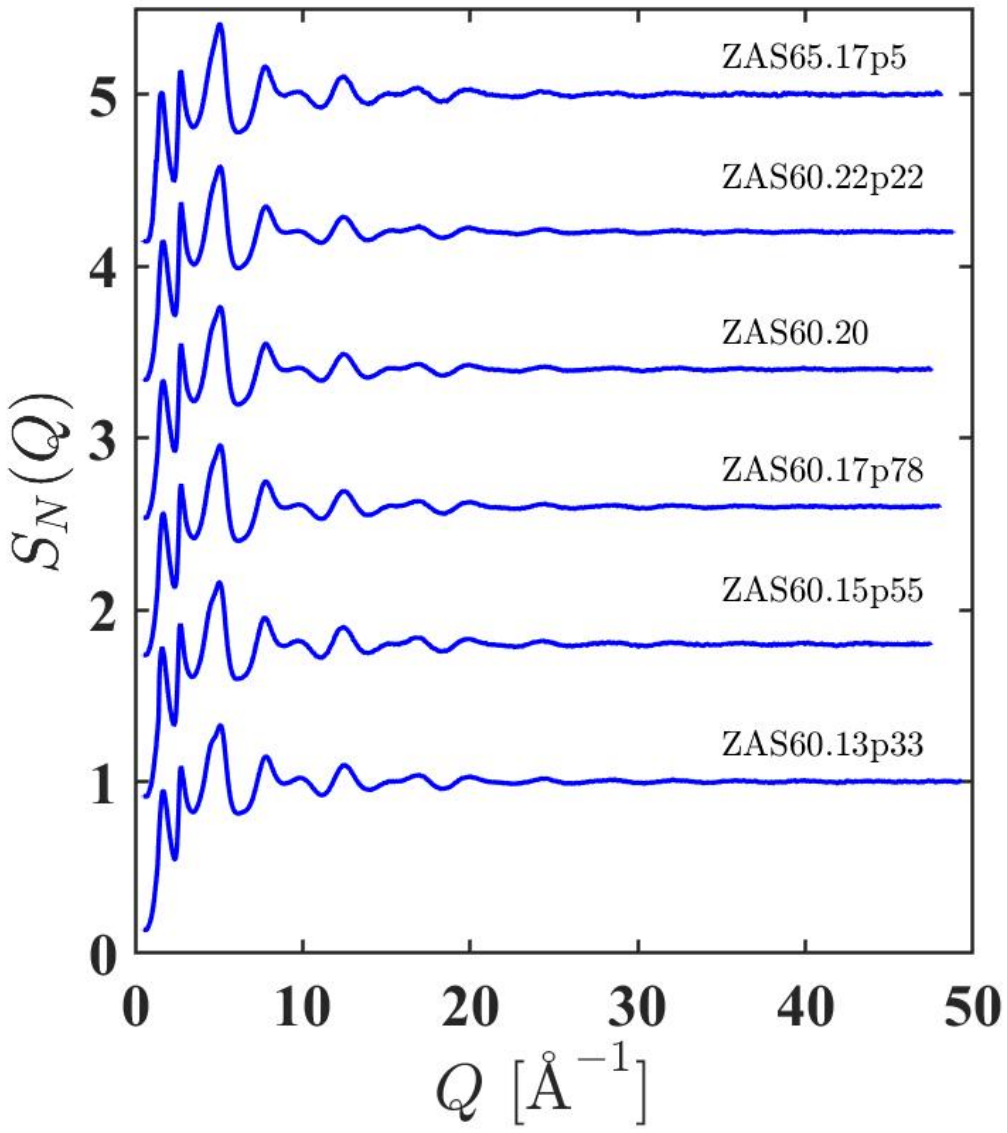

Figure 4-31: Total structure factors $S_N(Q)$ for the ZAS glasses along the 60 and 65 mol% SiO_2 tie-line. The error bars are smaller than the line thickness at most Q values. The curves are offset vertically for clarity of presentation.

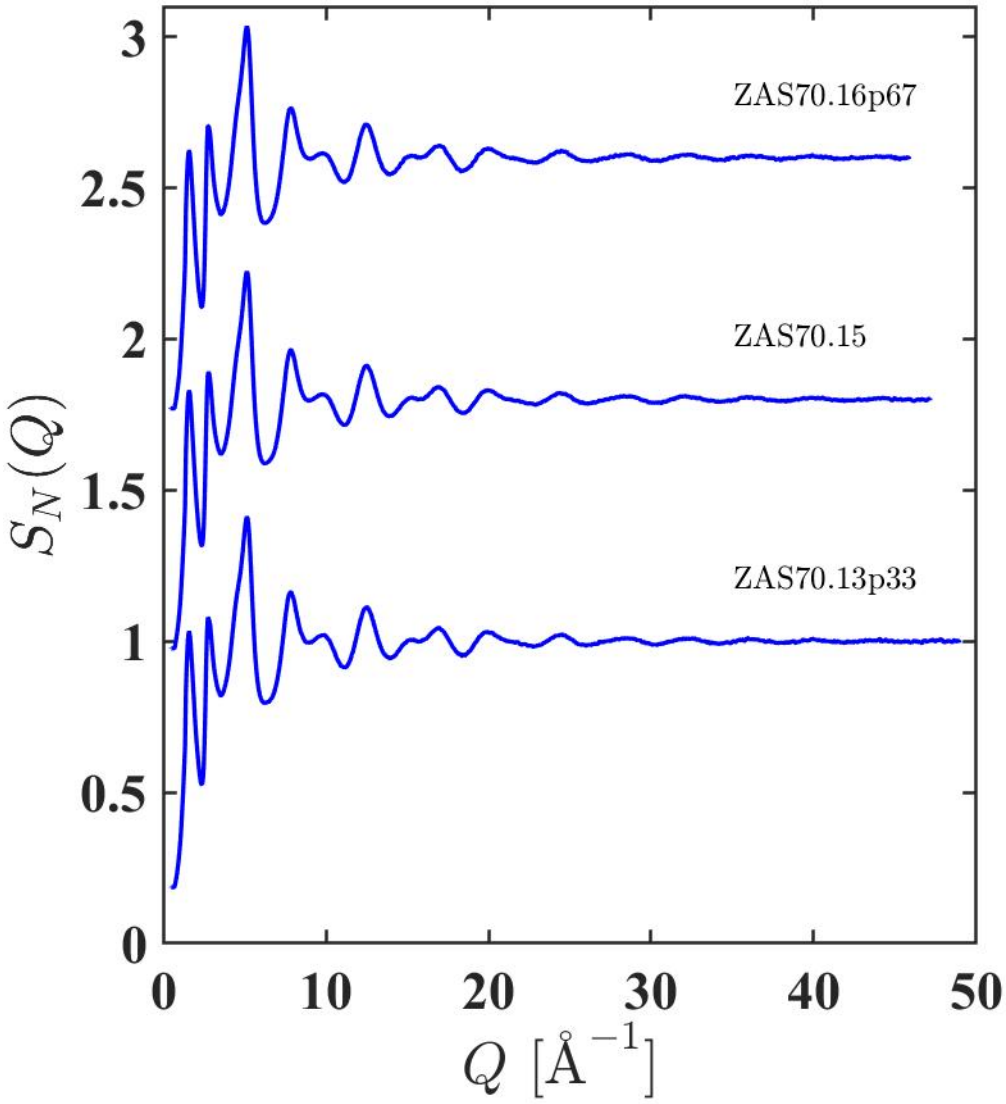

Figure 4-32: Total structure factors $S_N(Q)$ for the ZAS glasses along the 70 mol% SiO_2 tie-line. The error bars are smaller than the line thickness at most Q values. The curves are offset vertically for clarity of presentation.

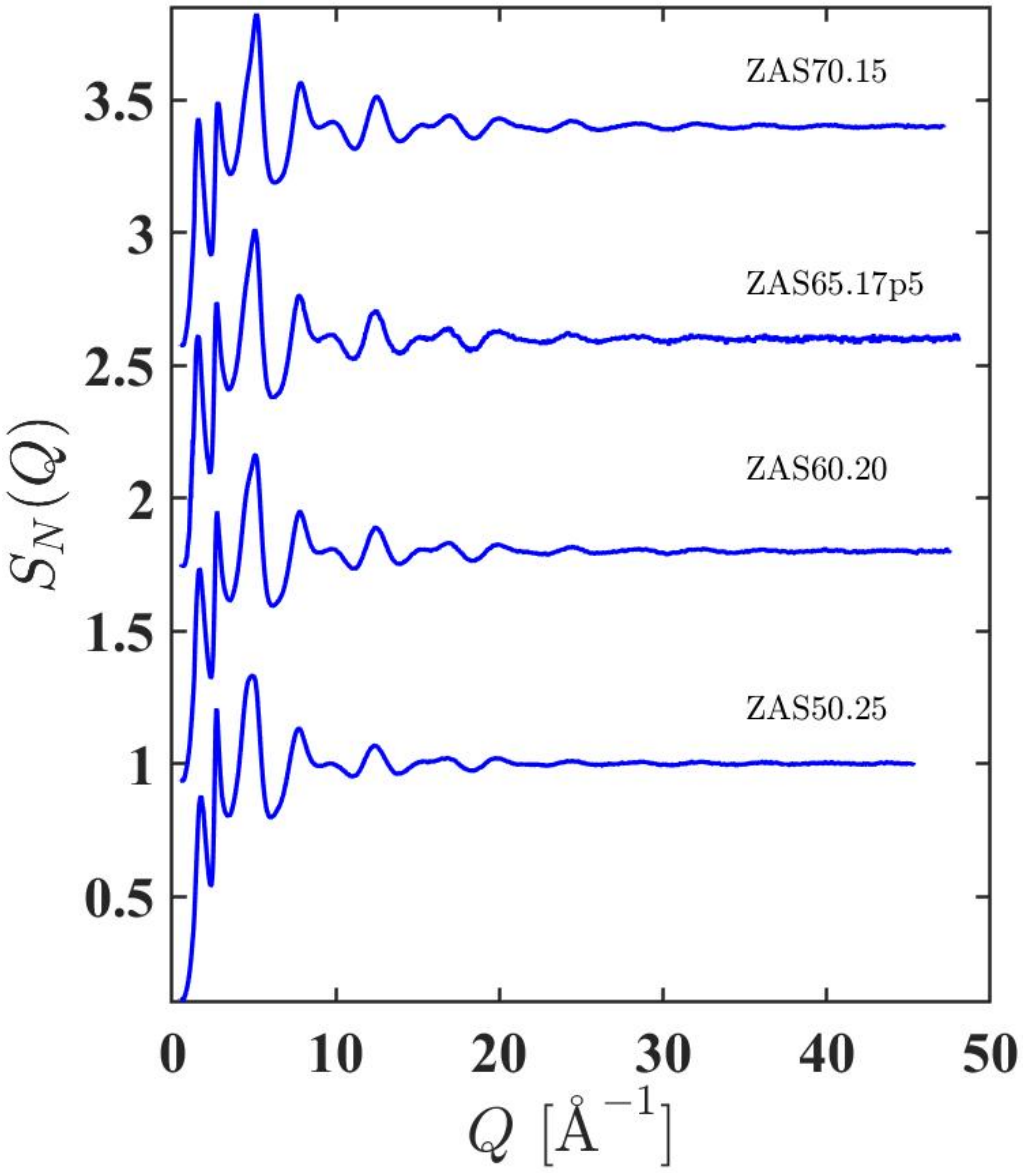

Figure 4-33: Total structure factors $S_N(Q)$ for the ZAS glasses along the $R = 1$ tie-line. The error bars are smaller than the line thickness at most Q values. The curves are offset vertically for clarity of presentation.

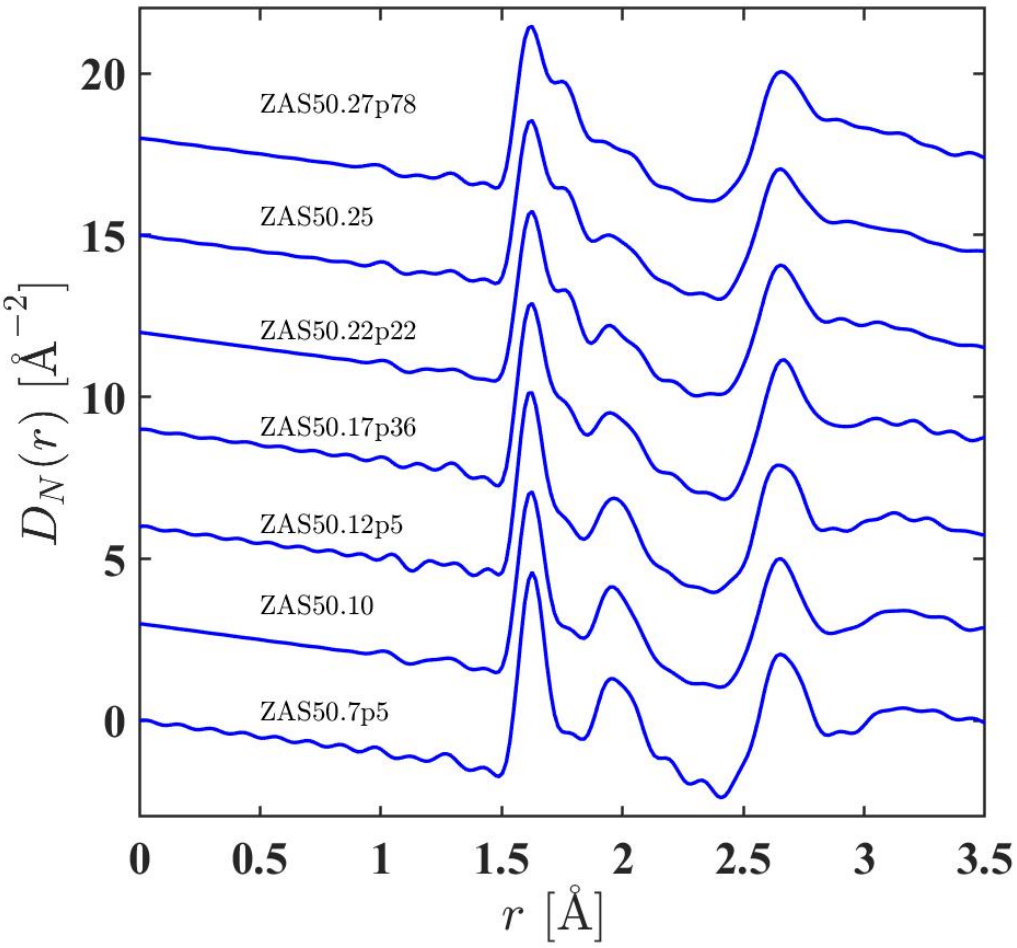

Figure 4-34: $D_N(r)$ functions for the ZAS glasses along the 50 mol% SiO_2 tie-line. The curves were obtained by Fourier transforming the corresponding reciprocal space data shown in figure 4-30 after spline fitting. The curves are offset vertically for clarity of presentation.

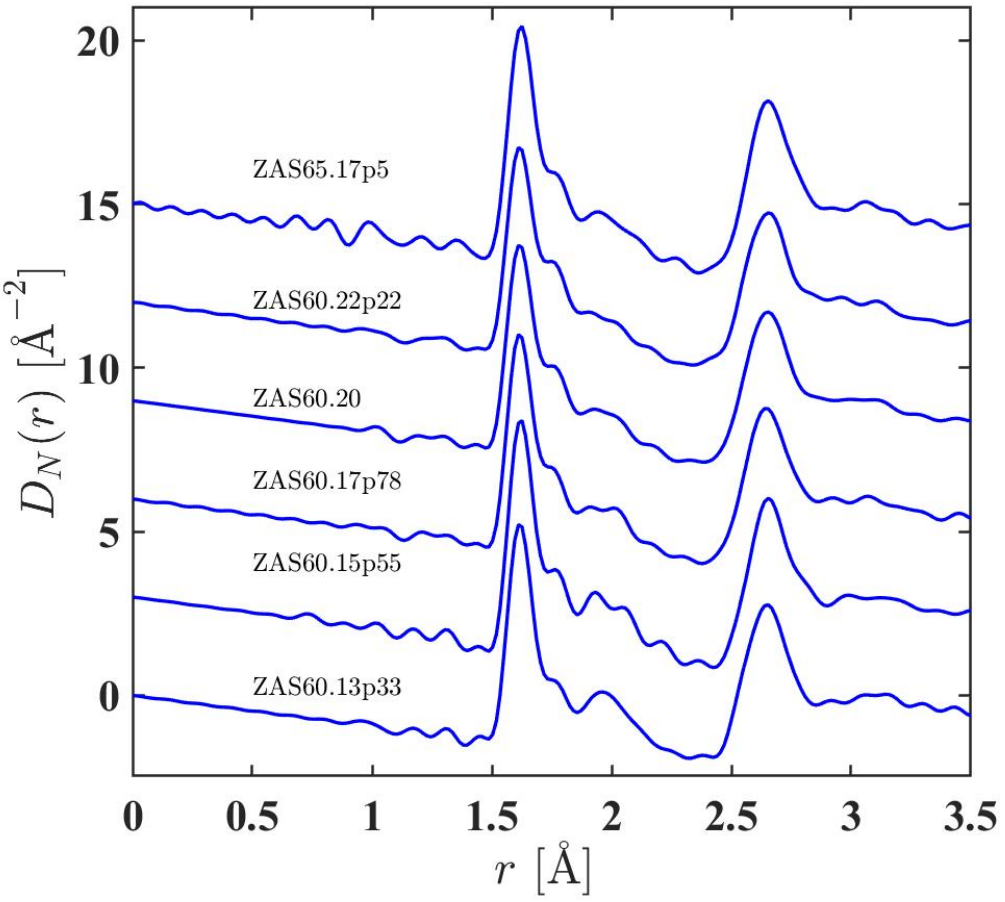

Figure 4-35: $D_N(r)$ functions for the ZAS glasses along the 60 and 65 mol% SiO_2 tie-line. The curves were obtained by Fourier transforming the corresponding reciprocal space data shown in figure 4-31. The curves are offset vertically for clarity of presentation.

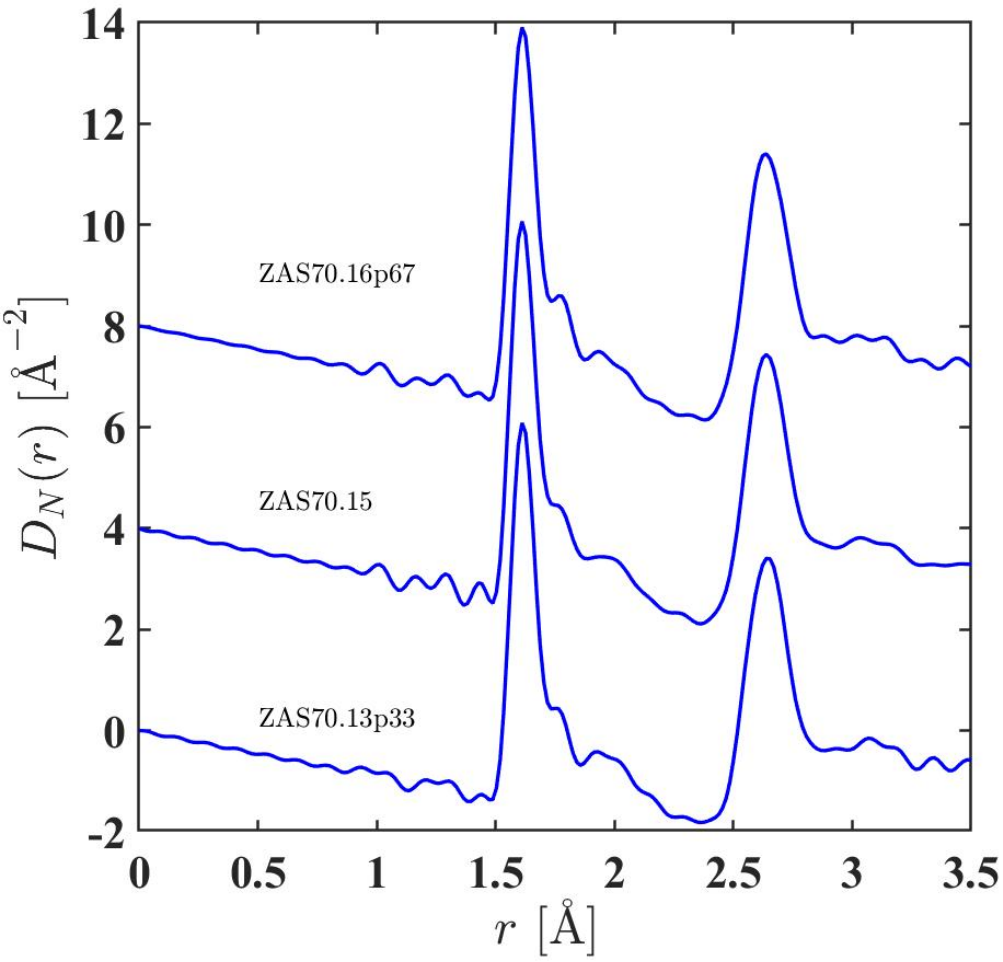

Figure 4-36: $D_N(r)$ functions for the ZAS glasses along the 70 mol% SiO_2 tie-line. The curves were obtained by Fourier transforming the corresponding reciprocal space data shown in figure 4-32. The curves are offset vertically for clarity of presentation.

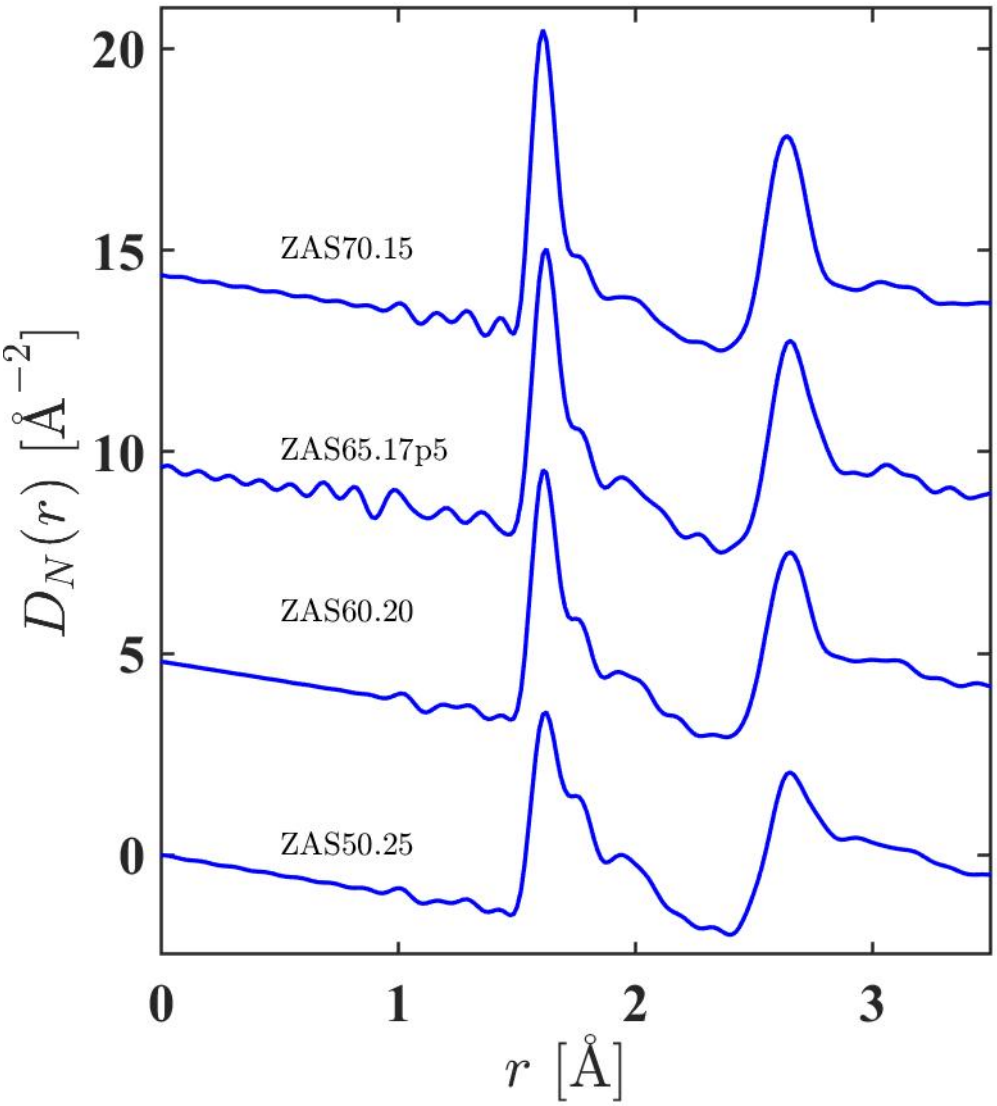

Figure 4-37: $D_N(r)$ functions for the ZAS glasses along the $R = 1$ tie-line. The curves were obtained by Fourier transforming the corresponding reciprocal space data shown in figure 4-37. The curves are offset vertically for clarity of presentation.

Sample	Atom pair	$r_{\alpha\beta}$[Å]	$\sigma_{\alpha\beta}$[Å]	$\bar{n}_{\alpha}^{\beta}$	R_{χ} [%]
ZAS50.7p5	Si-O	1.626(1)	0.047(5)	4*	6.82
	Al-O	1.761(1)	0.057(5)	4.08(5)	
	Zn-O	1.967(1)	0.078(5)	3.20(9)	
	Zn-O	2.134(1)	0.122(5)	1.51(9)	
	Zn-O (sum)			4.71(10)	
	O-O	2.650(1)	0.085(5)	3.60(10)	
ZAS50.10	Si-O	1.622(1)	0.052(5)	4*	6.41
	Al-O	1.774(1)	0.066(5)	4.07*	
	Zn-O	1.970(1)	0.075(5)	3.07(9)	
	Zn-O	2.150(1)	0.124(5)	1.59(9)	
	Zn-O (sum)			4.66(10)	
	O-O	2.650(1)	0.138(5)	3.98(10)	
ZAS50.12p5	Si-O	1.620(1)	0.050(5)	4*	6.87
	Al-O	1.762(1)	0.061(5)	4.06*	
	Zn-O	1.971(1)	0.079(5)	3.42(9)	
	Zn-O	2.179(1)	0.133(5)	1.44(9)	
	Zn-O (sum)			4.86(10)	
	O-O	2.650(1)	0.095(5)	3.92(10)	

Table 4.15: Parameters obtained from Gaussian peak fits to the $D_N(r)$ functions for the ZAS glasses along the 50 mol% SiO_2 tie-line. The fitted functions are shown in figure 4-38. The parameters denoted by an * are fixed. R_{χ} is given for the fitted range 1.30-2.65 Å.

Sample	Atom pair	$r_{\alpha\beta}$[Å]	$\sigma_{\alpha\beta}$[Å]	$\bar{n}_{\alpha}^{\beta}$	R_{χ} [%]
ZAS50.17	Si-O	1.623(1)	0.051(5)	4*	9.13
	Al-O	1.767(1)	0.064(5)	4.09*	
	Zn-O	1.965(1)	0.074(5)	2.98(9)	
	Zn-O	2.135(1)	0.129(5)	2.15(9)	
	Zn-O (sum)			5.13(10)	
	O-O	2.650(1)	0.086(5)	3.38(10)	
ZAS50.22p22	Si-O	1.620(1)	0.053(5)	4*	7.24
	Al-O	1.770(1)	0.067(5)	4.12*	
	Zn-O	1.972(1)	0.068(5)	2.81(9)	
	Zn-O	2.141(1)	0.127(5)	2.23(9)	
	Zn-O (sum)			5.04(10)	
	O-O	2.660(1)	0.105(5)	4.22(10)	
ZAS50.25	Si-O	1.619(1)	0.054(5)	4*	8.05
	Al-O	1.776(1)	0.072(5)	4.17*	
	Zn-O	1.977(1)	0.065(5)	2.63(9)	
	Zn-O	2.145(1)	0.136(5)	2.65(9)	
	Zn-O (sum)			5.29(10)	
	O-O	2.680(1)	0.106(5)	4.21(10)	
ZAS50.27p78	Si-O	1.619(1)	0.055(5)	4*	9.38
	Al-O	1.776(1)	0.074(5)	4.22*	
	Zn-O	1.988(1)	0.071(5)	3.18(9)	
	Zn-O	2.180(1)	0.136(5)	2.35(9)	
	Zn-O (sum)			5.53(10)	
	O-O	2.66(1)	0.105(5)	4.12(10)	

Table 4.16: Parameters obtained from Gaussian peak fits to the $D_N(r)$ functions for the ZAS glasses along the 50 mol% SiO_2 tie-line (continuation). The fitted functions are shown in figure 4-38. R_{χ} is given for the fitted range 1.30-2.66 Å.

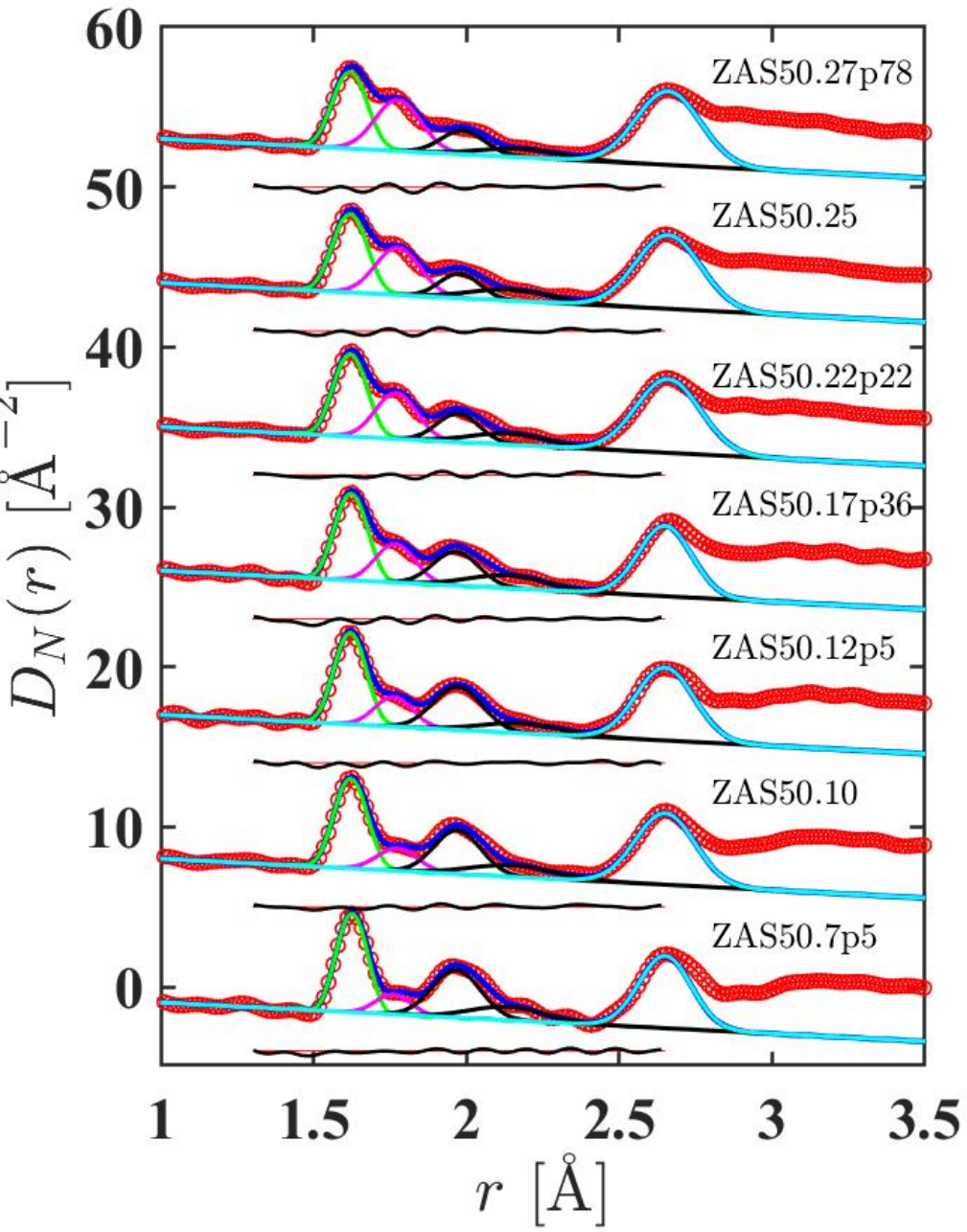

Figure 4-38: The fitted $D_N(r)$ functions for the ZAS glasses along the 50 mol% SiO_2 tie-line. The red circles are the data, the blue solid curves are the fits and the other curves show the contribution from Si-O (green), Al-O (magenta), Zn-O (black) and O-O (cyan) correlations. The displaced black solid curves gives the residual (fit subtracted from measured data). The O-O correlations are introduced to constrain the peaks fitted at small r values. The curves are offset vertically for clarity of presentation.

Sample	Atom pair	$r_{\alpha\beta}$[Å]	$\sigma_{\alpha\beta}$[Å]	$\bar{n}_{\alpha}^{\beta}$	R_{χ} [%]
ZAS60.13p33	Si-O	1.618(1)	0.050(5)	4*	6.55
	Al-O	1.771(1)	0.060(5)	4.13*	
	Zn-O	1.967(1)	0.071(5)	2.73(9)	
	Zn-O	2.123(1)	0.129(5)	2.26(9)	
	Zn-O (sum)			4.99(10)	
	O-O	2.647(1)	0.096(5)	4.37(10)	
ZAS60.15	Si-O	1.621(1)	0.049(5)	4*	6.75
	Al-O	1.770(1)	0.061(5)	4.17*	
	Zn-O	1.960(1)	0.070(5)	2.61(9)	
	Zn-O	2.105(1)	0.123(5)	2.79(9)	
	Zn-O (sum)			5.4(10)	
	O-O	2.650(1)	0.083(5)	3.87(10)	
ZAS60.17p78	Si-O	1.616(1)	0.051(5)	4*	7.77
	Al-O	1.769(1)	0.064(5)	4.09*	
	Zn-O	1.976(1)	0.074(5)	3.16(9)	
	Zn-O	2.166(1)	0.137(5)	2.34(9)	
	Zn-O (sum)			5.50(10)	
	O-O	2.650(1)	0.096(5)	4.38(10)	
ZAS60.20	Si-O	1.616(1)	0.052(5)	4*	7.68
	Al-O	1.775(1)	0.067(5)	4.14*	
	Zn-O	1.976(1)	0.068(5)	3.13(9)	
	Zn-O	2.165(1)	0.1220(5)	2.48(9)	
	Zn-O (sum)			5.62(10)	
	O-O	2.650(1)	0.099(5)	4.37(10)	
ZAS60.22p22	Si-O	1.616(1)	0.052(5)	4*	8.16
	Al-O	1.774(1)	0.064(5)	4.15*	
	Zn-O	1.971(1)	0.130(5)	2.75(9)	
	Zn-O	2.140(1)	0.100(5)	3.15(9)	
	Zn-O (sum)			5.90(10)	
	O-O	2.650(1)	0.110(5)	4.37(10)	
ZAS65.17p5	Si-O	1.622(1)	0.051(5)	4*	8.24
	Al-O	1.775(1)	0.062(5)	4.18*	
	Zn-O	1.949(1)	0.05(5)	2.00(9)	
	Zn-O	2.077(1)	0.112(5)	3.93(9)	
	Zn-O (sum)			5.93(10)	
	O-O	2.650(1)	0.086(5)	4.01(10)	

Table 4.17: Parameters obtained from Gaussian peak fits to the $D_N(r)$ functions for the ZAS glasses along the 60 and 65 mol% SiO_2 tie-line. The fitted functions are shown in figures 4-39 and 4-40. The parameters denoted by an * are fixed. R_{χ} is given for the fitted range 1.30-2.65 Å.

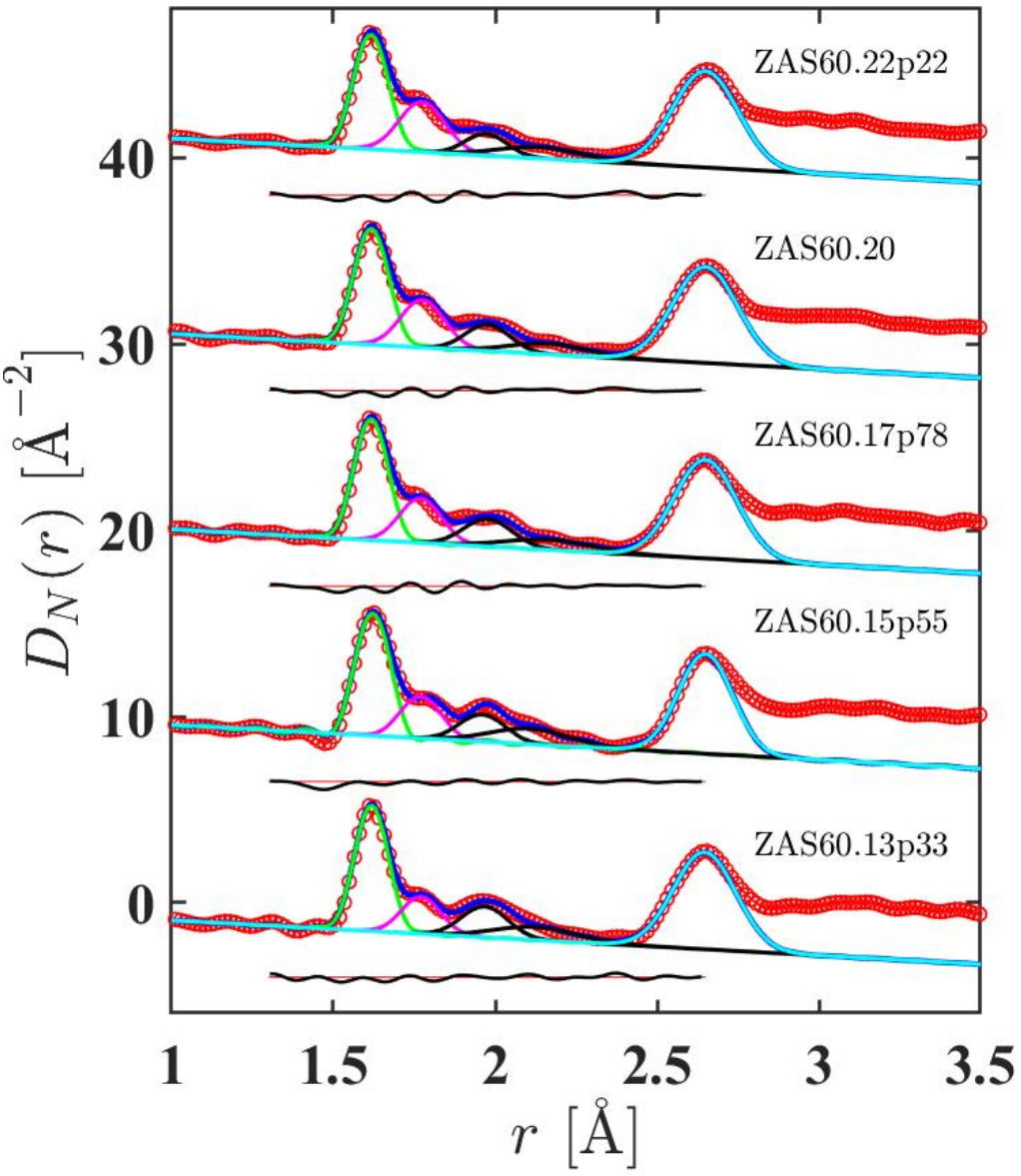

Figure 4-39: The fitted $D_N(r)$ functions for the ZAS glasses along the 60 mol% SiO_2 tie-line. The red circles are the data, the blue solid curves are the fits and the other curves show the contribution from Si-O (green), Al-O (magenta), Zn-O (black) and O-O (cyan) correlations. The displaced black solid curves gives the residual (fit subtracted from measured data). The O-O correlations are introduced to constrain the peaks fitted at smaller r values. The curves are offset vertically for clarity of presentation.

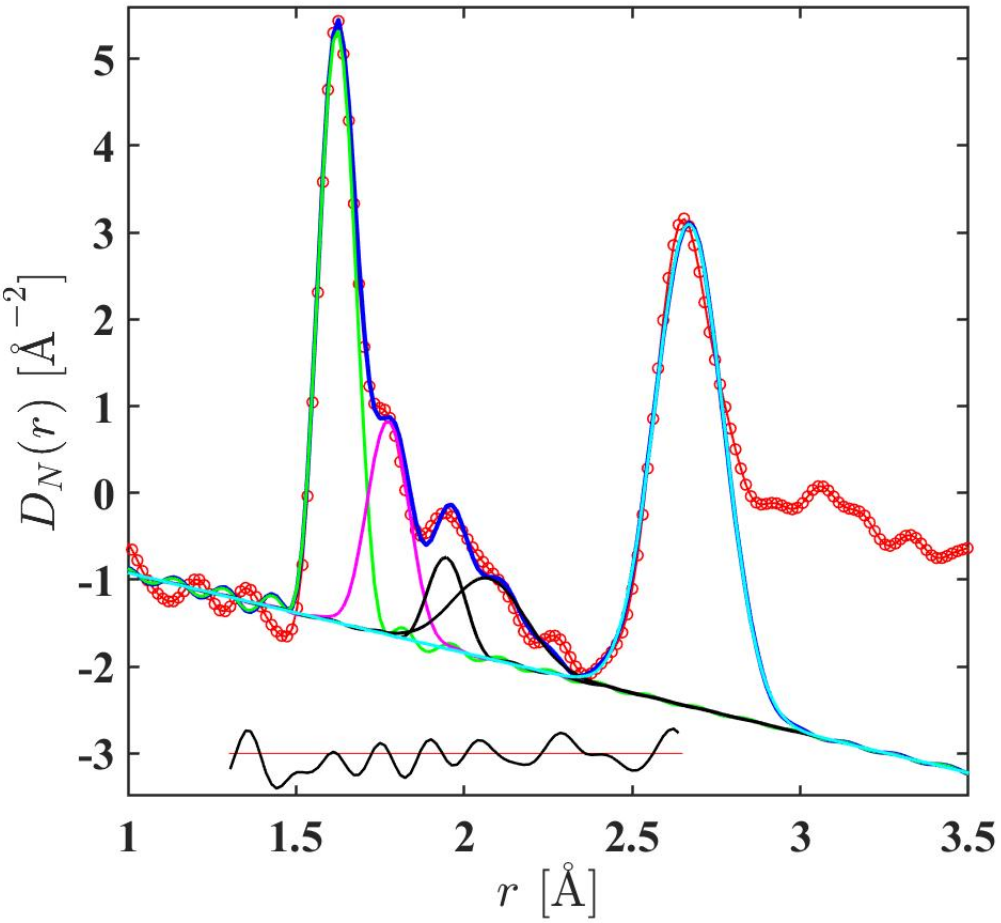

Figure 4-40: The fitted $D_N(r)$ function for the ZAS glass for the 65 mol% SiO_2. The red circles are the data, the blue solid curves are the fits and the other curves show the contribution from Si-O (green), Al-O (magenta), Zn-O (black) and O-O (cyan) correlations. The displaced black solid curve gives the residual (fit subtracted from measured data). The O-O correlation is introduced to constrain the peaks fitted at smaller r values.

Sample	Atom pair	$r_{\alpha\beta}$ [Å]	$\sigma_{\alpha\beta}$ [Å]	$\bar{n}_{\alpha}^{\beta}$	R_{χ} [%]
ZAS70.13p33	Si-O	1.615(1)	0.051(5)	4*	7.87
	Al-O	1.779(1)	0.061(5)	4.12*	
	Zn-O	1.973(1)	0.068(5)	3.13(9)	
	Zn-O	2.162(1)	0.126(5)	2.80(9)	
	Zn-O (sum)			5.93(10)	
	O-O	2.641(1)	0.091(5)	4.46(10)	
ZAS70.15	Si-O	1.614(1)	0.050(5)	4*	7.77
	Al-O	1.783(1)	0.066(5)	4.13*	
	Zn-O	1.977(1)	0.062(5)	2.62(9)	
	Zn-O	2.138(1)	0.136(5)	3.38(9)	
	Zn-O (sum)			6.00(10)	
	O-O	2.644(1)	0.094(5)	4.68(10)	
ZAS70.16p67	Si-O	1.614(1)	0.051(5)	4*	7.02
	Al-O	1.785(1)	0.068(5)	4.2*	
	Zn-O	1.988(1)	0.067(5)	3.65(9)	
	Zn-O	2.194(1)	0.109(5)	2.45(9)	
	Zn-O (sum)			6.10(10)	
	O-O	2.645(1)	0.096(5)	4.78(10)	

Table 4.18: Parameters obtained from Gaussian peak fits to the $D_N(r)$ functions for the ZAS glasses along the 70 mol% SiO_2 tie-line. The fitted functions are shown in figure 4-41. The parameters denoted by an * are fixed. R_{χ} is given for the fitted range 1.30-2.65 Å.

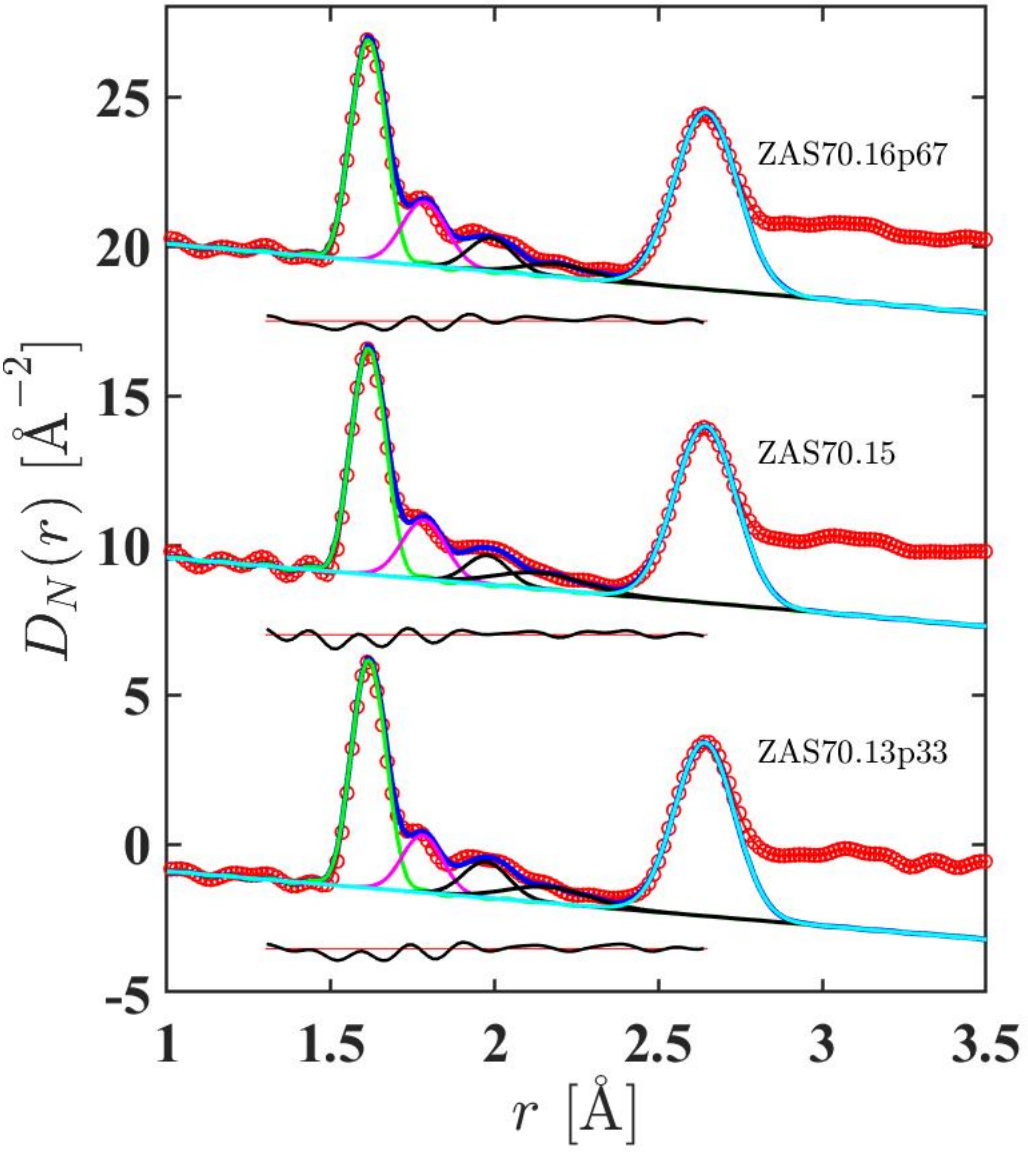

Figure 4-41: The fitted $D_N(r)$ functions for the ZAS glasses along the 70 mol% SiO_2 tie-line. The red circles are the data, the blue solid curves are the fits and the other curves show the contribution from Si-O (green), Al-O (magenta), Zn-O (black) and O-O (cyan) correlations. The displaced black solid curve gives the residual (fit subtracted from measured data). The O-O correlations are introduced to constrain the peaks fitted at smaller r values. The curves are offset vertically for clarity of presentation.

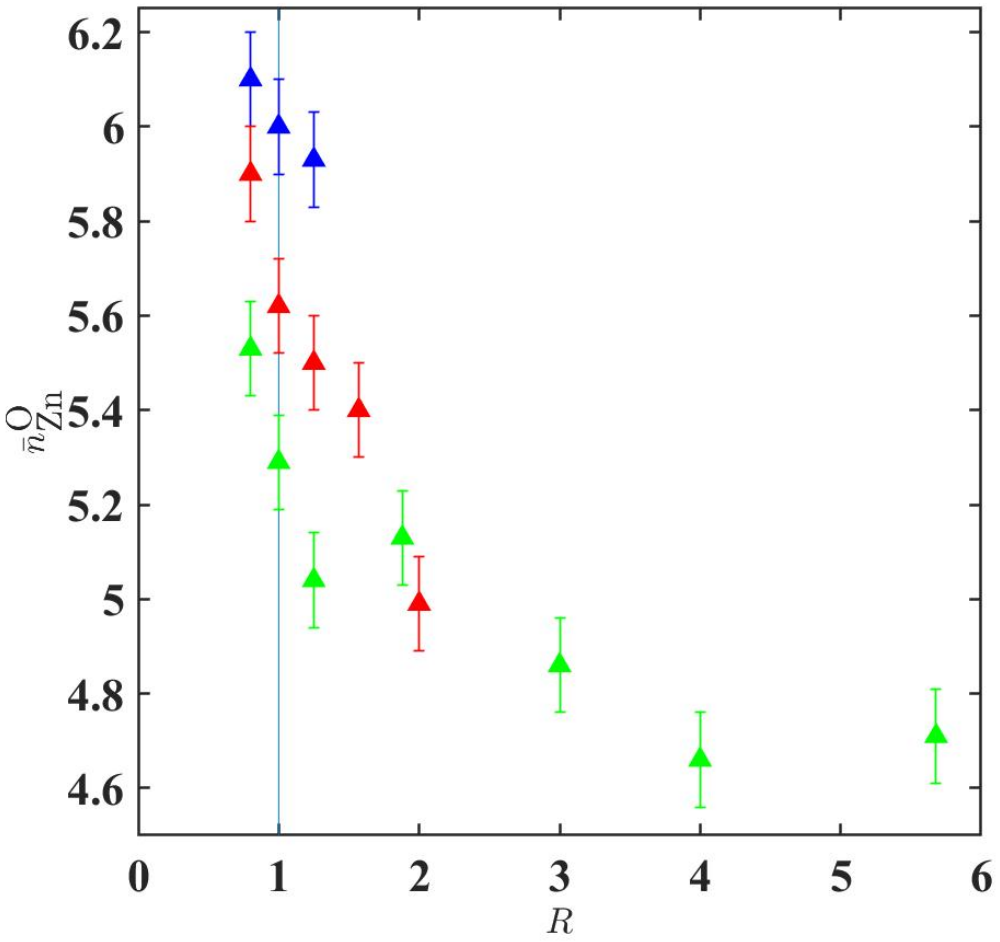

Figure 4-42: Zn-O coordination number as a function of R for the ZAS glasses obtained from the $D_N(r)$ fits. The green data points show the coordination numbers along the 50 mol% SiO_2 tie-line, red data points 60 mol% SiO_2 tie-line, black data point 65 mol% SiO_2 and the blue data points show the coordination numbers along the 70 mol% SiO_2 tie-line. The cyan line at $R = 1$ indicates the tectosilicate composition.

4.3.4 Raman Spectroscopy

Figures 4-43, 4-44, 4-45 and 4-46 show the Raman spectra for the batch 1 ZAS glasses. The Raman spectra can be divided in general into three regions for all the samples, more specifically, into low, middle and high frequency regions. The bands with the strongest intensity locate in the high frequencies from 800-1200 cm^{-1}, the bands with medium intensity are located between 400-800 cm^{-1} and the bands with low intensity are within 200-400 cm^{-1}.

The low-frequency regions contains information on ring sizes and their tetrahedral cations [103, 104]. The intermediate region contains several overlapping bands and can be analysed qualitatively in terms of the change in average bond strength of the network. The high-frequency region of the Raman spectra will contain information about the concentration of NBO and on Al/Si mixing [105, 106].

The most intense broad band at the range 1050-1200 cm^{-1} is related to the asymmetrical vibration Si-O^- in SiO_4 tetrahedra due to presence of other elements such as Al [107,108] and this band region broadens with SiO_2 content. It is interesting to notice that the stretching bands in Raman spectra can provide information on Q^n [109]. Literature data on Raman spectra of amorphous silicates indicate that bands are related to groups Q^0-Q^4 [109–119].

Raman spectra of amorphous silicates are characterized by a band centered at 1000 cm^{-1}, which is attributed to symmetric (atoms move in opposite directions with same strength towards the central atom) Si-O bond stretching modes and one centered at 500 cm^{-1} originating from intra-tetrahedral O-Si-O angle bending. The band centered at 1000 cm^{-1} can be decomposed as the sum of 5 bands: 800-850 cm^{-1} for Q^0; 900 cm^{-1} for Q^1; 950-1100 cm^{-1} for Q^2; 1100 cm^{-1} for Q^3 and 1150-1250 cm^{-1} for Q^4 [115, 120]. Thus, a band at about 1150 cm^{-1} in the ZAS glasses indicates the presence of Q^4 groups, i.e, four bridging oxygens in the silicate network. This is mainly seen for the ZAS glasses with 60 and 70 mol% SiO_2. The appearing band at 1100 cm^{-1} confirms the presence of Q^3 [113]. The intensities of bands at 1000 and 1100 cm^{-1} are also due to interlinking of Si-O-Al network. As the Al_2O_3 concentration increases, the band becomes broader and more asymmetric, the intensity decreases and shifts to lower frequencies.

The peak width can be used as a measure of the relative order of the Si-O network. A larger distribution of bond angles results in a wider Raman band. For compositions with $R > 1$, the larger FWHM of the ZAS glasses indicates that the higher field strength of the Zn^{2+} modifier increases the structural disorder.

The vibration at 970 cm^{-1} is due to stretching vibration of silicon-oxygen tetrahedra with two corners shared with aluminium-oxygen [121]. No bands in the range 900 cm^{-1} and 850-800 cm^{-1} indicate that there are no Q^1 or Q^0 groups.

A band centered at 780 cm^{-1} is caused by Si-O-Si in a tetrahedral network and AlO_4 units with three bridging oxygen atoms and one non-bridging oxygen [112,115,121,122]. For the compositions with $R = 1$ (Figure 4-46) the intensity of this band increased with increasing SiO_2 content.

AlO_6 octahedra is assigned to a Raman spectra band at 710 cm^{-1} in aluminosilicate glasses [117]. No such band appears in the ZAS glasses indicating that most of the aluminum atoms are in tetrahedral units. This is corroborated by ^{27}Al MAS NMR measurements shown in the previous section.

From the literature data in silicate and aluminosilicate glasses, there is a band at $\approx$ 650 cm^{-1} associated to bending vibration bridging bonds of Si-O-Si in Q^2 [118, 123], having two bridging oxygens. For the ZAS glasses, no such band appears.

The band between 485-590 cm^{-1} is related to the bending vibrations of Si-O-Si and Si-O-Al [123]. The observed region at 450 cm^{-1} is due to bending and stretching modes of Si-O-Si and bending vibrations of Al-O-Al and Al-O-Si [124]. The band 400-650 cm^{-1} is caused by bending vibrations of the bridging oxygen (BO) bonds for SiO_4 [124].

The region below 400 cm^{-1} is caused by vibration of network modifying cations and is associated to long range order. The peaks around 336 cm^{-1} are assigned to Zn-O in ZnO_4 units. However in the ZAS glasses there is no peak in this region suggesting that the presence of ZnO_4 tetrahedra is very unlikely. There is less literature data on the environment of octahedral ZnO_6 in the Raman spectra. Maysen et al [125] attributed a band centered at 904 cm^{-1} to the coupling of Si-O and Zn-O stretching vibrations. In other words SiO_4 connected with ZnO_6 octahedra by bridging oxygens Si-O-Zn.

Samples	Band 1	Band 2	Band 3	Band 4	Band 5
ZAS50.10	-	963	775	-	462
ZAS50.12p5	-	960	784	-	455
ZAS50.22p22	1068	946	779	592	462
ZAS50.25	1057	925	783	603	464
ZAS50.27p78	1083	925	792	601	479
ZAS60.13p33	-	993	792	607	453
ZAS60.17p78	1075	951	797	594	466
ZAS60.20	1083	923	804	608	453
ZAS60.22p22	1083	930	799	602	455
ZAS70.13p33	1068	935	797	605	473
ZAS70.15	1087	946	806	600	457
ZAS70.16p67	1070	953	797	596	450

Table 4.19: Bands position (in cm^{-1}) observed in Raman spectra of the batch 1 ZAS glasses.

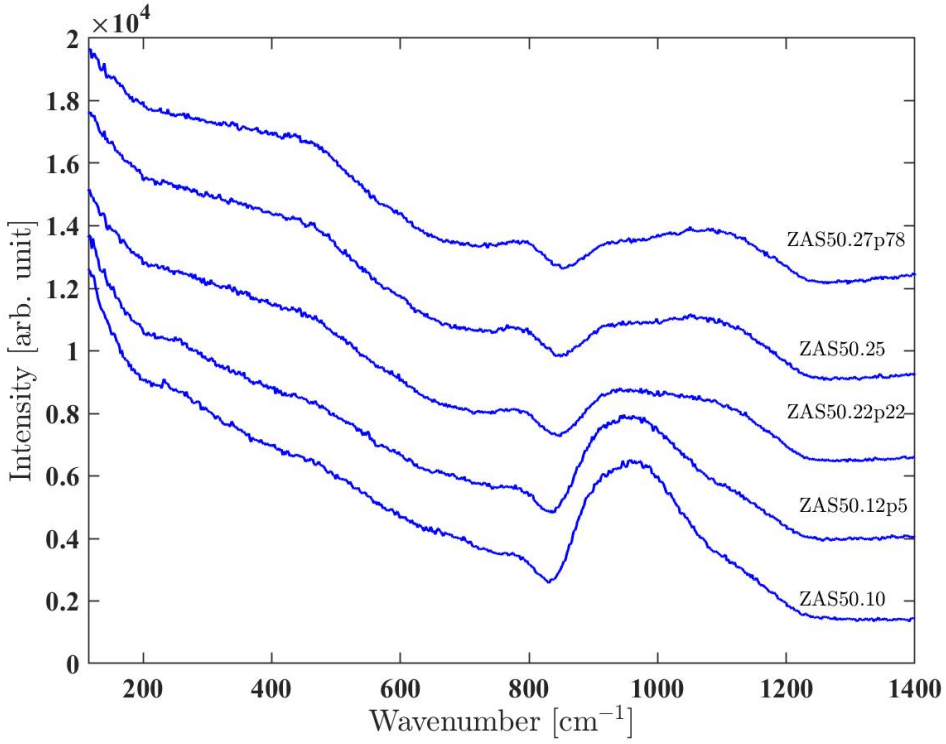

Figure 4-43: Raman spectra for the ZAS glasses along the 50 mol% SiO_2 tie-line. The curves are offset vertically for clarity of presentation.

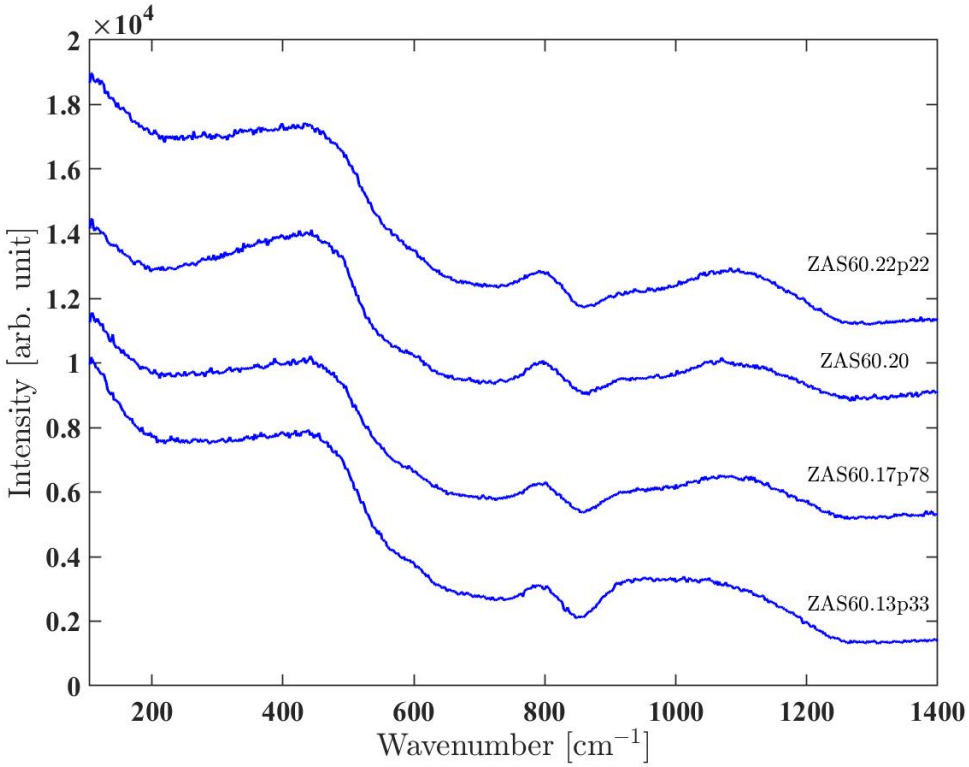

Figure 4-44: Raman spectra for the ZAS glasses along the 60 mol% SiO_2 tie-line. The curves are offset vertically for clarity of presentation.

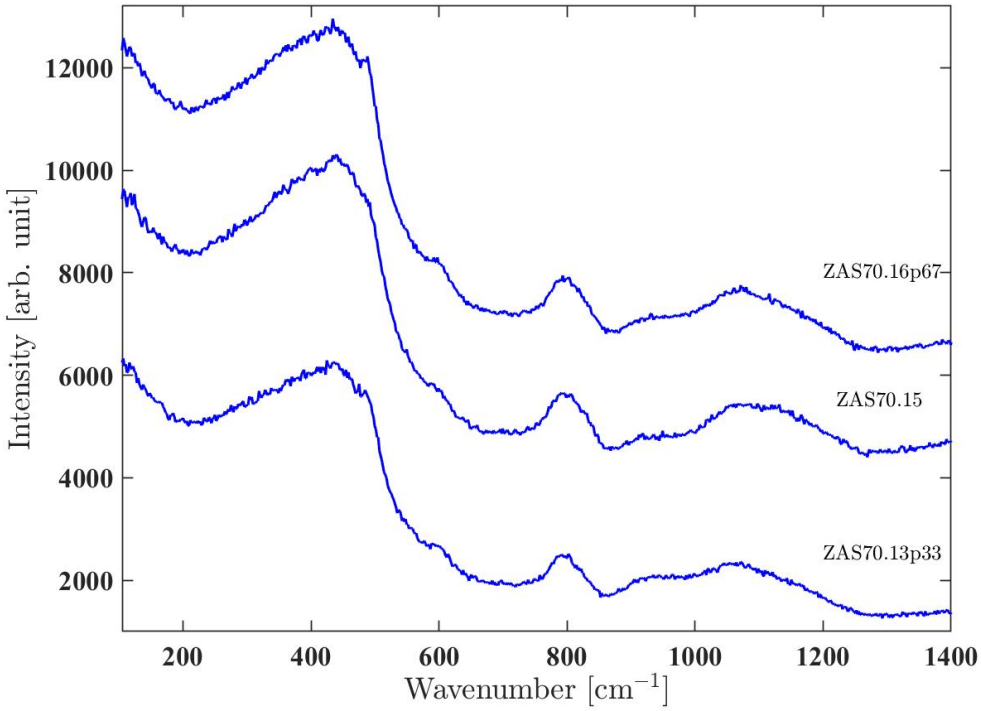

Figure 4-45: Raman spectra for the ZAS glasses along the 70 mol% SiO_2 tie-line. The curves are offset vertically for clarity of presentation.

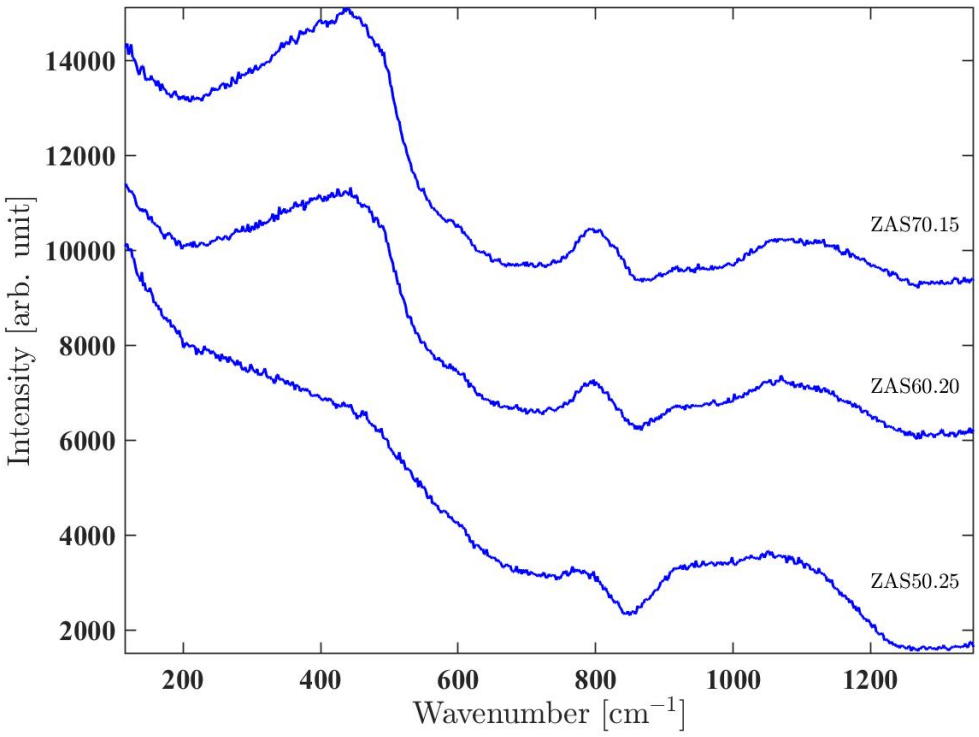

Figure 4-46: Raman spectra for the ZAS glasses along the $R = 1$ tie-line. The curves are offset vertically for clarity of presentation.

4.4 Discussion

The ^{29}Si MAS NMR and the neutron diffraction analysis on the crystalline Zn_2SiO_4 show tetrahedral coordination environments for Zn and Si. The minimum value of $\bar{n}_O^O = 3$ suggests that a SiO_4 tetrahedron is not connected to other SiO_4 units. This is corroborated by the sharp peak in the NMR measurements and an analysis of a cif (Figure 4-26) file where it is shown that there is no silicate network for willemite. Each oxygen of the group SiO_4 also forms a part of two neighboring Zn tetrahedra.

The willemite structure provided a starting point for fitting the structure of zinc aluminosilicate glasses. Zinc is mainly tetrahedrally coordinated with oxygen in crystals. However, in oxide glasses 5-fold coordinated zinc has also been found [73–77, 79, 82, 83, 126], including in the present work.

There is a variety of experimental techniques that have been used in order to provide a model that explains the structure of aluminosilicate glasses [91–96, 127, 128]. A recent model developed by Gammond et al [1] gives a possible explanation for these higher coordinated species observed in the X-ray diffraction results. The model is based on a simple set of reactions in which the silicon atoms remain fourfold coordinated. For the case of the ZAS system, ZnO reacts with Al_2O_3 according to the scheme

$$ZnO + Al_2O_3 \longrightarrow Zn^{2+} + 2[Al\emptyset_{4/2}]^-, \tag{4.1}$$

which generates network-forming Al(IV) atoms or with SiO_2 according to the scheme

$$ZnO + SiO_2 \longrightarrow Zn^{2+} + [Si\emptyset_{2/2}O_2]^{2-}, \tag{4.2}$$

O refers to an NBO atom. In equation 4.1, the Zn^{2+} ions behave as charge compensating species whereas in equation 4.2 the Zn^{2+} ions behave as network modifier species. Al_2O_3 can also react with SiO_2 by the following equation

$$Al_2O_3 + SiO_2 \longrightarrow [Al\emptyset_{4/2}]^- + Al^{3+} + [Si\emptyset_{2/2}O_2]^{2-}, \tag{4.3}$$

where Al^{3+} ions compensate the charge on the $[Al\emptyset_{4/2}]^-$ unit and modifies the SiO_2 network by the creation of NBO atoms. This aluminium species are going to be denoted as Al_{mcc} (modifier/charge compensator) and represent either Al(V), Al(VI) or a mixture of the two species.

On the Zn-O rich side of the phase diagram where $R \geqslant 1$, there is no reaction between Al_2O_3 and SiO_2. In this case, all the aluminium atoms are Al(IV) and these Al-centred tetrahedra are charge compensated by Zn^{2+} ions. The results are then consistent with the standard model of the structure of aluminosilicate glasses in which NBO atoms are absent at $R = 1$. On the Al_2O_3 rich side (peraluminous regime) of the phase diagram where $R < 1$, there is no reaction between ZnO and SiO_2. In this case, all the Zn^{2+} ions play a charge-compensating role. This changes in the glass network affect the Raman spectra along R, where the bands associated with Al are more prominent with higher R. The Raman spectra also enforces the presence of a silicate network in SiO_4 units.

The Zn-O coordination numbers are shown in figure 4-47 and the values are summarized in table 4.23, which also include the coordination numbers obtained by direct integration under the peaks in $D_N(r)$ after the application of a Lorch modification function and subtracting the contributions from the Si-O and Al-O coordination numbers. Figures 4-48, 4-49 and 4-50 show the average distances of $\bar{r}_{\mathrm{Si-O}}$, $\bar{r}_{\mathrm{Al-O}}$ and $\bar{r}_{\mathrm{Zn-O}}$ from $D_X(r)$ and $D_N(r)$ fits with R. Their respective values are listed in tables 4.21 and 4.22.

^{27}Al NMR results help to constrain the Al coordination environment for each glass. The peak centered at ≈1.76 Å is attributed to Al-O correlations and is also in agreement with previous aluminosilicate glass diffraction studies [80,129–131]. The presence of Al(V) is expected when the concentration of charge-balancing modifier cations is insufficient to stabilize all aluminium in tetrahedral configurations. The presence of Al(V) and Al(VI) provide a charge compensation in the glass network and can explain the presence of ZnO_x units in polyhedra sharing edges.

There is little variation with the glass composition and the overall mean value $\langle \bar{r}_{\mathrm{SiO}} \rangle = 1.619(7)$ Å for the neutrons and $\langle \bar{r}_{\mathrm{SiO}} \rangle = 1.621(7)$ Å for X-rays. This is consistent with a tetrahedral coordination environment for the silicon atoms. In comparison, the Al-O bond length increases in value as $R \longrightarrow 0$ in the peraluminous regime. For the Zn-O, the weighted mean bond distance is calculated as

$$\bar{r}_{\mathrm{ZnO}} = \frac{\int_{r_1}^{r_2} dr\ r\ g_{\mathrm{ZnO}}(r)}{\int_{r_1}^{r_2} dr\ g_{\mathrm{ZnO}}(r)}, \tag{4.4}$$

where $g_{\mathrm{ZnO}}(r)$ was obtained by summing the contributions of the fitted Gaussian functions, and r_1 and r_2 define the overall r-space extent of the Zn-O peak. The $\bar{r}_{\mathrm{ZnO}}$ corresponds to typical Zn-O bond lengths (Table 4.20) and, in accordance with the larger weighting of the Zn-O correlations in the X-ray diffraction work, it is more prominent

in $D_X(r)$ than $D_N(r)$. The results show larger mean Zn-O bond distances in the peraluminous regime where the model predicts a predominantly charge-compensating role for the Zn^{2+} ions.

In the peraluminous regime, the Al-O coordination numbers obtained from ^{27}Al MAS NMR experiments increase in value as $R \longrightarrow 0$. The Zn-O coordination number and bond distance both increase as R decreases from the limit $R \longrightarrow \infty$, where the glass contains no alumina and all the Zn^{2+} ions take a network modifying role, to the value $R = 1$, where most of the Zn^{2+} ions take a charge-compensating role. In this progression, the ratio $N_{\mathrm{NBO}}/N_{\mathrm{Zn}}$ decreases and has a minimum at the $R = 1$. The results therefore suggest a difference between the average coordination environments of charge-compensating versus network-modifying Zn^{2+} ions that is related to the availability of NBO atoms.

For the 50% SiO_2 glasses, $\bar{n}^{\mathrm{O}}_{\mathrm{Zn}}$ increases with increasing Al_2O_3 content varying from 4.67(10) to 5.45(10). The same trend happens for the 60% and 70% SiO_2 glasses, where $\bar{n}^{\mathrm{O}}_{\mathrm{Zn}}$ varies from 4.89(10) to 5.86(10).

In general, both BO and NBO atoms will contribute towards these coordination environments. There is however a greater probability of NBO atoms contributing in the $R \longrightarrow \infty$ limit, so the higher charge on NBO versus BO atoms favors a more compact coordination environment for the network-modifying species. Conversely, there is a smaller probability of NBO atoms contributing when $R = 1$, leading to a less compact coordination environment for the charge-compensating species. A comparison between the cations zinc and magnesium is presented in the next chapter with the calculations provided from the Gammond model [1].

Previous diffraction studies show that the addition of zinc in the soda-silica-based glasses resulted in $(ZnO_4)^{6-}$ tetrahedra added into the polymerized $(SiO_4)^{4-}$ matrix [132]. EXAFS experiments on silica based glasses including ZnO [126] reveals the presence of edge-sharing oxygen instead of the typical corner sharing (3-fold-coordinated) oxygen implying a tricluster over-coordinated silicon. However, there is not much information from diffraction studies on the simple ZnO-Al_2O_3-SiO_2 glass system. The results from this work suggest Zn cations partially incorporating in edge-sharing units provoking the formation of higher coordinated alumina species and playing the role of a network modifier and charge compensating species in the glass network.

Crystal	x	y	$1-x-y$	Polyhedron	Atom pair	Distance
ZnO	1.0	0	0	ZnO_4	Zn-O	1.978(9)
				SiO4	Si-O	1.62(1)
$ZnSiO_3$	0.5	0	0.5	ZnO_4	Zn-O	1.98(6)
				ZnO_6	Zn-O	2.14(15)
Zn_2SiO_4 - I	0.667	0	0.333	SiO_4	Si-O	1.59-1.64
				ZnO_4	Zn-O	1.94-1.99
Zn_2SiO_4 - II	0.667	0	0.333	SiO_4	Si-O	1.615
				ZnO_4	Zn-O	1.979(3)
$Zn_{27.33}Al_{55}Si_{137}O_{384}$	0.142	0.143	0.715	SiO_4	Si-O	1.65(6)
				AlO_4	Al-O	1.65(6)
				ZnO_3	Zn-O	2.18-2.23
$Zn_{35.5}Al_{71}Si_{121}O_{384}$	0.185	0.185	0.630	SiO_4	Si-O	1.64(6)
				AlO_4	Al-O	1.64(6)
				ZnO_3	Zn-O	2.10-2.23
				ZnO_6	Zn-O	2.14-2.77
$ZnAl_2O_4$	0.5	0.5	0	AlO_4	Al-O	1.945
				AlO_6	Al-O	1.914
				ZnO_4	Zn-O	1.945
				ZnO6	Zn-O	1.914

Table 4.20: The Si-O, Al-O and Zn-O coordination numbers and bond distances for several Zn-containing crystalline systems [133–137]. The aluminosilicates form zeolite structures [138, 139].

Samples	$\bar{r}_{\mathrm{Si-O}}$ [Å]	$\bar{r}_{\mathrm{Al-O}}$ [Å]	$\bar{r}_{\mathrm{Zn-O}}$ [Å]
ZAS50.7p5	1.626(1)	1.761(1)	2.010(10)
ZAS50.10	1.622(1)	1.774(1)	2.020(10)
ZAS50.12p5	1.620(1)	1.762(1)	2.020(10)
ZAS50.17p36	1.623(1)	1.767(1)	2.025(10)
ZAS50.22p22	1.620(1)	1.770(1)	2.036(10)
ZAS50.25	1.619(1)	1.775(1)	2.051(10)
ZAS50.27p78	1.619(1)	1.776(1)	2.056(10)
ZAS60.13p33	1.618(1)	1.771(1)	2.027(10)
ZAS60.15p55	1.622(1)	1.772(1)	2.025(10)
ZAS60.17p78	1.616(1)	1.769(1)	2.044(10)
ZAS60.20	1.617(1)	1.775(1)	2.047(10)
ZAS60.22p22	1.616(1)	1.774(1)	2.049(10)
ZAS65.17p5	1.622(1)	1.775(1)	2.026(10)
ZAS70.13p33	1.616(1)	1.779(1)	2.049(10)
ZAS70.15	1.614(1)	1.783(1)	2.056(10)
ZAS70.16p67	1.614(1)	1.785(1)	2.058(10)

Table 4.21: Average Si-O, Al-O and Zn-O distances for the ZAS glasses obtained from the $D_N(r)$ fits.

Samples	$\bar{r}_{\text{Si-O}}$ [Å]	$\bar{r}_{\text{Al-O}}$ [Å]	$\bar{r}_{\text{Zn-O}}$ [Å]
ZAS50.7p5	-	-	-
ZAS50.10	1.619(1)	1.779(2)	2.030(10)
ZAS50.12p5	1.626(1)	1.764(4)	2.038(10)
ZAS50.17p36	-	-	-
ZAS50.22p22	1.621(1)	1.778(1)	2.060(10)
ZAS50.25	1.631(2)	1.778(2)	2.080(10)
ZAS50.27p78	1.634(1)	1.776(2)	2.078(10)
ZAS60.13p33	1.617(1)	1.773(3)	2.053(10)
ZAS60.15p55	-	-	-
ZAS60.17p78	1.617(1)	1.770(1)	2.070(10)
ZAS60.20	1.619(1)	1.782(1)	2.077(10)
ZAS60.22p22	1.622(1)	1.789(1)	2.107(10)
ZAS65.17p5	-	-	-
ZAS70.13p33	1.619(1)	1.789(4)	2.102(10)
ZAS70.15	1.617(1)	1.789(1)	2.101(10)
ZAS70.16p67	1.618(1)	1.794(1)	2.068(10)

Table 4.22: Average Si-O, Al-O and Zn-O distances for the ZAS glasses obtained from the $D_X(r)$ fits.

Sample	XRD Fit	ND Fit	Integration
ZAS50.7p5	-	4.71(10)	4.52(10)
ZAS50.10	4.62(7)	4.66(10)	4.43(10)
ZAS50.12p5	4.84(7)	4.86(10)	4.46(10)
ZAS50.17	-	5.13(10)	4.83(10)
ZAS50.22p22	4.98(7)	5.04(10)	4.65(10)
ZAS50.25	5.22(7)	5.29(10)	4.95(10)
ZAS50.27p78	5.31(7)	5.53(10)	4.90(10)
ZAS60.13p33	4.88(7)	4.99(10)	4.54(10)
ZAS60.15	-	5.36(10)	5.03(10)
ZAS60.17p78	5.29(7)	5.50(10)	4.90(10)
ZAS60.20	5.36(7)	5.62(10)	4.83(10)
ZAS60.22p22	5.75(7)	5.90(10)	4.99(10)
ZAS65.17p5	-	5.93(10)	5.53(10)
ZAS70.13p33	5.82(7)	5.93(10)	4.97(10)
ZAS70.15	5.81(7)	6.00(10)	5.31(10)
ZAS70.16p67	5.94(7)	6.10(10)	5.33(10)

Table 4.23: Zn-O coordination numbers, $\bar{n}^{\text{O}}_{\text{Zn}}$, obtained by the $D_X(r)$ fits, $D_N(r)$ fits or by integration after the application of a Lorch [32] modification function.

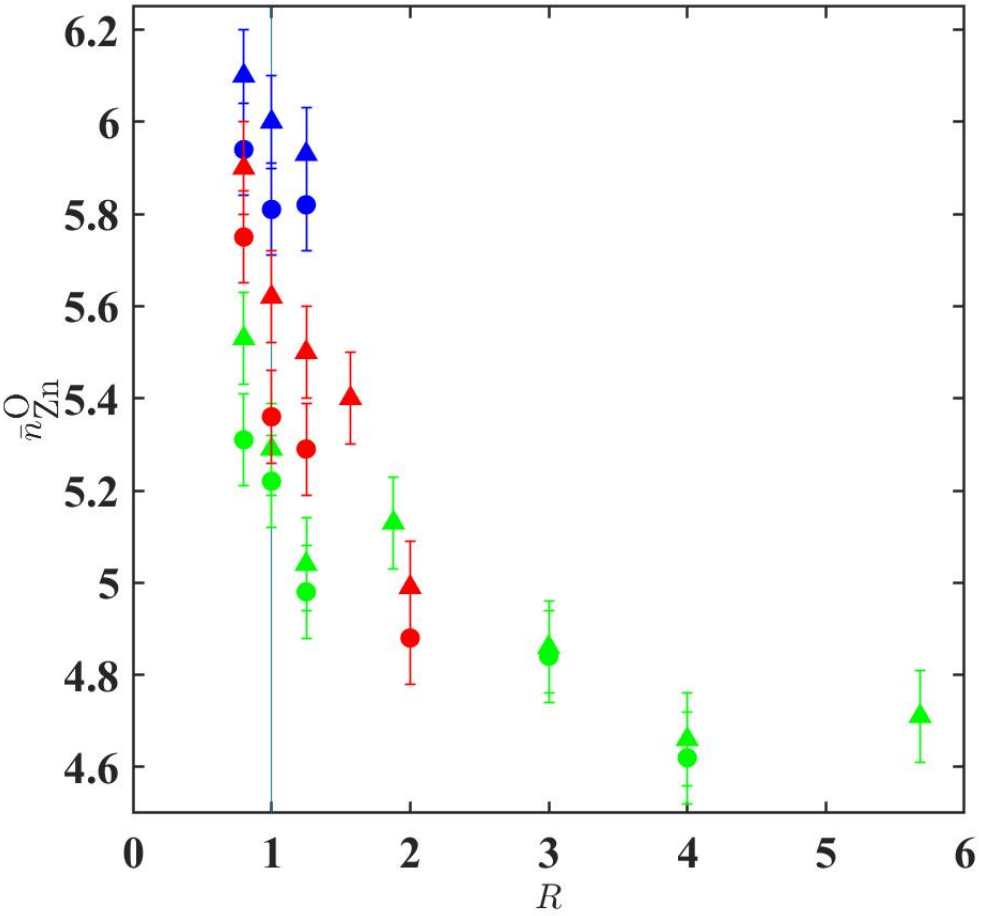

Figure 4-47: Zn-O coordination number for the ZAS glasses as a function of the ratio R, obtained from X-ray (circles) and neutron (triangles) diffraction data. The green data points show the coordination numbers along the 50 mol% SiO_2 tie-line. The red data points show the coordination numbers along the 60 mol% SiO_2 tie-line. The black data point show the coordination number for the 65 mol% SiO_2 and the blue data points show the coordination numbers along the 70 mol% SiO_2 tie-line. The cyan line at $R = 1$ indicates the tectosilicate region.

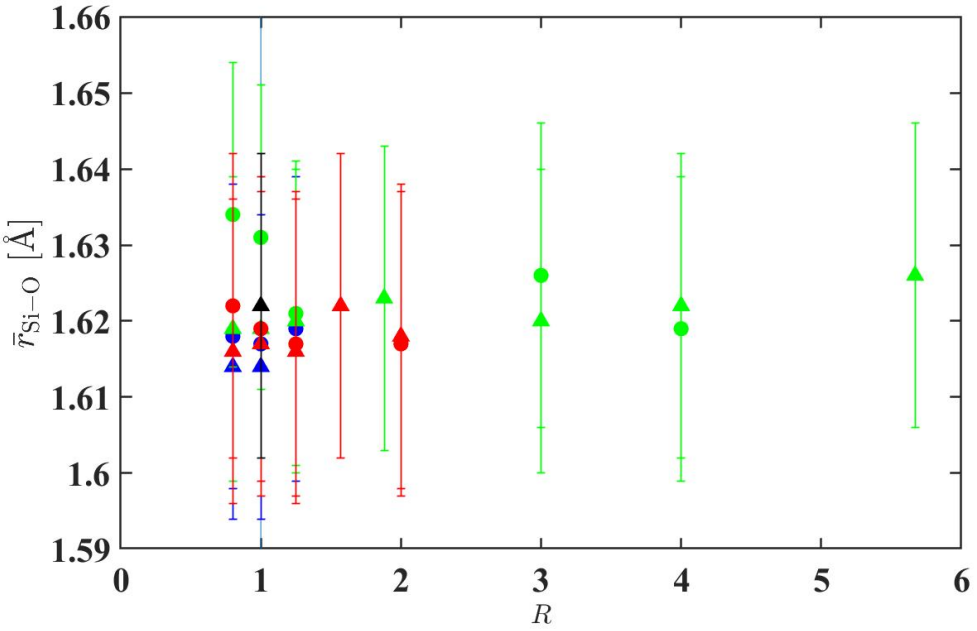

Figure 4-48: Average Si-O distances for the ZAS glasses as a function of the ratio R, obtained from X-ray (circles) and neutron (triangles) diffraction data. The green data points show the $\bar{r}_{\mathrm{Si\text{-}O}}$ values along the 50 mol% SiO_2 tie-line. The red data points show the $\bar{r}_{\mathrm{Si-O}}$ values along the 60 mol% SiO_2 tie-line. The black data point show the $\bar{r}_{\mathrm{Si-O}}$ value for the 65 mol% SiO_2 and the blue data points show the $\bar{r}_{\mathrm{Si-O}}$ value along the 70 mol% SiO_2 tie-line. The cyan line at $R = 1$ indicates the tectosilicate region.

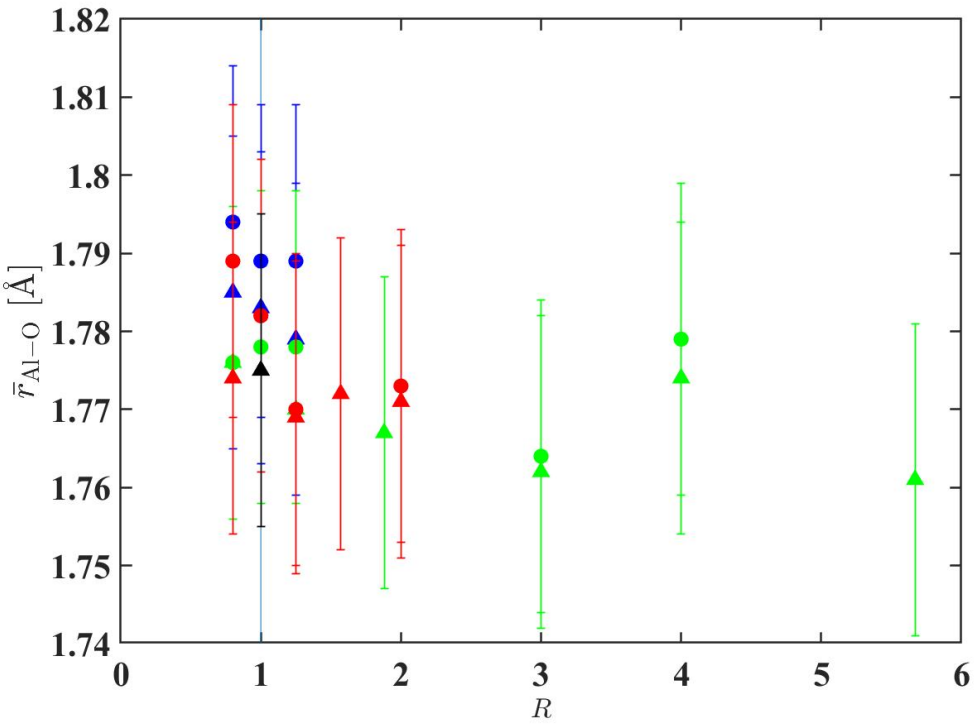

Figure 4-49: Average Al-O distances for the ZAS glasses as a function of the ratio R, obtained from X-ray (circles) and neutron (triangles) diffraction data. The green data points show the $\bar{r}_{\mathrm{Al\text{-}O}}$ values along the 50 mol% SiO_2 tie-line. The red data points show the $\bar{r}_{\mathrm{Al-O}}$ values along the 60 mol% SiO_2 tie-line. The black data point show the $\bar{r}_{\mathrm{Al-O}}$ value for the 65 mol% SiO_2 and the blue data points show the $\bar{r}_{\mathrm{Al-O}}$ value along the 70 mol% SiO_2 tie-line. The cyan line at $R = 1$ indicates the tectosilicate region.

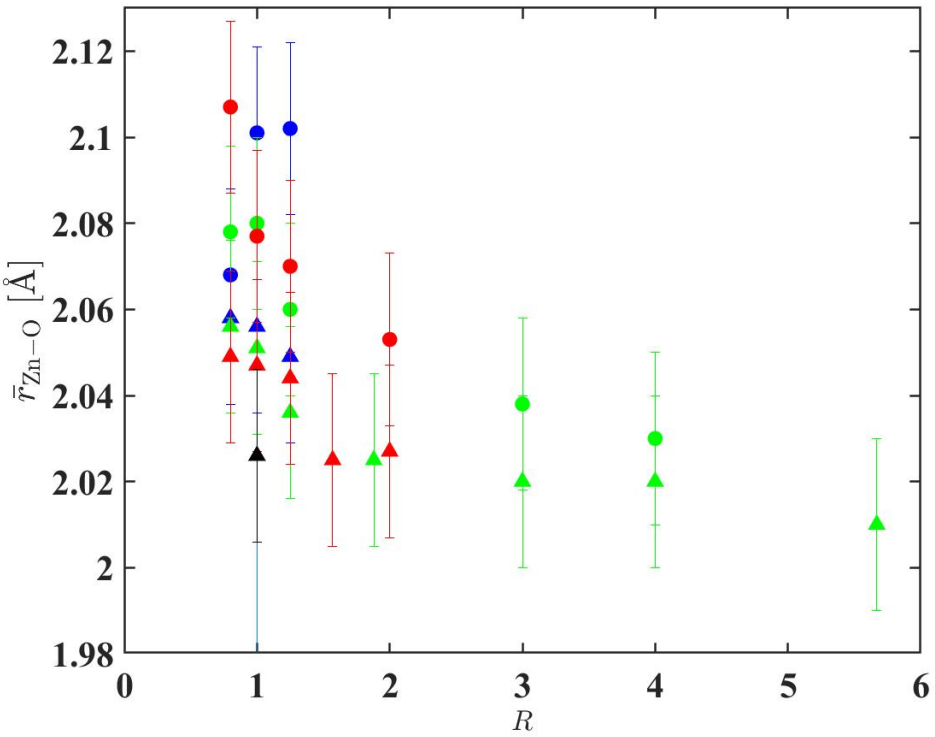

Figure 4-50: Average Zn-O distances for the ZAS glasses as a function of the ratio R, obtained from X-ray (circles) and neutron (triangles) diffraction data. The green data points show the $\bar{r}_{\mathrm{Zn\text{-}O}}$ values along the 50 mol% SiO_2 tie-line. The red data points show the $\bar{r}_{\mathrm{Zn-O}}$ values along the 60 mol% SiO_2 tie-line. The black data point show the $\bar{r}_{\mathrm{Zn-O}}$ value for the 65 mol% SiO_2 and the blue data points show the $\bar{r}_{\mathrm{Zn-O}}$ value along the 70 mol% SiO_2 tie-line. The cyan line at $R = 1$ indicates the tectosilicate region.

4.5 Conclusion

The structure of willemite and zinc aluminosilicate glasses was investigated using ^{27}Al MAS NMR, ^{29}Si MAS NMR, Raman spectroscopy and X-ray and neutron diffraction experiments. SiO_4 and ZnO_4 are the dominant species in willemite where there is the absence of a silicate network.

The compositions of the ZAS glasses were chosen in order to vary the ZnO:Al_2O_3 ratio at constant SiO_2 content across the glass forming region (Figure 4-2). The strategy is maximizing the change to the Zn-O coordination environment, which can vary from 4 to 6 according to crystallography data [138, 139]. In this work, a combination of ND, XRD and ^{27}Al MAS NMR is used to measure coordination environments of Zn-O and Al-O in the ZAS system.

The ^{27}Al MAS NMR parameters such as area of different Al species, $\delta(^{27}\mathrm{Al})$ and C_Q are sensitive to the structure and chemical bonding around this element. Therefore, variation of the parameters with composition provide valuable information on the atomic configuration and the degree of disorder/order by the appearance of NBOs and BOs. The results show that most of the aluminium atoms are in AlO_4 tetrahedra. There is also a significant fraction of aluminium atoms in fivefold coordinated Al(V) sites and a small fraction of aluminium atoms in sixfold coordinated Al(VI) sites. The proportion of Al(IV) atoms increases with the ZnO content along a constant mol% SiO_2 tie-line as the proportion of higher coordinated aluminium atoms decreases. The ^{27}Al MAS NMR results also constrained the X-ray and neutron diffraction data to extract $\bar{n}^{\mathrm{O}}_{\mathrm{Zn}}$ values with more accuracy.

The results from neutron and X-ray diffraction show that Zn is distributed between four-fold and five-fold coordinated sites which imply a dual structural role. Zn^{2+} is preferentially used for charge-stabilizing Al in tetrahedral configuration. The excess Zn^{2+} ions will then be used to create NBO around Si. An increase of the Al_2O_3 content in these glasses will attract zinc ions from the silicate network and increase the number of Si-O-Si and Si-O-Al bonds. An increase in SiO_2 content at the expense of ZnO will decrease the fraction of NBOs in the ZAS glasses. The predicted R dependence for the fractions of network-modifying and charge-compensating Zn^{2+} ions show that these species are structurally inequivalent, i.e, the mean Zn-O coordination number and bond distance are larger for the charge-compensating species.

Different structural units such as Si-O-Si, Al-O-Al, SiO_4 and AlO_4 tetrahedra were identified from the Raman spectra for different compositions of the batch 1 ZAS glasses.

The bands associated with ZnO_4 and ZnO_6 were not possible to identify with certainty. The Raman spectroscopy measurements confirm the expected changes in Q^n speciation with R. In this system, Al and Si are mainly in Q^4 species along the joint $R = 1$, and in depolymerized Q^2 and Q^3 units at high ZnO content.

The XRD, ND, ^{27}Al MAS NMR and Raman results confirm the mixing of the aluminosilicate network. The Zn^{2+} ions acting as charge-compensators for tetrahedral aluminum are found to have a similar effect on the network structure (Q^n speciation and Al/Si mixing) while they affect the network differently when they are in a modifying role.

Chapter 5

Structure of Magnesium Aluminosilicate Glasses

5.1 Introduction

Magnesia is present in many natural compounds and can be as abundant as silica in magmas, having played an important role in the differentiation of the primitive Earth [5, 140]. Although Al, Mg and Si are among the most abundant elements in the Earth [141], their role in the Earth's melt structure is still enigmatic. Understanding the structure of magnesium in amorphous aluminosilicates can provide a link between microscopic and macrosopic physico-chemical properties of melts, glasses and minerals.

Aluminosilicate glasses are of great importance due to their many industrial applications. They are cover glasses in personal electronic devices [142, 143], they are used in glass fiber as composite materials [67], as scaffolds for bone repair [144] and for bulk laser materials [145]. The presence of magnesium in these materials can change the properties of a glass such as viscosity [146, 147], glass transition temperature [148], the transmission of light in car windows [149] and the weathering rate of nuclear waste glasses [150]. For example, Si-based devices are deposited onto a flat glass substrate and alkaline earth oxides such as MgO, are introduced in the glass-making process in order to avoid high-mobility alkali ions that can migrate from the glass structure to damage these devices [143]. Here, MgO is used to decrease the liquid's temperature and consequently increasing its viscosity which is necessary for making flat glass sheets via the fusion-draw process, whilst helping to suppress crystallization.

Magnesium aluminosilicate (MAS) glasses possess very good mechanical and thermo-

mechanical properties such as (i) high fracture strength, which is important for accessing the high-temperature processing conditions; lower density, which is beneficial for making lighter weight products; low coefficient of thermal expansion, which can be used to advantage when matching the coefficient of the glass substrate to silicon in order to minimize thermal stress; (iv) have a high Young's modulus, which leads to stiffer glass that will exhibit less elastic distortion; and (v) a high chemical durability [151, 152]. MgO is also used to tune the compressive stress in display glass that is strengthened by ion exchange [153]. Its addition to Al_2O_3-SiO_2 improves the crack resistance, which can be adjusted, along with the hardness, by varying the glass composition.

The structural role of Mg atoms in these network-forming glasses is still ambiguous. This is due to the variety of conformations that Mg can adopt, where coordination numbers in the range from four to six or more are expected from the structural chemistry of its crystalline oxides [154–159] and the structural role of four-fold coordinated magnesium, which is sometimes regarded as a network-forming species [160] is still in debate. There is also the lack of definitive structural information from experiment. For example, information from ^{25}Mg MAS NMR experiments is scarce because of the low natural abundance (10%), low gyromagnetic ratio and significant quadrupole moment (nuclear spin I=5/2) of the ^{25}Mg isotope [161, 162].

Definitive experimental information on the dependence of the coordination environment of Mg^{2+} on the glass composition is therefore desirable in order to clarify the structural role of magnesium in disordered network structures. The structure of MAS glasses has been mainly investigated using Raman [163–166], IR [167], ^{29}Si and ^{27}Al MAS NMR [91, 168–170] spectroscopies. The traditional structural model of MAS glasses relies on the distinction between network forming Si and network modifying cations Mg^{2+}. Although Si is always in tetrahedral coordination at ambient pressure, Al can have various coordination numbers and consequently different structural roles. It is possible to distinguish three types of environments for the aluminium atoms, four-, five- and sixfold Al. SiO_4 and AlO_4 tetrahedral units are linked to each other through bridging oxygen (BO) atoms. When Mg^{2+} is added, additional oxygen atoms join the tetrahedral network by transforming BO atoms into non-bridging oxygen (NBO) atoms. As Al_2O_3 is added, the Mg^{2+} ions are expected to play a role of charge compensating species near the AlO_4 tetrahedra as shown by [127, 171]. For the glass forming composition $(MgO)_x(Al_2O_3)_y(SiO_2)_{(1-x-y)}$ where $R = x/y \geqslant 1$, the addition of Al_2O_3 causes the creation of AlO_4^- in the glass network and a reduction in the fraction of NBO. However, the same does not occur when $R < 1$ and the simple standard model cannot be applied.

In the present work X-ray diffraction experiments were carried out to study the struc-

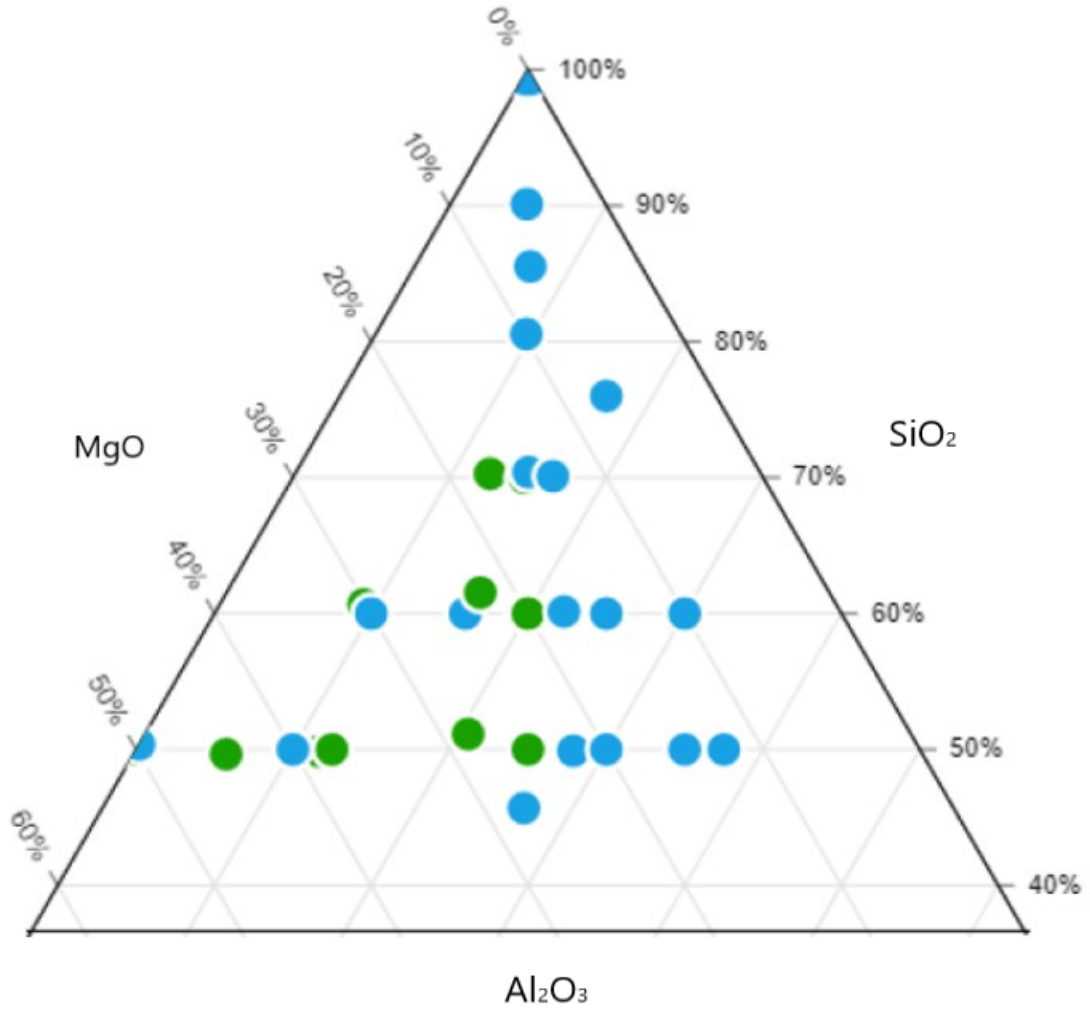

Figure 5-1: Diagram of the $(MgO)_x(Al_2O_3)_y(SiO_2)_{1-x-y}$ glass forming system studied by X-ray (this work, green) and neutron diffraction [40] (blue).

ture of $(MgO)_x(Al_2O_3)_y(SiO_2)_{(1-x-y)}$ glasses, where $0 \leqslant x \leqslant 1$, $0 \leqslant y \leqslant 1$ and $x + y \leqslant 1$. Figure 5-1 shows the studied MAS compositions. The aluminum speciation obtained from ^{27}Al MAS NMR experiments is used as a constraint in the interpretation of the measured pair distribution functions. A wide range of compositions was investigated along tie-lines in the ternary phase diagram where the silica content was kept constant at 50, 60 and 70 mol% silica. The $R = x/y = 1$ tie-line was also investigated. The results were then compared with neutron diffraction data for the same compositions and interpreted with the aid of a recently analytical model developed by Gammond et al [1] for the composition-dependent structure of aluminosilicate glasses.

Samples	Batch	MgO [mol%]	Al_2O_3 [mol%]	SiO_2 [mol%]
$MgSiO_3$	2	50	0	50
MAS50.06	1	44.43	5.92	49.65
MAS50.12	1	38.37	11.77	49.87
natMAS50.12p5	2	37.5	12.5	50
isoMAS50.12p5	2	37.5	12.5	50
MAS51.21	1	28.25	20.62	51.13
natMAS50.25	2	25.0	25.0	50
isoMAS50.25	2	25.0	25.0	50
MAS61.09	1	30.15	9.18	60.67
MAS62.16	2	22.27	16.19	61.54
natMAS60.20	1	20.0	20.0	60
isoMAS60.20	1	20.0	20.0	60
MAS70.12	1	17.28	12.44	70.28
MAS70.15	1	14.76	14.84	70.40

Table 5.1: Concentrations of MgO, Al_2O_3 and SiO_2 for each of the MAS samples.

5.2 Experiment

5.2.1 Sample Preparation

Two batches of magnesium aluminosilicate glasses were prepared as described below. Their respective concentrations are shown in table 5.1. The densities of the MAS samples were measured using a helium pycnometer (MICRO-ULTRAPYC 1200e) and their values are given in table 5.2.

The first batch of MAS samples was prepared at Corning Inc., USA. Powders of MgO (99.992%), Al_2O_3 (99.98%) and SiO_2 (99.99%) were mixed and heated inside a Pt crucible at 1650°C for 15 h. The glasses were quenched by pouring the liquid onto stainless steel, crushed and re-melted to guarantee sample homogeneity. Afterwards, they were annealed at 750°C for two hours to reduce internal stress. To check sample homogeneity, non-crystallization and absence of phase separation, the samples were observed in detail using a polarized light microscope [172].

The second batch of MAS samples was prepared at Bath, UK, where powders of MgO (Aldrich, $\geqslant$ 99.99%), SiO_2 (Alfa Aesar, 99.9%) and Al_2O_3 (Sigma-Aldrich, 99.998%) were used. Isotopically enriched samples prepared from powdered ISOFLEX ^{25}MgO (0.32% ^{24}Mg, 99.38 $\pm$ 0.04% ^{25}Mg, 0.30% ^{26}Mg) are labeled as isoMAS50.12p5, isoMAS50.25 and isoMAS60.20. Their corresponding compositions made using natural MgO will be denoted as natMAS50.12p5, natMAS50.25 and natMAS60.20. All the

starting materials were calcinated at 1000°C for 2 h within a Pt-10%Rh crucible. The isotopic and natural MAS50.12p5 and MAS50.25 samples were melted at 1550°C and 1650°C, respectively, and kept at their melted temperatures for 1 h. The glasses were quenched by using a copper block cooled in liquid nitrogen. The mass loss on melting was $< 0.3\%$, which was attributed to the loss of re-adsorbed water.

The isotopic and natural MAS60.20 samples were prepared by adding Al_2O_3 and SiO_2 to the isotopic and natural MAS50.25 samples. The samples were calcinated at 1000°C for 2 h within a Pt/10%Rh crucible and melted at 1550°C. The quenching method was identical to the samples mentioned above. The resulting glass was ground and remelted for a second time to ensure sample homogeneity. All the glasses were transparent and color-less. The mass loss was $\leq 0.46\%$ on the first melt and $\leq 0.29\%$ on the second melt, which was attributed to the loss of re-adsorbed water.

The $MgSiO_3$ glass of mass ≈ 3 g was made by mixing MgO (Alfa Aesar, $\geq 99.995\%$) and SiO_2 (Alfa Aesar, 99.9%) powders that had been calcined at 1000°C. The mixed powders were melted in a Pt/10%Rh crucible at 1650°C for 2 h and the melt was quenched by placing the bottom of the crucible in water. The sample was ground, and the melt and quench procedure was repeated. The overall mass loss during processing was $\approx 1\%$, which was probably related to the loss of re-adsorbed water.

The composition of each glass was measured using either inductively coupled plasma spectroscopy (batch 1 glasses) or it was taken from the batch composition (batch 2 glasses).

5.2.2 6-ID-D Experiment

Two sets of high energy X-ray diffraction experiments on the MAS samples were performed at room temperature using the 6-ID-D diffractomer at the Advanced Photon Source (APS), as discussed in section 3.2.2.

The first set of experiments (batch 1) was done with a photon energy of 100.334 keV corresponding to a wavelength of 0.1237 Å. The scattered X-rays were detected using a Varex 4343CT amorphous silicon flat panel detector, which was placed at a distance of 281.48 mm from the sample position. The second set of experiments (batch 2) was done with a photon energy of 100.233 keV corresponding to a wavelength of 0.1236 Å. The scattered X-rays were detected using the same detector, which was placed at a distance of 311.12 mm from the sample position.

The ground glasses were loaded into Kapton polyimide tubes (Figure 5-3) of 1.80(1) mm

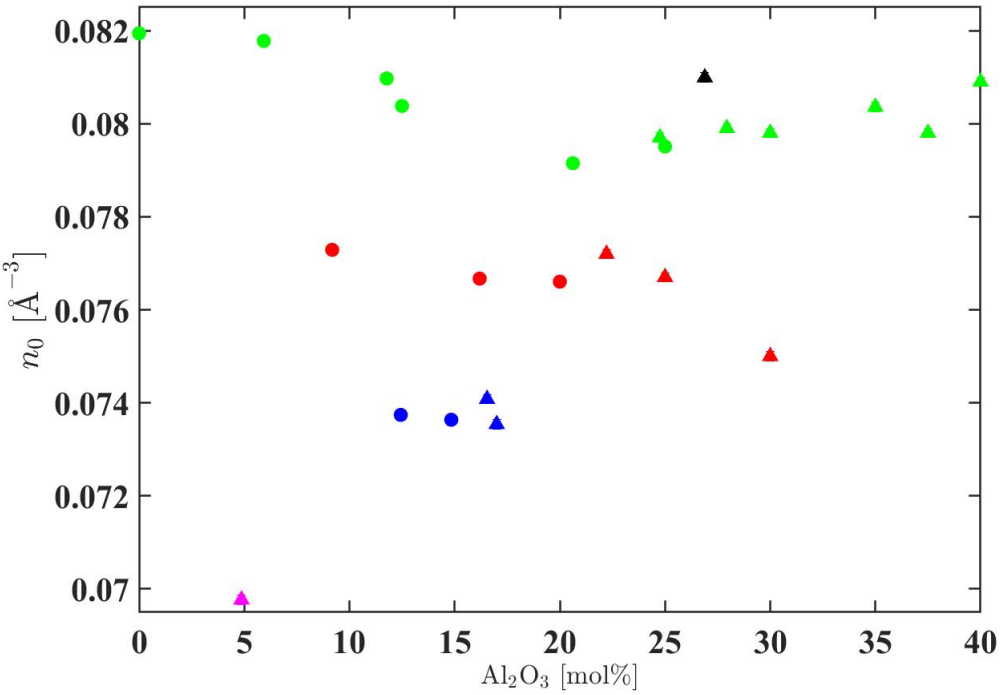

Figure 5-2: Number density, n_0, as a function of the Al_2O_3 content for the MAS glasses in this XRD work (circles) and from a ND work ([40], triangles). The green data points show the n_0 values along the 50 mol% SiO_2 tie-line. The red data points show the n_0 values along the 60 mol% SiO_2 tie-line and the blue data points show the n_0 values along the 70 mol% SiO_2 tie-line. The black data point corresponds to a MAS sample with 45.69 mol% SiO_2 and the magenta data point corresponds to a MAS sample with 90.12 mol% SiO_2.

Samples	ρ [g/cm^3]	ρ Corning Inc. [g/cm^3]	n_0 [Å^{-3}]
$MgSiO_3$	2.7318(6)	-	0.08194(2)
MAS50.06	2.7308(3)	2.723	0.081777(9)
MAS50.12	2.7075(4)	2.682	0.08097(1)
natMAS50.12p5	2.691(1)	-	0.08040(3)
isoMAS50.12p5	2.697(1)	-	0.08040(3)
MAS51.21	2.6510(4)	2.665	0.07915(1)
natMAS50.25	2.667(1)	-	0.07945(3)
isoMAS50.25	2.670(1)	-	0.07945(3)
MAS61.09	2.5812(2)	2.564	0.077288(6)
MAS62.16	2.5642(2)	2.565	0.076669(6)
natMAS60.20	2.558(1)	-	0.07660(3)
isoMAS60.20	2.576(1)	-	0.07660(3)
MAS70.12	2.4632(3)	2.456	0.073742(9)
MAS70.15	2.4609(3)	2.462	0.073636(9)

Table 5.2: The measured mass density, ρ, and corresponding number density, n_0, for the MAS samples. The density measured by Corning Inc. is also shown for comparison.

internal diameter and 0.051(6) mm wall thickness. Diffraction patterns were measured for each sample in its capillary, an empty capillary and the empty instrument. Figure 5-4 shows a two-dimensional image plate X-ray diffraction pattern for one of the MAS glass.

The FIT2D program [84] was used to correct the data for polarization of the beam effects before integrating to produce one dimensional diffraction pattern. It also calculates the sample to detector distance using a CeO_2 crystalline calibrant with a known scattering pattern. Some detector regions are covered by the beam stop or bad pixels. To overcome this problem a mask is applied such that it doesn't influence the results of integration.

Each data set is normalised to the incident beam by using the program PDFgetX2 [85], which obtains the pair distribution function from X-ray powder diffraction. Here, background scattering and attenuation effects are taken into account. The data are scaled to fit the sum of the Compton scattering [173] and self scattering contributions where the neutral atom form factors f_α(Q) were taken from the *International Tables of X-ray Crystallography* [174]. The Rayleigh-Thomson differential scattering cross-section is obtained by subtracting the Compton scattering and self-scattering.

Figure 5-3: MAS samples held in kapton polyimide tubes.

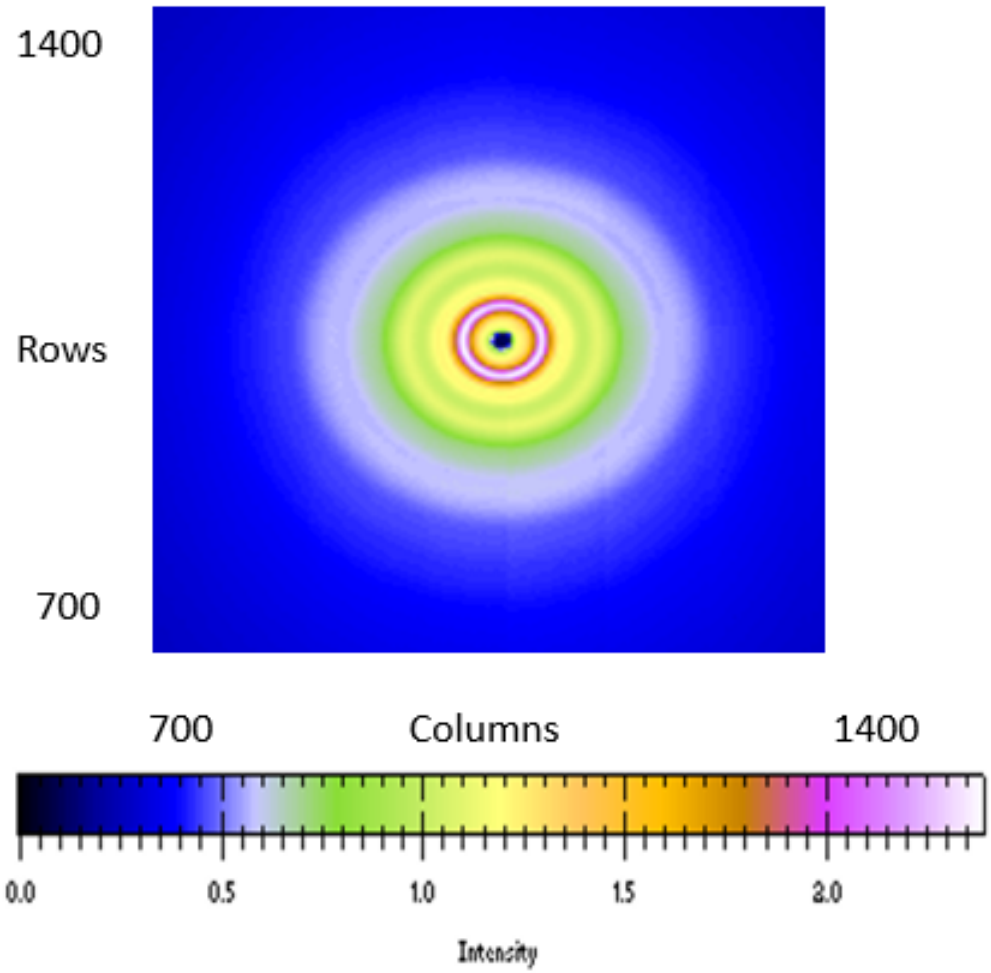

Figure 5-4: An example of a two-dimensional image plate X-ray diffraction patterns measured for the sample MAS51.21.

5.3 Results

Tables 5.3 and 5.4 show the values of the weighting factors for all pair correlations present in batch 1 at $Q = 0$. The Q dependent weighting factors are plotted in figure 5-5.

The X-ray total structure factors $S_X(Q)$ of MAS glasses are shown in figures 5-6, 5-7 and 5-8. For the glasses of batch 2, the structure factors were identical between natural (^{nat}Mg) and isotopic (^{25}Mg) samples, which was a good way to determine if the compositions were made accurately with the same composition. This is because isotopes are not distinguishable by X-rays. In contrast, neutron diffraction is sensitive to isotopes as neutron scattering amplitudes vary irregularly from one nuclide to another [175].

All $S_X(Q)$ functions have a three peak structure at small Q values which are listed in table 5.5, along with their respective $Q_{\max}$ used for Fourier transformation. These three main peaks are related to ordering on different real-space length scales [100] although the presence of overlapping partial structure factors with composition-dependent weighting factors makes it challenging to interpret. The first sharp diffraction peak (FSDP) occurs in the range from 1.70(1) to 1.95(1) Å^{-1} and is in agreement with previous X-ray diffraction experiments [127] on similar compositions for the magnesium aluminosilicate glasses. This peak becomes less broad and more intense as the SiO_2 content increases. The $S_X(Q)$ functions were Fourier transformed using a step modification function to get the total pair distribution functions $D_X(r)$. The total pair distribution functions are shown in figures 5-10, 5-11 and 5-12.

Figure 5-10 shows the $D_X(r)$ functions for the MAS glasses along the 50 mol% SiO_2 tie-line. The sample $MgSiO_3$ shows well defined peaks at $r \approx 1.6$ Å and $r \approx 2.0$ Å which correspond to Si-O and Mg-O peaks, respectively. The Mg-O peak includes a shoulder on the high r side which is typical of MAS glasses [127, 171, 176–179] but also for ZAS glasses [80, 82]. The peak at $r \approx 2.67$ Å is mainly due to O-O correlations originating from SiO_4 tetrahedra. The $D_X(r)$ fit is shown in Figure 5-14. When adding alumina to the glass network the first peak in $D_X(r)$ shifts to higher r (Figures 5-16, 5-18 and 5-19). A peak at around $r \approx 1.76$ Å is attributed to the Al-O distance in tetrahedral units. In contrast to neutron diffraction, it is not easy to identify Al-O contributions. For this reason neutron diffraction data [40] helped constrain the Al-O peak position for the same glass-forming compositions. The O-O peak remains at $r \approx 2.6$ Å for all compositions. All the MAS compositions show a peak in the range 3.1-3.2 Å which corresponds to the Mg-Si and Si-Si distances. There is also an overlap in that region from Al-Al and Al-Mg correlations that starts slightly before, around ≈ 3.0 Å. Above

Pair correlation α-β	MAS50.06	MAS50.12	MAS51.21
Si-O	0.224(3)	0.213(3)	0.201(3)
Al-O	0.054(3)	0.100(3)	0.162(3)
Mg-O	0.201(3)	0.164(3)	0.111(3)
O-O	0.365(3)	0.370(3)	0.378(3)
Si-Si	0.034(3)	0.031(3)	0.027(3)
Al-Al	0.002(3)	0.0068(7)	0.017(3)
Mg-Mg	0.028(3)	0.0181(7)	0.008(3)
Mg-Si	0.062(3)	0.0471(7)	0.030(3)
Mg-Al	0.015(3)	0.0222(7)	0.024(3)
Al-Si	0.016(3)	0.0289(7)	0.043(3)

Table 5.3: The ten weighting factors, $\omega_{\alpha\beta}$, at $Q = 0$ for batch 1 MAS samples from the 50 mol% SiO_2 tie-line.

3.5 Å there is an overlap between the different contributions which makes it difficult to extract information. The $D_X(r)$ fits for natural and isotopic samples of the same composition (Figures 5-15 and 5-17) are identical to each other as expected.

The $D_X(r)$ fits for the MAS glasses along the 60 and 70 mol% SiO_2 tie-lines show similar features to the 50 mol% SiO_2 tie-line although the peaks corresponding to Si-O are sharper and Mg-O is much smaller due to the low concentration of MgO in these samples. Tables 5.8, 5.9, 5.10 and 5.11 show the fitted parameters with the corresponding goodness-of-fit, R_χ, over the fitted range 1.30−2.76 Å for $MgSiO_3$ or 1.40−2.76 Å for the MAS samples. For each $D_X(r)$ fit one peak was assigned to Si-O correlations, one peak was assigned to Al-O correlations, two peaks were assigned to Mg-O correlations and one peak was assigned to O-O correlations. The average coordination numbers for Si-O correlations was fixed to 4 and the average coordination numbers for Al-O correlations were taken from ^{27}Al MAS NMR measurements [1,180]. The Mg-O peaks were constrained to have a minimum width of $\sigma = 0.05$ Å. For the isotopic enriched and corresponding natural MAS samples, the Mg-O coordination number was fixed from NDIS fits [180]. The Mg-O coordination numbers as a function of Al_2O_3 mol% are shown in figure 5-20.

Pair correlation α-β	MAS61.09	MAS62.16	MAS70.12	MAS70.15
Si-O	0.262(3)	0.248(3)	0.290(3)	0.284(3)
Al-O	0.079(3)	0.131(3)	0.103(3)	0.120(3)
Mg-O	0.130(3)	0.090(3)	0.071(3)	0.060(3)
O-O	0.386(3)	0.391(3)	0.403(3)	0.404(3)
Si-Si	0.044(3)	0.0394(3)	0.0520(7)	0.050(3)
Al-Al	0.041(3)	0.0109(3)	0.0065(7)	0.0089(7)
Mg-Mg	0.0109(7)	0.0052(3)	0.0032(7)	0.0022(7)
Mg-Si	0.044(3)	0.0285(7)	0.026(3)	0.021(3)
Mg-Al	0.0133(7)	0.0150(3)	0.0091(7)	0.0088(7)
Al-Si	0.0268(7)	0.0414(3)	0.037(3)	0.042(3)

Table 5.4: The ten weighting factors, $\omega_{\alpha\beta}$, at $Q = 0$ for batch 1 MAS samples from the 60 and 70 mol% SiO_2 tie-lines.

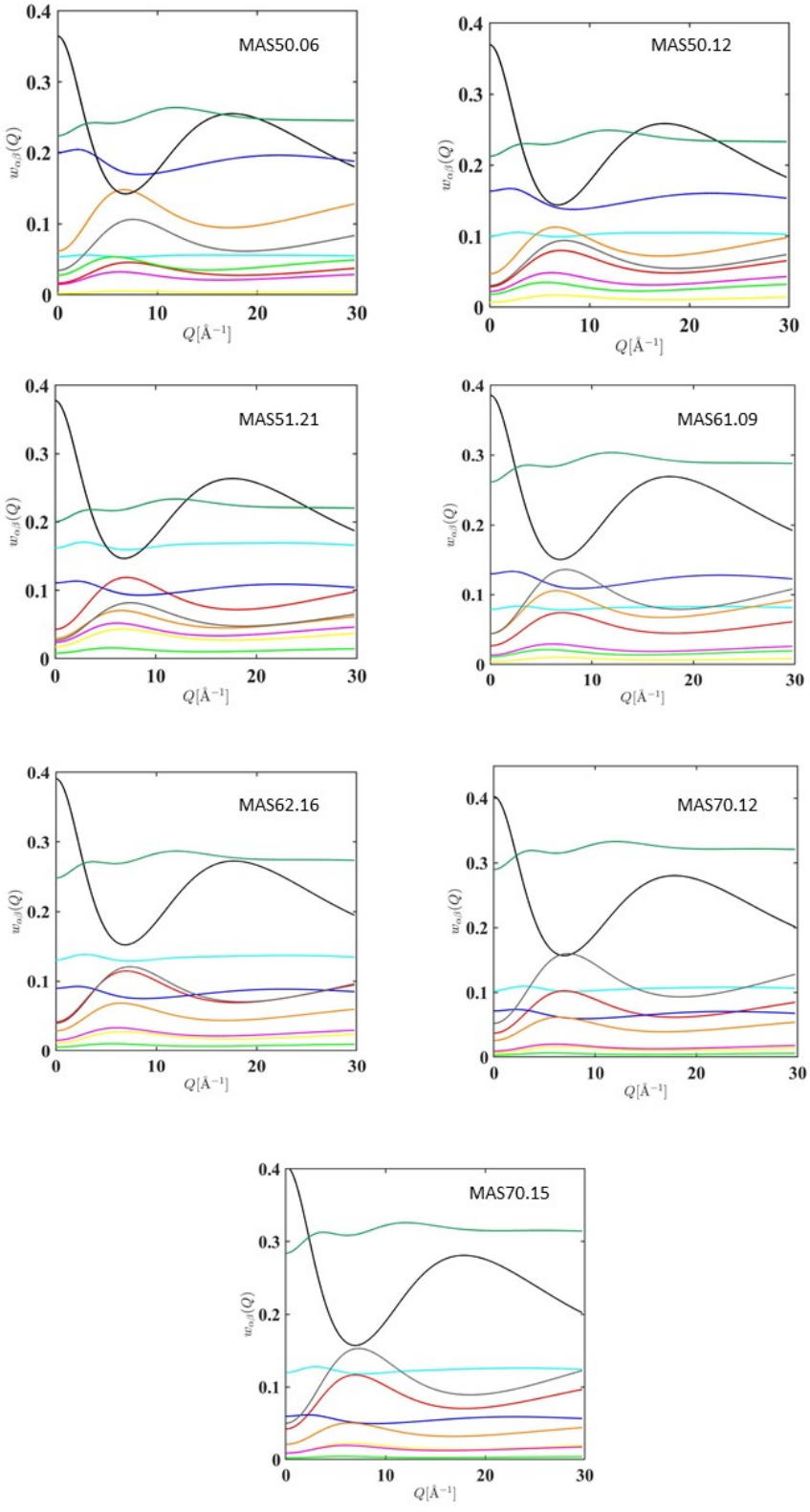

Figure 5-5: Weighting factors, $\omega_{\alpha\beta}(Q)$, plot for batch 1 MAS samples. The lines correspond to Al-Al (yellow), Al-Mg (pink), Al-O (cyan), Al-Si (red), Mg-Mg (green), Mg-O (blue), Mg-Si (orange), O-O (black) correlations, Si-O (dark green) and Si-Si (dark grey) correlations. Their respective values at $Q = 0$ are listed in tables 5.3 and 5.4.

Sample	Al(IV) [%]	Al(V) [%]	Al(VI) [%]	$\bar{n}^{\mathrm{O}}_{\mathrm{Al}}$
MAS50.06	91	9	0	4.09(5)
MAS50.12	91	9	0	4.09(5)
natMAS50.12p5	84	16	0	4.165(7)
isoMAS50.12p5	83	17	0	4.165(7)
MAS51.21	88	12	0	4.12(5)
natMAS50.25	75	25	0	4.27(7)
isoMAS50.25	75	21	4	4.27(7)
MAS61.09	94	6	0	4.06(5)
MAS62.16	86	13	1	4.15(5)
natMAS60.20	78	22	0	4.215(7)
isoMAS60.20	79	21	0	4.215(7)
MAS70.12	82	16	2	4.20(5)
MAS70.15	78	19	3	4.25(5)

Table 5.6: Al speciation in magnesium aluminosilicate glasses measured by ^{27}Al MAS NMR [1, 180] and the calculated average coordination number.

Sample	Q_{FSDP}[Å^{-1}]	Q_3[Å^{-1}]	Q_4[Å^{-1}]	Q_{max} [Å^{-1}]
$MgSiO_3$	1.917(1)	4.527(2)	6.464(2)	23.94
MAS50.06	1.891(1)	4.556(2)	6.473(2)	24.60
MAS50.12	1.856(1)	4.580(2)	6.51(2)	24.66
natMAS50.12p5	1.851(1)	4.591(2)	6.528(2)	25.78
isoMAS50.12p5	1.852(1)	4.592(2)	6.524(2)	25.78
MAS51.21	1.823(1)	4.610(2)	6.544(2)	25.80
natMAS50.25	1.828(1)	4.624(2)	6.561(2)	25.02
isoMAS50.25	1.828(1)	4.616(2)	6.565(2)	25.02
MAS61.09	1.764(1)	4.601(2)	6.507(2)	24.92
MAS62.16	1.755(1)	4.634(2)	6.540(2)	24.70
natMAS60.20	1.749(1)	4.651(2)	6.549(2)	25.88
isoMAS60.20	1.750(1)	4.648(2)	6.550(2)	25.88
MAS70.12	1.674(1)	4.670(2)	6.530(2)	24.86
MAS70.15	1.681(1)	4.683(2)	6.541(2)	23.70

Table 5.5: The positions of the first three peaks Q_{FSDP}, Q_3 and Q_4 in the $S_X(Q)$ functions for the MAS glasses shown in figures 5-6 and 5-7. The Q_{max} values used in the Fourier transform are also listed.

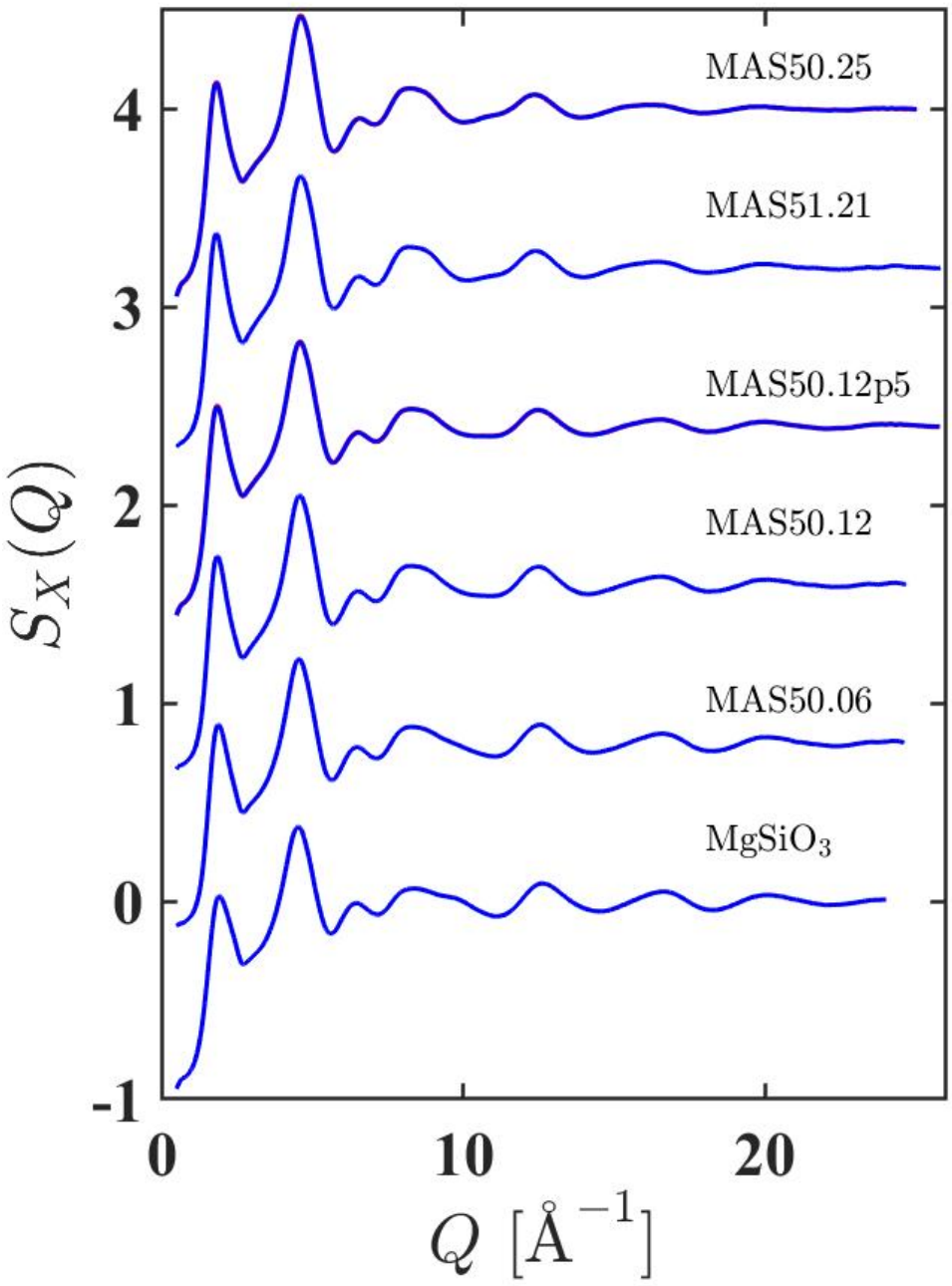

Figure 5-6: Total structure factors, $S_X(Q)$, for the magnesium aluminosilicate glasses along the 50 mol% SiO_2 tie-line. The blue solid curves are the natural samples. The red (underneath) solid curves are the isotopic samples MAS50.12p5 and MAS50.25. They are not possible to see because they are identical to their respective natural samples. The error bars are smaller than the line thickness at most Q values. The curves are offset vertically for clarity of presentation.

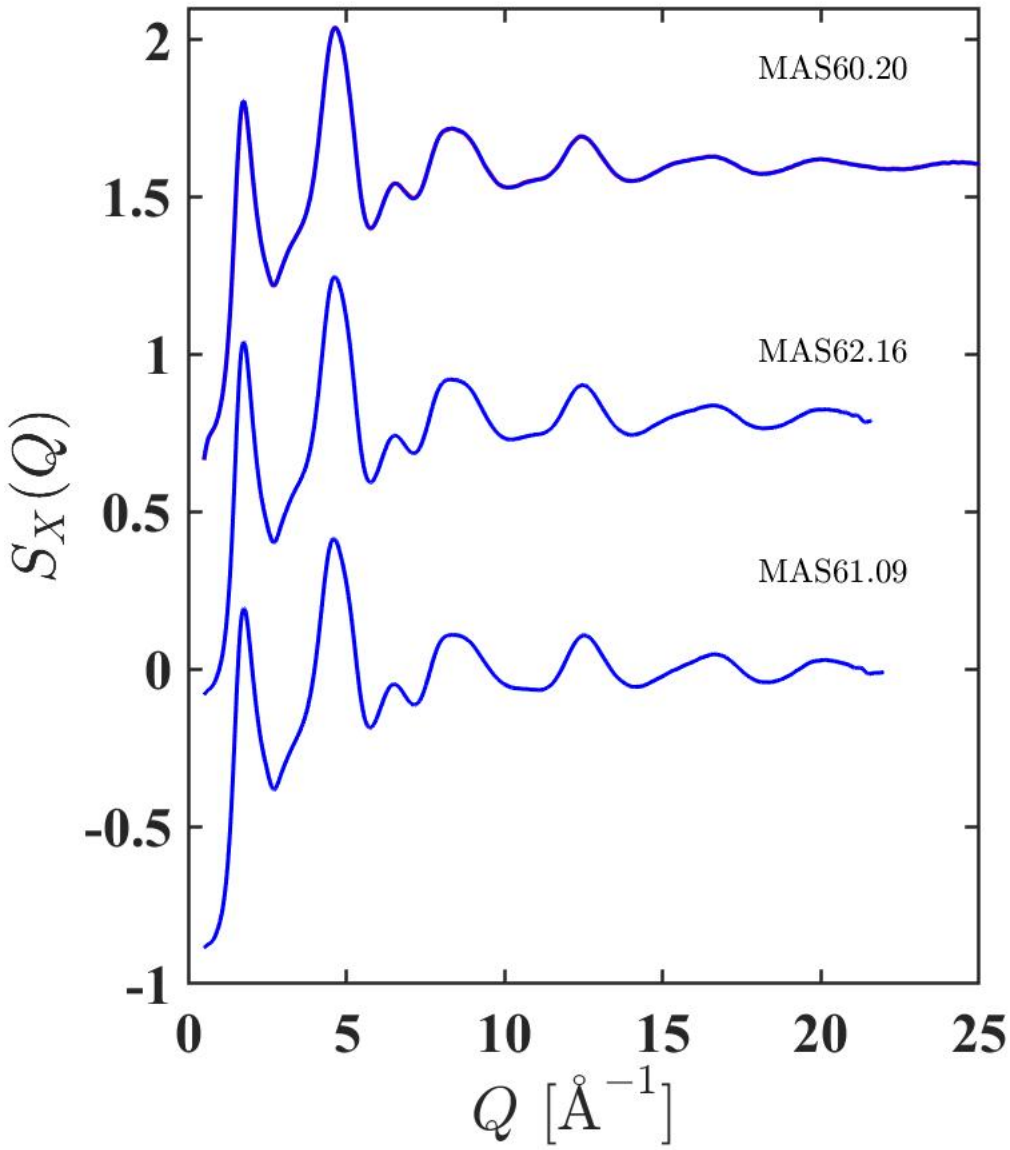

Figure 5-7: Total structure factors, $S_X(Q)$, for the magnesium aluminosilicate glasses along the 60 mol% SiO_2 tie-line. The blue solid curves are the natural samples. The red solid curve (underneath) is the isotopic sample MAS60.20. The isotopic sample is not possible to see because it is identical to the natural sample MAS60.20. The error bars are smaller than the line thickness at most Q values. The curves are offset vertically for clarity of presentation.

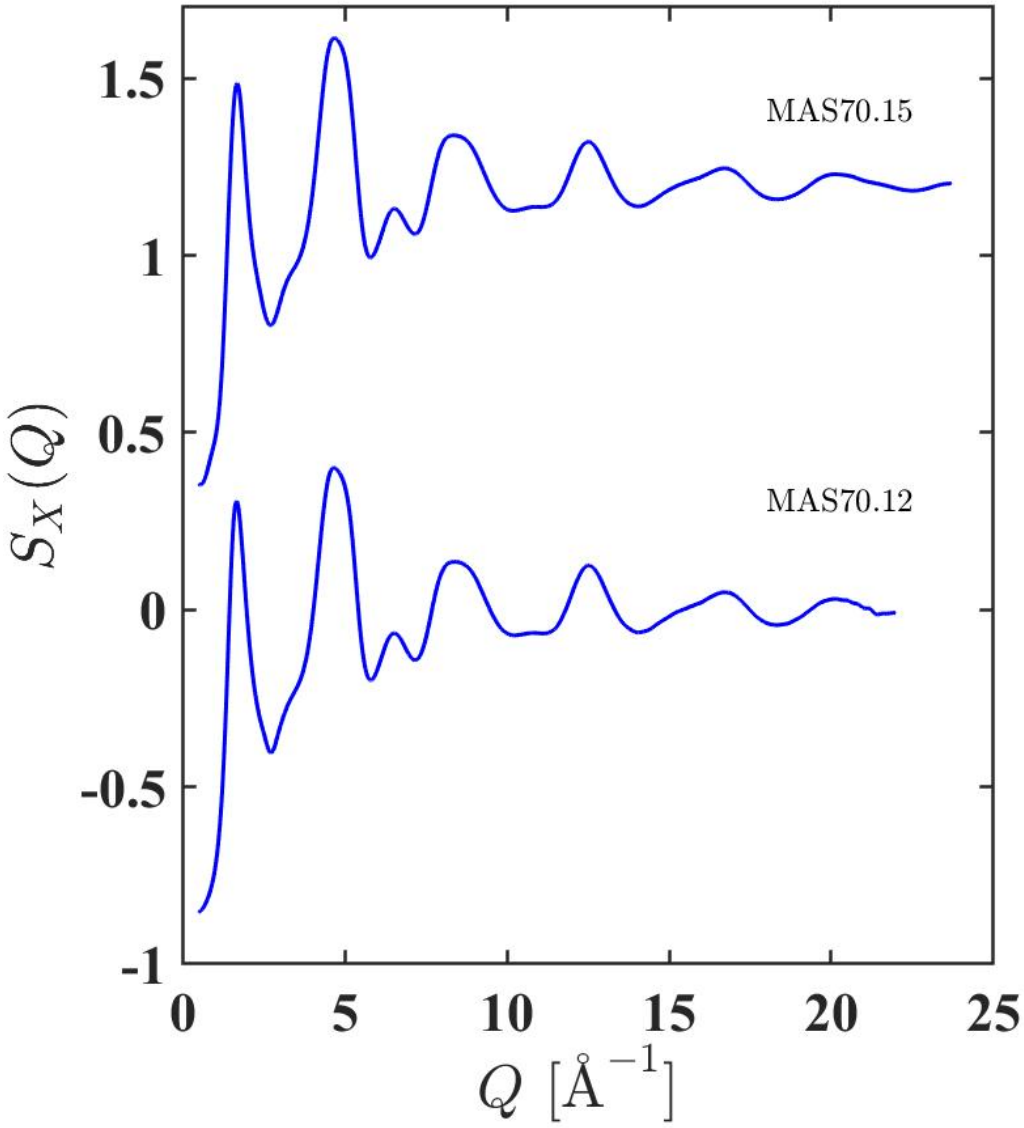

Figure 5-8: Total structure factors, $S_X(Q)$, for the magnesium aluminosilicate glasses along the 70 mol% SiO_2 tie-line. The error bars are smaller than the line thickness at most Q values. The MAS70.15 curve is offset vertically for clarity of presentation.

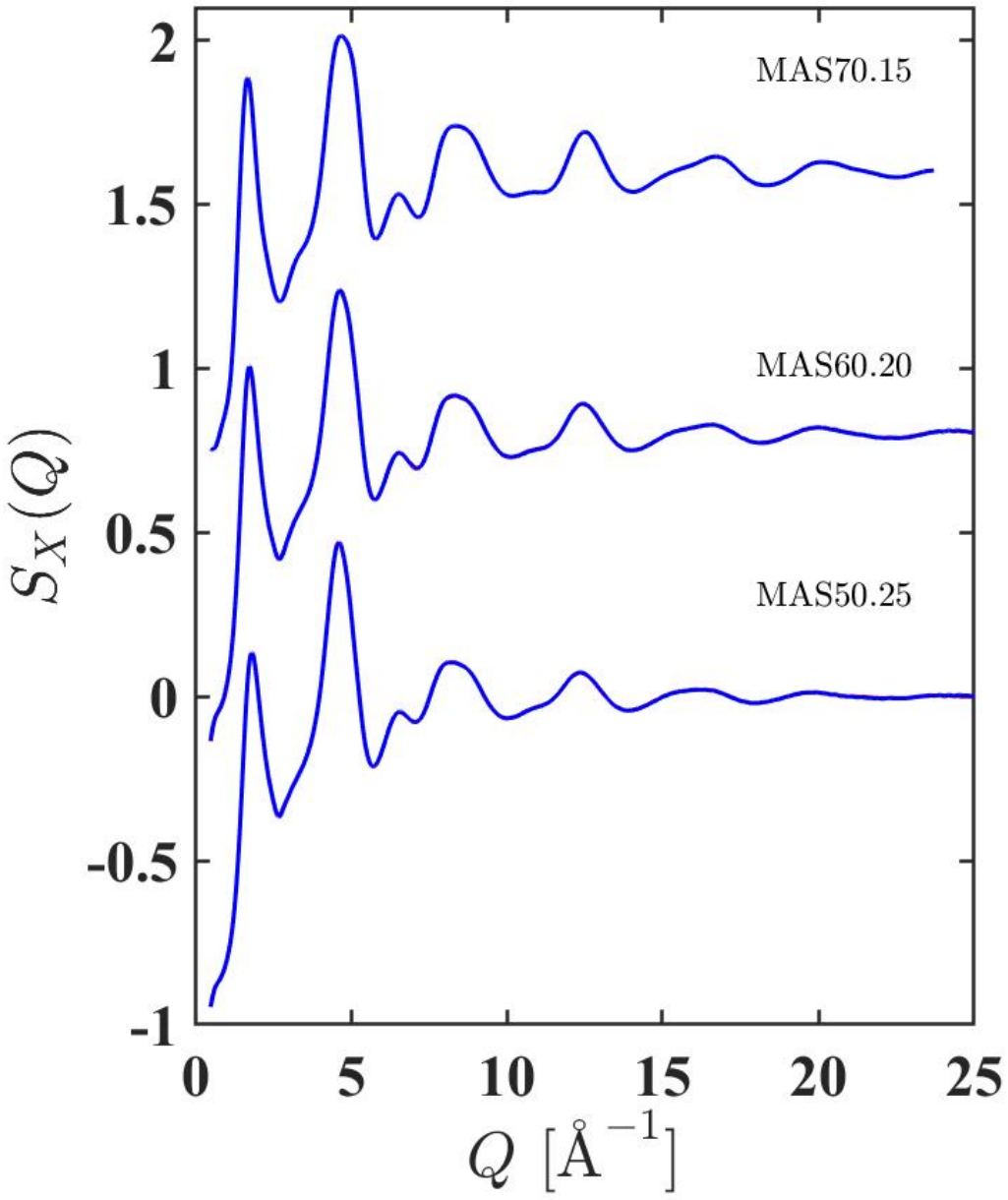

Figure 5-9: Total structure factors, $S_X(Q)$, for the magnesium aluminosilicate glasses along $R = 1$ tie-line. The blue solid curves are the natural samples. The red solid curves are the isotopic samples (MAS50.25 and MAS60.20). The error bars are smaller than the line thickness at most Q values. The curves are offset vertically for clarity of presentation.

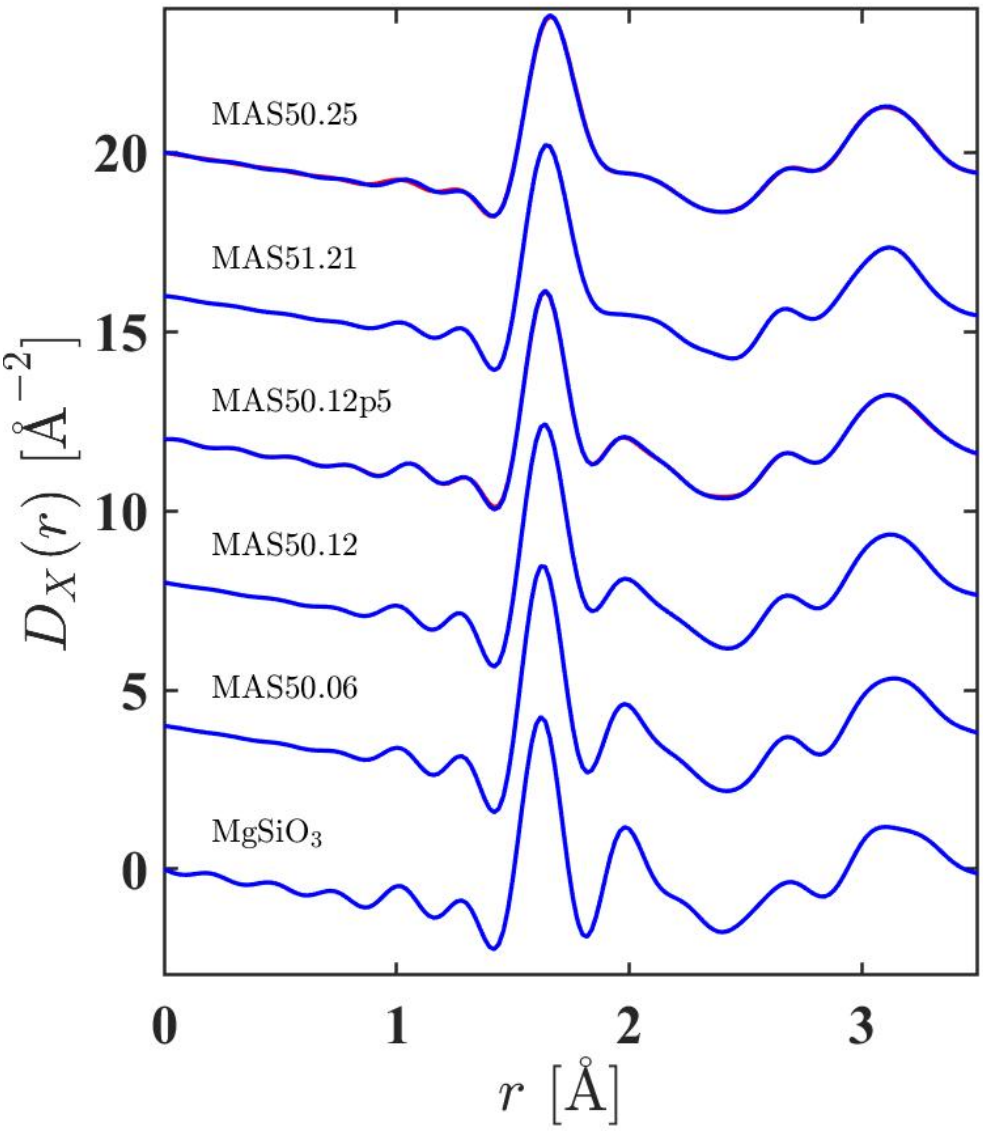

Figure 5-10: Total pair distribution functions, $D_X(r)$, for the MAS glasses along the 50 mol% SiO_2 tie-line. The curves were obtained by Fourier transforming the corresponding reciprocal space data shown in figure 5-6. The blue solid curves are the natural samples. The red solid curves (underneath) are the isotopic samples MAS50.12p5 and MAS50.25. The curves are offset vertically for clarity of presentation.

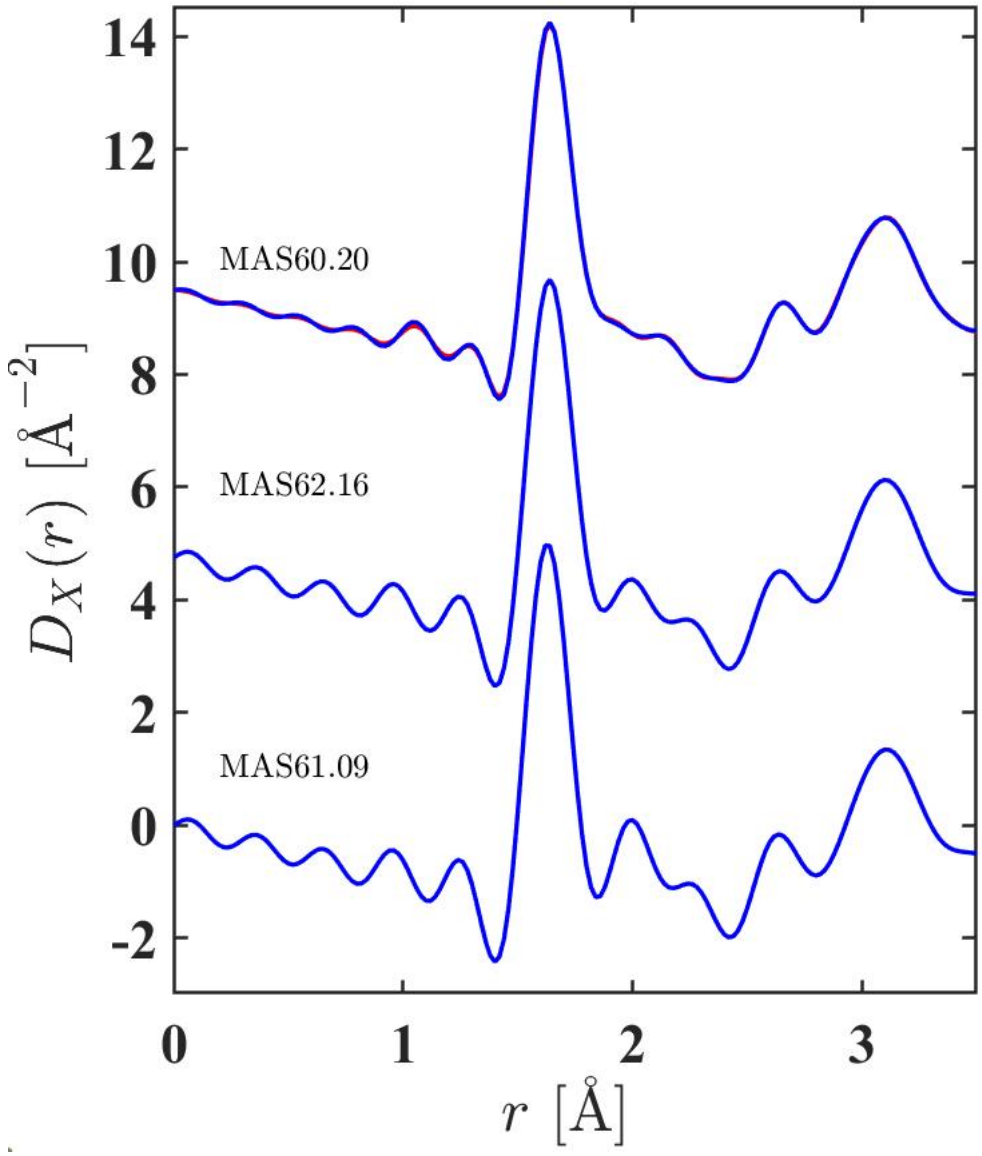

Figure 5-11: Total pair distribution functions, $D_X(r)$, for the MAS glasses along the 60 mol% SiO_2 tie-line. The curves were obtained by Fourier transforming the corresponding reciprocal space data shown in figure 5-7. The blue solid curves are the natural samples. The red solid curve (underneath) is the isotopic MAS60.20 sample. The curves are offset vertically for clarity of presentation.

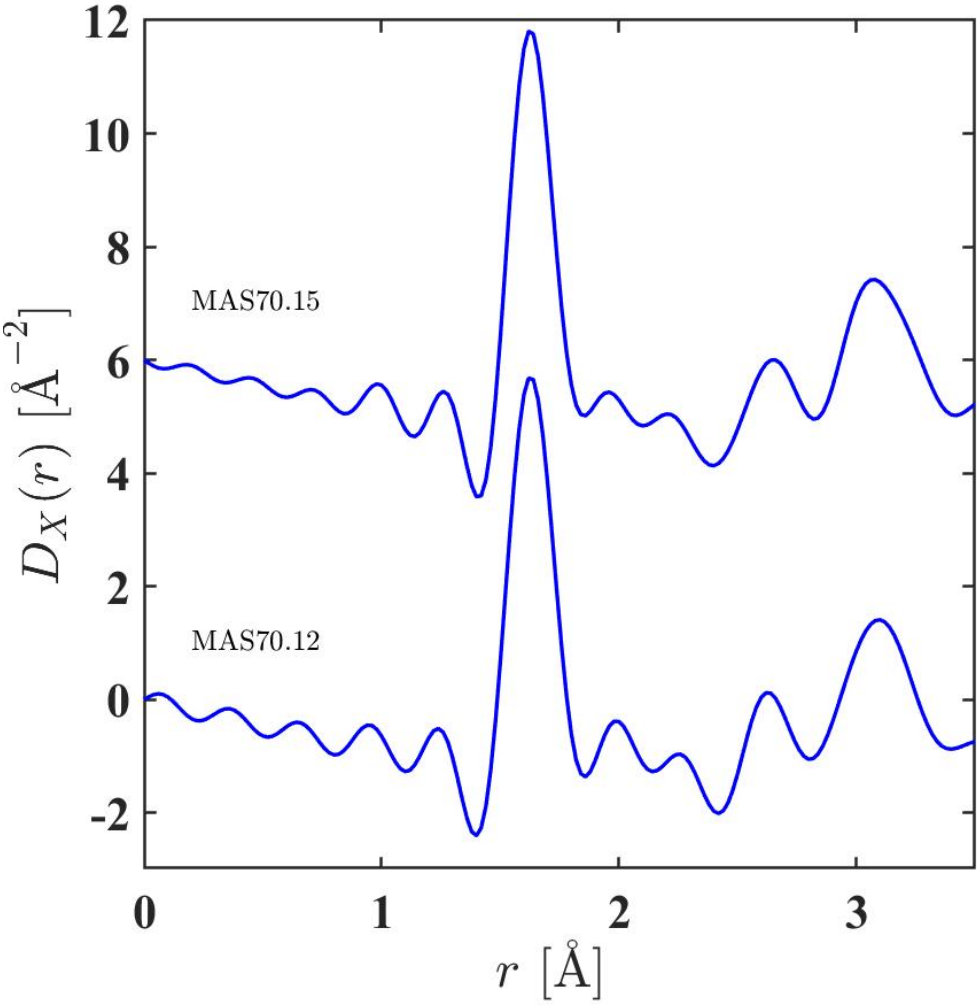

Figure 5-12: Total pair distribution functions, $D_X(r)$, for the MAS glasses along the 70 mol% SiO_2 tie-line. The curves were obtained by Fourier transforming the corresponding reciprocal space data shown in figure 5-8. The MAS70.15 curve is offset vertically for clarity of presentation.

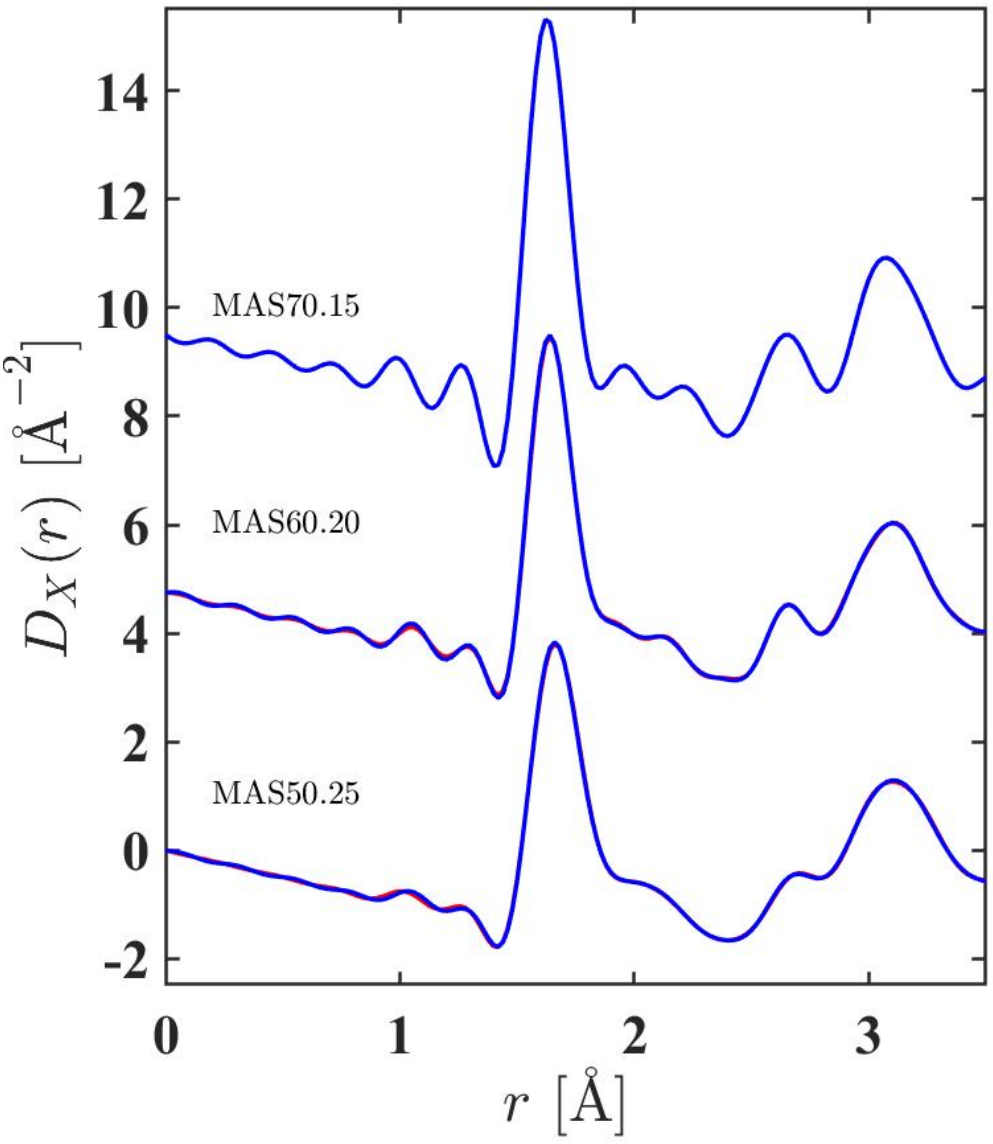

Figure 5-13: Total pair distribution functions, $D_X(r)$, for the MAS glasses along the $R = 1$ tie-line. The curves were obtained by Fourier transforming the corresponding reciprocal space data shown in figure 5-9. The blue solid curves are the natural samples. The red solid curves (underneath) are the isotopic samples MAS50.25 and MAS60.20. The curves are offset vertically for clarity of presentation.

Atom pair	$r_{\alpha\beta}$ [Å]	$\sigma_{\alpha\beta}$ [Å]	$\bar{n}_{\alpha}^{\beta}$	R_{χ} [%]
Si-O	1.624(3)	0.063(5)	3.90(28)	
Mg-O	1.983(4)	0.084(4)	3.06(5)	
Mg-O	2.175(8)	0.130(7)	1.82(5)	7.15
Mg-O (sum)			4.88(7)	
O-O	2.675(5)	0.125(4)	6.36(21)	

Table 5.7: Parameters obtained from Gaussian peak fits to the $D_X(r)$ function for glassy $MgSiO_3$. The fit is shown in figure 5-14. R_{χ} is given for the fitted range 1.30-2.76 Å.

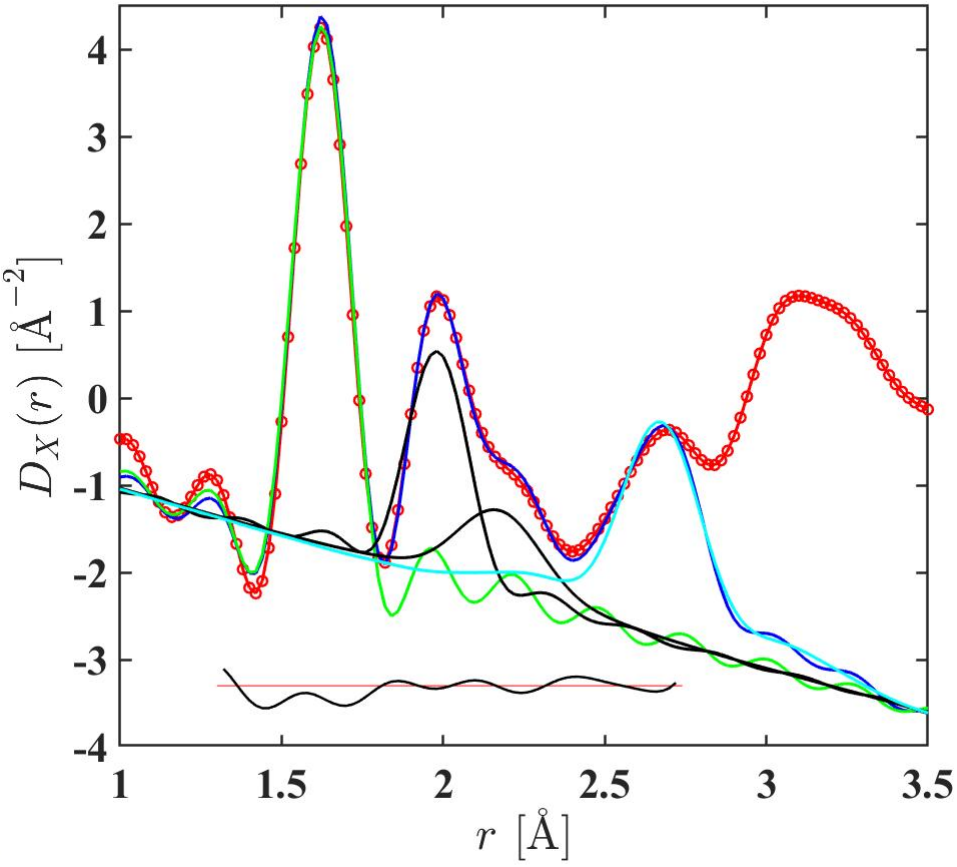

Figure 5-14: The fitted $D_X(r)$ function for glassy $MgSiO_3$. The red circles are the data, the blue solid curve is the fit and the other curves show the contribution from Si-O (green), Mg-O (black) and O-O (cyan) correlations. The displaced black solid curve gives the residual (fit subtracted from measured data). The O-O correlations are introduced to constrain the peaks fitted at smaller r values.

Sample	Atom pair	$r_{\alpha\beta}$ [Å]	$\sigma_{\alpha\beta}$ [Å]	$\bar{n}_{\alpha}^{\beta}$	R_{χ} [%]
MAS50.06	Si-O	1.627(3)	0.061(5)	4*	7.31
	Al-O	1.756(5)	0.110(5)	4.09*	
	Mg-O	1.991(4)	0.085(4)	3.01(5)	
	Mg-O	2.171(8)	0.110(7)	1.66(5)	
	Mg-O (sum)			4.67(7)	
	O-O	2.692(4)	0.135(3)	6.77(12)	
MAS50.12	Si-O	1.626(3)	0.061(5)	4*	6.85
	Al-O	1.760(5)	0.093(5)	4.09*	
	Mg-O	1.998(4)	0.082(4)	2.70(5)	
	Mg-O	2.163(8)	0.118(7)	2.03(5)	
	Mg-O (sum)			4.73(7)	
	O-O	2.689(4)	0.133(2)	6.44(11)	
isoMAS50.12p5	Si-O	1.6303(8)	0.0670(7)	4*	3.94
	Al-O	1.780(3)	0.113(2)	4.165*	
	Mg-O	2.020(5)	0.088(2)	3.17*	
	Mg-O	2.218(5)	0.107(5)	1.59*	
	Mg-O(sum)			4.76*	
	O-O	2.710(6)	0.154(4)	7.37(20)	
natMAS50.12p5	Si-O	1.6263(8)	0.063(1)	4*	5.27
	Al-O	1.780(3)	0.089(3)	4.165*	
	Mg-O	2.015(5)	0.076(2)	3.17*	
	Mg-O	2.208(5)	0.089(4)	1.59*	
	Mg-O (sum)			4.76*	
	O-O	2.712(8)	0.157(5)	7.55(27)	
MAS51.21	Si-O	1.629(3)	0.066(5)	4*	6.56
	Al-O	1.769(3)	0.100(5)	4.12*	
	Mg-O	2.033(4)	0.069(4)	2.59(5)	
	Mg-O	2.201(8)	0.102(7)	2.25(5)	
	Mg-O (sum)			4.84(7)	
	O-O	2.699(4)	0.142(3)	6.68(11)	
isoMAS50.25	Si-O	1.6429(6)	0.075(5)	4*	3.78
	Al-O	1.785(1)	0.127(1)	4.27*	
	Mg-O	2.072(6)	0.074(3)	2.43*	
	Mg-O	2.197(7)	0.125(6)	2.47*	
	Mg-O (sum)			4.90*	
	O-O	2.724(6)	0.159(4)	7.46(21)	

Table 5.8: Parameters obtained from Gaussian peak fits to the $D_X(r)$ functions for the MAS glasses along the 50 mol% SiO_2 tie-line. The fitted functions are shown in figures 5-15 and 5-16. R_{χ} is given for the range 1.40-2.76 Å. The parameters denoted by an * are fixed.

Sample	Atom pair	$r_{\alpha\beta}$ [Å]	$\sigma_{\alpha\beta}$ [Å]	$\bar{n}_{\alpha}^{\beta}$	R_{χ} [%]
natMAS50.25	Si-O	1.639(1)	0.074(9)	4*	3.63
	Al-O	1.784(2)	0.120(1)	4.27*	
	Mg-O	2.063(5)	0.068(3)	2.43*	
	Mg-O	2.200(5)	0.114(5)	2.47*	
	Mg-O (sum)			4.90*	
	O-O	2.721(6)	0.159(4)	7.46(20)	

Table 5.9: Parameters obtained from Gaussian peak fits to the $D_X(r)$ functions for MAS glasses along the 50 mol% SiO_2 tie-line (continuation). The fitted functions are shown in figures 5-15 and 5-16. R_{χ} is given for the range 1.40-2.76 Å. The parameters denoted by an * are fixed.

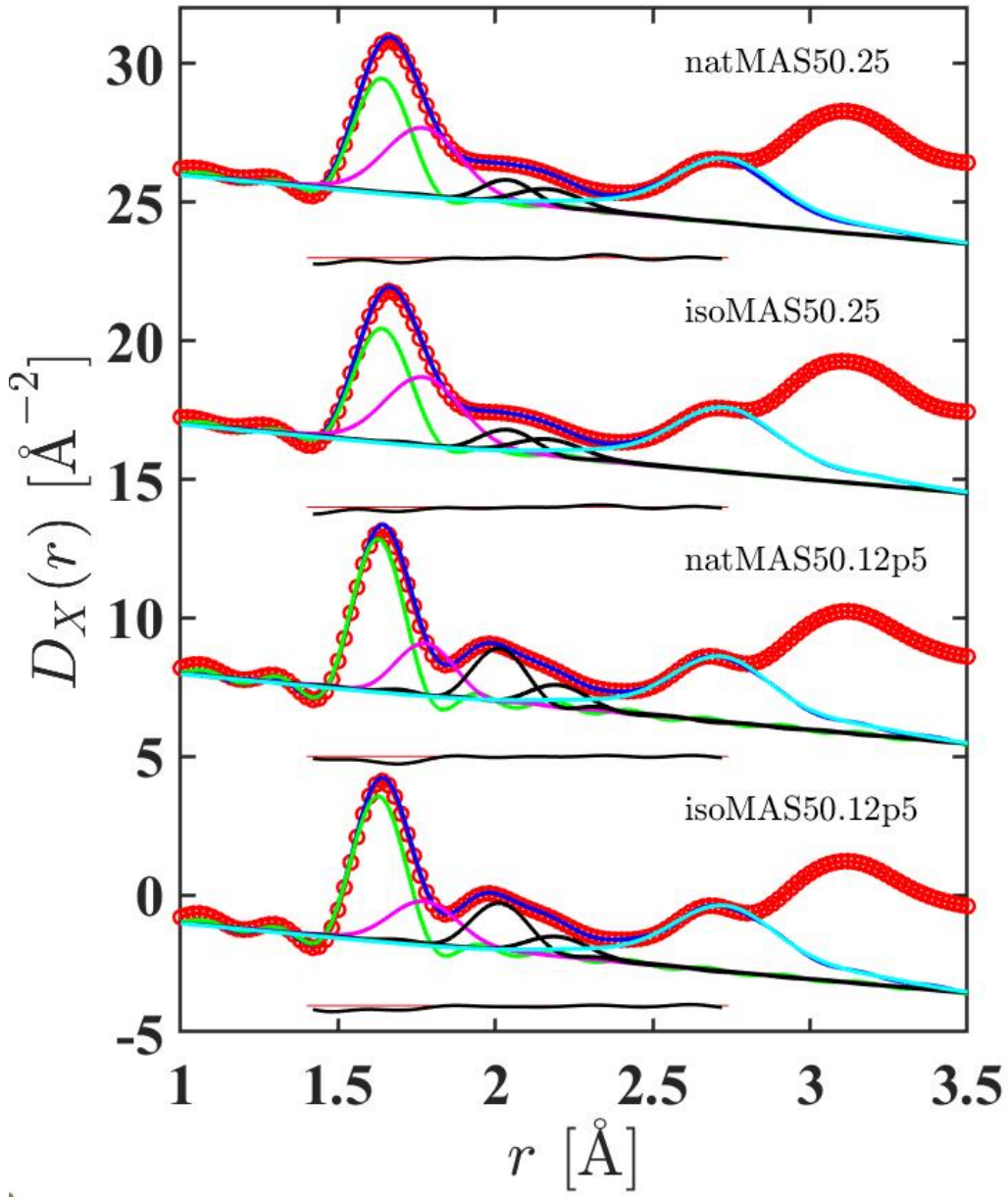

Figure 5-15: The fitted $D_X(r)$ functions for the isotopic MAS glasses and their corresponding natural compositions along the 50 mol% SiO_2 tie-line. The red circles are the data, the blue solid curves are the fits and the other curves show the contribution from Si-O (green), Al-O (magenta), Mg-O (black) and O-O (cyan) correlations. The displaced black solid curve gives the residual (fit subtracted from measured data). The O-O correlations are introduced to constrain the peaks fitted at smaller r values.

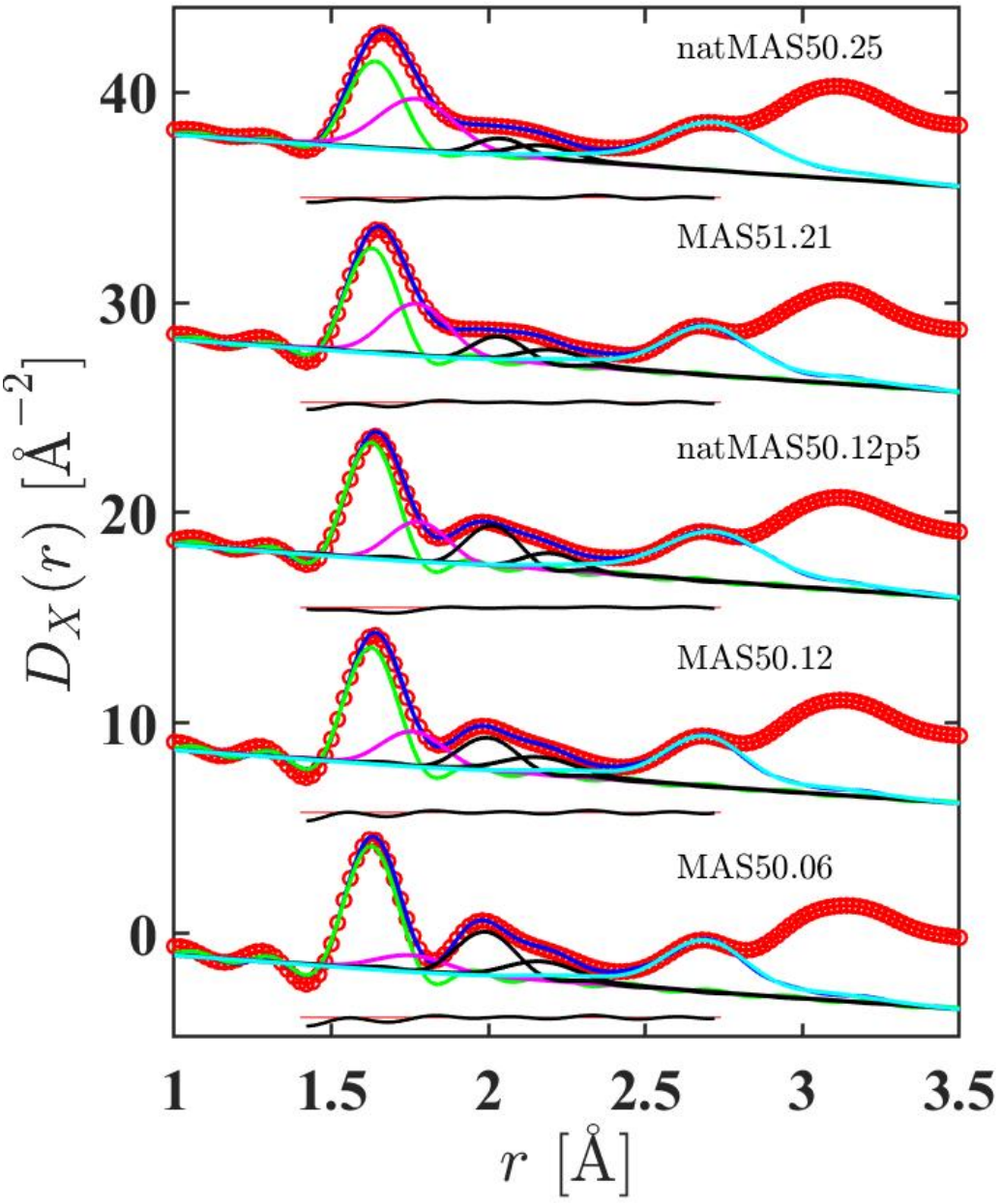

Figure 5-16: The fitted $D_X(r)$ functions for the natural MAS glasses along the 50 mol% SiO_2 tie-line. The red circles are the data, the blue solid curves are the fits and the other curves show the contribution from Si-O (green), Al-O (magenta), Mg-O (black) and O-O (cyan) correlations. The displaced black solid curve gives the residual (fit subtracted from measured data). The O-O correlations are introduced to constrain the peaks fitted at smaller r values.

Sample	Atom pair	$r_{\alpha\beta}$ [Å]	$\sigma_{\alpha\beta}$ [Å]	$\bar{n}_{\alpha}^{\beta}$	R_{χ} [%]
MAS61.09	Si-O	1.627(3)	0.061(5)	4*	4.58
	Al-O	1.771(5)	0.109(5)	4.06*	
	Mg-O	1.993(4)	0.059(4)	2.96(5)	
	Mg-O	2.197(8)	0.051(7)	1.71(5)	
	Mg-O (sum)			4.67(7)	
	O-O	2.678(4)	0.137(4)	6.45(8)	
MAS62.16	Si-O	1.629(3)	0.060(5)	4*	5.40
	Al-O	1.774(5)	0.110(5)	4.15*	
	Mg-O	2.035(4)	0.084(4)	3.24(5)	
	Mg-O	2.222(8)	0.050(7)	1.60(5)	
	Mg-O (sum)			4.84(7)	
	O-O	2.677(3)	0.133(2)	6.15(9)	
isoMAS60.20	Si-O	1.631(1)	0.0696(9)	4*	6.08
	Al-O	1.779(3)	0.125(3)	4.215*	
	Mg-O	2.063(10)	0.064(7)	2.165*	
	Mg-O	2.200(9)	0.114(9)	2.908*	
	Mg-O (sum)			5.07*	
	O-O	2.681(6)	0.138(4)	6.33(19)	
natMAS60.20	Si-O	1.628(1)	0.067(9)	4*	6.24
	Al-O	1.780(3)	0.116(4)	4.215*	
	Mg-O	2.053(6)	0.050(7)	2.165*	
	Mg-O	2.200(9)	0.099(7)	2.908*	
	Mg-O (sum)			5.07*	
	O-O	2.682(6)	0.139(5)	6.36(20)	

Table 5.10: Parameters obtained from Gaussian peak fits to the $D_X(r)$ functions for MAS glasses along the 60 mol% SiO_2 tie-line. The fitted functions are shown in figures 5-17 and 5-18. R_{χ} is given for the range 1.40-2.76 Å. The parameters denoted by an * are fixed.

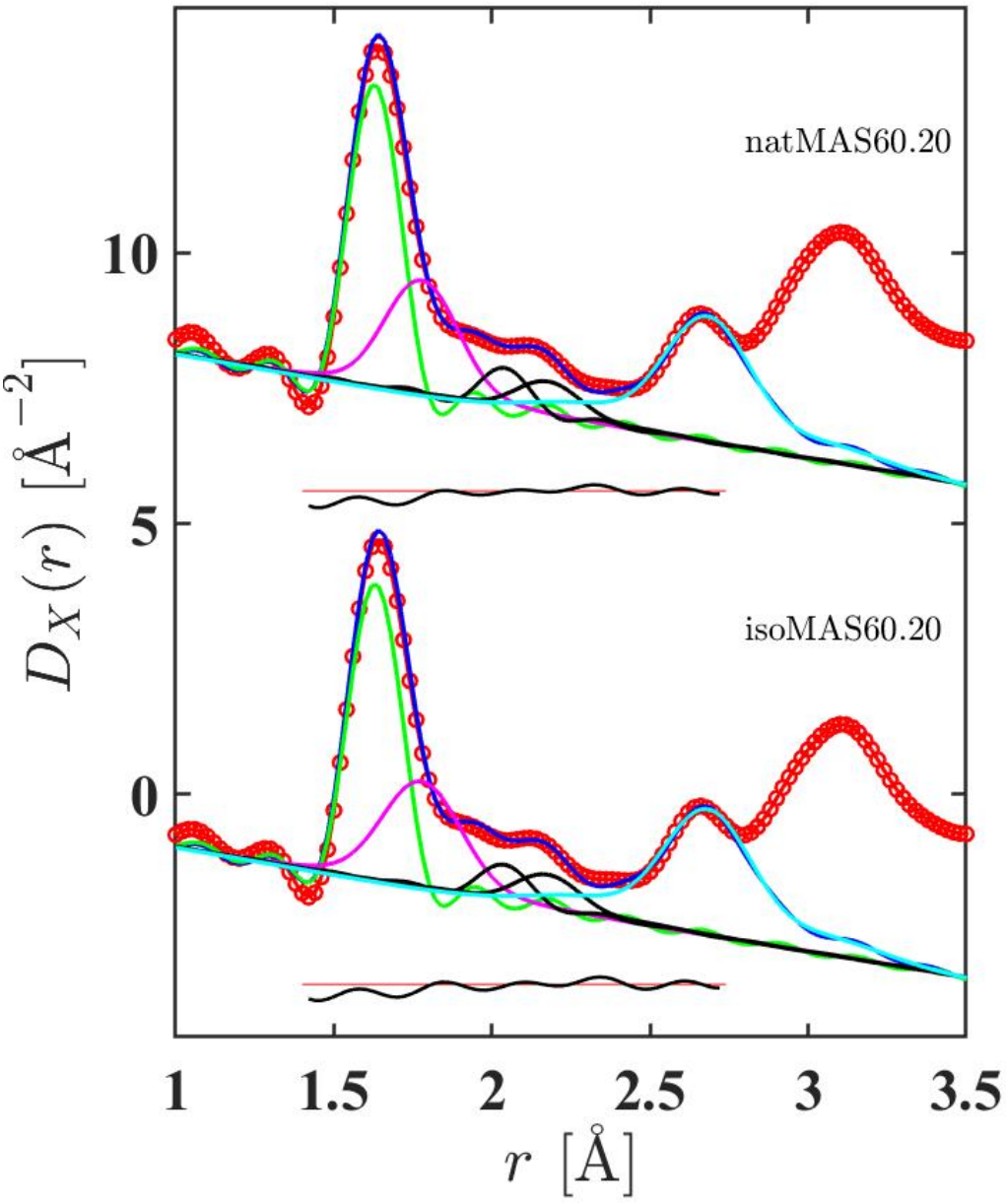

Figure 5-17: The fitted $D_X(r)$ functions for the isotopic MAS glass and its correspondent natural composition in the 60 mol% SiO_2. The red circles are the data, the blue solid curves are the fits and the other curves show the contribution from Si-O (green), Al-O (magenta), Mg-O (black) and O-O (cyan) correlations. The displaced black solid curve gives the residual (fit subtracted from measured data). The O-O correlations are introduced to constrain the peaks fitted at smaller r values.

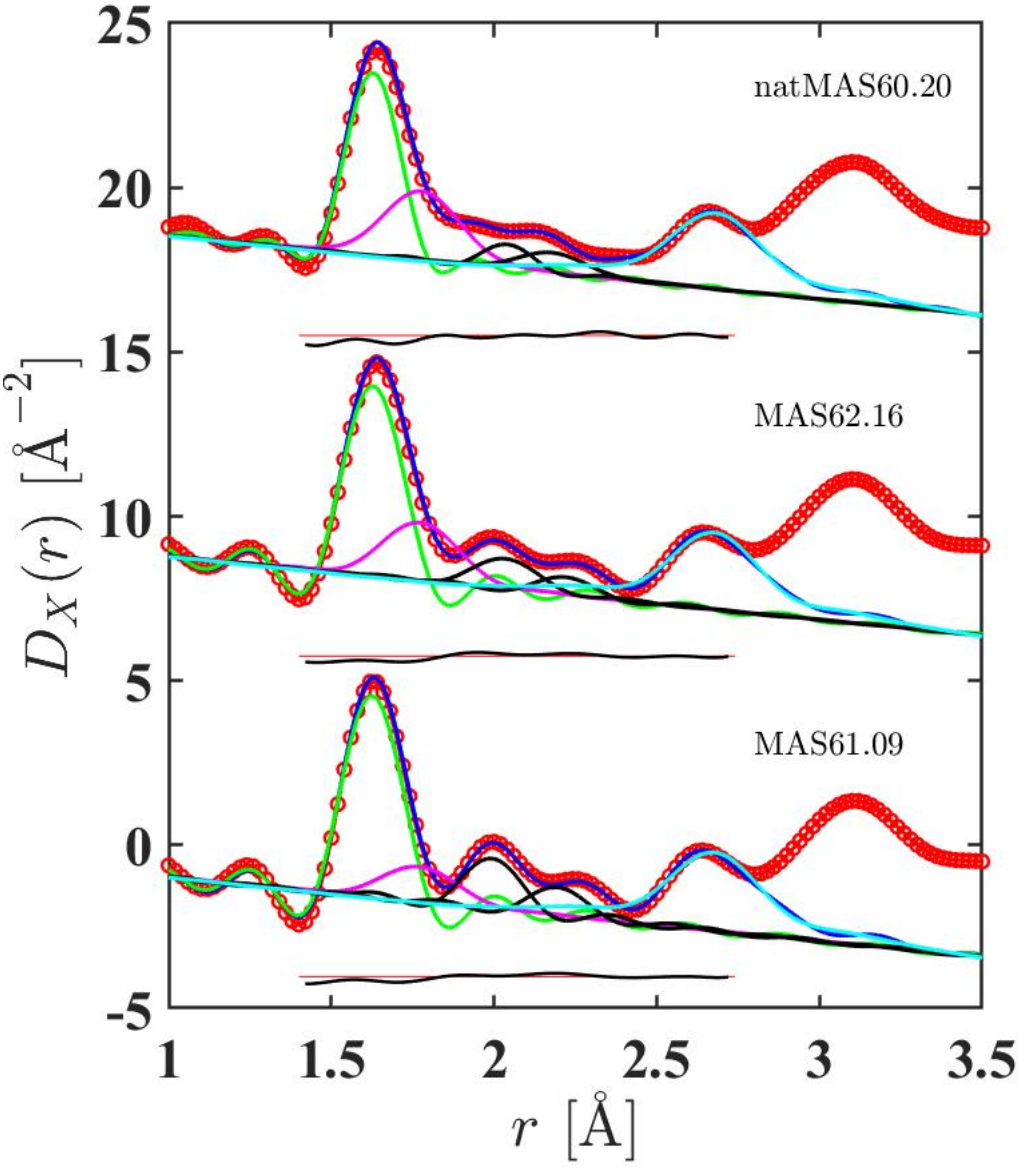

Figure 5-18: The fitted $D_X(r)$ functions for the natural MAS glasses along the 60 mol% SiO_2 tie-line. The red circles are the data, the blue solid curves are the fits and the other curves show the contribution from Si-O (green), Al-O (magenta), Mg-O (black) and O-O (cyan) correlations. The displaced black solid curve gives the residual (fit subtracted from measured data). The O-O correlations are introduced to constrain the peaks fitted at smaller r values.

Sample	Atom pair	$r_{\alpha\beta}$ [Å]	$\sigma_{\alpha\beta}$ [Å]	$\bar{n}_{\alpha}^{\beta}$	R_{χ} [%]
MAS70.12	Si-O	1.624(3)	0.063(5)	4*	6.01
	Al-O	1.794(5)	0.124(5)	4.20*	
	Mg-O	2.049(4)	0.075(4)	3.08(5)	
	Mg-O	2.250(8)	0.050(7)	1.80(5)	
	Mg-O (sum)			4.88(7)	
	O-O	2.648(3)	0.111(2)	5.49(9)	
MAS70.15	Si-O	1.625(3)	0.063(5)	4*	5.74
	Al-O	1.790(5)	0.130(5)	4.25*	
	Mg-O	2.066(4)	0.050(4)	2.84(5)	
	Mg-O	2.276(8)	0.061(7)	2.79(5)	
	Mg-O (sum)			5.63(7)	
	O-O	2.640(2)	0.098(2)	4.96(7)	

Table 5.11: Parameters obtained from Gaussian peak fits to the $D_X(r)$ functions for MAS glasses along the 70 mol% SiO_2 tie-line. The fitted functions are shown in figure 5-19. R_{χ} is given for the range 1.40-2.76 Å. The parameters denoted by an * are fixed.

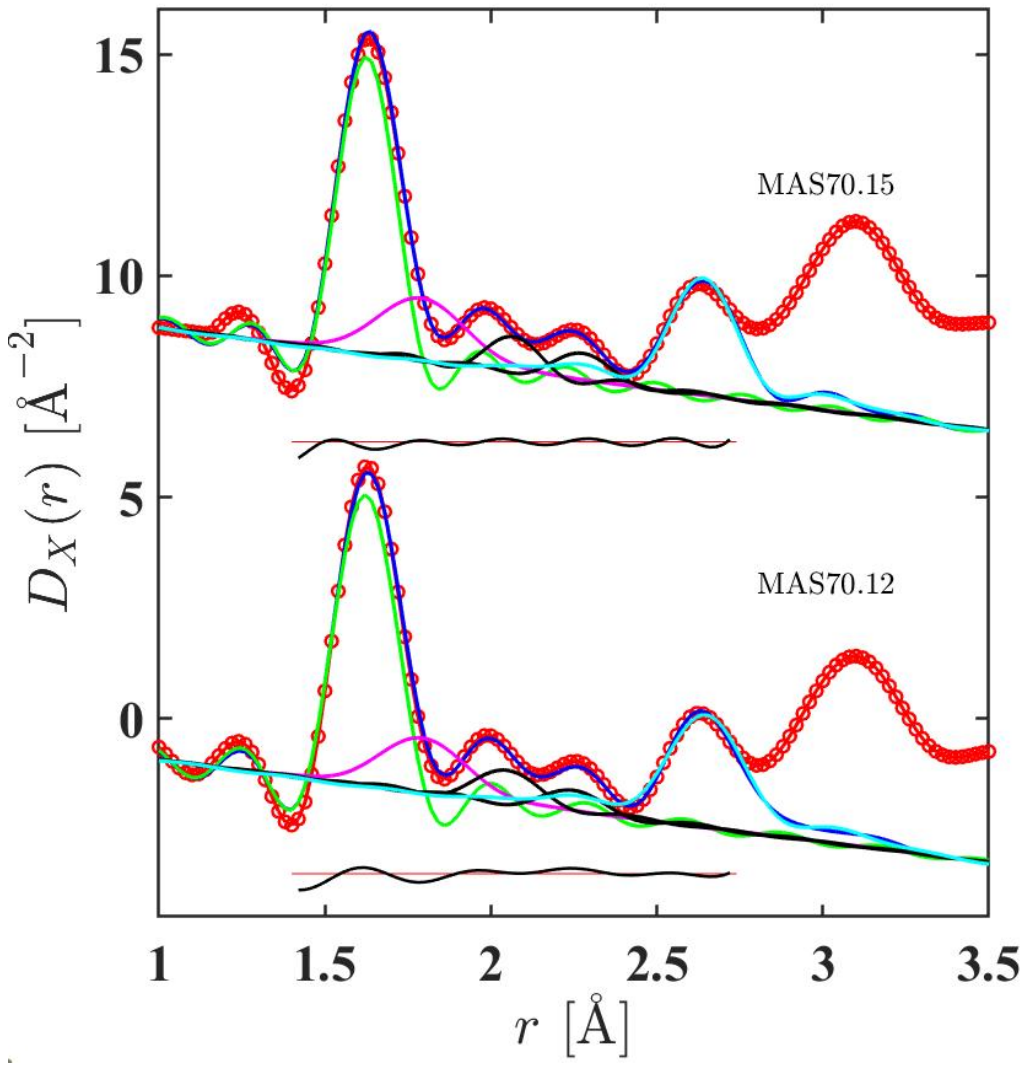

Figure 5-19: The fitted $D_X(r)$ functions for the natural MAS glasses along the 70 mol% SiO_2 tie-line. The red circles are the data, the blue solid curves are the fits and the other curves show the contribution from Si-O (green), Al-O (magenta), Mg-O (black) and O-O (cyan) correlations. The displaced black solid curve gives the residual (fit subtracted from measured data). The O-O correlations are introduced to constrain the peaks fitted at smaller r values.

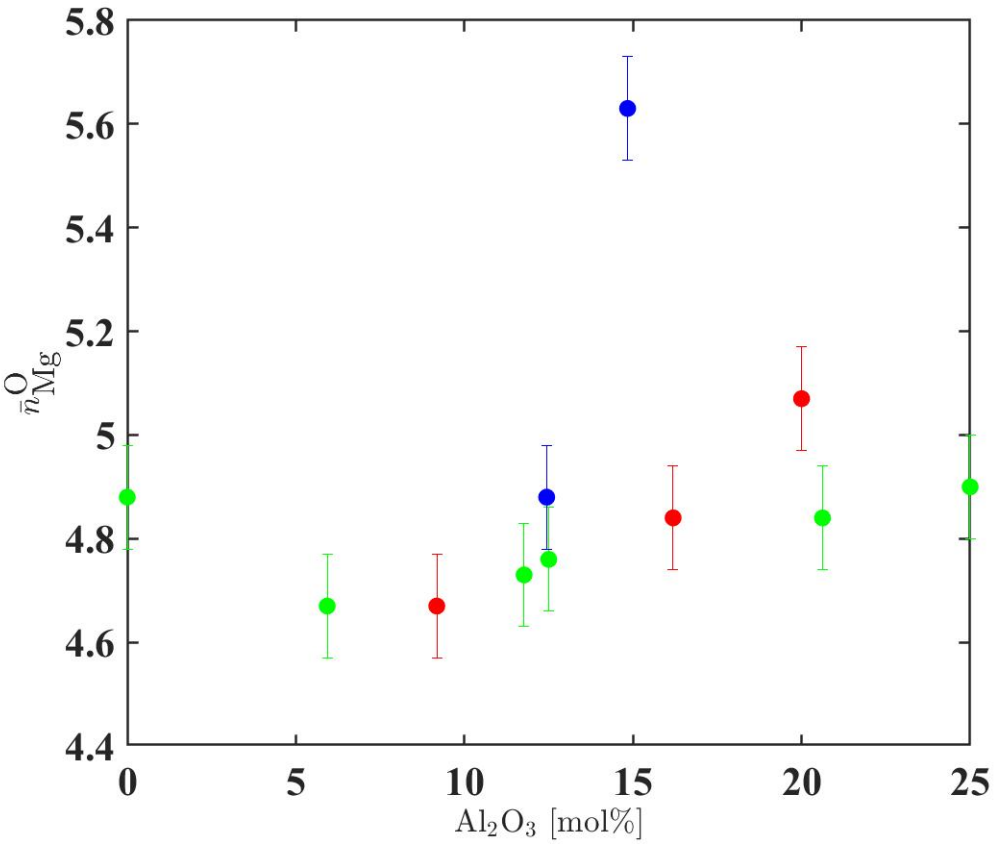

Figure 5-20: Mg-O coordination number as a function of the Al_2O_3 content obtained from the $D_X(r)$ fits. The green data points show the coordination numbers along the 50 mol% SiO_2 tie-line. The red data points show the coordination numbers along the 60 mol% SiO_2 tie-line and the blue data points show the coordination numbers along the 70 mol% SiO_2 tie-line.

5.4 Discussion

5.4.1 Model of magnesium aluminosilicate glasses

There is a variety of experimental techniques that have been used in order to provide a model that explains the structure of aluminosilicate glasses [91–96, 127, 128], which will be denoted here as the standard model. In the standard model, silica glass consists of a network of SiO_4 tetrahedral units linked to each other through bridging oxygen (BO) atoms [181, 182]. When a modifying oxide is added, such as MgO, additional oxygen atoms join the tetrahedral network by transforming BO atoms into non-bridging oxygen (NBO) atoms [183], i.e, O atoms that no longer form Si-O-Si bridges. The NBO atom has a local excess negative charge to which the positive charged modifying ion Mg^{2+} associates. Knowing the concentration of the modifying oxide is possible to calculate the average number of NBO atoms per Si-centred tetrahedral unit, which gives a quantitative description of the glass network. When alumina is added to the system, the Al atoms enter tetrahedral sites and join the network of corner-sharing units. Each Al(IV) species carries a charge, $(AlO_4)^-$, which requires a nearby charge-compensator from the Mg^{2+} to ensure charge neutrality. Mg^{2+} ions that stabilise Al(IV) in the network are taking a charge-compensating role and no longer create NBO atoms.

However, there is often contradictory values between the measured data and the one obtained by the standard model [128]. An example of this is the coordination environment of aluminum atoms in MO containing aluminosilicate glasses, where M denotes a metal atom like for example Mg or Zn. The standard model predicts only fourfold coordinated aluminum atoms for silica-rich compositions where $R \geqslant 1$, but experiments such as ^{27}Al MAS NMR often find a notable fraction of Al(V) and Al(VI) coordinated species in this region.

A recent model developed by Gammond et al [1] gives a possible explanation for these higher coordinated species observed in NMR. The model takes into account a parameter p ($0 \leqslant \mathrm{p} \leqslant 1$) which describes the weighting of competing reaction schemes for $(MO)_x(Al_2O_3)_y(SiO_2)_{1-x-y}$, where $0 \leqslant x \leqslant 1$, $0 \leqslant y \leqslant 1$ and $x + y \leqslant 1$. The value of p is found from the aluminium speciation measured in the composition regime where $R(x/y) \geqslant 1$, using solid-state ^{27}Al MAS NMR experiments on zinc-, calcium-, magnesium-, sodium- and potassium- aluminosilicate glasses [1]. p is dependent on the cation field strength F_{M}, where the standard model for amorphous aluminosilicates at $R \geqslant 1$ is recovered in the limit when F_{M} is small and $p = 1$.

Consider a glass network of fourfold coordinated Si atoms and Al(IV) atoms. These

two network former species are bound exclusively to oxygen atoms that are in non-bridging oxygen (NBO) or bridging oxygen (BO) sites. Consider A to be either Si or Al(IV), O-A coordination number has the value 1 for NBO and value 2 for BO. The Al(IV) atoms are at the center of $[Al\emptyset_{4/2}]^-$ units, where Ø denotes a BO atom. The Al(V) and Al(VI) atoms will be treated as network modifiers or charge-compensating species.

According to the model [1], MO reacts with Al_2O_3 and SiO_2 according to the following equations

$$MO + Al_2O_3 \longrightarrow M^{2+} + 2[Al\emptyset_{4/2}]^-, \tag{5.1}$$

$$MO + SiO_2 \longrightarrow M^{2+} + [Si\emptyset_{2/2}O_2]^{2-}. \tag{5.2}$$

O refers to an NBO atom. In equation 4.1, the M^{2+} ions behave as charge compensating species whereas in equation 4.2 the M^{2+} ions behave as network modifier species. Al_2O_3 can also react with SiO_2 following the equation

$$Al_2O_3 + SiO_2 \longrightarrow [Al\emptyset_{4/2}] + Al^{3+} + [Si\emptyset_{2/2}O_2]^{2-}, \tag{5.3}$$

where Al^{3+} ions compensate the charge on the $[Al\emptyset_{4/2}]^-$ unit and modifies the SiO_2 network by the creation of NBO atoms. These aluminium species are going to be denoted as Al_{mcc} (modifier/charge compensating) and represents either Al(V), Al(VI) or a mixture of the two species.

Al_{mcc} connects to the oxygen atoms in the network forming motifs in the same way as M^{2+}. In the modified random network model [184], two M^{2+} or Al_{mcc} species could share the same NBO atom and, therefore, appear as next-nearest neighbors. On the MO rich side, when $R \geqslant 1$, and according to equation 4.1 there are sufficient M^{2+} ions to compensate the charge on the network-forming $[Al\emptyset_{4/2}]^-$ units if all the aluminium is Al(IV). However, ^{27}Al NMR results show that although the Al(IV) atoms are in the majority, it is also possible to find Al(V) and Al(VI) in the glasses.

For this reason, it is convenient to write the glass composition as $[(MO)(Al_2O_3)]_{py}$ $[(MO)(SiO_2)]_{x-py}[(Al_2O_3)(SiO_2)]_{(1-p)y}(SiO_2)_{1-2x-2y+2py}$ to take into account the following reaction scheme

$$
\begin{aligned}
&py(\mathrm{MO} + \mathrm{Al_2O_3}) + (x - py)(\mathrm{MO} + \mathrm{SiO_2}) + (1 - p)y(\mathrm{Al_2O_3} + \mathrm{SiO_2}) \\
&+ (\mathrm{SiO_2})_{1-2x-2y+2py} \longrightarrow py(\mathrm{M^{2+}} + 2[\mathrm{Al\emptyset_{4/2}}]^-) + (x - py)(\mathrm{M^{2+}} + [\mathrm{Si\emptyset_{2/2}O}]^{2-}) \\
&+ (1 - p)y([\mathrm{Al\emptyset_{4/2}}]^- + \mathrm{Al^{3+}} + [\mathrm{Si\emptyset_{2/2}O_2}]^{2-}) + (1 - 2x - 2y + 2py)\mathrm{Si\emptyset_{4/2}}.
\end{aligned}
\tag{5.4}
$$

The fraction of Al(IV) will be

$$f_{\mathrm{Al(IV)}} = \frac{N_{\mathrm{Al(IV)}}}{N_{\mathrm{Al}}} = \frac{1+p}{2}, \tag{5.5}$$

where $N_{\mathrm{Al(IV)}}$ and N_{Al} are the number of fourfold coordinated aluminum atoms and total number of aluminum atoms, respectively. p determines the extent to which Al_2O_3 reacts with MO via equation 4.1 or with SiO_2 via equation 4.3.

If p=1, all the Al atoms are Al(IV) because there is no reaction between Al_2O_3 and SiO_2, so all the Al_2O_3 is charge compensated by MO. The results are then consisted with the standard model [128] for the structure of aluminosilicate glasses.

The fraction of NBO atoms is given by

$$f_{\mathrm{NBO}} = \frac{N_{\mathrm{NBO}}}{N_{\mathrm{O}}} = \frac{2(x + y - 2py)}{2 - x + y}, \tag{5.6}$$

where N_{NBO} is the number of NBO and N_{O} is the total number of oxygen atoms. The fraction of BO atoms is given by

$$f_{\mathrm{BO}} = \frac{N_{\mathrm{BO}}}{N_{\mathrm{O}}} = 1 - f_{\mathrm{NBO}}, \tag{5.7}$$

where N_{BO} is the number of BO atoms. The mean number of NBO atoms per Si atom is

$$\frac{N_{\mathrm{NBO}}}{N_{\mathrm{Si}}} = \frac{2(x + y - 2py)}{1 - x - y}, \tag{5.8}$$

where N_{Si} is the number of Si atoms. The mean number of BO atoms per Si atom is

$$\frac{N_{\mathrm{BO}}}{N_{\mathrm{Si}}} = 2 - \frac{N_{\mathrm{NBO}}}{N_{\mathrm{Si}}}. \tag{5.9}$$

The number of NBO atoms per tetrahedron is given by

$$\frac{N_{\mathrm{NBO}}}{N_{\mathrm{T}}} = \frac{N_{\mathrm{O}}}{N_{\mathrm{Si}} + N_{\mathrm{Al(IV)}}} f_{\mathrm{NBO}} = \frac{2(x + y - 2py)}{1 - x + py}, \tag{5.10}$$

where N_{T} is the number of tetrahedral units. The fraction of M atoms that are charge-compensating is written as

$$f_{\mathrm{M_{cc}}} = \frac{N_{\mathrm{M_{cc}}}}{N_{\mathrm{M}}} = \frac{py}{x}, \tag{5.11}$$

where $N_{\mathrm{M_{cc}}}$ is the number of charge compensating M atoms and N_{M} is the total number of M atoms. The fraction of M atoms that are network modifiers is written as

$$f_{\mathrm{M}_m} = \frac{N_{\mathrm{M_m}}}{N_{\mathrm{M}}} = 1 - f_{\mathrm{M_{cc}}} = \frac{x - py}{x}, \tag{5.12}$$

where $N_{\mathrm{M_m}}$ is the number of network modifying M atoms.

On the Al_2O_3 rich side, when $R < 1$, there is more than enough Al_2O_3 to react with all MO, so the excess will react with SiO_2 and higher coordinated Al^{3+} ions are created. The glass composition can be rewritten as $[(\mathrm{MO})(\mathrm{Al_2O_3})]_{px}[(\mathrm{MO})(\mathrm{SiO_2})]_{(1-p)x}$ $[(\mathrm{Al_2O_3})(\mathrm{SiO_2})]_{y-px}(\mathrm{SiO_2})_{1-2x-2y+2px}$ and the reaction scheme proceeds via

$$\begin{aligned} &px(\mathrm{MO} + \mathrm{Al_2O_3}) + (1-p)x(\mathrm{MO} + \mathrm{SiO_2}) + (y - px)(\mathrm{Al_2O_3} + \mathrm{SiO_2}) \\ &+ (\mathrm{SiO})_{1-2x-2y+2px} \longrightarrow\ px(\mathrm{M^{2+}} + 2[\mathrm{Al}\emptyset_{4/2}]^-) + (1-p)x(\mathrm{M^{2+}} \\ &+ [\mathrm{Si}\emptyset_{2/2}\mathrm{O_2}]^{2-}) + (y - px)([\mathrm{Al}\emptyset_{4/2}]^- + \mathrm{Al^{3+}} + [\mathrm{Si}\emptyset_{2/2}\mathrm{O_2}]^{2-}) \\ &+ (1 - 2x - 2y + 2px)\ \mathrm{Si}\emptyset_{4/2}. \end{aligned} \tag{5.13}$$

Unlike in the $R \geqslant 1$ systems, the $f_{\mathrm{Al(IV)}}$ depends on the glass composition and is written as

$$f_{\mathrm{Al(IV)}} = \frac{y + px}{2y}. \tag{5.14}$$

Consequently, $f_{\mathrm{NBO}} = \frac{2(x+y-2px)}{2-x+y}$; $\frac{N_{\mathrm{NBO}}}{N_{\mathrm{Si}}} = \frac{2(x+y-2px)}{1-x-y}$; $\frac{N_{\mathrm{NBO}}}{N_{\mathrm{T}}} = \frac{2(x+y-2px)}{1-x+px}$; $f_{\mathrm{M_{cc}}} = p$ and $f_{\mathrm{M_m}} = 1 - p$.

If $p = 1$, there is no reaction between MO and SiO_2 so all the M^{2+} ions have a charge compensating role. Figure 5-21 shows the dependence of f_{Al} on R found from ^{27}Al MAS NMR experiments on MAS and ZAS glasses.

For the regime $R \geqslant 1$, the ratio of the number of NBO to the number of atoms that play a network-modifying or charge-compensating role is given by

$$\frac{N_{\mathrm{NBO}}}{N_{\mathrm{M+Al}_{mcc}}} = \frac{2(x + y - 2py)}{x + (1 - p)y} = \frac{2(R + 1 - 2p)}{R + (1 - p)}, \tag{5.15}$$

where $N_{\mathrm{M+Al}_{mcc}} = N_{\mathrm{M}} + N_{\mathrm{Al_{mcc}}}$ and $N_{\mathrm{Al_{mcc}}}$ is the number of $\mathrm{Al_{mcc}}$ atoms. If the network is fully polymerized, NBO atoms are not generated and $N_{\mathrm{NBO}}/N_{\mathrm{M+Al_{mcc}}} = 0$. $\mathrm{Al_{mcc}}$ ions will not be generated by the reaction scheme of equation 4.3 and the reaction scheme of equation 4.2 does not apply such that all M atoms behave as charge-compensating species.

If the glass network is not fully polymerized $N_{\mathrm{NBO}}/N_{\mathrm{M+Al_{mcc}}} > 0$ and consequently some of the M and/or Al atoms adopt a network modifying role. The fraction of M plus Al atoms that form higher coordinated Al(V) and/or Al(VI) species is given by

$$f_{\mathrm{Al_{mcc}:M+Al}} = \frac{N_{\mathrm{Al_{mcc}}}}{N_{\mathrm{M}} + N_{\mathrm{Al}}} = \frac{(1 - p)y}{x + 2y}. \tag{5.16}$$

For the regime $R \leqslant 1$,

$$\frac{N_{\mathrm{NBO}}}{N_{\mathrm{M+Al_{mcc}}}} = \frac{2(x + y - 2px)}{x(1 - p) + y} = \frac{2[R(1 - 2p) + 1]}{R(1 - p) + 1}, \tag{5.17}$$

and

$$f_{\mathrm{Al_{mcc}:M+Al}} = \frac{y - px}{x + 2y}. \tag{5.18}$$

Figure 5-22 shows the dependence of $N_{\mathrm{NBO}}/N_{\mathrm{M+Al_{mcc}}}$ on R. In a fully polymerized network, the number of O-A bonds is given by $N_{\mathrm{O\text{-}A}} = 2N_{\mathrm{O}} = N_{\mathrm{O}}\bar{n}_{\mathrm{O}}^{\mathrm{A}}$, where $\bar{n}_{\mathrm{O}}^{\mathrm{A}}$ is the coordination number of A around O. For the case where NBO atoms exist,

$$N_{\mathrm{NBO}} = 2N_{\mathrm{O}} - N_{\mathrm{O\text{-}Si}} - N_{\mathrm{O\text{-}Al(IV)}}, \tag{5.19}$$

and

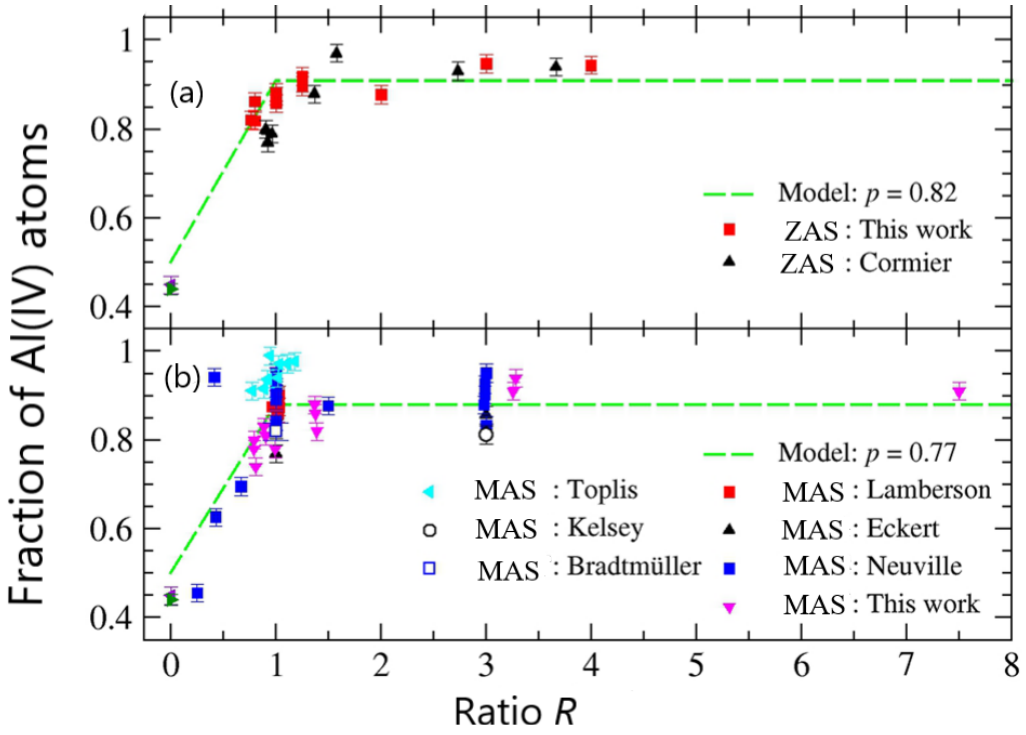

Figure 5-21: Fraction of Al(IV) atoms, $f_{\mathrm{Al(IV)}}$, as a function of R from ^{27}Al NMR experiments on the aluminosilicate glasses (a) ZAS (reference [80] and this work) and (b) MAS (references [97, 163, 172, 185, 186] and this work). The experimental results are compared to those from the model [1] (green curves).

$$f_{\mathrm{NBO}} = \frac{N_{\mathrm{NBO}}}{N_{\mathrm{O}}} = 2 - \bar{n}_{\mathrm{O}}^{\mathrm{Si}} - \bar{n}_{\mathrm{O}}^{\mathrm{Al(IV)}}. \tag{5.20}$$

Knowing that the number of A-O bonds is equal to the number of O-A bonds, $N_{\mathrm{A}}\bar{n}_{\mathrm{A}}^{\mathrm{O}} = N_{\mathrm{O}}\bar{n}_{\mathrm{O}}^{\mathrm{A}}$, then $c_{\mathrm{A}}\bar{n}_{\mathrm{A}}^{\mathrm{O}} = c_{\mathrm{O}}\bar{n}_{\mathrm{O}}^{\mathrm{A}}$ where $c_{\mathrm{A}} = \frac{N_{\mathrm{A}}}{N}$ is the atomic fraction of chemical species A and N is the total number of atoms. Equation 5.20 can then be written as

$$f_{\mathrm{NBO}} = 2 - \frac{c_{\mathrm{Si}}}{c_{\mathrm{O}}}\bar{n}_{\mathrm{Si}}^{\mathrm{O}} - f_{\mathrm{Al(IV)}}\frac{c_{\mathrm{Al}}}{c_{\mathrm{O}}}\bar{n}_{\mathrm{Al(IV)}}^{\mathrm{O}}. \tag{5.21}$$

The ratio of NBO atoms to i atoms, where i is any atom type is given as

$$\frac{N_{\mathrm{NBO}}}{N_{\mathrm{Si}}} = \frac{N_{\mathrm{O}}}{N_i}\frac{N_{\mathrm{NBO}}}{N_{\mathrm{O}}} = \frac{N_{\mathrm{O}}}{N_i}f_{\mathrm{NBO}} = \frac{c_{\mathrm{O}}}{c_{\mathrm{i}}}f_{\mathrm{NBO}}. \tag{5.22}$$

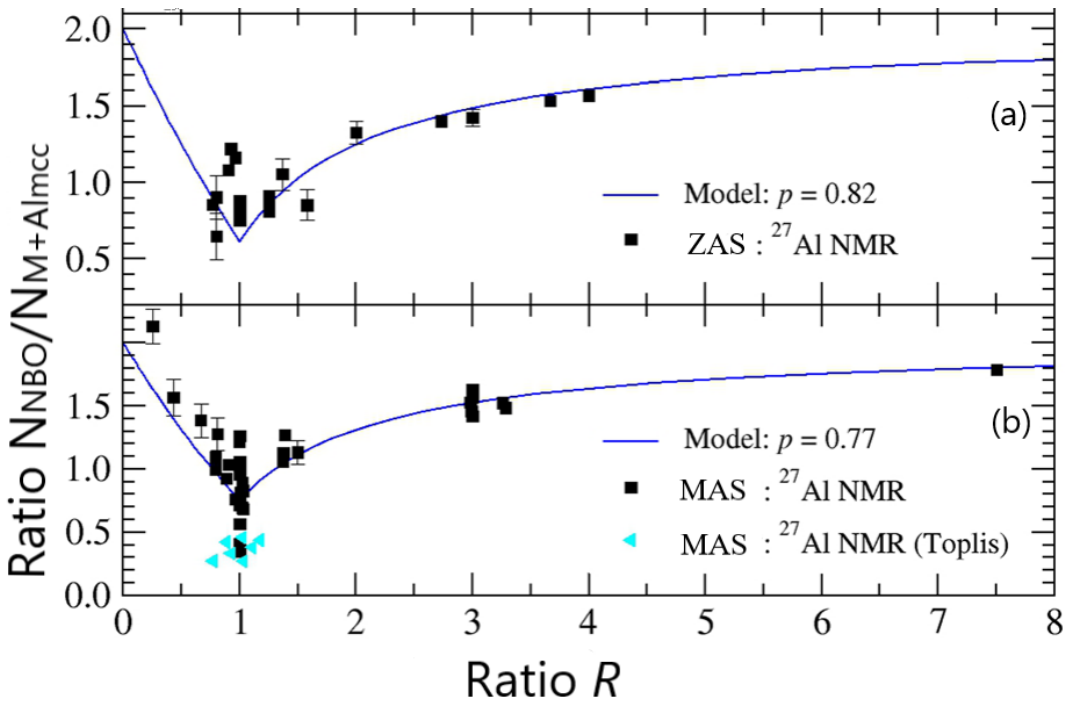

Figure 5-22: Dependence of $N_{\mathrm{NBO}}/N_{\mathrm{M+Al_{mcc}}}$ on the ratio R for (a) ZAS and (b) MAS glasses. The N_{NBO} were calculated using the model (blue curves) or using $N_{\mathrm{NBO}} = c_{\mathrm{O}} f_{\mathrm{NBO}}$ with f_{NBO} calculated from 5.21 and $f_{\mathrm{Al(IV)}}$ taken from the ^{27}Al MAS NMR experiments shown in figure 5-21 (black squares). In (b) the cyan data points are from Toplis et al [97].

5.4.2 Structure of M^{2+}

For $R \geqslant 1$, the average $\langle f_{\mathrm{Al(IV)}} \rangle$ is used to find the parameter p via the equation $p = 2\langle f_{\mathrm{Al(IV)}} \rangle - 1$. The model describes the overall trends in the experimental data, including the decrease in $f_{\mathrm{Al(IV)}}$ for the peraluminous regime when $R \to 0$ and more of the aluminum atoms adopt a network-modifying/charge compensating role. The cation field strength, F_{M}, can be defined as

$$F_{\mathrm{M}} = \frac{Z_{\mathrm{M}}}{r_{\mathrm{M}}^2}, \tag{5.23}$$

where Z_{M} is the formal charge on the M ions and r_{M} is the ion radius which corresponds to an M-O coordination number of six. Figure 5-23 shows the dependence of $\langle f_{\mathrm{Al(IV)}} \rangle$ and the parameter p on the cation field strength. For $F_{\mathrm{M}} > 0.575$, the results show a liner dependence given by

$$\langle f_{\mathrm{Al(IV)}} \rangle = -0.032(2)F_{\mathrm{M}} + 1.017(5) \tag{5.24}$$

or

$$p = -0.064(4)F_{\mathrm{M}} + 1.034(9). \tag{5.25}$$

$f_{\mathrm{Al(IV)}}$ decreases as F_{M} increases and for a tie-line with fixed mol% SiO_2, this reduction leads to an increase in the fraction of Al^{3+} ions that have roles of network modifiers. Consequently, it also leads to an increase in f_{NBO}, $N_{\mathrm{NBO}}/N_{\mathrm{Si}}$ and $N_{\mathrm{NBO}}/N_{\mathrm{T}}$.

Lee et al [168] define a degree of aluminum avoidance Q, which describes the extent to which Al-O-Al bonds are avoided on the glass-forming compositions. This parameter Q also decreases linearly as F_{M} increases according to the equation

$$Q = -0.104(10)F_{\mathrm{M}} + 1.058(23). \tag{5.26}$$

In the absence of Al-O-Al bonds $Q = 1$ and for a random distribution of Al/Si-O-Al/Si bonds $Q = 0$. For a specific glass composition, from equation 5.24 it is known that there will be less Al(IV) atoms to contribute to the glass network since lower field strength ions are replaced by higher field-strength ions.

More Al-O-Al bonds will be created in this replacement, according to equation 5.26. Al(V) and/or Al(VI) have a high probability of being involved in the distribution of

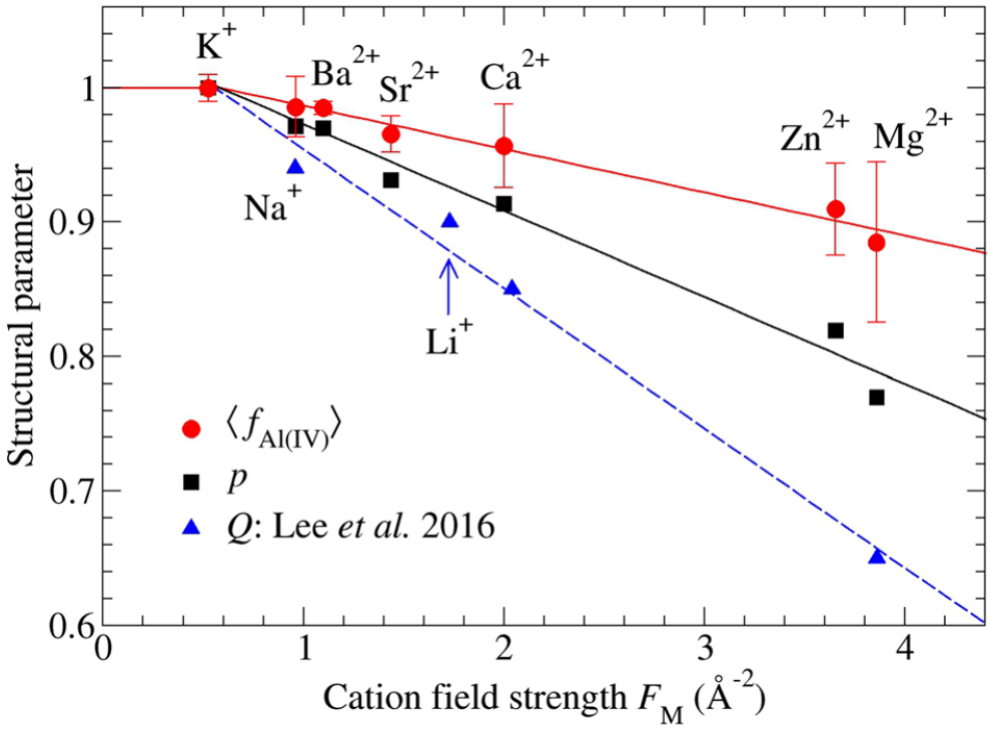

Figure 5-23: Dependence of $\langle f_{\mathrm{Al(IV)}} \rangle$ as evaluated for $R \geqslant 1$ and $p = 2\langle f_{\mathrm{Al(IV)}} \rangle - 1$ on the field strength F_{M} of the ions in aluminosilicate glasses. The linear fits to the data points are given by equations 5.24 and 5.25. Also shown is the aluminum avoidance parameter Q, where the linear fit is given by equation 5.26 [1, 168].

Al-O-Al bonds in the glass network since they become more numerous with increasing F_{M}.

Figure 5-24 shows the average Si-O, Al-O and Mg-O distances (listed in table 5.12) in MAS glasses obtained by the $D_X(r)$ fits and compared with D4c and SANDALS/GEM values. It is possible to observe the same trend for $\bar{r}^{\mathrm{O}}_{\mathrm{Mg}}$, $\bar{r}^{\mathrm{O}}_{\mathrm{Si}}$ and $\bar{r}^{\mathrm{O}}_{\mathrm{Al}}$ along the glass forming composition illustrating the success of the fitted Neutron and X-ray diffraction data. In general, the average distances were slightly higher for X-rays than Neutron fits. The measured distances $\bar{r}_{\mathrm{Si\text{-}O}}$ vary between $1.617(10) \leqslant r \leqslant 1.639(10)$ across the glass forming compositions revealing the persistence of SiO_4 tetrahedral sites which are predicted by the standard model [128]. The measured distance $\bar{r}_{\mathrm{Al\text{-}O}}$ is approximately constant for compositions with $R \geqslant 1$, where most of aluminum atoms associate with charge compensating Mg^{2+} to form tetrahedral sites. For compositions with $R \leqslant 1$ there is an increase of $\bar{r}_{\mathrm{Al\text{-}O}}$ which is caused by the increasing fraction of Al^{3+} ions that play a network modifying and/or charge compensating role and are associated with

Al(V) and Al(VI) coordinated species. From [1], these changes are due to network modifiers Mg^{2+} in compositions with $R \geqslant 2$ transforming into charge compensating species for compositions with $R \leqslant 2$. Therefore, there is no significant difference between network modifier and charge compensating Mg^{2+} environments. The $\bar{r}^{O}_{Mg}$ distance increases with Al_2O_3 and with SiO_2 content, where magnesium evolves from network modifier to charge compensating species. For compositions with $R = 1$, $\bar{r}_{Si\text{-}O}$ is higher for compositions with lower SiO_2 mol% and $\bar{n}^{O}_{Mg}$ tends to be higher for 60 and 70 mol% SiO_2. The increase on $\bar{r}_{Si\text{-}O}$ is attributed to an increase of Si-O-Al linkages.

Figure 5-25 shows a comparison of the $\bar{n}^{O}_{Mg}$ between the X-ray and neutron diffraction results using the D4c and SANDALS diffractometer taken from [40]. As an overall view, the $\bar{n}^{O}_{Mg}$ values on the D4c diffractometer are lower than the GEM diffractometer, which might be due to the smaller Q-range. The $\bar{n}^{O}_{Mg}$ are in overall agreement with each other with a $\approx 10\%$ difference and follow the same trend for $R \geqslant 1$ and $R \leqslant 1$. For compositions with $R > 1$ the coordination environment of Al varies in a range of 4.06(5) to 4.20(5) and $4.67(5) \leqslant \bar{n}^{O}_{Mg} \leqslant 4.88(7)$ for the same glass composition. In this regime, there are enough charge compensating Mg^{2+} ions to stabilise Al tetrahedral species. The presence of network modifier/charge compensating Al^{3+} ions in Al(V) and/or Al(VI) sites in this range of compositions is due to some fraction of Mg^{2+} ions acting as network modifier ions instead of stabilizing the formation of tetrahedral AlO_4. For $R = 1$ the X-ray measured values vary from $\bar{n}^{O}_{Mg} = 4.90(5)$ for the MAS50.25 glass to $\bar{n}^{O}_{Mg} = 5.63(6)$ for the MAS70.15 glass suggesting that the coordination environment of network modifiers and/or charge compensating Mg^{2+} ions is also dependent on the SiO_2 content. The higher $\bar{n}^{O}_{Mg}$ values can also be explained by the low MgO mol% and by the overlap between the Al-O and/or the O-O peaks since the Mg-O correlations have a significant tail at high r. As $R \to 0$, the neutron diffraction results also show higher $\bar{n}^{O}_{Mg}$ and $\bar{n}^{O}_{Al}$ due to the formation of network modifier/charge compensating Al^{3+} ions in a similar behavior to Mg^{2+} ions. The results from ^{27}Al NMR (Table 5.6) show that the majority of network modifying/charge compensating Al^{3+} in Al(V) sites (70-100%) and the remained are in Al(VI) sites.

Figures 5-27, 5-28 and 5-29 show a comparison between the coordination environments of Mg and Zn as a function of R for the 50, 60 and 70 mol% SiO_2 tie-line. Zn^{2+} and Mg^{2+} ions have very similar features for compositions with $R \geqslant 1$ and $R \leqslant 1$, indicative of the similar network modifier/charge compensating Mg^{2+} and Zn^{2+} ions behaviour. However, $\bar{n}^{O}_{Zn}$ are in general higher than $\bar{n}^{O}_{Mg}$ for compositions with $R \leqslant 1$. For compositions with R=1, $5.10(5) \leqslant \bar{n}^{O}_{Zn} \leqslant 5.65(10)$, illustrating a charge compensating role. Mg^{2+} and Zn^{2+} species are distributed between four-fold and five-

Sample	$\bar{r}_{\text{Si-O}}$ [Å]	$\bar{r}_{\text{Al-O}}$ [Å]	$\bar{r}_{\text{Mg-O}}$ [Å]
$MgSiO_3$	1.624(3)	-	2.042(2)
MAS50.06	1.627(3)	1.756(5)	2.044(2)
MAS50.12	1.626(3)	1.760(5)	2.058(2)
natMAS50.12p5	1.626(1)	1.780(3)	2.069(8)
isoMAS50.12p5	1.630(1)	1.780(3)	2.074(8)
MAS51.21	1.629(3)	1.770(5)	2.101(2)
natMAS50.25	1.639(1)	1.784(3)	2.124(8)
isoMAS50.25	1.643(1)	1.785(3)	2.127(8)
MAS61.09	1.627(3)	1.771(5)	2.057(2)
MAS62.16	1.629(3)	1.774(5)	2.087(2)
natMAS60.20	1.628(1)	1.780(3)	2.129(8)
isoMAS60.20	1.631(1)	1.779(3)	2.133(8)
MAS70.12	1.624(3)	1.794(5)	2.112(2)
MAS70.15	1.625(3)	1.790(5)	2.159(2)

Table 5.12: Average Si-O, Al-O and Mg-O distances for the MAS glasses shown in figure 5-24.

fold coordinated sites which was also found from [80]. From equation 5.23 and figure 5-23 it is known that Mg^{2+} ions have a higher cation field strength F_{M} than Zn^{2+} (Table 5.13). p increases with F_{M}, which suggests that Mg^{2+} ions are more likely to create NBO than Zn^{2+} and consequently preventing Al atoms from occupying tetrahedral sites. Figure 5-30 shows measurements on ^{27}Al MAS NMR done on MAS and ZAS glasses illustrating the similarity between these two ions. It is possible to observe for both ZAS and MAS samples that $\bar{n}^{\text{O}}_{\text{Al}}$ is predominantly dependent on the MO/Al_2O_3 ratio and not so much on the SiO_2 content which is predicted by the model. For compositions with $R \geqslant 1$ Al^{3+} will have a network forming role and will be incorporated in network forming sites as seen before. The sharp rise in $\bar{n}^{\text{O}}_{\text{Al}}$ seen in $R \to 0$ for the MAS and ZAS glasses is due of the network modifier/charge compensating Al^{3+} species since they cannot join into a tetrahedral network.

Ion	CN	r_M [Å]	F_M [Å^{-2}]
Mg^{2+}	4	0.57	6.16
	5	0.66	4.59
	6	0.72	3.86
	8	0.89	2.52
Zn^{2+}	4	0.60	5.56
	5	0.68	4.33
	6	0.74	3.65
	8	0.90	2.47
Ca^{2+}	6	1.00	2.00
	7	1.06	1.78
	8	1.12	1.59

Table 5.13: Cation field strength F_M for Mg^{2+}, Zn^{2+} and Ca^{2+} ions with different coordination numbers (CN). The ionic radii are taken from Shannon [187].

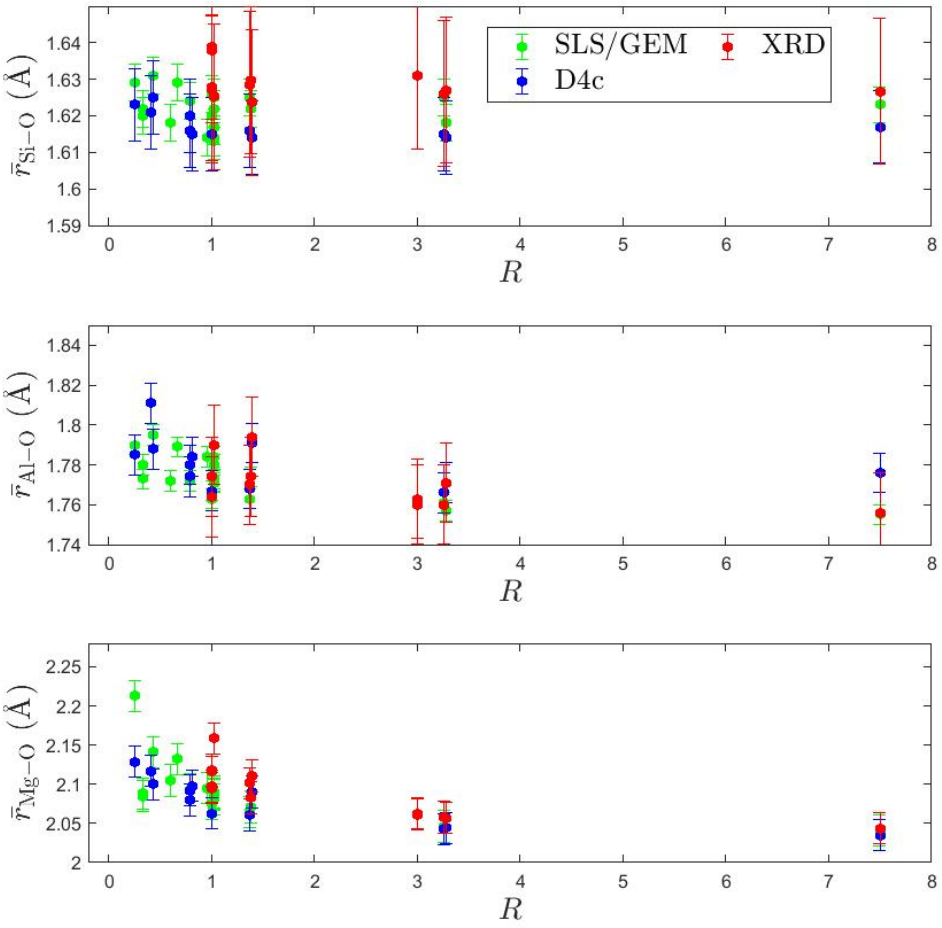

Figure 5-24: Average Si-O, Al-O and Mg-O distances for the MAS glasses using X-rays (red). The neutron data is also plotted for comparison [40] by using the SANDALS (black) and D4c (blue) diffractometers.

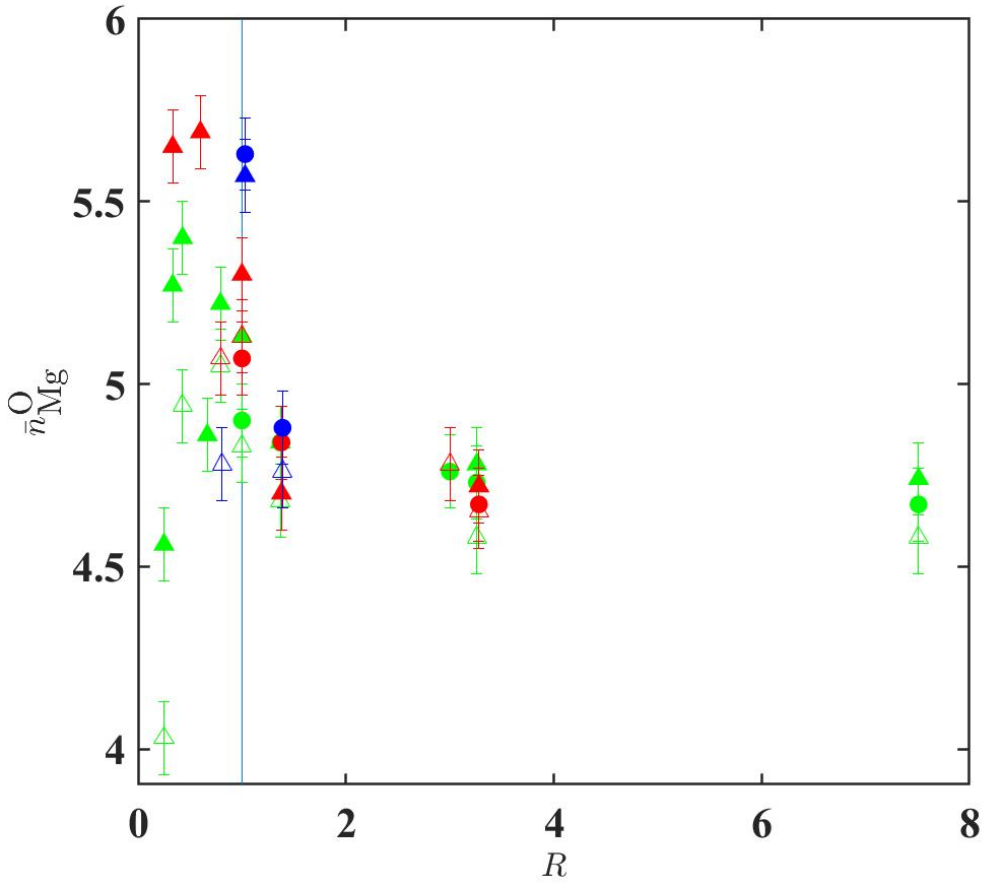

Figure 5-25: Coordination number of the MAS glasses as a function of the ratio R obtained from X-ray diffraction (circles) and neutron diffraction (triangles) data. For the neutron diffraction data, the filled triangles correspond to data obtained using the SANDALS or GEM diffractometers and the empty triangles correspond to data obtained using the D4c diffractometer [40]. The green data points show the coordination numbers along the 50 mol% SiO_2 tie-line. The red data points show the coordination numbers along the 60 mol% SiO_2 tie-line and the blue data points show the coordination numbers along the 70 mol% SiO_2 tie-line. The cyan line at $R = 1$ indicates the tectosilicate compositions.

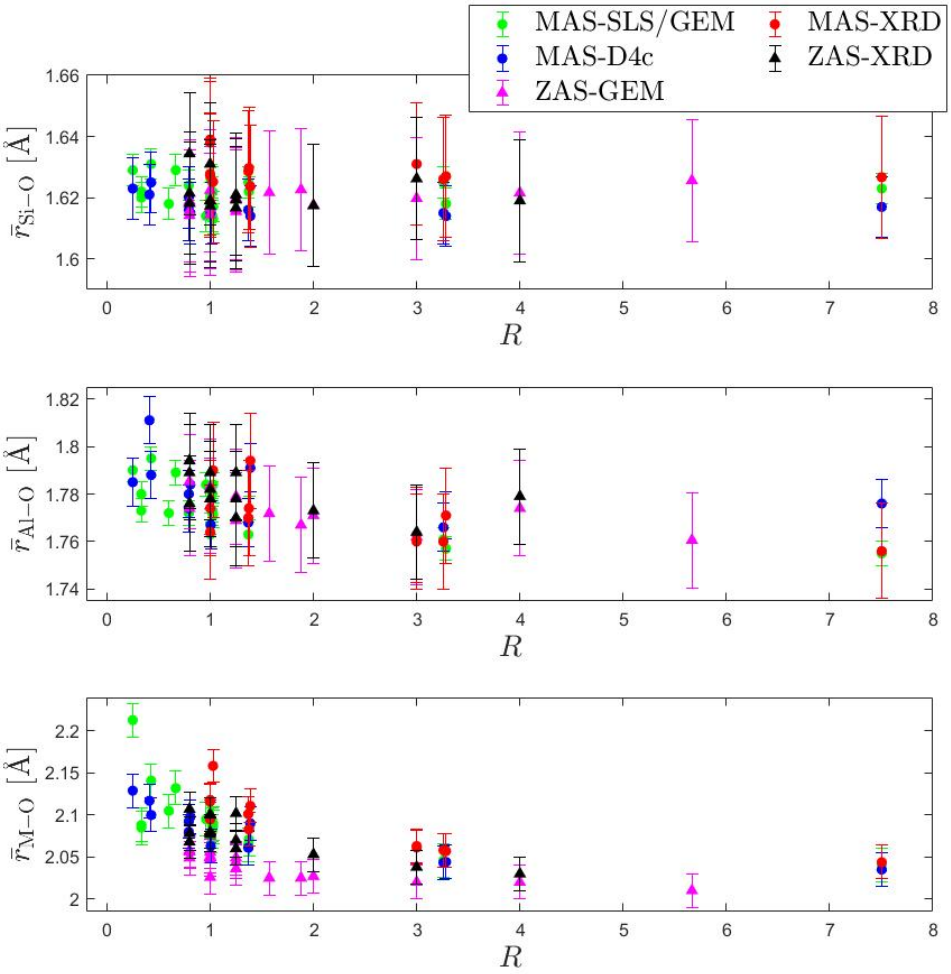

Figure 5-26: Average Si-O, Al-O and M-O (M = Mg or Zn) distances for the MAS and ZAS glasses using X-rays (triangles) and neutron data (circles) provided by the diffractometers 6-ID-D, GEM, SANDALS and D4c.

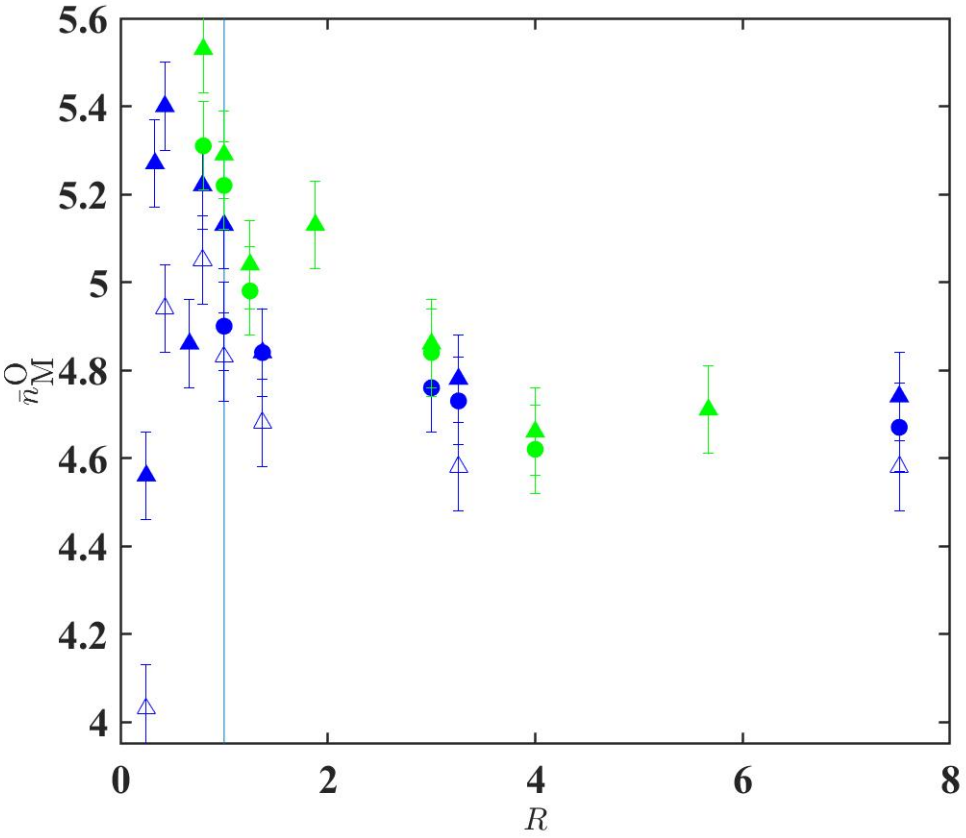

Figure 5-27: Coordination number of the MAS (blue) and the ZAS (green) glasses as a function of the ratio R= MO/Al_2O_3, where M is either Mg or Zn obtained from X-ray diffraction (circles) and neutron diffraction (triangles) data along the 50 mol% SiO_2 tie-line. For the ND, the filled triangles correspond to SANDALS (MAS glasses) and GEM (ZAS glasses) data. The empty triangles correspond to data obtained using D4c. The cyan line at $R = 1$ indicates the tectosilicate composition.

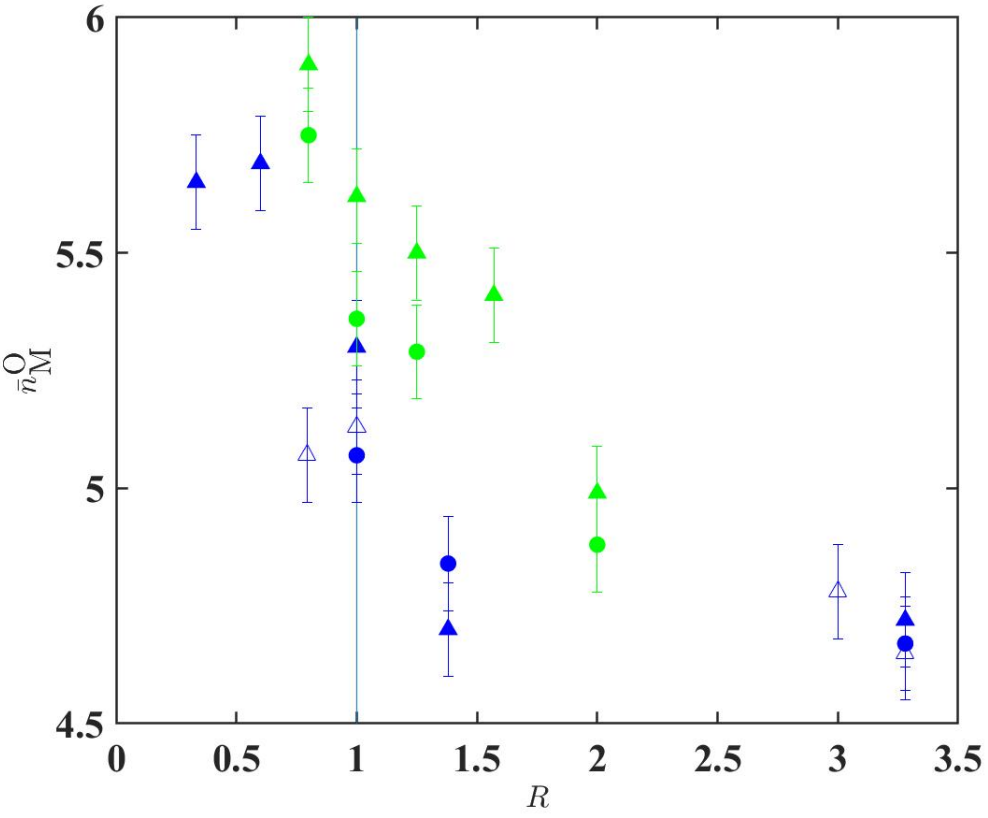

Figure 5-28: Coordination number of the MAS (blue) and the ZAS (green) glasses as a function of the ratio $R = MO/Al_2O_3$, where M is either Mg or Zn obtained from X-ray diffraction (circles) and neutron diffraction (triangles) data along the 60 mol% SiO_2 tie-line. For the ND, the filled triangles correspond to SANDALS (MAS glasses) and GEM (ZAS glasses) data. The empty triangles correspond to data obtained using D4c.

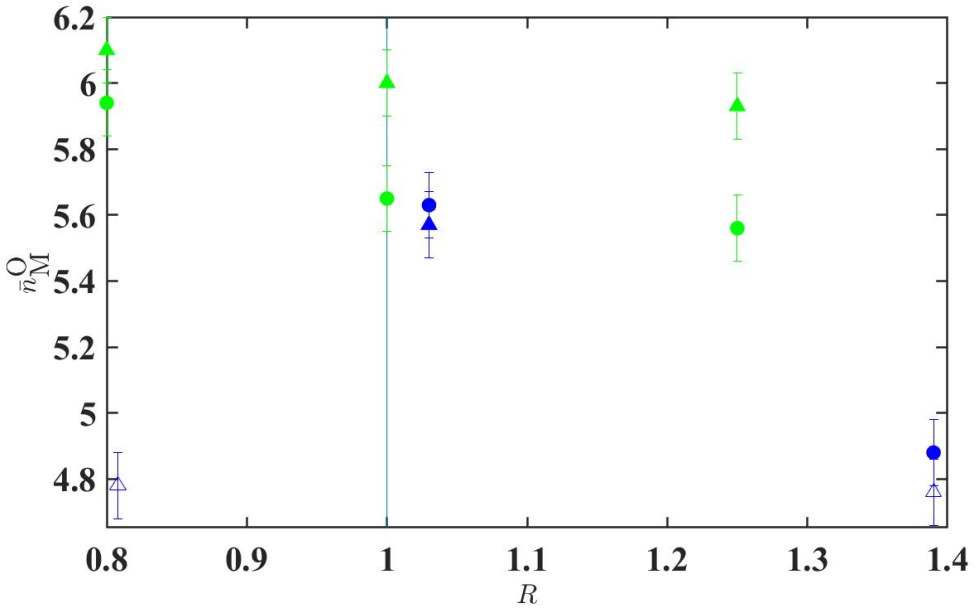

Figure 5-29: Coordination number of the MAS (blue) and the ZAS (green) glasses as a function of the ratio $R = \mathrm{MO}/\mathrm{Al_2O_3}$, where M is either Mg or Zn obtained from X-ray diffraction (circles) and neutron diffraction (triangles) data along the 70 mol% $\mathrm{SiO_2}$ tie-line. For the ND, the filled triangles correspond to SANDALS (MAS glasses) and GEM (ZAS glasses) data. The empty triangles correspond to data obtained using D4c.

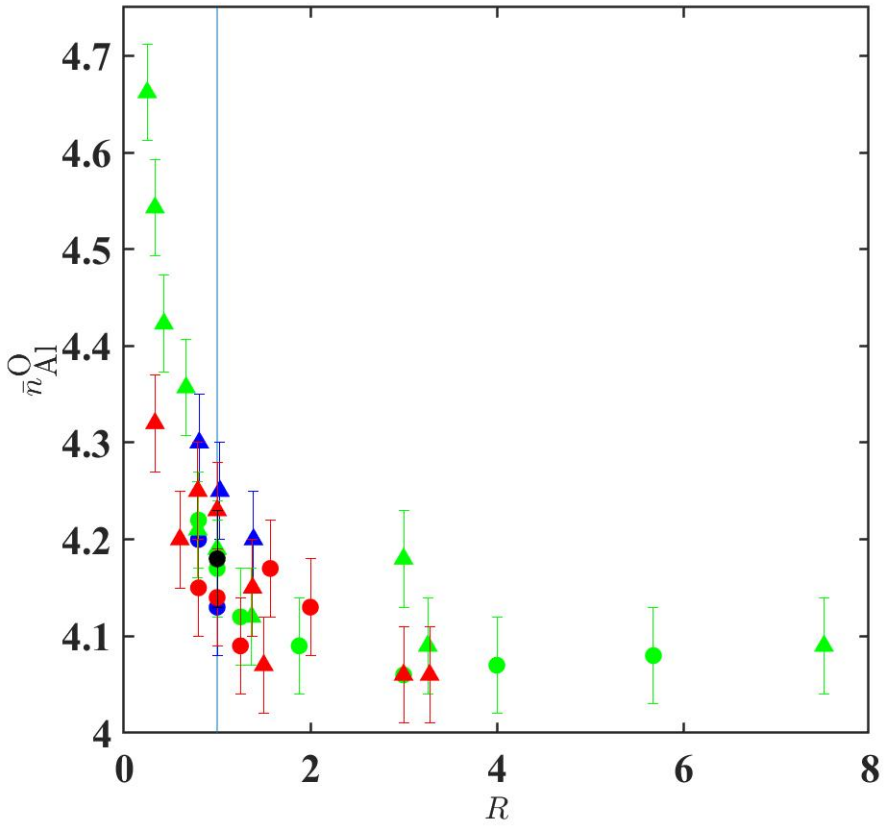

Figure 5-30: Coordination environment of aluminum as a function of R measured by ^{27}Al magic angle spinning NMR for the MAS (triangles) and ZAS (circles) glasses. The green color represents the 50 mol% SiO_2 tie-line, the red color represents the 60 mol% SiO_2 tie-line and the blue color represents the 70 mol% SiO_2 tie-line. The cyan line at $R = 1$ indicates the tectosilicate compositions.

5.5 Conclusion

The structure of $(MgO)_x(Al_2O_3)_y(SiO_2)_{1-x-y}$ glasses was investigated by X-ray pair distribution function analysis, aided by the results obtained from ^{27}Al MAS NMR spectroscopy. The results were compared with neutron diffraction [40] and with $(ZnO)_x$ $(Al_2O_3)_y(SiO_2)_{1-x-y}$ glasses (Chapter 4) for similar glass compositions and interpreted using the Gammond et al model [1] for aluminosilicate glasses. The model contains a single adjustable parameter that was set to the value $p = 0.77$ found from the mean fraction of Al(IV) atoms observed in the $R \geqslant 1$ regime from ^{27}Al MAS NMR experiments.

The $D_X(r)$ peaks corresponding to Si-O, Al-O and O-O correlations are narrow and symmetric, while those corresponding to Mg-O are broader and asymmetric resulting from a larger distribution of Mg and O atoms. The measured $D_X(r)$ functions exhibit a well defined peak at $r \approx 1.65$ Å due to Si-O and Al-O correlations. The fitted Si-O peak is well defined for all of the glass compositions with little or no variation in position, reflecting the persistence of Si-centered tetrahedral as a glass network former [188]. Neutron diffraction data was used to help constrain the Al-O peak positions due to the large neutron scattering length for this element.

^{27}Al MAS NMR spectroscopy was used to constrain the Al-O coordination number in the $D_X(r)$ fits. The majority of Al atoms exist in tetrahedral sites (AlO_4) although is also possible to observe significant amounts of AlO_5 and AlO_6 polyhedra for compositions with $R < 1$. The NMR results were helpful for the X-ray analysis because of the small contribution of Al(V) and Al(VI) and the overlap between the Si-O, Al-O and Mg-O peaks. The Gammond et al model [1] takes into account the presence of AlO_5 and AlO_6 polyhedra where Al atoms can have roles of network former, modifier and charge compensating species. The Al-O distances and $\bar{n}^{O}_{Al}$ values are also in agreement with the values obtained for similar compositions of $(ZnO)_x(Al_2O_3)_y(SiO_2)_{1-x-y}$ glasses shown in chapter 4, reflecting the similarity between Zn^{2+} and Mg^{2+} ions in the aluminosilicate glass network.

The magnesium environment gives a broad distribution of Mg-O bonds at 2.05(1) with a tail at $\approx$ 2.24(1) Å and a range of coordination numbers varying from 4.67(5) to 5.63(6). The measured Mg-O coordination number is $\bar{n}^{O}_{Mg} = 4.88(7)$ for $MgSiO_3$ glass where the Mg cations adopt a network-modifying role. As magnesia is replaced by alumina along the 50, 60 and 70 mol% SiO_2 tie-line in the MAS system, the Mg-O coordination number increases with the weighted bond distance as more Mg^{2+} ions adopt a charge-compensating role. The Mg-O coordination number for the isotopically

enriched samples was fixed to the value found from neutron diffraction with magnesium isotope substitution [180]. This was particularly useful because it removed uncertainty associated with overlap between the Mg-O and Al-O correlations and the Mg-O and O-O correlations in the $D_X(r)$ functions.

The model takes into account the fraction of NBO atoms where it is used to extract information on the glass network connectivity. The results are consistent with a glass network containing NBO and BO atoms where most of the Al(IV) atoms are in $[\mathrm{Al}\emptyset_{4/2}]^-$ units. The Mg^{2+} and Zn^{2+} ions are mainly in network modifier sites for the compositions with $R \geqslant 2$ and in charge compensating sites for the compositions with $R \leqslant 2$.

Chapter 6

Atomic Scale Structure of Diopside

6.1 Introduction

Crystalline $CaMgSi_2O_6$, most commonly known as diopside, is a pyroxene mineral constituent in basalts, eclogites and peridotites, which are widespread in crustal and upper mantle rocks [5, 189, 190]. It can also be found in meteoric rocks and interplanetary dust particles [191, 192]. Diopside has been studied in mineralogy and petrology where the atomic scale level of this mineral is still of major importance in the Earth sciences. The $MgSiO_3$-$CaSiO_3$ is a system where the network modifiers Mg and Ca have a glass formation region between the two end members, $MgSiO_3$ (enstatite) and $CaSiO_3$ (wollastonite). Its structure consists of single chains of corner-sharing SiO_4 tetrahedra connected by their apices with octahedral M1 sites that form a chain of edge-shared octahedra. In a similar way to the M1 sites, there is a second octahedral M2 site that is larger and more distorted than the M1 site allowing the introduction of larger cations. Ca atoms fill the M2 sites while Mg atoms fill the M1 sites (Figure 6-1). An investigation of the glassy state of these compositions provides a starting point for understanding the structure of Earth's mantle and interplanetary rock formation.

$CaMgSi_2O_6$ is also a member of the $CaO{-}MgO{-}Al_2O_3{-}SiO_2$ (CMAS) family of materials which plays an important role in commercial display glasses [12]. Additionally, diopside is a major product in metallurgical processing and it is a candidate for use as a bio-material due to its non-toxic and acid resistant nature [193].

For all the reasons mentioned above it is therefore interesting to study the network role of Mg^{2+} and Ca^{2+} ions in the glass structure. Although Ca^{2+} and Mg^{2+} have the same electrical charge Z the Mg^{2+} ion has a smaller radius and higher field strength than

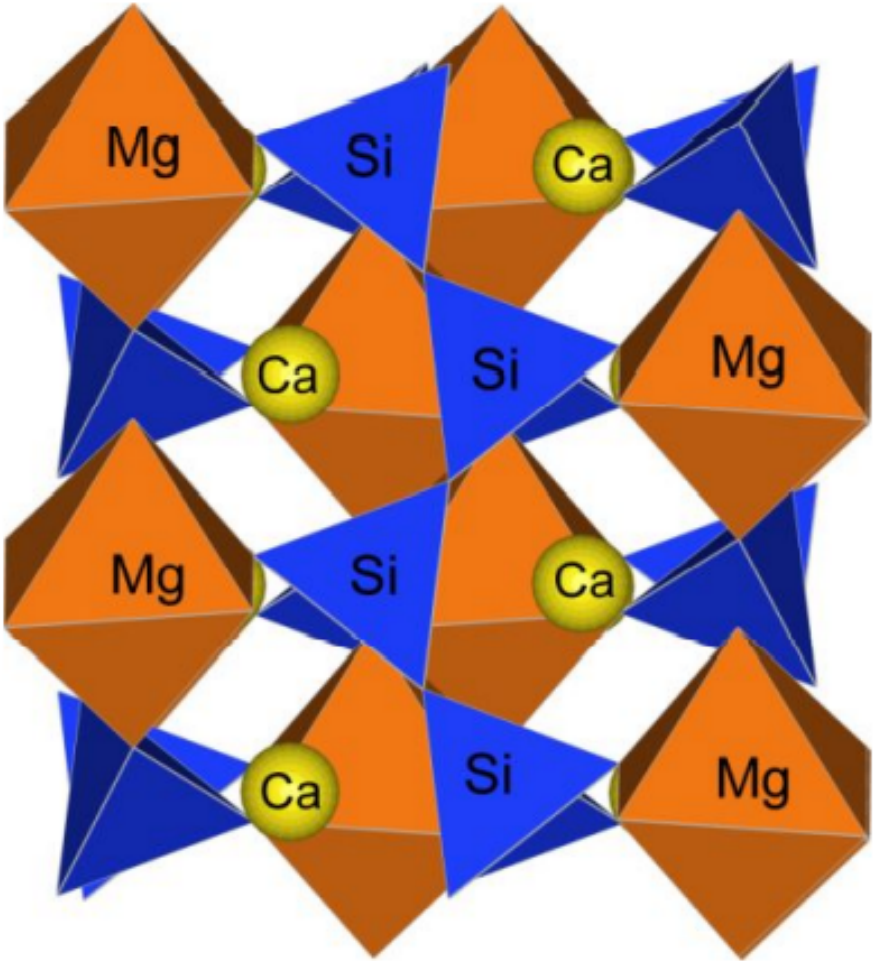

Figure 6-1: The atomic structure of diopside crystals [196].

Ca^{2+} [187]. Each cation may have specific "site" preferences, which adds some degree of disorder/order in the glass network and consequently affecting its configuration [194]. A Ca-Mg mixing is already known to contribute to the bulk thermodynamic properties: The configurational entropy at a constant temperature of $CaMgSi_2O_6$ liquid is higher than that of either end-member $MgSiO_3$ and $CaSiO_3$ melts at temperatures just above T_g [195].

In this chapter NDIS and XRD experiments were carried out on diopside glass to study its structure at an atomic level to understand the environment of Mg and Ca in the glass network.

6.2 Experiment

6.2.1 Sample Preparation

Two $CaMgSi_2O_6$, CMS, samples were prepared. One was enriched with ^{25}MgO and prepared at the Institut de Minéralogie, de Physique des Matériaux et de Cosmochimie, Sorbonne Université, Paris [177]. The other one containing ^{nat}MgO was prepared in Bath. The nominal composition was $(CaO)_{0.25}(MgO)_{0.25}(SiO_2)_{0.5}$. Table 6.1 gives the measured mass density ρ and corresponding number density, n_0, on the natural and isotopic diopside glasses.

The isotopically enriched diopside glass was made from powders of ^{25}MgO (0.81% ^{24}Mg, 98.79% ^{25}Mg, 0.40% ^{26}Mg), $CaCO_3$ (> 99%) and SiO_2 (> 99%). The decomposition of the carbonates was done by heating those powders at 800°C overnight. The powders were then ground together and melted at ≈ 1492°C for 1 h within a Pt-10%Rh crucible. The resulting melt was then quenched by putting the bottom of the crucible into water. The isotopic sample was grounded and melted again to ensure homogeneity.

The natural sample was prepared by mixing powders of $CaCO_3$ (Aldrich ⩾ 99.999%), ^{nat}MgO (Aldrich ⩾ 99.99%) and SiO_2 (Alfa Aesar 99.9%). All the raw materials were calcinated overnight at 800° C in a Pt-10% Rh crucible. A batch of ≈ 3 g was mixed by shaking a bottle with all the powders for ≈ 5 min and then transferred into another Pt-10%Rh crucible. The natural sample was melted at 1550°C for 1 h. The melt was quenched by placing the crucible on a copper block pre-cooled in liquid nitrogen. To ensure sample homogeneity the glass was ground and remelted at 1550°C for 1 h. The mass loss was 0.08% on the first melt and 0.15% on the second melt, which was attributed to the loss of water re-adsorbed during the preparation procedure. The final natural diopside sample was completely glassy (Figure 6-2).

Sample	ρ [g cm^{-3}]	n_0 [Å^{-3}]
natural	2.825(1)	0.0786(3)
isotopic	2.835(1)	0.0786(3)

Table 6.1: The measured mass density, ρ, and corresponding number density, n_0, for the natural and isotopically enriched CMS samples.

Figure 6-2: Natural diopside glass in a Pt-10%Rh crucible after quenching. The sample looks completely clear and glassy.

Species	b [fm]
^{nat}Mg	5.375(4)
^{24}Mg	5.66(3)
^{25}Mg	3.720(12)
^{26}Mg	4.89(15)
Isotopic	3.74(14)
Si	4.149(1)
Ca	4.70(1)
O	5.803(1)

Table 6.2: The bound coherent neutron scattering lengths $b_{^{y}\mathrm{Mg}}$, b_{Ca}, b_{Si} and b_{O} used in the neutron diffraction analysis. The b value of ^{25}Mg was taken from [180] and the other neutron scattering length values were taken from [38]. The scattering length of the isotopic diopside was calculated by taking into account that the sample was enriched with 0.81% ^{24}Mg, 98.79% ^{25}Mg and 0.40% ^{26}Mg. The scattering length of ^{nat}Mg was used for the natural diopside.

6.2.2 D4c Experiment

The neutron diffraction with isotopic substitution (NDIS) experiment was performed using the D4c diffractometer with an incident wavelength of 0.4958(1) Å. The sample powders of natural and isotopic CMS were loaded into a cylindrical vanadium can of 4.8 mm internal diameter and 0.1 mm wall thickness. Diffraction patterns were measured at room temperature ($\simeq$ 298 K) for the sample in the vanadium can, the empty can, the empty instrument and a vanadium rod of 6.08(1) mm diameter for normalisation purposes. A diffraction pattern was also measured for a slab of neutron absorbing $^{10}B_4C$ in order to estimate the effect of the sample's attenuation on the background count rate [101] at small scattering angles. Table 6.2 gives the bound coherent neutron scattering length of the elements used in the NDIS analysis.

6.2.3 6-ID-D Experiment

The high energy X-ray diffraction experiment on the isotopic and natural diopside was done at room temperature using the 6-ID-D diffractometer at the Advanced Photon Source. The photon energy of the square incident beam was 100.233 keV, corresponding to a wavelength of 0.1236 Å. The ground glasses were loaded into kapton polyimide tubes of 1.80(1) mm internal diameter and 0.051(6) mm wall thickness.

The scattered X-rays were detected using a Varex 4343CT amorphous silicon flat panel detector which was placed at a distance of 311(1) mm from the sample position as deduced from the diffraction pattern measured for crystalline CeO_2. Diffraction pat-

terns were measured for each sample in its capillary, an empty capillary and the empty instrument. The data were converted to one-dimensional diffraction patterns using FIT2D [84]. The program PDFgetX2 [85] was used for correction for background scattering, beam polarization, attenuation and Compton scattering.

6.3 Results

The total structure factors $F_N(Q)$ and $S_X(Q)$ measured by neutron and X-ray diffraction are shown in figures 6-4 and 6-13, respectively. The ND patterns indicate differences between the natural and the isotopic samples that is not observed using XRD which originates from neutrons being sensitive to the nuclei of elements.

The total pair distribution functions $D_N(r)$ and $D_X(r)$ are shown in figures 6-5 and 6-14, respectively. The first three major peaks in $D(r)$ correspond to Si-O (≈ 1.62 Å), Mg-O (≈ 2.00 Å) and CaO (≈ 2.40 Å) correlations. The fourth peak at ≈ 2.64 Å correspond to O-O correlations. Above 3.5 Å the overlap between different contributions makes the interpretation difficult. XRD data are dominated by elements with high atomic numbers (Ca>Si>Mg>O) while ND data are dominated by elements with a high scattering length ($b_{\mathrm{O}} > b_{\mathrm{Mg}} > b_{\mathrm{Ca}} > b_{\mathrm{Si}}$). The different sensitivities in these two diffraction techniques explain why Ca-O correlations are more predominant at 2.35 Å in the $D_X(r)$ function while in $D_N(r)$ they appear as a small shoulder at 2.33 Å. For this reason, XRD help constrain the Ca-O correlations when fitting the ND and NDIS data. There is overlap between Mg-O and Ca-O peaks in the $D_X(r)$ and $D_N(r)$ functions. The $\Delta D_{\mathrm{Mg}}(r)$ functions eliminate Ca-O correlations and help constrain the Mg-O correlations when fitting the $D_X(r)$ and $D_N(r)$ functions.

For all the fitted pair distribution functions a single Gaussian function was used for the nearest-neighbor Si-O correlations with the coordination number set to the value $\bar{n}^{\mathrm{O}}_{\mathrm{Si}} = 4$ found from ^{29}Si MAS NMR experiments [197, 198]. Two Gaussian functions were used for the Mg-O correlations with the coordination numbers set at the values found from fitting $\Delta D_{\mathrm{Mg}}(r)$ and a single Gaussian function was used for both the Ca-O and O-O correlations. Figure 6-3 shows the different weighting factors between ND, NDIS and XRD for the natural and isotopic $CaMgSi_2O_6$ glasses.

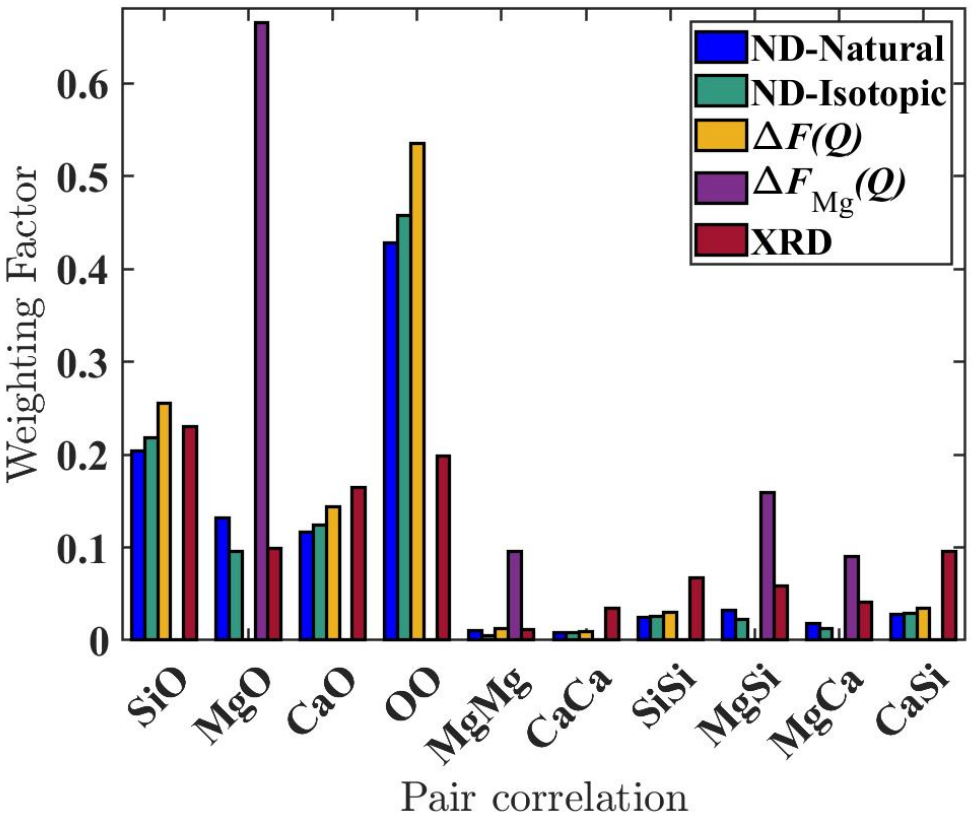

Figure 6-3: The weighting factors, $w_{\alpha\beta}(Q)$, given to the partial structure factors for the neutron diffraction totals (ND), neutron difference functions (NDIS) and X-ray diffraction (XRD). The XRD weighting factors were calculated at $Q = 0$.

6.3.1 Neutron Difraction

Total Structure Factors

Sample	w_{MgO}	w_{SiO}	w_{CaO}	w_{OO}	$\langle b \rangle$ [fm]	$G(0)$
isotopic	0.0980(5)	0.2174(5)	0.1231(5)	0.4561(5)	5.319(2)	-0.2658(3)
natural	0.1323(5)	0.2042(5)	0.1159(5)	0.4285(5)	5.156(2)	-0.2829(3)

Table 6.3: The neutron weighting factors for the partial pair distribution functions g_{MgO}, g_{SiO}, g_{CaO} and g_{OO} used in $D_N(r)$. The average neutron scattering length $\langle b \rangle$ and $G(0)$ values for the isotopic and natural diopside are also listed.

The positions of the first three peaks in the structure factors $F_N(Q)$ are listed in table 6.4 and the weighting factors for the partial pair distribution functions $g_{\mathrm{SiO}}(r)$, $g_{\mathrm{MgO}}(r)$, $g_{\mathrm{CaO}}(r)$ and $g_{\mathrm{OO}}(r)$ are shown in table 6.3. The measured $D_N(r)$ functions are shown in figure 6-5 and their respective fits are shown in figure 6-6.

According to $CaMgSi_2O_6$ crystal structures [199, 200] the first peak in real space at 1.62(1) Å is attributed to Si-O correlations within SiO_4 tetrahedral structural motifs. The second peak in real space at 2.06(1) Å is attributed to Mg-O correlations within edge-sharing MgO_4 tetrahedra. The shoulder at $\approx$ 2.38 Å is attributed to Ca-O correlations. For tetrahedral SiO_4 motifs with Si-O bond distances 1.62 Å the nearest neighbor O-O correlations are expected to be at $r_{\mathrm{OO}} = \sqrt{8/3} r_{\mathrm{SiO}} = 2.65$ Å. The O-O correlations were fitted in order to constrain the peaks fitted at small r- values. The parameters obtained from the fitted $D_N(r)$ functions are summarized in table 6.10 with the goodness-of-fit parameter R_χ calculated over the range 1.30-2.74 Å.

The $D_N(r)$ functions were firstly fitted by fixing the parameters from the $\Delta D_{\mathrm{Mg}}(r)$ and $\Delta D(r)$ fits and then refining the least amount of parameters starting by the peak widths.

Sample	Q_{FSDP}[Å^{-1}]	Q_{PP}[Å^{-1}]	Q_3[Å^{-1}]	Q_{max} [Å^{-1}]
natural	2.023(1)	2.835(1)	5.05(2)	23.65
isotopic	1.967(1)	2.815(1)	5.12(2)	23.65

Table 6.4: The positions of the first three peaks Q_{FSDP}, Q_{PP} and Q_3 in the $F_N(Q)$ functions shown in figure 6-4. Also given are the Q_{max} values used in the Fourier transformation.

Sample	Atom pair	$r_{\alpha\beta}$ [Å]	$\sigma_{\alpha\beta}$ [Å]	$\bar{n}_{\alpha}^{\beta}$	R_{χ} [%]
Natural	Si-O	1.622(3)	0.058(5)	4.00*	6.38
	Mg-O	1.977(4)	0.076(5)	2.61*	
	Mg-O	2.143(7)	0.146(5)	1.80*	
	Mg-O (sum)			4.40*	
	Ca-O	2.358(5)	0.156(5)	5.01(5)	
	O-O	2.657(3)	0.108(5)	4.99(10)	
Isotopic	Si-O	1.624(3)	0.058(5)	4.00*	5.43
	Mg-O	1.978(4)	0.074(5)	2.61*	
	Mg-O	2.143(7)	0.200(5)	1.80*	
	Mg-O (sum)			4.40*	
	Ca-O	2.350(5)	0.150(5)	5.01(5)	
	O-O	2.657(3)	0.107(5)	4.92(10)	

Table 6.5: Parameters obtained from Gaussian peak fits to the $D_N(r)$ functions for the isotopic and natural diopside glasses. The fitted functions are shown in figure 6-6. R_{χ} is given for the range 1.30-2.74 Å. The parameters denoted by an * are fixed and the Ca-O coordination number is constrained from the D_X(r) fits.

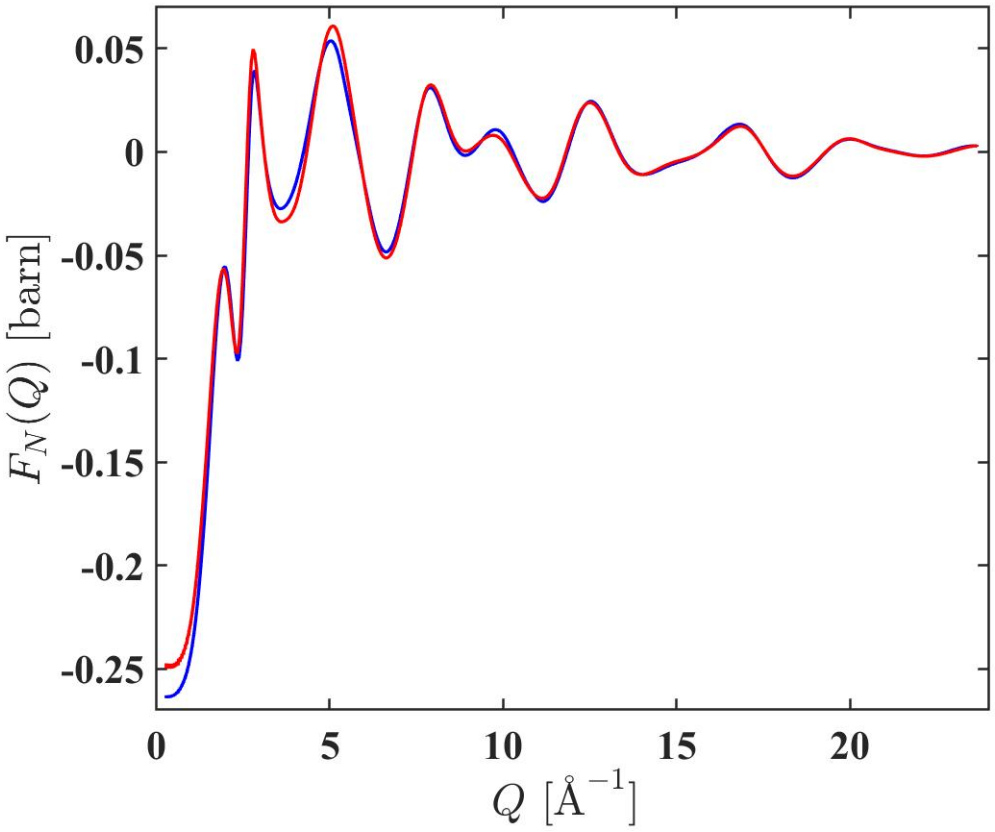

Figure 6-4: Total structure factors $F_N(Q)$ for the natural (blue) and isotopic (red) diopside glass. The error bars are smaller than the line thickness at most Q values. The curves are offset vertically for clarity of presentation.

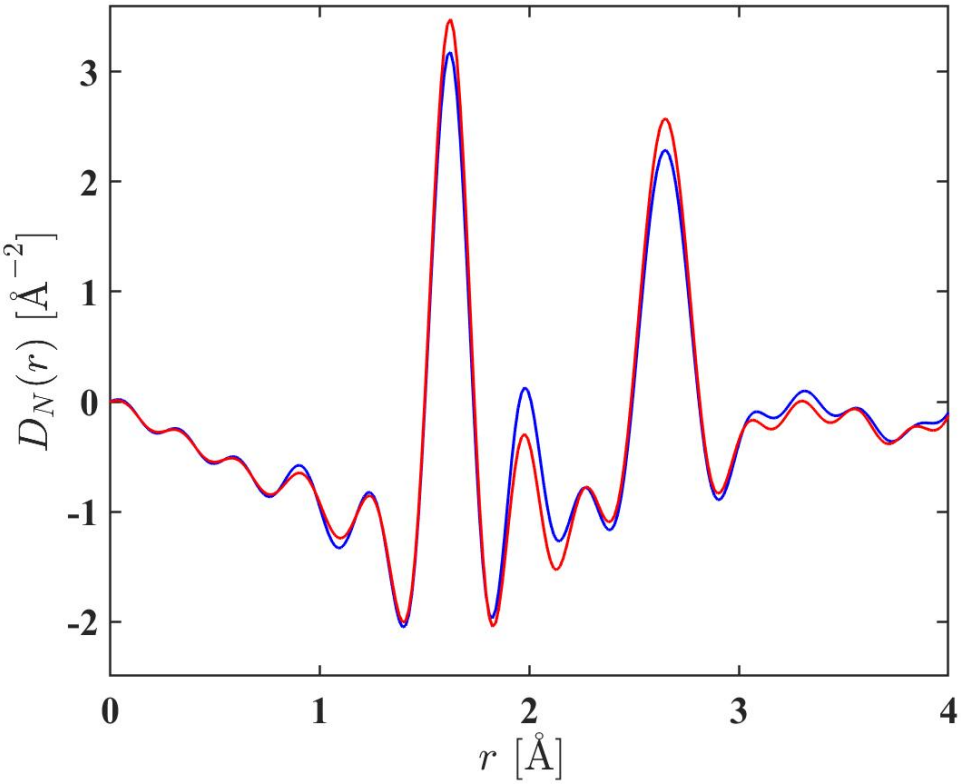

Figure 6-5: Total pair distribution functions $D_N(r)$ for the natural and isotopic diopside glasses. $D_N(r)$ was obtained by Fourier transforming the corresponding reciprocal data shown in figure 6-4 after spline fitting.

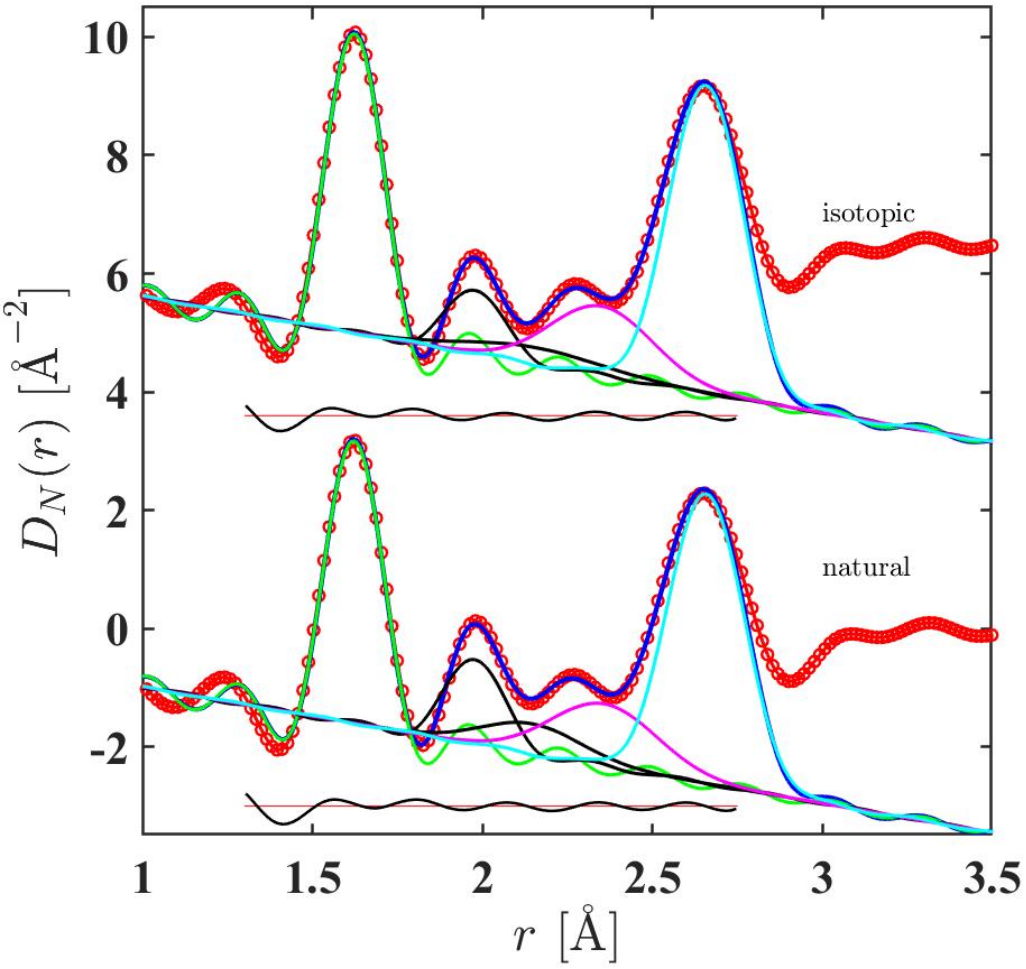

Figure 6-6: The fitted $D_N(r)$ functions for the natural and isotopic diopside glasses. The red circles are the data, the blue solid curves gives the fit and the other curves show the contribution from Si-O (green), Mg-O (black), Ca-O (magenta) and O-O (cyan) correlations. The displaced black solid curve gives the residual (fit subtracted from measured data). The O-O correlations are introduced to constrain the peaks fitted at smaller r values. The curves are offset vertically for clarity of presentation.

6.3.2 First-Order Difference Functions

By taking natural (^{nat}Mg) and isotopic (^{25}Mg) diopside it is possible to obtain site specific structural information by calculating difference functions from the natural and isotopic $F_N(Q)$ functions. The difference function ΔF_{Mg} eliminates pair-correlation functions that do not involve magnesium. The Mg$-\alpha$ correlations with $\alpha \neq$ Mg can also be eliminated by forming the difference function $\Delta F(Q)$. The difference functions $\Delta F_{\mathrm{Mg}}(Q)$ and $\Delta F(Q)$ therefore, lead to a simplification of the complexity of correlations associated with a single total structure factor. Chapter 2 gives the equations for both ΔF_{Mg} and $\Delta F(Q)$.

The first order difference functions $\Delta F_{\mathrm{Mg}}(Q)$ and $\Delta F(Q)$ are shown in figures 6-7 and 6-8 respectively. The position of the first three peaks in the $\Delta F_{\mathrm{Mg}}(Q)$ and $\Delta F(Q)$ functions are listed in table 6.6 and the weighting factors are listed in table 6.7. The $\Delta D_{\mathrm{Mg}}(r)$ and $\Delta D(r)$ functions are shown in figures 6-9 and 6-10, respectively. The $\Delta D_{\mathrm{Mg}}(r)$ function shows a sharp peak at $\approx$ 2.0 Å due to Mg-O correlations and a second major peak at 3.2 Å due to Mg-Mg and Mg-Ca correlations. A small shoulder is also observed at $\approx$ 2.8 Å which is attributed to Mg-Si correlations. Two peaks were used to fit Mg-O to cover the entire area and the peak attributed to Mg-Si correlations was fitted in order to extract $\bar{n}^{\mathrm{O}}_{\mathrm{Mg}}$ with more accuracy. The $\Delta D(r)$ function shows three major peaks due to Si-O ($\approx$ 1.62 Å), Ca-O ($\approx$ 2.35 Å) and O-O ($\approx$ 2.65 Å) correlations. The small peak at $\approx$ 2 Å is attributed to a Fourier transform artefact. The O-O correlations were fitted in order to constrain the peaks fitted at small r-values such as Ca-O correlations. To fit the Ca-O peak the $\bar{n}^{\mathrm{O}}_{\mathrm{Ca}}$ value was constrained from $D_X(r)$ fits. The $\Delta D_{\mathrm{Mg}}(r)$ and $\Delta D(r)$ fits are shown in figures 6-11 and 6-12, respectively. The parameters obtained from the fitted difference functions are summarized in table 6.8.

Function	Q_{FSDP}[Å^{-1}]	Q_{PP}[Å^{-1}]	Q_3[Å^{-1}]	Q_{max}[Å^{-1}]
$\Delta F_{\mathrm{Mg}}(Q)$	2.219(1)	4.193(1)	6.796(2)	20.7
$\Delta F(Q)$	1.862(1)	2.756(1)	5.237(2)	23.65

Table 6.6: The positions of the first three peaks Q_{FSDP}, Q_{PP} and Q_3 in the first-order difference functions shown in figures 6-9 and 6-10. Also given are the Q_{max} values used in the Fourier transformation.

Function	w_{MgO}	w_{MgSi}	w_{SiO}	w_{CaO}	w_{OO}	$G(0)$
$\Delta D_{\mathrm{Mg}}(r)$	0.6648(8)	0.1584(8)	-	-	-	-0.017(4)
$\Delta D(r)$	-	-	0.2550(8)	0.1444(8)	0.5349(8)	-0.099(4)

Table 6.7: The weighting factors for the difference functions used for fitting the $\Delta D_{\mathrm{Mg}}(r)$ and $\Delta D(r)$ functions. The $G(0)$ values are also given.

Difference Function	Atom pair	$r_{\alpha\beta}$ [Å]	$\sigma_{\alpha\beta}$ [Å]	$\bar{n}_{\alpha}^{\beta}$	R_{χ} [%]
$\Delta D_{\mathrm{Mg}}(r)$	Mg-O	1.975(4)	0.050(4)	2.61(3)	6.59
	Mg-O	2.143(8)	0.069(7)	1.80(3)	
	Mg-O (sum)			4.40(4)	
	Mg-Si	2.80(9)	0.180(7)	1.98(20)	
$\Delta D(r)$	Si-O	1.627(3)	0.059(5)	4.00*	6.26
	Ca-O	2.374(5)	0.123(5)	5.01(5)	
	O-O	2.653(5)	0.099(5)	4.58(10)	

Table 6.8: Parameters obtained from Gaussian peak fits to the first order difference functions of diopside. The fitted functions are shown in figures 6-11 and 6-12. For $\Delta D_{\mathrm{Mg}}(r)$, R_{χ} is given for the fitted range 1.70-2.80 Å. For $\Delta D(r)$, R_{χ} is given for the fitted range 1.30-2.74 Å. The parameter denoted by an * is fixed.

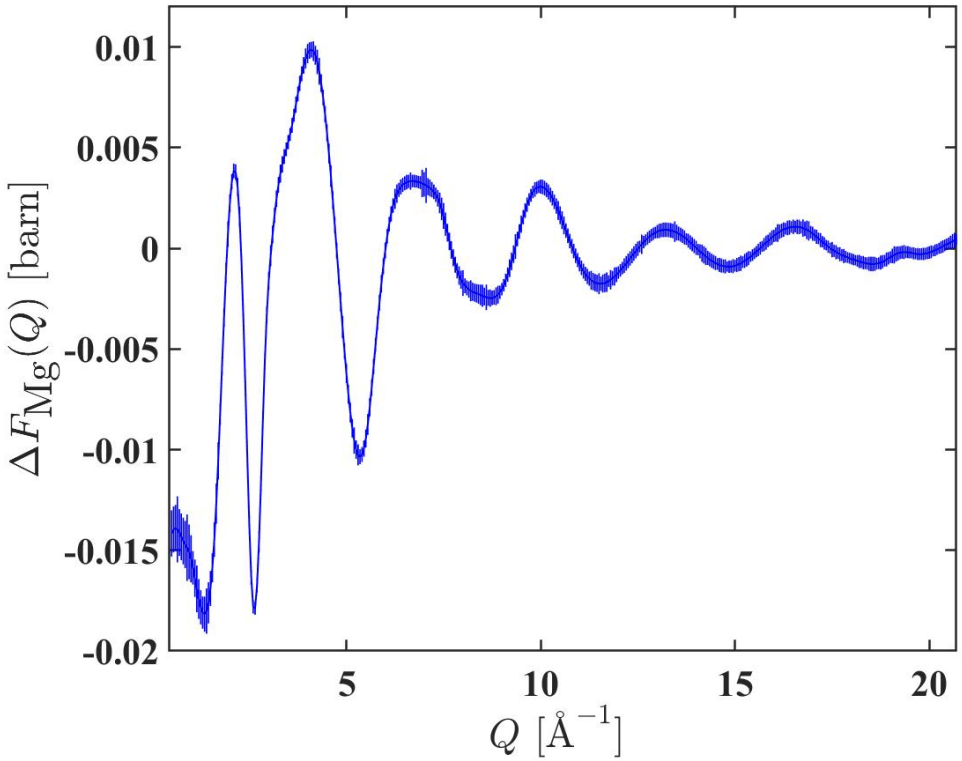

Figure 6-7: First-order difference function $\Delta F_{\mathrm{Mg}}(Q)$ for diopside. The vertical error bars are smaller than the line thickness at most Q values.

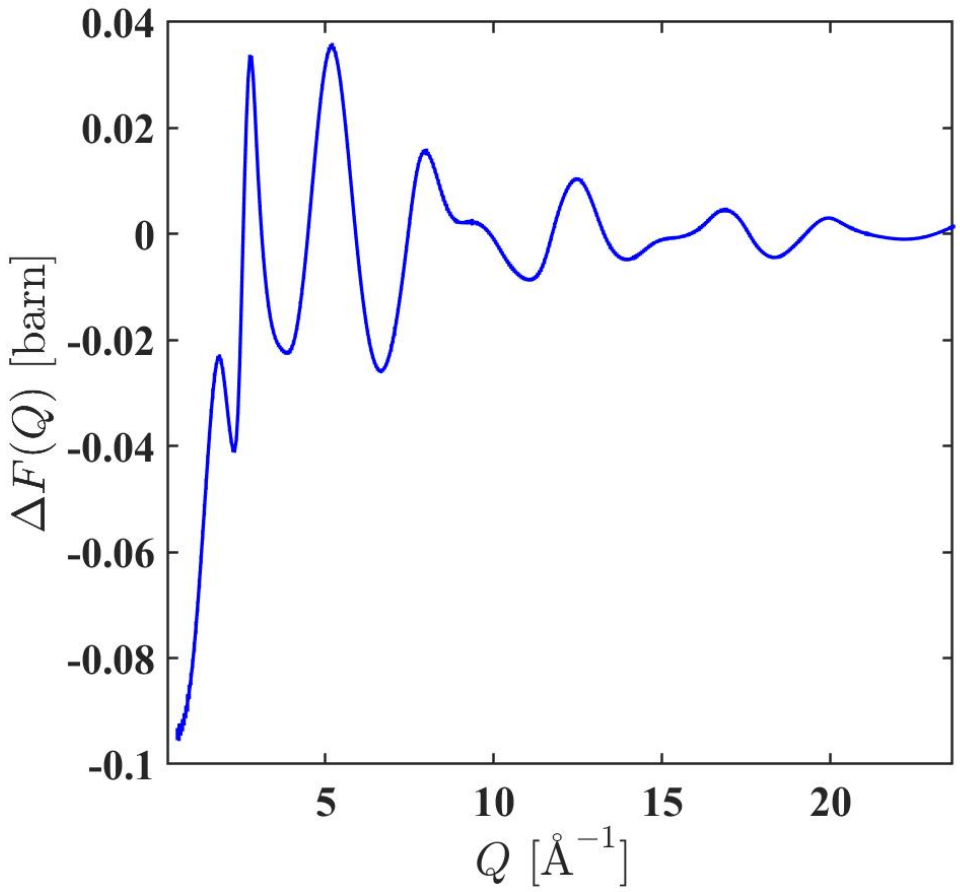

Figure 6-8: First-order difference function $\Delta F(Q)$ for diopside. The vertical error bars are smaller than the line thickness at most Q values.

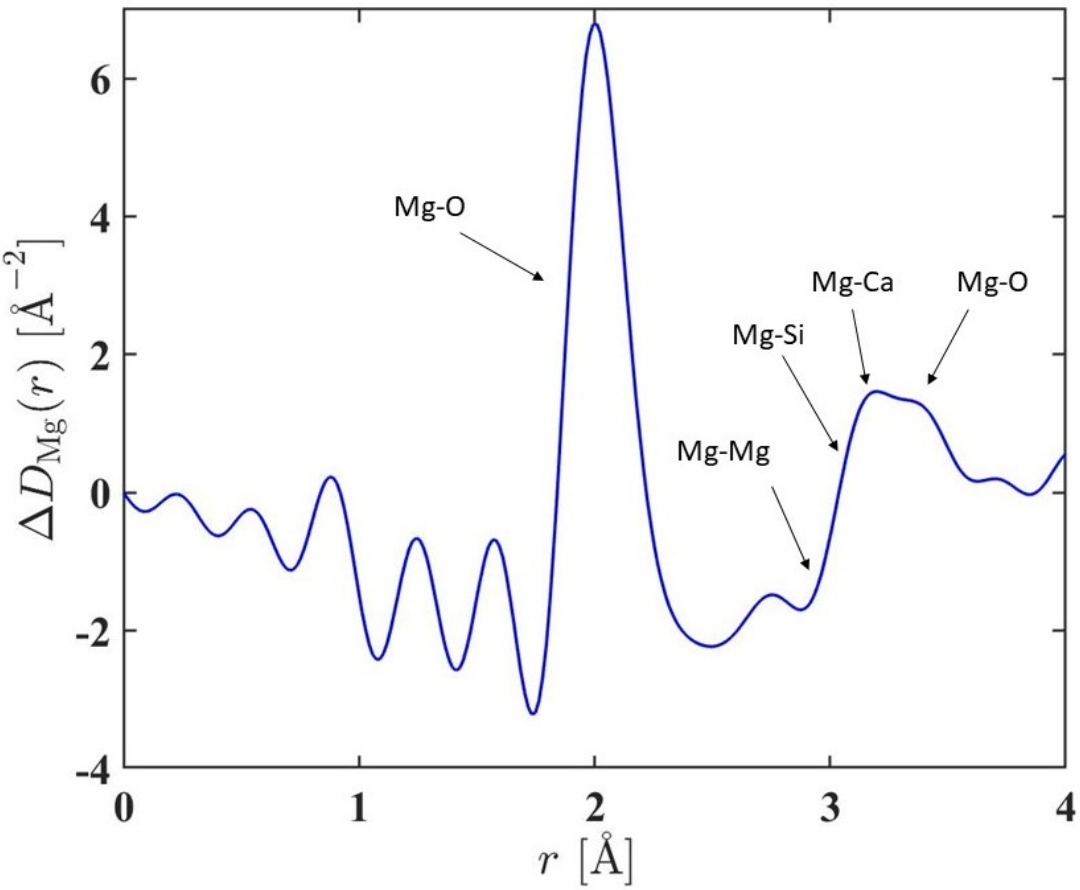

Figure 6-9: First-order difference pair distribution function $\Delta D_{\mathrm{Mg}}(r)$. The curve was obtained by Fourier transforming the corresponding reciprocal space data shown in figure 6-7 after spline fitting and truncated with $Q_{\mathrm{max}} = 20.7$ Å. Arrows indicate peak assignments based on the element-element distances found in the crystal structure [199–204].

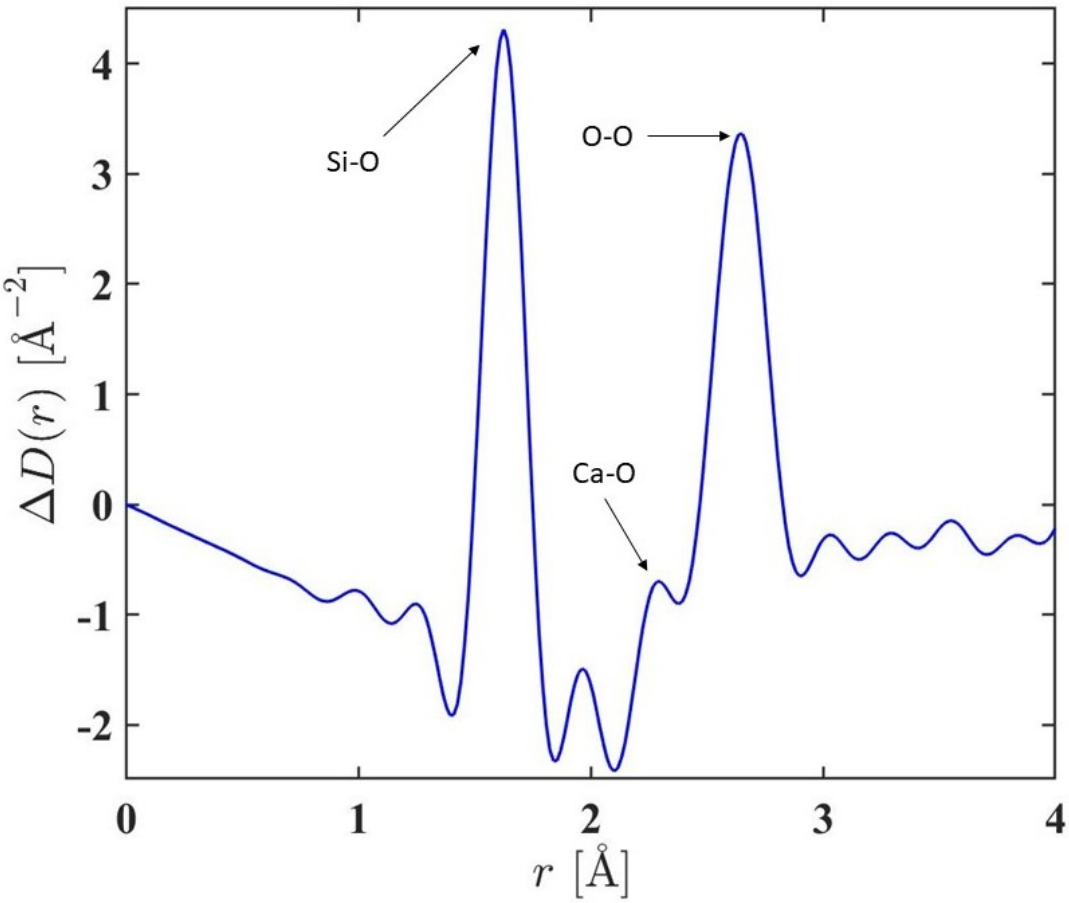

Figure 6-10: First-order difference pair distribution function $\Delta D(r)$. The curve was obtained by Fourier transforming the corresponding reciprocal space data shown in figure 6-8 after spline fitting and truncated with $Q_{\max} = 23.65$ Å. Arrows indicate peak assignments based on the element-oxygen distances found in the crystal structure [199–204].

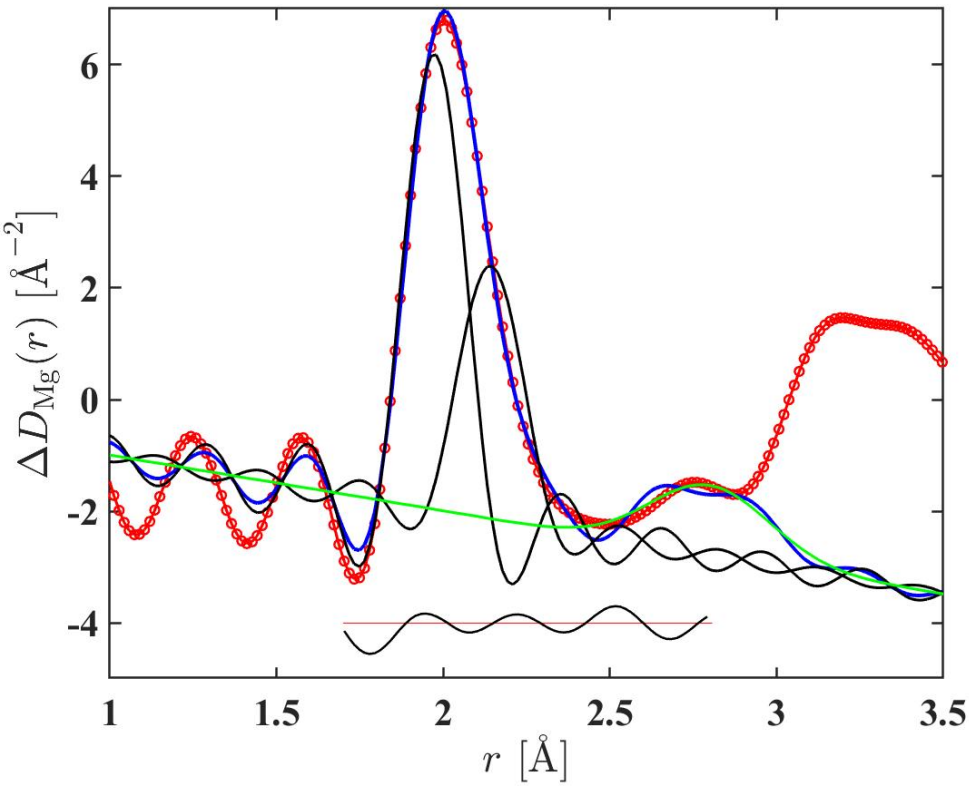

Figure 6-11: The fitted $\Delta D_{\mathrm{Mg}}(r)$ function for diopside. The red circles are the data, the blue solid curve gives the fit and the other curves show the contribution from Mg-O (black) and Mg-Si (green) correlations. The displaced black solid curve gives the residual (fit subtracted from measured data). The Mg-Si correlations are introduced to constrain the peaks fitted at small r values.

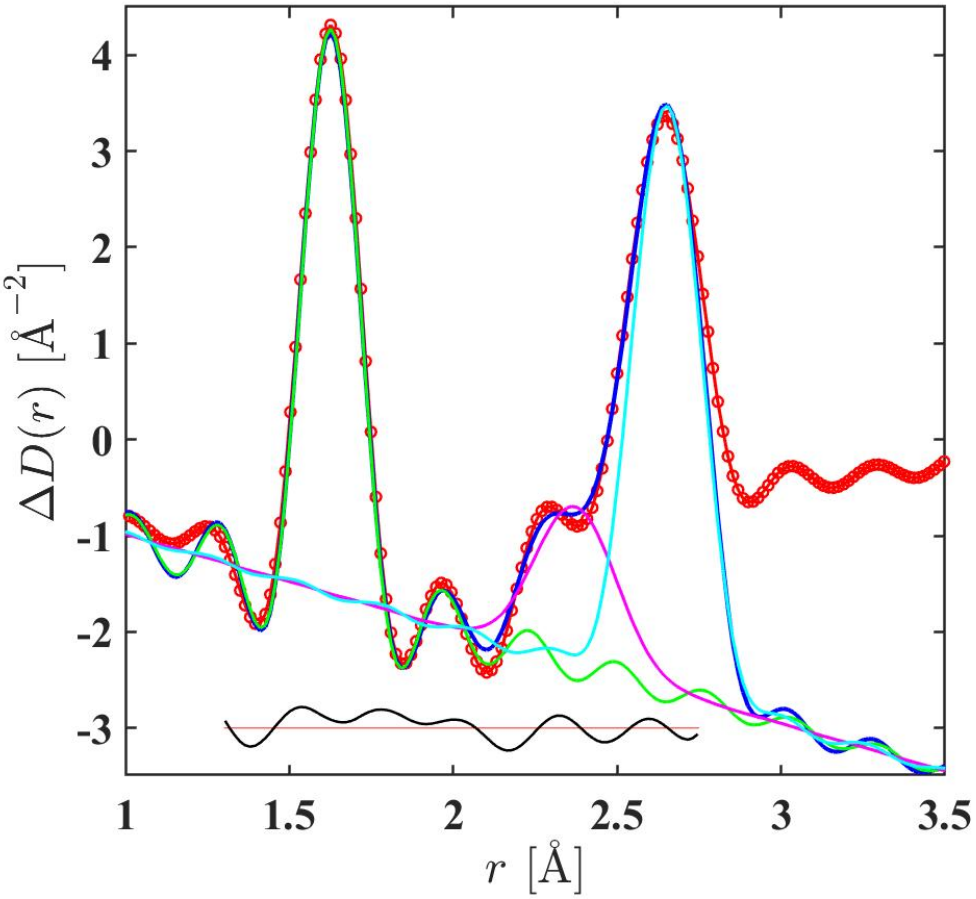

Figure 6-12: The fitted $\Delta D(r)$ function for diopside. The red circles are the data, the blue solid curve gives the fit and the other curves show the contribution from Si-O (green), Ca-O (magenta) and O-O (cyan) correlations. The displaced black solid curve gives the residual (fit subtracted from measured data). The O-O correlations are introduced to constrain the peaks fitted at small r values.

6.3.3 X-ray diffraction

The positions of the first three peaks in the structure factors, $S_X(Q)$, are listed in table 6.9. The $S_X(Q)$ functions for natural and diopside glasses are shown in figure 6-13. It is observed some differences between the two structure factors when plotted on top of each other, whereas for the isotopic and natural MAS glasses (Chapter 5) the $S_X(Q)$ functions were completely identical. This might be due to differences in composition between the isotopic and natural diopside samples. These small differences affect the Si-O peak height and the shape of Mg-O peak in the $D_X(r)$ functions as seen in figure 6-14.

The fitted $D_X(r)$ functions are shown in figure 6-15. The Ca-O peak is more prominent and the O-O correlations are much smaller as compared to the $D_N(r)$ functions. For both isotopic and natural samples the $\bar{n}^{\mathrm{O}}_{\mathrm{Mg}}$ value was fixed and peak positions of Mg-O correlations were constrained from the $\Delta D_{\mathrm{Mg}}(r)$ fit values. As a starting point of fitting the data, all the parameters are fixed according to the neutron difference function fits and then refined slowly except the Mg-O coordination numbers. The positions of Si-O, Mg-O, Ca-O and O-O correlations had a lower than 10% difference between the $D_X(r)$ and $D_N(r)$ fits.

A Ca-O coordination number of 5.01-5.06 was obtained with an associated bond distance of 2.353(5)-2.357(5) Å. The $\bar{n}^{\mathrm{O}}_{\mathrm{Ca}}$ value for the glasses may be larger than indicated if the distribution of nearest neighbors is asymmetric as found for the coordination environment of magnesium.

Sample	Q_{FSDP} [Å^{-1}]	Q_{PP} [Å^{-1}]	Q_3 [Å^{-1}]	Q_{max} [Å^{-1}]
Natural	2.121(1)	4.491(1)	5.937(2)	29.32
Isotopic	2.120(1)	4.503(1)	5.921(2)	29.32

Table 6.9: The positions of the first three peaks Q_{FSDP}, Q_{PP} and Q_3 in the $S_X(Q)$ functions shown in figure 6-13. The Q_{max} values used in the Fourier transformation are also listed.

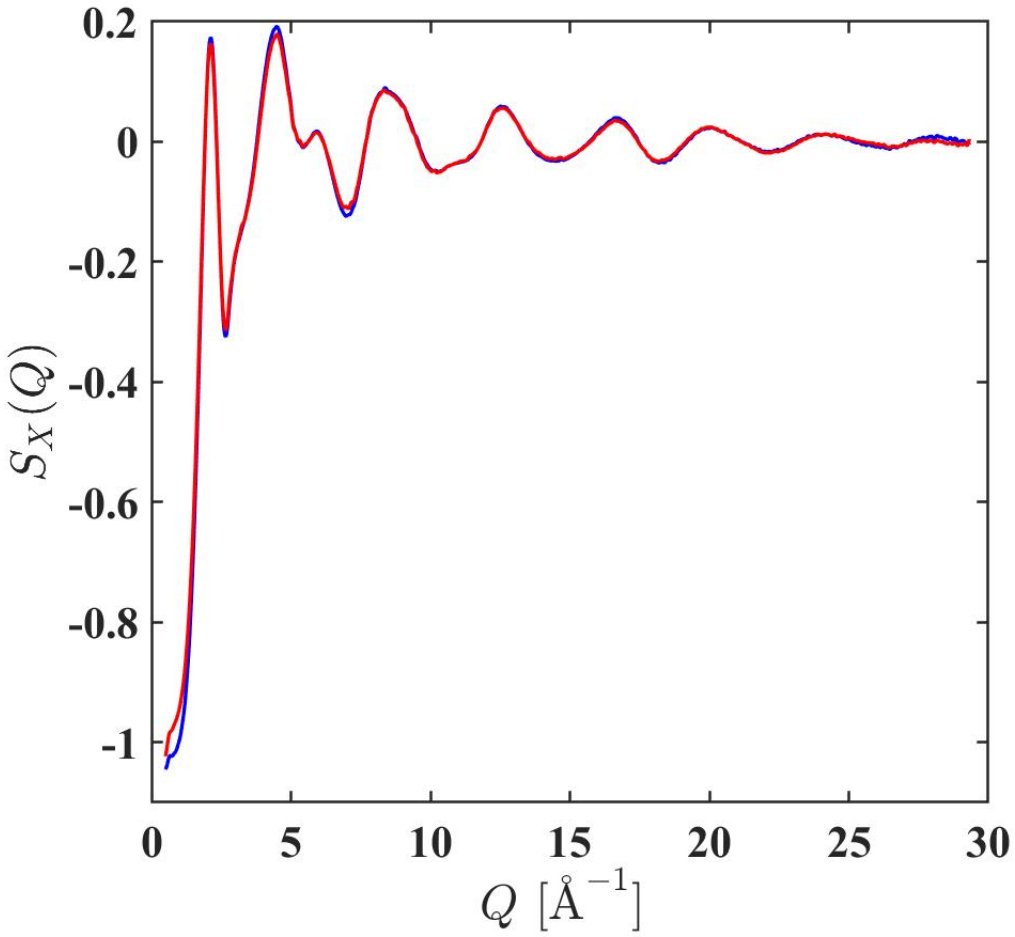

Figure 6-13: Total structure factors $S_X(Q)$ for the isotopic (red) and natural (blue) diopside glass. The vertical error bars are smaller than the line thickness at most Q values.

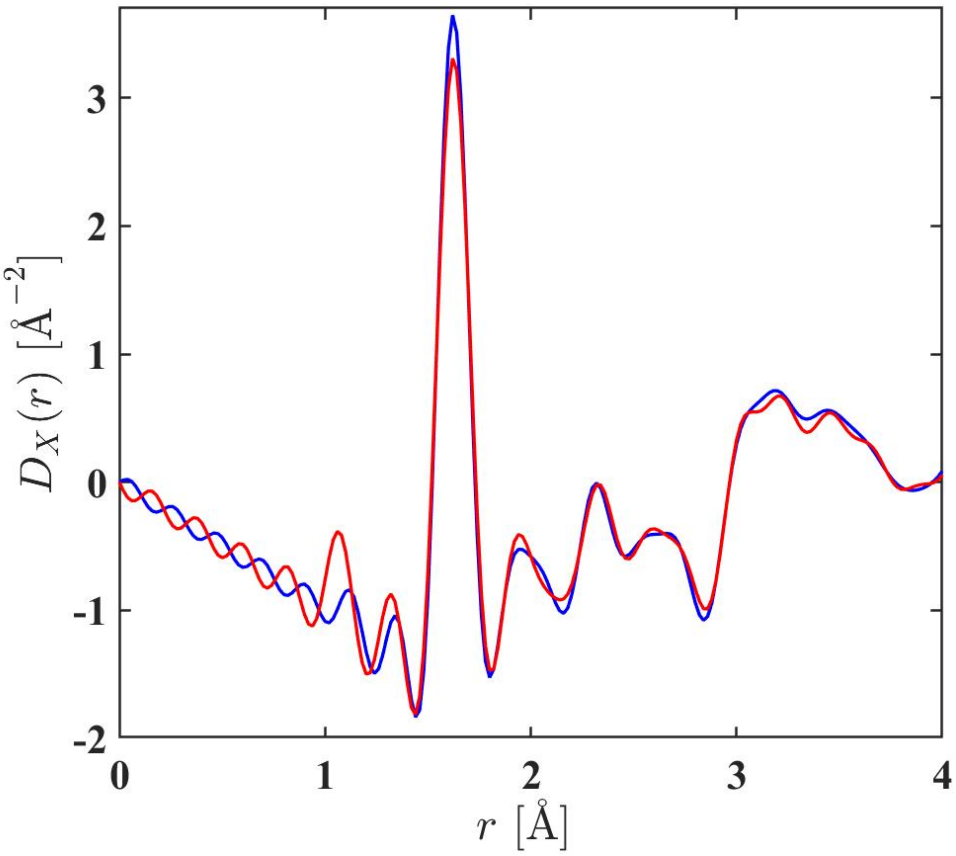

Figure 6-14: $D_X(r)$ functions for the natural and isotopic diopside glasses. $D_X(r)$ was obtained by Fourier transforming the reciprocal data shown in figure 6-13.

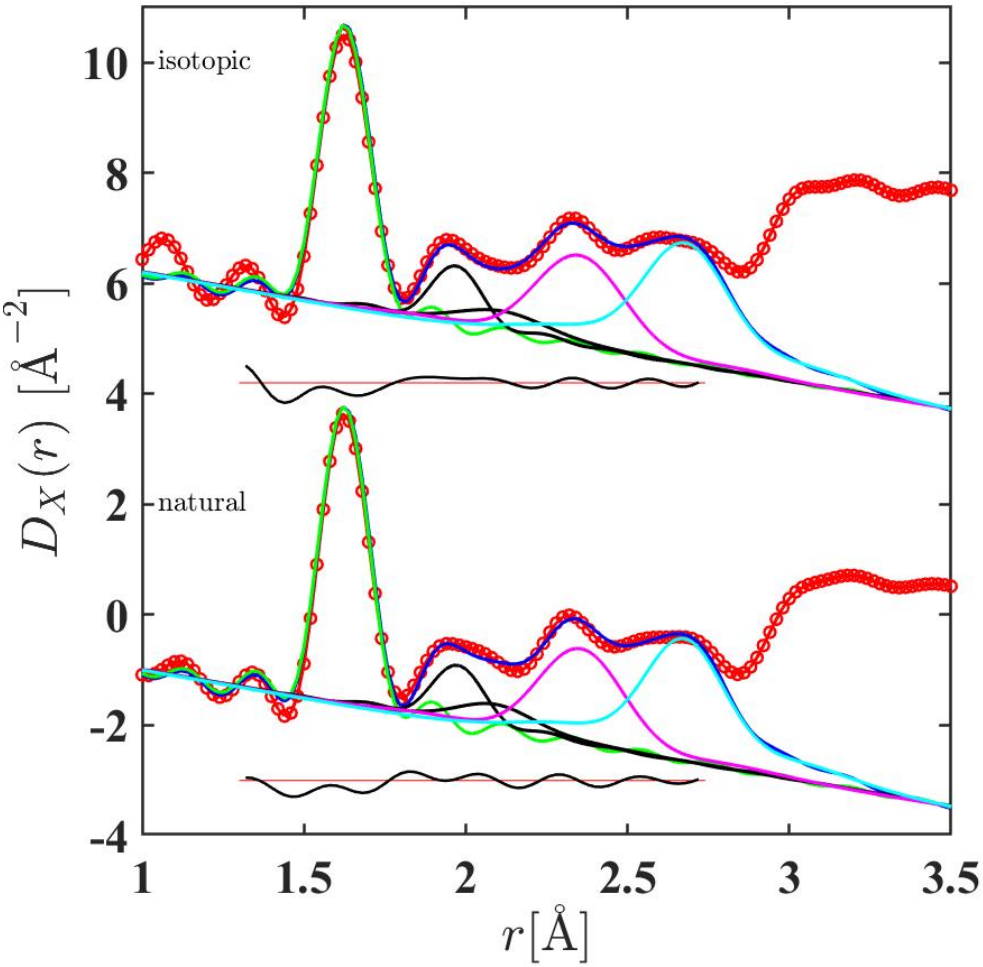

Figure 6-15: The fitted $D_X(r)$ functions for natural and isotopic diopside glasses. The red circles are the data, the blue solid curves shows the fits and the other curves show the contribution from Si-O (green), Mg-O (black), Ca-O (magenta) and O-O (cyan) correlations. The displaced black solid curve gives the residual (fit subtracted from measured data). The O-O correlations are introduced to constrain the peaks fitted at small r values.

Sample	Atom pair	$r_{\alpha\beta}$ [Å]	$\sigma_{\alpha\beta}$ [Å]	$\bar{n}_{\alpha}^{\beta}$	R_{χ} [%]
Isotopic	Si-O	1.626(1)	0.0653(9)	4*	11.59
	Mg-O	1.970(5)	0.071(4)	2.61*	
	Mg-O	2.112(2)	0.134(17)	1.80*	
	Mg-O (sum)			4.40*	
	Ca-O	2.353(5)	0.142(3)	5.01(13)	
	O-O	2.679(5)	0.133(3)	7.22(13)	
Natural	Si-O	1.6251(8)	0.0604(8)	4*	9.48
	Mg-O	1.976(5)	0.073(4)	2.61*	
	Mg-O	2.092(15)	0.116(12)	1.80*	
	Mg-O (sum)			4.40*	
	Ca-O	2.357(5)	0.137(4)	5.06(12)	
	O-O	2.676(4)	0.126(5)	6.94(14)	

Table 6.10: Parameters obtained from Gaussian peak $D_X(r)$ fits to the r-space functions for natural and isotopic diopside glasses. The fitted functions are shown in figure 6-15. The values denoted by an * are fixed. R_{χ} is given for the range 1.30-2.74 Å.

6.4 Discussion

Table 6.11 shows the fitted Ca-O and Si-O distances along with the calculated weighted Mg-O mean bond distance (Equation 2.12) using ND, NDIS and XRD. An average Si-O distance of 1.625(1) Å found for all the $D(r)$ functions corresponds to the nearest neighbour atomic separation of SiO_4 units.

The first Mg-O peak is broad and asymmetric which indicates a wide distribution of coordination environment for the Mg^{2+} ions. This variety leads to the broad distribution of electric-field gradient components at the magnesium position inferred from ^{25}Mg MAS NMR experiments on diopside glasses [198]. The $\Delta D_{\mathrm{Mg}}(r)$ fit gave an average coordination number of 4.40(4) O neighbors around Mg. This value indicates that the Mg environment is distributed mainly between Mg(IV) and Mg(V) species in between SiO_4 tetrahedra, as also seen for the MAS glasses (Chapter 5). The overall Mg-O coordination $\bar{n}^{\mathrm{O}}_{\mathrm{Mg}}$ (sum) obtained from the fitting procedure is in agreement with the value found directly from $\Delta D_{\mathrm{Mg}}(r)$ by using equation 2.11 to integrate under the first peak after the application of a Lorch modification function [32].

The $\bar{n}^{\mathrm{O}}_{\mathrm{Mg}}$ obtained is very similar to the value $\bar{n}^{\mathrm{O}}_{\mathrm{Mg}} = 4.50(8)$ found by Cormier et al [205] on $MgCaSi_2O_6$ studies using NDIS, XRD and Empirical Potential Structure Refinement (EPSR). A similar $\bar{n}^{\mathrm{O}}_{\mathrm{Mg}} = 4.50(5)$ value was found by Salmon et al [179] on $MgSiO_3$ studies using ND and molecular dynamic (MD) simulations. A recent NDIS study of $MgSiO_3$, enstatite, using the same $b_{^{25}\mathrm{Mg}}$ value (table 6.2) as in this work obtained $\bar{n}^{\mathrm{O}}_{\mathrm{Mg}} = 4.46$ [180]. This indicates a similar role for Mg in the silicate network for enstatite and diopside. The NDIS study also included an investigation of the sample MAS50.25 where it was found $\bar{n}^{\mathrm{O}}_{\mathrm{Mg}} = 4.90(4)$. The higher Mg-O coordination number for MAS50.25 in contrast to enstatite and diopside, suggests that Mg^{2+} ions charge compensate Al atoms in tetrahedral units. Figure 6-16 shows the difference function $\Delta D_{\mathrm{Mg}}(r)$ for the diopside and MAS50.25 glass. In both functions, the Mg-O peak has similar features in position (≈ 2.0 Å), height and width. However, the peak at ≈ 3.2 Å is higher for diopside than for MAS50.25 which is due to Mg-Ca correlations being greater than Mg-Al correlations.

In diopside and other investigated glasses, Mg-O coordination numbers of less than five indicate the presence of fourfold coordinated Mg^{2+} ions. For example, if only four and five-coordinated species are present in the glass and $f_{\mathrm{Mg(IV)}}$ denotes the fraction of four-coordinated Mg^{2+} ions, the mean coordination number is given by

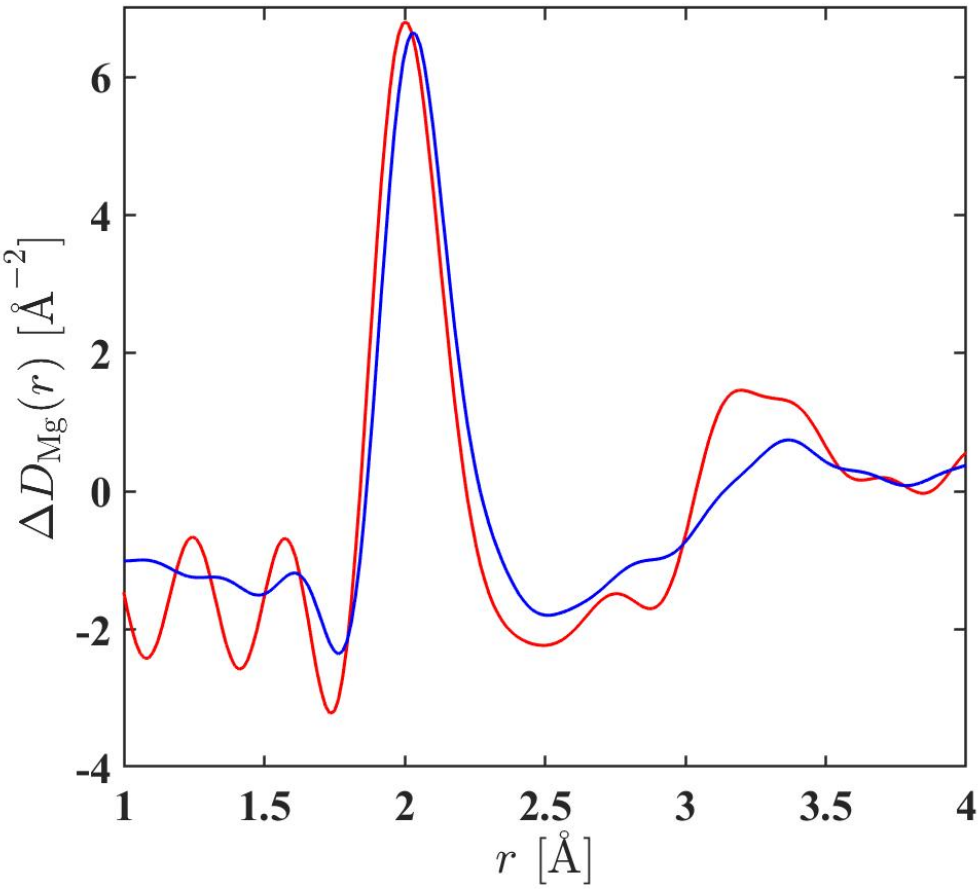

Figure 6-16: $\Delta D_{\mathrm{Mg}}(r)$ functions for diopside (red) and MAS50.25 (blue) [180].

Function	$\bar{r}_{\mathrm{MgO}}$ [Å]	$\bar{r}_{\mathrm{SiO}}$ [Å]	$\bar{r}_{\mathrm{CaO}}$ [Å]
ΔD_{Mg} or $\Delta D(r)$	2.036(8)	1.627(3)	2.374(5)
natural $D_N(r)$	2.033(8)	1.622(3)	2.358(5)
isotopic $D_N(r)$	2.031(8)	1.624(3)	2.350(5)
natural $D_X(r)$	2.016(8)	1.625(1)	2.357(5)
isotopic $D_X(r)$	2.019(8)	1.626(1)	2.353(5)

Table 6.11: Average Mg-O, Si-O and Ca-O distances for diopside obtained from ND, NDIS and XRD fits.

$$\bar{n}^{\mathrm{O}}_{\mathrm{Mg}} = 4f_{\mathrm{Mg(IV)}} + 5[1 - f_{\mathrm{Mg(IV)}}]. \tag{6.1}$$

It follows that $f_{\mathrm{Mg(IV)}} = 0.6$, which means that 60% of the magnesium is four-fold coordinated. There is no evidence, however, of Mg(IV) species adopting a network-forming role. For example, the Q^n speciation found from ^{29}Si MAS NMR experiments on glassy diopside [198], enstatite [206, 207] and wollastonite [198, 208, 209], where n denotes the number of bridging oxygen atoms per SiO_4 tetrahedron is similar in all these materials and the mean value $\langle n \rangle \simeq 2$ is consistent with a network-modifying role for Mg^{2+} [1].

Previous neutron and X-ray diffraction work on the $Mg_xCa_{1-x}SiO_3$ glasses were also done by [205,210,211]. The results show that the coordination environment of Mg varies from $4.35(5) \leq \bar{n}^{\mathrm{O}}_{\mathrm{Mg}} \leq 5.02(9)$ when the MgO content increases from 0 to 36.32 mol%. Even though the value $\bar{n}^{\mathrm{O}}_{\mathrm{Mg}} = 4.50(8)$ found for the same composition (diopside) is higher than the value $\bar{n}^{\mathrm{O}}_{\mathrm{Mg}} = 4.40(4)$ found in this work, it is expected from the total $D(r)$ functions were overlapping between Mg-O and Ca-O coexist. Indeed when the total $D_X(r)$ and $D_N(r)$ fits were not fixed to the $\bar{n}^{\mathrm{O}}_{\mathrm{Mg}} = 4.40(4)$ value, the coordination environment of Mg increased to $\approx 5.0(1)$ due to overlap between the different correlations.

The Ca-O bond length was estimated from the third peak position in $D_X(r)$ at ≈ 2.35 Å. The Ca-O coordination number obtained was $\bar{n}^{\mathrm{O}}_{\mathrm{Ca}} \approx 5$ but it is challenging extrapolating the value with certainty due to overlap between Ca-O and O-O correlations. Although there is no ND data with Ca isotopic substitution for the diopside glass, the results from this work can be compared to a study done with $CaSiO_3$ coupling neutron diffraction with ^{44}Ca/$^{\mathrm{nat}}$Ca isotopic substitution [212] where they found $\bar{n}^{\mathrm{O}}_{\mathrm{Ca}} = 6.15(17)$. In contrast with Mg, Ca cations are localized in a wide distribution of sites. The Ca coordination environment is predominantly Ca(V) with both Ca(VI) and Ca(VII) species

present in the glasses. For crystalline diopside Ca is eight-fold coordinated with oxygen and has a distance range of 2.227-2.389 Å under high pressure conditions [199,204] and distances of 2.352-2.717 Å at ambient conditions [201–203]. The average coordination environment of Ca is higher than that found for Mg in agreement with its lower field strength (Z/d^2).

The Mg coordination number implies the possibility of Mg^{2+} tetrahedral and octahedral configurations and a random mixing of $CaSiO_3$ and $MgSiO_3$. When the cations Mg^{2+} and Ca^{2+} are mixed, the cation distribution and ordering in the glass network originates from their ionic radius and charge. As these two cations have the same charge, upon MgO/CaO substitution there is no need to have significant charge redistribution in the glass structure and small network modifications can accommodate the differences in ionic radii and the distribution of the two cations in different sites.

Figure 6-17 shows the $D_N(r)$ functions for $CaSiO_3$ and $MgSiO_3$ glasses taken from Salmon et al [179]. The O-O peak at $\approx$ 2.6 Å is more prominent with a well-defined minimum in $MgSiO_3$ whereas in $CaSiO_3$ this peak is smaller and has a shoulder at $\approx$ 2.38 Å due to Ca-O correlations. Salmon et al [179] calculated the fractions of M-BO versus M-NBO bonds in $MSiO_3$ glasses obtained from (MD) simulations where M is either Mg or Ca. The results (Table 6.12) show that the proportion of BO around Ca is higher than for Mg indicating a preferential association of Ca with BO. The same trend was found for the $Mg_xSiO_3Ca_{1-x}$ glasses using Reverse Monte Carlo (RMC) modelling [211]. This was attributed to the lower field strength of Ca compared to Mg and thus its lower ability to charge-balance the negative charge around NBO sites. Mg(IV) species imply strong bonds and, thereby a BO atom that is connected to two SiO_4 and one MgO_4 would be over-bonded. Therefore, the oxygen connecting Mg to Si is preferentially a NBO atom. Ca^{2+} may also help convert Mg(IV) to Mg(V) sites. The high proportion of Ca-BO bonds may be explained by Ca atoms partly residing in more polymerized silicate-rich regions. Also, the distortion in the Ca polyhedra sites reflects the structural behaviour of oxygen. Some oxygens are in non-bridging sites and they connect directly the modifier to the network. The oxygens which occupy bridging sites in the network are weakly bonded to a modifier as shown in [213].

The connection of cations with the silicate network can be further probed from the Si-Mg and Si-Ca peak positions. In the Si-Mg correlations, a peak at 3.2 Å indicate corner-sharing polyhedra from EPSR studies [205]. Two distinct peaks are observed in the Ca-Si at 2.95 Å and 3.50 Å that are assigned to edge- and corner-sharing connectivity between SiO_4 tetrahedra and Ca polyhedra, respectively [214] with dominantly corner-sharing linkages.

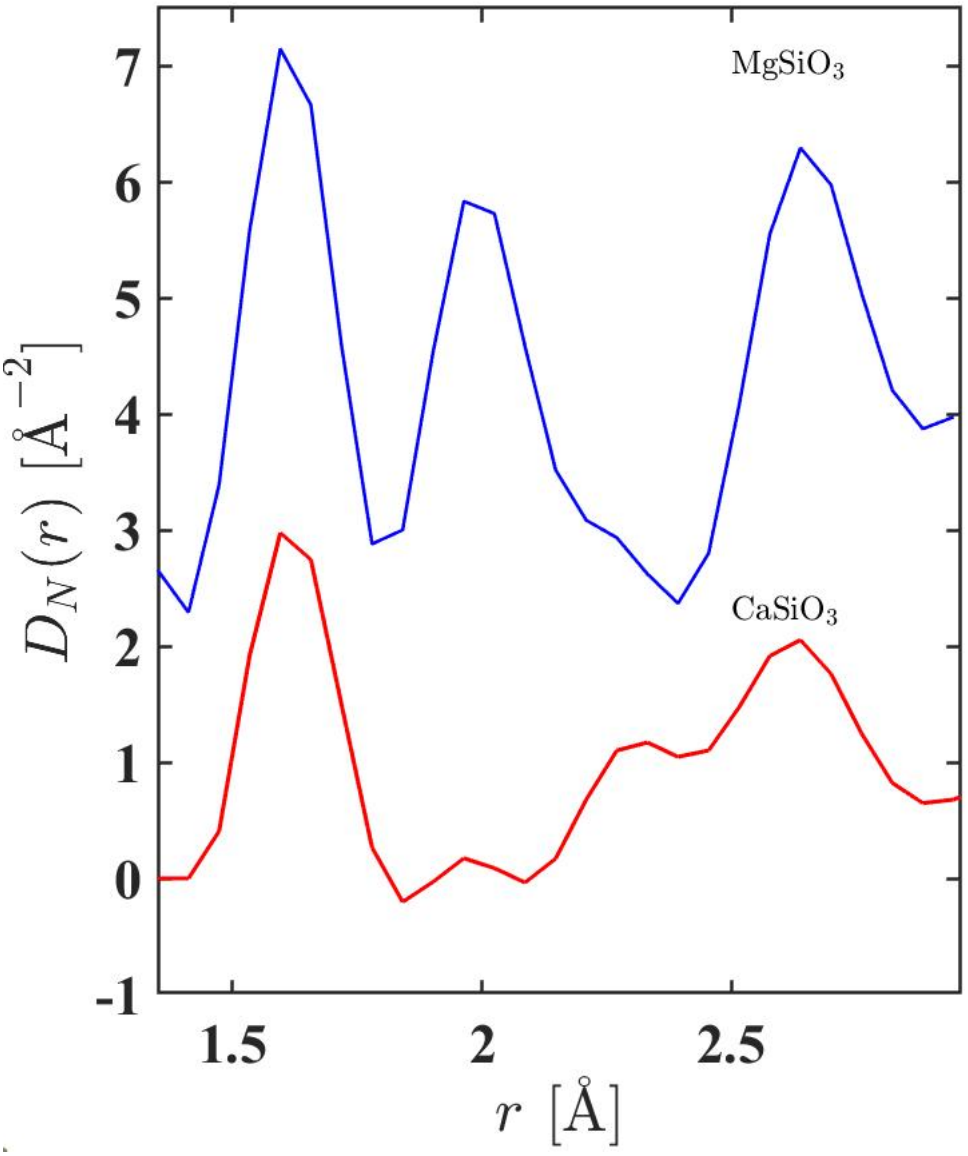

Figure 6-17: $D_N(r)$ functions for $MgSiO_3$ (blue) and $CaSiO_3$ (red) glasses taken from Salmon et al [179].

Sample	Ca-BO	Mg-BO	Ca-NBO	Mg-NBO	Reference
$MgSiO_3$	-	8.0(6)	-	91.5(6)	[179]
$CaSiO_3$	15.1(6)	-	84.8(9)	-	[179]
1.5CaO-0.5MgO-$2SiO_2$	15.8	7.2	84.2	92.8	[211]
0.5CaO-1.5MgO-$2SiO_2$	17.4	7.6	82.6	92.4	[211]

Table 6.12: The fractions of M-BO and M-NBO bonds on the $MgSiO_3$-$CaSiO_3$ join measured by MD simulations and RMC modelling.

Additionally, the entropy of mixing found from viscosity measurements on the pyroxene system $CaSiO_3$-$MgSiO_3$ in which Ca^{2+} was systematically replaced by Mg^{2+} is consistent with an ideal mixing hypothesis for these cations [215]. Likewise, the entropy of mixing found from viscosity measurements on the garnet system $Ca_3Al_2Si_3O_{12}$-$Mg_3Al_2Si_3O_{12}$ or the anorthite system $CaAl_2Si_2O_8$-$MgAl_2Si_2O_8$ in which Ca^{2+} was systematically replaced by Mg^{2+} is again consistent with an ideal mixing hypothesis for these cations [215, 216].

6.5 Conclusion

NDIS and XRD experiments were employed to investigate the structure of glassy $CaMgSi_2O_6$, with the experimental data fitted to determine the coordination environment of Mg and Ca in diopside glass. NDIS helps constrain the Mg-O coordination environment for the total $D_N(r)$ and $D_X(r)$ functions, while XRD helps constrain the Ca-O coordination environment and position due to the sensitivity of the radiation to elements with high atomic number.

The diffraction results show that the Mg and Ca cations have different environments. In particular, distinct local sites and their mixing may hold additional configurational entropies in order to accommodate the two specific environments. Mg^{2+} cations in the diopside glass are in smaller sites than in the corresponding pyroxene where they are 6-fold coordinated. Mg atoms are able to adopt diverse environments such as fourfold, fivefold and sixfold coordinated in glasses. Meanwhile, Ca is 8-fold coordinated in crystalline diopside but Ca(V), Ca(VI) and Ca(VII) species can also be present in the more disordered structures. This reflects the smaller size of Mg versus Ca and the significant intermixing of Ca^{2+} and Mg^{2+} ions in the glass network.

A Mg-O coordination number of $\bar{n}^{O}_{Mg} = 4.40(4)$ was found for $CaMgSi_2O_6$ in the present diffraction work. The Ca-O coordination number obtained from XRD is $\bar{n}^{O}_{Ca} = 5.01(13)$ for the isotopic glass and $\bar{n}^{O}_{Ca} = 5.06(12)$ for the natural glass. The errors on $\bar{n}^{O}_{Ca}$ take into account the overlap between the nearest neighbor Ca-O and O-O correlations. The coordination environment of magnesium tells us that it acts as a network modifier. Calcium also plays the role of a network modifier, having polyhedral Ca sites in the glass network.

Therefore, the ND and XRD results for the isotopic and natural diopside glass are consistent with network structures within tetrahedral SiO_4 units where Ca and Mg reside in a sub-octahedral coordination environments.

It would be helpful to have molecular dynamic simulations on both glasses to help interpret the network connectivity. An interesting next step would be to analyse isotopic and natural $CaMgSi_2O_6$ at higher pressures in similar conditions to where the mineral diopside is found in the Earth's mantle. Another suggestion for further work is investigating a various range of compositions along the $CaSiO_3$-$MgSiO_3$ joint to deeply understand the role of Ca^{2+} and Mg^{2+}. Diffraction techniques such as NDIS are important to isolate Mg-O and prevent overlap between Mg-O and Ca-O correlations for studying these different compositions.

Chapter 7

The NASICON system $\mathbf{Na_{1+x}Al_xGe_{2-x}(PO_4)_3}$

7.1 Introduction

The mechanisms and kinetics of crystal nucleation in glass-forming systems are vital for understanding the glass-forming ability of super-cooled liquids and the stability of glass against unwanted crystallization during fabrication or use. An example of these materials is the NASICON (Na Super Ionic Conductor) family which are known to have high ionic conductivity. The molecular formula of a NASICON is $A_xM_2(XO_4)_3$ where A is a monovalent cation (Na^+, Li^+, K^+), M is a tetravalent cation such as Ti^{4+} or Ge^{4+} and X can either be P^{5+} or Si^{4+}. The NASICON structure can be described as an arrangement of MO_6 octahedra linked by corners to XO_4 tetrahedra. There is therefore, a three dimensional $M_2(XO_4)_3$ arrangement with channels where A ions can easily move leading to very high ionic conductivities.

An example of these NASICON materials is the crystalline $NaGe_2(PO_4)_3$, where a negatively charged 3D framework of corner-sharing tetrahedral PO_4 and octahedral GeO_6 units (Figure 7-1) forms cavities in which the Na^+ ions reside [217]. It becomes fast ion conducting when a proportion of the Ge^{4+} cations are aliovalently substituted by Al^{3+}, and additional Na^+ enters interstitial sites to compensate for the charge deficit [218].

The initial work on the NASICON materials focused on pressed powders. However, it was discovered that they can also be prepared via the glass-ceramic route giving the significant advantage of moldable bulk materials [219]. The lithium analogues of these

materials nucleate internally and have already found commercial usage as separator membranes in lithium-air batteries and related systems [220–222].

Nucleation in the glass forming system can occur on the glass surface or internally. The control of nucleation to create a uniform distribution of crystallites of controllable size and shape throughout the bulk material is important for the production of glass ceramics that have uses ranging from cookwares to missile nose-cones [223]. For glass-forming silicates that show internal nucleation, macroscopic material properties such as the density, configurational entropy and frozen-in birefringence, suggest that the glass structure has a close resemblance to the phase formed on crystallization. The structure of $Na_{1+x}Ge_{2-x}Al_x(PO_4)_3$ materials (NAGP) with x=0, 0.4 or 0.8 was investigated using high real-space resolution neutron (ND) and X-ray diffraction (XRD). The aim was to understand the structural relationship between an ion-conducting glass ceramic and its precursor glass and to monitor the structural rearrangements that occur due to heat treatment near the glass transition temperature, T_g. The $x = 0$ composition will provide a reference for the Ge coordination. The $x = 0.4$ and 0.8 glasses will give information on how the local environment of Ge changes in the glassy precursor as Ge is replaced by Al and Na. Fast-sodium ion conductivity occurs in the crystalline materials with x=0.4 and 0.8 and originates from the incorporation of additional sodium ions into interstitial sites, as Al^{3+} replaces Ge^{4+} within the lattice. These solid electrolyte materials are best prepared by the glass-ceramics route, which indicates an internal nucleation mechanism [218, 224].

7.2 Experiment

7.2.1 Sample Preparation

The $Na_{1+x}Al_xGe_{2-x}(PO_4)_3$ glasses were made by mixing powders of Na_2CO_3 (Vetec, 99.5%), GeO_2 (Aldrich, 99.9%), Al_2O_3 (Aldrich, 99.9%) and $N_2H_9PO_4$ (Aldrich, 98%). The samples were first heated in a platinum crucible at 400 °C and 700 °C for 2 h and 4 h, respectively so Na_2CO_3 and $(NH_4)_2HPO_4$ will decompose. Then the temperature was raised to 1200 °C for 30 min to allow the complete melting. After being taken from the furnace, the melts were splat-cooled between stainless steel plates. The glasses were then broken and remelted for an additional 30 min at 1200 °C for better homogenization [218]. For each composition, part of the glass was kept in its as-prepared condition, part was annealed at a thermal treatment temperature T_{TT} near to T_{g} for a time chosen to relax the glass structure while minimizing the formation of crystallites, and part was annealed at T_{TT} for a time chosen to fully crystallize the material.

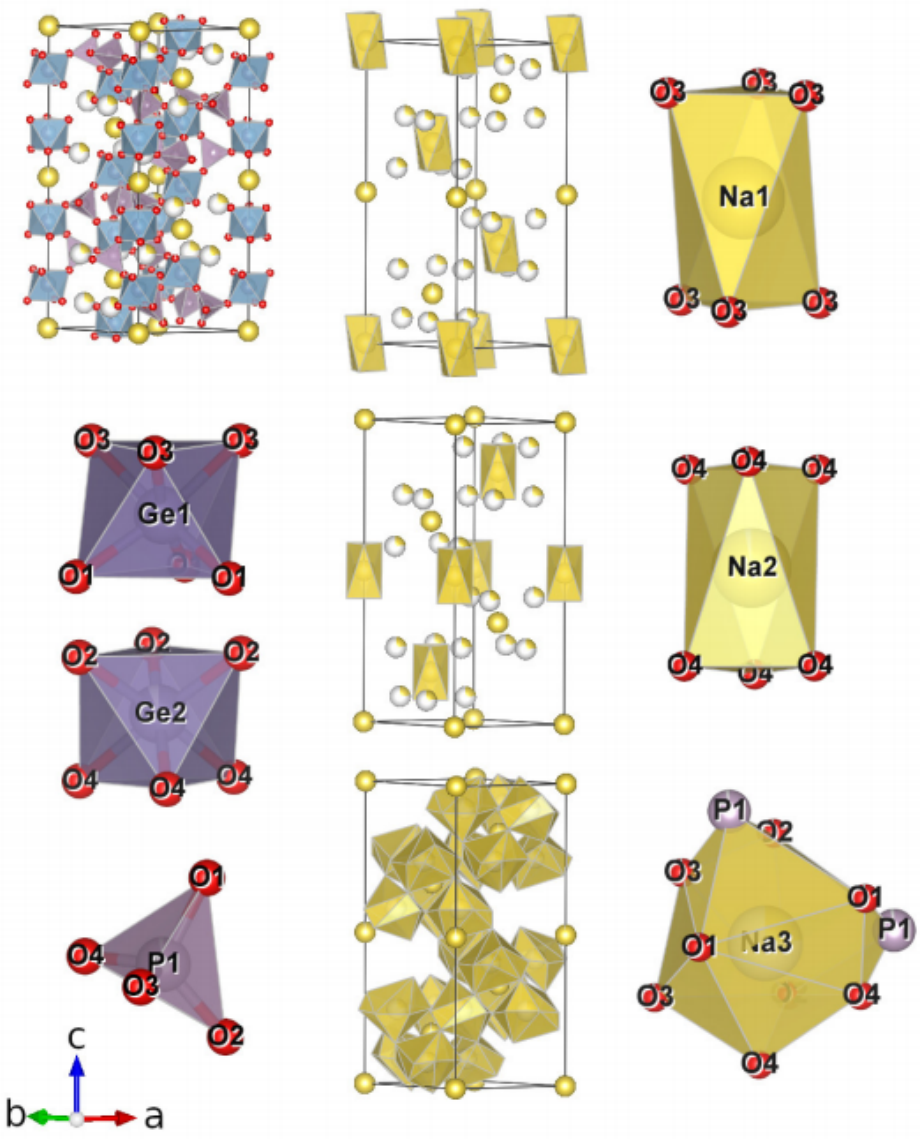

Figure 7-1: The R$\bar{3}$-type for the $NaGe_2(PO_4)_3$ crystal structure. The GeO_6 octahedra and PO_4 tetrahedra are shown bottom left and the sodium centered polyhedra are shown on the right. The positions of the different sodium centered polyhedra in the unit cell are shown in the center [225].

x	Na_2O [mol%]	Al_2O_3 [mol%]	GeO_2 [mol%]	P_2O_5 [mol%]
0	12.5	0.0	50.0	37.5
0.4	17.5	5.0	40.0	37.5
0.8	22.5	10.0	30.0	37.5

Table 7.1: Concentration of Na_2O, Al_2O_3, GeO_2 and P_2O_5 for the NAGP materials with $x = 0$, $x = 0.4$ and $x = 0.8$.

x	T_g [K]	ρ [g/cm^3]	n_0[Å^{-3}]
0	881(2)	3.2619(5)	0.07802(1)
0.4	845(2)	3.1006(5)	0.07736(1)
0.8	813(2)	2.9634(8)	0.07712(2)

Table 7.2: Parameters describing the glass transition temperature T_g, mass density ρ and corresponding number density n_0 for the as-prepared $Na_{1+x}Al_xGe_{2-x}(PO_4)_3$ glasses.

For the $x = 0$ composition, two additional parts of the as-prepared glass were taken for further investigation. One part was annealed at $T_{TT} = 873$ K for $t = 0.25$ h, and the other part was annealed at $T_{TT} = 876$ K for $t = 0.25$ h and $t = 0.5$ h. For the composition $x = 0.4$, one part of the as-prepared glass was annealed at $T_{TT} = 835$ K for $t = 2$ h and $t = 4$ h. The other part was annealed at $T_{TT} = 845$ K for $t = 2$ h and $t = 4$ h. For the composition $x = 0.8$ one part of the as-prepared glass was annealed at $T_{TT} = 810$ K for $t = 20$ h and the other part was annealed at $T_{TT} = 808$ K for $t = 30$ h.

The glass transition temperature T_g and crystallization temperatures T_x were measured for ∼20 mg monolithic samples using a differential scanning calorimeter (Netzsch DSC404) with a heating rate of 10 K/min. The mass densities of the as-prepared and annealed glasses was measured using a Quantachrome 1200e pycnometer operated with He gas. The density of the crystals was taken from the powder diffraction work [225]. Parameters describing the samples and their thermal history are listed in Tables 7.2, 7.3 and 7.4.

x	t_{cryst} [h]	ρ [g/cm^3]	n_0 [Å^{-3}]	T_{melt} [K]
0	17	3.659	0.08752	>1523
0.4	17	3.513	0.08753	1458(3)
0.8	55	3.385	0.08809	1362(3)

Table 7.3: Thermal treatment time t_{cryst} used to crystallize the as-prepared glass, mass density ρ and corresponding number density n_0 of the crystalline phase and melting point temperature T_{melt}. Densities were determined by crystallography.

x	T_x [K]	T_{TT} [K]	t_{anneal} [h]	T_g [K]	ρ [g/cm^3]	n_0 [Å^{-3}]
0	926(2)	873(1)	0.25	886(2)	3.3073(8)	0.07911(2)
		876(1)	0.25		3.3044(9)	0.07904(2)
		876(1)	0.5		3.3383(10)	0.07985(2)
0.4	905(2)	835(1)	2	851(2)	3.1640(10)	0.07894(2)
		835(1)	4		3.1635(7)	0.07895(2)
		845(1)	2		3.1498(6)	0.07859(2)
		845(1)	4		3.1515(17)	0.07865(4)
0.8	896(2)	808(1)	30	810(2)	3.0098(6)	0.07833(2)
		810(1)	20		3.0081(7)	0.07828(2)

Table 7.4: Crystallization temperature T_x and thermal treatment temperature T_{TT}, time t_{anneal} used to prepare the annealed glass from the as-prepared glass, glass transition temperature T_g, mass density ρ and corresponding number density n_0 for the annealed NAGP glasses.

7.2.2 D4c Experiment

A neutron diffraction experiment was carried out using the D4c diffractometer at the Institut Laue-Langevin in Grenoble with an incident neutron wavelength of $\lambda = 0.4955(1)$ Å. The powdered glasses were held in a cylindrical vanadium container of inner diameter 6.8 mm and wall thickness 0.1 mm. Diffraction patterns were measured at room temperature ($\simeq$ 298K) for each sample, an empty can, the empty instrument and a cylindrical vanadium rod of diameter 6.08 mm for normalization purposes.

A diffraction pattern was also measured for a slab of neutron absorbing $^{10}B_4C$ in order to estimate the effect of the sample's attenuation on the background count rate at small scattering angles. The counting times for the empty container and the sample in the container were optimized to decrease the statistical error on the container-corrected intensity [101].

7.2.3 6-ID-D Experiment

The high energy X-ray diffraction experiment on $Na_{1+x}Al_xGe_{2-x}(PO_4)_3$ was done at room temperature using the 6-ID-D diffractometer at the APS. The photon energy of the square incident beam was 80.02 keV, corresponding to a wavelength of 0.155 Å. The ground glasses were loaded into kapton polyimide tubes of 1.80(1) mm internal diameter and 0.051(6) mm wall thickness.

The scattered X-rays were detected using a Varex 4343CT amorphous silicon flat panel detector which was placed at a distance of 271.93(6) mm from the sample position as deduced from the diffraction pattern measured for crystalline CeO_2. Diffraction patterns were measured for each sample in its capillary, an empty capillary and the empty instrument. The data were converted to one-dimensional diffraction patterns using FIT2D [84]. The program PDFgetX2 [85] was used for corrections for background scattering, beam polarization, attenuation and Compton scattering.

7.3 Results

Figures 7-2, 7-3 and 7-4 show the differences in weighting factors between X-rays and neutrons for the compositions $x = 0$, $x = 0.4$ and $x = 0.8$. From the graph bars it is inferred that correlations involving Ge will be more perceptive to X-rays whereas O-O correlations are more sensitive to neutrons.

The crystalline NAGP samples were previously studied by NMR and Rietveld refinement [218, 225] and the results are shown in figures 7-5 and listed in table 7.5. ^{27}Al MAS NMR experiments on the as-prepared and annealed glasses showed that Al exists in a mixture of AlO_4, AlO_5 and AlO_6 (Figure 7-5). For the crystalline NAGP the NMR results show a predominant presence of AlO_6 sites. For the annealed glasses with $x = 0.4$ and $x = 0.8$, there was no significant change on the AlO coordination environment when the time of annealing increased. The structure factors, $S(Q)$, measured by neutron and X-ray diffraction are shown in figures 7-6, 7-7, 7-8, 7-15 and 7-16. For the annealed glasses, the XRD patterns indicate a small amount of crystalline material for the $x = 0$ and $x = 0.8$ samples that is not observed using ND. This may originate from the differences between the Q space resolution of the diffractometers.

Figures 7-19, 7-20 and 7-21 show the $D(r)$ functions for the crystalline NAGP with $x = 0$, $x = 0.4$ and $x = 0.8$, respectively. For the composition $x = 0$, the first peak at 1.52 Å and the second peak at 1.86 Å originate from P-O and Ge-O correlations, respectively and the third peak has contributions from Na-O and O-O correlations. A single peak was used to represent the P-O correlations. A single peak was also used to represent the Ge-O correlations in the ND work, whereas two peaks were used to represent these correlations in the XRD work because of the large atomic number of Ge (Z = 32) which makes the results particularly sensitive to the germanium coordination environment. For the Na-O correlations, a single peak was fitted with the coordination number fixed to the value found from crystallography [225]. Two peaks were fitted for the O-O correlations because each BO is shared between a PO_4 tetrahedron and a GeO_6 octahedron. The coordination numbers were fixed at $\bar{n}^{O}_{O} = 3$ and $\bar{n}^{O}_{O} = 4$ according to crystallography.

For the as-prepared glass, the ND and XRD data sets were fitted using two Gaussian peaks to represent P-O correlations and one Gaussian peak to represent Ge-O correlations. Additional peaks at larger r (Na-O and O-O correlations) were used to constrain the fits at lower r and coordination numbers were fixed according to crystallography. The results gave a P-O coordination number $\bar{n}^{O}_{P} \approx 4$ and an average Ge-O coordination number $\bar{n}^{O}_{Ge} \sim 5$, smaller than the value 6 found from the crystalline phase.

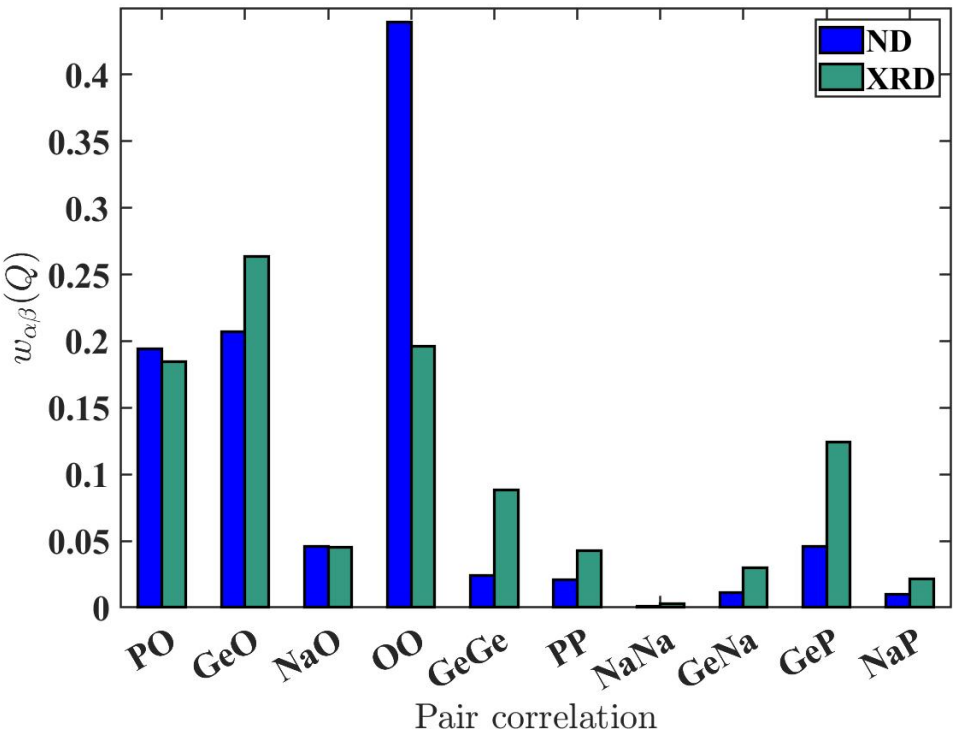

Figure 7-2: The weighting factors $w_{\alpha\beta}(Q)$ of the partial pair distribution functions for the neutron diffraction (ND) versus X-ray diffraction (XRD) experiments on the NAGP glasses with $x = 0$. The X-ray values were calculated for $Q = 0$.

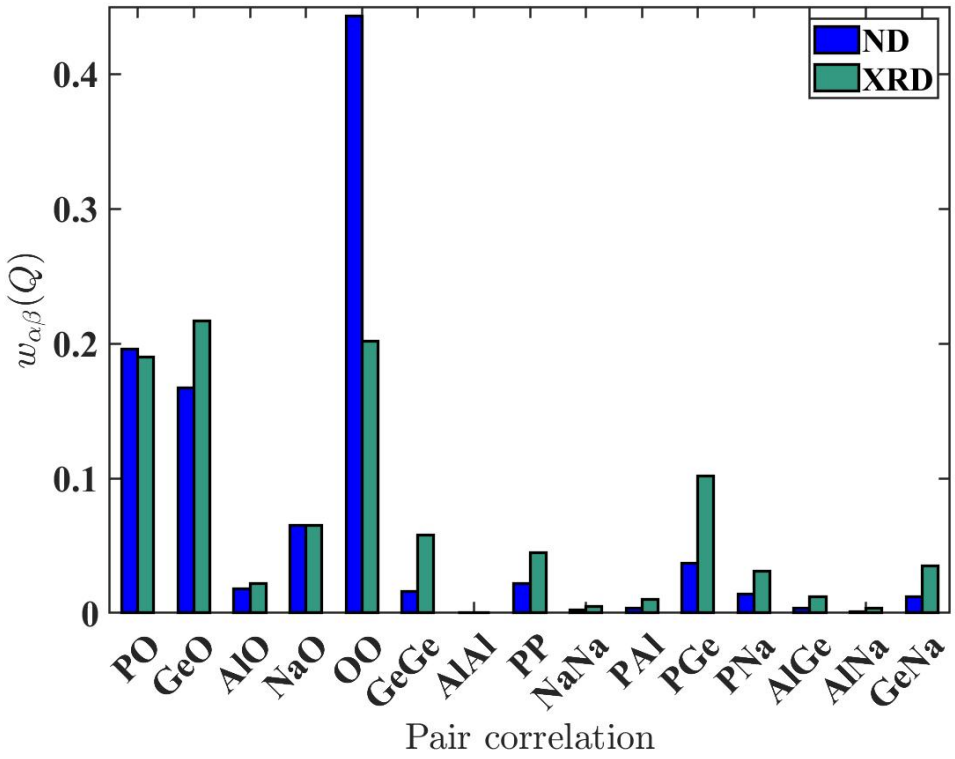

Figure 7-3: The weighting factors $w_{\alpha\beta}(Q)$ of the partial pair distribution functions for the neutron diffraction (ND) versus X-ray diffraction (XRD) experiments on the NAGP glasses with $x = 0.4$. The X-ray values were calculated for $Q = 0$.

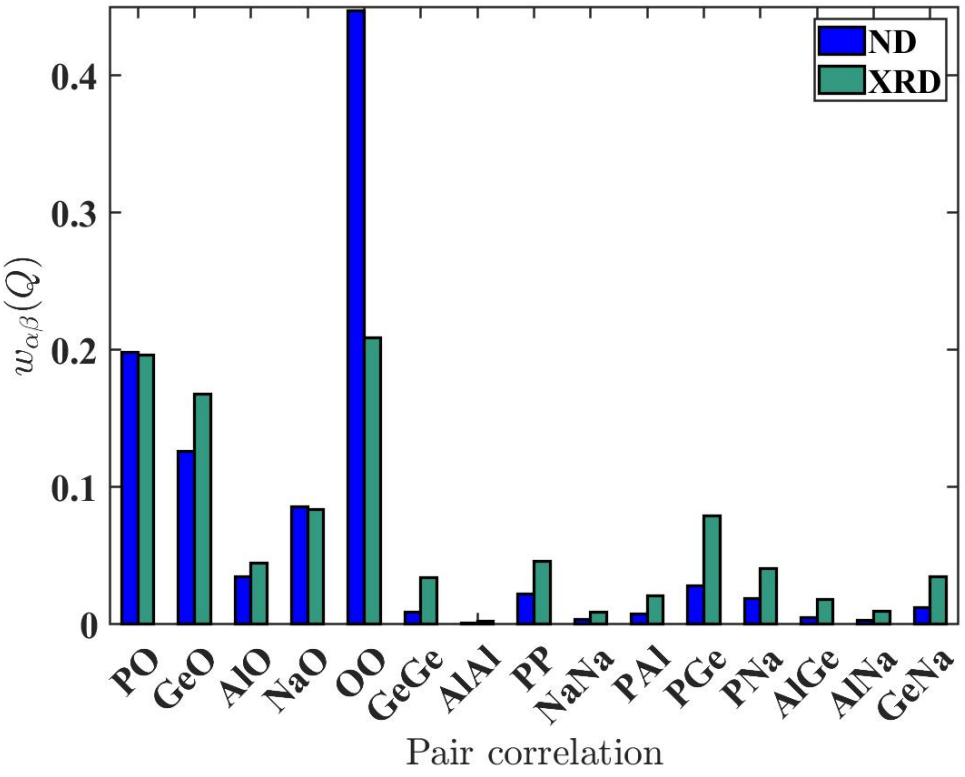

Figure 7-4: The weighting factors $w_{\alpha\beta}(Q)$ of the partial pair distribution functions for the neutron diffraction (ND) versus X-ray diffraction (XRD) experiments on the NAGP glasses with $x = 0.8$. The X-ray values were calculated for $Q = 0$.

x	Condition	T_{TT} [K]	t [h]	Al(IV) [%]	Al(V) [%]	Al(VI) [%]	$\bar{n}^{\mathrm{O}}_{\mathrm{Al}}$
	as-prepared	-	-	37.2	39.8	23.0	4.86(6)
	annealed	835(1)	2	33	33	34	5.01(6)
0.4	annealed	835(1)	4	34	33	33	4.99(6)
	annealed	845(1)	2	32.9	37.9	27.7	4.96(6)
	annealed	845(1)	4	34	32	34	5.00(6)
	crystal	-	-	2.5	11.5	86.1	5.84(8)
	as-prepared	-	-	39.6	35.7	24.3	4.85(6)
0.8	annealed	810(1)	20	36.4	33.0	30.6	4.94(6)
	annealed	808(1)	30	36	32	32	4.96(6)
	crystal	-	-	10.5	6.4	83.1	5.73(8)

Table 7.5: The Al speciation in NAGP with $x = 0.4$ and $x = 0.8$ found from ^{27}Al MAS NMR experiments. The mean Al-O coordination number is also given. The error on the fraction of Al in a fourfold, fivefold or sixfold coordination environment is $\pm 2\%$ [225].

The fits of the as-prepared glasses were used as starting parameters for fitting the annealed glasses. The results do not show a change in $\bar{n}^{\mathrm{O}}_{\mathrm{P}}$, but $\bar{n}^{\mathrm{O}}_{\mathrm{Ge}}$ increased. It was not possible to see a significant change in Ge-O coordination number with different time or temperature of annealing between the annealed glasses with same composition.

For the compositions with $x > 0$ the $D_N(r)$ and $D_X(r)$ functions for crystalline and glassy NAGP are shown in figures 7-12, 7-13, 7-14, 7-19, 7-20 and 7-21. The first peak at $\simeq 1.52$ Å is attributed to P-O correlations but the second peak at $\simeq 1.86$ Å will have contributions both from Ge-O and Al-O. The parameters describing the Gaussian peaks for the Al-O correlations were constrained using the information obtained from ^{27}Al MAS NMR. The third peak was treated in the same way as for the crystalline NAGP with $x = 0$, i.e, two O-O peaks set to $\bar{n}^{\mathrm{O}}_{\mathrm{O}} = 3$ and $\bar{n}^{\mathrm{O}} = 4$ found from Rietveld refinements [225].

In the $D(r)$ fits for the glassy materials, three Gaussian peaks were used to represent Al-O correlations for 4-, 5- and 6-fold coordinated aluminium atoms. The peak positions for 4- and 5-fold coordinated aluminium atoms were set to 1.76 Å and 1.84 Å, respectively, which are the Al-O bond lengths calculated using the bond valence method [226]. The position of the peak for sixfold coordinated aluminium atoms was set to the average Al-O bond length of 1.86 Å found from the X-rays. The width of the Gaussian peak describing AlO_4 units was set to 0.05 Å which is a typical value for AlO_4 units in alumino-phosphate glasses [227] and the width of the Gaussian peak describing AlO_6 units was set to 0.07 Å. The width of the Gaussian peak describing AlO_5 units was set in between these values to 0.06 Å.

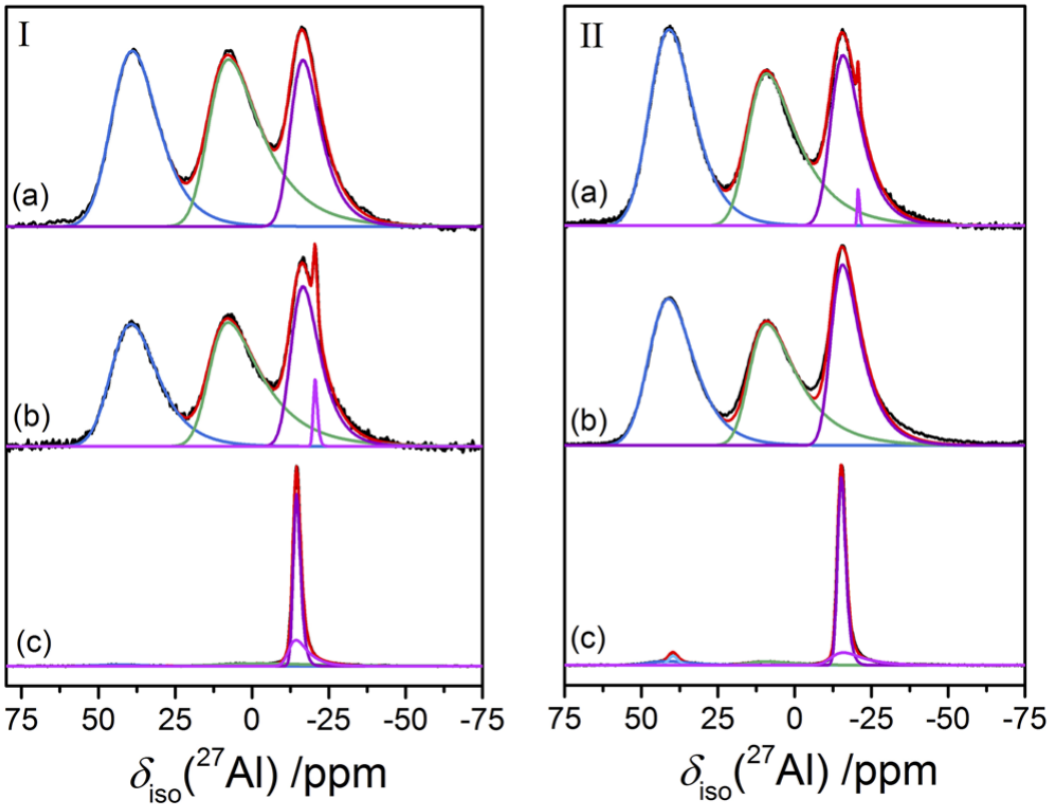

Figure 7-5: The single-pulse ^{27}Al MAS NMR spectra (black curves) measured for (a) as-prepared glassy, (b) annealed glassy and (c) crystalline NAGP with (I) $x = 0.4$ or (II) $x = 0.8$. The Czjzek fits to the spectral components are given for Al(IV) (blue), Al(V) (green) and Al(VI) (magenta). The sum of the fitted functions is given by the red curve.

x	Condition	Q_{FSDP}	Q_{PP}	Q_3	Q_{max}
0	as-prepared	1.806(1)	3.135(1)	5.326(2)	23.40
	annelead at 873 K for 0.25 h	1.803(1)	3.143(1)	5.341(2)	22.95
	annealed at 876 K for 0.25h	1.836(1)	3.145(1)	5.337(2)	23.60
	annealed at 876 K for 0.5h	1.783(1)	3.176(1)	5.398(2)	23.70
0.4	as-prepared	1.818(1)	3.076(1)	5.335(2)	23.10
	annealed at 835 K for 2h	1.851(1)	3.088(1)	5.341(2)	22.80
	annealed at 835 K for 4h	1.849(1)	3.097(1)	5.337(2)	23.15
	annealed at 845 K for 2h	1.857(1)	3.075(1)	5.407(2)	22.95
	annealed at 845 K for 4h	1.804(1)	3.131(1)	5.324(2)	23.70
0.8	as-prepared	1.843(1)	3.03(1)	5.343(2)	22.90
	annealed at 810 K for 20h	1.860(1)	3.053(1)	5.342(2)	23.60
	annealed at 808 K for 30h	1.848(1)	3.055(1)	5.322(2)	23.25

Table 7.6: The positions (in $\mathrm{Å}^{-1}$) of the first three peaks Q_{FSDP}, Q_{PP} and Q_3 in the $S_N(Q)$ functions. Also given are the $\mathrm{Q_{max}}$ values used for the Fourier transformation.

7.3.1 Neutron Difraction

The positions of the first three peaks in the $S_N(Q)$ functions are listed in table 7.6 and the weighting factors for the partial pair distribution functions $g_{\mathrm{PO}}(r)$, $g_{\mathrm{AlO}}(r)$, $g_{\mathrm{GeO}}(r)$, $g_{\mathrm{NaO}}(r)$ and $g_{\mathrm{OO}}(r)$ are given in table 7.7. For the annealed glasses with $x = 0.4$ and $x = 0.8$, the differences in the $S_N(Q)$ functions are very small when the annealing time is increased (maintaining the same T_{TT}) and the coordination environment of Ge-O showed differences $\approx 10\%$.

The total pair distribution functions $D_N(r)$ are shown in figures 7-9, 7-10 and 7-11. The first two peaks in $D_N(r)$ correspond to P-O, Al-O and Ge-O correlations. Although Na-O correlations are expected at $r \approx 2.5$ Å, the large neutron scattering length and atomic concentration of O in NAGP makes the O-O correlations dominate the third peak. The $D_N(r)$ fits are shown in figures 7-12, 7-13 and 7-14. Their respective fitted parameters are listed in tables 7.8, 7.9, 7.10 and 7.11.

For the as-prepared glasses, the results give a coordination number of $\bar{n}^{\mathrm{O}}_{\mathrm{P}} = 4.00(3)$ and $\bar{n}^{\mathrm{O}}_{\mathrm{P}} = 4.01(3)$ for $x = 0.4$ and $x = 0.8$, respectively. For $x > 0$, a reduction in the average Ge-O coordination number is observed as more aluminium is added to the glass structure. The coordination environment of Ge is $\bar{n}^{\mathrm{O}}_{\mathrm{Ge}} = 4.94(5)$ and $\bar{n}^{\mathrm{O}}_{\mathrm{Ge}} = 4.64(5)$ for the compositions $x = 0.4$ and $x = 0.8$, respectively. The results do not show a change in the coordination environment of phosphorous. However, for the annealed glasses, the coordination number of Ge increases relative to the as-prepared glass.

x	w_{PO}	w_{AlO}	w_{GeO}	w_{NaO}	w_{OO}	$G(0)$
0	0.19432(10)	-	0.20669(4)	0.04583(2)	0.4396(3)	-0.3405(4)
0.4	0.19596(10)	0.0175667(7)	0.16675(3)	0.06471(4)	0.4433(3)	-0.3231(4)
0.8	0.19763(10)	0.035433(3)	0.12613(2)	0.08391(6)	0.4471(3)	-0.3069(4)

Table 7.7: The weighting factors (in barn) for the partial pair distribution functions of the NAGP glasses used in the $D_N(r)$ fits.

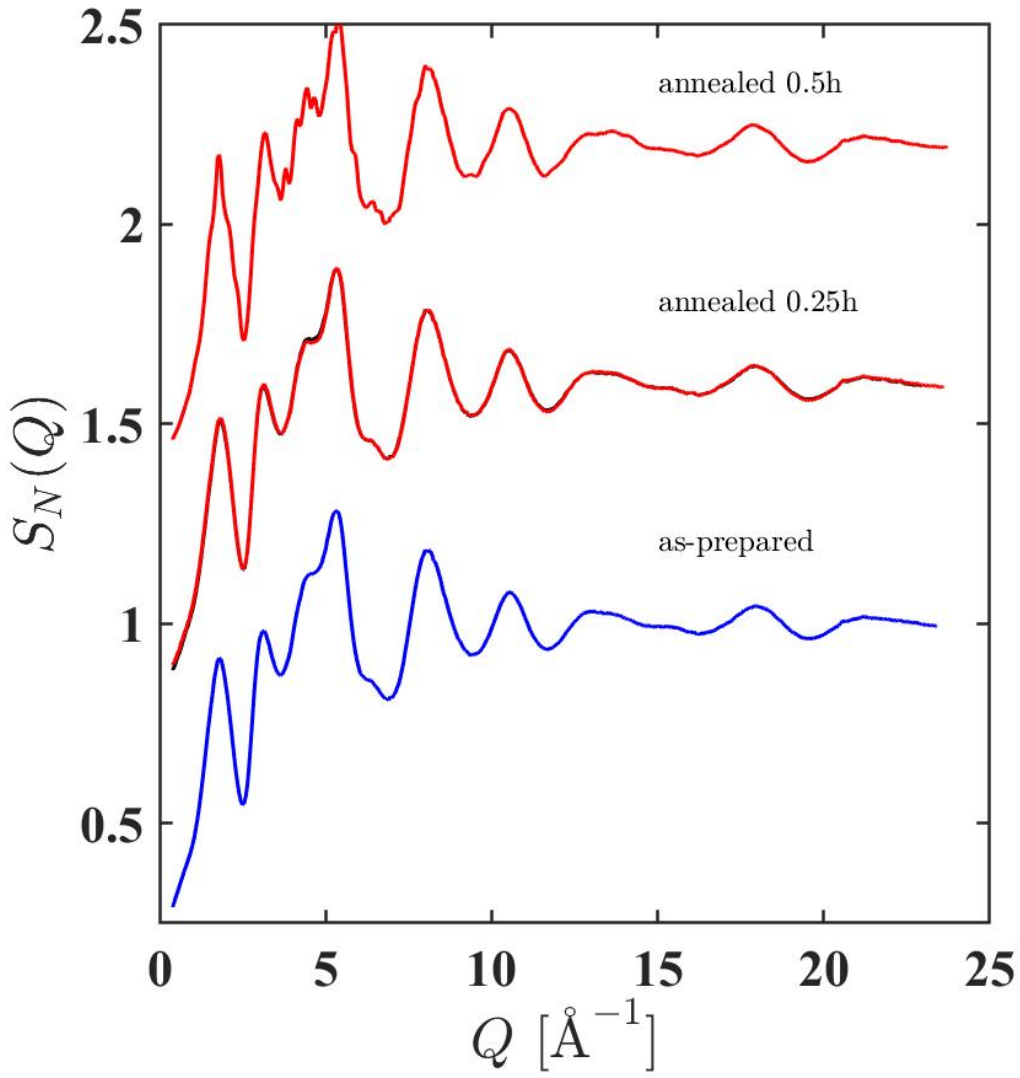

Figure 7-6: $S_N(Q)$ functions for the as-prepared (blue) and annealed (black and red) NAGP glasses with $x = 0$. For the glasses annealed for $t = 0.25$ h, the black solid curve (underneath) corresponds to $T_{\mathrm{TT}} = 873$ K and the red solid curve corresponds to $T_{\mathrm{TT}} = 876$ K. The error bars are smaller than the line thickness at most Q values. The curves are offset vertically for clarity of presentation.

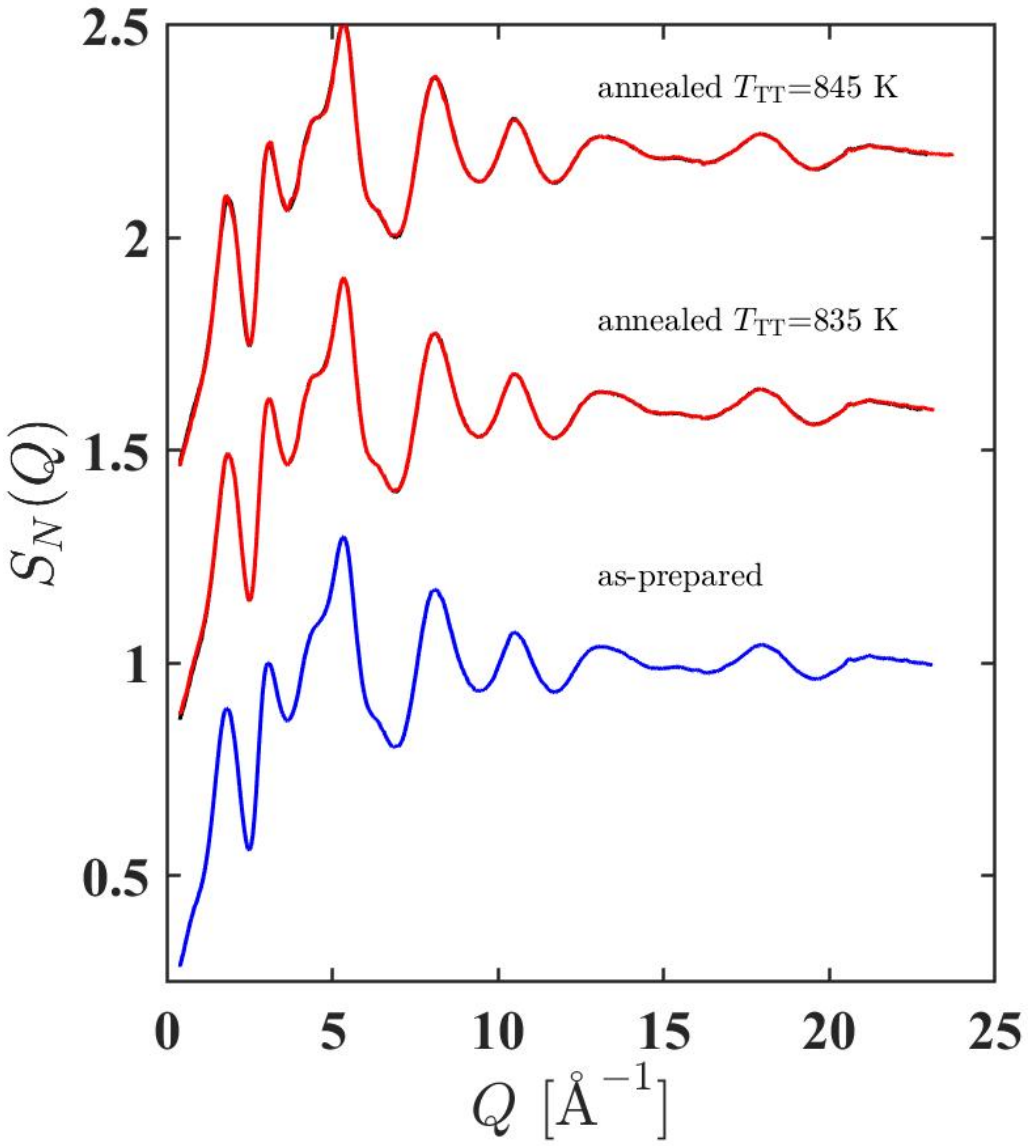

Figure 7-7: $S_N(Q)$ functions for the as-prepared (blue) and annealed (black and red curves) NAGP glasses with $x = 0.4$. For the glasses annealed at $T_{TT} = 835$ K and $T_{TT} = 845$ K, the black solid curves (underneath) corresponds to an annealing time of $t = 2$ h and the red solid curves corresponds to an annealing time of $t = 4$ h. The error bars are smaller than the line thickness at most Q values. The curves are offset vertically for clarity of presentation.

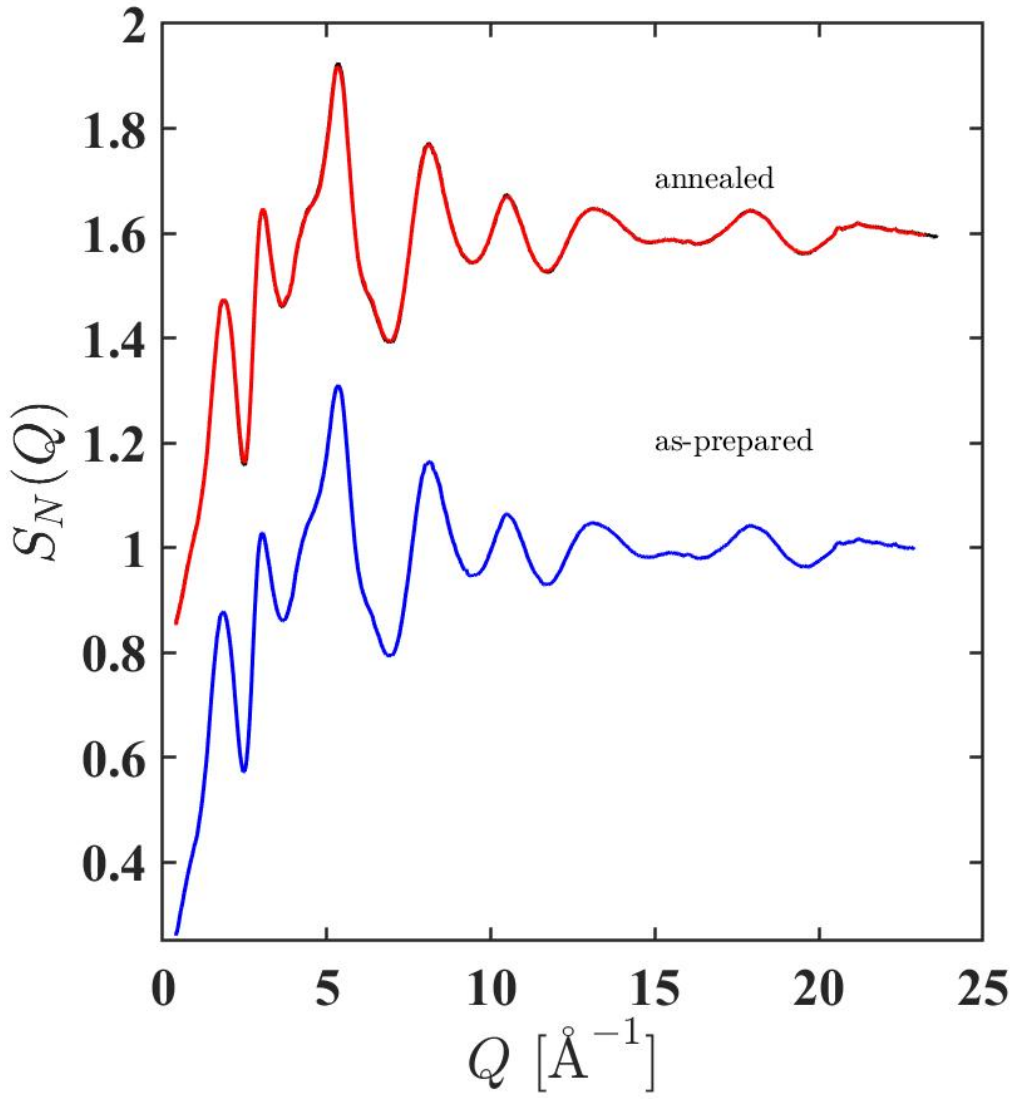

Figure 7-8: $S_N(Q)$ functions for the as-prepared (blue) and annealed (black and red) NAGP glasses with $x = 0.8$. For the annealed glasses, the black solid curve (underneath) corresponds to an annealing time of $t = 20$ h. The red solid curve represents the glass annealed for $t = 30$ h. The error bars are smaller than the line thickness at most Q values. The curves are offset vertically for clarity of presentation.

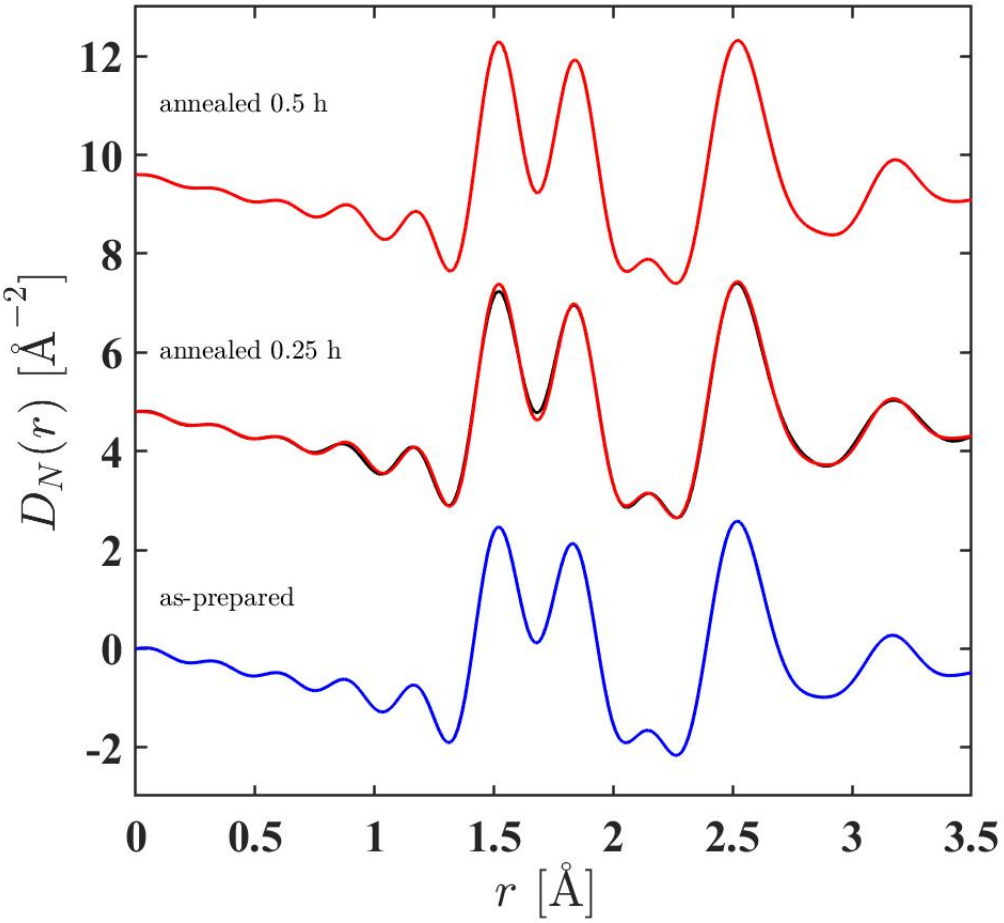

Figure 7-9: $D_N(r)$ functions for the as-prepared (blue) and annealed (red and black) NAGP glasses with $x = 0$. For the glasses annealed for $t = 0.25$ h, the black solid curve (underneath) corresponds to $T_{\mathrm{TT}} = 873$ K and the red solid curve corresponds to $T_{\mathrm{TT}} = 876$ K. The curves were obtained by Fourier transforming the corresponding reciprocal data shown in Figure 7-6 after spline fitting. The curves are offset vertically for clarity of presentation.

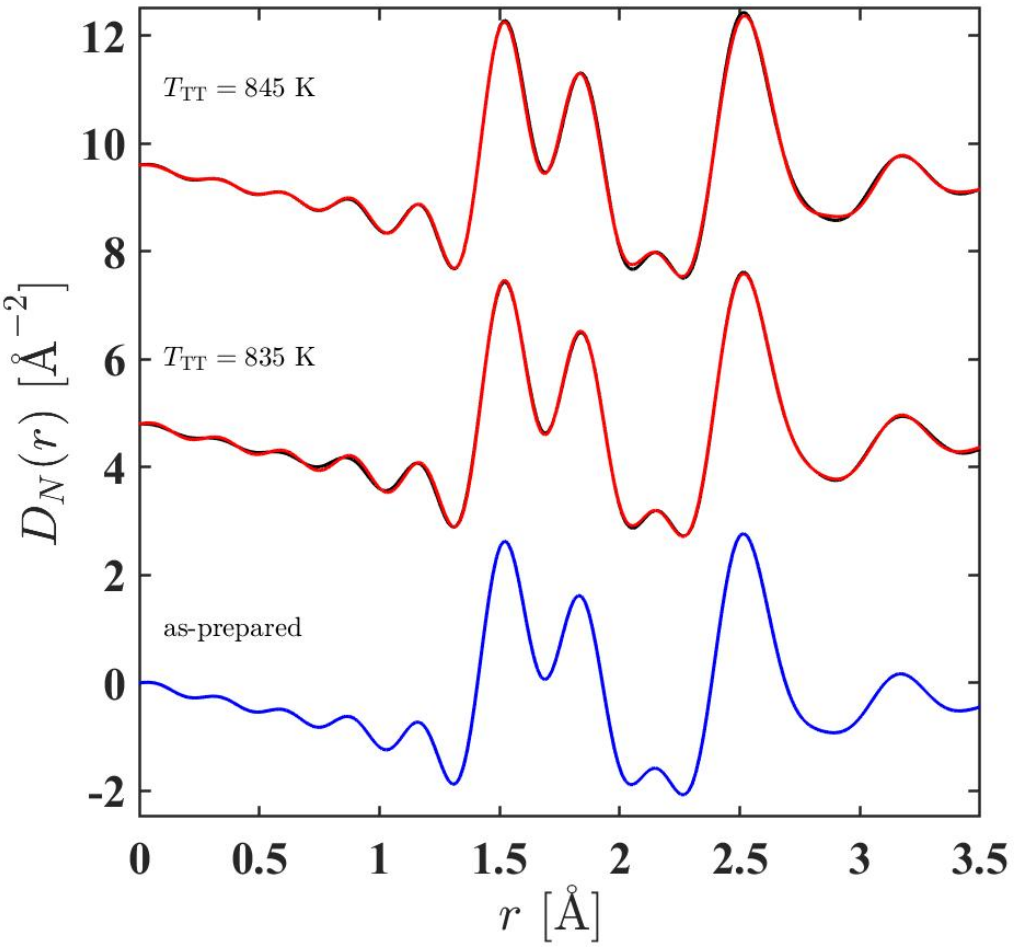

Figure 7-10: $D_N(r)$ functions for the as-prepared (blue) and annealed (red and black) NAGP glasses with $x = 0.4$. For the glasses annealed at $T_{\mathrm{TT}} = 835$ K and $T_{\mathrm{TT}} = 845$ K, the black solid curves (underneath) corresponds to an annealing time of $t = 2$ h and the red solid curves corresponds to an annealing time of $t = 4$ h. The curves were obtained by Fourier transforming the corresponding reciprocal data shown in Figure 7-7 after spline fitting. The curves are offset vertically for clarity of presentation.

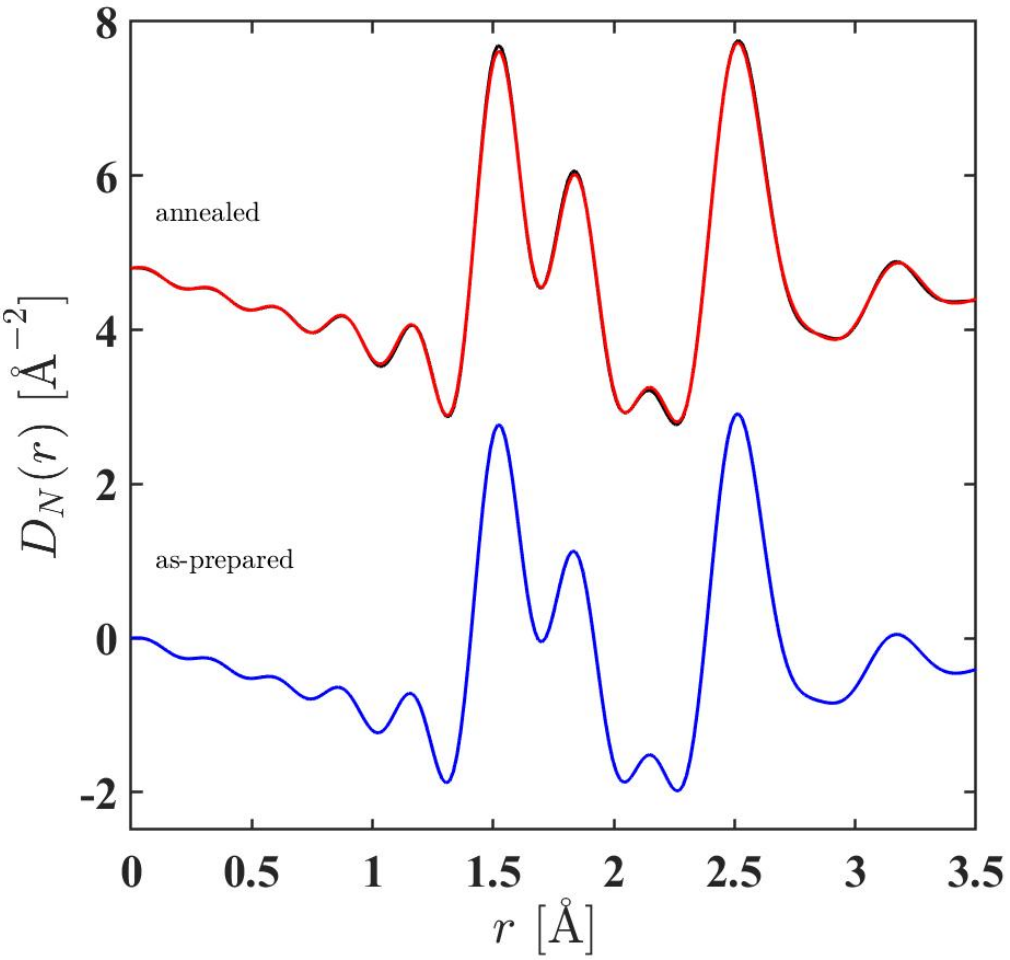

Figure 7-11: $D_N(r)$ functions for the as-prepared (blue) and annealed (red and black) NAGP glasses with $x = 0.8$. For the annealed glasses, the black solid curve (underneath) corresponds to the glass annealed for $t = 20$ h. The red solid curve represents the glass annealed for $t = 30$ h. The curves were obtained by Fourier transforming the corresponding reciprocal data shown in Figure 7-8 after spline fitting. The curves are offset vertically for clarity of presentation.

Sample	T_{TT} [K]	t [h]	Atom pair	$r_{\alpha\beta}$ [Å]	$\sigma_{\alpha\beta}$ [Å]	n_α^β	R_χ [%]
			P-O	1.501(4)	0.021(5)	2.01(2)	
			P-O	1.587(5)	0.081(5)	1.99(2)	
			P-O (sum)			4.00(3)	
As-prepared	-	-	Ge-O	1.823(5)	0.092(6)	5.12(5)	3.25
			Na-O	2.433*	0.300(9)	6*	
			O-O	2.507(5)	0.081(5)	3*	
			O-O	2.644(5)	0.150(8)	3.02(8)	
			P-O	1.507(4)	0.025(5)	2.01(2)	
			P-O	1.578(5)	0.089(6)	1.99(2)	
			P-O (sum)			4.00(3)	
Annealed	873	0.25	Ge-O	1.829(5)	0.092(6)	5.18(5)	3.57
			Na-O	2.433*	0.300(9)	6*	
			O-O	2.507(5)	0.082(6)	3*	
			O-O	2.644(5)	0.150(8)	3.16(8)	
			P-O	1.498(4)	0.022(5)	2.00(2)	
			P-O	1.584(5)	0.069(6)	1.99(2)	
			P-O (sum)			3.99(3)	
Annealed	876	0.25	Ge-O	1.831(5)	0.089(6)	5.09(5)	2.81
			Na-O	2.433*	0.300(9)	6*	
			O-O	2.507(5)	0.086(6)	3*	
			O-O	2.635(5)	0.150(8)	3.15(8)	
			P-O	1.491(4)	0.010(5)	2.00(2)	
			P-O	1.588(5)	0.054(6)	1.99(2)	
			P-O (sum)			3.99(3)	
Annealed	876	0.5	Ge-O	1.835(5)	0.086(6)	5.21(5)	2.32
			Na-O	2.433*	0.279(9)	6*	
			O-O	2.500(5)	0.083(6)	3*	
			O-O	2.635(5)	0.129(8)	3.05(8)	

Table 7.8: Parameters obtained from Gaussian peak fits to the $D_N(r)$ functions for the as-prepared and annealed NAGP glasses with $x = 0$. The fixed parameters are denoted by an *. R_χ is given for the range 1.20-2.70 Å. The fitted functions are shown in Figure 7-12.

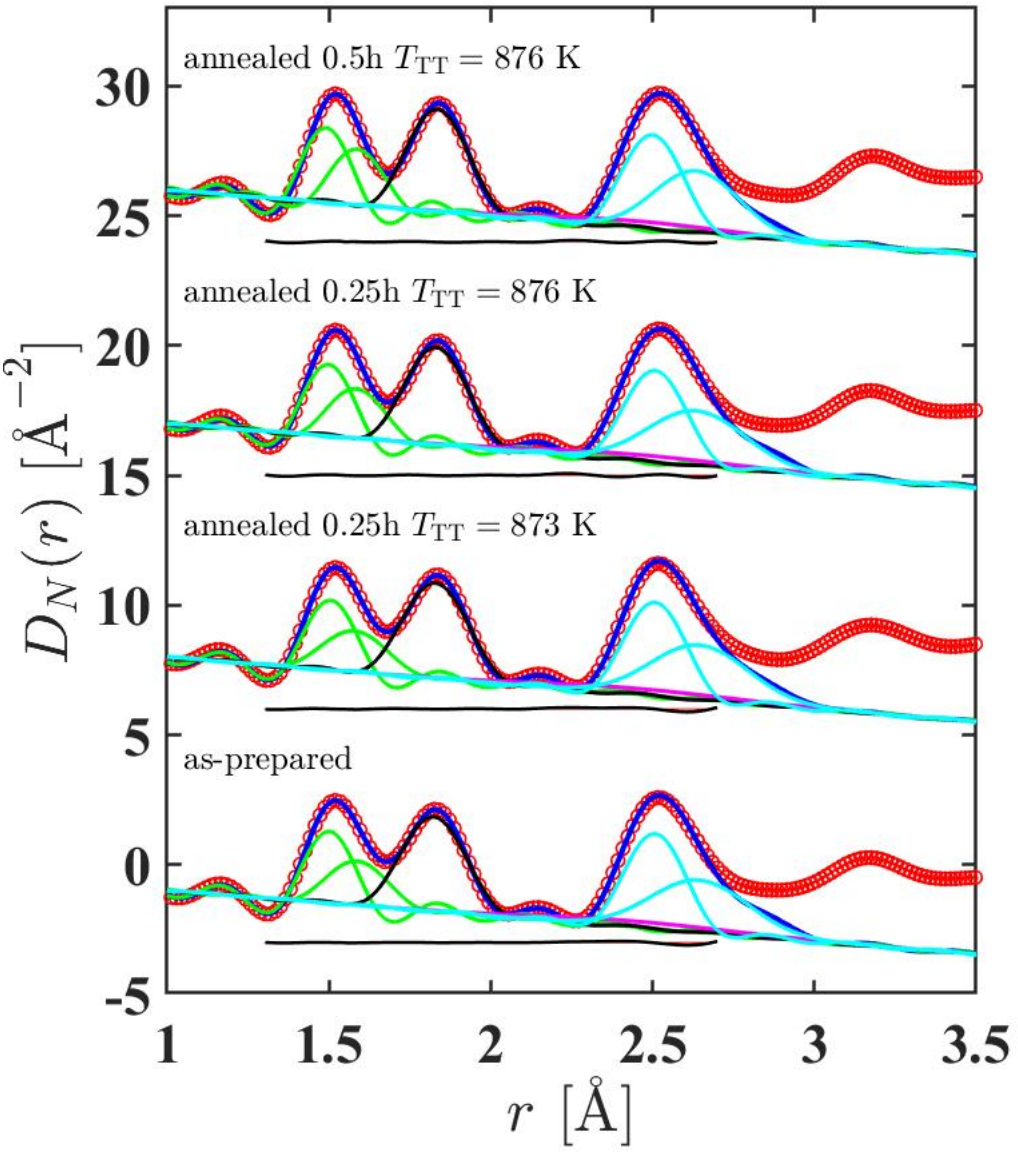

Figure 7-12: The fitted $D_N(r)$ functions for the as-prepared and annealed NAGP glasses with $x = 0$. The red circles are the data, the blue solid curves are the fits and the other curves show the contribution from the P-O (green), Ge-O (black), Al-O (yellow), Na-O (magenta) and O-O (cyan) correlations. The displaced black solid curve gives the residual (fit subtracted from the measured data). The Na-O and O-O correlations are introduced to constrain the peaks fitted at smaller r values. The curves are offset vertically for clarity of presentation.

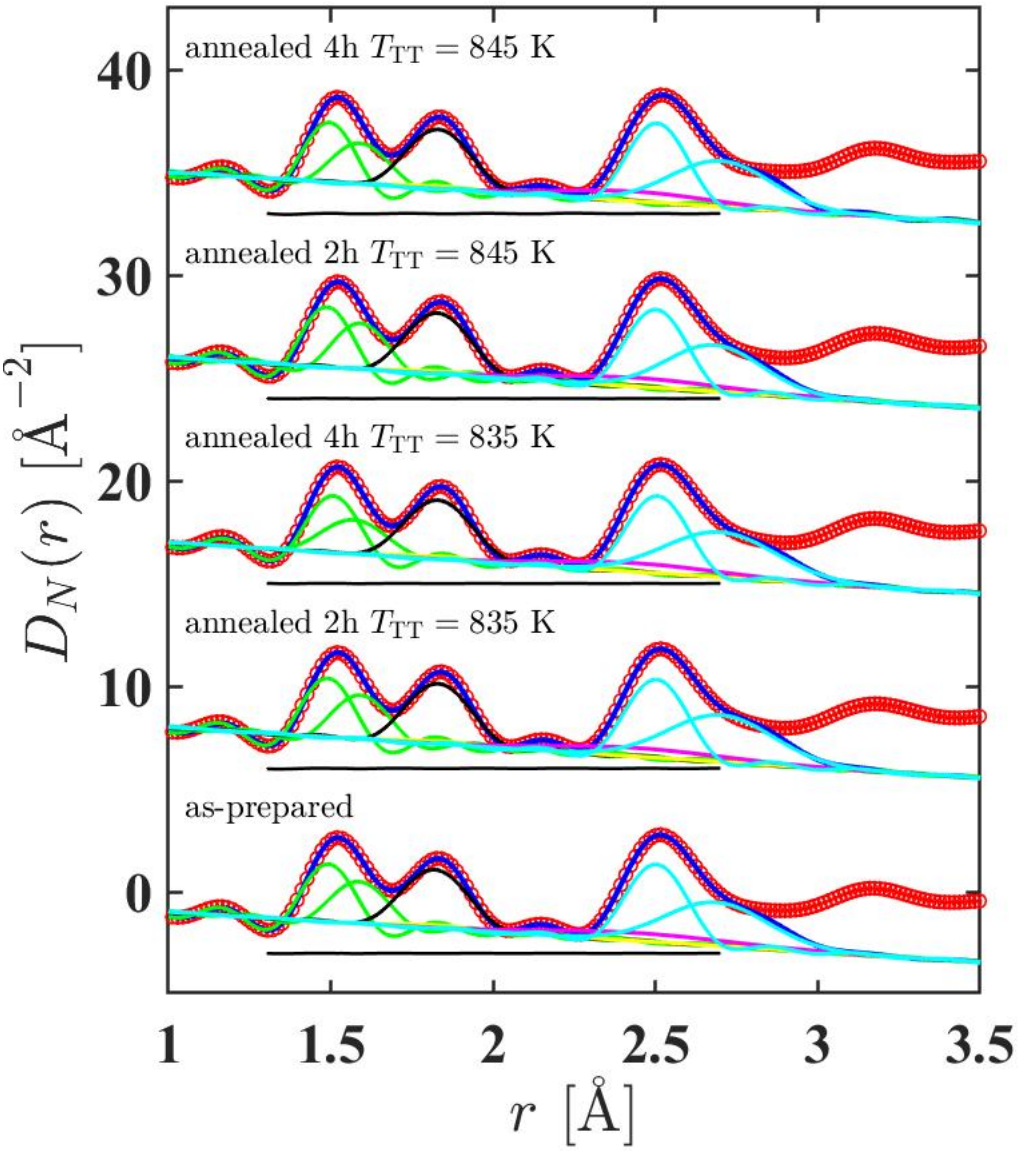

Figure 7-13: The fitted $D_N(r)$ functions for the as-prepared and annealed NAGP glasses with $x = 0.4$. The red circles are the data, the blue solid curves are the fits and the other curves show the contribution from the P-O (green), Ge-O (black), Al-O (yellow), Na-O (magenta) and O-O (cyan) correlations. The displaced black solid curve gives the residual (fit subtracted from the measured data). The Na-O and O-O correlations are introduced to constrain the peaks fitted at smaller r values. The curves are offset vertically for clarity of presentation.

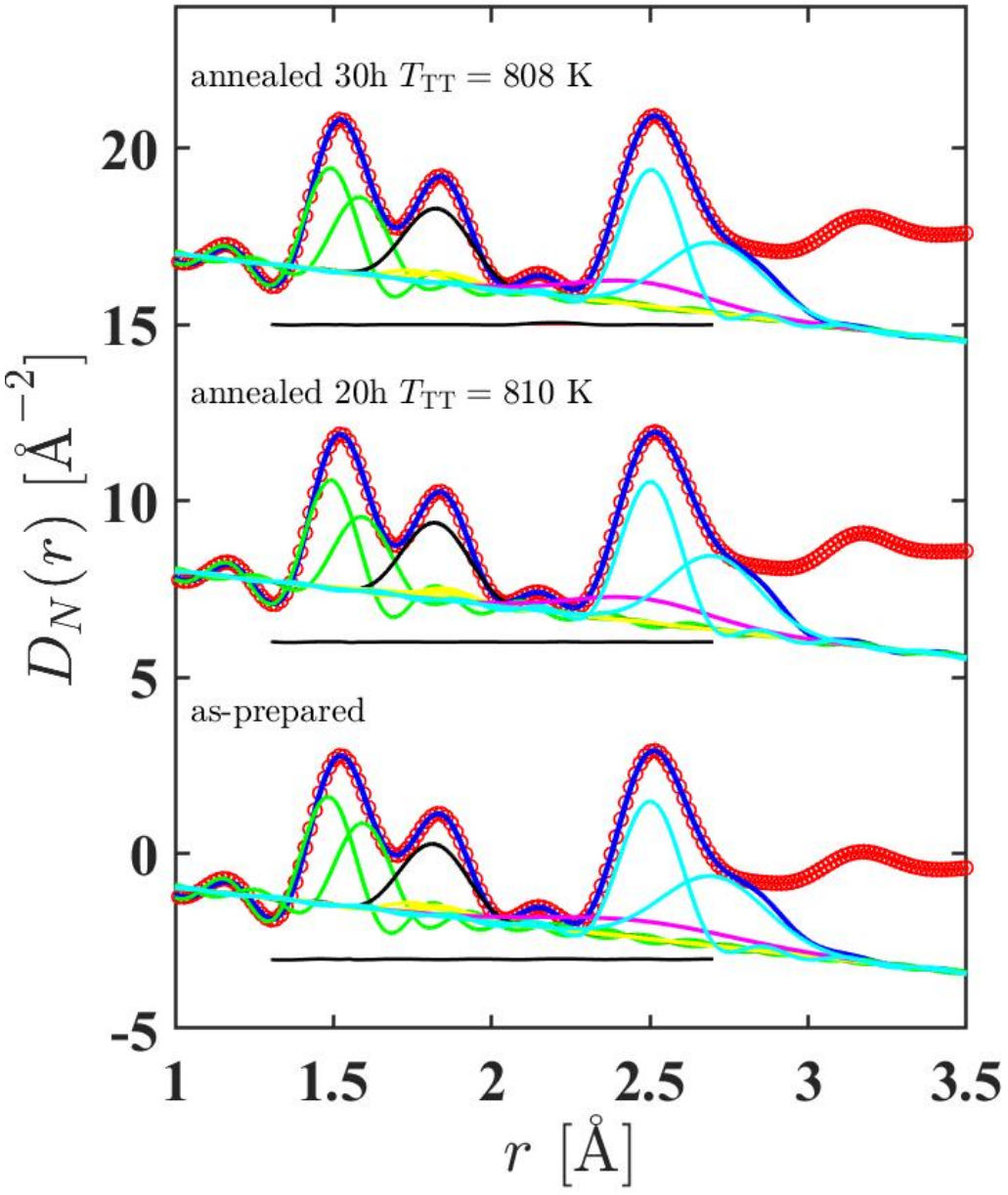

Figure 7-14: The fitted $D_N(r)$ functions for the as-prepared and annealed NAGP glasses with $x = 0.8$. The red circles are the data, the blue solid curves are the fits and the other curves show the contribution from the P-O (green), Ge-O (black), Al-O (yellow), Na-O (magenta) and O-O (cyan) correlations. The displaced black solid curve gives the residual (fit subtracted from the measured data). The Na-O and O-O correlations are introduced to constrain the peaks fitted at small r values. The curves are offset vertically for clarity of presentation.

Atom pair	$r_{\alpha\beta}$ [Å]	$\sigma_{\alpha\beta}$ [Å]	$\bar{n}_{\alpha}^{\beta}$	R_{χ} [%]
P-O	1.494(4)	0.025(5)	2.00(2)	
P-O	1.587(5)	0.064(6)	2.00(2)	
P-O (sum)			4.00(3)	
Ge-O	1.820(5)	0.094(6)	4.94(5)	
Al-O	1.76*	0.05*	1.488*	0.375
Al-O	1.84*	0.06*	1.99*	
Al-O	1.86*	0.07*	1.38*	
Al-O (sum)			4.86	
Na-O	2.436*	0.282(9)	6.61*	
O-O	2.503(5)	0.080(6)	3*	
O-O	2.686(5)	0.158(8)	3.30(8)	

Table 7.9: Parameters obtained from Gaussian peak fits to the D_N(r) functions for the as-prepared glass with $x = 0.4$. The fixed parameters are denoted by an *. R_{χ} is given for the range 1.20-2.70 Å. The fitted function is shown in Figure 7-13.

Sample	T_{TT} [K]	t [h]	Atom pair	$r_{\alpha\beta}$ [Å]	$\sigma_{\alpha\beta}$ [Å]	$\bar{n}_\alpha^\beta$	R_χ [%]
Annealed	835	2	P-O	1.491(4)	0.020(5)	2.01(2)	0.665
			P-O	1.590(5)	0.057(6)	2.01(2)	
			P-O (sum)			4.02(3)	
			Ge-O	1.831(5)	0.090(6)	4.97(5)	
			Al-O	1.76*	0.05*	1.32*	
			Al-O	1.84*	0.06*	1.65*	
			Al-O	1.86*	0.07*	2.04*	
			Na-O	2.436*	0.262(9)	6.61*	
			O-O	2.504(5)	0.079(6)	3*	
			O-O	2.700(5)	0.161(8)	3.64(8)	
Annealed	835	4	P-O	1.509(4)	0.024(5)	2.00(2)	0.478
			P-O	1.571(5)	0.088(6)	2.00(2)	
			P-O (sum)			4.00(3)	
			Ge-O	1.830(5)	0.096(6)	5.11(5)	
			Al-O	1.76*	0.05*	1.36*	
			Al-O	1.84*	0.06*	1.65*	
			Al-O	1.86*	0.07*	1.98*	
			Na-O	2.436*	0.255(9)	6.61*	
			O-O	2.506(5)	0.081(6)	3*	
			O-O	2.698(5)	0.171(8)	3.73(8)	
Annealed	845	2	P-O	1.490(4)	0.012(5)	2.00(2)	0.377
			P-O	1.591(5)	0.052(6)	2.00(2)	
			P-O (sum)			4.00(3)	
			Ge-O	1.829(5)	0.091(6)	5.05(5)	
			Al-O	1.76*	0.05*	1.316*	
			Al-O	1.84*	0.06*	1.895*	
			Al-O	1.86*	0.07*	1.752*	
			Na-O	2.436*	0.255(9)	6.61*	
			O-O	2.502(5)	0.079(6)	3*	
			O-O	2.680(5)	0.146(8)	3.26(8)	
Annealed	845	4	P-O	1.495(4)	0.020(5)	2.01(2)	0.955
			P-O	1.590(4)	0.068(6)	2.01(2)	
			P-O (sum)			4.02(3)	
			Ge-O	1.831(5)	0.093(6)	4.99(5)	
			Al-O	1.76*	0.05*	1.36*	
			Al-O	1.84*	0.06*	1.60*	
			Al-O	1.86*	0.07*	2.04*	
			Na-O	2.436*	0.229(9)	6.61*	
			O-O	2.505(5)	0.079(6)	3*	
			O-O	2.701(5)	0.155(8)	3.43(8)	

Table 7.10: Parameters obtained from Gaussian peak fits to the $D_N(r)$ functions measured for the annealed NAGP glasses with $x = 0.4$. The fixed parameters are denoted by an *. R_χ is given for the range 1.20-2.70 Å. The fitted functions are shown in Figure 7-13.

Sample	T_{TT} [K]	t [h]	Atom pair	$r_{\alpha\beta}$ [Å]	$\sigma_{\alpha\beta}$ [Å]	$\bar{n}_{\alpha}^{\beta}$	R_{χ} [%]
As-prepared	-	-	P-O	1.486(4)	0.010(7)	2.01(2)	0.517
			P-O	1.594(5)	0.045(7)	2.00(2)	
			P-O (sum)			4.01(3)	
			Ge-O	1.818(5)	0.096(6)	4.64(5)	
			Al-O	1.76*	0.05*	1.584*	
			Al-O	1.84*	0.06*	1.785*	
			Al-O	1.86*	0.07*	1.482*	
			Al-O (sum)			4.85	
			Na-O	2.467*	0.300(9)	6.85*	
			O-O	2.503(5)	0.080(7)	3*	
			O-O	2.701(5)	0.165(8)	3.15(8)	
Annealed	810	20	P-O	1.490(4)	0.010(7)	2.01(2)	0.460
			P-O	1.590(5)	0.053(7)	2.01(2)	
			P-O (sum)			4.02(3)	
			Ge-O	1.828(5)	0.098(6)	4.97(5)	
			Al-O	1.76*	0.05*	1.456*	
			Al-O	1.84*	0.06*	1.65*	
			Al-O	1.86*	0.07*	1.836*	
			Al-O (sum)			4.94	
			Na-O	2.467*	0.220(9)	6.85*	
			O-O	2.503(5)	0.079(7)	3*	
			O-O	2.702(5)	0.147(8)	2.97(8)	
Annealed	808	30	P-O	1.494(4)	0.024(7)	2.01(2)	1.171
			P-O	1.585(5)	0.059(7)	1.98(2)	
			P-O (sum)			3.99(3)	
			Ge-O	1.828(5)	0.101(6)	5.02(5)	
			Al-O	1.76*	0.05*	1.44*	
			Al-O	1.84*	0.06*	1.60*	
			Al-O	1.86*	0.07*	1.92*	
			Al-O (sum)			4.96	
			Na-O	2.467*	0.220(9)	6.85*	
			O-O	2.505(5)	0.081(7)	3*	
			O-O	2.702(5)	0.159(8)	3.07(8)	

Table 7.11: Parameters obtained from Gaussian peak fits to the $D_N(r)$ functions measured for the as-prepared and annealed NAGP glasses with $x = 0.8$. The fixed parameters are denoted by an *. R_{χ} is given for the range 1.20-2.70 Å. The fitted functions are shown in Figure 7-14.

7.3.2 X-ray Difraction

x	Q_{FSDP} [Å^{-1}]	Q_{PP} [Å^{-1}]	Q_3 [Å^{-1}]	Q_{max} [Å^{-1}]
0				
as-prepared	1.945(1)	4.434(2)	6.550(3)	24.24
annealed	1.934(1)	4.42(2)	6.497(3)	24.18
crystal	-	-	-	24.98
0.4				
as-prepared	2.038(1)	4.444(2)	6.479(3)	23.92
annealed	2.088(1)	4.418(2)	6.467(3)	24.34
crystal	-	-	-	23.54
0.8				
as-prepared	2.088(1)	4.449(2)	6.443(3)	23.86
annealed	2.142(1)	4.425(2)	6.443(3)	24.10
crystal	-	-	-	24.14

Table 7.12: The positions of the first three peaks Q_{FSDP}, Q_{PP} and Q_3 in the $S_X(Q)$ functions. Also given are the $\mathrm{Q_{max}}$ values used in the Fourier transformation. The annealed glasses corresponds to $t = 0.25$ h at $T_{\mathrm{TT}} = 873$ K for $x = 0$; $t = 2$ h at $T_{\mathrm{TT}} = 845$ K for $x = 0.4$; and $t = 20$ h at $T_{\mathrm{TT}} = 810$ K for $x = 0.8$.

The positions of the first three peaks in the $S_X(Q)$ functions are listed in table 7.12. As in the neutrons, the $S_X(Q)$ functions for the glassy materials show a peak at ≈ 0.85 Å^{-1}, which indicates ordering on a length scale of $2\pi/Q = 7.4$ Å [100]. The total pair distribution functions $D_X(r)$ for the crystalline and glassy materials are shown in figures 7-17 and 7-18, respectively. The $D_X(r)$ fits are shown in figures 7-19, 7-20 and 7-21. Their respective fitted parameters are listed in tables 7.13, 7.14 and 7.15.

The fitted $D_X(r)$ function for the crystalline material with $x = 0$ gave $\bar{n}_{\mathrm{P}}^{\mathrm{O}} = 3.88(4)$ and $\bar{n}_{\mathrm{Ge}}^{\mathrm{O}} = 5.90(4)$. The P-O coordination number found from fitting is smaller than the value $\bar{n}_{\mathrm{P}}^{\mathrm{O}} = 4$ expected from ^{31}P MAS NMR and Rietveld refinement [225] but according to diffraction analyses on phosphate materials [227–229] a P-O coordination number smaller than 4 is typical. A possible explanation for this observation is the Q space resolution of the diffractometer [230,231]. However, the inclusion of a second peak increases the P-O coordination number to 4, which suggests a broader distribution of P-O distances than found by fitting a single peak. The Ge-O distances of 1.847(1) and 1.871(1) Å are in agreement with the short and long average Rietveld Ge-O distances of 1.841 Å and 1.873 Å, respectively.

For the compositions with $x > 0$ the P-O coordination numbers are 3.85(3) and 3.91(3) for $x = 0.4$ and $x = 0.8$, respectively. The $\bar{n}^{\mathrm{O}}_{\mathrm{Ge}}$ obtained were 5.97(2) and 5.97(4) for $x = 0.4$ and $x = 0.8$, respectively. The Ge-O coordination number is consistent with the powder diffraction value $\bar{n}^{\mathrm{O}}_{\mathrm{Ge}} = 6$. The P-O coordination number remain relatively constant for the glassy NAGP but the $\bar{n}^{\mathrm{O}}_{\mathrm{Ge}}$ reduced in these disordered structures.

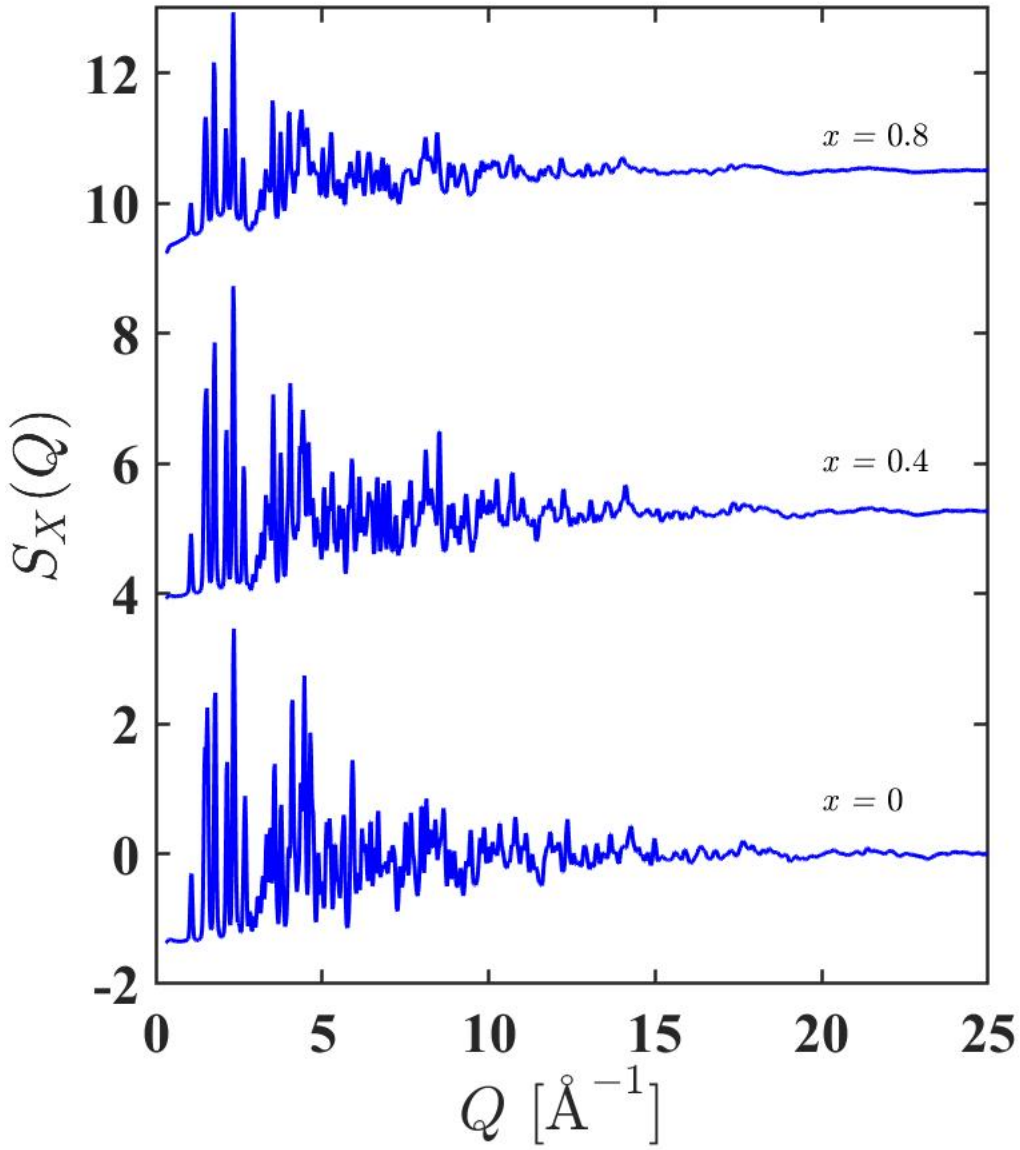

Figure 7-15: The total structure factors $S_X(Q)$ for crystalline NAGP with $x = 0$, 0.4 and 0.8. The vertical error bars are smaller than the line thickness at most Q values. The curves are offset vertically for clarity of presentation.

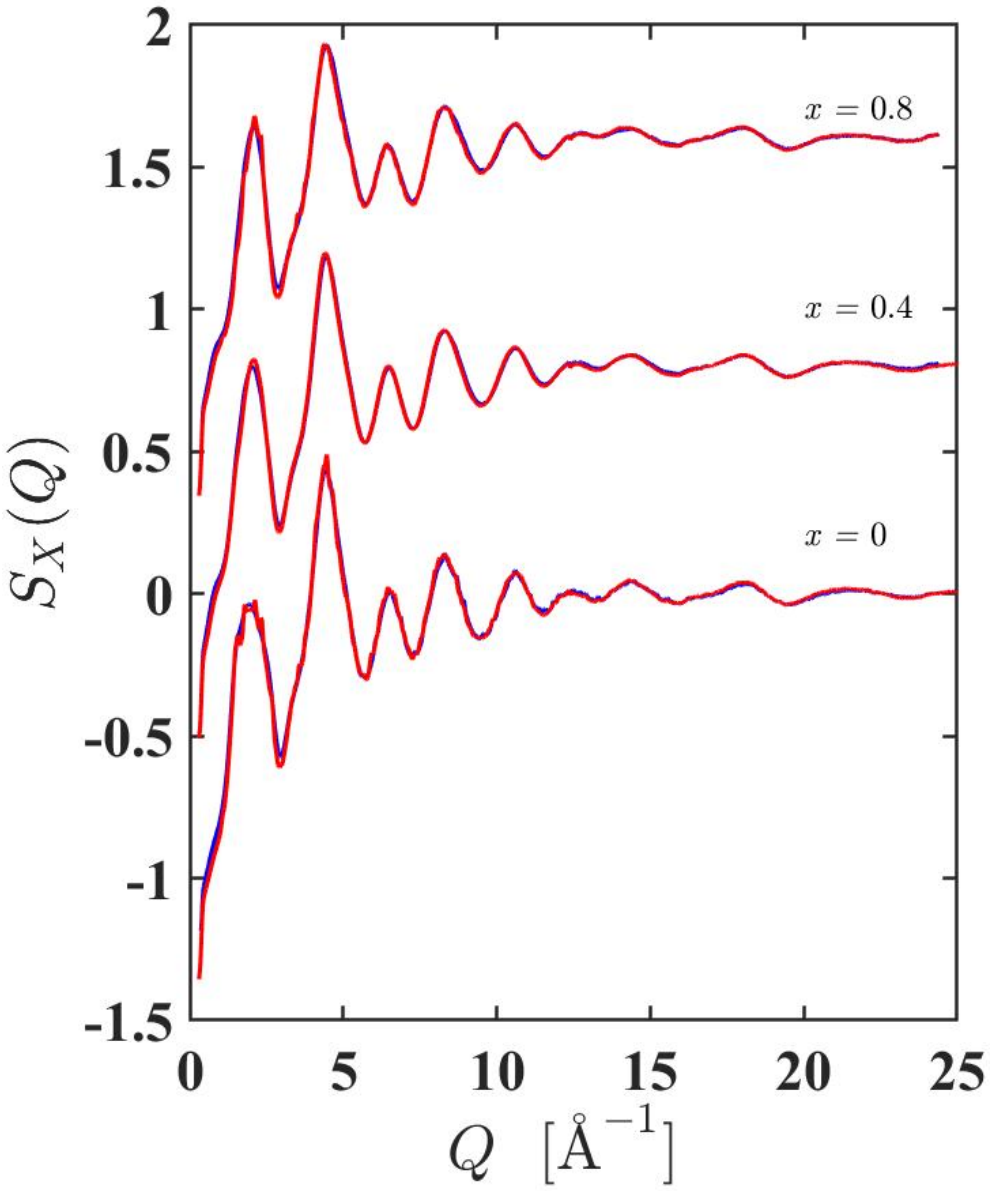

Figure 7-16: The total structure factors $S_X(Q)$ for the as-prepared (blue) versus annealed (red) NAGP glasses with $x = 0$, 0.4 and 0.8. The annealed glasses correspond to $t = 0.25$ h at $T_{\rm TT} = 873$ K for the composition $x = 0$; $t = 2$ h at $T_{\rm TT} = 845$ K for the composition $x = 0.4$; and $t = 20$ h at $T_{\rm TT} = 810$ K for the composition $x = 0.8$. The vertical error bars are smaller than the line thickness at most Q values. The curves are offset vertically for clarity of presentation.

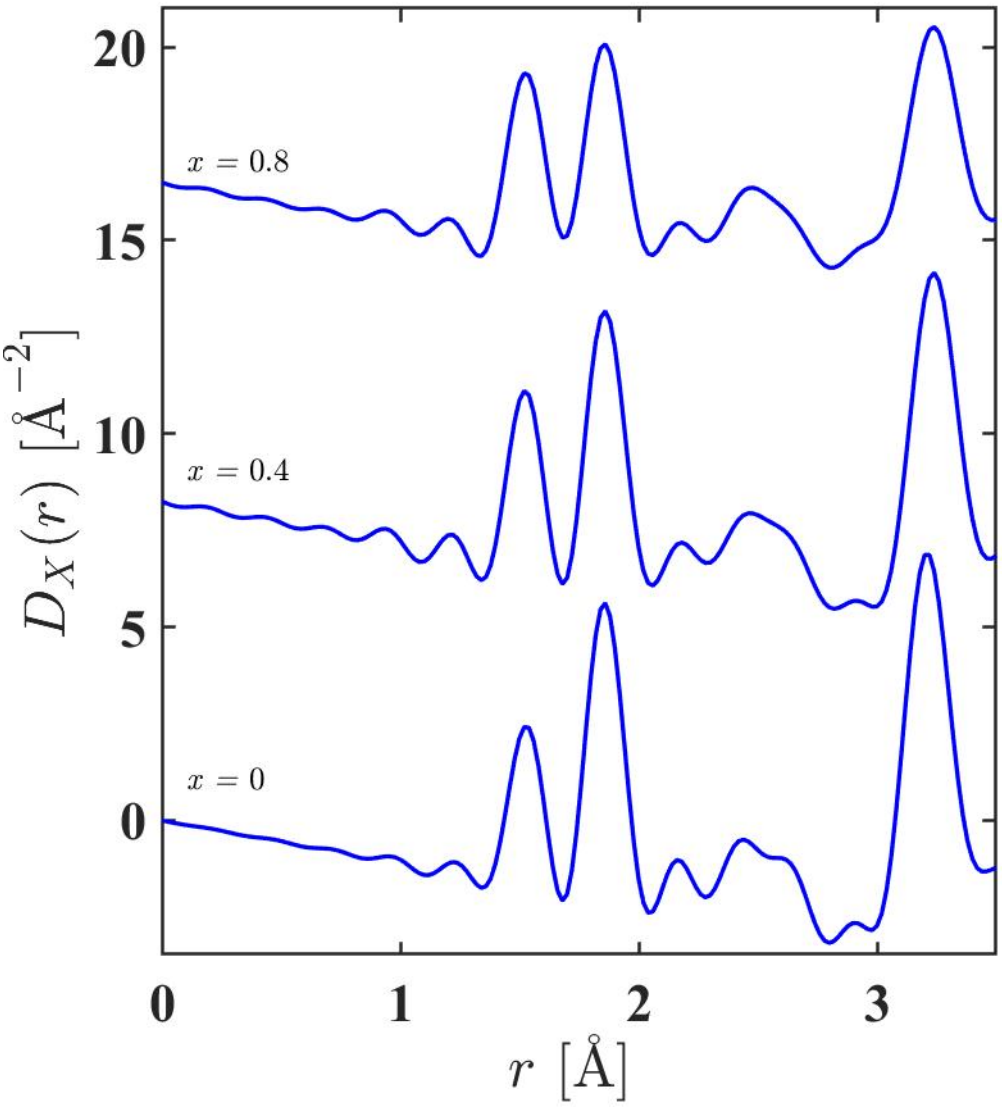

Figure 7-17: Total pair distribution functions $D_X(r)$ for the NAGP crystals. The blue curves were obtained by Fourier transforming the corresponding reciprocal data shown in Figure 7-15. The curves are offset vertically for clarity of presentation.

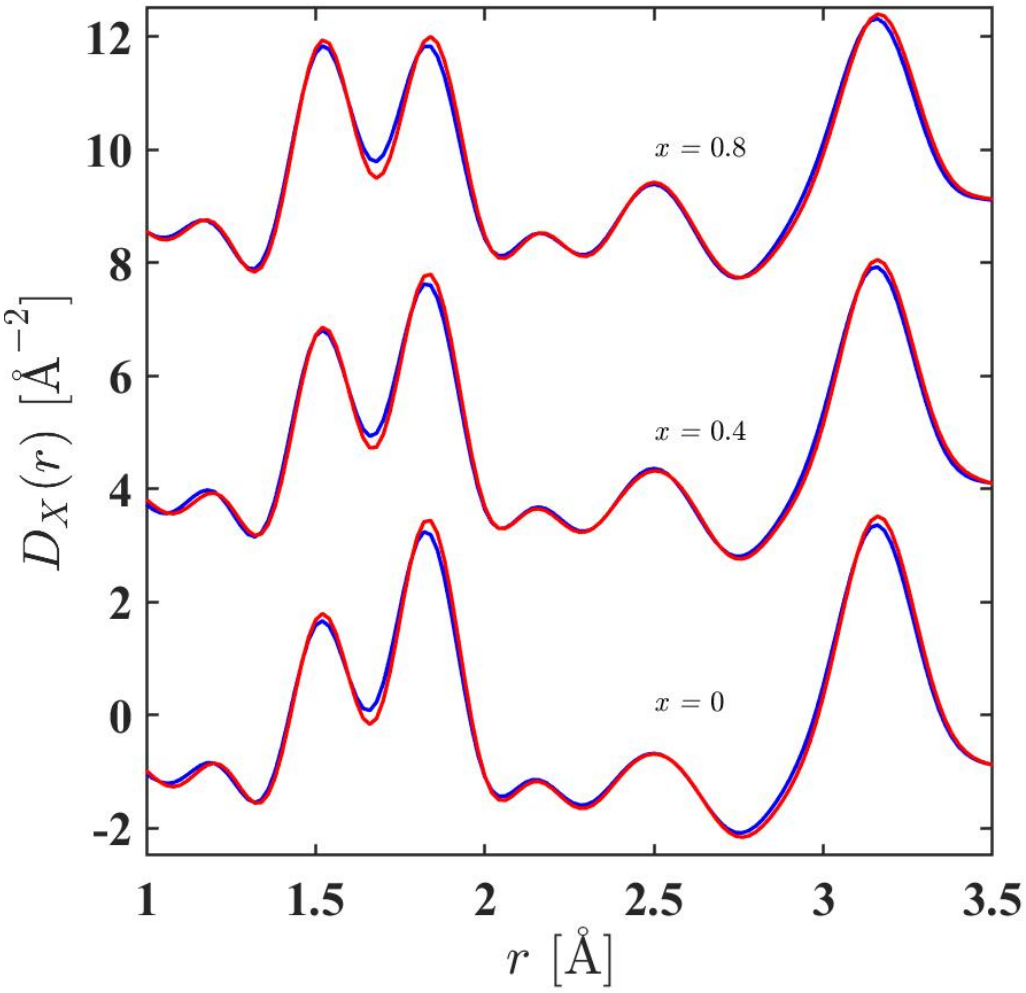

Figure 7-18: Total pair distribution functions $D_X(r)$ for the as-prepared (blue) and annealed NAGP glasses (red). The curves were obtained by Fourier transforming the corresponding reciprocal data shown in Figure 7-16. The curves are offset vertically for clarity of presentation.

x	Atom pair	$r_{\alpha\beta}$ [Å]	$\sigma_{\alpha\beta}$ [Å]	$\bar{n}_\alpha^\beta$	R_χ [%]
0	P-O	1.526(1)	0.037(2)	1.94(3)	2.95
	P-O	1.538(2)	0.073(2)	1.94(2)	
	P-O (sum)			3.88(4)	
	Ge-O	1.847(1)	0.049(1)	2.95(3)	
	Ge-O	1.871(1)	0.074(1)	2.95(3)	
	Ge-O(sum)			5.90(4)	
	Na-O	2.310(1)	0.139(8)	6*	
	O-O	2.459(2)	0.076(2)	3*	
	O-O	2.607(2)	0.091(2)	4*	
0.4	P-O	1.527(1)	0.026(1)	1.92(2)	1.31
	P-O	1.530(1)	0.069(1)	1.93(2)	
	P-O (sum)			3.85(3)	
	Ge-O	1.845(1)	0.049(1)	2.98(1)	
	Ge-O	1.880(1)	0.078(1)	2.99(1)	
	Ge-O (sum)			5.97(2)	
	Al-O	1.86*	0.091(3)	6*	
	Na-O	2.329(1)	0.122(2)	6.61*	
	O-O	2.466(1)	0.071(1)	3*	
	O-O	2.616(1)	0.074(1)	4*	
0.8	P-O	1.521(1)	0.048(1)	1.96(2)	3.60
	P-O	1.539(1)	0.055(1)	1.95(2)	
	P-O (sum)			3.91(3)	
	Ge-O	1.832(1)	0.068(1)	3.00(3)	
	Ge-O	1.890(1)	0.080(1)	2.97(3)	
	Ge-O (sum)			5.97(4)	
	Al-O	1.86*	0.097(3)	6*	
	Na-O	2.338(3)	0.128(3)	6.85*	
	O-O	2.493(1)	0.056(1)	3*	
	O-O	2.661(1)	0.086(1)	4*	

Table 7.13: Parameters obtained from Gaussian peak fits to the $D_X(r)$ functions measured for crystalline NAGP. The fixed parameters are denoted by an *. R_χ is given for the range 1.30-2.70 Å. The fitted functions are shown in Figures 7-19 ($x = 0$), 7-20 ($x = 0.4$) and 7-21 ($x = 0.8$).

x	Atom pair	$r_{\alpha\beta}$ [Å]	$\sigma_{\alpha\beta}$ [Å]	$\bar{n}_{\alpha}^{\beta}$	R_{χ} [%]
	P-O	1.522(1)	0.043(1)	1.96(2)	
	P-O	1.560(3)	0.104(2)	1.96(3)	
	P-O (sum)			3.92(4)	
0	Ge-O	1.825(1)	0.089(1)	4.98(2)	4.10
	Na-O	2.310(1)	0.067(2)	6*	
	O-O	2.459(2)	0.139(8)	3*	
	O-O	2.607(2)	0.076(2)	4*	
	P-O	1.520(2)	0.067(2)	1.97(3)	
	P-O	1.548(2)	0.074(2)	2.02(3)	
	P-O (sum)			3.99(4)	
	Ge-O	1.825(1)	0.088(1)	4.86(3)	
	Al-O	1.76*	0.05*	1.488*	
0.4	Al-O	1.84*	0.06*	1.99*	4.88
	Al-O	1.86*	0.07*	1.38*	
	Al-O (sum)			4.86	
	Na-O	2.329(1)	0.091(3)	6.61*	
	O-O	2.466(1)	0.122(2)	3*	
	O-O	2.616(1)	0.071(1)	4*	
	P-O	1.516(1)	0.054(1)	1.95(1)	
	P-O	1.560(1)	0.080(1)	1.95(2)	
	P-O (sum)			3.90(2)	
	Ge-O	1.824(1)	0.094(1)	4.72(2)	
	Al-O	1.76*	0.05*	1.584*	
0.8	Al-O	1.84*	0.06*	1.785*	3.34
	Al-O	1.86*	0.07*	1.482*	
	Al-O (sum)			4.85	
	Na-O	2.338(3)	0.097(3)	6.85*	
	O-O	2.493(1)	0.128(3)	3*	
	O-O	2.661(1)	0.056(1)	4*	

Table 7.14: Parameters obtained from Gaussian peak fits to the $D_X(r)$ functions measured for the as-prepared NAGP glasses. The fitted functions are shown in Figures 7-19 ($x = 0$), 7-20 ($x = 0.4$) and 7-21 ($x = 0.8$). Fixed parameters are denoted by an *. R_{χ} is given for the range 1.30-2.70 Å.

x	Atom pair	$r_{\alpha\beta}$ [Å]	$\sigma_{\alpha\beta}$ [Å]	$\bar{n}^{\alpha}_{\beta}$	R_χ [%]
	P-O	1.529(2)	0.062(2)	1.95(3)	
	P-O	1.542(2)	0.075(2)	1.98(3)	
	P-O (sum)			3.93(4)	
0	Ge-O	1.830(1)	0.084(1)	5.09(2)	4.66
	Na-O	2.310(1)	0.067(2)	6*	
	O-O	2.459(2)	0.139(8)	3*	
	O-O	2.607(2)	0.076(2)	4*	
	P-O	1.524(1)	0.053(1)	1.95(1)	
	P-O	1.555(1)	0.080(1)	1.95(1)	
	P-O (sum)			3.90(1)	
	Ge-O	1.831(1)	0.086(1)	4.95(1)	
	Al-O	1.76*	0.05*	1.316*	
0.4	Al-O	1.84*	0.06*	1.895*	2.80
	Al-O	1.86*	0.07*	1.752*	
	Al-O (sum)			4.96	
	Na-O	2.329(1)	0.091(3)	6.61*	
	O-O	2.466(1)	0.122(2)	3*	
	O-O	2.616(1)	0.071(1)	4*	
	P-O	1.522(1)	0.051(1)	1.95(1)	
	P-O	1.553(1)	0.079(1)	1.95(1)	
	P-O (sum)			3.90(2)	
	Ge-O	1.835(1)	0.091(1)	4.82(2)	
	Al-O	1.76*	0.05*	1.456*	
0.8	Al-O	1.84*	0.06*	1.65*	3.18
	Al-O	1.86*	0.07*	1.836*	
	Al-O (sum)			4.94	
	Na-O	2.338(3)	0.097(3)	6.85*	
	O-O	2.493(1)	0.128(3)	3*	
	O-O	2.661(1)	0.056(1)	4*	

Table 7.15: Parameters obtained from Gaussian peak fits to the $D_X(r)$ functions measured for the annealed NAGP glasses. The fitted functions are shown in Figures 7-19 ($x = 0$), 7-20 ($x = 0.4$) and 7-21 ($x = 0.8$). Fixed parameters are denoted by an *. R_χ is given for the range 1.30-2.70 Å.

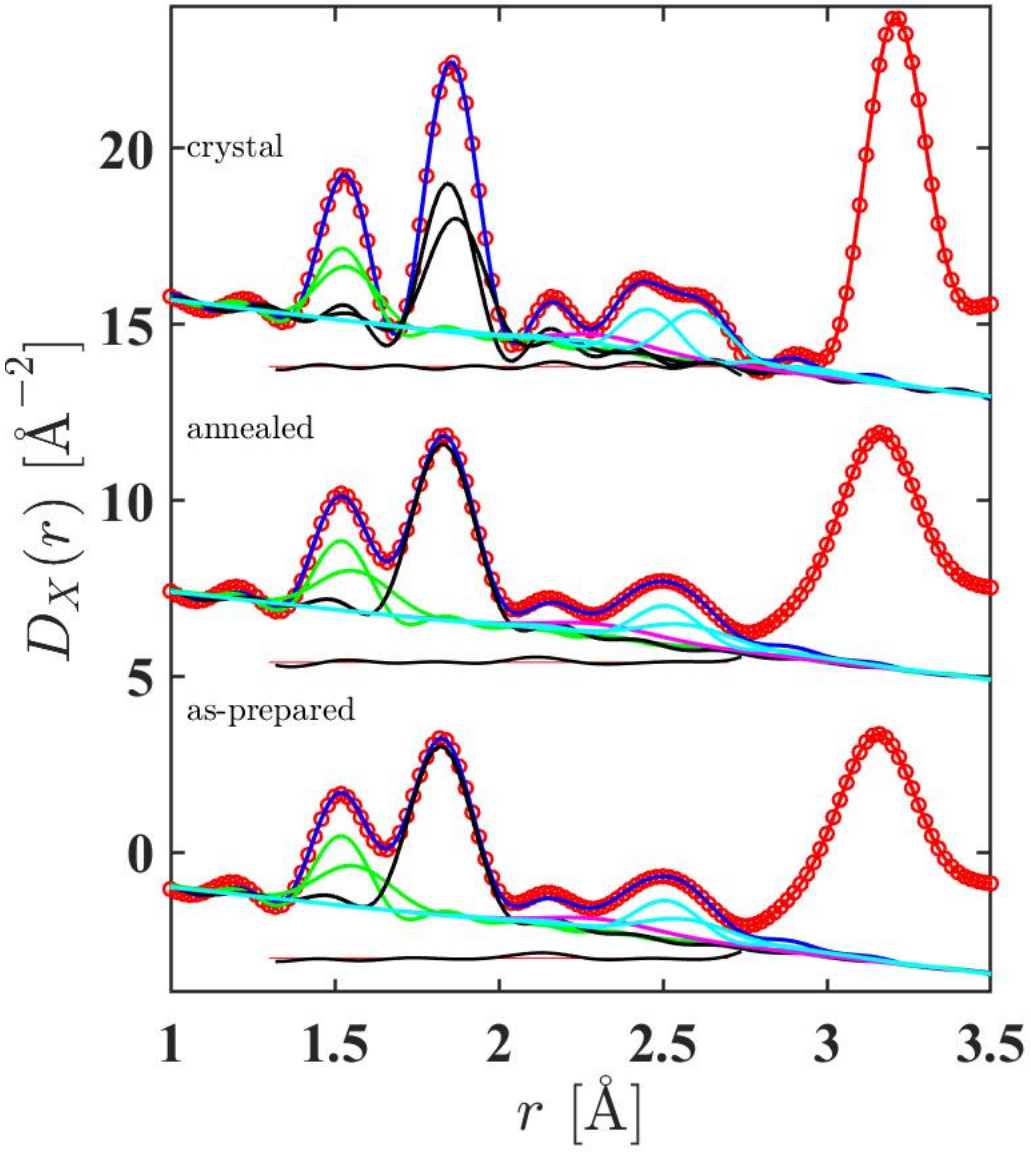

Figure 7-19: The fitted $D_X(r)$ functions for crystalline, as-prepared glass and annealed glass ($T_{\mathrm{TT}} = 873$ K) with $x = 0$. The red circles are the data, the blue solid curves are the fits and the other curves show the contribution from the P-O (green), Ge-O (black), Na-O (magenta) and O-O (cyan) correlations. The displaced black solid curves gives the residual (fit subtracted from the measured data). The Na-O and O-O correlations are introduced to constrain the peaks fitted at smaller r values. The curves are offset vertically for clarity of presentation.

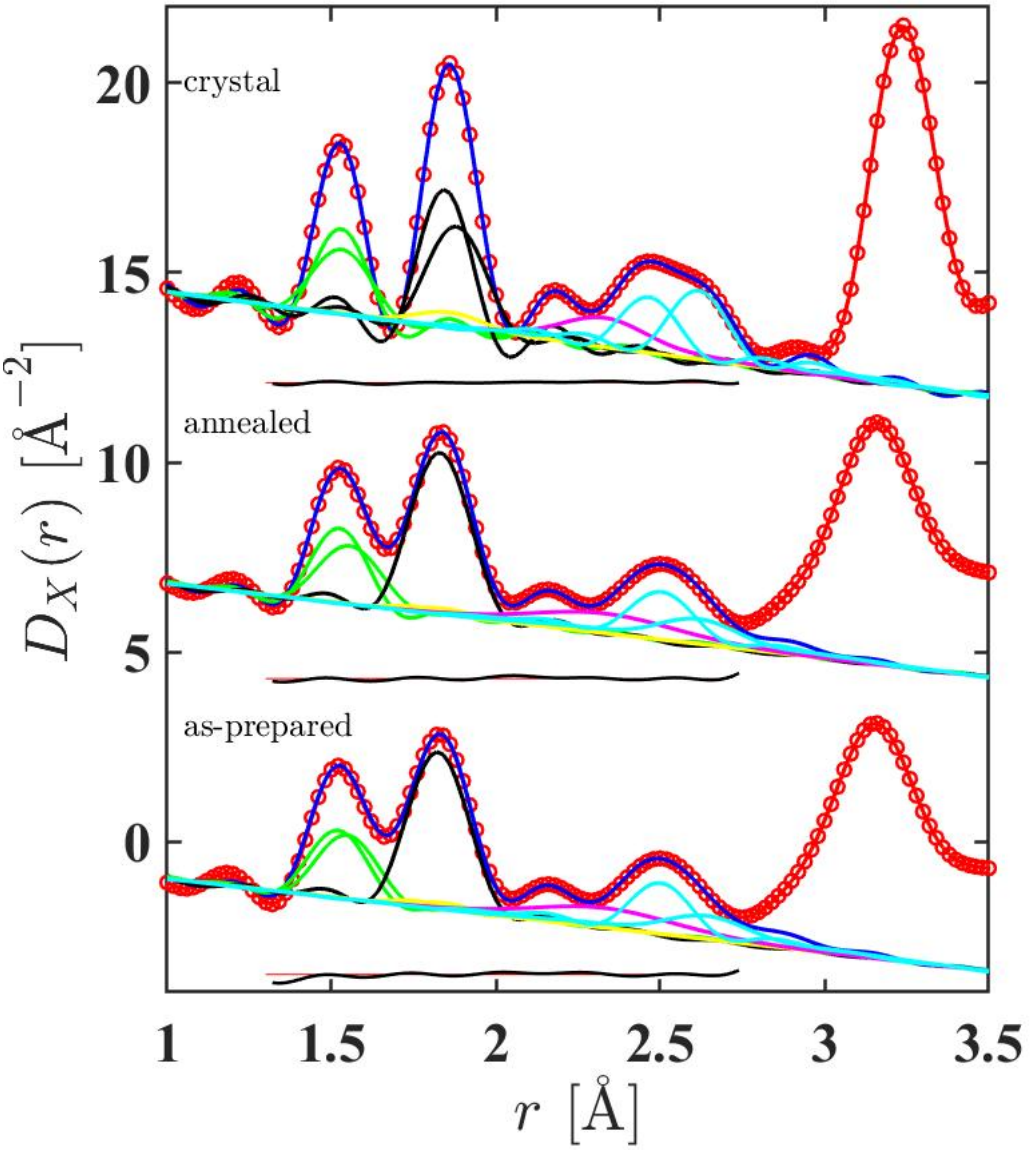

Figure 7-20: The fitted $D_X(r)$ functions for crystalline, as-prepared glass and annealed glass ($T_{\mathrm{TT}} = 845$ K) with $x = 0.4$. The red circles are the data, the blue solid curves are the fits and the other curves show the contribution from the P-O (green), Ge-O (black), Al-O (yellow), Na-O (magenta) and O-O (cyan) correlations. The displaced black solid curve gives the residual (fit subtracted from the measured data). The Na-O and O-O correlations are introduced to constrain the peaks fitted at smaller r values.

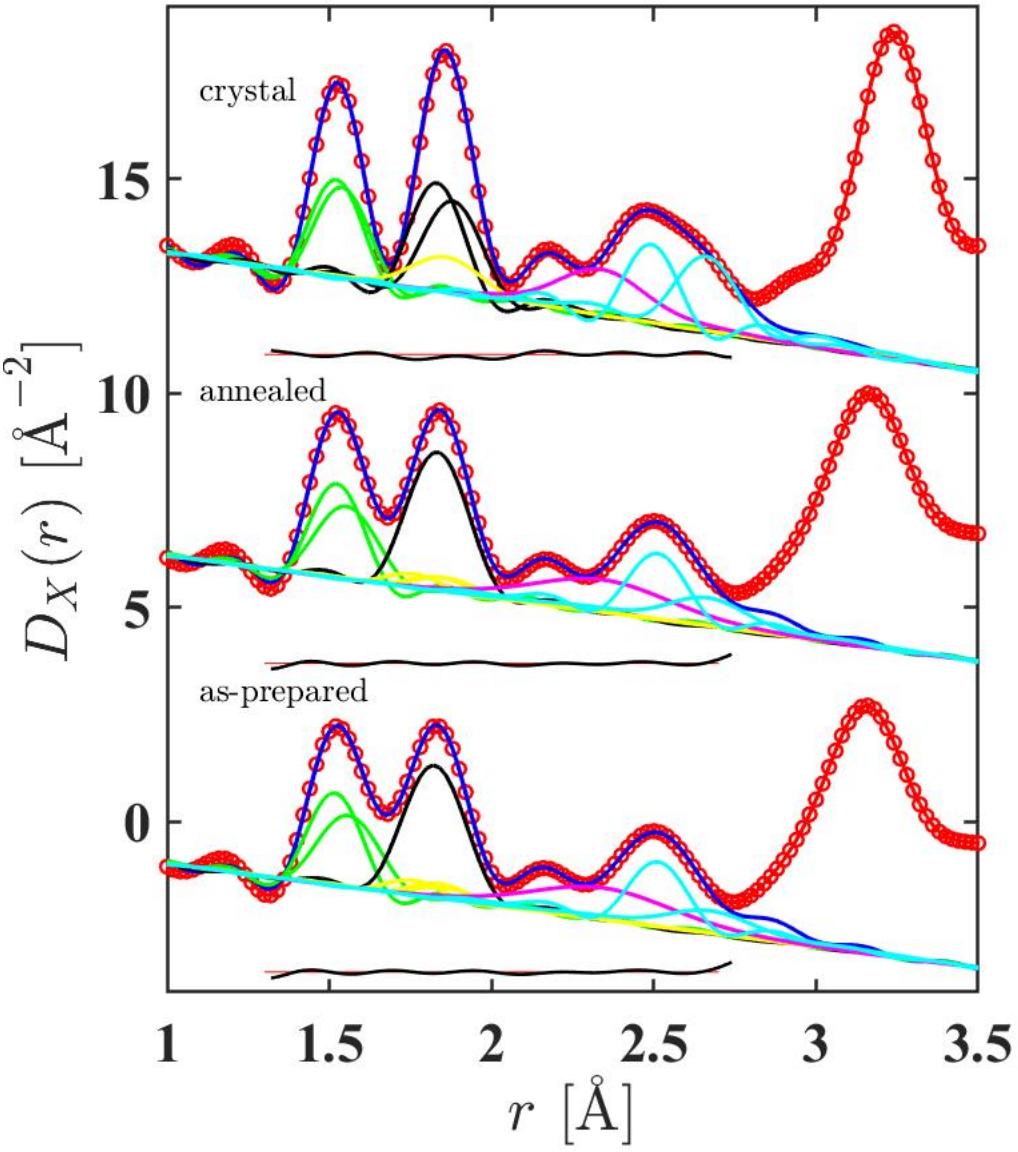

Figure 7-21: The fitted $D_X(r)$ functions for crystalline, as-prepared glass and annealed glass ($T_{\rm TT}$ = 810 K) NAGP with $x = 0.8$. The red circles are the data, the blue solid curves are the fits and the other curves show the contribution from the P-O (green), Ge-O (black), Al-O (yellow), Na-O (magenta) and O-O (cyan) correlations. The displaced black solid curve gives the residual (fit subtracted from the measured data). The Na-O and O-O correlations are introduced to constrain the peaks fitted at smaller r values. The curves are offset vertically for clarity of presentation.

7.4 Discussion

Table 7.16 summarizes the mean distances and coordination numbers for the P-O and Ge-O correlations obtained from $D_N(r)$ and $D_X(r)$ fits by calculating the direct average. The diffraction results for the glasses show that Ge-O coordination numbers are smaller than $\bar{n}^{\mathrm{O}}_{\mathrm{Ge}} = 6$, which indicates the presence of polyhedral GeO_5 and/or GeO_4 units. This observation of a substantial difference between the crystal and glass structures is supported by solid-state NMR experiments [224].

x	Material	r_{PO} [Å]	r_{PO} [Å]	$\bar{n}^{\mathrm{O}}_{\mathrm{P}}$ (sum)	r_{GeO} [Å]	$\bar{n}^{\mathrm{O}}_{\mathrm{Ge}}$
0	as-prepared	1.513(13)	1.573(15)	3.97(3)	1.826(2)	5.07(7)
	annealed (a)	1.512(17)	1.568(26)	3.97(4)	1.831(1)	5.11(2)
	annealed (b)	1.498(4)	1.584(5)	3.99(3)	1.831(5)	5.09(5)
	annealed (c)	1.491(4)	1.588(5)	3.99(3)	1.835(5)	5.21(5)
	crystal	1.517(10)	1.546(10)	3.93(5)	1.858(1)	5.94(3)
0.4	as-prepared	1.509(15)	1.568(19)	3.99(1)	1.826(2)	4.93(8)
	annealed (d)	1.491(4)	1.590(5)	4.02(3)	1.831(5)	4.97(5)
	annealed (e)	1.509(4)	1.571(5)	4.00(3)	1.830(5)	5.11(5)
	annealed (f)	1.507(18)	1.572(17)	3.95(5)	1.831(1)	5.07(12)
	annealed (g)	1.495(4)	1.590(4)	4.02(3)	1.831(5)	4.99(5)
	crystal	1.513(14)	1.545(13)	3.93(7)	1.861(2)	6.02(3)
0.8	as-prepared	1.510(12)	1.571(15)	3.96(4)	1.824(4)	4.84(12)
	annealed (h)	1.509(14)	1.571(18)	3.95(5)	1.833(2)	4.97(15)
	annealed (i)	1.494(4)	1.585(5)	3.99(3)	1.828(5)	5.02(5)
	crystal	1.512(10)	1.546(8)	3.98(5)	1.857(3)	6.03(4)

Table 7.16: The mean P-O and Ge-O bond distances and coordination numbers obtained from Gaussian peak fits to the r-space functions measured using ND and XRD for the as-prepared, annealed and crystalline NAGP samples. The shorter and longer P-O distances, obtained by representing the nearest neighbor P-O correlations are distinguished. (a) annealed glass with $T_{\mathrm{TT}} = 873$ K for 0.25 h, (b) annealed glass with $T_{\mathrm{TT}} = 876$ K for 0.25 h and (c) annealed glass with $T_{\mathrm{TT}} = 876$ K for 0.5 h. (d) annealed glass with $T_{\mathrm{TT}} = 835$ K for 2 h. (e) annealed glass with $T_{\mathrm{TT}} = 835$ K for 4 h. (f) annealed glass with $T_{\mathrm{TT}} = 845$ K for 2 h. (g) annealed glass with $T_{\mathrm{TT}} = 845$ K for 4 h. (h) annealed glass with $T_{\mathrm{TT}} = 810$ K for 20 h. (i) annealed glass with $T_{\mathrm{TT}} = 808$ K for 30 h.

In the crystals, ^{27}Al NMR shows that Al is six-fold coordinated but in glasses and annealed glasses it is 4- 5- and 6-fold coordinated. The results on ^{31}P NMR for the

Material	Species	Area [%]	δ_{iso} [ppm]	FWHM [ppm]
Glass: As-prepared	$P^{(3)}$	68	-25.3	17.5
	$P^{(4)}$	32	-36.5	16.9
Glass: Annealed at T = 873 K for 0.25 h	$P^{(3)}$	63	-24.8	16.6
	$P^{(4)}$	37	-36.3	15.3
Glass: Annealed at T = 876 K for 0.25 h	$P^{(3)}$	61	-24.8	17.0
	$P^{(4)}$	39	-36.3	15.5
Glass: Annealed at T = 876 K for 0.5 h	$P^{(3)}$	49	-24.8	17.0
	$P^{(4)}$	48	-36.3	15.3
	$P^{(4)}_{cryst}$	3	-37.3	2.7
Crystal	$P^{(4)}$	100	-37.4	1.0

Table 7.17: Deconvolution of the ^{31}P MAS NMR spectra for as-prepared, annealed and crystalline NAGP with $x = 0$. The parameters describe the fractional area, δ_{iso}, and FWHM of the peaks fitted to the spectra. For one of the annealed glasses the crystalline contribution to the line shape is indicated by a subscript. The errors on the fitted areas are $\pm 1\%$. The errors on δ_{iso} and the FWHM are ± 0.5 ppm.

composition with $x = 0$ (Figure 7-22) show that $P^{(3)}$ units are the majority of phosphate species in the glasses [224,225], where the superscript denotes the number of BO atoms per P atom. The spectrum of the as-prepared glass can be deconvoluted into two Gaussian components at ≈ -25.3 ppm and ≈ -36.5 ppm [Figure 7-22(a)]. For the NAGP crystals the spectrum differs significantly from the glasses, indicating that the local structures in the glassy and crystalline materials are quite different. The spectrum for the crystalline material has a chemical shift at ≈ -37.4 ppm [Figure 7-22(d)], which characterizes a $P^{(4)}_{4Ge}$ where phosphorous is connected to four sixfold coordinated Ge atoms. For the annealed glasses [Figures 7-22(b) and 7-22(c)] the data shows that the material remains amorphous. However, some line shape changes indicates a structural re-arrangement in the glass caused by nucleation. Table 7.17 shows that the the principal line shape involves a change to the ratio of the relative areas of the two line shape components, indicating a moderate increase in the fraction of $P^{(4)}$ units, which has the same local coordination environment as the crystalline phase. For the sample annealed at $T_{TT} = 876$ K for 0.5 h the change in peak areas is more dramatic where a small amount of crystalline material is also detected.

To elucidate the observed changes between glassy and crystalline NAGP, a model was proposed based on the oxygen coordination number [228]. Assuming that all oxygen atoms occupy either NBO or BO sites with coordination numbers of one or two then the fraction of NBO atoms is given by

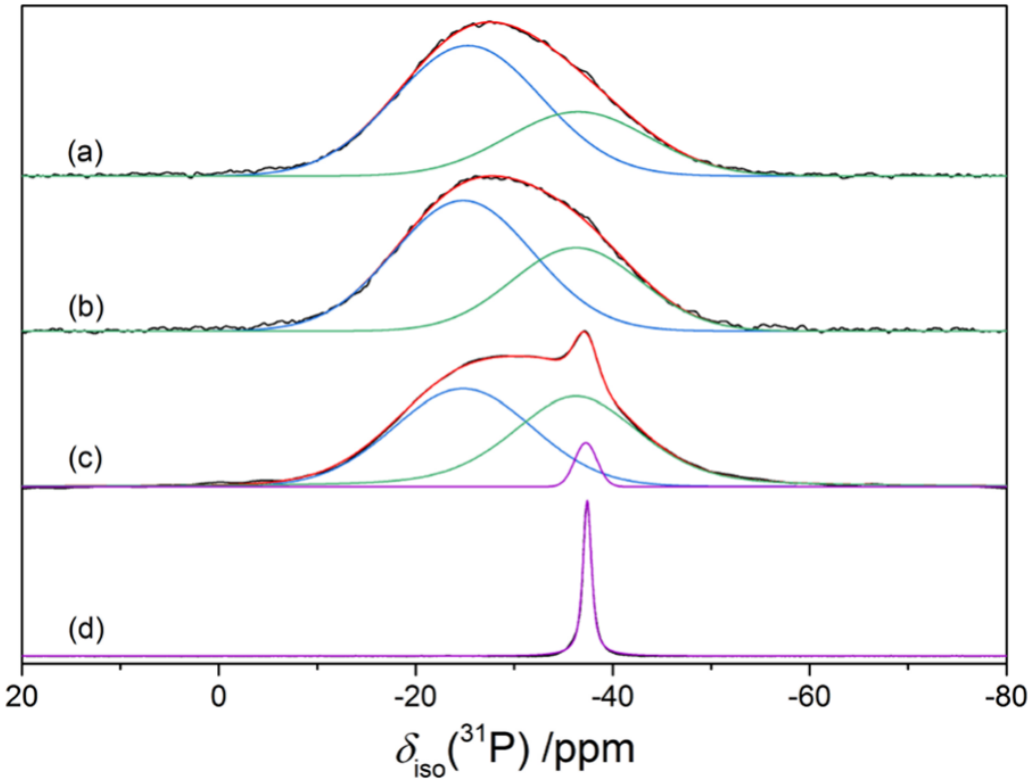

Figure 7-22: The single-pulse ^{31}P MAS NMR spectra (black curves) measured for the NAGP materials with $x = 0$: (a) as-prepared glass, (b) glass annealed at $T_{TT} = 873$ K for 0.25 h, (c) glass annealed at $T_{TT} = 876$ K for 0.5 h, and (d) crystalline material. In (a)-(c), two Gaussian peaks (blue and green) are used to fit the spectra. In (c), an additional small peak (violet) represents a small amount of crystalline material. The sum of fitted functions is given by the red curve. In (d), the spectrum is fitted to a Gauss-Lorentz curve (violet).

$$f_{\mathrm{NBO}} = N_{\mathrm{NBO}}/N_{\mathrm{O}} = 2 - \bar{n}_{\mathrm{O}}^{\mathrm{P}} - \bar{n}_{\mathrm{O}}^{\mathrm{Ge}} - \bar{n}_{\mathrm{O}}^{\mathrm{Al}}, \tag{7.1}$$

where N_{NBO} is the number of NBO and N_{O} is the total number of oxygen atoms. For a fully polymerized network

$$\bar{n}_{\mathrm{O}}^{\mathrm{P}} + \bar{n}_{\mathrm{O}}^{\mathrm{Ge}} + \bar{n}_{\mathrm{O}}^{\mathrm{Al}} = 2 \tag{7.2}$$

and $f_{\mathrm{NBO}} = 0$. For a fully depolymerised network

$$\bar{n}_{\mathrm{O}}^{\mathrm{P}} + \bar{n}_{\mathrm{O}}^{\mathrm{Ge}} + \bar{n}_{\mathrm{O}}^{\mathrm{Al}} = 1 \tag{7.3}$$

and $f_{\mathrm{NBO}} = 1$. The number of O-β bonds between atoms of chemical species β and oxygen is equal to the number of β-O bonds, i.e, $N_{\mathrm{O}}\bar{n}_{\mathrm{O}}^{\beta} = N_{\beta}\bar{n}_{\beta}^{\mathrm{O}}$, such that

$$c_{\mathrm{O}}\bar{n}_{\mathrm{O}}^{\beta} = c_{\beta}\bar{n}_{\beta}^{\mathrm{O}}. \tag{7.4}$$

Hence, the fraction of NBO atoms can be re-written as

$$f_{\mathrm{NBO}} = (2c_{\mathrm{O}} - c_{\mathrm{P}}\bar{n}_{\mathrm{P}}^{\mathrm{O}} - c_{\mathrm{Ge}}\bar{n}_{\mathrm{Ge}}^{\mathrm{O}} - c_{\mathrm{Al}}\bar{n}_{\mathrm{Al}}^{\mathrm{O}})/c_{\mathrm{O}}. \tag{7.5}$$

The number of NBO atoms per phosphorus atom is given by $N_{\mathrm{NBO}}/N_{\mathrm{P}} = (c_{\mathrm{O}}/c_{\mathrm{P}})f_{\mathrm{NBO}}$ where N_{P} is the number of phosphorus atoms. The number of BO atoms per phosphorus atom can be written as

$$N_{\mathrm{BO}}/N_{\mathrm{P}} = 4 - (c_{\mathrm{O}}/c_{\mathrm{P}})f_{\mathrm{NBO}}, \tag{7.6}$$

assuming $\bar{n}_{\mathrm{P}}^{\mathrm{O}} = 4$. The nearest neighbor O-O coordination number is written as

$$\bar{n}_{\mathrm{O}}^{\mathrm{O}} = f_{\mathrm{NBO}}\bar{n}_{\mathrm{NBO}}^{\mathrm{O}} + f_{\mathrm{BO}}\bar{n}_{\mathrm{BO}}^{\mathrm{O}}, \tag{7.7}$$

where the fraction of BO atoms $f_{\mathrm{BO}} = 1 - f_{\mathrm{NBO}}$.

For the NAGP crystals with $x = 0$ the network connectivity is based on a corner sharing tetrahedral PO_4 and octahedral GeO_6 units in which each BO atom is shared between a tetrahedron and an octahedron (Figure 7-1). Each BO atom has three nearest-neighbor O atoms within a tetrahedron and four nearest-neighbor O atoms within an octahedron such that $\bar{n}_{\mathrm{O}}^{\mathrm{O}} = \bar{n}_{\mathrm{BO}}^{\mathrm{O}} = 7$, as determined by the Rietveld refinement on the crystalline

NAGP [225]. For these samples, $f_{\mathrm{NBO}} = 0$ since the Al^{3+} ions substitute at the sites of the Ge^{4+} ions such that $\bar{n}^{\mathrm{O}}_{\mathrm{Al}} = \bar{n}^{\mathrm{O}}_{\mathrm{Ge}} = 6$. For the case of the glasses, the coordination numbers take values smaller than six, so NBO atoms appear. As the composition changes from $x = 0$ to $x = 0.8$ the fraction of NBO atoms increases leading to an increase in $N_{\mathrm{NBO}}/N_{\mathrm{P}}$ and a decrease in $N_{\mathrm{NBO/Na}}$ [Figures 7-24(c)-7-24(e)].

The $D_X(r)$ and $D_N(r)$ fits for the annealed glasses shows a small increase in the Ge-O and Al-O coordination numbers as compared to the as-prepared glasses, which leads to a reduction in f_{NBO} as well as in both $N_{\mathrm{NBO}}/N_{\mathrm{P}}$ and $N_{\mathrm{NBO}}/N_{\mathrm{Na}}$. The $N_{\mathrm{NBO}}/N_{\mathrm{P}}$ ratios are consistent with a mixture of $P^{(3)}$ and $P^{(4)}$ species, as found from ^{31}P NMR experiments.

A structural model developed by Gammond et al [225] for the NAGP glasses, known as the super-structural model, suggests $\bar{n}^{\mathrm{O}}_{\mathrm{Ge}}$ and $\bar{n}^{\mathrm{O}}_{\mathrm{Al}}$ values that are larger than four in which the phosphate species are constrained to be either $P^{(3)}$ or $P^{(4)}$. The Ren and Eckert model [232] for sodium phosphosilicate glasses provides a starting point where super-structural units contain sixfold coordinated silicon atoms (Figure 7-23). The formula of $x = 0$, can be rewritten as $(Na_2P_6GeO_{18})_{1/8}(GeO_2)$. BO atoms will be denoted by Ø and the number of BO atoms per Ge or P atom will be denoted by a superscript. In the Ren and Eckert model the part of the glass $Na_2P_6GeO_{12}$ is built from the super-structural units $[Ge^{(6)}P^{(3)}_6Ø_{10}Ø_{4/2}O_6]^{2-}$, where the negative charge on a unit is compensated by two Na^+ ions. The other part of the glass, GeO_2, is built from charge neutral corner-sharing tetrahedral $Ge^{(4)}$ units. So the model contains $P^{(3)}$, $Ge^{(4)}$, $Ge^{(5)}$ and $Ge^{(6)}$ motifs. All NBO atoms will reside in the $P^{(3)}$ species carrying a partial charge of -(2/6)e = -0.33e and e is the elementary charge.

The model gives $\bar{n}^{\mathrm{O}}_{\mathrm{Ge}} = 4.5$ with $x = 0$, which is smaller than the value found from diffraction experiments (Table 7.16). However, a larger Ge-O coordination number can be obtained by using the NBO atoms within the $P^{(3)}$ motifs of a super-structural unit to convert $Ge^{(4)}$ to $Ge^{(6)}$ units according to the scheme

$$2\left[P^{(3)}Ø_{3/2}O\right] + Ge^{(4)}Ø_{4/2} \longrightarrow 2\left[P^{(4)}Ø_{4/2}\right]^{+} + \left[Ge^{(6)}Ø_{6/2}\right]^{2-}. \qquad (7.8)$$

In the crystal structures determined by Rietveld refinement [225], $P^{(4)}$–Ø–$P^{(4)}$ linkages are absent, i.e, the phosphate chains in the model dissociate as $Ge^{(6)}$ species join to expand a super-structural unit.

Consider a fraction, y, of the $Ge^{(4)}$ atoms to be converted to $Ge^{(6)}$ units. The propor-

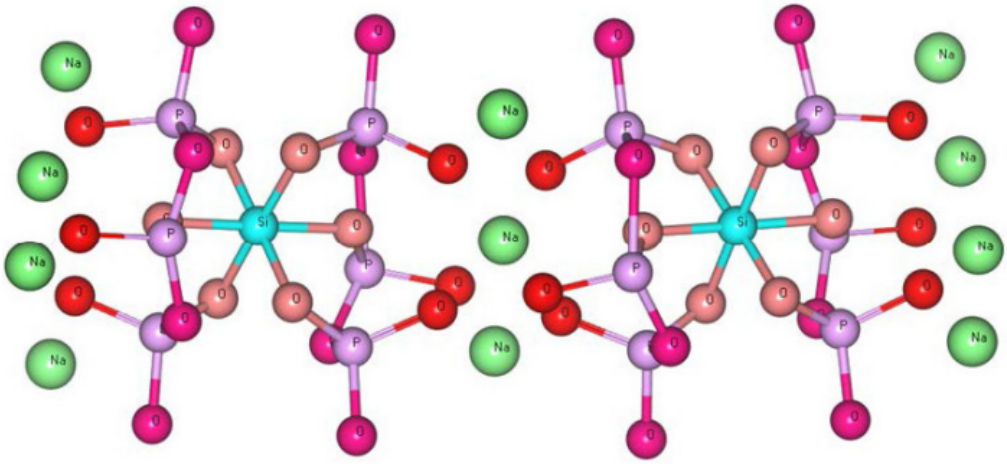

Figure 7-23: Two of the $[Si^{(6)}P_6^{(3)}Ø_{10}Ø_{4/2}O_6]^{2-}$ super-structural units in the model of Ren and Eckert [232] for $Na_2P_6SiO_{18}$ glass, where charge-shuttling ensures that the NBO atoms in the P^3 phosphate motifs carry a partial negative charge.

tion of the initial super-structural units are converted to $[Ge^{(6)}P_6^{(4)}Ø_6\ Ø_{18/2}]^{4+}$ units according to the equation

$$\begin{aligned} &Na^+ + \frac{1}{2}\left[Ge^{(6)}P_6^{(3)}Ø_{10}Ø_{4/2}O_6\right]^{2-} + \frac{3y}{2}Ge^{(4)}Ø_{4/2} + \frac{3(1-y)}{2}Ge^{(4)}Ø_{4/2} \longrightarrow \\ &Na^+ + \frac{(1-y)}{2}\left[Ge^{(6)}P_6^{(3)}Ø_{10}Ø_{4/2}O_6\right]^{2-} + \frac{y}{2}\left[Ge^{(6)}P_6^{(4)}Ø_6Ø_{18/2}\right]^{4+} + \\ &\frac{3y}{2}\left[Ge^{(6)}Ø_{6/2}\right]^{2-} + \frac{3(1-y)}{2}Ge^{(4)}Ø_{4/2}. \end{aligned} \tag{7.9}$$

In the $\left[Ge^{(6)}P_6^{(4)}Ø_6Ø_{18/2}\right]^{4+}$ units each of the six $P^{(4)}$ motifs has three BO atoms without involving $P^{(4)} - Ø - P^{(4)}$ linkages.

The coordination number of Ge-O can be rewritten as

$$\bar{n}^{O}_{Ge} = 4f_{Ge^{(4)}} + 6f_{Ge^{(6)}}, \tag{7.10}$$

where $f_{\mathrm{Ge}^{(i)}}$ is the fraction of $\mathrm{Ge}^{(i)}$ atom, and $f_{\mathrm{Ge}^{(4)}} + f_{\mathrm{Ge}^{(6)}} = 1$. From equation 7.9,

$$f_{\mathrm{Ge}^{(6)}} = (1 + 3y)/4, \tag{7.11}$$

which gives $\bar{n}^{\mathrm{O}}_{\mathrm{Ge}} = 3(y + 3)/2$. The fraction of NBO atoms is written as

$$f_{\mathrm{NBO}} = (1 - y)/4, \tag{7.12}$$

and $f_{\mathrm{NBO}} + f_{\mathrm{BO}} = 1$ The phosphate units are either $\mathrm{P}^{(3)}$ or $\mathrm{P}^{(4)}$ motifs. $\mathrm{P}^{(3)}$ has one NBO and $\mathrm{P}^{(4)}$ has only BO. The fraction of $\mathrm{P}^{(3)}$ species is given by

$$f_{\mathrm{P}^{(3)}} = N_{\mathrm{NBO}}/N_{\mathrm{P}} = (1 - y), \tag{7.13}$$

$f_{\mathrm{P}^{(3)}} + f_{\mathrm{P}^{(4)}} = 1$ and $N_{\mathrm{NBO}}/N_{\mathrm{P}} + N_{\mathrm{BO}}/N_{\mathrm{P}} = 4$. The number of NBO atoms per sodium atom is

$$N_{\mathrm{NBO}}/N_{\mathrm{Na}} = 3(1 - y), \tag{7.14}$$

and $N_{\mathrm{NBO}}/N_{\mathrm{Na}} + N_{\mathrm{BO}}/N_{\mathrm{Na}} = 12$. In the $y = 1$ limit, $\bar{n}^{\mathrm{O}}_{\mathrm{Ge}} = 6$ and $f_{\mathrm{NBO}} = 0$ such that $f_{\mathrm{P}^{(4)}} = 1$.

Table 7.18 gives the parameters for NAGP with $x = 0$ predicted by the Gammond model. The average Ge-O coordination number for the composition $x = 0$ is $\bar{n}^{\mathrm{O}}_{\mathrm{Ge}} = 5.07(7)$ for the as-prepared glass versus $\bar{n}^{\mathrm{O}}_{\mathrm{Ge}} = 5.11(2)$ for the annealed glass. For the as-prepared glass $y = 0.382(44)$ and it follows that $f_{\mathrm{NBO}} = 0.154(11)$, $f_{\mathrm{P}^{(3)}} = 0.618(20)$ and $N_{\mathrm{NBO}}/N_{\mathrm{Na}} = 1.85(13)$. For the annealed glass, $y = 0.407(13)$, $f_{\mathrm{NBO}} = 0.148(3)$, $f_{\mathrm{P}^{(3)}} = 0.593(20)$and $N_{\mathrm{NBO}}/N_{\mathrm{Na}} = 1.78(4)$. The $\mathrm{P}^{(3)}$:$\mathrm{P}^{(4)}$ ratio is therefore 1.62:1 for the as-prepared glass versus 1.46(8):1 for the annealed glass. Then by converting $\mathrm{P}^{(3)}$ to $\mathrm{P}^{(4)}$ motifs the super-structural units grow on thermal annealing in order to generate $\mathrm{Ge}^{(6)}$ from $\mathrm{Ge}^{(4)}$ units.

In the crystal, the $\mathrm{P}^{(3)}$ chains dissociate as $\mathrm{Ge}^{(6)}$ motifs are created, so all the phosphate tetrahedra are $\mathrm{P}^{(4)}$ units. The results in table show that the super-structural units can grow when the glasses are thermally annealed by converting $\mathrm{P}^{(3)}$ to $\mathrm{P}^{(4)}$ motifs in order to accommodate more $\mathrm{Ge}^{(6)}$ units. This finding is also supported by the NMR results (Figure 7-22). Therefore, the super-structural units provide the nucleation sites for crystal growth via an internal nucleation mechanism.

Condition	glass as-prepared	glass annealed 873 K for 0.25 h	glass annealed 876 K for 0.25 h	annealed 876K for 0.5 h
$\bar{n}^{O}_{Ge}$	5.07(7)	5.11(2)	5.09(5)	5.21(5)
y	0.382(44)	0.407(13)	0.393(33)	0.473(33)
f_{NBO}	0.154(11)	0.148(3)	0.152(8)	0.132(8)
N_{NBO}/N_{Na}	1.85(13)	1.78(4)	1.82(10)	1.58(10)
$f_{P^{(3)}}/f_{P^{(4)}}$	1.62(22)	1.46(6)	1.54(16)	1.11(11)
$f_{P^{(3)}}/f_{P^{(4)}}$	2.13(6)	1.70(5)	1.56(4)	0.96(3)

Table 7.18: Parameters predicted for the $x = 0$ composition by the super-structural model. The calculated ratio $f_{P^{(3)}}/f_{P^{(4)}}$ is compared to the measured in the ^{31}P MAS NMR experiments.

The electrical conductivity in the NASICON system is predominantly ionic where the ionic conductivity is given by $\sigma = ne\mu$, where n is the effective carrier concentration, e is the charge on the mobile Na^+ ions and μ is the ion mobility [233]. For the NAGP crystals the electrical conductivity [Figure 7-24(a) and 7-24(b)] increases by almost two orders of magnitude and the activation energy, E_a, decreases as as the composition changes from $x = 0$ to $x = 0.8$ when Ge^{4+} ions are substituted by Al^{3+} ions and additional Na^+ ions are introduced to compensate for charge deficit. The substitution for Al^{3+} ions does not create NBO atoms, i.e, $f_{NBO} = 0$ as seen from the super-structural model. The conductivity is between 3.2 and 40 times larger than that of the as-prepared glass.

For the glass, the composition dependence of conductivity for the crystals is roughly matched by scaling [Figure 7-24(a)]. σ also increases with x but the mobility of these ions is much smaller in the more disordered glass structure. NBO atoms appear in the glass as part of $P^{(3)}$ motifs on the super-structural units. They are negatively polarized and probably influence the Na^+ ion mobility, although the role that they play is still unclear.

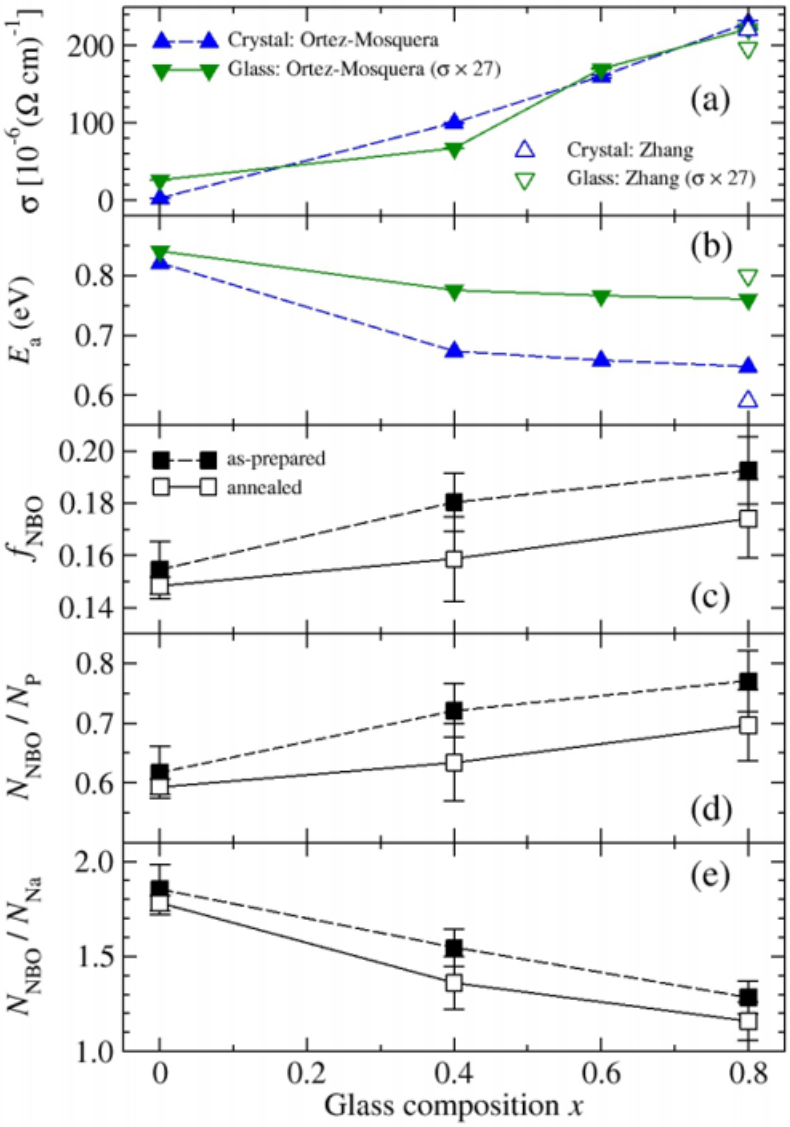

Figure 7-24: Composition dependence of the (a) electrical conductivity σ at 573 K and (b) activation energy E_a in crystalline versus as-prepared glassy NAGP. (c)-(e) Several of the parameters describing the NBO atoms in as-prepared vs annealed NAGP glasses. In (a) and (b), the crystalline materials were obtained from the as-prepared glass either (i) by thermal annealing at a temperature in the range 917-939 K for 3 h or (ii) by two stage process in which crystals were first nucleated by heating for 2 h at a temperature between $T_g = 851$ K and $T_x = 937$ K and the resultant material was then annealed at 1023 K for 18 h. In (a) the results for the glass are scaled by a factor of 27. In (b) the error bars are smaller than the triangle size. For the $x = 0$ composition, the annealed glass corresponds to $T_{TT} = 873$ K. For the $x = 0.4$ composition, the annealed glass corresponds to $T_{TT} = 845$ K [225].

7.5 Conclusion

The structure of crystalline $Na_{1+x}Al_xGe_{2-x}(PO_4)_3$ with x= 0, 0.4 and 0.8 was investigated using X-ray diffraction. The results indicate tetrahedral PO_4 units where the distribution of P-O distances is broader and can be accommodated by using two Gaussian peaks to describe the nearest-neighbor P-O correlations. The ionic conductivity increases with x as more Na^+ ions are introduced. The ion transport does not involve NBO atoms because they are absent from the crystal structures. These results therefore conform the expected NASICON structure.

The structure of the as-prepared and annealed NAGP glasses was investigated by neutron and X-ray diffraction. The pair-distribution function analysis used ^{31}P and ^{27}Al NMR results to help interpret the data. The Ge-O and Al-O coordination numbers are lower than the value 6 found for crystalline samples, which indicates the presence of NBOs. The Ge-O coordination number is higher for the annealed than for the as-prepared glasses. However, no significant change in the Ge-O coordination number was observed between the different annealing times. These results show that substantial structural reorganisation must be undertaken during the crystallization process.

The conductivity of the glass increases with concentration of Na^+ ions, where at the same time there is an increase in both f_{NBO} and the ratio NBO:P but a decrease in the ratio NBO:Na. The effect of NBO atoms in the Na^+ ion mobility is in need of further investigation. A structural model is proposed for the $x = 0$ by adapting the Ren and Eckert model [232] for phosphosilicate glasses. In the model, the structure can be modified by using the donor function of a doubly-bonded NBO on a $P^{(3)}$ to convert $Ge^{(4)}$ atoms to higher coordinated Ge atoms, thereby converting $P^{(3)}$ to $P^{(4)}$ motifs and increasing the size of a super-structural unit. The $P^{(4)}$ species have a formal positive charge, so they do not attract sodium ions. Accordingly, they interact more weakly with Na^+ ions than the $P^{(3)}$ species. An explanation for the structural model is provided by a deconvolution of the ^{31}P MAS NMR spectra [225] for the as-prepared glass.

When the glass is thermally annealed, the ^{31}P MAS NMR spectra show a small increase in the fraction of $P^{(4)}$ species [225], indicating a further progression to the super-structural unit. This modification is also seen by a moderate increase in the Ge coordination number found from the diffraction experiments and a reduction in f_{NBO}. The $P^{(4)}$ species generated within the modified super-structural units by the reaction of $P^{(3)}$ motifs with $Ge^{(4)}$ units therefore provide the nucleation sites for crystal growth via an internal nucleation mechanism.

Chapter 8

The $Na_{1+x}Ti_2Si_xP_{3-x}O_{12}$ system for solid electrolyte applications

8.1 Introduction

The scientific and technological challenges of finding new devices that can store energy and replace energy sources such as fossil fuels has boosted the development of batteries. Among the batteries that are widely used in electrical cars and in electronic devices such as cell phones and notebooks are those containing lithium ions. Although the technology of these batteries has improved in recent years, there is a limited natural abundance of Li and its limited geographic distribution has launch a search for less expensive alternatives. Studies in recent years have shown that sodium based batteries constitute an excellent alternative for energy storage since it is also widely available and has less toxicity than lithium [234–237].

Here, sodium (Na) super-ionic conductor (NASICON) materials have received significant attention in view of their large sodium-ion conductivity and structural stability in the solid state [238–240]. An example is provided by the crystalline $NaTi_2(PO_4)_3$ [241, 242] where the crystal structure is based on a negatively-charged framework of corner-sharing TiO_6 octahedra and tetrahedral PO_4 units. Each octahedral TiO_6 is connected to six tetrahedral units and each tetrahedral PO_4 is connected to four octahedral units [243, 244]. The Na^+ ions reside in the interstitial sites of the framework and are free to move around these sites. A strategy for increasing the ionic conductivity of $NaTi_2(PO_4)_3$ is to replace P^{5+} ions by Si^{4+} ions and thereby increase the Na^+ content of the material, thus ensuring charge neutrality [245–247].

These $Na_{1+x}Ti_2Si_xP_{3-x}O_{12}$ (NTSP) materials can be made via a glass-ceramic route, although the extent to which P^{5+} ions are replaced by Si^{4+} ions remains unclear [242, 248, 249]. The glass-ceramic route can reduce the porosity of the final materials and control its micro-structure via thermal treatment. Hence, there is an interest in the structure of the parent glass and how it evolves as the system crystallizes. In the NASICON system $Na_{1+x}Al_xGe_{2-x}(PO_4)_3$ (NAGP) with $x = 0$, 0.4 and 0.8, the internal crystal nucleation proceeds via super-structural units that are built into the glass structure (Chapter 7). Vitreous NASICONs are also of interest because they contain five-fold and/or sixfold coordinated network-forming units, thus transcending Zachariasen's rules for glass formation [181]. In this chapter, the structure of $Na_{1+x}Ti_2Si_xP_{3-x}O_{12}$ glasses with $x = 0.8$ and $x = 1.0$ was investigated by combining X-ray and neutron diffraction. This combination offers an effective way to obtain information on the coordination environment of Ti-O since it's correlations with other elements have a negative weighting in neutron diffraction because of the negative neutron scattering length of Ti [38] versus a large positive weighting in X-ray diffraction due to the large atomic number of Ti (Z = 22).

8.2 Experiment

8.2.1 Sample Preparation

Powders of sodium carbonate (Na_2CO_3, Vetec 99.9%), titanium dioxide (TiO_2, Aldrich > 99.9%), dihydroxy ammonium phosphate ($(NH_4)_2HPO_4$, Aldrich > 98%) and silicon dioxide (SiO_2, Zetasil2 > 99%) were used as starting materials. All the reagents were mixed in a rotary ball mill with alumina balls for 12 h, after which they were placed in a platinum crucible and heated for 6 h to temperatures ranging from 400 to 700 °C to remove volatile compounds such as CO_2 from the Na_2CO_3 and NH_3 and H_2O from $(NH_4)_2HPO_4$ [242].

The homogenized mixture was then heated to temperatures of 1400 - 1500 °C for 30 minutes and the resulting liquid was splat-cooled (pressed between two metal plates). The glassy materials were grey and optically opaque (Figure 8-1) due to the presence of titanium and were investigated in their as-prepared state.

The characteristic temperatures of the NTSP glasses (Table 8.1), namely glass transition temperature (T_g) and crystallization temperature (T_x) were determined by differential scanning calorimetry (Netzsch DSC404) [242] with a heating rate of 10 °C/min and a temperature range of 30-1000 °C.

Figure 8-1: NTSP glass with composition $x = 1.0$.

x	Na_2O	TiO_2	SiO_2	P_2O_5	T_g	T_x	ρ	n_0
0.8	18.8	41.7	16.7	22.9	677	729	2.8719(9)	0.0775(1)
1.0	20.0	40.0	20.0	20.0	635	758	2.8397(4)	0.0767(1)

Table 8.1: Nominal composition and characteristic temperatures of the NTSP precursor glasses. T_g (K) is the glass transition temperature, T_x (K) is the onset of the crystallization temperature. ρ is the measured mass density (g/cm^3) and n_0 is the corresponding number density (Å^{-3}).

8.2.2 D4c Experiment

The neutron diffraction experiment was carried out using the D4c diffractometer at the Institut Laue-Langevin in Grenoble with an incident neutron wavelength of $\lambda = 0.4955(1)$ Å. The samples were held at room temperature (∼298 K) in a cylindrical vanadium container of inner diameter 6.8 mm and wall thickness 0.1 mm. Diffraction patterns were measured for each sample in its container, the empty container, the empty instrument and a cylindrical vanadium rod of diameter 6.08 mm for normalization purposes. A diffraction pattern was also measured for a slab of neutron absorbing $^{10}B_4C$ in order to estimate the effect of the sample's attenuation to the background count rate [101] at small scattering angles.

The counting times for the empty container and the sample in the container were optimized to decrease the statistical error on the container-corrected intensity [101].

x	w_{SiO}	w_{PO}	w_{TiO}	w_{NaO}	w_{OO}	$G(0)$
0.8	0.06577(6)	0.2230(9)	-0.1361(3)	0.1296(9)	0.6888(5)	-0.1991(3)
1.0	0.08107(9)	0.2005(7)	-0.1343(3)	0.1419(11)	0.6803(5)	-0.1975(3)

Table 8.2: The neutron weighting factors (in barn) for the partial pair distribution functions of the NTSP glasses with $x = 0.8$ and $x = 1.0$ used in the $D_N(r)$ fits.

8.2.3 6-ID-D Experiment

The high energy X-ray diffraction experiment on the $Na_{1+x}Ti_2Si_xP_{3-x}O_{12}$ was done at room temperature using the 6-ID-D diffractometer at the APS. The photon energy of the square incident beam was 100.233 keV, corresponding to a wavelength of 0.1236 Å. The ground glasses were loaded into kapton polyimide tubes of 1.80(1) mm internal diameter and 0.051(6) mm wall thickness.

The scattered X-rays were detected using a Varex 4343CT amorphous silicon flat panel detector that was placed at ≈ 311(1) mm from the sample position as deduced from the

x	Q_{FSDP} [Å^{-1}]	Q_{PP} [Å^{-1}]	Q_3 [Å^{-1}]	Q_{max} [Å^{-1}]
0.8	1.587(1)	2.824(1)	5.286(2)	23.40
1.0	1.549(1)	2.814(1)	5.307(2)	22.45

Table 8.3: The positions of the first three peaks Q_{FSDP}, Q_{PP} and Q_3 in the $S_N(Q)$ functions. Also given are the Q_{max} values used in the Fourier transformation.

diffraction pattern measured for crystalline CeO_2. Diffraction patterns were measured for each sample in its capillary, an empty capillary and the empty instrument. The data were converted to one-dimensional diffraction patterns using FIT2D [84]. The program PDFgetX2 [85] was used to correct for background scattering, beam polarization, attenuation and Compton scattering.

8.3 Results

The measured $S(k)$ functions for neutrons and X-rays are shown in figures 8-4 and 8-7, respectively. It is observed a difference between ND and XRD in accordance with the different weighting factors for the partial structure factors (Figures 8-2 and 8-3). The $S_X(Q)$ function for $x = 1.0$ show a small Bragg peak at $\simeq 1.55$ Å, which is indicative of a small amount of crystallization.

8.3.1 Neutron diffraction

The position of the first three peaks in $S_N(Q)$ are listed in table 8.3. The total pair distribution functions $D_N(r)$ are shown in figure 8-5 and the weighting factors of the partial pair distribution functions are given in table 8.2.

The $D_N(r)$ fits are shown in figure 8-6. The first peak at $\simeq 1.55$ Å is attributed to P-O and Si-O correlations and the second peak at $\simeq 1.95$ Å is attributed to Ti-O correlations. The latter appears as a negative peak because of the negative scattering length of Ti. In the crystalline structure of $NaTi_2(PO_4)_3$, the nearest neighbor Na-O correlations appear at around 2.29-2.50 Å. For tetrahedral PO_4 and SiO_4 motifs with P-O and Si-O bond distances 1.526 Å and 1.647 Å, respectively, the nearest neighbor O-O correlations are expected to be at $r_{\mathrm{OO}} = \sqrt{8/3} r_{\mathrm{PO}} = 2.492$ Å and $r_{\mathrm{OO}} = \sqrt{8/3} r_{\mathrm{SiO}} = 2.692$ Å. The Na-O and O-O correlations in the $D_N(r)$ functions were fitted in order to constrain the peaks fitted at small r values. The fitted parameters are summarized in table 8.4.

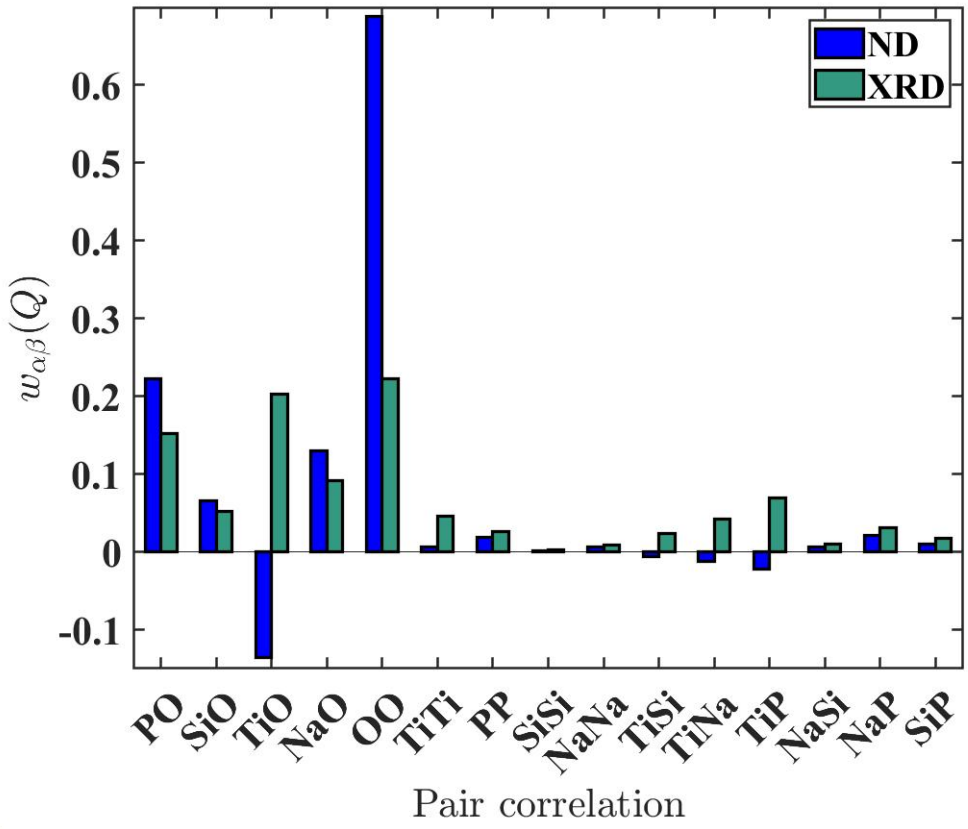

Figure 8-2: The weighting factors $w_{\alpha\beta}(Q)$ of the partial pair distribution functions for the neutron diffraction (ND) versus X-ray diffraction (XRD) experiments on the NTSP glasses with $x = 0.8$. The X-ray values were calculated for $Q = 0$.

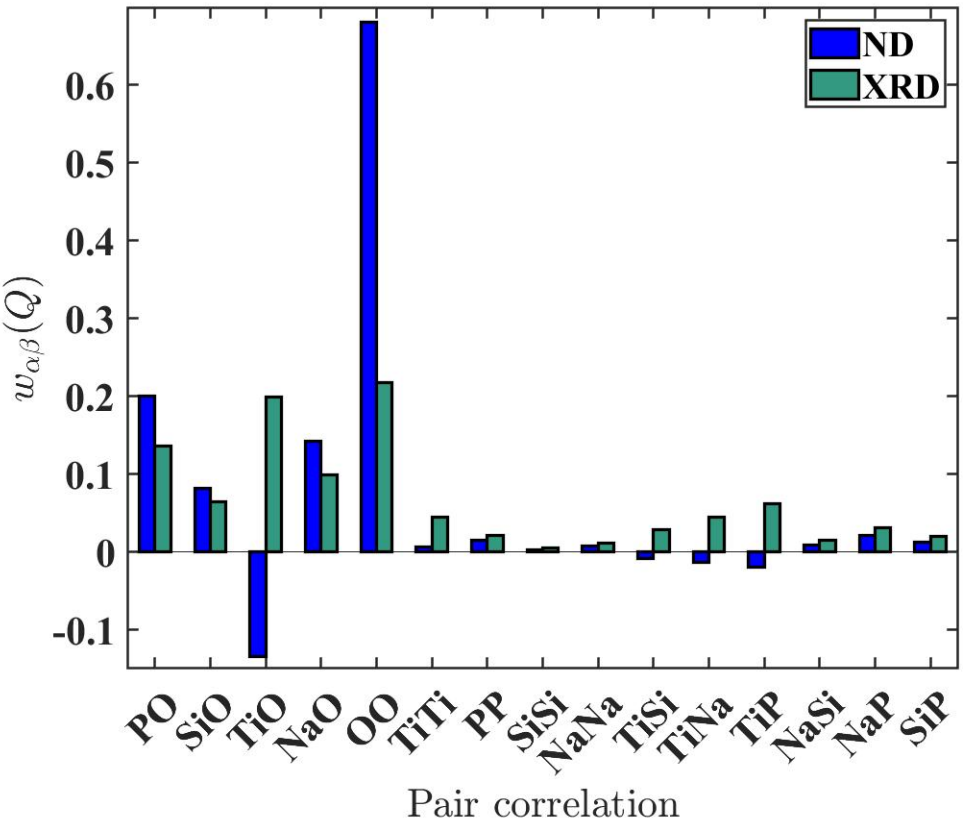

Figure 8-3: The weighting factors $w_{\alpha\beta}(Q)$ of the partial pair distribution functions for the neutron diffraction (ND) versus X-ray diffraction (XRD) experiments on the NTSP glasses with $x = 1.0$. The X-ray values were calculated for $Q = 0$.

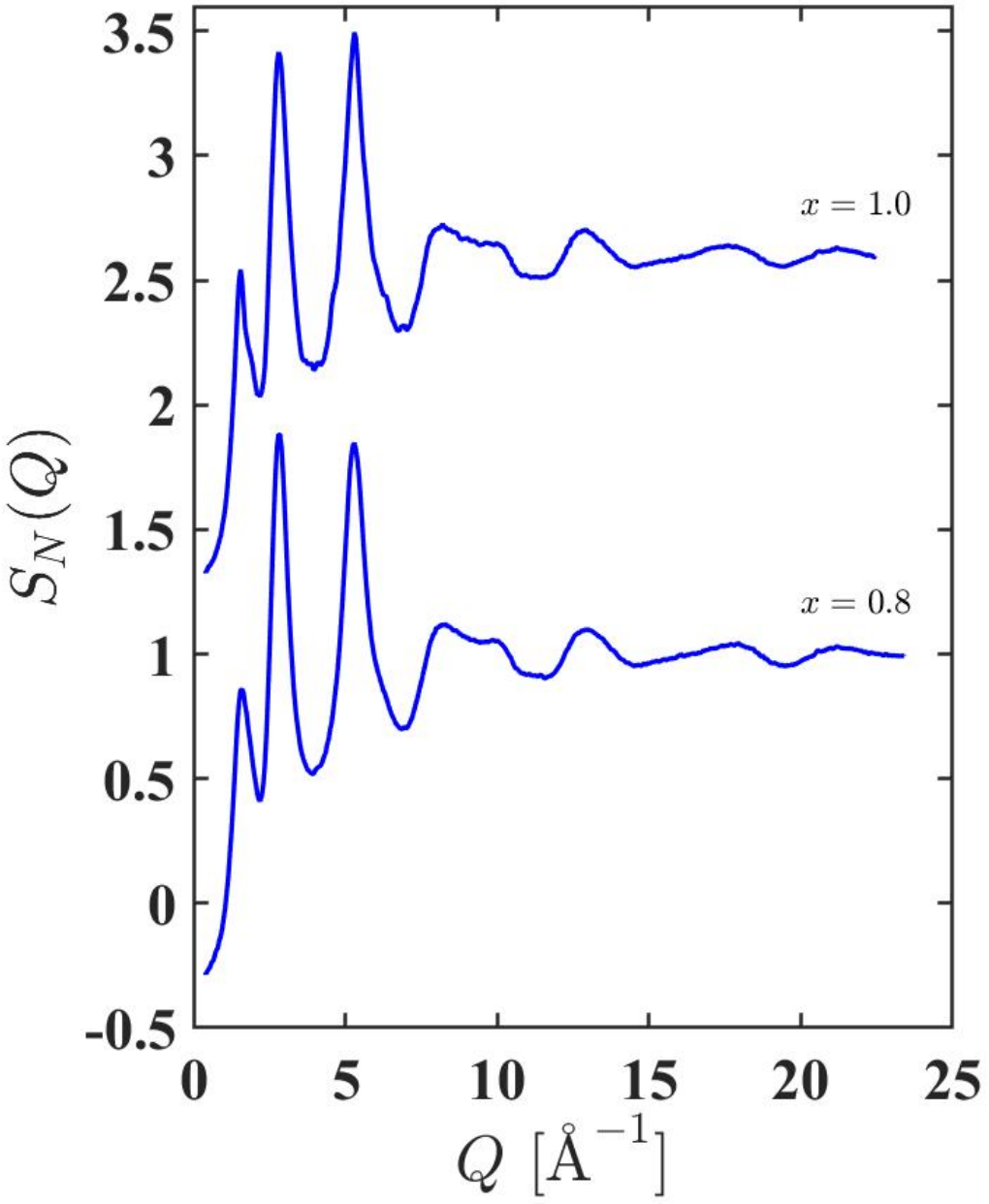

Figure 8-4: The $S_N(Q)$ functions for glassy NTSP. The vertical error bars are smaller than the line thickness at most Q values. The $x = 1.0$ data sets are shifted for clarity of presentation.

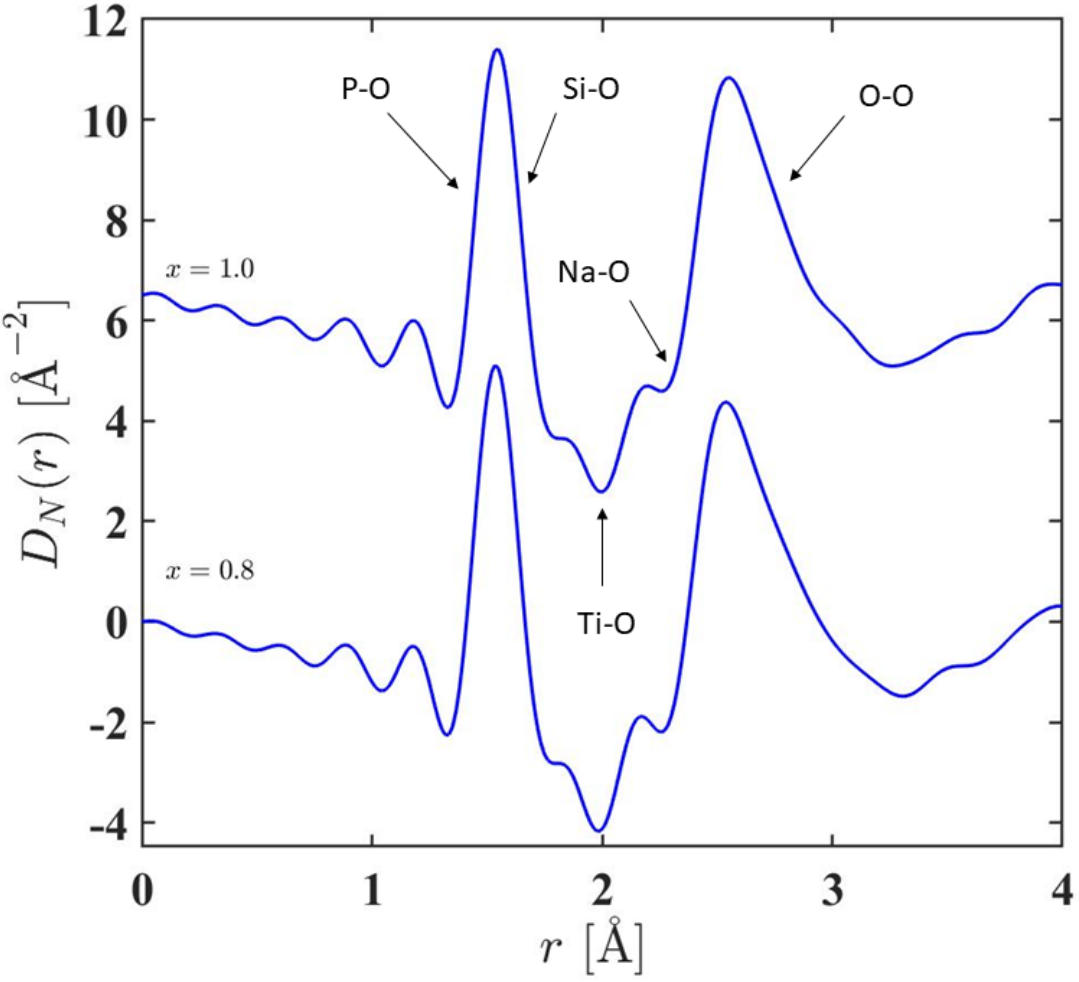

Figure 8-5: Total pair distribution functions $D_N(r)$ for the NTSP glasses. The curves were obtained by Fourier transforming the reciprocal data shown in figure 8-4 after spline fitting. The $x = 1.0$ data sets are shifted for clarity of presentation. Arrows indicate peak assignments based on the element-oxygen distances found in the crystal structures [243–247]. Although Na-O correlations are expected at $r \approx 2.5$ Å, the large neutron scattering length and atomic concentration of O in NTSP glasses means that O-O correlations dominate the third peak. The peak assigned to Ti-O is negative relative to the other correlations.

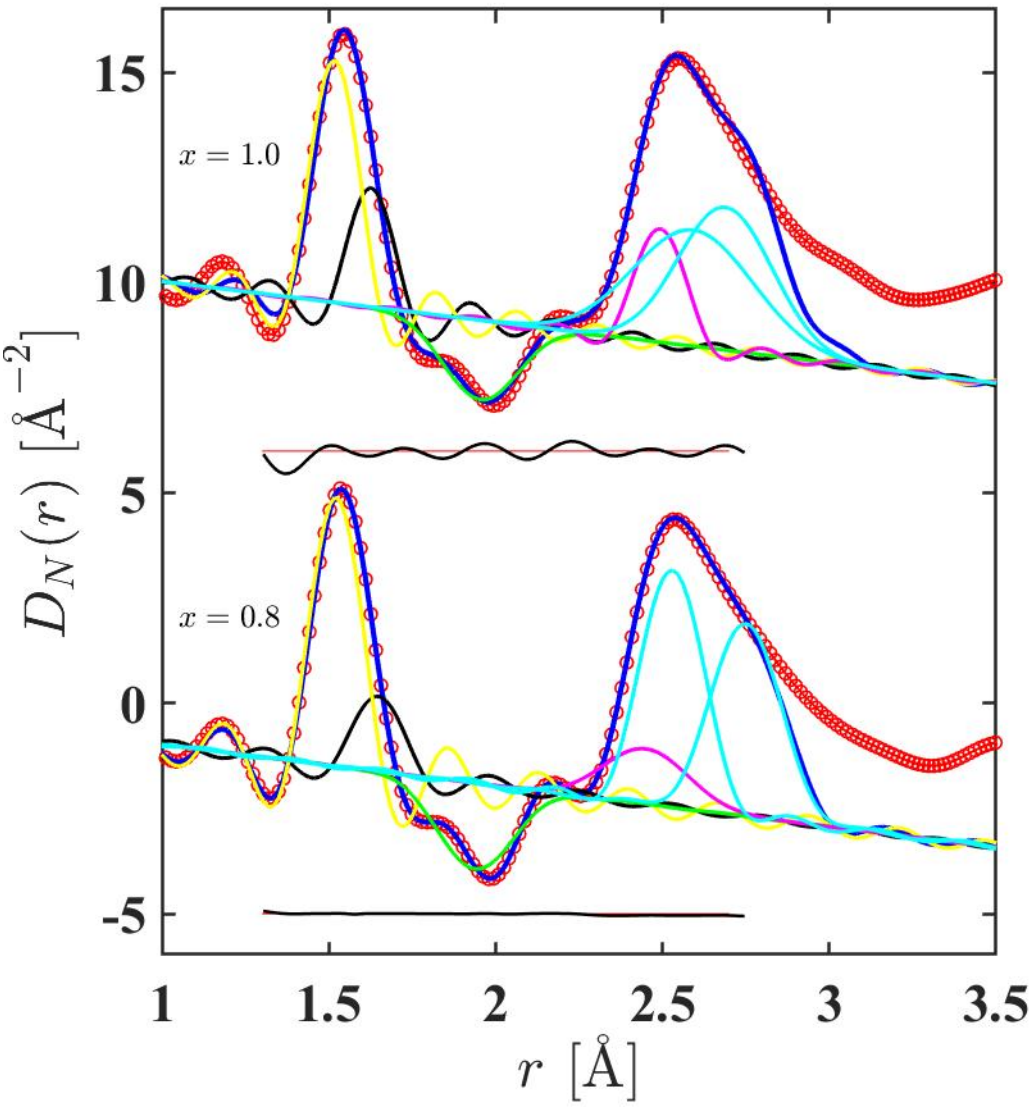

Figure 8-6: The fitted $D_N(r)$ functions for glassy NTSP. The red circles are the data, the blue solid curves are the fits and the other curves show the contribution from P-O (yellow), Si-O (black), Ti-O (green), Na-O (magenta) and O-O (cyan) correlations. The displaced black solid curve gives the residual (fit subtracted from the measured data). The Na-O and O-O correlations are introduced to constrain the peaks fitted at smaller r values.

x	Atom pair	$r_{\alpha\beta}$ [Å]	$\sigma_{\alpha\beta}$ [Å]	$\bar{n}_{\alpha}^{\beta}$	R_{χ} [%]
0.8	P-O	1.522(2)	0.026(5)	4.01(2)	0.843
	Si-O	1.648(3)	0.020(4)	4.01(2)	
	Ti-O	1.939(4)	0.110(6)	5.16(4)	
	Na-O	2.450(5)	0.125(6)	5.00(5)	
	O-O	2.529(5)	0.087(6)	3.00(5)	
	O-O	2.750(5)	0.101(6)	3.00(5)	
1.0	P-O	1.517(2)	0.041(4)	4.01(2)	5.35
	Si-O	1.623(3)	0.005(5)	4.01(2)	
	Ti-O	1.955(4)	0.111(6)	4.85(4)	
	Na-O	2.493(5)	0.057(6)	5.00(5)	
	O-O	2.592(5)	0.180(6)	3.00(5)	
	O-O	2.689(5)	0.141(6)	3.00(5)	

Table 8.4: Parameters obtained from Gaussian peak fits to the $D_N(r)$ functions for glassy NTSP. The fitted functions are shown in figure 8-6. R_{χ} is given for the fitted range 1.30-2.75 Å.

8.3.2 X-ray diffraction

The positions of the first three peaks in $S_X(Q)$ are listed in table 8.5. The total pair distribution functions $D_X(r)$ are illustrated in figure 8-8. The $D_X(r)$ fits are shown in figure 8-9 and the fitted parameters are listed in table 8.6. In a similar way to $D_N(r)$, the first peak in $D_X(r)$ is attributed to P-O and Si-O correlations and the second peak is attributed to Ti-O where the latter in the case of the X-rays appears as a peak, on account of the large atomic number of Ti ($Z = 22$). The third peak is attributed to Na-O and O-O correlations and is much smaller compared to $D_N(r)$ due to the small weighting factor for O-O correlations.

x	Q_{FSDP} [Å^{-1}]	Q_3 [Å^{-1}]	Q_4 [Å^{-1}]	Q_{max} [Å^{-1}]
0.8	2.085(2)	4.192(2)	6.172(2)	27.12
1.0	2.180(2)	4.195(2)	6.239(2)	25.88

Table 8.5: The position of the first three peaks Q_{FSDP}, Q_3 and Q_4 in the $S_X(Q)$ functions for the glassy NTSP. Also given are the Q_{max} values used in the Fourier transformation.

x	Atom pair	$r_{\alpha\beta}$ [Å]	$\sigma_{\alpha\beta}$ [Å]	$\bar{n}^{\alpha}_{\beta}$	R_{χ} [%]
0.8	P-O	1.535(1)	0.038(1)	4.01(1)	5.98
	Si-O	1.659(1)	0.038(3)	4.01(1)	
	Ti-O	1.949(1)	0.108(1)	5.17(4)	
	Na-O	2.322(1)	0.138(2)	5.02(5)	
	O-O	2.510(1)	0.063(2)	3.01(5)	
	O-O	2.690(1)	0.075(1)	3.35(5)	
1.0	P-O	1.531(1)	0.032(1)	4.01(1)	5.81
	Si-O	1.658(1)	0.010(5)	4.01(1)	
	Ti-O	1.954(1)	0.111(1)	4.87(3)	
	Na-O	2.331(1)	0.140(2)	5.00(5)	
	O-O	2.509(1)	0.076(2)	3.01(5)	
	O-O	2.690(1)	0.080(1)	3.39(5)	

Table 8.6: Parameters obtained from Gaussian peak fits to the $D_X(r)$ functions for glassy NTSP. The fitted functions are shown in figure 8-9. R_{χ} is given for the fitted range 1.30-2.74 Å.

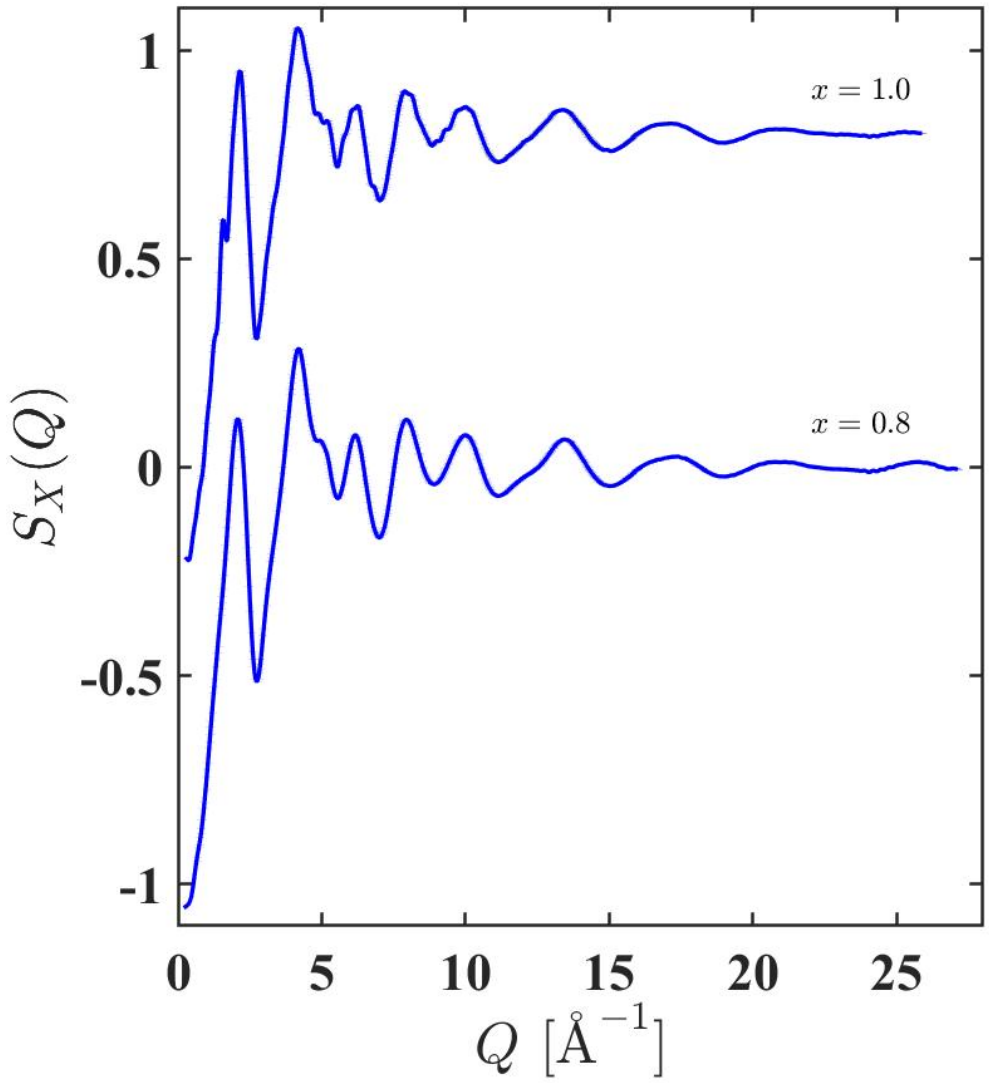

Figure 8-7: The $S_X(Q)$ functions for glassy NTSP. The vertical error bars are smaller than the line thickness at most Q values. The $x = 1.0$ data sets are shifted for clarity of presentation.

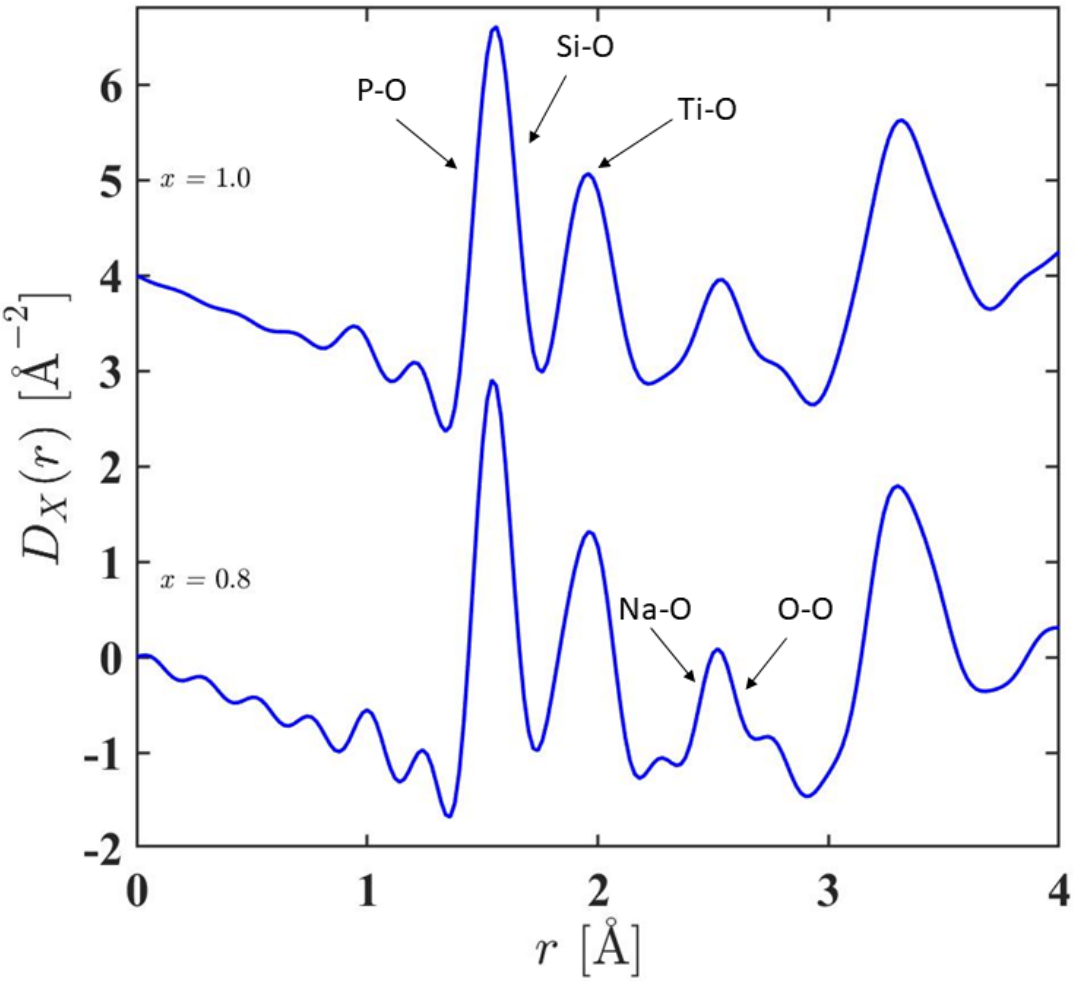

Figure 8-8: Total pair distribution functions $D_X(r)$ for the NTSP glasses. $D_X(r)$ was obtained by Fourier transforming the reciprocal data shown in figure 8-7. The $x = 1.0$ data sets are shifted for clarity of presentation. Arrows indicate peak assignments based on the element-oxygen distances found in the crystal structures [243–247].

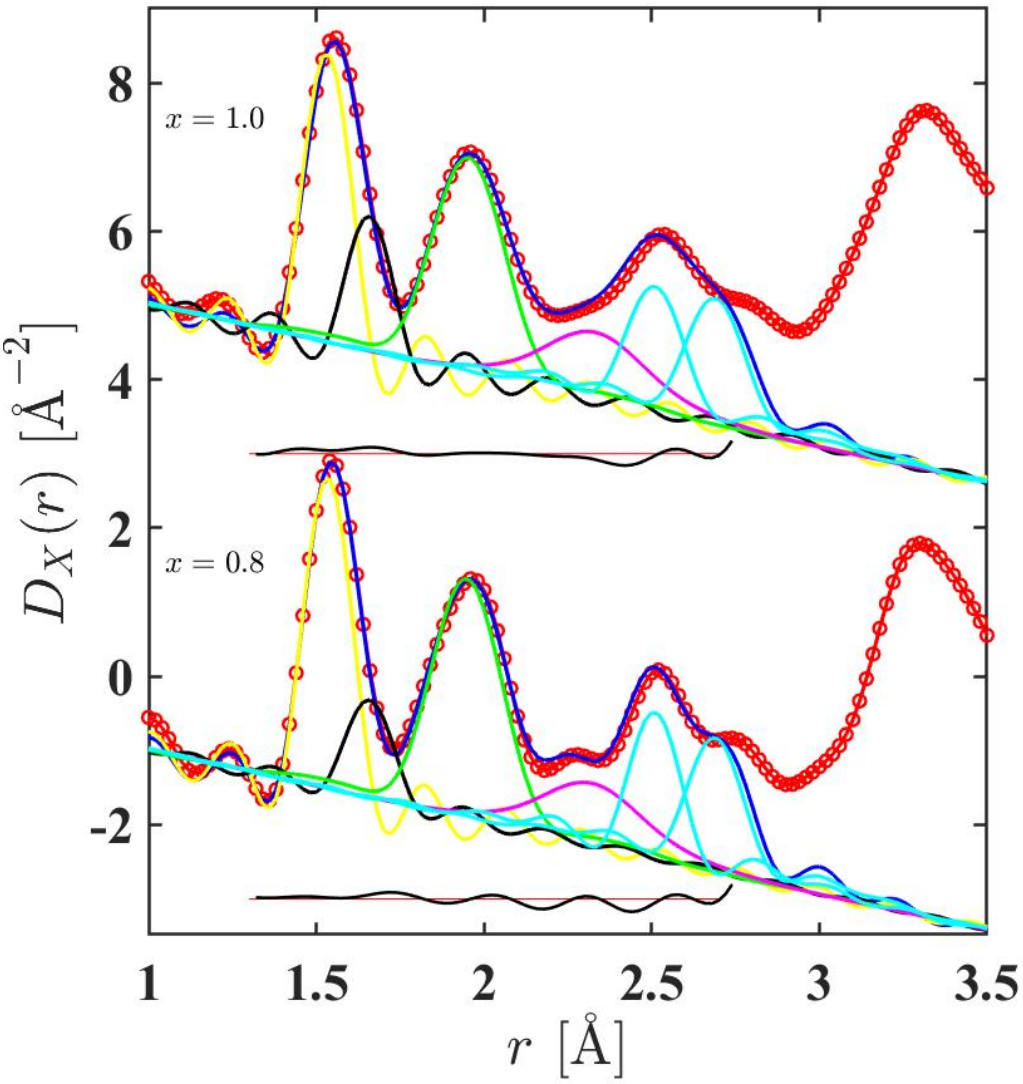

Figure 8-9: The fitted $D_X(r)$ functions for glassy NTSP. The red circles are the data, the blue solid curves are the fits and the other curves show the contribution from P-O (yellow), Si-O (black), Ti-O (green), Na-O (magenta) and O-O (cyan) correlations. The displaced black solid curve gives the residual (fit subtracted from the measured data). The Na-O and O-O correlations are introduced to constrain the peaks fitted at smaller r values.

8.4 Discussion

The neutron and X-ray diffraction results are consistent with a glass structure containing tetrahedral PO_4 and SiO_4 motifs. The mean Si-O bond length of 1.647 Å is 8% longer than the mean P-O bond length of 1.526 Å leading to tetrahedral volumes of 2.293 and 1.825 $Å^3$, respectively. Hence, the volume of a SiO_4 tetrahedron is 26% larger than that of a PO_4 tetrahedron. In the crystal structure of $Na_5Ti_2(Si_2O_9)(PO_4)$ tetrahedral SiO_4 and PO_4 units coexist [250, 251], the Si-O bond length is 4-5% longer than the mean P-O bond length, leading to a tetrahedral volume that is 12-17% larger for SiO_4 compared to PO_4.

The difference between the Si-O and the P-O bond lengths found for the NTSP system is likely to inhibit the incorporation of Si into the P sites of the NASICON $NaTi_2(PO_4)_3$ crystal structure. For example, in experiments on the $Na_{1+x}Ti_yZr_{2-y}Si_xP_{3-x}O_{12}$ system ($0 \leq x \leq 3$, $0 \leq y \leq 2$) the aim was to find the influence on the ionic conductivity of substituting Zr^{4+} by Ti^{4+} ions at fixed x. It was suggested that the framework for the fully titanium substituted NASICON with $y = 2$ does not accept the substitution of PO_4 by SiO_4 groups [25].

In the previous chapter, the ionic conductivity of the NAGP system increased with concentration of Na^+ ions by replacing Ge^{4+} ions at the octahedral sites of the crystal structure by Al^{3+} ions. An increase in conductivity with x for the NTSP materials is also observed (Figure 8-10) in an electrical characterization study done by [242]. As can be seen from figure 8-10, the inclusion of silicon leads to a considerable decrease in the activation energy when compared to that of the glass produced without silicon (NTP). When adding silicon the ionic conductivity of the NTSP samples increased by up to four orders of magnitude, where the composition $x = 1.0$ exhibits the lowest activation energy (0.31 eV) and the highest ionic conductivity of 1.0×10^{-4} S cm^{-1} at room temperature and 1.7×10^{-2} S cm^{-1} at 300 °C.

This was attributed not only to the increase of sodium ion concentration but also to the expansion of the NASICON unit cell in response to the introduction of larger Si^{4+} cations. The increase of the unit cell volume enables sodium ions to move more easily in the NASICON crystal structure, which is reflected in the decrease in activation energy. However, there is a decrease in the fraction of the NASICON phase formed at $x \geqslant 1.0$ as the silicon is increased, which is accompanied by a sharp rise in the fraction of the crystalline phase $Na(TiO)(PO_4)$ as determined by Rietveld refinement studies [242]. A progressive instability of the NASICON phase with increasing x has also been found in other studies [249].

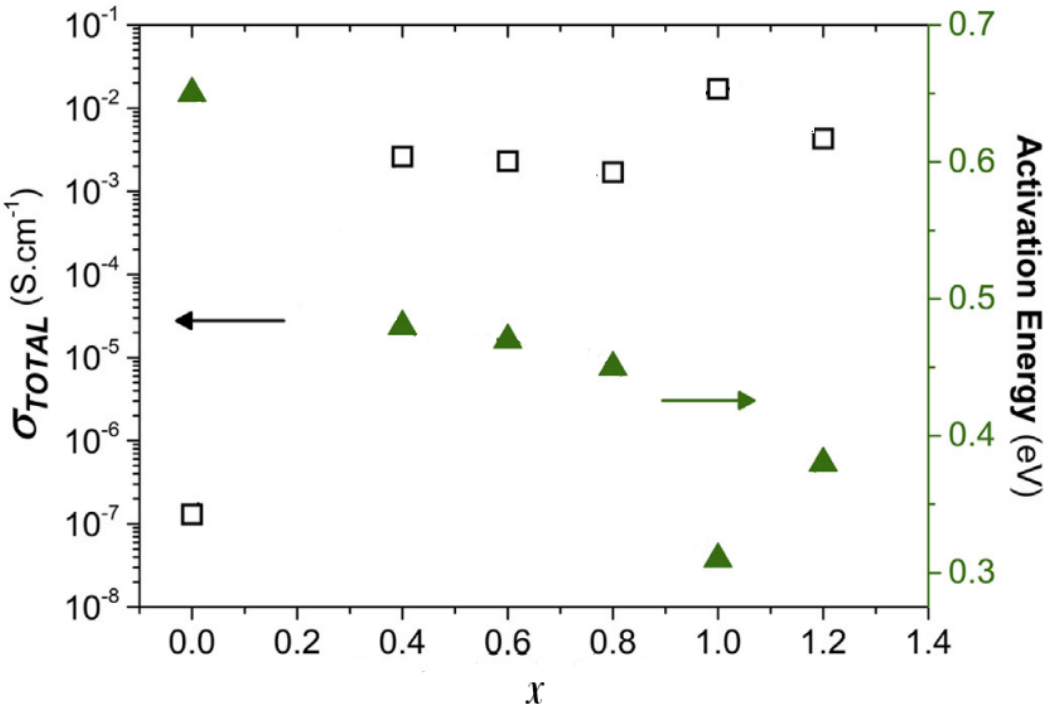

Figure 8-10: Variation of σ_{Total} at 300 °C and activation energy as a function of silica content x in the $Na_{1+x}Ti_2Si_xP_{3-x}O_{12}$ system. The values were taken from [242].

In crystalline $NaTi_2(PO_4)_3$ the Ti atoms are in an octahedral coordination environment with three short Ti-O bonds of 1.884-1.896 Å and three long Ti-O bonds of 1.964-2.107 Å [243, 244]. For the NTSP glasses investigated in this work the Ti-O bond length was expected to increase with the Ti-O coordination number to allow the Ti-centered polyhedra to incorporate a larger number of oxygen nearest neighbors. The mean Ti-O bond length is, however, 1.944 Å for $x = 0.8$ and 1.955 Å for $x = 1.0$. These results do not appear to be related to a distortion of the Ti-centered polyhedra because the peak width for the Ti-O nearest neighbors is comparable in both of the glass compositions. The mean Ti-O coordination number is 5.17(4) for $x = 0.8$ versus 4.87(3) for $x = 1.0$. The Ti coordination environment is sub-octahedral as found for the coordination environment of Ge and Al in the NAGP glass system (chapter 7).

8.5 Conclusion

The neutron and X-ray diffraction results for $Na_{1+x}Ti_2Si_xP_{3-x}O_{12}$ with $x = 0.8$ and $x = 1.0$ are consistent with network structures containing tetrahedral PO_4 and SiO_4 units with the Ti atoms residing in a sub-octahedral coordination environment.

The substitution of Si for P in the NASICON structure is possible. It would be helpful to have molecular simulations on the samples and to know the extent to which the P-O and Si-O bond lengths in the glass vary with the nature of the NASICON system, to help assess the viability of substituting PO_4 by SiO_4 units in NASICON materials. Full crystallization studies on $Na_{1+x}Ti_2Si_xP_{3-x}O_{12}$ will be interesting to provide information on the Na sites which would also help to further constrain the XRD and ND data, where there is overlap of Na-O and O-O correlations in the $D(r)$ functions.

Chapter 9

Overall Conclusions and Future Perspectives

In this work diffraction techniques were used to study the atomic level structure in aluminosilicate glasses and crystalline and glassy NASICON materials. The combination of the diffraction results with ^{27}Al and ^{31}P MAS NMR has allowed a detailed investigation of the structure of these materials.

The results of ND, XRD and ^{27}Al MAS NMR for $(ZnO)_x(Al_2O_3)_y(SiO_2)_{1-x-y}$ glasses show that most of the aluminum atoms are in a AlO_4 tetrahedra but AlO_5 and AlO_6 species are also present in the glass network. Tetrahedral SiO_4 is present in all the glass compositions. The NMR results helped extract the local coordination environment of Zn atoms with more accuracy. Zinc is used for charge-stabilizing Al in tetrahedral configuration (charge-compensating role) but when there is an excess of Zn^{2+} ions ($R > 1$ regime) they create NBO atoms in the glass network (network modifier role). It would be helpful to have more compositions in the peraluminous regime to be able to have a complete understanding of zinc in aluminosilicate glasses and compare with magnesium in this region. Using aerodynamic levitation for sample preparation would be helpful in order to extend the glass-forming region and give a wider view in the zinc behaviour.

$(MgO)_x(Al_2O_3)_y(SiO_2)_{1-x-y}$ glasses were investigated by X-ray diffraction and combined with ^{27}Al MAS NMR spectroscopy experiments to constrain structural information on the Al-O coordination number and to be able to extract the Mg-O coordination number. The results were interpreted with the aid of a structural model developed for amorphous aluminosilicate. In the case of $R = x/y > 1$, the glass structure consists

primarily of SiO_4 and AlO_4 tetrahedral units which are linked through bridging oxygen (BO) atoms. The Mg^{2+} ions either associate with non-bridging oxygen atoms or stabilise the formation of Al-centred tetrahedral units by balancing the negative charge associated with AlO_4. For compositions with the case of $R < 1$, there are an insufficient number of Mg^{2+} ions to stabilise all the Al^{3+} in tetrahedral geometries. In this regime where there is an alumina excess, Al^{3+} ions behave in a similar way to Mg^{2+} ions, i.e, as modifiers/charge-compensating species. The X-ray diffraction results were in agreement with previous neutron diffraction work done on these samples.

Neutron diffraction with isotope substitution was used to measure the structure of diopside, $CaMgSi_2O_6$. The diffraction results show a broad asymmetric distribution of Mg-O nearest neighbors. The measured coordination number is $\bar{n}^{O}_{Mg} = 4.40(5)$ where the Mg^{2+} ions adopt a network-modifying role. The results demonstrate the power of neutron diffraction with magnesium isotope substitution to provide unambiguous site-specific information on the glass structure. In particular, it removes the uncertainty associated with the overlap between the Mg-O and Ca-O correlations in the fitted functions. A different range of compositions along the MgO-CaO-SiO_2 system is needed to further investigate the role of Mg^{2+} and Ca^{2+}. Another interesting study would be analysing the isotopic and natural $CaMgSi_2O_6$ at higher pressures in similar conditions to where the mineral diopside is found in the Earth's mantle.

The structure of crystalline and glassy $Na_{1+x}Al_xGe_{2-x}(PO_4)_3$ with $x = 0$, $x = 0.4$ or $x = 0.8$ was investigated by X-ray and neutron diffraction. ^{27}Al MAS NMR experiments helped constrain the Al-O coordination number in the pair distribution function analysis. ^{31}P MAS NMR helped interpreting the diffraction results and supported the structural model based on the formation and growth of $Na_2P_6GeO_{18}$ super-structural units. The results for the amorphous materials revealed a significant fraction of sub-octahedral Ge/Al-centred units, whereas in the crystalline materials Ge and Al are present in octahedral units. For the more disordered structures NBOs appear. The effect of NBOs in the sodium ion mobility is in need of further investigation in these disordered structures. Further work in molecular dynamic simulations may help elucidate this behaviour.

Finally the structure of glassy $Na_{1+x}Ti_2Si_xP_{3-x}O_{12}$ with $x = 0.8$ or $x = 1.0$ was investigated by X-ray and neutron diffraction. The results are consistent with network structures comprising tetrahedral PO_4 and SiO_4 units. Here the Ti atoms reside in a sub-octahedral coordination environment in a similar way to Ge. Further work to study this NASICON structure is needed, especially with a wider range of compositions to help assess the viability of substituting PO_4 by SiO_4 units. Diffraction results on

the full crystalline materials could help interpret the nucleation growth in the more disordered structures. ^{31}P MAS NMR results would be helpful to elucidate the effect of the phosphorous atoms in crystalline and glassy materials. This could help to infer if the super-structural units within a $Ti^{(4)}$ are present as in the $Na_{1+x}Al_xGe_{2-x}(PO_4)_3$ system.

Bibliography

[1] L. V. D. Gammond, R. E. Youngman, A. Zeidler, B. G. Aitken and P. S. Salmon. Structural model for amorphous aluminosilicates. *The Journal of Chemical Physics*, 156(6):064503, 2022.

[2] J. D. Musgraves, J. Hu and L. Calvez. *Springer handbook of glass.* Springer, 2019.

[3] E. Le Bourhis. *Glass: Mechanics and Technology.* WILEY-VCH, Weinheim, 2008.

[4] I. M. Awan M. Y. Nadeem and M. F. Wasiq. Optical properties of boro-germanate glass systems. *Modern Physics Letters B*, 21(15):955–963, 2007.

[5] Y. Kono C. Sanloup. *Magmas under pressure: Advances in high-pressure experiments on structure and properties of melts.* Elsevier, 2018.

[6] M. I. Ojovan and W. E. Lee. *New developments in glassy nuclear wasteforms.* Nova Publishers, 2007.

[7] J. S. McCloy and A. Goel. Glass-ceramics for nuclear-waste immobilization. *MRS Bulletin*, 42(3):233–240, 2017.

[8] J. R. Jones. Review of bioactive glass: from Hench to hybrids. *Acta biomaterialia*, 9(1):4457–4486, 2013.

[9] J. R. Jones, L. M. Ehrenfried and L. L. Hench. Optimising bioactive glass scaffolds for bone tissue engineering. *Biomaterials*, 27(7):964–973, 2006.

[10] J. R. Jones P. Sepulveda and L. L. Hench. In vitro dissolution of melt-derived 45S5 and sol-gel derived 58S bioactive glasses. *Journal of Biomedical Materials Research: An Official Journal of The Society for Biomaterials, The Japanese*

Society for Biomaterials, and The Australian Society for Biomaterials and the Korean Society for Biomaterials, 61(2):301–311, 2002.

[11] J. E. Shelby. Properties and structure of B_2O_3–GeO_2 glasses. *Journal of Applied Physics*, 45(12):5272–5277, 1974.

[12] A. K. Varshneya. *Fundamentals of inorganic glasses*. Elsevier, 2013.

[13] K. J. Rao. *Structural Chemistry of Glasses*. Elsevier Science Ltd, Oxford, First edition, 2002.

[14] M. Cable. Classical Glass Technology. In J. Zarzycki, editor, *Glasses and Amorphous Materials*, volume 9, chapter 1. Wiley-VCH, Weinheim, 1991.

[15] P. H. Gaskell. Models for the Structure of Amorphous Solids. In J. Zarzycki, editor, *Glasses and Amorphous Materials*, volume 9, chapter 4. Wiley-VCH, Weinheim, 1991.

[16] H. G. Pfaender. *Schott Guide to Glass*. Springer Science, London, second edition, 1996.

[17] M. Douay, W. X. Xie, T. Taunay, P. Bernage, P. Niay, P. Cordier, B. Poumellec, L. Dong, J. F. Bayon, H. Poignant and E. Delevaque. Densification involved in the UV-based photosensitivity of silica glasses and optical fibers. *Journal of Lightwave technology*, 15(8):1329–1342, 1997.

[18] Gorilla Glass. https://www.corning.com/gorillaglass/worldwide/en.html. (accessed: 28.07.2022).

[19] H. Scholze. New possibilities for variation of glass structure. *Journal of Non-Crystalline Solids*, 73(1-3):669–680, 1985.

[20] J. H. Campbell, J. S. Hayden and A. Marker. High-power solid-state lasers: a laser glass perspective. *International Journal of Applied Glass Science*, 2(1):3–29, 2011.

[21] P. Y. Shih. Properties and FTIR spectra of lead phosphate glasses for nuclear waste immobilization. *Materials Chemistry and Physics*, 80(1):299–304, 2003.

[22] A. S. Pinheiro, Z. M. Da Costa, M. J. V. Bell, V. Anjos, N. O. Dantas and S. T. Reis. Thermal characterization of iron phosphate glasses for nuclear waste disposal. *Optical Materials*, 33(12):1975–1979, 2011.

[23] T. Okura, T. Miyachi and H. Monma. Properties and vibrational spectra of magnesium phosphate glasses for nuclear waste immobilization. *Journal of the European Ceramic Society*, 26(4-5):831–836, 2006.

[24] I. Ahmed, A. J. Parsons, G. Palmer, J. C. Knowles, G. S. Walker and C. D. Rudd. Weight loss, ion release and initial mechanical properties of a binary calcium phosphate glass fibre/PCL composite. *Acta biomaterialia*, 4(5):1307–1314, 2008.

[25] K. Shimazu, Y. Yamamoto, Y. Saito, and O. Nakamura. Electrical conductivity and Ti^{4+} ion substitution range in NASICON system. *Solid State Ionics*, 79:106–110, 1995.

[26] D. S. Sivia. *Elementary Scattering Theory For X-ray and Neutron Users*. Oxford University Press, 2011.

[27] K. J. Pizzey. *Glasses under extreme conditions*. PhD thesis, University of Bath, Department of Physics, 2015.

[28] H. E. Fischer, A. C. Barnes and P. S. Salmon. Neutron and X-ray Diffraction Studies of Liquids and Glasses. *Reports on Progress in Physics*, 69(1):233–299, 2006.

[29] G. Placzek. The Scattering of Neutrons by Systems of Heavy Nuclei. *Physical Review*, 86(3):377–388, 1952.

[30] T. E. Faber and J. M. Ziman. A theory of the electrical properties of liquid metals. *Philosophical Magazine*, 11(153), 1965.

[31] J. E. Enderby, D. M. North and P. A. Egelstaff. The partial structure factors of liquid Cu-Sn. *Philosophical Magazine*, 14(131):961–970, 1966.

[32] E. Lorch. Neutron diffraction by germania, silica and radiation-damaged silica glasses. *Journal of Physics C: Solid State Physics*, 2(2):229, 1969.

[33] R. A. Martin, P. S. Salmon, H. E. Fischer and G. J. Cuello. Structure of dysprosium and holmium phosphate glasses by the method of isomorphic substitution in neutron diffraction. *Journal of Physics: Condensed Matter*, 15(49):8235–8252, 2003.

[34] D. I. Grimley, A. C. Wright and R. N. Sinclair. Neutron scattering from vitreous silica IV. Time-of-flight diffraction. *Journal of Non-Crystalline Solids*, 119(1):49–64, 1990.

[35] D. A. Keen. A comparison of various commonly used correlation functions for describing total scattering. *Journal of Applied Crystallography*, 34(2):172–177, 2001.

[36] H. H. Paalman and C.J. Pings. Numerical Evaluation of X-Ray Absorption Factors for Cylindrical Samples and Annular Sample Cells. *Journal of Applied Physics*, 33:2635–2639, 1962.

[37] A. K. Soper and P. A. Egelstaff. Multiple scattering and attenuation of neutrons in concentric cylinders: I. Isotropic first scattering. *Nuclear Instruments and Methods*, 178(2-3):415–425, 1980.

[38] V. F. Sears. Neutron scattering lengths and cross sections. *Neutron News*, 3(3):26–37, 1992.

[39] A. C. Hannon Private Communication. (25.05.2020).

[40] L. V. D. Gammond. *Hot Science Under Pressure*. PhD thesis, University of Bath, Department of Physics, 2021.

[41] Scipy Curve Fitting Optimization. https://docs.scipy.org/doc/scipy/reference-/generated/scipy.optimize.curve-fit.html. (accessed: 04.02.2022).

[42] M. O. Jones, A. D. Taylor and S. F. Parker. Neutron scattering studies of catalyst systems at the ISIS neutron spallation source. *Applied Petrochemical Research*, 2:97–104, 2012.

[43] ISIS Neutron and Muon Source. https://www.isis.stfc.ac.uk/Pages/How-ISIS-works.aspx. (accessed: 10.02.2022).

[44] ISIS Neutron and Muon Source. https://www.isis.stfc.ac.uk/Pages/How-ISIS-works–in-depth.aspx. (accessed: 21.04.2020).

[45] D. A. J. Whittaker. *The Structure and Dynamics of Fundamental Glasses by Neutron and X-ray Scattering Techniques.* PhD thesis, University of Bath, Department of Physics, 2012.

[46] Alex C. Hannon. Results on disordered materials from the GEneral Materials diffractometer, GEM, at ISIS. *Nuclear Instruments and Methods in Physics Research*, 1(551):88–107, 2005.

[47] GEneral Materials Diffractometer. http://www.isis2.isis.rl.ac.uk/dirsordered/gem/gem-home. (accessed: 18.07.2019).

[48] H. Schober. An introduction to the theory of nuclear neutron scattering in condensed matter. *Journal of Neutron Research*, 17(3-4):109–357, 2014.

[49] A. Polidori. *Structure of disordered materials: from geological fluids to network glasses*. PhD thesis, University of Bath, Department of Physics, 2016.

[50] H. E. Fischer, G. J. Cuello, P. Palleau, D. Feltin, A. C. Barnes, Y. S. Badyal and J. M. Simonson. D4c: A very high precision diffractometer for disordered materials. *Applied Physics A*, 74(160), 2002.

[51] D4 - Disordered Materials Diffractometer. https://www.ill.eu/users/instruments-instruments-list/d4/description/instrument-layout/. (accessed: 18.07.2019).

[52] J. W. E. Drewitt. *Structure of copper halide melts, rare earth chalcogenide glasses and glassy germania at high pressure*. PhD thesis, University of Bath, Department of Physics, 2009.

[53] The Advanced Photon Source. http://www.anl.gov. (accessed: 29.07.2019).

[54] Beamline 6-ID-D: High Energy Scattering. http://www.aps.anl.gov/Beamlines-Directory/. (accessed: 10.02.2022).

[55] L. B. Skinner, C. J. Benmore and J. B. Parise. Area detector corrections for high quality synchrotron X-ray structure factor measurements. *Nuclear Instruments and Methods in Physics Research Section A: Accelerators, Spectrometers, Detectors and Associated Equipment*, 662(1):61–70, 2012.

[56] F. A. Jenkins and E. Segre. The quadratic Zeeman effect. *Physical Review*, 55(1):52, 1939.

[57] A. Samoson, T. Tuherm, J. Past, A. Reinhold, T. Anupõld and I. Heinmaa. New horizons for magic-angle spinning NMR. *New Techniques in Solid-State NMR*, pages 15–31, 2005.

[58] G. Wu, D. Rovnyak and R. G. Griffin. Quantitative multiple-quantum magic-angle-spinning NMR spectroscopy of quadrupolar nuclei in solids. *Journal of the American Chemical Society*, 118(39):9326–9332, 1996.

[59] Magic Angle Spinning NMR. https://commons.wikimedia.org/wiki/File:Magic-AngleSpinning.svg. (accessed: 01.08.2022).

[60] J. R. Ferraro. *Introductory Raman Spectroscopy*. Elsevier, 2003.

[61] E. Smith and G. Dent. *Modern Raman spectroscopy: a practical approach*. John Wiley & Sons, 2019.

[62] N. Colthup. *Introduction to infrared and Raman spectroscopy*. Elsevier, 2012.

[63] P. R. G. D. J. Graves and D. Gardiner. Practical raman spectroscopy. *Springer*, 10:978–3, 1989.

[64] C. V. Raman and K. S. Krishnan. A new type of secondary radiation. *Nature*, 121(3048):501–502, 1928.

[65] C. J. Sayers. *Charge density wave phenomena in trigonal transition metal dichalcogenides*. PhD thesis, University of Bath, 2020.

[66] Raman Confocal Microscope RENISHAM INVIA. https://researchportal.bath.ac.uk/en/equipments/raman-confocal-microscope-renisham-invia. (accessed: 29.07.2022).

[67] A. Smrček. Compositions of industrial glasses. In *Fiberglass and Glass Technology*, pages 229–266. Springer, 2010.

[68] P. Yaowakulpattana, T. Wakasugi, S. Kondo and K. Kadono. Effect of Alkaline and Alkaline-Earth Metal Oxides Addition on the Glass Formation and Crystallization of ZnO-Al_2O_3-SiO_2 Glasses. *Engineering Journal*, 19(3):21–34, 2015.

[69] A. R. Molla, A. M. Rodrigues, S. P. Singh, R. P. Lancelotti, E. D. Zanotto, A. C. M. Rodrigues, M. R. Dousti, A. S. S. de Camargo, C. J. Magon and Igor De Anciães Almeida Silva. Crystallization, mechanical, and optical properties of transparent, nanocrystalline gahnite glass-ceramics. *Journal of the American Ceramic Society*, 100(5):1963–1975, 2017.

[70] K. H. Klaska, J. C. Eck and D. Pohl. New investigation of willemite. *Acta Crystallographica Section B: Structural Crystallography and Crystal Chemistry*, 34(11):3324–3325, 1978.

[71] M. Takesue, H. Hayashi, J. R. Smith and L. Richard. Thermal and chemical methods for producing zinc silicate (willemite): a review. *Progress in Crystal Growth and Characterization of Materials*, 55(3-4):98–124, 2009.

[72] L. Cormier and S. Zhou. Transition metals as optically active dopants in glass-ceramics. *Applied Physics Letters*, 116(26):260503, 2020.

[73] D. Ehrt and S. Flügel. Properties of Zinc Silicate Glasses and Melts. *Journal of Materials Science and Engineering A1*, 1:312–320, 2011.

[74] D. Ehrt, H. T. Vu, A. Herrmann and G. Völksch. Luminescent ZnO-Al_2O_3-SiO_2 glasses and glass ceramics. *Advanced Materials Research*, 39:231–236, 2008.

[75] D. Ehrt. The effect of ZnO, La_2O_3, PbO and Bi_2O_3 on the properties of binary borate glasses and melts. *Physics and Chemistry of Glasses-European Journal of Glass Science and Technology Part B*, 47(6):669–674, 2006.

[76] M. Peng, D. Chen, J. Qiu, X. Jiang and C. Zhu. Bismuth-doped zinc aluminosilicate glasses and glass-ceramics with ultra-broadband infrared luminescence. *Optical Materials*, 29(5):556–561, 2007.

[77] A. Goel, S. Kapoor, A. Tilocca, R. R. Rajagopalb and J. M. F. Ferreirab. Structural role of zinc in biodegradation of alkali-free bioactive glasses. *Journal of Materials Chemistry B*, 1:3073–3082, 2013.

[78] P. W. R. Osinaga, R. H. M. Grande, R. Y. Ballester, M. R. L. Simionato, C. R. M. D. Rodrigues and A. Muench. Zinc sulfate addition to glass-ionomer-based cements: influence on physical and antibacterial properties, zinc and fluoride release. *Dental Materials*, 19(3):212–217, 2003.

[79] K. R. Bright, C. P. Gerba and P. A. Rusin. Rapid reduction of Staphylococcus aureus populations on stainless steel surfaces by zeolite ceramic coatings containing silver and zinc ions. *Journal of Hospital Infection*, 52(4):307–309, 2002.

[80] G. Calas, L. Cormier, L. Galoisy and P. Jollivet. Structure–property relationships in multicomponent oxide glasses. *Comptes Rendus Chimie*, 5(12):831–843, 2002.

[81] X. Liu, M. Kanzaki and X. Xue. Crystal structures of Zn_2SiO_4 III and IV synthesized at 6.5–8 GPa and 1273 K. *Physics and Chemistry of Minerals*, 40(6):467–478, 2013.

[82] A. Novikov. *Structure and dynamics of aluminosilicate glasses and melts.* PhD thesis, Université D'Orléans, 2016.

[83] L. Jiazhi, S Ying and H. Guanging. An investigation of relationship between phase separation and crystallization of ZnO-Al2O3-SiO2 glasses. *Journal de Physique Colloques*, 43(C9):C9–231, 1982.

[84] A. P. Hammersley. Fit2d internal report esrf-98-ha01t. *ESRF, Grenoble, France*, 1998.

[85] X. Qiu, J. W. Thompson and S. J. L. Billinge. PDFgetX2: a GUI-driven program to obtain the pair distribution function from X-ray powder diffraction data. *Journal of Applied Crystallography*, 37(4):678–678, 2004.

[86] D. Massiot, F. Fayon, M. Capron, I. King, S Le Calvé, B. Alonso, J. Durand, B. Bujoli, Z. Gan and G. Hoatson. Modelling one-and two-dimensional solid-state NMR spectra. *Magnetic resonance in chemistry*, 40(1):70–76, 2002.

[87] M. Leśniak, J. Partyka, M. Gajek and M. Sitarz. FTIR and MAS NMR study of the zinc aluminosilicate ceramic glazes. *Journal of Molecular Structure*, 1171:17–24, 2018.

[88] J. S. Hartman, A. Narayanan, S. S. Rigby, D. R. Sliwinski, N. M. Halden and A. D. Bain. Heterogeneities in sol–gel-derived paramagnetics-doped forsterites and willemites—Electron microprobe analysis and stretched-exponential ^{29}Si MAS NMR spin–lattice relaxation studies. *Canadian Journal of Chemistry*, 85(1):56–65, 2007.

[89] M. A. Camblor and M. E. Davis. ^{29}Si MAS NMR spectroscopy of tectozincosilicates. *Journal of Physical Chemistry*, 98(50):13151–13156, 1994.

[90] I. Atkinson, E. M. Anghel, C. Munteanu, M. Voicescu and M. Zaharescu. ZrO_2 influence on structure and properties of some alkali lime zinc aluminosilicate glass ceramics. *Ceramics International*, 40(5):7337–7344, 2014.

[91] D. R. Neuville, L. Cormier, V. Montouillout and D. Massiot. Local Al site distribution in aluminosilicate glasses by ^{27}Al MQMAS NMR. *Journal of Non-Crystalline Solids*, 353(2):180–184, 2007.

[92] P. Florian, N. Sadiki, D. Massiot and J. P. Coutures. ^{27}Al NMR study of the structure of lanthanum-and yttrium-based aluminosilicate glasses and melts. *Journal of Physical Chemistry B*, 111(33):9747–9757, 2007.

[93] A. Jaworski, B. Stevensson, B. Pahari, K. Okhotnikov and M. Eden. Local structures and Al/Si ordering in lanthanum aluminosilicate glasses explored by advanced ^{27}Al NMR experiments and molecular dynamics simulations. *Physical Chemistry Chemical Physics*, 14(45):15866–15878, 2012.

[94] S. Iftekhar, B. Pahari, K. Okhotnikov, A. Jaworski, B. Stevensson, J. Grins and M. Eden. Properties and structures of RE_2O_3–Al_2O_3–SiO_2 (RE= Y, Lu) glasses probed by molecular dynamics simulations and solid-state NMR: the roles

of aluminum and rare-earth ions for dictating the microhardness. *Journal of Physical Chemistry C*, 116(34):18394–18406, 2012.

[95] A. Jaworski, B. Stevensson and M. Eden. The bearings from rare-earth (RE= La, Lu, Sc, Y) cations on the oxygen environments in aluminosilicate glasses: a study by solid-state ^{17}O NMR, molecular dynamics simulations, and DFT calculations. *Journal of Physical Chemistry C*, 120(24):13181–13198, 2016.

[96] J. F. Stebbins and Z. Xu. NMR evidence for excess non-bridging oxygen in an aluminosilicate glass. *Nature*, 390(6655):60–62, 1997.

[97] M. E. Smith M. J. Toplis, S. C. Kohn and I. J. F. Poplett. Fivefold-coordinated aluminum in tectosilicate glasses observed by triple quantum MAS NMR. *American Mineralogist*, 85(10):1556–1560, 2000.

[98] M. Ren, J. Y. Cheng, S. P. Jaccani, S. Kapoor, R. E. Youngman, L. Huang, J. Du and A. Goel, Ashutosh. Composition–structure–property relationships in alkali aluminosilicate glasses: A combined experimental–computational approach towards designing functional glasses. *Journal of Non-Crystalline Solids*, 505:144–153, 2019.

[99] M. M. Smedskjaer, R. E. Youngman, and J. C. Mauro. Impact of ZnO on the structure and properties of sodium aluminosilicate glasses: Comparison with alkaline earth oxides. *Journal of Non-Crystalline solids*, 381:58–64, 2013.

[100] P. S. Salmon and A. Zeidler. Ordering on different length scales in liquid and amorphous materials. *Journal of Statistical Mechanics: Theory and Experiment*, 2019(11):114006, 2019.

[101] P. S. Salmon. The structure of molten and glassy 2: 1 binary systems: An approach using the Bhatia—Thornton formalism. *Proceedings of the Royal Society of London. Series A: Mathematical and Physical Sciences*, 437(1901):591–606, 1992.

[102] C. F. Macrae, I. Sovago, S. J. Cottrell, P. T. A. Galek, P. McCabe, E. Pidcock, M. Platings, G. P. Shields, J. S. Stevens, M. Towler and P. A. Wood. Mercury 4.0: From visualization to analysis, design and prediction. *Journal of Applied Crystallography*, 53(1):226–235, 2020.

[103] D. R. Neuville, L. Cormier and D. Massiot. Al coordination and speciation in calcium aluminosilicate glasses: Effects of composition determined by ^{27}Al MQ-MAS NMR and Raman spectroscopy. *Chemical geology*, 229(1-3):173–185, 2006.

[104] T. K. Bechgaard, A. Goel, R. E. Youngman, J. C. Mauro, S. J Rzoska, M. Bockowski, L. R. Jensen and M. M. Smedskjaer. Structure and mechanical properties of compressed sodium aluminosilicate glasses: Role of non-bridging oxygens. *Journal of Non-Crystalline Solids*, 441:49–57, 2016.

[105] T. K. Bechgaard, G. Scannell, L. Huang, R. E. Youngman, J. C. Mauro and M. M. Smedskjaer. Structure of MgO/CaO sodium aluminosilicate glasses: Raman spectroscopy study. *Journal of Non-Crystalline Solids*, 470:145–151, 2017.

[106] D. R. Neuville, L. Cormier, V. Montouillout, P. Florian, F. Millot, J.-C. Rifflet and D. Massiot, Dominique. Structure of Mg-and Mg/Ca aluminosilicate glasses: ^{27}Al NMR and Raman spectroscopy investigations. *American Mineralogist*, 93(11-12):1721–1731, 2008.

[107] M. Okuno, N. Zotov, M. Schmücker and H. Schneider. Structure of SiO_2–Al_2O_3 glasses: Combined X-ray diffraction, IR and Raman studies. *Journal of Non-Crystalline Solids*, 351(12-13):1032–1038, 2005.

[108] K. M. Kaky, G. Lakshminarayana, S. O. Baki, Y. H. Taufiq-Yap, I. V. Kityk and M. A. Mahdi. Structural, thermal, and optical analysis of zinc boroaluminosilicate glasses containing different alkali and alkaline modifier ions. *Journal of Non-Crystalline Solids*, 456:55–63, 2017.

[109] V. Labet and P. Colomban. Vibrational properties of silicates: A cluster model able to reproduce the effect of "SiO_4" polymerization on Raman intensities. *Journal of Non-Crystalline Solids*, 370:10–17, 2013.

[110] M. Rokita, W. Mozgawa and M. Handke. The influence of Na^+ and Ca^{2+} ions on the SiO_2–$AlPO_4$ materials structure—IR and Raman studies. *Journal of Molecular Structure*, 596(1-3):171–178, 2001.

[111] M. Handke and W. Mozgawa. Vibrational spectroscopy of the amorphous silicates. *Vibrational Spectroscopy*, 5(1):75–84, 1993.

[112] M. Sitarz, M. Handke and W. Mozgawa. Identification of silicooxygen rings in SiO_2 based on IR spectra. *Spectrochimica Acta Part A: Molecular and Biomolecular Spectroscopy*, 56(9):1819–1823, 2000.

[113] M.Sitarz. The structure of simple silicate glasses in the light of Middle Infrared spectroscopy studies. *Journal of non-crystalline solids*, 357(6):1603–1608, 2011.

[114] W. Mozgawa, M. Sitarz and M. Rokita. Spectroscopic studies of different aluminosilicate structures. *Journal of Molecular Structure*, 511:251–257, 1999.

[115] W. Mozgawa and M. Sitarz. Vibrational spectra of aluminosilicate ring structures. *Journal of Molecular Structure*, 614(1-3):273–279, 2002.

[116] P. Colomban and O. Paulsen. Non-destructive determination of the structure and composition of glazes by Raman spectroscopy. *Journal of the American Ceramic Society*, 88(2):390–395, 2005.

[117] C. Huang and E. C. Behrman. Structure and properties of calcium aluminosilicate glasses. *Journal of Non-Crystalline Solids*, 128(3):310–321, 1991.

[118] S. A. Brawer and W. B. White. Raman spectroscopic investigation of the structure of silicate glasses (II). Soda-alkaline earth-alumina ternary and quaternary glasses. *Journal of Non-Crystalline Solids*, 23(2):261–278, 1977.

[119] S. A. Brawer and W. B. White. Raman spectroscopic investigation of the structure of silicate glasses. I. The binary alkali silicates. *Journal of Chemical Physics*, 63(6):2421–2432, 1975.

[120] P. Colomban, A. Tournie and L. Bellot-Gurlet. Raman identification of glassy silicates used in ceramics, glass and jewellery: a tentative differentiation guide. *Journal of Raman Spectroscopy: An International Journal for Original Work in all Aspects of Raman Spectroscopy, Including Higher Order Processes, and also Brillouin and Rayleigh Scattering*, 37(8):841–852, 2006.

[121] A. Yadav, S. Kumar and P. Singh. A review of the structures of oxide glasses by Raman spectroscopy. *RSC Advances*, 5(83):67583–67609, 2015.

[122] S. Petrescu, M. Constantinescu, E. M. Anghel, I. Atkinson, M. Olteanu and M. Zaharescu. Structural and physico-chemical characterization of some soda lime zinc alumino-silicate glasses. *Journal of Non-Crystalline solids*, 358(23):3280–3288, 2012.

[123] M. Rokita, M. Handke and W. Mozgawa. Spectroscopic studies of the amorphous SiO_2–$AlPO_4$ materials. *Journal of Molecular Structure*, 511:277–280, 1999.

[124] N. Santha, S. Shamsudeen, N. Karunakaran, I. Thachan and J. Naseemabeevi. Spectroscopic, dielectric and optical properties of $60ZnO$–$30B_2O_3$–$10SiO_2$ glass–Al_2O_3 composites. *International Journal of Applied Ceramic Technology*, 8(5):1042–1049, 2011.

[125] B. O. Mysen, D. Virgo and C. M. Scarfe. Relations between the anionic structure and viscosity of silicate melts—a Raman spectroscopic study. *American Mineralogist*, 65(7-8):690–710, 1980.

[126] A. B. Rosenthal and S. H. Garofalini. Structural Role of Zinc Oxide in Silica and Soda-Silica Glasses. *Journal of the American Ceramic Society*, 70(11):821–826, 1987.

[127] M. Guignard and L. Cormier. Environments of Mg and Al in MgO–Al_2O_3–SiO_2 glasses: A study coupling neutron and X-ray diffraction and Reverse Monte Carlo modeling. *Chemical Geology*, 256(3-4):111–118, 2008.

[128] M. Eden. Update on ^{27}Al NMR studies of aluminosilicate glasses. In *Annual Reports on NMR Spectroscopy*, volume 101, pages 285–410. Elsevier, 2020.

[129] S. D. Shastri V. Petkov, S. J. L. Billinge and B. Himmel. Polyhedral units and network connectivity in calcium aluminosilicate glasses from high-energy X-ray diffraction. *Physical Review Letters*, 85(16):3436, 2000.

[130] L. Cormier, D. R. Neuville and G. Calas. Structure and properties of low-silica calcium aluminosilicate glasses. *Journal of Non-Crystalline Solids*, 274(1-3):110–114, 2000.

[131] L. Hennet, J. W. E. Drewitt, D. R. Neuville, V. Cristiglio, J. Kozaily, S. Brassamin, D. Zanghi and H. E. Fischer. Neutron diffraction of calcium aluminosilicate glasses and melts. *Journal of Non-Crystalline Solids*, 451:89–93, 2016.

[132] T. R. Stechert, M. J. D. Rushton and R. W. Grimes. Predicted mechanism for enhanced durability of zinc containing silicate glasses. *Journal of the American Ceramic Society*, 96(5):1450–1455, 2013.

[133] S. C. Abrahams and J. L. Bernstein. Remeasurement of the structure of hexagonal ZnO. *Acta Crystallographica Section B: Structural Crystallography and Crystal Chemistry*, 25(7):1233–1236, 1969.

[134] N. Morimoto, Y. Nakajima, S. Syono, S. Akimoto and Y. Matsui. Crystal structure of pyroxene-type $ZnSiO_3$ and $ZnMgSi_2O_6$. *Acta Crystallographica Section B: Structural Crystallography and Crystal Chemistry*, 31(4):1041–1049, 1975.

[135] T. Tangcharoen, W. Klysubun, T. Jiraroj and C. Kongmark. Cation exchange in Ni–Cu–Zn aluminate spinels revealed by EXAFS. *Journal of Solid State Chemistry*, 292:121695, 2020.

[136] F. Marumo and Y. Syono. The crystal structure of Zn_2SiO_4-II, a high-pressure phase of willemite. *Acta Crystallographica Section B: Structural Crystallography and Crystal Chemistry*, 27(10):1868–1870, 1971.

[137] R. F. Samigullina, A. P. Tyutyunnik, I. N. Gracheva, T. I. Krasnenko, N. A. Zaitseva and T. A. Onufrieva. Hydrothermal synthesis of α-Zn_2SiO_4: V phosphor, determination of oxidation states and structural localization of vanadium ions. *Materials Research Bulletin*, 87:27–33, 2017.

[138] S. M. Seo, H. S. Kim, M. Park and W. T. Lim. Synthesis and structural refinement of fully dehydrated fully Zn^{2+}-exchanged zeolite Y (FAU), $|Zn_{35.5}|[Si_{121}Al_{71}O_{384}]$-FAU. *Journal of Porous Materials*, 18(1):47–56, 2011.

[139] K. Steff. Comment on "Synthesis of Fully Dehydrated Fully Zn^{2+}-Exchanged Zeolite Y and Its Crystal Structure Determined by Pulsed-Neutron Diffraction". Cationic Zinc Clusters Formally Containing Zn (I) in the Sodalite Cavities of Zeolite Y (FAU). *Journal of Physical Chemistry B*, 109(28):13840–13841, 2005.

[140] S. Jahn and P. A. Madden. Modeling Earth materials from crustal to lower mantle conditions: A transferable set of interaction potentials for the CMAS system. *Physics of the Earth and Planetary Interiors*, 162(1-2):129–139, 2007.

[141] C. R. Hammond. *The elements*, volume 81. CRC press Boca Raton, FL, 2000.

[142] A. K. Varshneya. Chemical strengthening of glass: lessons learned and yet to be learned. *International Journal of Applied Glass Science*, 1(2):131–142, 2010.

[143] M. Dejneka and T. J. Kiczenski. Display glass. In *Springer Handbook of Glass*, pages 1521–1553. Springer, 2019.

[144] Q. Fu, E. Saiz, M. N. Rahaman and A. P. Tomsia. Toward strong and tough glass and ceramic scaffolds for bone repair. *Advanced Functional Materials*, 23(44):5461–5476, 2013.

[145] J. H. Campbell, J. S. Hayden and A. Marker. High-power solid-state lasers: a laser glass perspective. *International Journal of Applied Glass Science*, 2(1):3–29, 2011.

[146] C. A. Scamehorn and C. A. Angell. Viscosity-temperature relations and structure in fully polymerized aluminosilicate melts from ion dynamics simulations. *Geochimica et Cosmochimica Acta*, 55(3):721–730, 1991.

[147] M. J. Toplis and D. B. Dingwell. Shear viscosities of CaO-Al_2O_3-SiO_2 and MgO-Al_2O_3-SiO_2 liquids: Implications for the structural role of aluminium and the degree of polymerisation of synthetic and natural aluminosilicate melts. *Geochimica et Cosmochimica Acta*, 68(24):5169–5188, 2004.

[148] D. B. Dingwell. Relaxation in silicate melts; some applications. *Reviews in Mineralogy and Geochemistry*, 32(1):21–66, 1995.

[149] S. Rossano. Spectroscopic study of silicate glass structure. Application to the case of iron and magnesium. *Universite Paris-Est Marne-la-Vallee*, 2008.

[150] E. Curti. Glass dissolution parameters: update for 'Entsorgungsnachweis'. *Paul Scherrer Institute PSI*, 2003.

[151] P. Wange, T Höche, C. Rüssel and J. D. Schnapp. Microstructure-property relationship in high-strength MgO–Al_2O_3–SiO_2–TiO_2 glass-ceramics. *Journal of Non-Crystalline Solids*, 298(2-3):137–145, 2002.

[152] M. Dittmer, M. Müller and C. Rüssel. Self-organized nanocrystallinity in $MgOAl_2O_3$–SiO_2 glasses with ZrO_2 as nucleating agent. *Materials Chemistry and Physics*, 124(2-3):1083–1088, 2010.

[153] T. M. Gross. Chemical strengthening of glass. In *Springer handbook of glass*, pages 273–296. Springer, 2019.

[154] T. Yamanaka and Y. Takéuchi. Order-disorder transition in $MgAl_2O_4$ spinel at high temperatures up to 1700°C. *Zeitschrift für Kristallographie-Crystalline Materials*, 165(1-4):65–78, 1983.

[155] S. Sasaki, K. Fujino and Y. Takéuchi. X-ray determination of electron-density distributions in oxides, MgO, MnO, CoO, and NiO, and atomic scattering factors of their constituent atoms. *Proceedings of the Japan Academy, Series B*, 55(2):43–48, 1979.

[156] N. Morimoto and K. Koto. The crystal structure of orthoenstatite. *Zeitschrift für Kristallografie*, 129(1-4):65–83, 1969.

[157] P. B. Moore and J. V. Smith. Crystal structure of β-Mg_2SiO_4: Crystal-chemical and geophysical implications. *Physics of the Earth and Planetary Interiors*, 3:166–177, 1970.

[158] H. Xu, P. J. Heaney, P. Yu and H. Xu. Synthesis and structure of a stuffed derivative of α-quartz, $Mg_{0.5}AlSiO_4$. *American Mineralogist*, 100(10):2191–2198, 2015.

[159] E. P. Meagher. The crystal structures of pyrope and grossularite at elevated temperatures. *American Mineralogist: Journal of Earth and Planetary Materials*, 60(3-4):218–228, 1975.

[160] S. J. Watts, R. J. Hill, M. D. O'Donnell and R. V. Law. Influence of magnesia on the structure and properties of bioactive glasses. *Journal of Non-Crystalline Solids*, 356(9-10):517–524, 2010.

[161] K. Shimoda, Y. Tobu, M. Hatakeyama, Moriaki, T. Nemoto and K. Saito. Structural investigation of Mg local environments in silicate glasses by ultra-high field ^{25}Mg 3QMAS NMR spectroscopy. *American Mineralogist*, 92(4):695–698, 2007.

[162] J. C. C. Freitas and M. E. Smith. Recent advances in solid-state ^{25}Mg NMR spectroscopy. *Annual Reports on NMR Spectroscopy*, 75:25–114, 2012.

[163] D. R. Neuville, L. Cormier, V. Montouillout, P. Florian, F. Millot, J. Rifflet and D. Massiot. Structure of Mg-and Mg/Ca aluminosilicate glasses: ^{27}Al NMR and Raman spectroscopy investigations. *American Mineralogist*, 93(11-12):1721–1731, 2008.

[164] B. O. Mysen and M. J. Toplis. Structural behavior of Al^{3+} in peralkaline, metaluminous, and peraluminous silicate melts and glasses at ambient pressure. *American Mineralogist*, 92(5-6):933–946, 2007.

[165] F. A. Seifert, B. O. Mysen and D. Virgo. Three-dimensional network structure of quenched melts (glass) in the systems SiO_2–$NaAlO_2$, SiO_2–$CaAl_2O_4$ and SiO_2–$MgAl_2O_4$. *American Mineralogist*, 67(7-8):696–717, 1982.

[166] B. O. Mysen, D. Virgo and F. A. Seifert. The structure of silicate melts: implications for chemical and physical properties of natural magma. *Reviews of Geophysics*, 20(3):353–383, 1982.

[167] C. I. Merzbacher and W. B. White. The structure of alkaline earth aluminosilicate glasses as determined by vibrational spectroscopy. *Journal of Non-Crystalline Solids*, 130(1):18–34, 1991.

[168] S. K. Lee, H. I. Kim, E. J. Kim, K. Y. Mun and S Ryu. Extent of disorder in magnesium aluminosilicate glasses: insights from ^{27}Al and ^{17}O NMR. *Journal of Physical Chemistry C*, 120(1):737–749, 2016.

[169] C. I. Merzbacher, B. L. Sherriff, J. S. Hartman and W. B. White. A high-resolution ^{29}Si and ^{27}Al NMR study of alkaline earth aluminosilicate glasses. *Journal of Non-Crystalline Solids*, 124(2-3):194–206, 1990.

[170] C. I. Merzbacher and W. B. White. The structure of alkaline earth aluminosilicate glasses as determined by vibrational spectroscopy. *Journal of Non-Crystalline Solids*, 130(1):18–34, 1991.

[171] M. Guignard, L. Cormier, V. Montouillout, N. Menguy, D. Massiot and A. C. Hannon. Environment of titanium and aluminum in a magnesium alumino-silicate glass. *Journal of Physics: Condensed Matter*, 21(37):375107, 2009.

[172] L. A. Lamberson. *Influence of Atomic Structure on Plastic Deformation in Tectosilicate Calcium-Aluminosilicate, Magnesium-Aluminosilicate and Calcium-Galliosilicate Glasses*. PhD thesis, Cornwell University, 2016.

[173] D. T. Cromer. Compton scattering factors for aspherical free atoms. *Journal of Chemical Physics*, 50(11):4857–4859, 1969.

[174] E. N. Maslen, A. G. Fox and M. A. O'Keefe. X-ray scattering. *Dordrecht: Kluwer*, 2006.

[175] G. E. Bacon and M. Blackman. *Applications of neutron diffraction in chemistry*. Reader's Digest Young Families, 1963.

[176] L. Dien, P. Mingsheng and T. Murata. Coordination and local structure of magnesium in silicate minerals and glasses; Mg K-edge XANES study. *Canadian Mineralogist*, 37(1):199–206, 1999.

[177] L. Cormier and G. J. Cuello. Mg coordination in a $MgSiO_3$ glass using neutron diffraction coupled with isotopic substitution. *Physical Review B*, 83(22):224204, 2011.

[178] M. C. Wilding, C. J. Benmore, J. A. Tangeman, and S. Sampath. Evidence of different structures in magnesium silicate liquids: coordination changes in forsterite-to enstatite-composition glasses. *Chemical Geology*, 213(1-3):281–291, 2004.

[179] P. S. Salmon, G. S. Moody, Y. Ishii, K. J. Pizzey, A. Polidori, M. Salanne, A. Zeidler, M. Buscemi, H. E. Fischer, C. L. Bull, S. Klotz, R. Weber, C. J. Benmore and S. G. MacLeod. Pressure induced structural transformations in amorphous $MgSiO_3$ and $CaSiO_3$. *Journal of Non-Crystalline Solids: X*, 3:1–14, 2019.

[180] H. Mohamadi, R. Mendes Da Silva, A. Zeidler, L. V. D. Gammond, F. Gehlhar, M. D. O. Jr, H. Eckert, R. E. Youngmann, B. G. Aitken, H. E. Fischer, H. Kohlmann, L. Cormier, C. J. Benmore and P. S. salmon. Structure of diopside, enstatite and magnesium aluminosilicate glasses: A joint approach between using neutron and X-ray diffraction and solid-state NMR. In preparation.

[181] W. H. Zachariasen. The atomic arrangement in glass. *Journal of the American Chemical Society*, 54(10):3841–3851, 1932.

[182] A. C. Wright. Neutron scattering from vitreous silica. V. The structure of vitreous silica: What have we learned from 60 years of diffraction studies? *Journal of Non-Crystalline solids*, 179:84–115, 1994.

[183] B. E. Warren and J. Biscob. Fourier analysis of x-ray patterns of soda-silica glass. *Journal of the American Ceramic Society*, 21(7):259–265, 1938.

[184] G. N. Greaves. EXAFS and the structure of glass. *Journal of Non-Crystalline Solids*, 71(1-3):203–217, 1985.

[185] K. E. Kelsey, J. R. Allwardt, and J. F. Stebbins, Jonathan F. Ca–Mg mixing in aluminosilicate glasses: an investigation using ^{17}O MAS and 3QMAS and ^{27}Al MAS NMR. *Journal of Non-Crystalline Solids*, 354(40-41):4644–4653, 2008.

[186] H. Bradtmuller, T. Uesbeck, H. Eckert, T. Murata, S. Nakane and H. Yamazaki. Structural origins of crack resistance on magnesium aluminoborosilicate glasses studied by solid-state NMR. *Journal of Physical Chemistry C*, 123(24):14941–14954, 2019.

[187] R. D. Shannon and C. T. Prewitt. Effective ionic radii in oxides and fluorides. *Acta Crystallographica Section B: Structural Crystallography and Crystal Chemistry*, 25(5):925–946, 1969.

[188] A. Zeidler, K. Wezka, R. F. Rowlands, D. A. J. Whittaker, P. S. Salmon, A. Polidori, J. W. E. Drewitt, S. Klotz, H. E. Fischer and M. C. Wilding, C. L. Bull, M. G. Tucker and M. Wilson. High-pressure transformation of SiO_2 glass from a tetrahedral to an octahedral network: A joint approach using neutron

diffraction and molecular dynamics. *Physical Review Letters*, 113(13):135501, 2014.

[189] H.Yang and S. Ghose. High temperature single crystal X-ray diffraction studies of the ortho-proto phase transition in enstatite, $Mg_2Si_2O_6$ at 1360 K. *Physics and Chemistry of Minerals*, 22(5):300–310, 1995.

[190] R. M. Thompson and R. T. Downs. Model pyroxenes II: Structural variation as a function of tetrahedral rotation. *American Mineralogist*, 89(4):614–628, 2004.

[191] R. M. Canup. Accretion of the Earth. *Philosophical Transactions of the Royal Society A: Mathematical, Physical and Engineering Sciences*, 366(1883):4061–4075, 2008.

[192] R. Christoffersen and P. R. Buseck. Mineralogy of interplanetary dust particles from the "olivine" infrared class. *Earth and Planetary Science Letters*, 78(1):53–66, 1986.

[193] A. Potysz, B. Mikoda and M. Napieraj. (Bio) dissolution of Glassy and Diopside-Bearing Metallurgical Slags: Experimental and Economic Aspects. *Minerals*, 11(3):262, 2021.

[194] I. Farnan, P. J. Grandinetti, J. H. Baltisberger, J. F. Stebbins, U. Werner, M. A. Eastman and A. Pines. Quantification of the disorder in network-modified silicate glasses. *Nature*, 358(6381):31–35, 1992.

[195] J. F. Stebbins. Temperature effects on the network structure of oxide melts and their consequences for configurational heat capacity. *Chemical Geology*, 256(3-4):80–91, 2008.

[196] P. S. Young. *Structure and Properties of Quaternary Ca-Mg Aluminosilicate glasses and melts in diopside-tschermakite join.* PhD thesis, Seoul National University, 2010.

[197] M. D. O. Jr, H. Damasceno, P. S. Salmon and H. Eckert. Analysis and Information Content of Quadrupolar NMR in Glasses: ^{25}Mg NMR in Vitreous $MgSiO_3$ and $CaMgSi_2O_6$. *Journal of Magnetic Resonance Open*, page 100067, 2022.

[198] J. Schneider, V. R. Mastelaro, H. Panepucci and E. D. Zanotto. ^{29}Si MAS–NMR studies of Q^n structural units in metasilicate glasses and their nucleating ability. *Journal of Non-Crystalline Solids*, 273(1-3):8–18, 2000.

[199] A. M. Plonka, P. Dera, P. Irmen, M. L. Rivers, L. Ehm and J. B. Parise. β-diopside, a new ultrahigh-pressure polymorph of $CaMgSi_2O_6$ with six-coordinated silicon. *Geophysical Research Letters*, 39(24), 2012.

[200] M. Cameron, S. Sueno, C. T. Prewitt and J. J. Papike. High-temperature crystal chemistry of acmite, diopside, hedenbergite jadeite, spodumene and ureyite. *American Mineralogist: Journal of Earth and Planetary Materials*, 58(7-8):594–618, 1973.

[201] J. R. Clark. Crystal-chemical characterization of clinopyroxenes based on eight new structure refinements. *Mineral.Soc.Amer.Spec.Pap.*, 2:31–50, 1969.

[202] E. Bruno, S. Carbonin and G. Molin. Crystal structures of Ca-rich clinopyroxenes on the $CaMgSi_2O_6$-$Mg_2Si_2O_6$ join. *Tschermaks Mineralogische und Petrographische Mitteilungen*, 29(4):223–240, 1982.

[203] S. Sasaki, K. Fujino, Y. Takeuchi and R. Sadanaga. On the estimation of atomic charges by the X-ray method for some oxides and silicates. *Acta Crystallographica Section A: Crystal Physics, Diffraction, Theoretical and General Crystallography*, 36(6):904–915, 1980.

[204] R. M. Thompson and R. T. Downs. The crystal structure of diopside at pressure to 10 GPa. *American Mineralogist*, 93(1):177–186, 2008.

[205] L. Cormier, L. Hennet, G. Lelong, G. J. Cuello and A. Bytchkov. Structure from glass to melt: a case study along the $MgSiO_3$-$CaSiO_3$ join using neutron and X-ray diffraction. *Comptes Rendus. Géoscience*, 354(S1):1–20, 2022.

[206] S. Sen, H. Maekawa and G. N. Papatheodorou. Short-range structure of invert glasses along the pseudo-binary join $MgSiO_3$–Mg_2SiO_4: Results from ^{29}Si and ^{25}Mg MAS NMR Spectroscopy. *Journal of Physical Chemistry B*, 113(46):15243–15248, 2009.

[207] M. C. Davis, K. J. Sanders, P. J. Grandinetti, S. J. Gaudio and S. Sen. Structural investigations of magnesium silicate glasses by ^{29}Si 2D magic-angle flipping NMR. *Journal of Non-Crystalline Solids*, 357(15):2787–2795, 2011.

[208] P. Zhang, P. J. Grandinetti and J. F. Stebbins. Anionic species determination in $CaSiO_3$ glass using two-dimensional ^{29}Si NMR. *Journal of Physical Chemistry B*, 101(20):4004–4008, 1997.

[209] D. C. Kaseman, A. Retsinas, A. G. Kalampounias, G. N. Papatheodorou and S. Sen. *Q*-speciation and network structure evolution in invert calcium silicate glasses. *Journal of Physical Chemistry B*, 119(26):8440–8445, 2015.

[210] L. Cormier, G. Calas and G. J. Cuello. Structural study of Ca-Mg and K-Mg mixing in silicate glasses by neutron diffraction. *Journal of Non-crystalline Solids*, 356(44-49):2327–2331, 2010.

[211] L. Cormier and G. J. Cuello. Structural investigation of glasses along the $MgSiO_3$–$CaSiO_3$ join: Diffraction studies. *Geochimica et Cosmochimica Acta*, 122:498–510, 2013.

[212] M. C. Eckersley, P. H. Gaskell, A. C. Barnes and P. Chieux. Structural ordering in a calcium silicate glass. *Nature*, 335(6190):525–527, 1988.

[213] N. Binsted, G. N. Greaves and C. M. B. Henderson. An EXAFS study of glassy and crystalline phases of compositions $CaAl_2Si_2O_8$ (anorthite) and $CaMgSi_2O_6$ (diopside). *Contributions to Mineralogy and Petrology*, 89(2-3):103–109, 1985.

[214] K. Gong, V. O. Özçelik, K. Yang and C. E. White. Density functional modeling and total scattering analysis of the atomic structure of a quaternary CaO–MgO–Al_2O_3–SiO_2 (CMAS) glass: Uncovering the local environment of calcium and magnesium. *Physical Review Materials*, 5(1):015603, 2021.

[215] D. R. Neuville and P. Richet. Viscosity and mixing in molten (Ca, Mg) pyroxenes and garnets. *Geochimica et Cosmochimica Acta*, 55(4):1011–1019, 1991.

[216] D. R. Neuville and C. Le Losq. Link between medium and long-range order and macroscopic properties of silicate glasses and melts. *Reviews in Mineralogy and Geochemistry*, 87(1):105–162, 2022.

[217] D. Zhao, Z. Xie, J.-M. Hu, H. Zhang, W. Zhang, S.-L. Yang and W.-D. Cheng. Structure determination, electronic and optical properties of $NaGe_2P_3O_{12}$ and $Cs_2GeP_4O_{13}$. *Journal of Molecular Structure*, 922(1-3):127–134, 2009.

[218] J. F. Ortiz-Mosquera, A. M. Nieto-Muñoz and A. C. M Rodrigues. Precursor glass stability, microstructure and ionic conductivity of glass-ceramics from the $Na_{1+x}Al_xGe_{2-x}(PO_4)_3$ NASICON series. *Journal of Non-Crystalline Solids*, 513:36–43, 2019.

[219] J. Fu. Fast Li^+ ion conducting glass-ceramics in the system Li_2O–Al_2O_3–GeO_2–P_2O_5. *Solid State Ionics*, 104(3-4):191–194, 1997.

[220] H. Eckert and A. C. M. Rodrigues. Ion-conducting glass-ceramics for energy-storage applications. *MRS Bulletin*, 42(3):206–212, 2017.

[221] A. M. Rodrigues, J. L. Narváez-Semanate, A. A. Cabral and A. C. M. Rodrigues. Determination of crystallization kinetics parameters of a $Li_{1.5}Al_{0.5}Ge_{1.5}(PO_4)_3$ (LAGP) glass by differential scanning calorimetry. *Materials Research*, 16(4):811–816, 2013.

[222] Y. Inda, T. Katoh and M. Baba. Development of all-solid lithium-ion battery using Li-ion conducting glass-ceramics. *Journal of power sources*, 174(2):741–744, 2007.

[223] G. H. Beall. Dr. S. Donald (Don) Stookey (1915–2014): Pioneering Researcher and Adventurer. *Frontiers in Materials*, 3:37, 2016.

[224] H. Bradtmüller, A. M. Nieto-Muñoz, J. F. Ortiz-Mosquera, A. C. M. Rodrigues and H. Eckert. Glass-to-crystal transition in the NASICON glass-ceramic system $Na_{1+x}Al_xM_{2-x}(PO_4)_3$ (M= Ge, Ti). *Journal of Non-Crystalline Solids*, 489:91–101, 2018.

[225] L. V. D. Gammond, H. Auer, R. Mendes Da Silva, A. Zeidler, J. F. Ortiz-Mosquera, A. M. Nieto-Muñoz, A. C. M. Rodrigues, I. d'Anciães Almeida Silva, H. Eckert, C. J. Benmore and P. S. Salmon. Structure of crystalline and amorphous materials in the NASICON system $Na_{1+x}Al_xGe_{2-x}(PO_4)_3$. *Journal of Chemical Physics*, 155(7):074501, 2021.

[226] N. E. Brese and M. O'Keeffe. Bond-valence parameters for solids. *Acta Crystallographica Section B: Structural Science*, 47(2):192–197, 1991.

[227] R. A. Martin, P. S. Salmon, D. L. Carroll, M. E. Smith and A. C. Hannon. Structure and thermal properties of yttrium alumino-phosphate glasses. *Journal of Physics: Condensed Matter*, 20(11):115204, 2008.

[228] U. Hoppe, N. P. Wyckoff, R. K. Brow, M. Von Zimmermann and A. C. Hannon. Structure of Na_2O–GeO_2–P_2O_5 glasses by X-ray and neutron diffraction. *Journal of non-crystalline solids*, 390:59–69, 2014.

[229] U. Patel, R. M. Moss, K. M. Z. Hossain, A. R. Kennedy, E. R. Barney, I. Ahmed and A. C. Hannon. Structural and physico-chemical analysis of calcium/strontium substituted, near-invert phosphate based glasses for biomedical applications. *Acta biomaterialia*, 60:109–127, 2017.

[230] D. I. Grimley, A. C. Wright and R. N. Sinclair. Neutron scattering from vitreous silica IV. Time-of-flight diffraction. *Journal of Non-Crystalline Solids*, 119(1):49–64, 1990.

[231] M. Affatigato. *Modern glass characterization*. John Wiley & Sons, 2015.

[232] J. Ren and H. Eckert. Superstructural units involving six-coordinated silicon in sodium phosphosilicate glasses detected by solid-state NMR spectroscopy. *Journal of Physical Chemistry C*, 122(48):27620–27630, 2018.

[233] S. V. Pershina, B. D. Antonov, A. S. Farlenkov and E. G. Vovkotrub. Glass-ceramics in $Li_{1+x}Al_xGe_{2-x}(PO_4)_3$ system: the effect of Al_2O_3 addition on microstructure, structure and electrical properties. *Journal of Alloys and Compounds*, 835:155281, 2020.

[234] Y. Wang, R. Chen, T. Chen, H. Lv, G. Zhu, L. Ma, C. Wang, Z. Jin and J. Liu. Emerging non-lithium ion batteries. *Energy Storage Materials*, 4:103–129, 2016.

[235] Y. Fang, J. Zhang, L. Xiao, X. Ai, Y. Cao and H. Yang. Phosphate framework electrode materials for sodium ion batteries. *Advanced Science*, 4(5):1600392, 2017.

[236] H. Kang, Y. Liu, K. Cao, Y. Zhao, L. Jiao, Y. Wang and H. Yuan. Update on anode materials for Na-ion batteries. *Journal of Materials Chemistry A*, 3(35):17899–17913, 2015.

[237] N. Tapia-Ruiz, A. R. Armstrong, H. Alptekin, M. A. Amores, H. Au, J. Barker, R. Boston, W. R. Brant, J. M. Brittain and Y. Chen. 2021 Roadmap for sodium-ion batteries. *Journal of Physics: Energy*, 3(3):031503, 2021.

[238] N. Anantharamulu, K. Koteswara Rao, G. Rambabu, B. Vijaya Kumar, V Radha and M. Vithal. A wide-ranging review on Nasicon type materials. *Journal of Materials Science*, 46(9):2821–2837, 2011.

[239] S. Chen, C. Wu, L. Shen, C. Zhu, Y. Huang, K. Xi, J. Maier and Y. Yu. Challenges and perspectives for NASICON-type electrode materials for advanced sodium-ion batteries. *Advanced Materials*, 29(48):1700431, 2017.

[240] B. Singh, Z. Wang, S. Park, G. S. Gautam, J. Chotard, L. Croguennec, D. Carlier, A. K. Cheetham, C. Masquelier and P. Canepa. A chemical map of NaSICON electrode materials for sodium-ion batteries. *Journal of Materials Chemistry A*, 9(1):281–292, 2021.

[241] H. Zhang, B. Qin, D. Buchholz and S. Passerini. High-efficiency sodium-ion battery based on NASICON electrodes with high power and long lifespan. *ACS Applied Energy Materials*, 1(11):6425–6432, 2018.

[242] A. M. Nieto-Munoz, J. F. Ortiz-Mosquera and A. C. M. Rodrigues. Novel sodium superionic conductor of the $Na_{1+y}Ti_2Si_yP_{3-y}O_{12}$ series for application as solid electrolyte. *Electrochimica Acta*, 319:922–932, 2019.

[243] Y. A. Ivanov, E. L. Belokoneva, Y. K. Egorov-Tismenko, M. A. Simonov, and N. Belov. Crystal structure of Na, Ti orthophosphate $NaTi_2[PO_4]_3$. *Soviet Physics Doklady*, 25:420, 1980.

[244] J. Liu, D. Chang, P. Whitfield, Y. Janssen, X. Yu, Y. Zhou, J. Bai, J. Ko, K. Nam, L. Wu, Y. Zhu, M. Feygenson, G. Amatucci, A. Van der Ven, X. Yang and P. Khalifah. Ionic conduction in cubic $Na_3TiP_3O_9N$, a secondary Na-ion battery cathode with extremely low volume change. *Chemistry of Materials*, 26(10):3295–3305, 2014.

[245] H. Y. P. Hong. Crystal structures and crystal chemistry in the system $Na_{1+x}Zr_2Si_xP_{3-x}O_{12}$. *Materials Research Bulletin*, 11(2):173–182, 1976.

[246] J. B. Goodenough, H. Y. P. Hong and J. A. Kafalas. Fast Na^+-ion transport in skeleton structures. *Materials Research Bulletin*, 11(2):203–220, 1976.

[247] J. Fu. Fast Li^+ Ion Conduction in Li_2O-Al_2O_3-TiO_2-SiO_2-P_2O_2 Glass-Ceramics. *Journal of the American Ceramic Society*, 80(7):1901–1903, 1997.

[248] A. Kishioka, Y. Miyazawa, K. Itatani, F. S. Howell and M. Kinoshita,. Preparation and properties of phosphate glasses and glass-ceramics containing large amounts of titanium (IV). *Journal of the Ceramic Society of Japan*, 102(1182):155–159, 1994.

[249] H. Takahashi A. Tsuji and T. Oi. Preparation of ion exchangers in the hydrogen form from $M_{1+x}Ti_2P_{3-x}Si_xO_{12}$ (M= Li, Na) crystals and glass-ceramics and their characterization. *Journal of Materials Chemistry*, 13(3):542–549, 2003.

[250] R. K. Rastsvetaeva, V. I. Simonov and N. V. Belov. Crystalline structure of lomonosovite, $Na_5Ti_2Si_2O_7PO_4O_2$. *Doklady Akademii Nauk*, 197(1):81–84, 1971.

[251] N. V. Belov, G. S. Gavrilova, L. P. Solov'eva and A. D. Halilov. The more precisely determined structure of lomonosovite. *Doklady Akademii Nauk*, 235(5):1064–1067, 1977.